

University of Alberta Library




0 1620 2672472 2

91D-055

Ex LIBRIS
UNIVERSITATIS
ALBERTAE NSIS





Digitized by the Internet Archive
in 2025 with funding from
University of Alberta Library

<https://archive.org/details/0162026724722>

UNIVERSITY OF ALBERTA

RELEASE FORM

NAME OF AUTHOR

Flávio Massayuki Kuwajima

TITLE OF THESIS

Behavior of Shotcrete in
Shallow Tunnels

DEGREE FOR WHICH THESIS

WAS PRESENTED

Doctor of Philosophy

YEAR THIS DEGREE GRANTED

Spring, 1991

Permission is hereby granted to UNIVERSITY OF ALBERTA LIBRARY to reproduce single copies of this thesis and to lend or sell such copies for private, scholarly or scientific research purposes only.

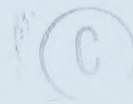
The author reserves other publication rights, and neither the thesis nor extensive extracts from it may be printed or otherwise reproduced without the author's written permission.

UNIVERSITY OF ALBERTA

BEHAVIOR OF SHOTCRETE IN SHALLOW TUNNELS

by

FLAVIO MASSAYUKI KUWAJIMA



A THESIS

SUBMITTED TO THE FACULTY OF GRADUATE STUDIES AND RESEARCH
IN PARTIAL FULFILLMENT OF THE REQUIREMENTS FOR THE DEGREE
OF DOCTOR OF PHILOSOPHY

DEPARTMENT OF CIVIL ENGINEERING

EDMONTON, ALBERTA

SPRING, 1991

THE UNIVERSITY OF ALBERTA
FACULTY OF GRADUATE STUDIES AND RESEARCH

The undersigned certify that they have read, and recommend to the Faculty of Graduate Studies and Research, for acceptance, a thesis entitled *Behavior of Shotcrete in Shallow Tunnels* submitted by Flavio Massayuki Kuwajima in partial fulfilment of the requirements for the degree of Doctor of Philosophy.

DEDICATION

To Katian and Maria Alice

Parameters of shotcrete for interpretation of lining instrumentation and for lining design are suggested. These parameters were obtained having mind the short term response of tunnelling, but studies suggested that they may be in the safe side, in terms of design for the long term.

The analytical procedure for liner calculation can take into account the rate of construction and shows that the faster the construction rates, the larger the convergences and the smaller the thrusts. This procedure also allows the calculation of internal loads developments in the lining during the tunnel construction.

Practical applications are presented for the analysis of the NATM 'Northbound Tunnel' of the South Light Rail Transit System (SLRT) in Edmonton.

ACKNOWLEDGEMENTS

I am indebted to Dr. Z. Eisenstein, not only for his support and guidance throughout this research programme but also for invaluable engineering lessons I learned during these years. I am grateful for the very special attention I received, especially towards the end of this work. I am also grateful to Dr. J.G. MacGregor, for his continued encouragement and advice on the laboratory investigations of shotcrete behavior. Appreciation is extended to the other members of my committee, for their review and constructive criticism.

Financial assistance came from a variety of sources including the Conselho Nacional de Desenvolvimento Científico e Tecnológico (CNPq - Brazil), Instituto Tecnológico de Aeronáutica (São José dos Campos, Brazil), the National Sciences and Engineering Research Council of Canada, the Department of Civil Engineering of the University of Alberta, the City of Edmonton and the Myer Horowitz Graduate Scholarship.

During the field instrumentation I worked side by side with the friendly staffs from Thurber Consultants Ltd. which would require a long list for acknowledgments; special thanks are due to Gloria Gerber, Robin Tweedie, Murray Harris and James Hogan. For field instrumentation and also laboratory tests, the cooperation by Gerry Cyre, Steve Gamble, Christine Hereygers and Jay Khajuria were fully appreciated. During this phase, important informations of the project were obtained from Dr. José Brandt. Dr. Garry Briggs kindly provided the accelerator for the shotcrete tested in laboratory.

Dr. Arsenio Negro Jr., as in many other thesis, was a major driving force in the development of this thesis. He encouraged me to pursue the subject of this thesis and it is likely that I would never have found the light at the end of tunnel without his help.

Dr. Heinrich Heinz contributed to this thesis in many occasions and I am especially thankful for his review of the manuscripts and the positive suggestions. Murray Harris and Kofi Addo also reviewed the text and contributed with clarifying discussions.

Dr. Mauro Santos, Dr. José Napoleão, Noboru Yomemitsu, Dr. João Küpper, Selmo Kuperman, Dr. Paulo Branco, Dr. André Assis and Dr. Júlio Alencar helped me in different ways.

Finally, this work could never be completed without the help of Maria Alice, who was present in each critical stage of this thesis. Above all, I could have not survived without her love and especially her patience.

TABLES OF CONTENTS

Chapter	Page
1. INTRODUCTION.....	1
1.1 Foreword	1
1.2 Aims of this thesis	3
1.3 Scope and Thesis Organization	4
2. CASE HISTORY: SOUTH LRT EXTENSION TUNNEL.....	9
2.1 Foreword	9
2.2 Description of the Project	10
2.2.1 SLRT Project	10
2.2.2 NATM Tunnels	10
2.3 Description of the Instrumentation	12
2.3.1 General.....	12
2.3.2 Ground Instrumentation.....	12
2.3.3 Lining Instrumentation	13
2.3.3.1 Foreword	13
2.3.3.2 Direct Load Measurement.....	13
2.3.3.3 Indirect Load Measurement	15
2.4 Considerations for Lining Instrumentation.....	16
2.4.1 Relative Stiffness: Compression Gages.....	16
2.4.2 Temperature Compensations	18
2.5 Preliminary Back Analysis.....	20
2.5.1 Foreword.....	20
2.5.2 Method used for the Analysis	22
2.5.3 Commented Application of the Method.....	24
2.5.4 Analysis of Results.....	30

2.6 Comments and Summary	33
3. FLAT JACK TEST	66
3.1 Introduction	66
3.2 Tests Using Conventional Procedure.....	66
3.2.1 Brief Review of Current Practice.....	67
3.2.2 Application of the LNEC Test Procedure	68
3.3 Characteristics of the Mini Flat Jack Test.....	71
3.3.1 Equipment Description.....	71
3.3.2 Test Procedure Investigations	73
3.3.2.1 Jack Calibration	73
3.3.2.2 Laboratory simulation.....	75
3.3.2.3 Test Procedure Deviations	83
3.4 In Situ Measurements	87
3.4.1 Foreword.....	87
3.4.2 Tests at SLRT South Bound Tunnel	88
3.4.3 Complementary Tests.....	92
3.5 Summary and Conclusions.....	97
4. EARLY AGE PROPERTIES OF THE SHOTCRETE	128
4.1 Introduction	128
4.2 Laboratory Tests Organization.....	133
4.3 Control and Strength Tests.....	136
4.4 Determination of Elastic Parameters	145
4.5 Short Term Creep Tests	152
4.5.1 Introduction.....	152
4.5.2 Testing Procedures	153
4.5.3 Interpretation through Rheological Models.....	154

4.6 Stress Independent Deformations	162
4.6.1 Introduction.....	162
4.6.2 Testing Procedure.....	163
4.7 Stress Controlled Tests	176
4.8 Strain Controlled Tests	186
4.9 Summary and Conclusions.....	205
5. EFFECT OF TUNNEL ADVANCING RATE ON LINING LOADING.....	279
5.1 Introduction	279
5.2 Analytical Approximation.....	279
5.2.1 Foreword.....	279
5.2.2 Tunnel Advance Simulation using 2D Model	281
5.2.3 Simulation of Tunnel Advance Rate using 2D Model	282
5.3 Limitations and Extensions of the Analytical Approximation.....	292
5.3.1 Simplifications in Yuen's (1979) Solution	292
5.3.2 Horizontal to Vertical Stress Ratio	297
5.3.3 Gravitational Stress Gradient.....	301
5.4 Applications.....	302
5.4.1 Tunneling Response for Different Rates of Construction	302
5.4.2 Adjustments for Non Linear Ground Response.....	305
5.5 Summary and Conclusions.....	306
6. PRACTICAL APPLICATIONS	325
6.1 Introduction	325
6.2 Interpretation of Strain Measurements in SLRT Lining Instrumentation.....	325
6.2.1 Constitutive Relations of Shotcrete.....	325
6.2.2 Shrinkage Compensation.....	329

6.2.3 Temperature Compensation.....	331
6.2.4 Evaluation of the Stress Dependent Strains.....	334
6.3 Load Evaluation based on SLRT Lining Instrumentation.....	339
6.3.1 Total Pressure Cells.....	339
6.3.2 Loads in Shotcrete and Steel Ribs.....	339
6.3.3 Load Share between Shotcrete and Steel Ribs	340
6.4 Analysis of Results	343
6.4.1 Predicted Values for Design Purposes	343
6.4.2 Comparison between Measured and Calculated Values.....	347
6.5 Summary and Recommendations	351
7. SUMMARY AND CONCLUSIONS.....	376
7.1 Introduction	376
7.2 Field Measurements	376
7.3 Shotcrete Behavior at the Early Ages.....	378
7.4 Analytical Procedure.....	382
7.5 Practical Applications	383
7.5.1 Interpretation of Lining Instrumentation.....	383
7.5.2 Design.....	384
7.5.3 Conclusions from SLRT Tunnel Analysis	385
BIBLIOGRAPHY	388
APPENDIX A - Data from Soil Instrumentation of the SLRT Project.....	402
APPENDIX B - Data from Lining Instrumentation of the SLRT Project.....	446
APPENDIX C - Data from Flat Jack Tests	475
APPENDIX D - Data from Creep Tests in Shotcrete at Early Age	488

List of Tables

Table	Page
2.1 Quaternary Geology of Edmonton Area (modified from May and Thomson, 1978).....	36
2.2 Classification of prediction (modified after Lambe, 1973)	37
2.3 Preliminary Simplified Estimates of Loads from Lining Instrumentation.....	37
3.1 Test Conditions for Flat Jack Calibrations	101
3.2 Calibration Factor for Flat Jack Test.....	101
3.3 Calibration Factor for Eccentric Loading, Test ELNRH	102
3.4 Summary of In Situ Tests, SLRT/NATM South Bound Tunnel	102
4.1 Measured and Calculated Convergence at Paraiso Tunnels, São Paulo (modified from Negro, 1989).....	211
4.2 Water-Cement Ratio Reported in Literature for Shotcrete.....	212
4.3 Composition of the Shotcrete Simulated in Laboratory	212
4.4 Summary of Compression Tests: Strength	213
4.5 Parameters for Strength Estimation According to Equation 4.1.....	213
4.6 Data Used for Comparison of Results in Figures 4.10 and 4.13.....	214
4.7 Summary of Test Series STA and STB	215
4.8 Geometric Restriction to Obtain Reliable Measurement, According to ASTM 2845 (relation 4.11)	216
4.9 Relations between Young's Modulus and Strength Used for Shotcrete	216
4.10 Summary of Data Used in Figure 4.18 (Modified after Byfors, 1980)	217
4.11 Parameters of Equation 4.12.....	218

Table	Page
4.12 Summary of Creep Tests Coefficients (Eq. 4.16) Obtained by Curve Fittings for Different Time Intervals ($\Delta t'$), Series CRSG	219
4.13 Summary of Curve Fittings, Series CRSG, According to Equations 4.24 and 4.25.....	220
4.14 Summary of Loading Stages and Viscoelastic Parameters Assumed in Stress Controlled Tests, Series CRMST and CRSLP	221
4.15 Assumptions Used in Strain Analysis of the Stress Controlled Tests	223
4.16 Parameters of Equation 4.26 for the Deformations Imposed during Strain Controlled Tests	224
4.17 Equations and Parameters Used to Describe Deformation for Stress Analysis of Test CRSCO1	224
4.18 Assumptions Used to Perform Stress Analysis in Strain Controlled Test, CRSCO1	225
4.19 Equations and Parameters Used to Describe Deformation for Stress Analysis of Test CRSCO2	226
4.20 Assumptions Used to Perform Stress Analysis in Strain Controlled Test, CRSCO2	227
4.21 Equations and Parameters Used to Describe Deformation for Stress Analysis of Test CRSCO3	228
4.22 Assumptions Used to Perform Stress Analysis in Strain Controlled Test, CRSCO3	229
5.1 Parameters Used in the Axisymmetric Simulations for Lined Tunnels Shown in Figure 5.5	310
5.2 Range of Values for the Parameters of Ground-Structure Interaction Problem Investigated to Evaluate the Applicability of Simplified Equation 5.11, for the present application	310
5.3 Rate of Advance of some Recent Urban Tunnels Built in São Paulo by the NATM (modified from Negro, 1989)	311

Table	Page
5.4 Values for the Parameters in Hanafy and Emery (1982) Simulation used to Evaluate the Applicability of ADVRATE for Conditions of $K_0 \neq 1$	312
5.5 Values for the Parameters used to Evaluate the Influence of Gravitational Stress Gradient on Liner Loads	312
5.6 Parameters of Lined Tunnel Simulation using ADVRATE to Investigate Convergence and Thrust Developments for Different Rates of Construction Advancing	313
5.7 Results of the Application of Design Method for NATM Tunnels (modified from Negro, 1988)	313
6.1 Instruments used for shrinkage and thermal strain compensations in SLRT lining instrumentation.....	356
A.1 Location for Settlement Points.....	403
A.2 Location of Multipoint Extensometers	404
A.3 Location of Inclinometers and Piezometers.....	404
B.1 Timetable of Tunnel Lining Instrumentation.....	447

List of Figures

Figure	Page
1.1 Construction Scheme of Tunnel Lining Loaded during Early Ages	7
1.2 Effect of Shotcrete Stiffness Development on the Magnitude of Loading in Tunnel Lining (modified from Heinz and Rocha, 1990)	8
2.1 Overview of SLRT Project (modified from Phelps and Brandt, 1988)	38
2.2 Typical Scheme for Excavation of NATM Tunnels	39
2.3 Chronologic Advance of North-Bound Tunnel Construction: Heading and Invert positions	40
2.4 Layout of NATM Tunnel Instrumentation	41
2.5 Shotcrete Body with Embedded Compression Gage.....	42
2.6 Stress Concentration Factor for different Stages of Shotcrete Curing	42
2.7 Measured Temperature from Gages Embedded in Shotcrete, Section C2I, Springline Region.....	43
2.8 Difference of Strain Measured by Embedded Vibrating Wire and Standard Compressometer, Temperature Compensation Factor	43
2.9 Measured Strains from Dummy Gages Embedded in Shotcrete Panels and Left inside the Tunnel	44
2.10 Measured Strains from Gages Embedded in Shotcrete, Section C2I, Crown Region.....	44
2.11 Measured Strains from Compression Gages Embedded in Shotcrete, Floor Region, Temperature Compensated	45
2.12 Measured Vertical Displacement Profile, Multipoint Extensometer, C2-M1	45
2.13 Suggested Sequence of Steps for Shallow Tunnel Design (modified from Negro, 1988: 1161).....	46

Figure	Page
2.14 Calculation Sheet with Geometric Ground Properties Data and Tunnel Closure at Lining Activation (modified from Negro, 1988)	47
2.15 Calculation Sheet for Estimates of the Stress Release and Ground Stiffness at the Section the Lining is Activated	48
2.16 Calculation Sheet for 2D Stability Verification and Lining-Ground Interaction Analysis (modified from Negro, 1988).....	49
2.17 Calculation Sheet for Iterative Analysis of the Lining-Ground Interaction, (modified from Negro, 1988).....	50
2.18 Calculation Sheets for Iterative Analysis of the Lining Ground Interaction and for Subsurface and Surface Settlements (modified from Negro, 1988).....	51
2.19 Geotechnical Profile and In Situ Tests at Instrumented Section Site	52
2.20 Coefficients of the U and K Relationship for the Crown of an Unlined Shallow Tunnel, ($1.5 < H/D < 3.0$) as a Function of the Distance to the Face (modified from Negro, 1988: 792)	53
2.21 Slopes of the Arbitrary Axis used to Obtain the NNRC Represented as a Function of H/D, for $K = 0.8$ (modified from Negro, 1988:1061).....	53
2.22 Relationships between α_{ref} and the Friction Angle for $K_0 = 0.8$ (modified from Negro, 1988: 1062).....	54
2.23 NNGRCs for Tunnel Crown, Calculated for $K_0 = 0.8$ (modified from Negro, 1988:1063)	54
2.24 Variations of λ' for the Tunnel Crown, Calculated for $K_0 = 0.8$ (modified from Negro, 1988:1076).....	55
2.25 Lower and Upper Bound Solutions for Tunnel Collapse Pressure in a Frictional and Cohesive Soil , $\phi = 30^\circ$, (modified from Negro, 1988: 1099)	55
2.26 Notations and Conventions used in Hartmann's Solution (modified from Negro, 1988:1124).....	56

Figure	Page
2.27 Lining Stresses, Displacements and Internal Forces Given by Hartmann's Solution (modified from Negro, 1988: 1125)	57
2.28 Normalized Subsurface Settlements for $H/D = 3$, $K_0 = 0.8$ and $\phi = 30^\circ$, Calculated for Increasing Amount of Stress Release (modified from Negro, 1988: 979).....	58
2.29 Normalized Surface Settlements for $H/D = 3$, $K_0 = 0.8$ and $\phi = 30^\circ$, Calculated for Increasing Amount of Stress Release (modified from Negro, 1988: 980).....	58
2.30 Measured and Calculated Transverse Settlement Distribution	59
2.31 Measured and Calculated Settlement at Crown Region	59
2.32 Measured Horizontal Displacement Profile, Perpendicular to Tunnel Axis, Slope Indicator, C2-I2	60
2.33 Measured and Calculated Radial Stresses at Soil-Lining Interface	61
2.34 Bending Moment and Thrust Calculated and Results from Preliminary Simplified Interpretation of Embedded Gages	61
3.1 Layout of LNEC Flat Jack Test (modified from Rocha et al., 1966).....	103
3.2 Longitudinal Cross Section of SLRT Lining, NATM Tunnels	103
3.3 Layout of Mini Flat Jack.....	104
3.4 Load Transmission Characteristics of Flat Jack.....	105
3.5 Tests of Installation of Vibrating Wire Strain Gages (VW) on Concrete Cylinders	105
3.6 Layout of Installation of Vibrating Wire Strain Gages	106
3.7 Layout of Laboratory Mini Flat Jack Test.....	107
3.8 Relative Displacements during the First Cutting, Laboratory Tests	108
3.9 Relative Displacements during Jack Pressurization Stage, Test CLNRH.....	108

Figure	Page
3.10 Illustration of Pressure Transmission Deficiency	109
3.11 Layout of Test FLDV	110
3.12 Temperature Readings taken by RTDs during Cutting, Test FLDV	111
3.13 Temperature Readings taken by Thermistors during Cutting, Test FLDV	111
3.14 Relative Displacements during the First Cutting, Test ELNRH.....	112
3.15 Relative Displacements during Jack Pressurization Stage, Test ELNRH	112
3.16 Geometrical Parameters used to describe In Situ Test Location	113
3.17 Relative Displacements during the First Cutting, In Situ Test IST2/2	114
3.18 Relative Displacements during Jack Pressurization Stage, In Situ Test IST3/1	114
3.19 Relative Displacement Readings recorded by Thermally Protected Gage VW10 and for Unprotected VW7, during Cutting, Test FLDV	115
3.20 Cross Section of Tunnels where Complementary In Situ Tests were Performed	116
3.21 Relative Displacement Readings during Thermal Equalization, Complementary In Situ Tests.....	117
3.22 Temperature Reading Variation during Thermal Equalization, Complementary In Situ Tests.....	117
3.23 Relative Displacement Readings during the First Cutting, Complementary In Situ Tests.....	118
3.24 Temperature Reading Variation during the First Cutting, Complementary In Situ Tests.....	118
3.25 Lay Out of the Cutting Plane of Test ISJK.....	119
3.26 Scheme of Curved Path of Cutting Front	119

Figure	Page
3.27 Relative Displacement Readings during Second Cutting and Slot Cleaning, Complementary In Situ Tests.....	120
3.28 Temperature Reading Variation during Second Cutting and Slot Cleaning, Complementary In Situ Tests.....	120
3.29 Relative Displacement Readings during Pressurization Stage, Complementary In Situ Tests.....	121
3.30 Temperature Reading Variation during Pressurization Stage, Complementary In Situ Tests.....	121
3.31 Stress Concentration around a Tunnel, Elastic Solution	122
3.32 Relative Displacements during Cutting, Laboratory Tests (modified from Abdunur, 1985).....	122
4.1 Grain Size Distribution of Gravel and Sands.....	230
4.2 Histogram of Unit Weight Measured in Cores Taken at SLRT Site and Specimens Cast in Laboratory	230
4.3 Strength Evaluated Using Cores Taken from Panels of Shotcrete Made at the SLRT Site.....	231
4.4 Strength Evaluated Using Cores Taken from SLRT Tunnels Lining.....	231
4.5 Strength Measured Using Specimens Cast in Laboratory	232
4.6 Basic Appearance of the Strength Gain in a Log-Log Chart (modified from Byfors, 1980).....	232
4.7 Schematic Effect of the w/c Ratio on the Relative Strength Gain (modified from Byfors, 1980)	233
4.8 Effect of the w/c Ratio on the Relative Strength Development.....	233
4.9 Influence of w/c Ratio on Parameter A_1 (Equation 4.4)	234
4.10 Comparison of Strength Development with Published Data	234
4.11 Stress-Strain Fittings and Measured Values During Compression Tests, Series STA	235

Figure	Page
4.12 Stress-Strain Fittings and Measured Values During Compression Tests, Series STB	235
4.13 Elastic Modulus Development Measured by Different Procedures	236
4.14 Poisson's Ratio Measured Using Ultrasonic Technique	236
4.15 Development of Dynamic and Static Poisson's Ratio (modified from Anson, 1966)	237
4.16 Ratio Between Conventional and Initial Tangent Modulus as Function of Strength	237
4.17 Ratio Between Initial Tangent Modulus Measured in Conventional and Ultrasonic Tests.....	238
4.18 Measured and Calculated Relations between Conventional Young's) Modulus and Strength.....	238
4.19 Basic Rheological Models: (a) Kelvin Model; (b) Maxwell Model (modified from Neville, 1970)	239
4.20 Freudenthal and Roll's Model (modified from Neville, 1970)	239
4.21 Three Elements Viscoelastic Model	240
4.22 Measured and Calculated Values of Creep Test, CRSG4H.....	240
4.23 Measured and Calculated Values of Creep Test, CRSG8H.....	241
4.24 Measured and Calculated Values of Creep Test, CRSG12H.....	241
4.25 Measured and Calculated Values of Creep Test, CRSG16H.....	242
4.26 Measured and Calculated Values of Creep Test, CRSG24H.....	242
4.27 Measured and Calculated Values of Creep Test, CRSG36H.....	243
4.28 Measured and Calculated Values of Creep Test, CRSG78H.....	243
4.29 Measured and Calculated Values of Creep Test, CRSG168H.....	244
4.30 Summary of Specific Deformation Values, Creep Tests.....	244
4.31 Summary of Viscosity Values, Creep Tests	245

Figure	Page
4.32 Strain Measured in the Lining of the Langener Tunnel and Calculated Stress (modified from Schubert, 1988)	245
4.33 Comparison of Short Term Creep Tests with Published Data.....	246
4.34 Evaluation of Thermal Coefficient of Expansion	246
4.35 Temperature Development in Specimen Cast in Laboratory.....	247
4.36 Temperature Development in Specimen Cast in Laboratory, Detail for the First Forty Hours.....	247
4.37 Age Dependency at Early Age for the Coefficient of Thermal Expansion Based on Data from Literature (modified from Byfors, 1980).....	248
4.38 Plastic Shrinkage (modified from Vironnaud, 1960).....	248
4.39 Temperature from Instruments Installed in Compensating Panels	249
4.40 Temperature from Instruments Installed Close to the Tunnel Floor.....	249
4.41 Temperature from Instruments Installed Close to the Tunnel Springline.....	250
4.42 Temperature from Instruments Installed Close to the Tunnel Crown.....	250
4.43 Deformation Development from Laboratory Specimens at Very Early Stages	251
4.44 Estimation of Strain for the Interval 4 to 7 Hours Based on Temperature Difference	251
4.45 Shrinkage Measured in Laboratory for Specimens Subjected to Different Environmental Conditions	252
4.46 Shrinkage from Instruments Installed in Compensating Panels	252
4.47 Shrinkage from Instruments Installed in Longitudinal Direction of the Tunnel, Close to the Floor	253

Figure	Page
4.48 Shrinkage from Instruments Installed in Longitudinal Direction of the Tunnel, Close to the Springline and to the Crown	253
4.49 Shrinkage from Instruments Installed in Longitudinal Direction of the Tunnel, Close to the Springline and to Crown: Long Term Oscillation.....	254
4.50 Load Path Applied in Stress Controlled Tests	254
4.51 Load Deviations in Stress Controlled Tests at Early Stages.....	255
4.52 Relative Error of Applied Load, Test CRSLP2	255
4.53 Strain Development for Load Applied According to Equation 4.19	256
4.54 Superposition of Strains of Two Load Increments	256
4.55 Measured and Calculated Strains, Test CRMST1.....	257
4.56 Difference of Measured and Calculated Strains, Test CRMST1	257
4.57 Measured and Calculated Strains, Test CRMST2.....	258
4.58 Difference of Measured and Calculated Strains, Test CRMST2	258
4.59 Measured and Calculated Strains, Test CRMST3.....	259
4.60 Difference of Measured and Calculated Strains, Test CRMST3	259
4.61 Measured and Calculated Strains, Test CRMST4.....	260
4.62 Difference of Measured and Calculated Strains, Test CRMST4	260
4.63 Measured and Calculated Strains, Test CRSLP1	261
4.64 Difference of Measured and Calculated Strains, Test CRSLP1	261
4.65 Measured and Calculated Strains, Test CRSLP2.....	262
4.66 Difference of Measured and Calculated Strains, Test CRSLP2	262
4.67 Typical Strain Development Observed in Instruments Installed in the Tunnel Lining and Applied in Strain Controlled Tests	263
4.68 Deformations Measured in Strain Controlled Tests	263

Figure	Page
4.69	Stress Measured in Strain Controlled Tests 264
4.70	Temperature of the Specimens in Strain Controlled Tests 264
4.71	Temperature of the Air During Strain Controlled Tests..... 265
4.72	Measured and Assumed Strains before 10 Hours, Test CRSCO1..... 265
4.73	Measured and Calculated Stresses before 10 Hours, Test CRSCO1..... 266
4.74	Difference of Measured and Calculated Stresses before 10 Hours, Test 266
4.75	Measured and Assumed Strains after 10 Hours, Test CRSCO1 267
4.76	Measured and Calculated Stresses after 10 Hours, Test CRSCO1..... 267
4.77	Difference of Measured and Calculated Stresses after 10 Hours, Test CRSCO1..... 268
4.78	Measured and Assumed Strains before 10 Hours, Test CRSCO2..... 268
4.79	Measured and Calculated Stresses before 10 Hours, Test CRSCO2..... 269
4.80	Difference of Measured and Calculated Stresses before 10 Hours, Test 269
4.81	Measured and Assumed Strains after 10 Hours, Test CRSCO2 270
4.82	Measured and Calculated Stresses after 10 Hours, Test CRSCO2..... 270
4.83	Difference of Measured and Calculated Stresses after 10 Hours, Test CRSCO2..... 271
4.84	Measured and Assumed Strains before 10 Hours, Test CRSCO3..... 271
4.85	Measured and Calculated Stresses before 10 Hours, Test CRSCO3..... 272

Figure	Page
4.86 Measured and Calculated Strains between 10 to 18 Hours, Test CRSCO3.....	272
4.87 Measured Stress between 10 to 18 Hours, Test CRSCO3	273
4.88 Measured and Assumed Strains after 18 Hours, Test CRSCO3	273
4.89 Measured and Calculated Stresses after 18 Hours, Test CRSCO3.....	274
4.90 Measured and Calculated Thermal Strains after 18 Hours, Test CRSCO3.....	274
4.91 Stress Development Including the Compressometer Compensation, Test CRSCO3	275
4.92 Stress Development Including the Compressometer Compensation, Test CRSCO1	275
4.93 Stress Development Including the Compressometer Compensation, Test CRSCO2.....	276
5.1 Techniques to Emulate Tunnel Advance Effect using Two Dimensional Model	314
5.2 Three-Dimensional Arching near the Face of an Advancing Tunnel (modified from Eisenstein et.al., 1984).....	315
5.3 Analysis of Tunnel Advancing using Two-Dimensional F.E.M. Simulation (modified from Ohnishi et al., 1982).....	316
5.4 Curve Fitting of Tunnel Convergence versus Distance from Tunnel Face for $K_0 = 1$	317
5.5 Comparison between axisymmetric FEM Simulation and Analytical Approximation for $K_0 = 1$	317
5.6 Strain Development as Fitted to Strain Readings in SLRT Shotcrete Lining, for Advancing Rate $A_d = 4$ m/day	318
5.7 Stress Development for Strain Controlled Deformation as Measured in Typical Instrument in SLRT Tunnel, with Advancing Rate $A_d = 4$ m/day	318

5.8	Comparison between Convergence Calculated by 3D FEM Simulation and Analytical Approximation for Points at Crown and Floor, Unlined Tunnel.....	319
5.9	Comparison between Convergence Calculated by 3D FEM Simulation and Analytical Approximation for Points at Springline, Unlined Tunnel.....	319
5.10	Comparison between Convergence Calculated by 3D FEM Simulation and Analytical Approximation for Points at Crown and Floor, Lined Tunnel	320
5.11	Comparison between Convergence Calculated by 3D FEM Simulation and Analytical Approximation for Points at Springline, Lined Tunnel	320
5.12	Comparison between Thrust Calculated by Analytical Approximation and Einstein and Schwartz (1979) Method for Points at Crown and Floor, Lined Tunnel	321
5.13	Comparison between Thrust Calculated by Analytical Approximation and Einstein and Schwartz (1979) for Points at Springline, Lined Tunnel	321
5.14	Effect of the Gravitational Stress Gradient on Thrust Calculated in Lining, for Tunnels at Different Depths.....	322
5.15	Effect of the Gravitational Stress Gradient on Bending Moment Calculated in Lining, for Tunnels at Different Depths.....	322
5.16	Development of Lined Tunnel Convergence with Tunnel Face Advancing, according to Results from ADVRATE Simulations.....	323
5.17	Development of Thrust in Lining with Tunnel Face Advancing, according to Results from ADVRATE Simulations.....	323
5.18	Development of Lined Tunnel Convergence with Time, according to Results from ADVRATE Simulations	324
5.19	Development of Thrust in Lining with Time, according to Results from ADVRATE Simulations	324
6.1	Elastic Modulus Development as a Function of Age	357

6.2	Shrink Fit of Composite Tube Assemblage	357
6.3	Simplified Evaluation of Thermal Stresses using Equation 6.10 for the SLRT Tunnel Geometry	358
6.4	Construction Progress of the SLRT Northbound Tunnel close to the Lining Instrumentation.....	358
6.5	Compensated Measurements from Vibrating Wire Strain Gages Embedded in Crown Region, Section C2I.....	359
6.6	Compensated Measurements from Vibrating Wire Strain Gages Embedded in Springline Region, Section C2I	359
6.7	Compensated Measurements from Vibrating Wire Strain Gages Embedded in Crown Region, Section C2II	360
6.8	Compensated Measurements from Vibrating Wire Strain Gages Embedded in Floor Region, Section C2II	360
6.9	Strain Measured in Steel Rib in the Crown Region, Section C2I	361
6.10	Strain Measured in Steel Rib in Springline and Floor Regions, Section C2I.....	361
6.11	Strain Measured in Steel Rib in Springline and Floor Regions, Section C2II	362
6.12	Strain Measured in Steel Rib in Springline and Floor Regions, Section C2III	362
6.13	Compensated Measurements from Total Pressure Cell Installed at Soil-Lining Interface.....	363
6.14	Distribution of Lining Thickness Measured in NATM Tunnels at SLRT Extension	363
6.15	Calculated and Measured Thrusts in SLRT Tunnel Lining, for Points close to Crown	364
6.16	Calculated and Measured Bending Moments in SLRT Tunnel Lining, for Points close to Crown	364

Figure	Page
6.17	Calculated and Measured Thrusts in SLRT Tunnel Lining, for Points close to Springline 365
6.18	Calculated and Measured Bending Moments in SLRT Tunnel Lining, for Points close to Springline..... 365
6.19	Calculated and Measured Thrusts in SLRT Tunnel Lining, for Points close to Floor 366
6.20	Calculated and Measured Bending Moments in SLRT Tunnel Lining, for Points close to Floor 366
6.21	Calculation Sheet with Geometric Ground Properties Data and Tunnel Closure at Lining Activation..... 367
6.22	Calculation Sheet for Estimations of the Stress Release and Ground Stiffness at the Section the Lining is Activated 368
6.23	Calculation Sheet for 2D Stability Verification and Lining-Ground Interaction Analysis 369
6.24	Calculation Sheet for Iterative Analysis of the Lining-Ground Interaction 370
6.25	Calculation Sheets for Iterative Analysis of the Lining Ground Interaction and for Subsurface and Surface Settlements 371
6.26	Measured and Calculated Transverse Settlement Distributions..... 372
6.27	Measured and Calculated Settlements at Crown Region..... 372
6.28	Comparison between Calculated and Measured Values of Thrust in SLRT Shotcrete Lining, using different Techniques 373
6.29	Comparison between Calculated and Measured Values of Bending Moment in SLRT Shotcrete Lining, using different Techniques 373
6.30	Comparison between Calculated and Measured Radial Pressures of Ground on SLRT Shotcrete Lining 374
6.31	Bending Moments and Thrusts Measured in a Section of Subway in Vienna (modified from Golser et al, 1989) 374

Figure	Page
6.32	Distribution of Strength of Shotcrete Measured in Cores Taken from Panel and Tunnel Lining, South SLRT NATM Tunnel 375
6.33	Surface Settlements Caused by the Construction of North Bound and South Bound NATM Tunnels 375
A.1	Installation Details for Shallow Settlement Point 405
A.2	Installation Details for Deep Settlement Point and Bench Mark 406
A.3	Installation Details for Multipoint Extensometer 407
A.4	Anchor Assembly Detail of Multipoint Extensometer U. of A. Type 408
A.5	Installation Details of Anchor Assembly for Multipoint Extensometer 409
A.6	Inclinometer Installation Details 410
A.7	Installation Procedure for Standpipe Piezometer H85-1 (modified from Hardy, 1985) 411
A.8	Transverse Settlement Distribution. Early Warning Section (C1) Shallow Settlement Points 412
A.9	Measured Vertical Displacements with Tunnel Heading Advancing, C1-S1 412
A.10	Measured Vertical Displacements with Tunnel Heading Advancing, C1-S2 413
A.11	Measured Vertical Displacements with Tunnel Heading Advancing, C1-S3 413
A.12	Measured Vertical Displacements with Tunnel Heading Advancing, C1-S4 414
A.13	Measured Vertical Displacements with Tunnel Heading Advancing, C1-S5 414
A.14	Measured Vertical Displacements with Tunnel Heading Advancing, C1-S6 415

Figure	Page
A.15 Measured Vertical Displacements with Tunnel Heading Advancing, C1-S7	415
A.16 Transverse Settlement Distribution, Main Section C2-1, Shallow Settlement Points	416
A.17 Transverse Settlement Distribution, Main Section C2-2, Shallow Settlement Points	416
A.18 Transverse Settlement Distribution, Main Section C2-3, Shallow Settlement Points	417
A.19 Transverse Settlement Distribution, Main Section C2-4, Shallow Settlement Points	417
A.20 Measured Vertical Displacements with Tunnel Heading Advancing, C2-S1	418
A.21 Measured Vertical Displacements with Tunnel Heading Advancing, C2-S2	418
A.22 Measured Vertical Displacements with Tunnel Heading Advancing, C2-S3	419
A.23 Measured Vertical Displacements with Tunnel Heading Advancing, C2-S4	419
A.24 Measured Vertical Displacements with Tunnel Heading Advancing, C2-S5	420
A.25 Measured Vertical Displacements with Tunnel Heading Advancing, C2-S6	420
A.26 Measured Vertical Displacements with Tunnel Heading Advancing, C2-S7	421
A.27 Measured Vertical Displacements with Tunnel Heading Advancing, C2-S8	421
A.28 Measured Vertical Displacements with Tunnel Heading Advancing, C2-S9	422
A.29 Measured Vertical Displacements with Tunnel Heading Advancing, C2-S10	422

Figure	Page
A.30 Measured Vertical Displacements with Tunnel Heading Advancing, C2-S11	423
A.31 Measured Vertical Displacements with Tunnel Heading Advancing, C2-S12	423
A.32 Measured Vertical Displacements with Tunnel Heading Advancing, C2-S13	424
A.33 Measured Vertical Displacements with Tunnel Heading Advancing, C2-S14	424
A.34 Measured Vertical Displacements with Tunnel Heading Advancing, C2-S15	425
A.35 Measured Vertical Displacements with Tunnel Heading Advancing, C2-S16	425
A.36 Measured Vertical Displacements with Tunnel Heading Advancing, C2-S17	426
A.37 Measured Vertical Displacements with Tunnel Heading Advancing, C2-S18	426
A.38 Measured Vertical Displacements with Tunnel Heading Advancing, C2-S19	427
A.39 Measured Vertical Displacements with Tunnel Heading Advancing, C2-S20	427
A.40 Measured Vertical Displacements with Tunnel Heading Advancing, C2-S21	428
A.41 Measured Vertical Displacements with Tunnel Heading Advancing, C2-S22	428
A.42 Measured Vertical Displacements with Tunnel Heading Advancing, C1-DSP1 (Deep Settlement Point)	429
A.43 Measured Vertical Displacements with Tunnel Heading Advancing, C2-DSP6 (Deep Settlement Point)	429
A.44 Measured Vertical Displacements with Tunnel Heading Advancing, C2-DSP7 (Deep Settlement Point)	430

Figure	Page
A.45 Measured Vertical Displacements with Tunnel Heading Advancing, C2-DSP8 (Deep Settlement Point)	430
A.46 Measured Vertical Displacement Profile, Multipoint Extensometer C1-M1	431
A.47 Measured Vertical Displacement Profile, Multipoint Extensometer C1-M2	431
A.48 Measured Vertical Displacement Profile, Multipoint Extensometer C2-M1	432
A.49 Measured Vertical Displacement Profile, Multipoint Extensometer C2-M2	432
A.50 Measured Vertical Displacement Profile, Multipoint Extensometer C2-M3	433
A.51 Measured Vertical Displacement Profile, Multipoint Extensometer C2-M4	433
A.52 Measured Vertical Displacement Profile, Multipoint Extensometer C2-M5	434
A.53 Measured Vertical Displacement Profile, Multipoint Extensometer C2-M6	434
A.54 Measured Vertical Displacement Profile, Multipoint Extensometer C2-M7	435
A.55 Measured Horizontal Displacement Profile, Perpendicular to Tunnel Axis, Slope Indicator C1-I1	436
A.56 Measured Horizontal Displacement Profile, Parallel to Tunnel Axis, Slope Indicator C1-I1	437
A.57 Measured Horizontal Displacement Profile, Perpendicular to Tunnel Axis, Slope Indicator C2-I1	438
A.58 Measured Horizontal Displacement Profile, Parallel to Tunnel Axis, Slope Indicator C2-I1	439
A.59 Measured Horizontal Displacement Profile, Perpendicular to Tunnel Axis, Slope Indicator C2-I2	440

A.60	Measured Horizontal Displacement Profile, Parallel to Tunnel Axis, Slope Indicator C2-I2	441
A.61	Measured Horizontal Displacement Profile, Perpendicular to Tunnel Axis, Slope Indicator C2-I3	442
A.62	Measured Horizontal Displacement Profile, Parallel to Tunnel Axis, Slope Indicator C2-I3	443
A.63	Measured Horizontal Displacement Profile, Perpendicular to Tunnel Axis, Slope Indicator C2-I4	444
A.64	Measured Horizontal Displacement Profile, Parallel to Tunnel Axis, Slope Indicator C2-I4	445
B.1	Layout of Vibrating Wire Strain Gages (VW) Installed in Tunnel Lining.....	448
B.2	Layout of Total Pressure Cells (TPC) Installed in Tunnel Lining.....	449
B.3	Layout of Compression Gages (CG) Installed in Tunnel Lining.....	450
B.4	Layout of Resistance Strain Gages (RS) Bonded on Steel Ribs	451
B.5	Measured Strains from Gages Embedded in Shotcrete, Section C1I, Crown Region, Large Overcut	452
B.6	Measured Temperatures from Gages Embedded in Shotcrete, Section C1I, Crown Region, Large Overcut.....	452
B.7	Measured Strains from Gages Embedded in Shotcrete, Section C1I, Floor Region.....	453
B.8	Measured Temperatures from Gages Embedded in Shotcrete, Section C1I, Floor Region	453
B.9	Measured Strains from Gages Embedded in Shotcrete, Section C2I, Crown Region.....	454
B.10	Measured Temperatures from Gages Embedded in Shotcrete, Section C2I, Crown Region	454

Figure	Page
B.11 Measured Strains from Gages Embedded in Shotcrete, Section C2I, Crown Region.....	455
B.12 Measured Temperatures from Gages Embedded in Shotcrete, Section C2I, Crown Region	455
B.13 Measured Strains from Gages Embedded in Shotcrete, Section C2I, Springline Region	456
B.14 Measured Temperatures from Gages Embedded in Shotcrete, Section C2I, Springline Region.....	456
B.15 Measured Strains from Gages Embedded in Shotcrete, Section C2I, Springline Region	457
B.16 Measured Temperatures from Gages Embedded in Shotcrete, Section C2I, Springline Region.....	457
B.17 Measured Strains from Gages Embedded in Shotcrete, Section C2I, Floor Region.....	458
B.18 Measured Temperatures from Gages Embedded in Shotcrete, Section C2I, Floor Region	458
B.19 Measured Strains from Gages Embedded in Shotcrete, Section C2II, Crown Region	459
B.20 Measured Temperatures from Gages Embedded in Shotcrete, Section C2II, Crown Region.....	459
B.21 Measured Strains from Gages Embedded in Shotcrete, Section C2II, Crown Region	460
B.22 Measured Temperatures from Gages Embedded in Shotcrete, Section C2II, Crown Region.....	460
B.23 Measured Strains from Gages Embedded in Shotcrete, Section C2II, Crown Region, Block Fall	461
B.24 Measured Temperatures from Gages Embedded in Shotcrete, Section C2II, Crown Region, Block Fall.....	461
B.25 Measured Strains from Gages Embedded in Shotcrete, Section C2II, Springline Region.....	462

Figure	Page
B.26 Measured Temperatures from Gages Embedded in Shotcrete, Section C2II, Springline Region	462
B.27 Measured Strains from Gages Embedded in Shotcrete, Section C2II, Floor Region	463
B.28 Measured Temperatures from Gages Embedded in Shotcrete, Section C2II, Floor Region.....	463
B.29 Measured Strains from Gages Embedded in Shotcrete, Section C2II, Floor Region	464
B.30 Measured Temperatures from Gages Embedded in Shotcrete, Section C2II, Floor Region.....	464
B.31 Measured Strains from Gages Embedded in Shotcrete, Section C2III, Crown Region	465
B.32 Measured Temperatures from Gages Embedded in Shotcrete, Section C2III, Crown Region.....	465
B.33 Measured Strains from Gages Embedded in Shotcrete, Section C2III, Crown Region	466
B.34 Measured Temperatures from Gages Embedded in Shotcrete, Section C2III, Crown Region.....	466
B.35 Measured Strains from Gages Embedded in Shotcrete, Section C2III, Springline Region	467
B.36 Measured Temperatures from Gages Embedded in Shotcrete, Section C2III, Springline Region.....	467
B.37 Measured Strains from Gages Embedded in Shotcrete, Section C2III, Floor Region	468
B.38 Measured Temperatures from Gages Embedded in Shotcrete, Section C2III, Floor Region.....	468
B.39 Measured Strains from Dummy Gages Embedded in Shotcrete Panels and left inside the Tunnel.....	469
B.40 Measured Temperatures from Dummy Gages Embedded in Shotcrete Panels and left inside the Tunnel.....	469

Figure	Page
B.41 Measured Pressures by Total Pressure Cells Installed at Interface Soil-Shotcrete, Temperature Compensated.....	470
B.42 Measured Temperatures in Total Pressure Cells Installed at Interface Soil-Shotcrete	470
B.43 Measured Strains from Compression Gages Embedded in Shotcrete, Crown Region, Temperature Compensated	471
B.44 Measured Strains from Compression Gages Embedded in Shotcrete, Floor Region, Temperature Compensated	471
B.45 Measured Strains from Resistance Gages Bonded in Steel Ribs, Section C2I, Heading, Temperature Compensated	472
B.46 Measured Strains from Resistance Gages Bonded in Steel Ribs, Section C2I, Invert, Temperature Compensated	472
B.47 Measured Strains from Resistance Gages Bonded in Steel Ribs, Section C2II, Invert, Temperature Compensated.....	473
B.48 Measured Strains from Resistance Gages Bonded in Steel Ribs, Section C2III, Heading, Temperature Compensated.....	473
B.49 Measured Strains from Resistance Gages Bonded in Steel Ribs, Section C2III, Invert, Temperature Compensated	474
C.1 Flat Jack Test CLMR1, Pressurization Stage.....	476
C.2 Flat Jack Test CLMR2, Pressurization Stage.....	477
C.3 Flat Jack Test CLNRH, Pressurization Stage	478
C.4 Relative Displacements during the First Cutting, In Situ Test IST1/1	479
C.5 Relative Displacements during Jack Pressurization Stage, In Situ Test IST1/1	479
C.6 Relative Displacements during the First Cutting, In Situ Test IST1/2	480
C.7 Relative Displacements during Jack Pressurization Stage, In Situ Test IST1/2	480

Figure	Page
C.8	Relative Displacements during the First Cutting, In Situ Test IST1/3 481
C.9	Relative Displacements during Jack Pressurization Stage, In Situ Test IST1/3 481
C.10	Relative Displacements during the First Cutting, In Situ Test IST2/1 482
C.11	Relative Displacements during Jack Pressurization Stage, In Situ Test IST2/1 482
C.12	Relative Displacements during the First Cutting, In Situ Test IST2/2 483
C.13	Relative Displacements during Jack Pressurization Stage, In Situ Test IST2/2 483
C.14	Relative Displacements during the First Cutting, In Situ Test IST2/3 484
C.15	Relative Displacements during the First Cutting, In Situ Test IST3/1 485
C.16	Relative Displacements during Jack Pressurization Stage, In Situ Test IST3/1 485
C.17	Relative Displacements during the First Cutting, In Situ Test IST3/2 486
C.18	Relative Displacements during Jack Pressurization Stage, In Situ Test IST3/2 486
C.19	Relative Displacements during the First Cutting, In Situ Test IST3/3 487
C.20	Relative Displacements during Jack Pressurization Stage, In Situ Test IST3/3 487
D.1	Measured and Calculated Strains, Test CRSG4H..... 489
D.2	Measured and Assumed Stresses, CRSG4H 489
D.3	Measured and Calculated Strains, Test CRSG8H..... 490

Figure	Page
D.4 Measured and Assumed Stresses, CRSG8H	490
D.5 Measured and Calculated Strains, Test CRSG12H	491
D.6 Measured and Assumed Stresses, CRSG12H	491
D.7 Measured and Calculated Strains, Test CRSG16H	492
D.8 Measured and Assumed Stresses, CRSG16H	492
D.9 Measured and Calculated Strains, Test CRSG24H	493
D.10 Measured and Assumed Stresses, CRSG24H	493
D.11 Measured and Calculated Strains, Test CRSG36H	494
D.12 Measured and Assumed Stresses, CRSG36H	494
D.13 Measured and Calculated Strains, Test CRSG78H	495
D.14 Measured and Assumed Stresses, CRSG78H	495
D.15 Measured and Calculated Strains, Test CRSG168H	496
D.16 Measured and Assumed Stresses, CRSG168H	496

List of Plates

Plate		Page
2.1	Excavator used at SLRT Project for Construction of NATM Tunnels.....	62
2.2	Loader used at SLRT Project for Construction of NATM Tunnels.....	62
2.3	Detail of Total Pressure Cell Fixation to Ground, before Application of Shotcrete	63
2.4	View of Compression Gages Fixed to Steel Cages	63
2.5	View of Compression Gages Fixed to Steel Mesh.....	64
2.6	View of Resistance Strain Gages Bonded to Steel Ribs.....	64
2.7	Installation of Vibrating Wire Strain Gages	65
3.1	Stress Application System used in Mini Flat Jack Tests Performed in Laboratory.....	123
3.2	Insertion of Mini Flat Jack into Slot during Laboratory Tests	123
3.3	In Situ Trial Test using LNEC's Procedure	124
3.4	Detail of Shotcrete Surface Irregularities	124
3.5	Installation of Gage Points using Holding Frame	125
3.6	Installation of Vibrating Wire Strain Gages for Mini Flat Jack Test	125
3.7	Cutting Saw Assembled at Tunnel Crown and in Position for Cutting the Shotcrete	126
3.8	Installation of Vibrating Wire Strain Gages model VSM-4000	126
3.9	Installation of Thermal Protection on Strain Gages in Mini Flat Jack Test.....	127
3.10	Detail of Sealing Application in Thermal Protection to the Strain Gages	127

Plate		Page
4.1	View of Hydraulic System and Twin Shotcrete Specimens used during Creep and Stress Controlled Tests.....	277
4.2	Shotcrete Specimen Assembled for Creep and Stress Controlled Test.....	277
4.3	View of Equipments used for Strain Controlled Tests.....	278
4.4	Shotcrete Specimen Assembled for Strain Controlled Test	278

1. INTRODUCTION

1.1 Foreword

The technology of tunnel construction in soft ground has undergone substantial development in recent years. Among the construction methods in practice, the New Austrian Tunneling Method (NATM) has proved to be one of the most economically competitive, particularly for shallow tunnels or tunnels of non circular cross section. In spite of the discussions concerned with the designation 'NATM' (e.g., Muller, 1978; Golser, 1979; Brown, 1981), the method is unique because of its flexibility during construction. By allowing modifications on the basis of locally available equipment and construction practice or by adjusting the construction procedure due to variability of the ground condition, the method is highly versatile. Although this technique has been extensively applied to tunnelling in soil, very little is known about the load transfer processes between the ground and the shotcrete lining during construction. The understanding of the ground-shotcrete interaction is of great importance since this type of lining is not only used in this method as a temporary lining but also as a permanent lining (e.g., Selmer-Olsen, 1976; Cruz et al., 1982; Simondi et al., 1982; Onuma et al., 1985).

Another method of tunnel support which has lately received increasing attention uses extruded concrete linings (e.g., Babendererde, 1986; Okada et al., 1989). This construction procedure uses a special tunnel boring machine (TBM), which creates a closed and pressurized space between tubbing shuttering and the ground (Figure 1.1). Fresh concrete, constituting the future lining, is pumped or compressed into this space. By regulating the level of pressure, it is possible to control surface settlements above the tunnel. This technique is particularly useful in the case of very restrictive settlement requirements, usually dictated by buildings or other structures close to the tunnel alignment.

The shotcrete in the NATM and the extruded lining have one feature in common: the lining is loaded at an early age of the concrete hardening process, as illustrated in Figure 1.1. In order to assess the soil-lining load transfer mechanism, it is essential to know the behavior of the shotcrete (or pumped concrete) in this period. However, the literature review has shown that very little is known about the behavior of shotcrete during the early ages, indicating a necessity for further investigation. Figure 1.2 (Heinz and Rocha, 1990) showed that the structural model used for design would have a significant influence on the loading expected in the lining. In their example, the authors presented calculations for two values of lining thickness, based on numerical simulations performed by Erdmann (1983). It could be inferred that a simple plane strain model predicts heavier loads on the lining than the three dimensional model despite the use of the same shotcrete elastic modulus in both simulations ($E_c = 15 \text{ GPa}$). It is of interest to note that in the plane strain model, the excavation and installation of the lining occur simultaneously, while in the more realistic three dimensional simulation, the ground near the tunnel face is allowed to deform prior to lining installation, with a corresponding stress release. For the hypothesis considering the elastic modulus development during the early ages (Erdmann, 1983: 188), an even lower value could be found. If, besides the elastic modulus development considered above, one also considers creep deformations, then the loads expected should be even lighter. If these hypotheses could be confirmed, substantial saving in the cost of the lining production could be achieved. In addition, more realistic rheological properties of the lining would yield a more accurate safety evaluation. So, the designer could make a better assessment of the usual compromise between economy and risk involved in tunnelling.

In order to account for these lining characteristics in a numerical model, a highly complex simulation would be necessary. Ideally, the simulation should consider the following:

1. three dimensional nature of the problem

2. non-linearity of the ground
3. development of the deformation properties of the lining
4. lining creep deformations (also function of age)
5. lining temperature variation
6. lining shrinkage deformations
7. lining plastic shrinkage and/or autogenous volumetric changes

The model should also simulate different rates of tunnel construction, since the lining stiffness and the level of loading in the lining are functions of the shotcrete age and proximity of the tunnel face respectively.

Although the numerical methods currently available (e.g., Finite Element Method-FEM; Boundary Element Method-BEM) do permit the use of very complex constitutive laws for the material to be simulated, they are not commonly used in tunnelling practice. Besides the usual shortage of time and budget faced by common projects, the reason to avoid numerical modelling may be explained on the basis of results from a recent survey carried out among practitioners around the world (Negro, 1988: 570), which suggested that simplicity with reliability is the most important requirement in a calculation procedure to be used in day to day tunnelling practice.

It therefore seems that if one intends to include a short term behavior of the shotcrete in a design method and make it useful for practitioners, the use of a complex numerical simulation should be avoided. Simplicity should be pursued and the actual behavior of the shotcrete (or concrete) at early ages should be assessed. Once the solution or design recommendations are obtained, they should be checked against case histories or prototype tests.

1.2 Aims of this thesis

The aims of the present work are to:

1. identify the mechanisms involved in the load transfer process in a shotcrete lining loaded during the early ages in shallow tunnels excavated in soft ground,
2. improve the state of knowledge of the level of loading in the lining and provide recommendations for design of soft ground shallow tunnels under conditions stated above,
3. provide a measuring method which estimates loads in the linings under the above conditions, to be applied in the observational method (Peck, 1969).

Although all the tests and analyses were done with the NATM tunnel construction technique in mind, it is believed that some of the findings in the present investigation can be extended to cases of extruded concrete linings. The extruded concrete lining was not investigated because of the very limited information available in literature.

Simple solutions are pursued, aiming at facilitating the absorption of the results by practitioners. Due to the complex rheological characteristics of the shotcrete and the three dimensional nature of the load transfer mechanism of the ground-lining interaction, it was necessary to introduce semi-empirical factors in some of the solutions to preserve simplicity.

1.3 Scope and Thesis Organization

It is recognized that besides the rheological behavior of shotcrete, there are several other variables involved in the design of a NATM tunnel in soft ground. A recent design method developed by Negro (1988) takes into account most of the relevant variables, such as the non-linearity of the soil and the stress release prior to lining activation. This method has been verified against several case histories, yielding good estimates of ground displacements and lining loads.

For the case of NATM tunnels, however, the method requires the input of a single shotcrete elastic modulus. Negro (op. cit.: 591) recognizes the necessity of adopting a reduced shotcrete modulus, since 'most of the interaction processes between the soil and

lining takes place while the shotcrete is young'. However, the selection of this shotcrete modulus was not carried out in detail and the value $E_c = 10 \text{ GPa}$ implicitly suggested in the original method, may be regarded as somewhat arbitrary. Accordingly, the need was felt for further investigation, and a variant of Negro's method is proposed.

Since design procedures such as the one mentioned above are conveniently applied in association with the 'observational method' (Peck, 1969), it was also appropriate to monitor load development in the shotcrete lining. An economical and fast procedure to measure the average stress in the lining, termed the 'mini flat jack', was developed and is subsequently presented in this thesis.

Chapter 2 presents the instrumentation used to monitor the construction of the NATM tunnel of the South Extension of the Light Rail Transit (SLRT) project in Edmonton. This case history is used as the major source of reference in the investigation of the soil-lining interaction presented herein. The monitoring program included instruments to define displacement field in the ground as well as the strains and loads in the lining. The interpretation of these instruments revealed the difficulty to obtain the loads in the shotcrete lining and the necessity to understand the behavior of the shotcrete at the early ages. A preliminary analysis of the instrumentation is presented and Negro's (op. cit.) method is introduced by presenting a commented calculation.

Chapter 3 presents modifications and improvements introduced to the 'flat jack test' procedure, as proposed by Rocha et al. (1966). The original procedure was developed for measurement of in situ stress in rock masses. The modified procedure was developed to obtain the average stresses in shotcrete linings.

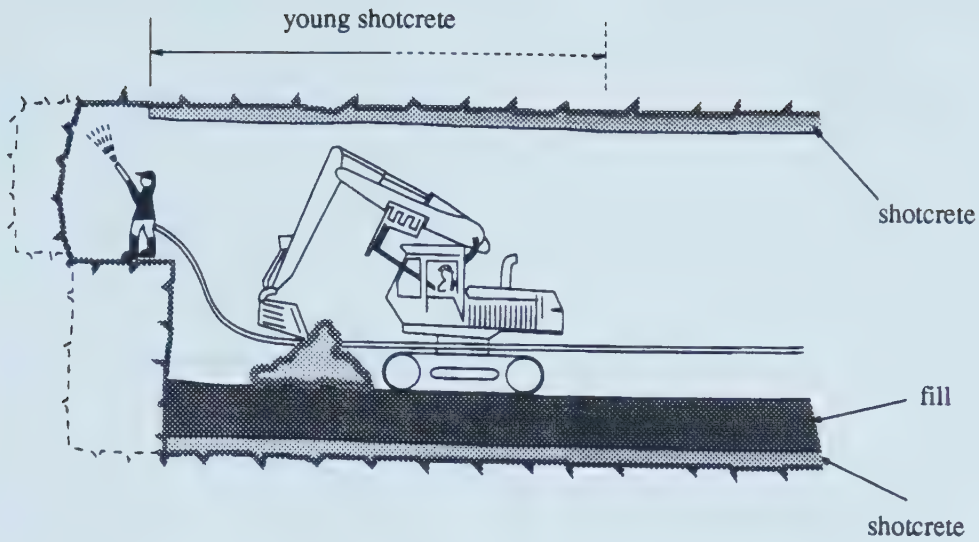
Chapter 4 presents the investigations carried out to obtain the early age properties of the shotcrete. These investigations were based on laboratory tests, tunnel construction control tests, field measurements and data published by other authors. The variation of compressive strength, elastic modulus, creep, shrinkage and temperature with time are

presented. A simplified viscoelastic model is proposed for the calculation of stress dependent deformations.

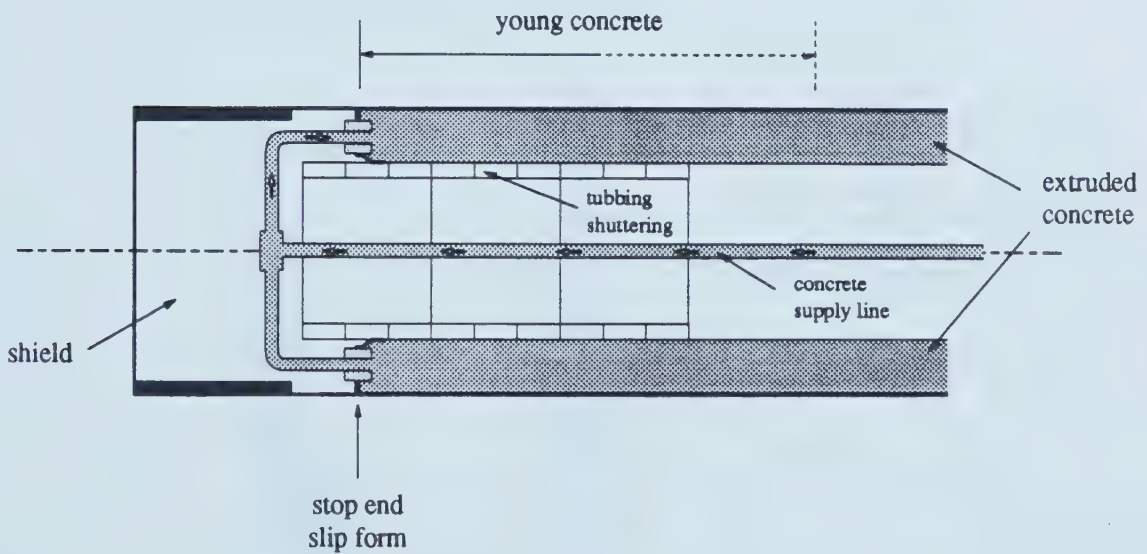
Chapter 5 presents the analytical approximation for the ground-lining interaction problem to be used in connection with the design method developed by Negro (op. cit.). In order to analyze the short term behavior of the shotcrete, an analytical approximation based on the viscoelastic solution derived by Yuen (1979) was developed. The new solution incorporates the rate of tunnel construction.

In Chapter 6, the results of the investigations presented in the previous chapters are applied to a practical purpose. A procedure for interpretation of stress development in the lining is presented, based on strain measurements in the field. Variants of Negro's method are also suggested in order to take the short term behavior of the shotcrete into account. The measurements of the SLRT case history are used to check the adequacy of these procedures.

Chapter 7 summarizes the findings of this research and presents the main conclusions. Recommendations for further investigations related to this subject are also included.



a) Typical scheme for excavation of NATM in soft-ground



b) Typical scheme for extruded concrete lining application (modified from Babendererde, 1986)

Figure 1.1 Construction Scheme of Tunnel Lining Loaded during Early Ages

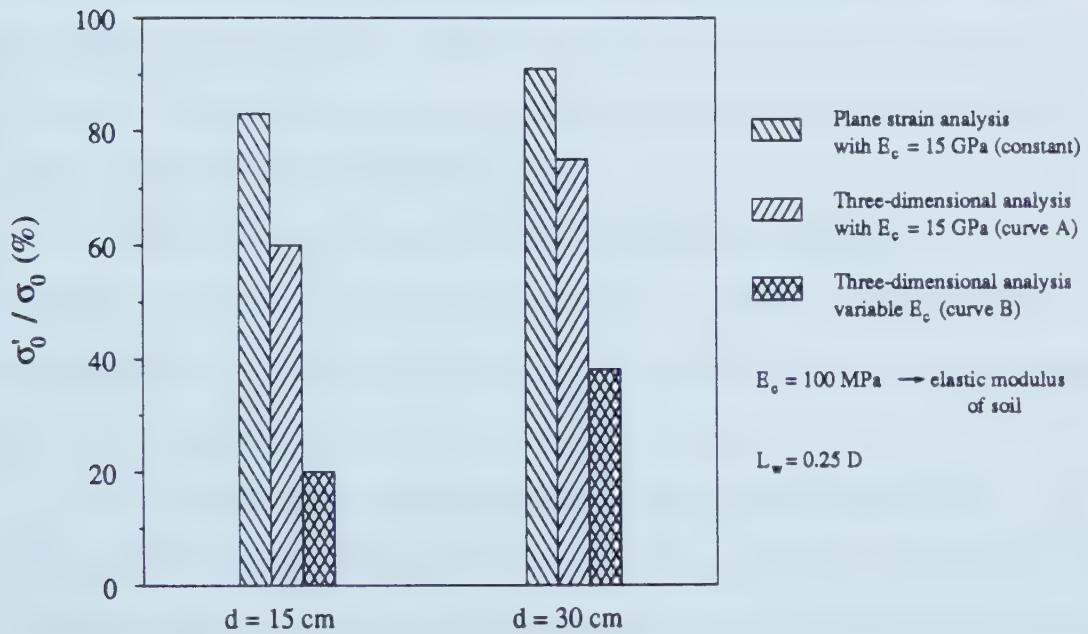
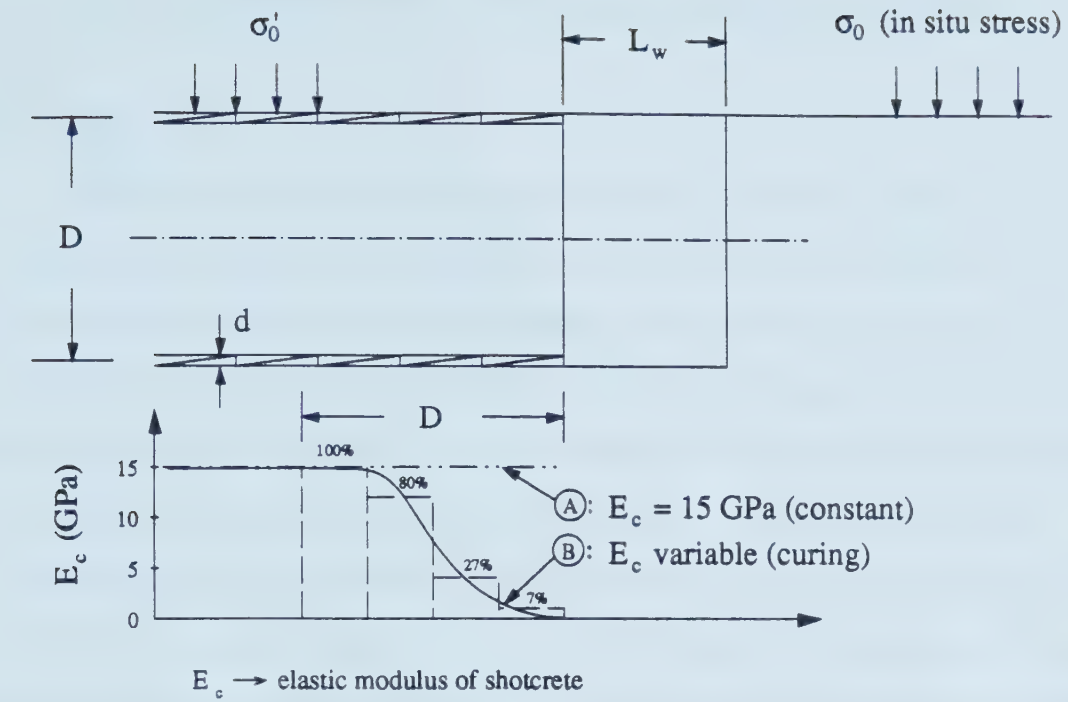


Figure 1.2 Effect of Shotcrete Stiffness Development on the Magnitude of Loading in Tunnel Lining (modified from Heinz and Rocha, 1990)

2. CASE HISTORY: SOUTH LRT EXTENSION TUNNEL

2.1 Foreword

This chapter focuses on the monitoring program carried out during the construction of a shallow tunnel located in an urban area. Since the objective was to follow the ground-lining interaction mechanism, both soil and shotcrete were instrumented. The ground instrumentation was performed using the conventional techniques and they will not be discussed in great detail because their interpretation does not constitute a subject of research compared with the shotcrete instrumentation interpretation. One should refer to Cording et al. (1975) and Dunnicliff and Green (1988) for an overview of ground monitoring and to El-Nahhas (1977), El-Nahhas (1980) and Branco (1981) for technical information on the devices used in the present investigation. However, the interpretation of the lining instruments, especially related to load measurements, does constitute a subject for discussion. For this reason, special attention was devoted to this topic during the instrumentation design and will be discussed in greater detail in this and subsequent chapters.

The monitoring of the load acting on the lining was considered the key information for a proper assessment of the soil-lining interaction mechanism. The instrumentation was intended to provide load development with time and with tunnel advance, with special attention to the short term behavior.

This chapter presents the instrumentation and problems related to its interpretation. Later it will be seen that for a proper interpretation of the load acting on the lining, intensive laboratory investigations were necessary. These results are presented in Chapters 3 and 4, and a complete instrumentation interpretation will be shown in Chapter 6. However, a preliminary interpretation based on an available method at the time the tunnel was under construction is also presented in this chapter. It was used as a

guide for the schedule of the instrument readings and also to evaluate the quality of construction.

2.2 Description of the Project

2.2.1 SLRT Project

The City of Edmonton has been involved in the development of a Light Rail Transit (LRT) system since the early 1970's. It has been implemented in stages, and at the time the instrumentation was carried out (summer 1987), approximately one-half of the northeast-southwest line was built. The first stage, the northeast leg, started to operate in 1978 and the second stage, the central leg, was completed in 1983. These two stages have a total length of 10.3 km, and 1.5 km of this runs underground, through the downtown area.

The development of the system had then entered a new phase, designated as the South LRT Extension (SLRT). The case history that will be presented in this chapter was a portion of this extension. In this stage, shown in Figure 2.1a, the tunnels were constructed from the Corona Station (end of the central leg) to the North Portal, at the margin of the North Saskatchewan River. A bridge would then be constructed across the river and the SLRT lines are now being constructed to expand the system. The main purpose of this extension is to connect the business center of Edmonton with the south areas in general and with the University of Alberta campus in particular. The campus area, beside its obvious educational role, is a major center for health care, cultural and sporting activities (Eisenstein and Sorensen, 1986).

2.2.2 NATM Tunnels

Figure 2.1a shows that the SLRT Extension was constructed using both the Tunnel Boring Machine (TBM) and the New Austrian Tunnelling Method (NATM). The instrumentation was installed in the Northbound Tunnel, between the Corona Station and

the Crossover Cavity. Figure 2.1b shows a simplified geological profile (Hardy, 1986) along the NATM tunnels and Table 2.1 presents a summary of the quaternary geology of the Edmonton area.

Figure 2.2 shows the typical scheme of excavation of the NATM tunnels and some construction details. This figure presents the initial support system, composed of wire mesh (102X102 MW 13.3X MW 13.3), steel ribs (W 150X14) typically spaced at 1 m and a shotcrete layer with a nominal thickness of 18 cm. A permanent lining of reinforced concrete was then placed to a final diameter of 5.4 m. The investigation and instrumentation presented in this thesis were restricted to the initial support system. The amount of cement used in the shotcrete mix within the instrumented sections was 350 kg/m^3 . The water-cement ratio (w/c) was between 0.4 and 0.5 and the accelerator-cement ratio (a/c) was 0.05. The liquid accelerator was composed of potassium hydroxide. The cement was Type 50 (sulfur resistant) and the maximum diameter of the aggregates was of the order of 1.9 cm. The pump and mixers used in this construction were located at the Crossover cavity (Fig. 2.1a) and the shotcrete was applied using the 'Dry Method'. The composition and the properties of the shotcrete will be discussed extensively in Chapter 4.

The heading and bench (Fig. 2.2) were both excavated using a conventional hydraulic excavator (Plate 2.1) and the soil was removed from the face area by a loader (Plate 2.2). The rate of construction of the Northbound tunnel was of the order of 5.0 m per two-ten hour shifts a day (Fig. 2.3). Spilling of 1.6 m long was occasionally used at the crown when instability was detected. The occurrence of water-bearing sand lenses within the till (generally favorable material for tunneling) were the only potential geotechnical obstacle for the construction. Since the amount and the pressure of water found in these lenses were low and the extent of the sand around the tunnel crown was limited, they did not lead to any major construction problem.

2.3 Description of the Instrumentation

2.3.1 General

Figure 2.1 shows the positions of all sections that were instrumented along the tunnels of the SLRT project. Sections A1 and A2 were set to monitor construction by the TBM technique in sand, B1 and B2 for TBM excavated through till and C1 and C2 for NATM excavated through till. The instruments installed to monitor construction of the Northbound NATM tunnel are the subject of this chapter. They can be divided in two groups: those for monitoring the ground movements and those for monitoring the load build-up in the lining.

This instrumentation program was intended to be used as a construction control of the NATM tunnels and as investigation of the soil-lining load transfer mechanism. The design of the instrumentation was done by this author and the installation and monitoring involved staff from the Civil Engineering Department of the University of Alberta and Thurber Consultants Ltd. All the data from the instrumentation were stored in a microcomputer, and the analysis software (Kuwajima et al., 1988) generated charts and tables necessary for construction control.

2.3.2 Ground Instrumentation

Figure 2.4 shows the layout of the instrumented sections C1 or "Early Warning Section" and C2's or "Main Section Series". Section C1 was located in the region where the excavation of the Northbound NATM tunnel began, and it was intended to monitor the quality of the construction procedure in the early stages. The major source of data for the ground response was designed to be taken from the Main Section Series (C2), and for this reason they comprised a much larger number of instruments.

The ground instrumentation included shallow and deep settlement points, vertical multipoint extensometers, inclinometers and piezometers. Appendix A presents the locations of these instruments in terms of chainage and offset (Tables A.1 to A.3) and

also the scheme of installation (Figures A.1 to A.7). The shallow settlement points were installed according to local practice, two meters below the ground surface, in order to avoid movement caused by ground freezing. The deep settlement points were installed at the tunnel center line, half meter above the crown elevation. The vertical multipoint extensometers were magnetic type and the inclinometers were installed in a vertical line in order to measure horizontal displacements. The piezometers were ordinary standpipes.

2.3.3 Lining Instrumentation

2.3.3.1 Foreword

The problems related to interpretation of concrete lining instrumentation are well known. The difficulty to obtain stress from strain measurements in concrete is well reported by Shepherd and Wilson (1960), England and Illston (1965), Hornby and Noltingk (1973), Brierley and Cording (1976), Jones (1976:138), Schubert (1988). The problems are due to stress independent strains such as shrinkage and temperature changes and also time-dependent creep deformations. This problem is aggravated in the case of NATM tunnels, where the shotcrete is loaded at early age. During this period, the curing shotcrete exhibits a complex mechanical behavior which changes with the age. The interpretation of load measurement devices (Voort, 1976; Benecz et al., 1977; Baumann, 1985) is often a focus of criticism, usually related to stress concentration factor due to stiffness differences and also installation imperfections.

The main purpose of this instrumentation was to measure the loads transferred from the ground to the lining, and the instruments used in this work are divided into direct and indirect load measurement devices.

2.3.3.2 Direct Load Measurement

Two types of direct measurement devices were used in the lining instrumentation: total pressure cells and 'stress gages'. The former were commercial earth pressure cells

manufactured by Geokon, model 4800EC, which were equipped with vibrating wire pressure gages. The 'stress gages' were manufactured at the machine shop of the Department of Civil Engineering, University of Alberta, following the measurement concepts presented by Loh (1952).

The total pressure cells (TPC) were installed at the soil-lining interface, oriented to measure radial stresses. After the excavation and the installation of the ribs were completed, the soil was scraped to obtain a surface as plane as possible to place the TPC. Grouting or any other type of filling was not used in order to avoid possible voids induced by dynamic impacts during the shotcrete application. The pressure cell was then installed against the soil using three clamps applied to the outer ring of the TPC. Plate 2.3 illustrates this stage of installation for TPC991, which was placed at the crown region (Figure B.2). The steel mesh was then installed and shotcrete was applied. Five instruments of this type were installed and complete locations and their readings can be found in Appendix B. As these instruments were not thermally compensated, thermistors were assembled close to the pressure gages for temperature measurements which were used for compensation *a posteriori*.

Plate 2.4 shows the "stress gages", which were composed of three instruments of different lengths. The left, right and center instruments were 13.97 cm, 8.89 cm and 3.81 cm long respectively. All of them were 2.54 cm diameter, made of mild steel and were basically hollow cylinders. The thickness of the tube wall was calculated to provide an equivalent stiffness expected of the average shotcrete Young's modulus (secant modulus), 10 GPa. Resistance strain gages were bonded onto the surfaces of these cylinders using full bridge connections. The lengths of these gages were different to allow interpretation of in situ stresses based on a stress concentration factor (Loh, op. cit.). This type of interpretation will be discussed in more detail later.

These gages were assembled in cages (Plate 2.4) which were then attached to the steel mesh of the shotcrete lining (Plate 2.5). The cages were assembled in such a way to

locate the gages close to the mid thickness of the shotcrete lining. As these instruments are only applicable to compressive loads, they will be referred to as compressive gages. The installation locations are shown in Appendix B, Figure B.3.

2.3.3.3 Indirect Load Measurement

The indirect load measurement devices were vibrating wire strain gages embedded in the shotcrete and resistance strain gages bonded to the steel ribs.

Plate 2.6 shows a steel ribs where gages were bonded to both upper and lower inner flanges (Figure B.4). The resistance strain gages were installed using the conventional bonding techniques, followed by application of a layer of epoxy and a layer of silicone. This procedure was intended to protect the gages against the shotcrete impact, damping the mechanical shocks of the aggregates and improving the water tightness. Full bridge configuration was used for each measuring point which offered thermal and cable length compensation for the reading of this instruments. As the cable length compensation is limited by the quality of the cable itself, the reading stations for this type of gage was kept as close as possible to the instrumented section (about 5 m). During the lining shooting operation, these instruments presented a high rate of impairment: 46% of the instruments were lost just after the lining was placed.

Plate 2.7 shows the vibrating wire strain gages installed at the steel mesh. The installation was similar to that described for compression gages, using the same kind of cage. There were two different cages for the vibrating wire strain gages: one type of cage shown at the upper side of Plate 2.7 was used to install a single instrument close to the mid thickness of the lining, and another type shown in the lower side of Plate 2.7 where two gages were installed. This type of cage was designed to locate one instrument 3 cm from the shotcrete surface and another one 8 cm below, close to the steel mesh. The configuration with two gages would allow interpretation of bending moments. Because these gages were sensitive to temperature variations, thermistors were incorporated in the

sensor at each measuring point. The vibrating wire strain gages and the type of thermistor used in this instrumentation were not affected by the cable length. For this reason, the reading station could be brought to the surface through a small shaft (20 cm diameter) at the tunnel crown, 36 m behind the instrumented section. Complete location of these instruments can be found in Appendix B, Figure B.1.

Stress-independent deformations of shotcrete, specially during the curing period, due to processes like temperature variation and shrinkage are well known. Wooden panels were prepared, assembled with cages and vibrating wire strain gages similar to those installed in the lining. As soon as an instrumented section was covered by shotcrete, the wooden panel was also filled with the same shotcrete applied by the same operator. These panels were left inside the tunnel close to the instrumented section to provide strain compensation for the interpretation of the shotcrete lining response.

2.4 Considerations for Lining Instrumentation

2.4.1 Relative Stiffness: Compression Gages

The dynamic impact of aggregates on the instruments was taken into account during the design of the compression gages, however, the severity of the shocks was far beyond expectation. As a consequence, the rate of breakage during shooting of the lining was extremely high: 67% of the instruments were destroyed. The rest of them gave erratic readings that were not very useful.

Nevertheless the concepts used for their development could be helpful in illustrating the complexity of the lining instrumentation: as the shotcrete hardens, the relative stiffness between the lining and the gage changes with time. Therefore, the interpretation of the instruments will be a function of time. Consider a cylindrical gage embedded in a shotcrete body, as illustrated in Figure 2.5. E_s is the shotcrete Young's modulus, E_g is the gage Young's modulus, σ_s is the stress acting in the shotcrete and σ_g is the stress acting in the gage. If E_s is equal to E_g , σ_s will be equal to σ_g , which is the

perfect case, i.e., the gage is indicating the surrounding stress. However, E_g usually is different from E_s , causing difference between σ_s and σ_g , i.e. the gage is indicating different stress from the surrounding shotcrete. In general, they can be related to each other and Loh (1952) proposed the following equation:

$$\sigma_g = \sigma_s (1 + C_s) \quad [3.1]$$

where C_s = the stress concentration factor.

Applying the theory of elasticity and assuming that the end surfaces of the gages are perfectly rigid plates, Loh (1951) derived the following expressions for C_s :

For $L > \pi (1 - \mu_s^2) R$,

$$C_s = \frac{\frac{E_g}{E_s} - 1}{1 + \frac{\pi R}{L} \frac{E_g}{E_s} \frac{1 - \mu_s^2}{2 - \frac{\pi R}{L} (1 - \mu_s^2)}} \quad [3.2]$$

and for $L < \pi (1 - \mu_s^2) R$,

$$C_s = \frac{\frac{E_g}{E_s} - 1}{1 + \frac{\pi R}{L} \frac{E_g}{E_s} (1 - \mu_s^2)} \quad [3.3]$$

where μ_s is the Poisson's ratio of the shotcrete.

Figure 2.6 is a graphical representation of these equations. Observing this figure and Equation 3.1, it becomes clear that knowing the gage geometry (radius R and length L , Figure 2.5) and its Young's modulus is not enough to perform a proper interpretation of the gage readings. It is necessary to know the shotcrete Young's modulus and Poisson's ratio. These parameters, however, are not well known especially at early ages, and the Young's modulus varies widely after the gage is installed (from few kPa to tens of GPa, Figure 4.13). A test shown in Chapter 4 (Figure 4.14) indicated that the Poisson's ratio of the shotcrete after 10 hours of aging is almost constant and close to 0.3. In this case, it is

possible to apply Equation 3.2 for gages with $L/R > 2.9$. Substituting Equation 3.2 in 3.1, one finds two unknowns: E_g and σ_s , which is the in situ stress.

If two instruments of different lengths are used ($L/R > 2.9$), the problem can be solved. Three instruments were used ($L/R=3$, $L/R=7$ and $L/R=11$) to improve the accuracy and also check the Poisson's ratio assumption. Therefore, the compression gages (set of three instruments) were intended to allow measurement of stress without the knowledge of the Young's modulus and Poisson's ratio of the shotcrete. Actually these parameters can be found during the interpretation, by applying Equations 3.1 and 3.2.

2.4.2 Temperature Compensations

Temperature compensation for instrumentation usually is understood in two different ways: compensation to eliminate thermal stresses and compensation to eliminate the zero drift. The second one will be used throughout this thesis.

Figure 2.7 shows a typical temperature variation of the shotcrete lining at the springline. These are measurements taken by thermistors in the vibrating wire strain gages. In this figure, the initial time represents the moment the instruments were covered by shotcrete.

All the instruments which used resistance strain gages (bonded to the ribs and compression gages) were connected using full bridge configuration, therefore thermal compensation was provided. The manufacturer of the total pressure cells (TPC) provided the temperature correction factor for each pressure transducer. The readings these instruments were corrected by applying this factor to the temperature variation. This approach is clearly a simplification of the problem, as the pressure cell and the hydraulic oil inside it dilate differently from each other and the surrounding soil and shotcrete also present different thermal dilations. A careful temperature compensation would include all these factors but compared with the influence of other details on the readings, like

installation imperfections (Sauer and Sharma, 1977, Heinz, 1984, Negro, 1988), the assumption described above was considered adequate.

The readings of the vibrating wire strain gages were also sensitive to temperature variations and had to be corrected¹. The thermal dilation of the gage wire could change its tension which would indicate a strain value different from the one experienced by the shotcrete where it was embedded. The calibration cannot be done by simply changing the temperature of an instrument immersed in air or water and taking measurements. This procedure could be highly affected by the coefficient of thermal expansion of the tube that constitutes the 'body' of the gage. Note that this steel tube was designed to follow all the deformations imposed by the material in which the gage would be embedded, therefore it does not take part in the problem under discussion.

Note in Figure 2.7 that the widest variations of temperature occur approximately in the first 50 hours. Also, it will be shown (Figure 4.13) that in this period, the Young's modulus of the shotcrete was very low, especially before 12 hours of age. In this case, the stiffness of the vibrating wire strain gage could affect the readings (the gage is designed to be used in well cured concrete). For these reasons, a calibration was chosen to solve the problem. It comprised a vibrating wire strain gage embedded in concrete similar to that used in the tunnel lining, starting readings at around 10 hours of age. This procedure would partially compensate the relative stiffness problem, if it were to occur.

In order to obtain the temperature variation, some trials were done applying external control of heat. This procedure proved to be inadequate because either the temperature change was too low or the gradient of temperature within the specimen was too high for the time limit imposed on the test: 10 to 50 hour old specimen. The solution was to allow changes of temperature in the specimen due to its own curing heat. Three tests were performed (Figure 2.8) and the difference in the range of temperature variation

¹ The working principle of the instruments is considered out of the scope of this thesis, and general informations can be found in Hanna, 1985.

was caused by different amounts of accelerator used in each test. The temperature during the first 50 hours typically increased sharply to a peak (see Chapter 4) at approximately 8 hours of age and then decreased at a much lower rate. The results of the tests shown in Figure 2.8 were taken in this second period, where the maximum temperature difference within the specimen was under 0.3 °C.

The specimen was 15 cm diameter and 45 cm high, and followed the preparation procedure for the creep tests presented in Chapter 4. The vibrating wire strain gage was placed in the center of the specimen while it was being cast in a cylindrical mold. At six hours of age, the mold was taken out and the specimen was covered by a layer of paraffin to minimize deformations related to shrinkage. At eight hours of age, a standard compressometer described in ASTM C469 (to be discussed in Chapter 4) was attached to the specimen before readings were recorded. Note that this compressometer was immersed in air at constant temperature (within 0.1 °C) and was used as the nominally correct deformations. The vibrating wire strain gage was immersed in the concrete which was changing temperature. The difference between them is the reading deviation, and the slope of the lines shown in Figure 2.8 are the temperature compensation factor (average = $-6.6 \times 10^{-6} \text{ mm/mm/}^\circ\text{C}$). The linear pattern shown, specially in the case of test TEMP3, suggested that at low shotcrete stiffness (region of higher temperature) the readings were not affected. For this reason, this value was applied throughout the strain readings.

2.5 Preliminary Back Analysis

2.5.1 Foreword

During the design of the lining instrumentation, two classes of measurements were considered crucial for data interpretation: the compensating panels of shotcrete and the compression gages.

Figure 2.9 presents the data from the compensating panels of the vibrating wire strain gages, which would allow for compensation of stress-independent deformations (thermal and shrinkage) of readings of instruments embedded in the shotcrete lining. The stress and time dependent components are then left. However, if one makes use of these values to compensate readings from the lining as those shown in Figure 2.10, the results would not be accurate. This would indicate that loads decreased with the tunnel face advancing, and in some cases it could even indicate tensile thrust. In Chapter 4, it will be shown that the moisture content of the soil plays a major role in shrinkage deformations of the shotcrete. As the contact between the compensating panels and soil was poor, the data could not be used.

Figure 2.11 presents the data from the only set of three compression gages which were not damaged during lining shooting. The instrument CG106 corresponded to the short gages ($L=3.81$ cm), while CG206 was the intermediate ($L=8.89$ cm) and CG306 the longest one ($L=13.97$ cm). Theoretically (Equations 3.1 and 3.2) the series CG206 should give strains higher than CG106, as opposed to those shown in Figure 2.11. These gages had the function of indicating stresses in key points and their results could be helpful in interpreting vibrating wire strain gage readings.

The data presented above from compensating panels and compression gages did not produce the expected results and complementary intensive laboratory and site investigations became necessary. Two main outputs resulted from it: an in situ test for the shotcrete lining and determination of the behavioral parameters for the shotcrete at the early ages. The former is presented in Chapter 3 and it represents the solution found to avoid conventional instrumentation due to interpretation difficulties caused by the extremely complex behavior of the shotcrete in the short term. Chapter 4 presents the shotcrete parameters at early age.

A detailed interpretation of the lining instrumentation cannot be presented without the results to be shown in Chapters 3, 4 and 5. However, preliminary

interpretation of the field data will be carried out by making a simplification in the analysis: an equivalent secant modulus for the lining behavior will be assumed. This equivalent Young's modulus was set to 10 GPa as many authors have already suggested (e.g. Negro, 1988) and it will include all the intervenient factors such as curing, non linearity, time dependency, etc.

All the data collected in this instrumentation are presented in Appendices A and B, and only the results related to the preliminary interpretation will be presented here. Although the lining instrumentation was the most problematic one, some of the instruments installed for soil monitoring also indicated some difficulties. The multipoint extensometers gave erratic readings and unusual response during monitoring: settlements larger at the surface than close to the tunnel crown (Figure 2.12) when the opposite should be expected. The reason seems to be related to the bentonite slurry (Figure A.3) which was injected in the extensometer borehole. Due to legal problems beyond control of the SLRT project management, the schedule for the installation of the instrumentation was reduced drastically. As a result, the soil instruments were installed between one to four weeks before the tunnel crossed the instrumented sections. The reading from the multipoint extensometers C2-M1 (Figure 2.12) indicated accommodation of the magnet points (sudden changes of the readings) associated with the consolidation of the bentonite slurry. Excellent performance resulted from the same type of instruments at the extension of the SLRT lines. These were installed with identical procedure, in similar type of soil, by the same crew (Thurber Consultant Ltd.) but the installation anticipated the first readings by approximately one year. Similar problems also might be present for the slope indicator but in this case the changes of the readings probably would be reduced due to the not yet well cured bentonite slurry (Figure A.6).

2.5.2 Method used for the Analysis

The preliminary interpretation of the field data had two main purposes: immediate assessment of the quality of construction and instrumentation just after the data were collected and an examination of the capability of a method of design that could meet the special interests of the present research. This special interest was the ground-lining interaction in the short term and calculations should be sensitive to this feature.

The method of design proposed by Negro (1988) was chosen for this purpose, and it is one of the few methods available that integrates the calculation for the ground and lining in a consistent way. The procedure allows lining load predictions and settlement estimates taking into account some of the most important factors controlling the tunnel behavior. These are:

1. the effect of the relative position of a horizontal, stress free ground surface;
2. the action of gravitational body forces generating a stress gradient across the tunnel profile;
3. the non-uniformity of the in-situ stresses generated by a stress ratio different from unity;
4. the non-linear response exhibited by soils in terms of their stress-strain relationship, including the dependence on hydrostatic and deviatoric stress levels;
5. the delayed activation of the lining generating ground movements and associated stress and stiffness changes in the ground prior to support application;
6. the interactive nature of the load transfer process developed between the soil and the support;

Moreover, the method was exhaustively checked against a large number of case histories and sensible results were obtained for both ground and lining responses. The method is limited to tunnel construction with good ground control, or in other words, the method cannot be applied to construction with near collapse ground condition. A comprehensive summary of Negro's method was presented by Eisenstein and Negro, 1990 and a flow chart of its application is presented in Figure 2.13. For more details, the

reader should refer to Negro's (1988) thesis for a fully explained example of using the design approach.

Lambe (1973) proposed a classification of types of predictions in geotechnical engineering which is presented in Table 2.2. This classification is particularly interesting due to the attention Lambe gave to the availability of the instrumentation data at the time of calculations:

"...The Profession is in great need of simple techniques to make type A predictions. Even though type B predictions may be helpful, they are normally not nearly as useful as type A predictions. Type C predictions are autopsies. Our professional literature contains the results of more type C1 predictions than of any other type. Autopsies can of course be very helpful in contributing to our knowledge. However, one must be suspicious when an author used type C1 predictions to 'prove' that any prediction technique is correct ..."

Numerical methods available today permit simulation of extremely complex conditioning like "birth and death" of elements, intricate boundary conditions, sophisticated constitutive laws, etc. This technique can be applied for prediction type A or C, but it is usually not suitable for prediction type B, especially when feedback from instrumentation data is required to adjust the construction design. This procedure is often used in NATM tunnel construction, where the observational method is applied. This is an extra reason for the choice of Negro's method, and due to the ease of its application, one may even perform adjustment of parameters at site, using a simple programmable pocket calculator.

2.5.3 Commented Application of the Method

Negro (1988) presented a set of calculation sheets to facilitate the sequence of calculations involved in the method. The results of the analyses for the SLRT tunnel are presented in Figures 2.14 to 2.18. The calculations using the method for this case history

were originally done by Negro (1987) as type "A" prediction (Lambe, 1973), but due to changes in the tunnel alignment, they were modified. As these modifications were restricted to adapt to the new alignment, besides the fact that this author knew the results of the instrumentation at the time of the recalculation, the results seem to remain very close to prediction type "A".

Figure 2.19 presents the soil and SPT profile from boreholes H85-1, H85-36 and H85-38 (Hardy, 1986), which are shown in plan view in Figure 2.4. Pressuremeter test results (Thurber, 1980) are also shown in Figure 2.19 for borehole S80-1 (plan view in Figure 2.4) in the tunnel construction area, and another, S80-2, done at Jasper Avenue between 104 St. and 103 St. (5 blocks east from the construction site).

The first item (Geometry) in Figure 2.14 presents two dimensions necessary for the calculations: H , the distance between the tunnel crown and the surface and D , the diameter of the tunnel resulting in a H/D of 1.23. As most of the parametric charts available in Negro's method were limited to the range $1.5 < H/D < 6$, extrapolations were necessary.

The next item presents the ground properties γ (unit weight) and K_0 (horizontal to vertical stress ratio), values of which are well known to local practitioners (e.g. Thurber, 1980). The strength parameters c , ϕ and R_f are used in the hyperbolic model (Duncan and Chang, 1970), which is used to evaluate the deformation and stiffness degradation of the ground. Therefore, these parameters should be set for the most representative soil, in this case, the glacial till. The values of c , ϕ and R_f shown in Figure 2.14 resulted from interpretation of data presented by Wittebolle (1983) for tests done in till specimens taken from a site located at 106 St. and 100 Ave., a few blocks from the construction site.

The calculation method was originally developed for cohesionless material, with $R_f = 0$. However, by introducing adjustment in the friction angle ϕ_a and ϕ_e in Figure 2.14, the method can also be applied to cohesive material with $R_f \neq 1$ respectively. The in situ initial tangent modulus of the ground (E_{ti}) can be calculated from the hyperbolic model

(Duncan and Chang, 1970), by applying the in situ stress σ_1 and σ_3 and using Janbu's (1963) coefficients K and n . Note that in this case, one will be assuming a homogeneous ground. However, Figure 2.19 shows that this is not the case, and in situ values of E_u were taken from pressuremeter tests. The SPT profiles were used as guidelines to obtain the values of E_u at the locations required by the method: half diameter above the crown, at the springline and half diameter below the floor. The value of E_u corresponding to the point half diameter above the crown was not taken at this exact location, but as the average value nearby due to the sharp variation of properties presented in the region.

Item 3 (Figure 2.14) is the evaluation of tunnel closure at the moment the lining is activated. This part of the design method was developed using 3D numerical simulations of full face tunnel excavations, as opposed to the staged construction of this case history. In the case of NATM tunnel construction, Negro (1988: 1175) suggested that one may assume lining activation when the shotcrete ring is closed at the floor. Figure 2.2 shows that the distance between the excavation front and the invert closure (parameter X in Figure 2.14) was around 3 to 5 meters, and an average value of 4 m was used for the calculations. Having the parameters X/D and K_0 , the method provides charts like that presented in Figure 2.20 for the tunnel crown to obtain the normalized radial closure U for the three points of interest around the tunnel boundary: crown, springline and floor. From the normalized values, one can calculate the actual radial displacements u_r . They represent the displacement of the tunnel contour, at the moment the lining was activated.

The next step consists of the evaluation of the ground stress release and ground stiffness at the point of support activation. This part of the method was developed using 2D finite element simulations assuming the hyperbolic model (Duncan and Chang, 1970) for the ground. These simulations were performed using the conventional technique of proportionally manipulating the boundary forces at the contour of the tunnel. At the beginning of each simulation, these boundary forces were set equal to the initial in situ stresses, reproducing the equilibrium state where construction did not introduce any

disturbance: the tunnel is very far². As tunnel construction starts and approaches the 2D section, the stresses are released and the tunnel contour starts to converge. This is simulated by reducing the boundary forces, which eventually will be zero, for the case the tunnel face has already passed the section and is very far away: all the stress dissipation due to the tunnel construction have occurred. Some point between these extremes, the lining would be installed and activated. Note that if one delays the installation of the tunnel lining, larger deformations and shear stresses will undergo in the ground until the lining activation. For the hyperbolic model assumed for the soil, this will translate in stiffness degradation of the ground around the tunnel. Obviously, the reverse is also true.

Similarly, the delay of the lining installation will affect the load transferred from the soil to the support. Calculations in Figure 2.15 evaluate these effects, represented by the stress and stiffness reduction factors. In order to facilitate the application of the method, these results were presented using normalized parameters. In some cases, the results were normalized two times. The calculations presented in Figure 2.15, item 4, are reference values used for the second normalization. Although the reference values were chosen to obtain maximum accuracy of the normalization, they are arbitrary values and don't have any particular physical meaning. U_{ref} and α_{ref} can be considered as an axis used to reduce a family of homothetic curves into a single one at the second normalization. However, as charts presented in the method were reduced using specific values of U_{ref} and α_{ref} , the user should take the same values. Using the charts corresponding to the given H/D , K_0 and $(m-1)$, one would find the values presented in item 4 (Figure 2.15).

The next step is the determination of the amount of stress release and ground stiffness change at the time of lining activation. The stress release parameter λ is

² This approximation mimics the actual three-dimensional stress changes or arching process that leads to smaller ground loads being transferred to the lining as a result of the interaction process within the soil (Negro, 1988: 1131)

obtained by using the twice normalized ground response curve, illustrated in Figure 2.23 for a point at the crown. The derivative of this curve is used to obtain the stiffness reduction parameter λ' (Figure 2.24). The same procedure is repeated for the springline and floor, and results are shown in item 5, Figure 2.15.

At this point, we have already estimated the tunnel closure and evaluated the state of stress and stiffness of the ground at lining activation. However, in order to validate these calculations before the lining is applied, it is necessary to ensure that this condition can be reached, i.e., the construction is stable. A two-dimensional stability verification is made, and it is presented in item 6, Figure 2.16. A lower bound solution was applied ($P_1/\gamma D$ from D'Escatha and Mandel, 1974) for the state of stress calculated in item 5 ($\bar{\alpha}$) of Figure 2.15. The chart used for this purpose is presented in Figure 2.25, which also presents an upper bound solution (Atkinson et al., 1975) offered as a reference value for the other extreme limit.

The next design step is the ground-lining interaction analysis. Figure 2.26 presents the notation and conventions used in Hartmann's derivations (1970 and 1972) and Figure 2.27 shows the solution. This solution was chosen among others because it was the only one that makes full allowance for the non-uniform stress field existing in a shallow tunnel, which is generated by in situ stress ratios different from unity and by the action of gravity. The original solution treats both the soil and lining as linear elastic, isotropic and homogeneous materials. The opening is assumed to be circular, the ground mass is represented by an infinite plate and the lining by a weightless thin cylindrical shell of constant thickness. The ground surface is represented by a stress-free horizontal surface and the lining is assumed to be installed in the opening before any displacement occurs in the ground.

This last assumption does not reflect the usual tunnel construction sequence, as deformations do occur in the ground before the activation of the lining. In fact, they have already been calculated in item 3 (Figure 2.14) and this effect can be understood as part

of the load being carried by the ground. This delay of the lining activation, or reduction of ground loads, can be introduced in Hartmann's solution by reducing the unit weight. This decrease is related to the amount of stress release $\bar{\alpha}$ until the lining activation and therefore the reduced unit weight is $\gamma_{\text{red}} = \gamma (1 - \bar{\alpha})$. Also, this delay of lining activation will allow the non-linear soil to deform, and as a result, degradation of the ground stiffness around the tunnel will take place. This effect is taken into account by applying the ratio between the stiffness at the moment of lining activation to the initial one (λ'/λ'_i) to the initial tangent modulus E_{ti} , as presented in item 5 (Figure 2.15).

Applying these corrections to the ground parameters (γ_{red} and \bar{E}_t) in Hartmann's solution, one would obtain the results shown in item 7 (Figure 2.16). The Young's modulus of the shotcrete was set as 10 GPa, according to reasoning presented earlier. Note that during this lining-ground interaction, extra deformation occurred in the ground, which in turn will promote further degradation of the soil stiffness. The difference between the modulus of the ground (\bar{E}_t) before the lining-ground interaction and after it (\bar{E}_t)_{new} is related to this stiffness reduction. The calculation is repeated with this new modulus, in an iterative process, until the difference between \bar{E}_t and (\bar{E}_t)_{new} are negligible (Figure 2.17). Note that v_{z0}'' represents the heave of the tunnel contour, resulting from the gradient of stress due to the gravitational forces, calculated by Hartmann's solution.

Finally, using normalized charts for the condition of the final equilibrium, subsurface and surface settlements can be calculated (Figure 2.18) using charts as those presented in Figures 2.28 and 2.29, respectively. Negro (1988) noticed that the surface settlement trough was typically non-conservative when compared with field measurements. For this reason, it was suggested a correction on the maximum calculated distortion (γ_c) by a factor of 1.4. The shape of the trough is assumed to follow a normal probability curve, and the results are also presented in Figure 2.18.

2.5.4 Analysis of Results

The reduction of the soil displacement data are trivial and the results are compared with the calculated values in Figures 2.30 to 2.32. The interpretation of the lining instrumentation data, to obtain loads, was done using a very simplified assumption for the reason already presented. The parameters assumed are shown in Table 2.3 and results are compared in Figures 2.33 and 2.34.

The dimensionless crown displacement U shown in Figure 2.14 is smaller than 1.0, which is an indication of good ground control condition necessary for the application of the method. Another index to analyze the ground condition is the factor of safety against ground collapse as shown in Figure 2.16. Although the value 1.46 seems to be fairly low, Negro (1988: 1326) observed that urban tunnels designed for and built under 'good ground control' conditions (as opposed to near collapse ground condition) typically presented a factor of safety between 1.2 and 1.7. Moreover, due to these low values, non-linear response should be expected as considerable departures from linear response is observed for factors of safety less than 2 to 3. This demonstrates the necessity of using non-linear models to analyze the ground for cases similar to the SLRT case history: shallow urban tunnels.

The excavation of any tunnel causes settlements of the ground above it, which has the potential of damaging structures adjacent to its alignment. It is well known that structural malfunctioning is not caused only by the amount of settlement, but specifically by differential settlement. Therefore the settlement trough distribution is of interest and the results presented in Figure 2.20 refer to the equilibrium state after the completion of tunnel excavation. The field data are presented for four cross sections (C2-1 to C2-4) and the location of these instruments is shown in Figure 2.4. The calculated values are those commented above and presented in item 9, Figure 2.28. Figure 2.30 shows that Negro's method produced very good estimates of the settlement trough and the original calculation (item 9 in Figure 2.18) and the correction of the maximum distortion, γ_c ,

presented good boundaries: the former for overall absolute values of settlement and the latter for the differential settlement.

Figure 2.31 shows the deep settlement points installed 0.5 m above the tunnel crown at the tunnel alignment. The initial readings of the instruments C2-DSP7 and C2-DSP8 were taken just when the tunnel face was close to them, and for this reason, they present incomplete settlement development with tunnel heading advancing. C2-DSP6 presented irregular readings, probably due to local over-excavation at the crown, and its data were disregarded. C1-DPS1 presented final readings of the order of 13.2 mm, while the calculated value was 13.4 mm (iteration 3, Figure 2.17). However, the good agreement must be considered with some caution. In the calculation of the settlement at the crown, the tunnel heave³ v_{z0}'' was added to obtain the final value $u_{ff} = u_r + \Delta u_r + v_{z0}''$. The equation to obtain v_{z0}'' is shown in Figures 2.16 and 2.17, and it is part of Hartmann's original analytical solution. Note, however, that the heave v_{z0}'' is a function of r_1 , which is the radius of an arbitrary circle at which the vertical heave displacement is set equal to zero. For practical applications, r_1 should be smaller than either a tangent from the tunnel axis to a stiffer horizon below the tunnel or one to the ground surface. Although this approach entails an indeterminate degree of approximation to the ground movement estimate, it has little effect on the load distribution. It is also suggested that neglecting the heave component will lead to slightly conservative estimates of field settlement.

Note that the displacement of the crown after the activation of the lining, represented by $\Delta u_r + v_{z0}''$ in Figure 2.17, would be 0.9 mm upwards. Field data presented in Figure 2.31 show downward movements, with an average value of 1.6 mm. Note however, that this value closely agrees with the calculation, if one neglects the heave ($v_{z0}'' = 0$), i.e., displacement after the lining activation would be represented only by Δu_r .

³ this tunnel heave can be considered as a result of the unbalanced stress, between the upper and lower region of the countour, causing the tunnel perimeter to "float". This movement is upward (heave) because the stresses at the upper portion are smaller than those at the bottom due to the gravitational distribution.

The convergence of the springline is not affected by this parameter, as the heave is orthogonal to its direction. Figure 2.32 presents the comparison of the horizontal movement measured by C2-I2 (Figure 2.4 and Table A.3), showing field displacements smaller than the calculated values. As mentioned earlier, the slope indicators could have their readings reduced due to the poorly cured grouting, at the moment the tunnel was crossing the instrumented sections.

In any case, this discussion will not be complete without appraising on the lining activation assumption. Two approximations resulted when considering $X = 4$ m and $E_c = 10$ GPa in Figure 2.14. The former had converted the actual sequential excavation construction (Figure 2.2) into an equivalent full face excavation assumed by the design method. The latter, $E_c = 10$ GPa, had assumed an equivalent secant modulus for the ground-lining interaction phase (Figures 2.16 and 2.17), which should take into account factors like: deformation modulus development, early age creep, shrinkage, thermal deformations, etc. Since both considerations are interconnected, a rational solution to find equivalent parameters for the design method cannot be completed without a better knowledge of the shotcrete behavior.

Figure 2.33 presents the calculated radial stress of the soil acting against the lining according to Negro's method. This figure also shows the field measurements taken by the total pressure cells (Figures B.2 and B.42, appendix B), including the pressure gage temperature compensation. It is recognized that the installation did not provide a perfect contact at the soil-pressure cell interface which explains the low readings observed in Figure 2.33.

Figure 2.34 presents the thrusts as calculated by Negro's method and the values from the lining instrumentation resulting from an extremely simplified interpretation. Data presented in Appendix B show oscillations in strain readings and also a wide variation of temperature. This indicates the necessity of compensating the total strain readings by the stress independent components, if one intends to obtain loads from these

data. As mentioned earlier, the readings of the vibrating wire strain gages installed in stress free panels which were supposed to provide compensation components to be used for interpretation, failed to fulfill their functions. The application of the temperature compensation factor to the readings of vibrating wire strain gages as presented in item 2.4.2, did not drastically change the value of final readings. The necessity for better knowledge of the behavior of the shotcrete parameters to permit a proper interpretation of the readings has already been pointed out. For the purpose of this preliminary interpretation, only what was considered 'well behaved' instruments will be used. As crucial information of the shotcrete behavior was not available in this stage of interpretation, this arbitrary criterium chose only instruments which were installed in pairs and their reading developments were similar and asymptotic. The instruments embedded in shotcrete were interpreted assuming a equivalent secant modulus for the shotcrete of 10 GPa and thickness of 18 cm, and no kind of correction was applied to the readings. The strain gages bonded to the ribs were thermally compensated (reading compensation), and a linear elastic model was assumed for the interpretation.

Table 2.3 shows the results and comments on this interpretation, and the values can only be used as an index or rough estimation of the actual values. A complete set of the lining instrumentation readings are presented in Appendix B. The results shown in Figure 2.34 are in reasonable agreement: thrusts calculated and measured in shotcrete have similar values. The ratio between the product of Young's modulus and the area (EA) of the rib to the shotcrete was approximately 18% while the results in Figure 2.34 indicated around 20%. As an illustration, the calculated bending moments are also presented in Figure 2.34, which are proportional to the stress variations along the lining thickness.

2.6 Comments and Summary

This chapter presented the case history to be used in this thesis: the South LRT extension tunnel. The SLRT project was described and the soil and lining instrumentation used to monitor the tunnel construction were introduced. Emphasis was laid on the lining instrumentation due to the difficulty of its interpretation.

This difficulty has been recognized because the design stages of the instrumentation and studies were carried out to examine two of the factors necessary to be compensated for during interpretation: relative stiffness and temperature. A compression gage was developed to solve the relative stiffness problem based on the concept of stress concentration factor (Loh, 1952). Despite the effort expended in designing these gages and preparing special setups to obtain compensating strain for embedded vibrating wire strain gages, it was not possible to perform a reliable interpretation of data for the lining. Both of these measures yielded poor performances and a complete interpretation was only possible after an extensive program of laboratory tests was carried out. For future investigations, one should be aware that the high breakage of the resistance gages was not solely caused by the direct impact of the shotcrete to the instruments. During the shooting of the lining, blocks of shotcrete often fell from the crown region, pulling the instrument cables. It is believed that this mechanism damaged most of the resistance gages, and it is suggested that the cables be fixed firmly to the cage or steel mesh.

A preliminary interpretation of the field data was presented for two purposes: immediate assessment of the instrumentation and an examination of results using Negro's (1988) design method. This method was chosen because it is one of the few methods that integrates the calculations for the ground and the lining in a consistent way. A commented application of this method to the case history is presented and the most important aspects of the method are introduced. A preliminary simplified interpretation of the instruments installed in the lining is presented as index values for evaluation of the loads. Although the comparison of results presented reasonable agreement, the necessity

to investigate many of the aspects involving the soil-ground interaction and their impact on tunnel design became evident.

The investigations carried out in this thesis led to the evaluation of the loads acting in the lining based on the instrumentation data. However, due to its complexity and the limitations of the results (there is not enough information to ensure the applicability of the results presented for shotcrete on situations or compositions different from those studied here), a practical alternative to evaluate loads in tunnels linings was felt necessary. The in situ flat jack test, which provides a reliable means to evaluate loads, is presented in Chapter 3.

The flat jack test is a solution *a posteriori* but designers need to provide values *a priori*. The laboratory tests presented in Chapter 4 were investigations carried out to meet this requirement. Tests were conducted to evaluate deformation and strength properties of the shotcrete with age. Creep at early age, temperature development and shrinkage were other aspects examined. However, these results cannot be applied directly in design methods as those used in this chapter. As presented in item 2.5.3, Negro's method which is similar to most of the design methods assumes the lining to be a linear elastic material. The value of 10 GPa used in the calculations may be considered arbitrary and further investigations may be necessary. Also in this method, the delay of the lining activation is taken into account in a simplified way by assuming that the equivalent lining is activated when the invert is closed. In order to provide a rational solution for these interrelated parameters (equivalent secant modulus and the position of the lining activation) investigations were conducted. They are presented in Chapter 5, where the results from the laboratory (Chapter 4) were used in a parametric analysis applying a simplified analytical solution to simulate different rates of tunnel construction.

Finally, Chapter 6 presents a complete interpretation of the results where the other aspects of interest are investigated as pointed out in item 2.5.4.

Table 2.1 Quaternary Geology of Edmonton Area (modified from May and Thomson, 1978)

Quaternary	Holocene	Alluvium, Organic deposits, recent lake deposits
	Pleistocene	Lacustrine sand, silt and clay, organic deposits, aeolian sand and silt, river Alluvium
		Till
		Sand and sandy gravel, some silt and clay
		Till
Tertiary (undivided)		Saskatchewan gravels and sands

Table 2.2 Classification of prediction (modified after Lambe, 1973)

Prediction type	When prediction made	Results at time prediction made
A	Before event	-
B	During event	Not known
B1	During event	Known
C	After event	Not known
C1	After event	Known

Table 2.3 Preliminary Simplified Estimates of Loads from Lining Instrumentation

INSTRUMENTS		Strain	Young's modulus	Load	observations
Type	Designation	10×10^{-6} m/m	GPa	kN/m	
embedded in shotcrete	VW16 VW17	225	10	405	readings of VW16 and VW17 developed fairly close, Figure B.11
embedded in shotcrete	VW28 VW29	150	10	270	the difference between readings of VW28 and VW29 was approximately 100×10^{-6} m/m at beginning, decreasing with time, Figure B.15
embedded in shotcrete	VW36 VW37	150	10	270	VW36 constant around 150×10^{-6} m/m and VW37 increasing. Value of VW36 was assumed for calculations, Figure B.25
bounded in steel ribs	RS64 RS65	150	200	44.5	average value at pathamar 200-400 hours, Figure B.47
bounded in steel ribs	RS72 RS73	75	200	22.2	average value at 200-400 hours, Figure B.44

(1) thickness of shotcrete assumed for calculation: 18 cm

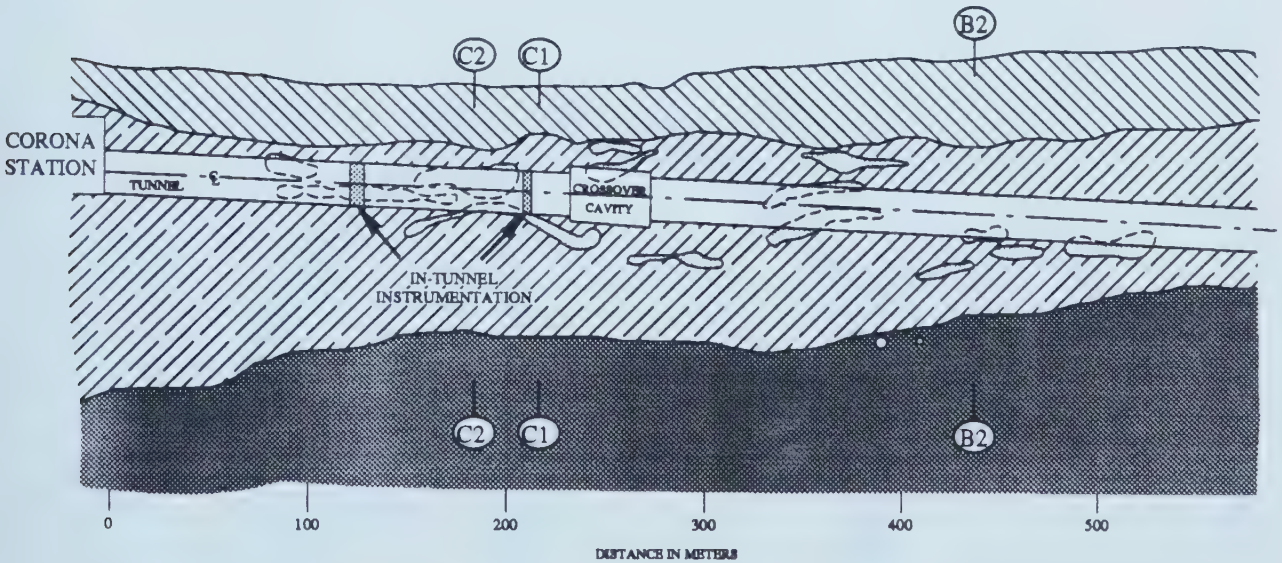
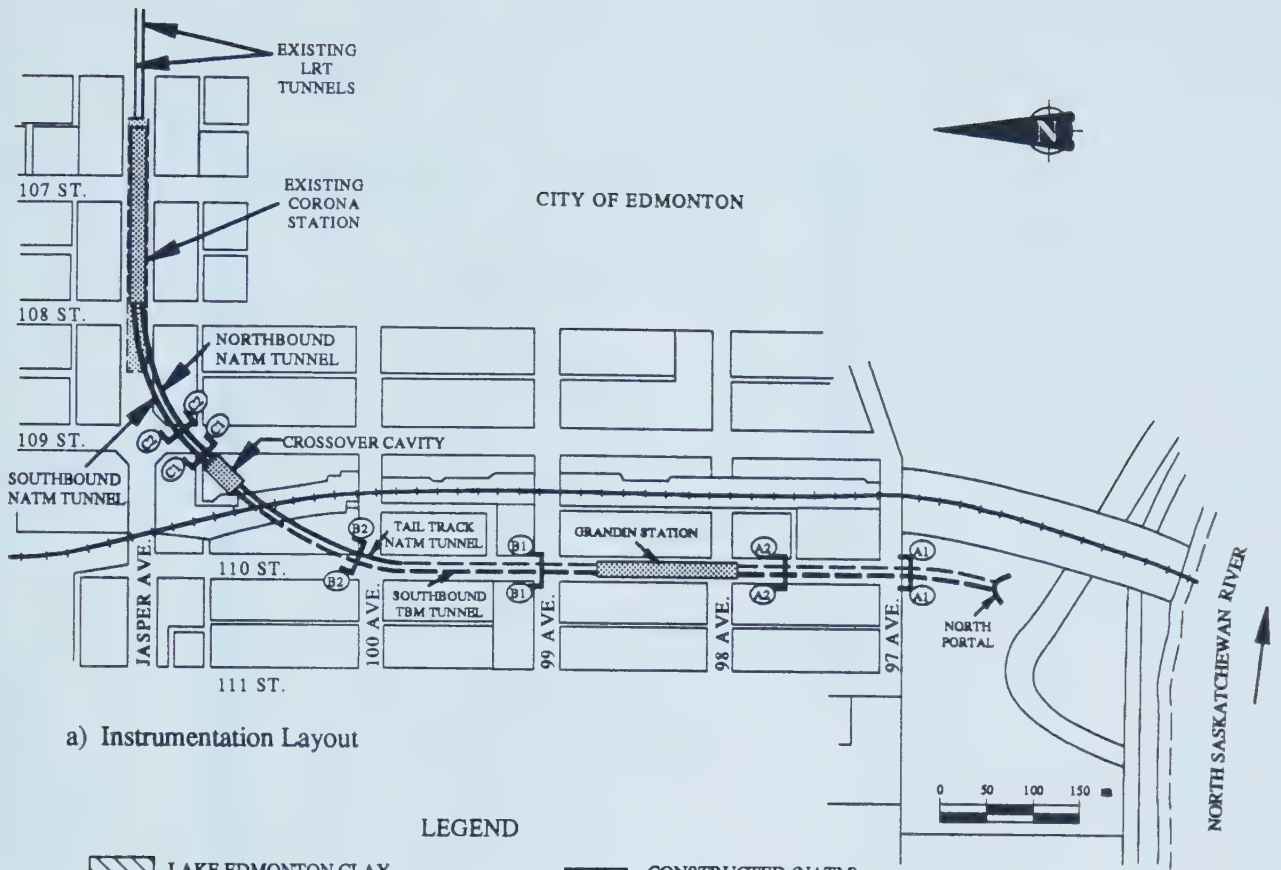


Figure 2.1 Overview of SLRT Project (modified from Phelps and Brandt, 1988)

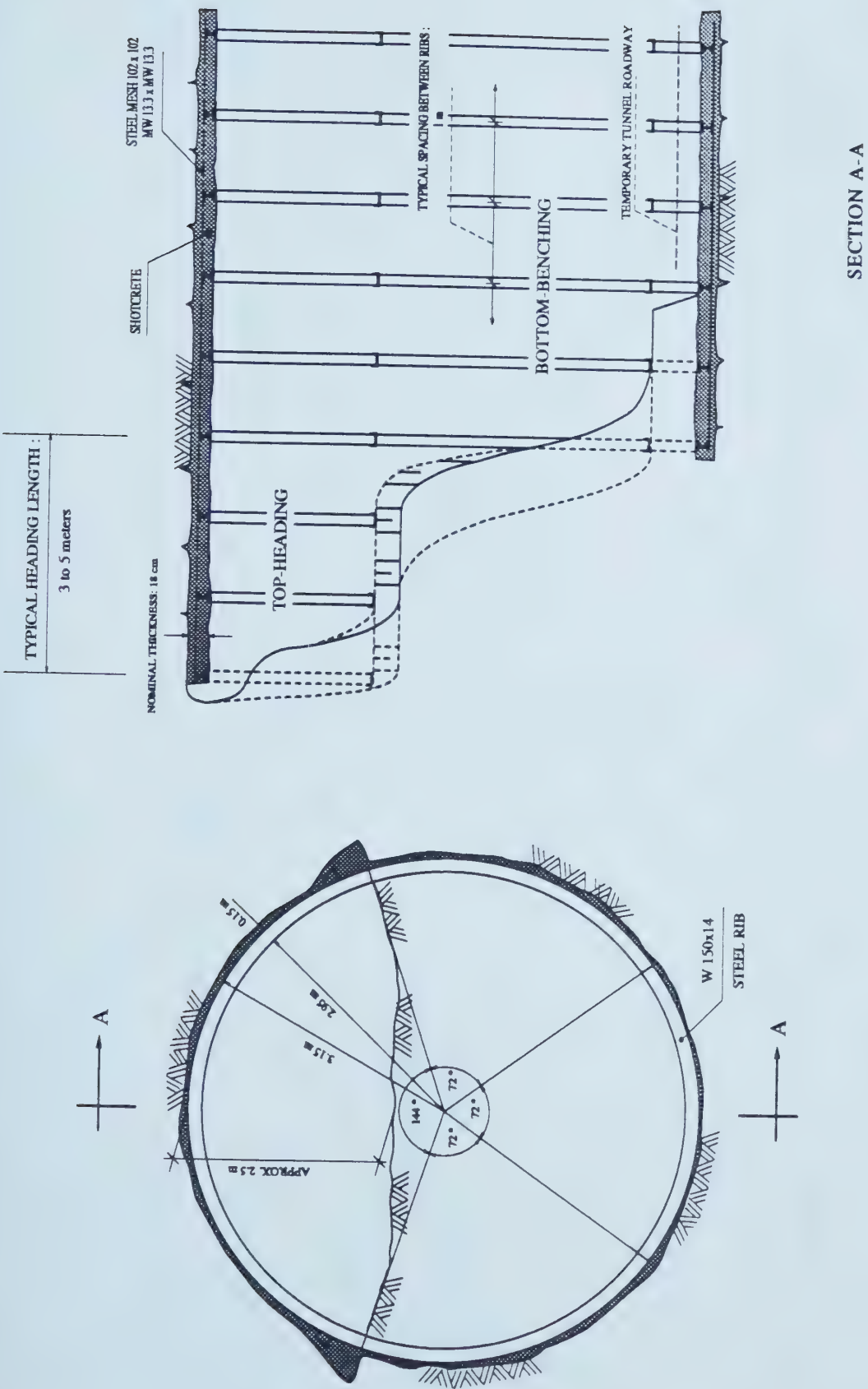


Figure 2.2 Typical Scheme for Excavation of NATM Tunnels

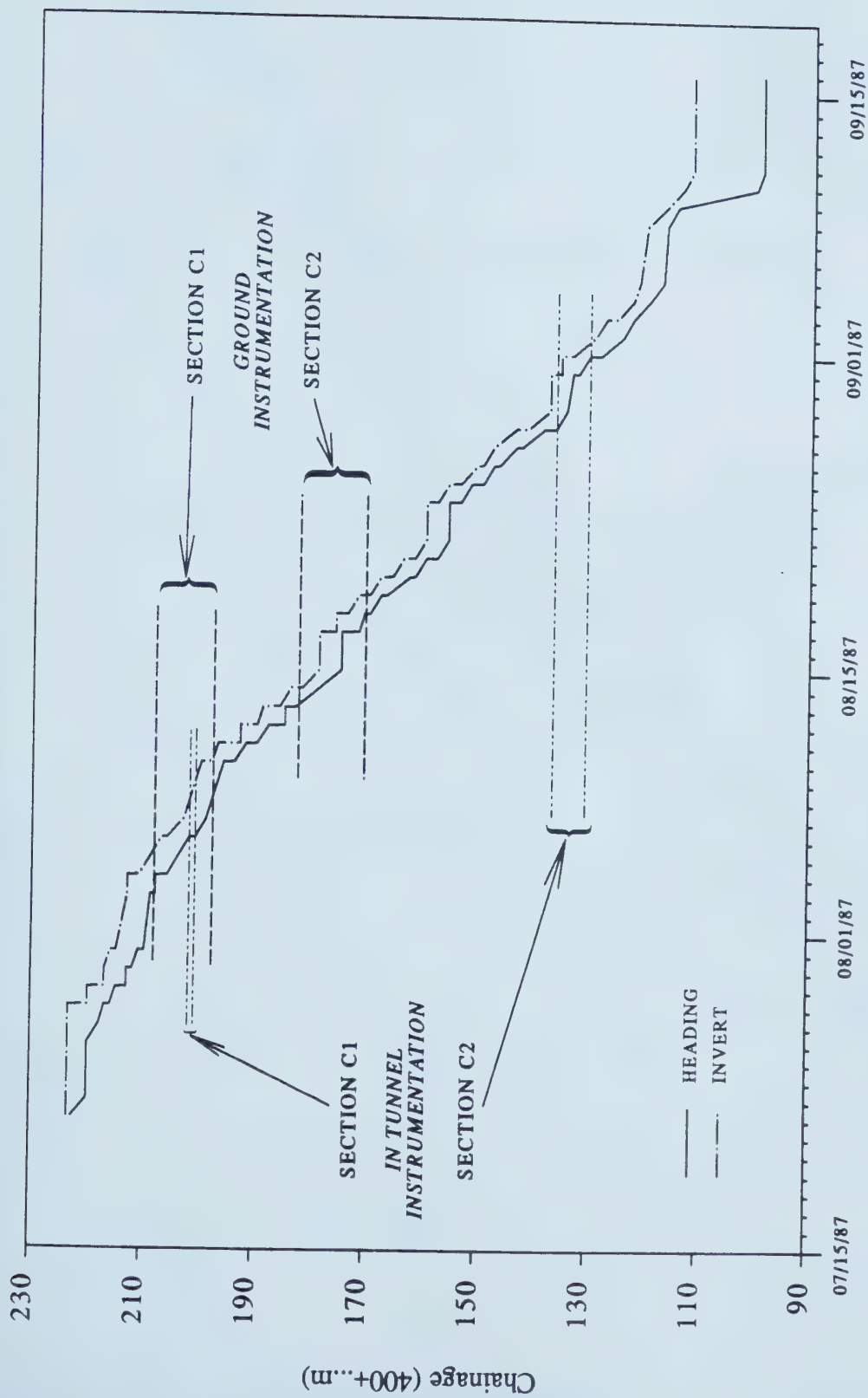


Figure 2.3 Chronologic Advance of North-Bound Tunnel Construction: Heading and Invert positions

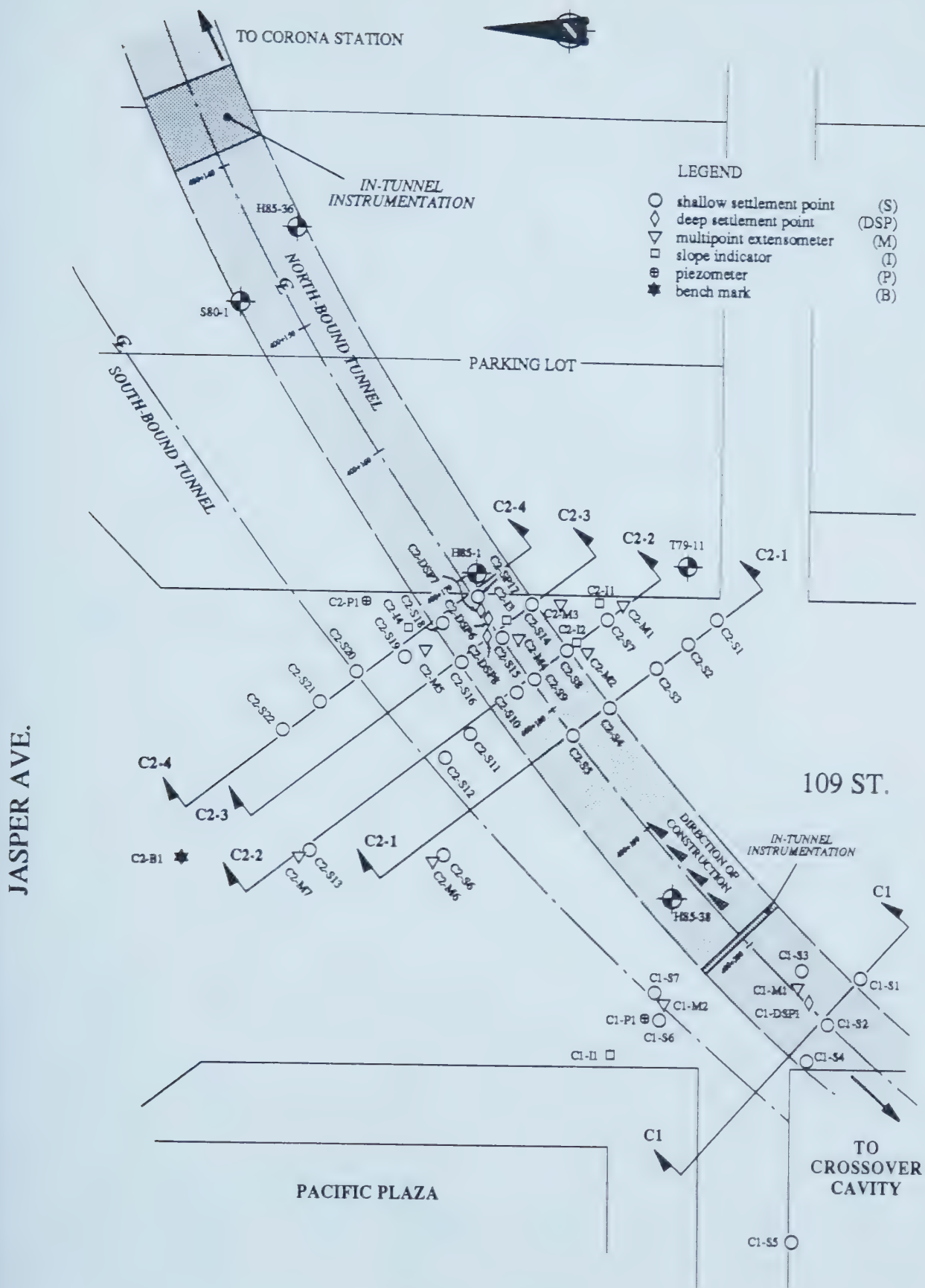


Figure 2.4 Layout of NATM Tunnel Instrumentation

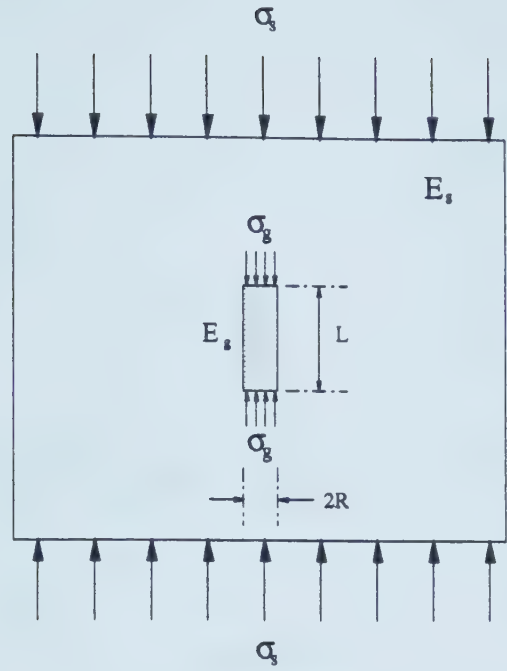


Figure 2.5 Shotcrete Body with Embedded Compression Gage

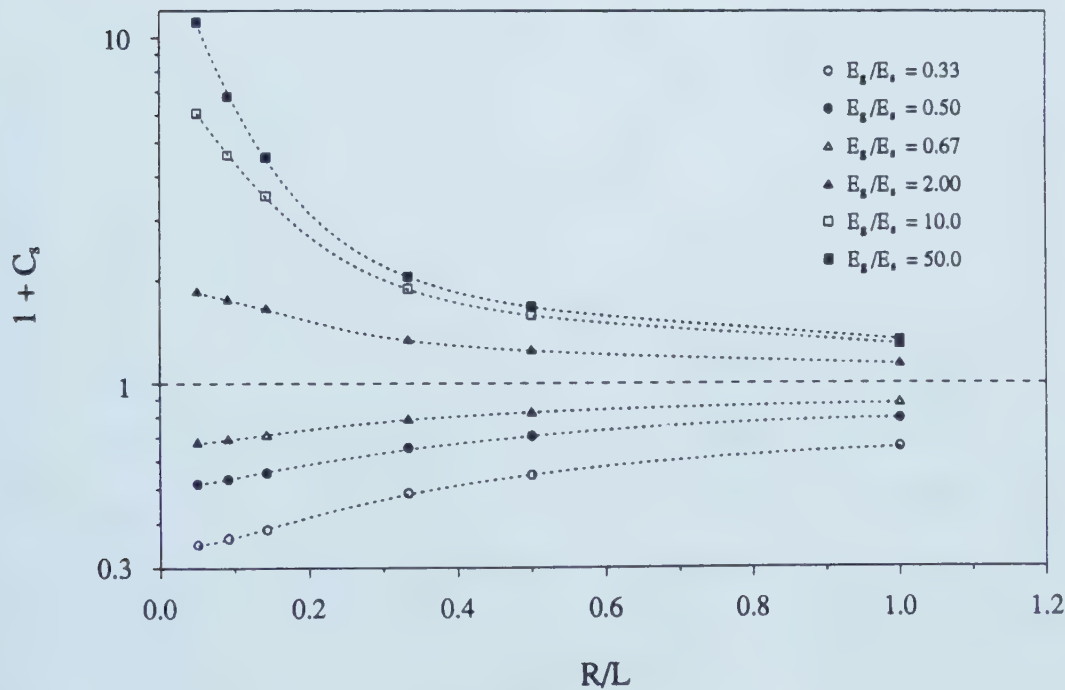


Figure 2.6 Stress Concentration Factor for different Stages of Shotcrete Curing

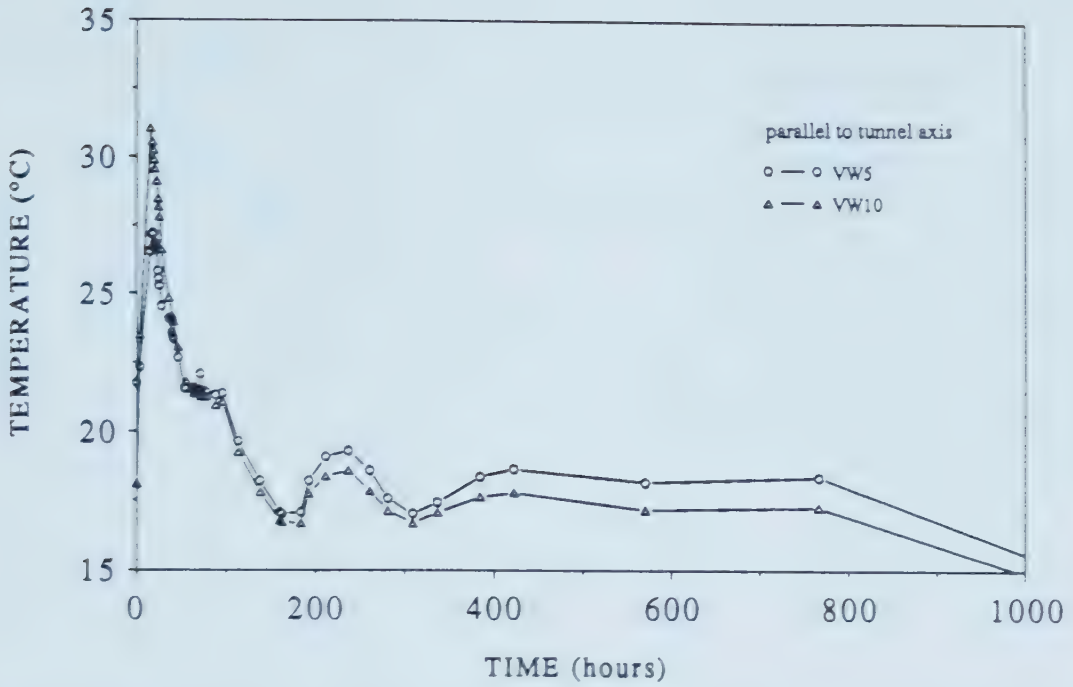


Figure 2.7 Measured Temperature from Gages Embedded in Shotcrete, Section C2I, Springline Region

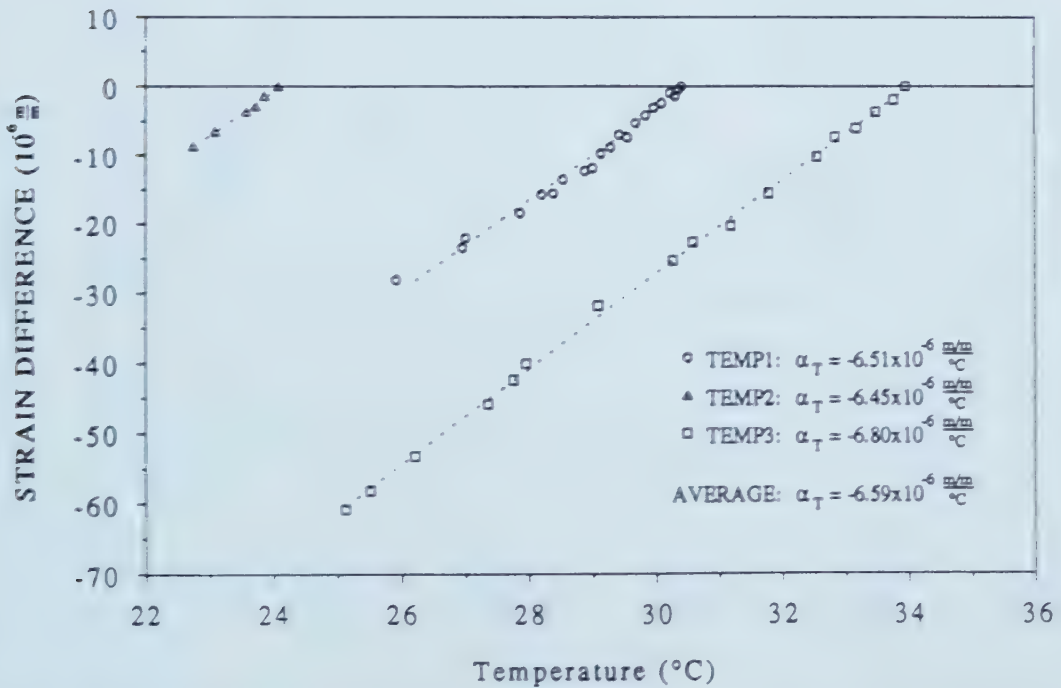


Figure 2.8 Difference of Strain Measured by Embedded Vibrating Wire and Standard Compressometer, Temperature Compensation Factor

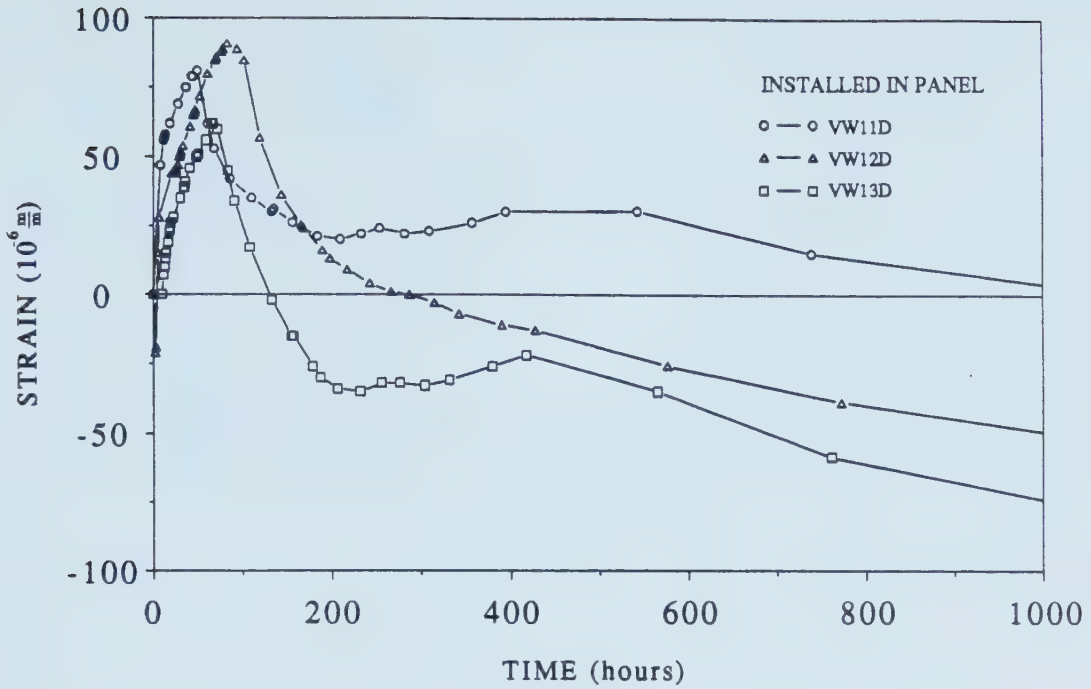


Figure 2.9 Measured Strains from Dummy Gages Embedded in Shotcrete Panels and Left inside the Tunnel

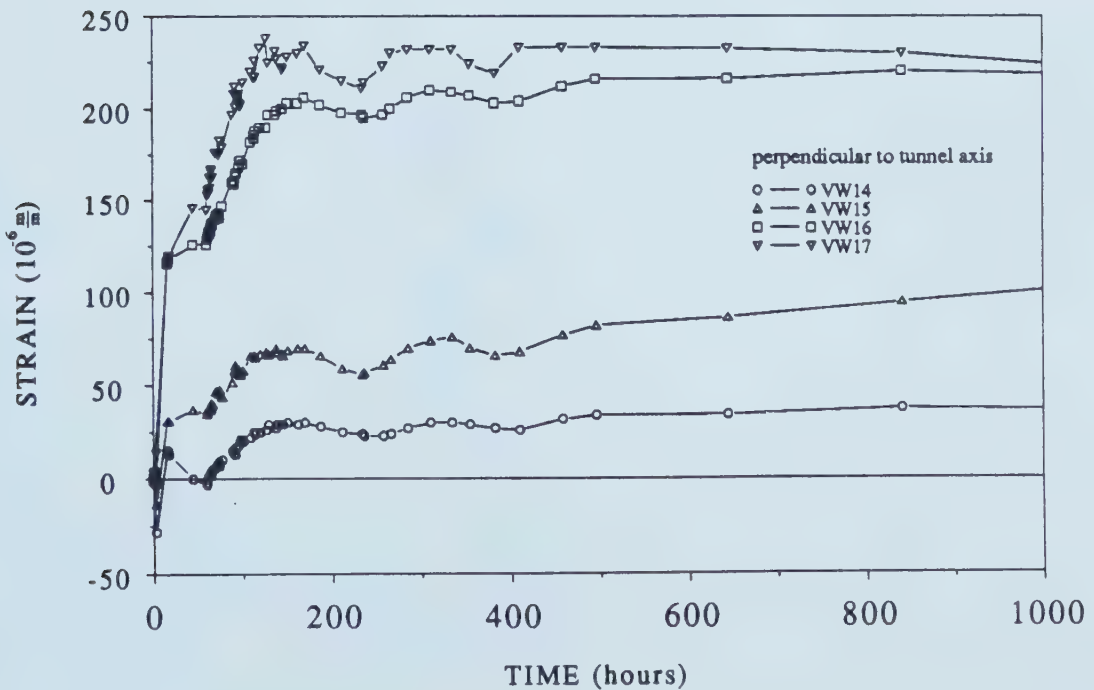


Figure 2.10 Measured Strains from Gages Embedded in Shotcrete, Section C2I, Crown Region

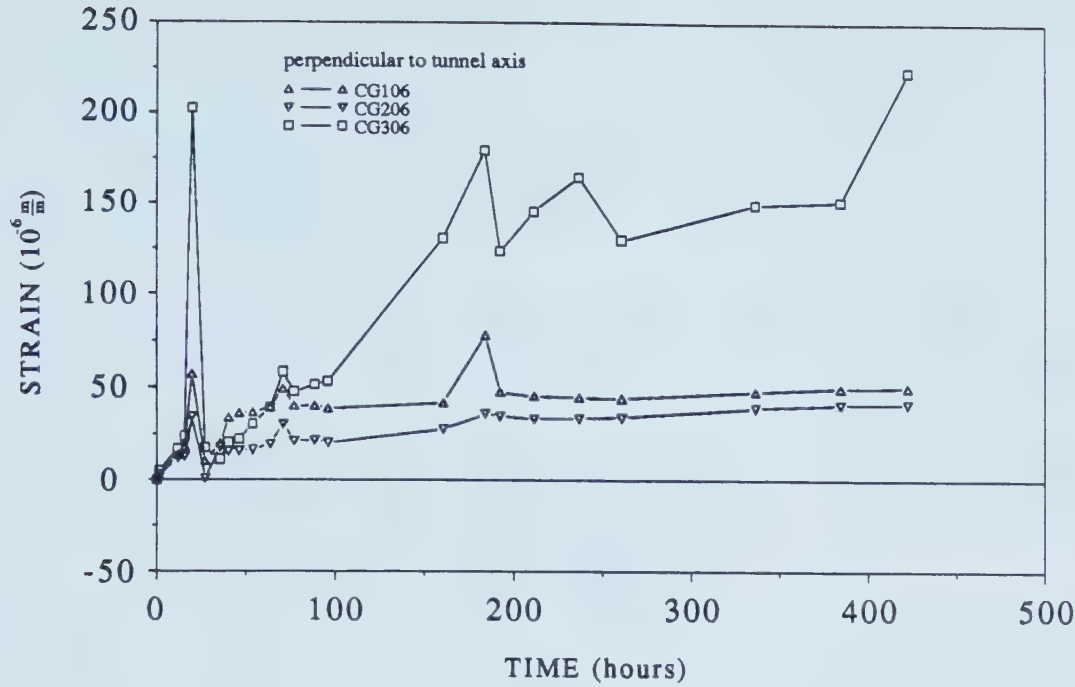


Figure 2.11 Measured Strains from Compression Gages Embedded in Shotcrete, Floor Region, Temperature Compensated

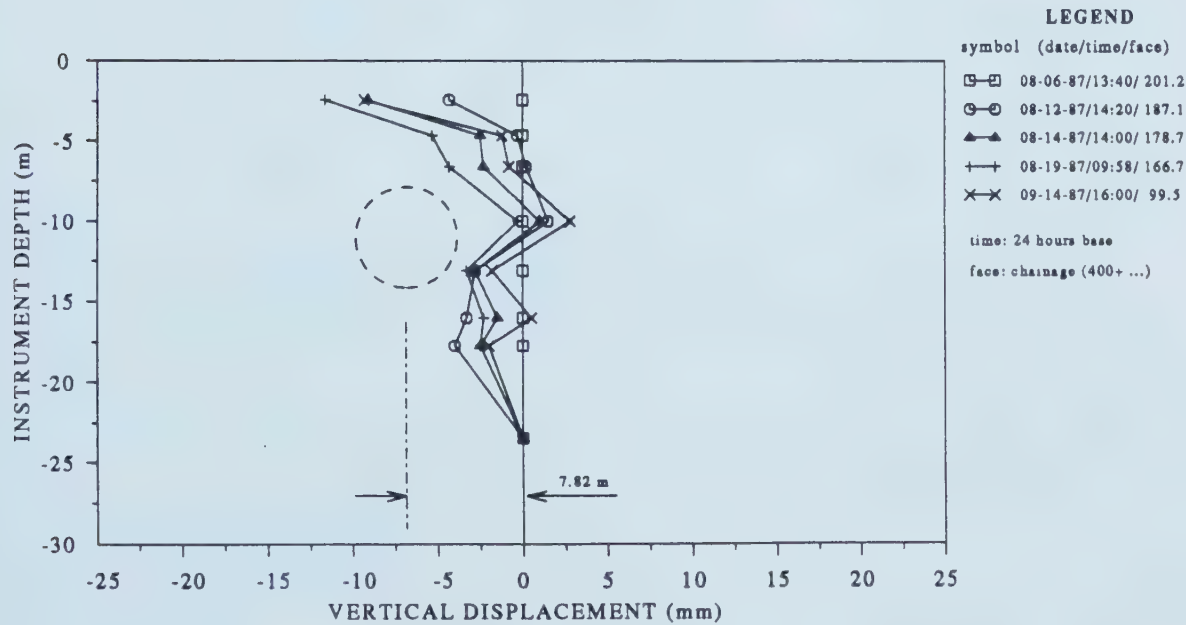


Figure 2.12 Measured Vertical Displacement Profile, Multipoint Extensometer, C2-M1

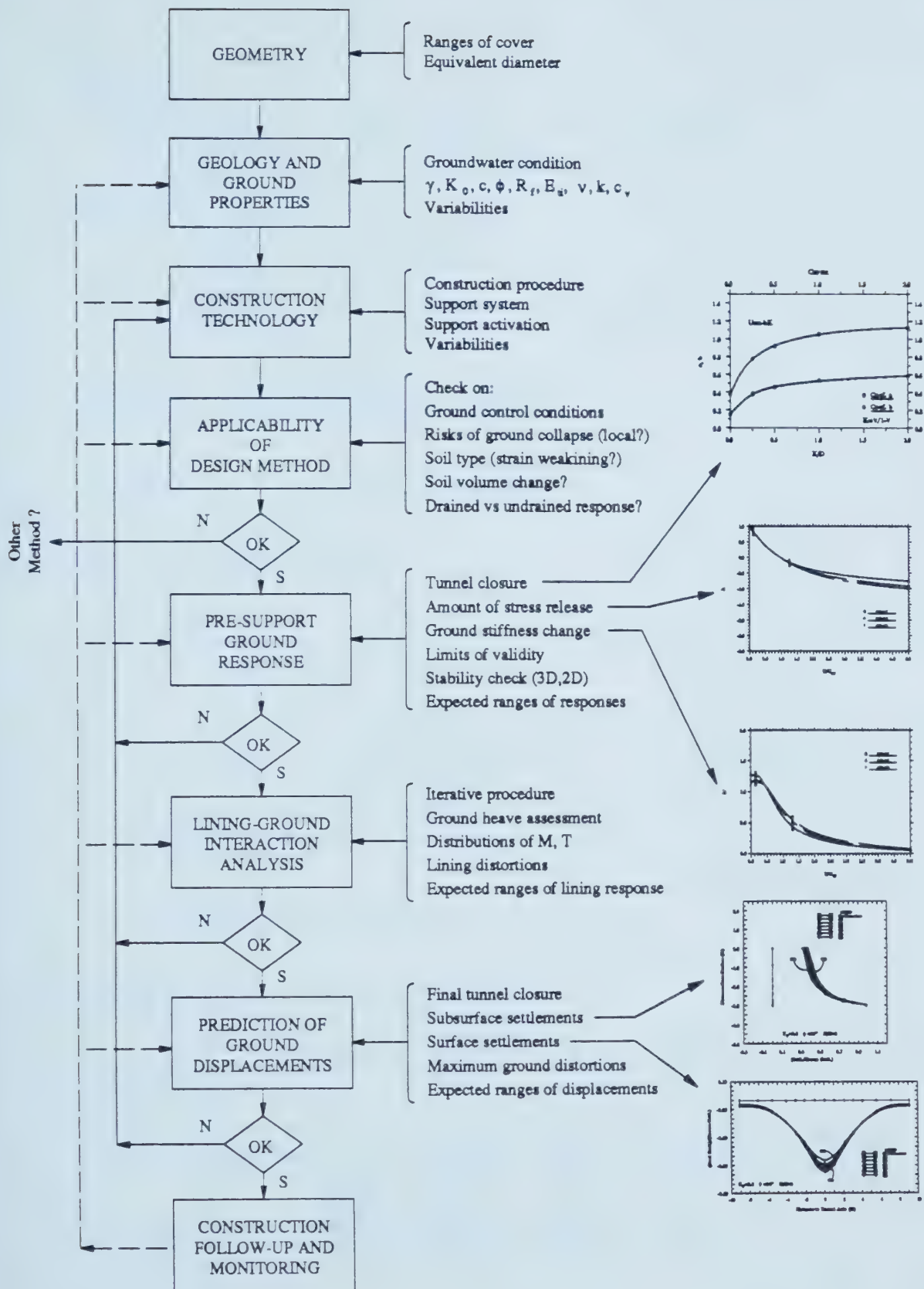


Figure 2.13 Suggested Sequence of Steps for Shallow Tunnel Design (modified from Negro, 1988: 1161)

1. GEOMETRY

$H =$
(crown to surface)

$D =$
(diameter of the tunnel)

$H/D =$

2. GROUND PROPERTIES

$\gamma =$

$K_0 =$

$(\sigma_3)_{axis} =$

$c =$

$\phi =$

$R_f =$

$\phi_a = \arcsin \left(\frac{1 + (\sigma_3/c) \tan (\phi)}{1 + (\sigma_3/c) \sec (\phi)} \right) =$

$\phi_o = \arcsin (1 - R_f + R_f \csc \phi_a)^{-1} =$

$(m-1) = \frac{2 \sin \phi_o}{1 - \sin \phi_o} =$

$K =$

$n =$

$p_a =$

$\mu =$

(Janbu's parameter, 1963)

$E_u = K p_a \left(\frac{\sigma_3}{p_a} \right)^n \left(1 - \frac{R_f (1 - \sin \phi) (\sigma_1 - \sigma_3)}{2 c \cos \phi + 2 \sigma_3 \sin \phi} \right)^2$

(Duncan and Chang, 1970)

Location	σ_3	σ_1	E_u (MPa)
1/2D above C	-	-	40
at S	-	-	69
1/2D below F	-	-	26

(from pressurimeter tests)
(Thurber, 1980: Figure 2.18))

3. TUNNEL CLOSURE AT LINING ACTIVATION

$X =$
(face to lining closure)

$X/D =$

$K_0 =$

$u_r = (D \sigma_{ro} / E_u) U$

Location	U	σ_{ro} (kPa)	$D \sigma_{ro} / E_u$	u_r (mm)
C	0.585	155.40	0.0245	14.3
S	0.459	174.72	0.0160	7.3
F	0.343	281.40	0.0682	23.4

(σ_{ro} : initial radial in situ stress)

Figure 2.14 Calculation Sheet with Geometric Ground Properties Data and Tunnel Closure at Lining Activation (modified from Negro, 1988)

4. REFERENCE VALUES

$H/D =$ 1.23 $K_0 =$ 0.8 $(m - 1) =$ 2.82

	$1 - \Sigma_{ref} = \alpha_{ref}$	α_{ref} / U_{ref}	U_{ref}
C	0.630	0.82	0.768
S	0.605	1.12	0.540
F	0.470	2.03	0.232

5. STRESS RELEASE AND STIFFNESS CHANGE AT LINING ACTIVATION

	U	U/U_{ref}	Beyond Limit?	λ	λ'
C	0.585	0.761	NO	0.175	0.725
S	0.459	0.850	NO	0.1	0.63
F	0.343	1.481	NO	-0.35	0.7

STRESSES : $\Sigma = 1 - (1 - \lambda) \alpha_{ref}$

	$(1 - \lambda)$	Σ
C	0.825	0.480
S	0.9	0.456
F	1.35	0.366

$\bar{\Sigma} = (\Sigma_C + 2\Sigma_S + \Sigma_F)/4 =$ 0.439

$\bar{\alpha} = 1 - \bar{\Sigma} =$ 0.561

$\gamma_{red} = \gamma \bar{\Sigma} =$ 8.784 kN/m³

STIFFNESS : $E_t = (\lambda'/\lambda'_i) E_d$

	λ'_i	E_d / λ'_i	E_t (MPa)
C	1.28	31.25	22.66
S	1.43	48.25	30.40
F	1.01	25.74	18.02

$\bar{E}_t = (E_{tC} + 2E_{tS} + E_{tF})/4 =$ 25.37 MPa

Figure 2.15 Calculation Sheet for Estimates of the Stress Release and Ground Stiffness at the Section the Lining is Activated

6. 2D STABILITY VERIFICATION

$$\bar{\alpha} = \boxed{0.561} \quad \bar{\sigma}_{ro} = \frac{1+K_0}{2} \gamma \left(H + \frac{D}{2} \right) = \boxed{196.5 \text{ kPa}} \quad \phi = \boxed{33^\circ} \quad c/\gamma D = \boxed{0.05} \quad H/D = \boxed{1.23}$$

(approximation for calculation : $\phi = 30^\circ$, $c/\gamma D = 0$)

$$\therefore P_1/\gamma D = \boxed{0.2} \quad P_1 = \boxed{25.2 \text{ kPa}} \quad \alpha_1 = 1 - P_1/\bar{\sigma}_{ro} = \boxed{0.872}$$

$$FS = \frac{[(1 - K_0)(1 + K_0) + \alpha_1]}{[(1 - K_0)(1 + K_0 + \bar{\alpha})]} = \boxed{1.46}$$

7. LINING-GROUND INTERACTION

GEOMETRY : $Z_0 = \boxed{10.92 \text{ m}} \quad r_0 = \boxed{3.15 \text{ m}} \quad r_1 = \boxed{10.92 \text{ m}}$

SOIL : $\bar{E}_t = \boxed{25.37 \text{ MPa}} \quad \mu = \boxed{0.35} \quad \gamma_{red} = \boxed{8.78 \text{ kN/m}^3} \quad K_0 = \boxed{0.8}$

LINING : $E_t = \boxed{10000 \text{ MPa}} \quad \mu_s = \boxed{0.25} \quad d = \boxed{0.18 \text{ m}} \quad I_s = \boxed{4.86 \cdot 10^{-4} \text{ m}^4}$

ITERATION NO.: 1 $\bar{E}_t = \boxed{25.37 \text{ MPa}} \quad \alpha = \boxed{32.44} \quad \beta = \boxed{8.83 \cdot 10^{-3}}$

	u_r (mm)	Δu_r (mm)	$u_{rf} =$ $u_r + \Delta u_r + v_{so}^*$	U	U/ U_{ref}	λ'	E_t (MPa)	σ_r (kPa)
C	14.32	2.37	13.14	0.537	0.699	0.825	25.78	66.37
S	7.32	-1.66	5.67	0.355	0.658	0.84	40.53	89.21
F	23.39	2.67	29.61	0.434	1.875	0.59	15.19	90.19

$$v_{so}^* = \frac{(1+\mu)(3-4\mu)}{4(1-\mu)E_t} \gamma_{red} r_0^2 \ln \frac{r_0}{r_1} = \boxed{3.55 \text{ mm}} \quad (\bar{E}_t)_{new} = (E_{tc} + 2E_{ts} + E_{tf})/4 = \boxed{30.51 \text{ MPa}}$$

Figure 2.16 Calculation Sheet for 2D Stability Verification and Lining-Ground Interaction Analysis (modified from Negro, 1988)

ITERATION NO.: 2

$\bar{E}_t =$

30.51 MPa

$\alpha =$

26.97

$\beta =$

$7.34 \cdot 10^{-3}$

	u_r (mm)	Δu_r (mm)	$u_{rf} =$ $u_r + \Delta u_r + v_{zo}^*$	U	U/ U_{ref}	λ'	E_t (MPa)	σ_r (kPa)
C	14.32	2.05	13.42	0.548	0.714	0.8	25.00	65.84
S	7.32	-1.33	6.00	0.376	0.696	0.805	38.84	88.87
F	23.39	2.32	28.66	0.420	1.816	0.605	15.57	89.39

$v_{zo}^* = \frac{(1+\mu)(3-4\mu)}{4(1-\mu)\bar{E}_t} \gamma_{red} r_0^2 \ln \frac{r_0}{r_1} =$

2.95 mm

$(\bar{E}_t)_{new} = (E_{tc} + 2E_{ts} + E_{tf})/4 =$

29.73 MPa

ITERATION NO.: 3

$\bar{E}_t =$

29.73 MPa

$\alpha =$

27.83

$\beta =$

$7.57 \cdot 10^{-3}$

	u_r (mm)	Δu_r (mm)	$u_{rf} =$ $u_r + \Delta u_r + v_{zo}^*$	U	U/ U_{ref}	λ'	E_t (MPa)	σ_r (kPa)
C	14.32	2.102	13.38	0.546	0.711	0.8	25.00	65.93
S	7.32	-1.379	5.94	0.373	0.690	0.805	38.84	88.94
F	23.39	2.378	28.81	0.423	1.825	0.6	15.45	89.53

$v_{zo}^* = \frac{(1+\mu)(3-4\mu)}{4(1-\mu)\bar{E}_t} \gamma_{red} r_0^2 \ln \frac{r_0}{r_1} =$

3.04 mm

$(\bar{E}_t)_{new} = (E_{tc} + 2E_{ts} + E_{tf})/4 =$

29.53 MPa

$\bar{E}_t \equiv (\bar{E}_t)_{new} \Rightarrow$ end of iteration

ITERATION NO.: _

$\bar{E}_t =$

$\alpha =$

$\beta =$

	u_r (mm)	Δu_r (mm)	$u_{rf} =$ $u_r + \Delta u_r + v_{zo}^*$	U	U/ U_{ref}	λ'	E_t (MPa)	σ_r (kPa)
C								
S								
F								

$v_{zo}^* = \frac{(1+\mu)(3-4\mu)}{4(1-\mu)\bar{E}_t} \gamma_{red} r_0^2 \ln \frac{r_0}{r_1} =$

$(\bar{E}_t)_{new} = (E_{tc} + 2E_{ts} + E_{tf})/4 =$

Figure 2.17 Calculation Sheet for Iterative Analysis of the Lining-Ground Interaction, (modified from Negro, 1988)

8. SUBSURFACE SETTLEMENTS

CROWN SETTL. = 13.38 mm

$U/U_{ref} = 0.711$

$\lambda_c = 0.22$

$\alpha_c = (1 - \lambda_c) \alpha_{ref} = 0.49$

$K_0 = 0.8$

$\phi = 33$

Depth Z (m)	Z/H	SETTLEMENT/CROWN SETTL.			SETTLEMENT NT (mm)
		H/D=1.5	H/D=3	H/D=1.23	
0	0	0.52	0.375	0.5461	7.30
2.59	0.333	0.59	0.44	0.617	8.25
4.53	0.583	0.665	0.5	0.6947	9.29
6.47	0.833	0.8	0.655	0.8261	11.05
7.12	0.916	0.875	0.765	0.8948	11.97
7.77	1	1	1	1	13.38

9. SURFACE SETTLEMENTS

$\alpha_c = 0.49$

$K_0 = 0.8$

$\phi = 33$

DIST. Y(m)		0	3.15	6.3	12.6	18.9
Y/D		0	0.5	1.0	2.0	3.0
SETTL. CROWN SETTL.	H/D=1.50	0.52	0.46	0.365	0.21	0.13
	H/D=3.00	0.375	0.365	0.335	0.245	0.175
	H/D=1.23	0.546	0.477	0.370	0.204	0.122
SETTL. (mm)		7.30	6.38	4.95	2.72	1.63

MAX. DISTOR : $\gamma_c = 1 : 2207$

Trough correction:

$\gamma_{cc} = 1.4 \gamma_c \Rightarrow \gamma_{cc} = 1 : 1576$

$i = 0.606 \frac{s_{max}}{\gamma_{cc}}$

$s = s_{max} e^{-x^2/2i^2}$ (settlement trough : normal probability curve)

where s_{max} is the surface settlement as calculated for $Y/D=0$ in item 9

Figure 2.18 Calculation Sheets for Iterative Analysis of the Lining Ground Interaction and for Subsurface and Surface Settlements (modified from Negro, 1988)

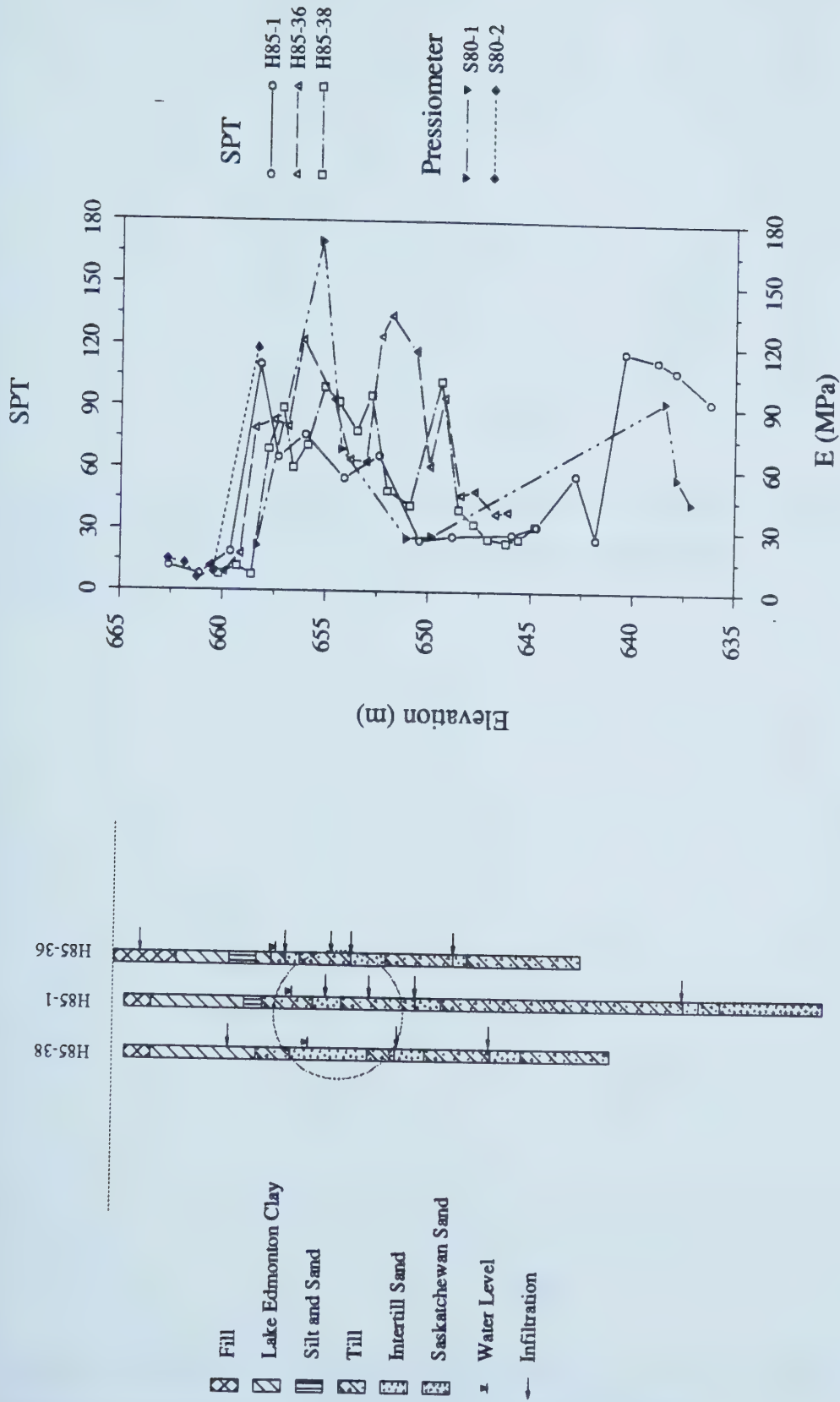


Figure 2.19 Geotechnical Profile and In Situ Tests at Instrumented Section Site

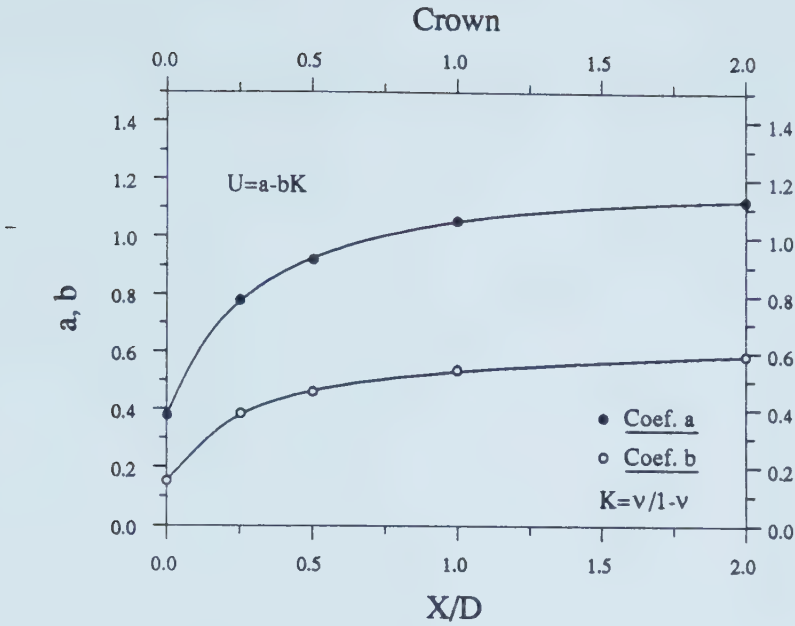


Figure 2.20 Coefficients of the U and K Relationship for the Crown of an Unlined Shallow Tunnel, ($1.5 < H/D < 3.0$) as a Function of the Distance to the Face (modified from Negro, 1988: 792)

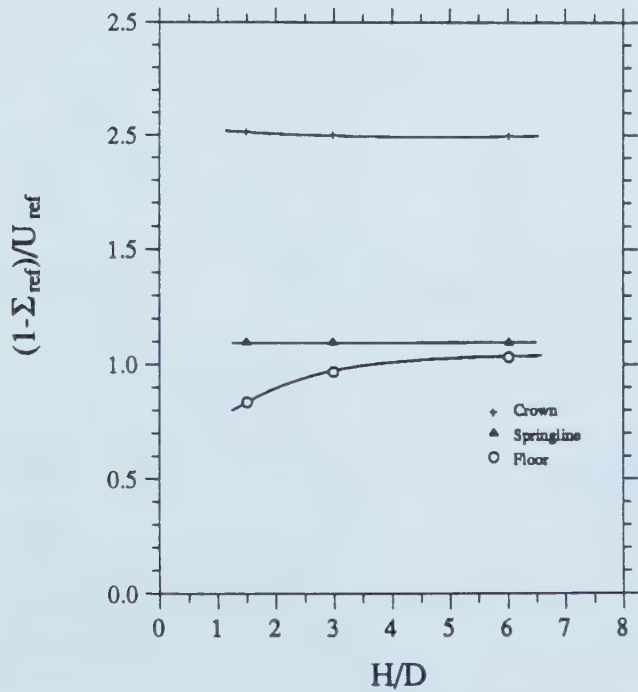


Figure 2.21 Slopes of the Arbitrary Axis used to Obtain the NNRC Represented as a Function of H/D , for $K = 0.8$ (modified from Negro, 1988:1061)

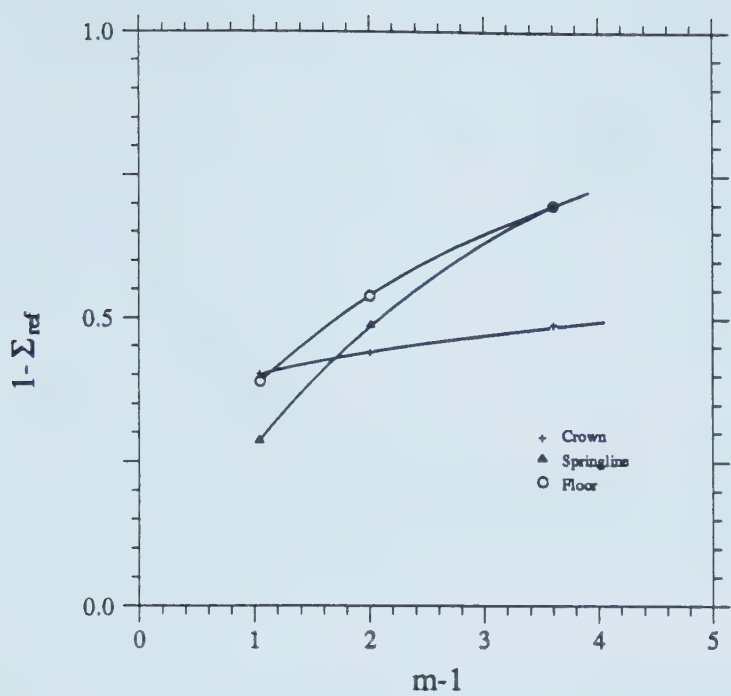


Figure 2.22 Relationships between α_{ref} and the Friction Angle for $K_0=0.8$ (modified from Negro, 1988: 1062)

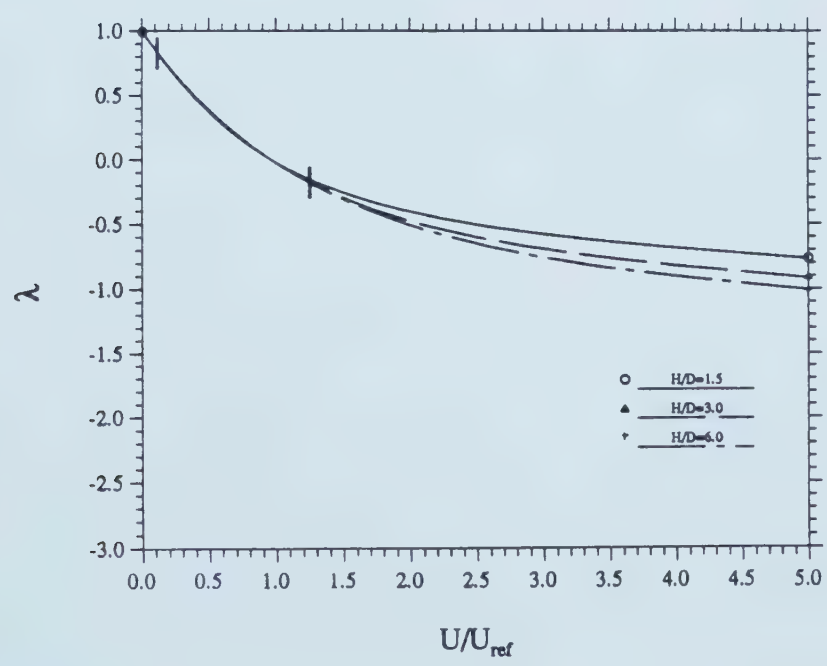


Figure 2.23 NNGRCs for Tunnel Crown, Calculated for $K_0=0.8$ (modified from Negro, 1988:1063)

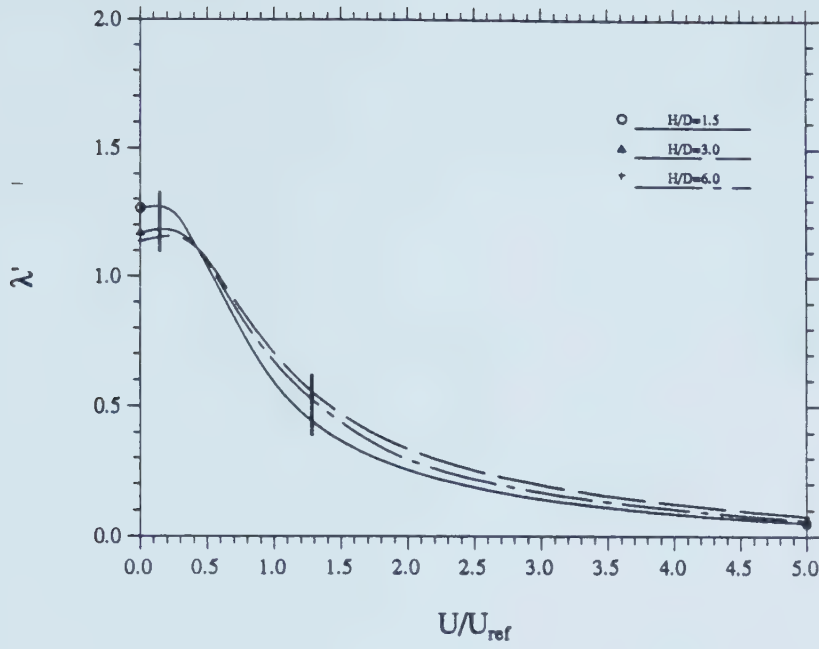


Figure 2.24 Variations of λ' for the Tunnel Crown, Calculated for $K_0=0.8$ (modified from Negro, 1988:1076)

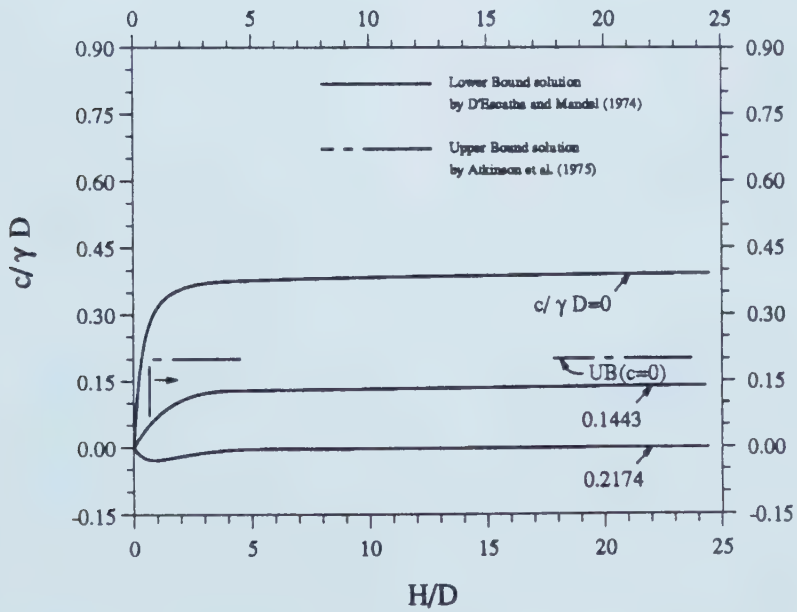


Figure 2.25 Lower and Upper Bound Solutions for Tunnel Collapse Pressure in a Frictional and Cohesive Soil, $\phi=30^\circ$, (modified from Negro, 1988: 1099)

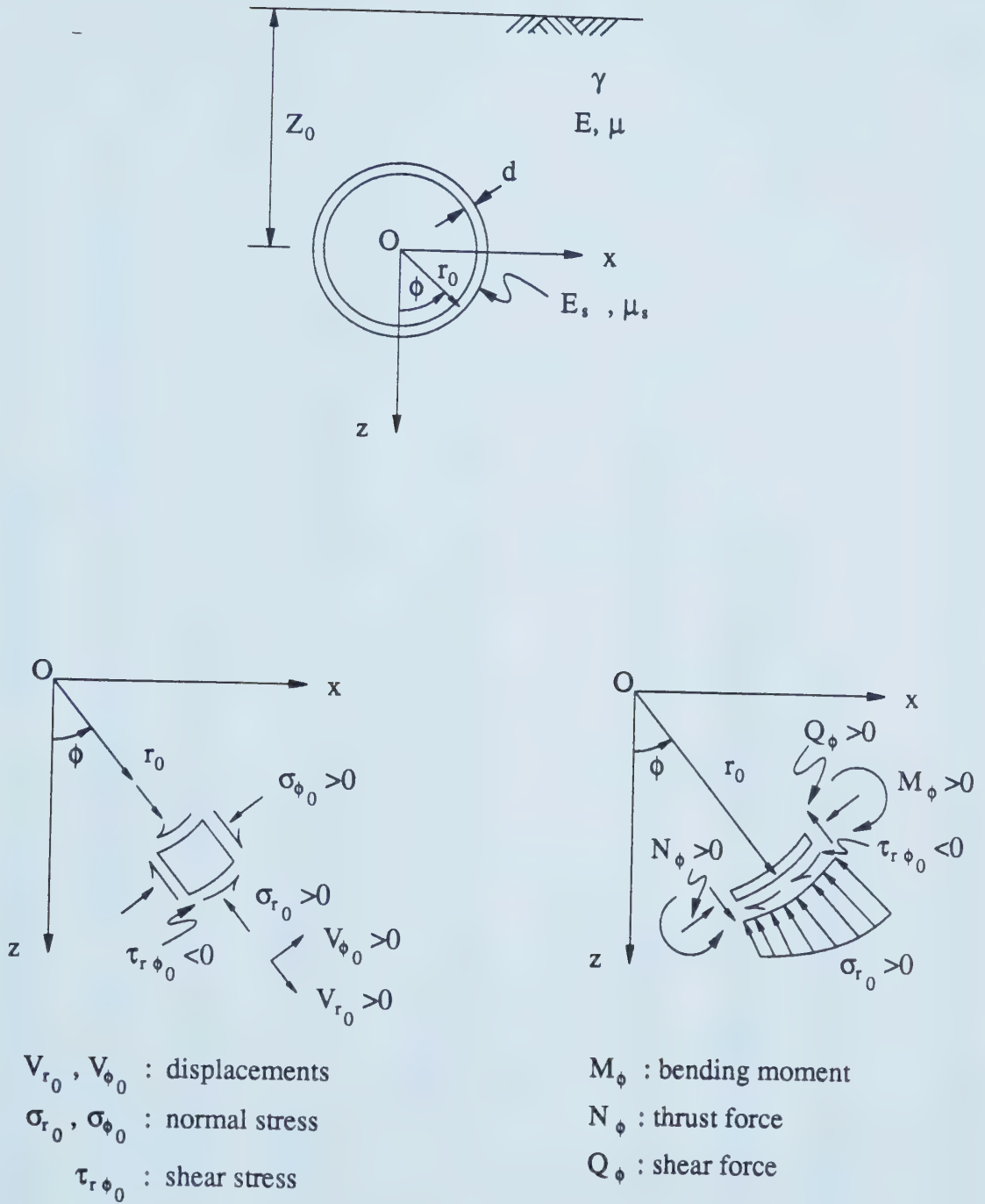


Figure 2.26 Notations and Conventions used in Hartmann's Solution (modified from Negro, 1988:1124)

$$(7.1) \quad \frac{\alpha}{E} = \frac{E_s A_s (1+\mu)}{E r_0 (1-\mu_s^2)} \quad \beta = \frac{E_s I_s (1+\mu)}{E r_0^3 (1-\mu_s^2)} \quad (7.2)$$

$$\sigma_{r0} = \frac{(1+K)(\alpha+\beta)}{2(1+\alpha+\beta)} \gamma_{r0} + \frac{(1+K)\alpha}{4(1+\alpha)} \gamma_{r0} \cos \phi - \frac{(1-K)(3-4\mu)(\alpha-9\beta-12\alpha\beta)}{2(1+(3-2\mu)\alpha+3(5-6\mu+4(3-4\mu)\alpha)\beta)} \gamma_{r0} \cos(2\phi) - \frac{(1-K)(3-4\mu)(\alpha-32\beta-72\alpha\beta)}{4(1+(5-4\mu)\alpha+8(7-8\mu+9(3-4\mu)\alpha)\beta)} \gamma_{r0} \cos(3\phi) \quad (7.3)$$

$$\sigma_{\phi 0} = \frac{(1+K)(2+\alpha+\beta)}{2(1+\alpha+\beta)} \gamma_{r0} + \frac{2+\alpha+(K-\mu-\mu_s)(4+3\alpha)}{4(1-\mu)(1+\alpha)} \gamma_{r0} \cos \phi - \frac{(1-K)(4+(3+4\mu)\alpha+3(11-12\mu+4(3-4\mu)\alpha)\beta)}{2(1+(3-2\mu)\alpha+3(5-6\mu+4(3-4\mu)\alpha)\beta)} \gamma_{r0} \cos(2\phi) - \frac{(1-K)(4+(5+4\mu)\alpha+8(16-16\mu+9(3-4\mu)\alpha)\beta)}{4(1+(5-4\mu)\alpha+8(7-8\mu+9(3-4\mu)\alpha)\beta)} \gamma_{r0} \cos(3\phi) \quad (7.4)$$

$$\tau_{r\phi 0} = \frac{(1+K)\alpha}{4(1+\alpha)} \gamma_{r0} \sin \phi - \frac{(1-K)(3-4\mu)(1+6\beta)\alpha}{1+(3-2\mu)\alpha+3(5-6\mu+4(3-4\mu)\alpha)\beta} \gamma_{r0} \sin(2\phi) - \frac{3(1-K)(3-4\mu)(1+24\beta)\alpha}{4(1+(5-4\mu)\alpha+8(7-8\mu+9(3-4\mu)\alpha)\beta)} \gamma_{r0} \sin(3\phi) \quad (7.5)$$

$$\mathbf{v}_{r0} = \mathbf{v}_{r0}' + \mathbf{v}_{r0}'' \cos \phi \quad (7.6)$$

$$\mathbf{v}_{r0}' = -\frac{1+\mu}{E} \left[\frac{1+K}{2(1+\alpha+\beta)} \gamma_{r0} \gamma_0 + \frac{(1+K)}{8(1+\alpha)} \gamma_{r0}^2 \cos \phi + \frac{(1-K)(3-4\mu)(1+2\alpha)}{2(1+(3-2\mu)\alpha+3(5-6\mu+4(3-4\mu)\alpha)\beta)} \gamma_{r0} \gamma_0 \cos(2\phi) + \frac{(1-K)(3-4\mu)(1+3\alpha)}{8(1+(5-4\mu)\alpha+8(7-8\mu+9(3-4\mu)\alpha)\beta)} \gamma_{r0}^2 \cos(3\phi) \right] \quad (7.7)$$

$$\mathbf{v}_{\phi 0} = \mathbf{v}_{\phi 0}' + \mathbf{v}_{\phi 0}'' \cos \phi \quad (7.8)$$

$$\mathbf{v}_{\phi 0}' = \frac{1+\mu}{E} \left[-\frac{1+K}{8(1+\alpha)} \gamma_{r0}^2 \sin \phi + \frac{(1-K)(3-4\mu)(1+\alpha+3\beta)}{2(1+(3-2\mu)\alpha+3(5-6\mu+4(3-4\mu)\alpha)\beta)} \gamma_{r0} \gamma_0 \sin(2\phi) + \frac{(1-K)(3-4\mu)(1+\alpha+16\beta)}{8(1+(5-4\mu)\alpha+8(7-8\mu+9(3-4\mu)\alpha)\beta)} \gamma_{r0}^2 \sin(3\phi) \right] \quad (7.9)$$

$$\mathbf{v}_{\infty}'' = \frac{(1+\mu)(3-4\mu)}{4(1-\mu)E} \gamma_{r0}^2 \ln \frac{r_0}{r_1} \quad (7.10)$$

$$N_{\phi} = \frac{(1+K)(\alpha+\beta)}{2(1+\alpha+\beta)} \gamma_{r0} \gamma_0 + \frac{(1+K)\alpha^2}{4(1+\alpha)} \gamma_{r0}^2 \cos \phi - \frac{(1-K)(3-4\mu)(\alpha+3\beta+12\alpha\beta)}{2(1+(3-2\mu)\alpha+3(5-6\mu+4(3-4\mu)\alpha)\beta)} \gamma_{r0} \gamma_0 \cos(2\phi) - \frac{(1-K)(3-4\mu)(\alpha+4\beta+36\alpha\beta)}{4(1+(5-4\mu)\alpha+8(7-8\mu+9(3-4\mu)\alpha)\beta)} \gamma_{r0}^2 \cos(3\phi) \quad (7.11)$$

$$M_{\phi} = -\frac{(1+K)\beta}{2(1+\alpha+\beta)} \gamma_{r0}^2 + \frac{3(1-K)(3-4\mu)(1+2\alpha)\beta}{2(1+(3-2\mu)\alpha+3(5-6\mu+4(3-4\mu)\alpha)\beta)} \gamma_{r0}^2 \cos(2\phi) + \frac{(1-K)(3-4\mu)(1+3\alpha)\beta}{1+(5-4\mu)\alpha+8(7-8\mu+9(3-4\mu)\alpha)\beta} \gamma_{r0}^3 \cos(3\phi) \quad (7.12)$$

$$Q_{\phi} = -\frac{3(1-K)(3-4\mu)(1+2\alpha)\beta}{(1+(3-2\mu)\alpha+3(5-6\mu+4(3-4\mu)\alpha)\beta)} \gamma_{r0} \gamma_0 \sin(2\phi) - \frac{3(1-K)(3-4\mu)(1+3\alpha)\beta}{1+(5-4\mu)\alpha+8(7-8\mu+9(3-4\mu)\alpha)\beta} \gamma_{r0}^2 \sin(3\phi) \quad (7.13)$$

Figure 2.27 Lining Stresses, Displacements and Internal Forces Given by Hartmann's Solution (modified from Negro, 1988: 1125)

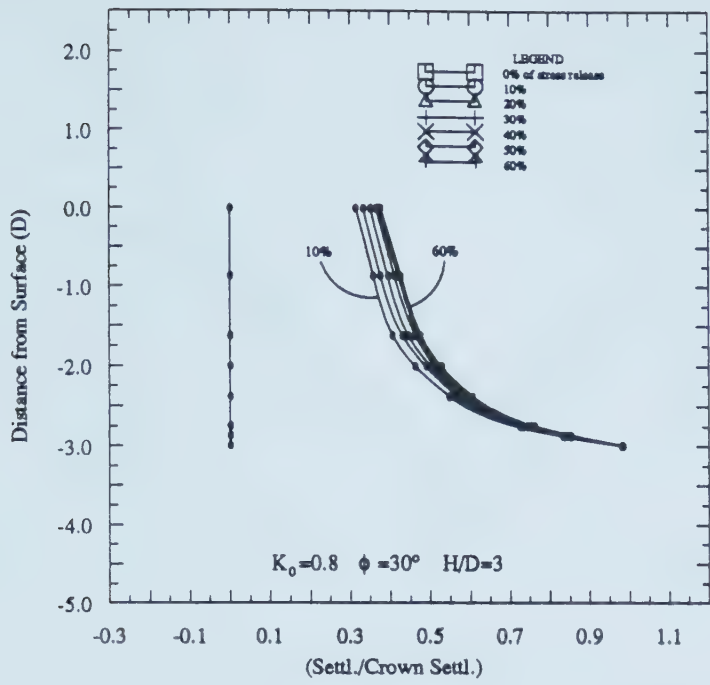


Figure 2.28 Normalized Subsurface Settlements for $H/D=3$, $K_0=0.8$ and $\phi=30^\circ$, Calculated for Increasing Amount of Stress Release (modified from Negro, 1988: 979)

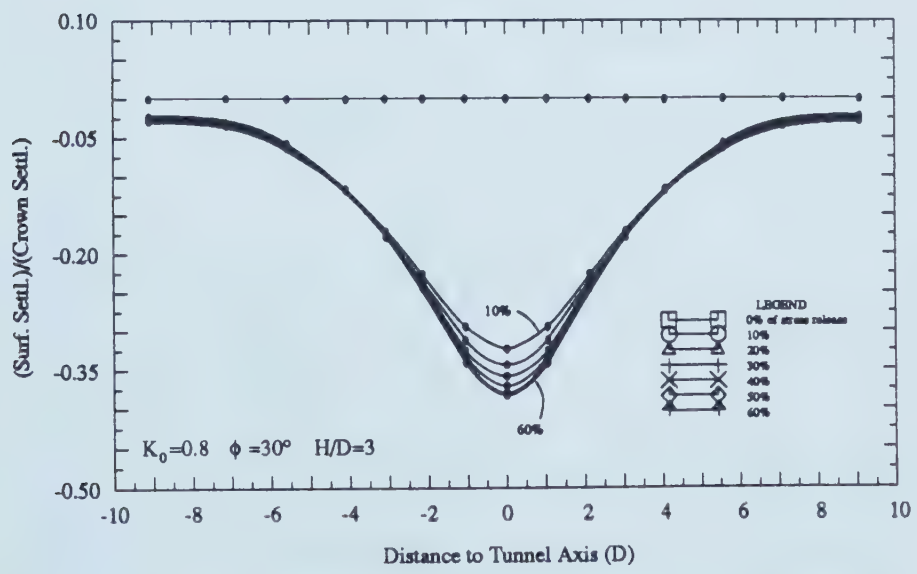


Figure 2.29 Normalized Surface Settlements for $H/D=3$, $K_0=0.8$ and $\phi=30^\circ$, Calculated for Increasing Amount of Stress Release (modified from Negro, 1988: 980)

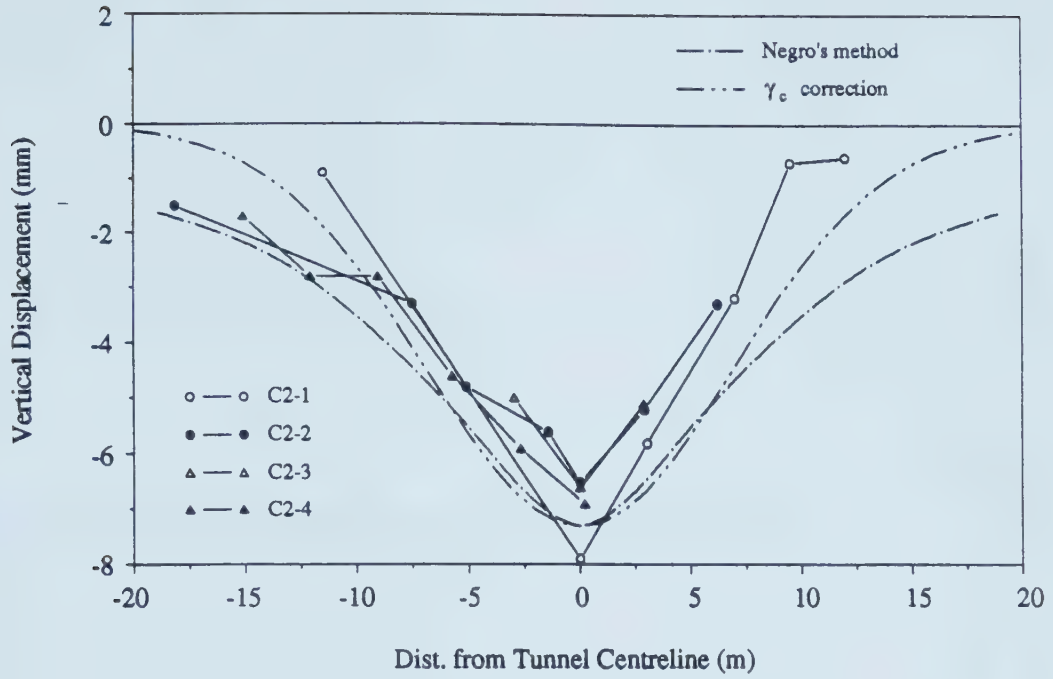


Figure 2.30 Measured and Calculated Transverse Settlement Distribution

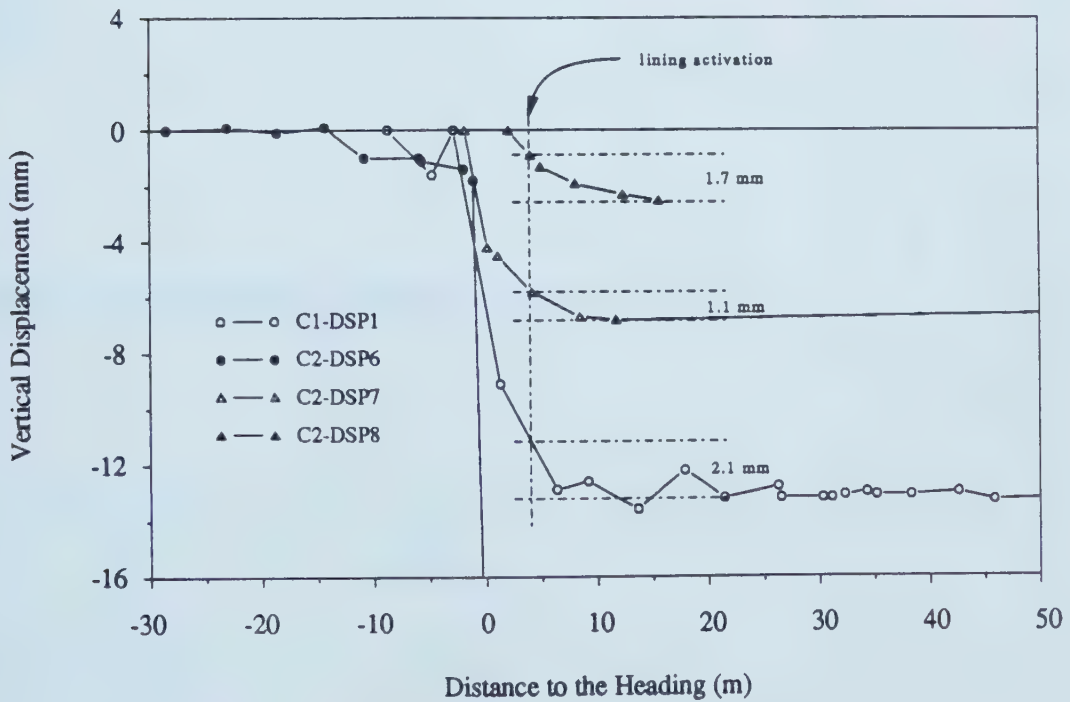


Figure 2.31 Measured and Calculated Settlement at Crown Region

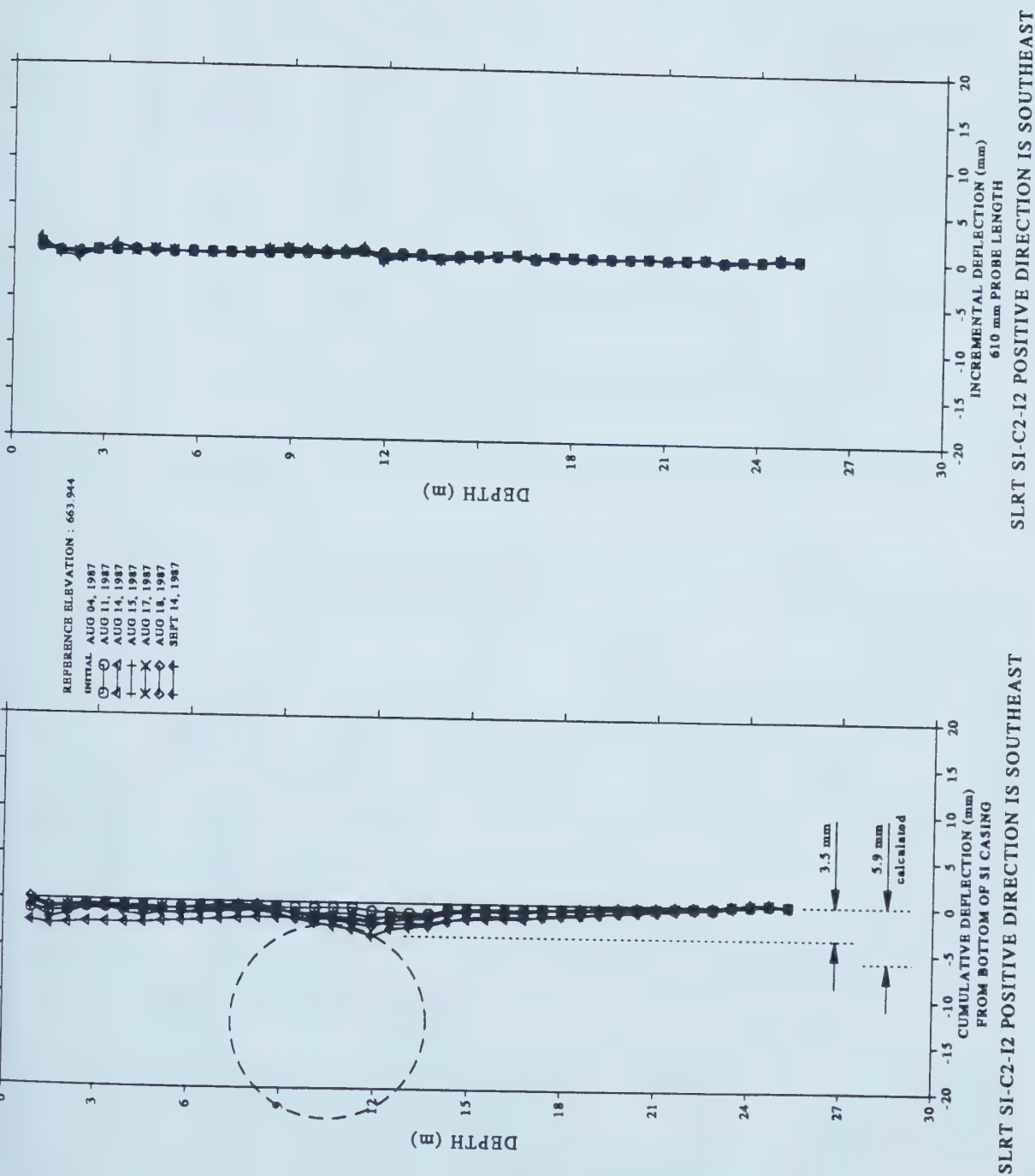


Figure 2.32 Measured Horizontal Displacement Profile, Perpendicular to Tunnel Axis, Slope Indicator, C2-I2

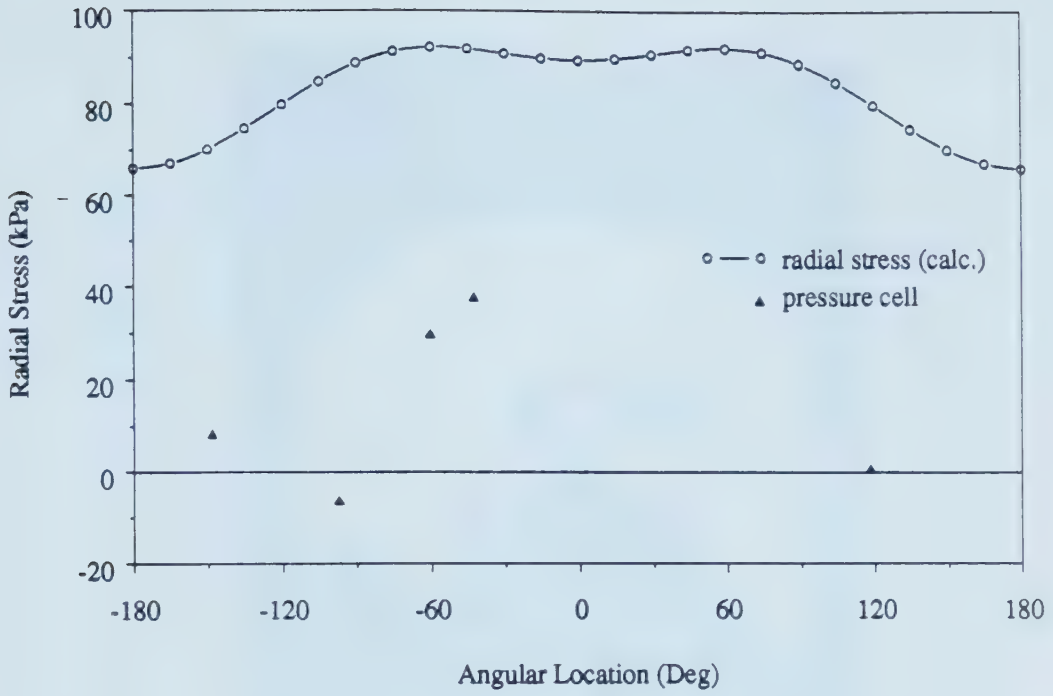


Figure 2.33 Measured and Calculated Radial Stresses at Soil-Lining Interface

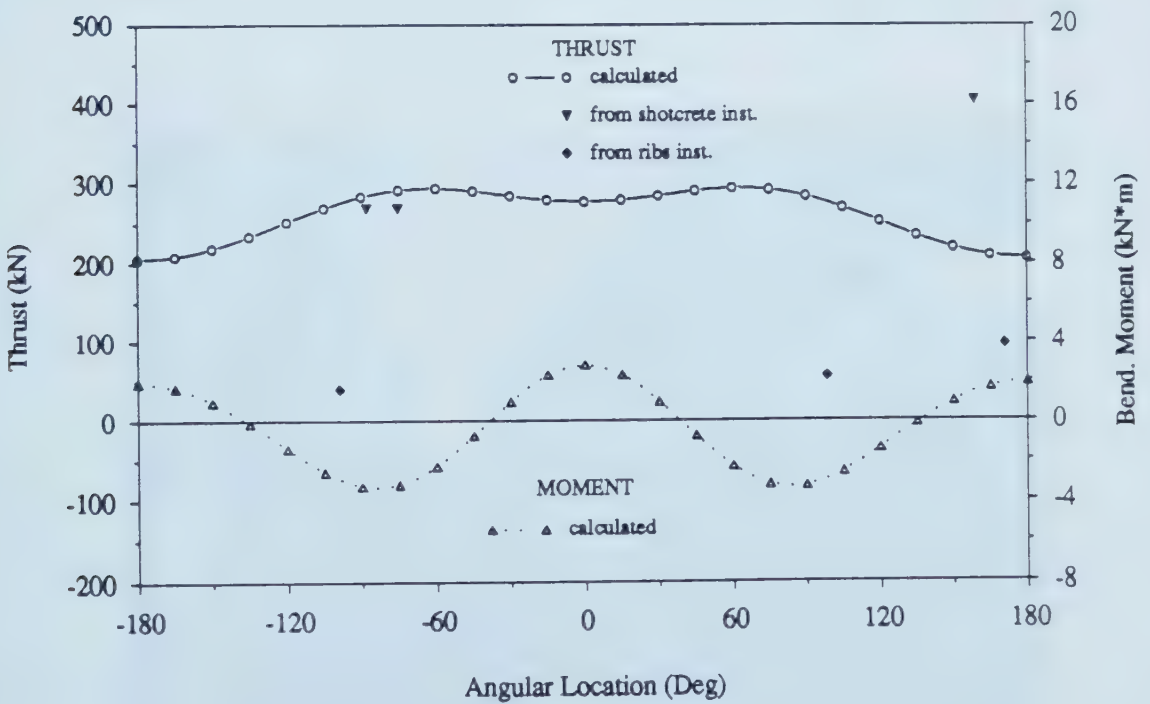


Figure 2.34 Bending Moment and Thrust Calculated and Results from Preliminary Simplified Interpretation of Embedded Gages



Plate 2.1 Excavator used at SLRT Project for Construction of NATM Tunnels



Plate 2.2 Loader used at SLRT Project for Construction of NATM Tunnels

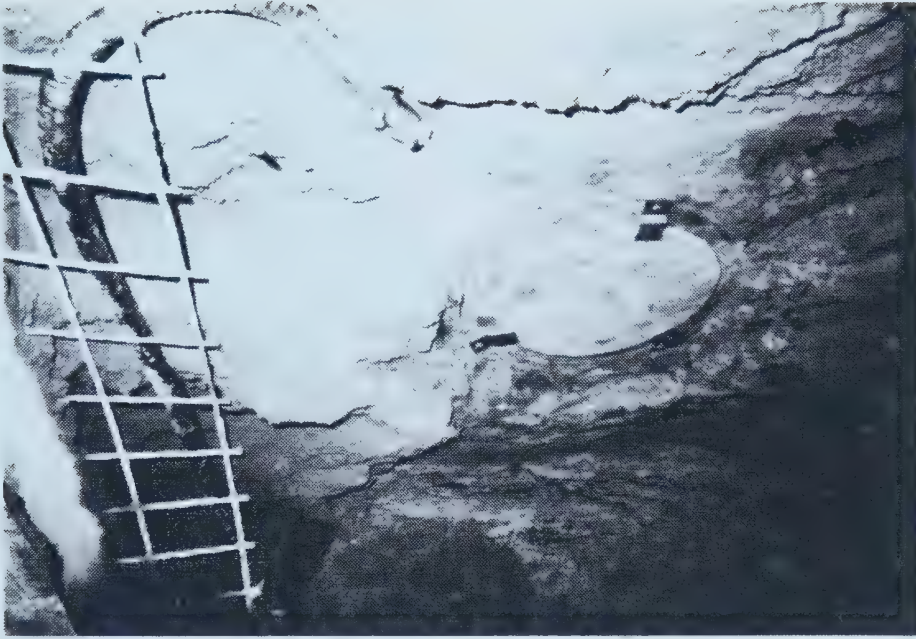


Plate 2.3 Detail of Total Pressure Cell Fixation to Ground, before Application of Shotcrete

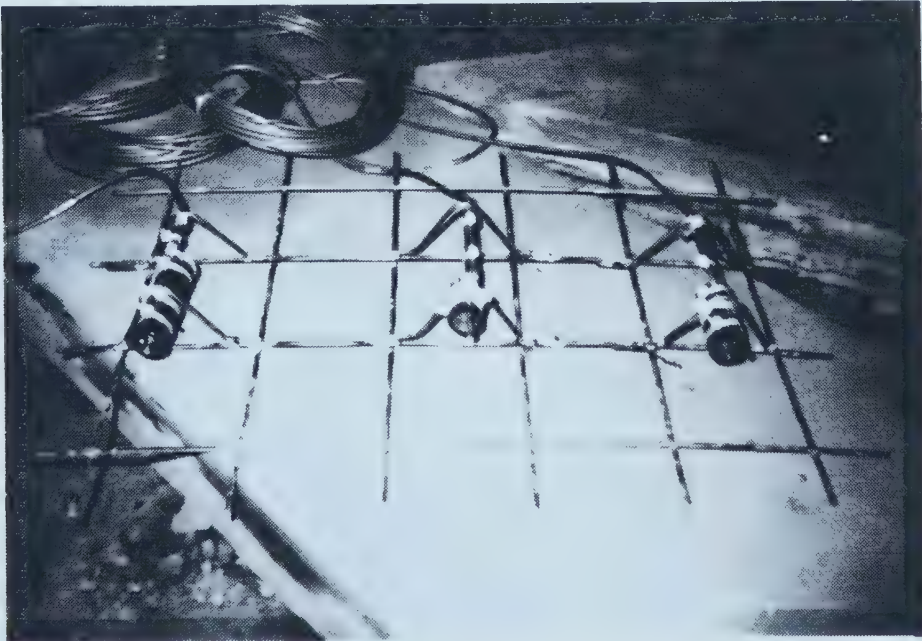


Plate 2.4 View of Compression Gages Fixed to Steel Cages

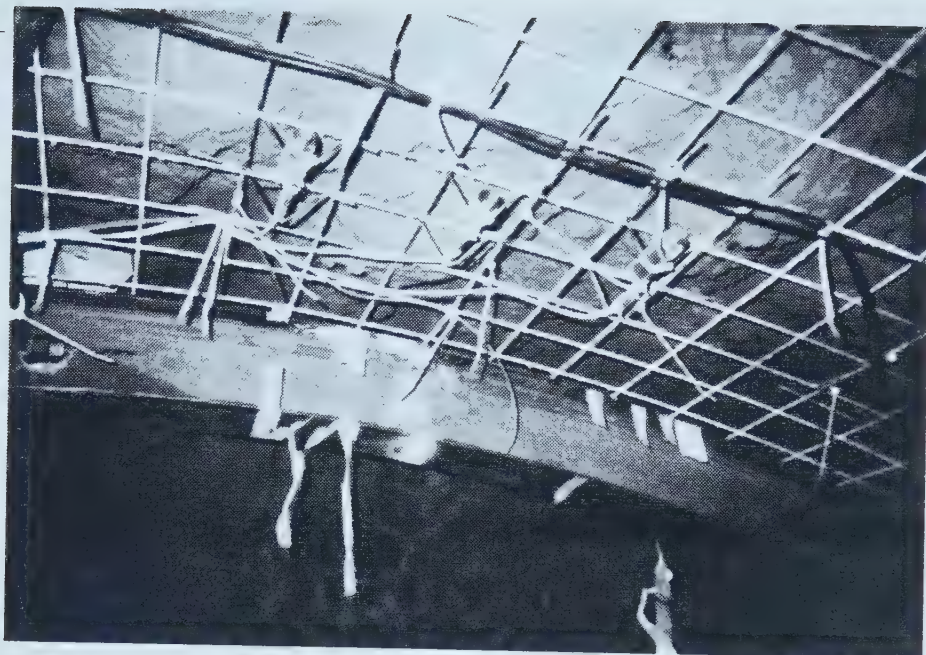


Plate 2.5 View of Compression Gages Fixed to Steel Mesh

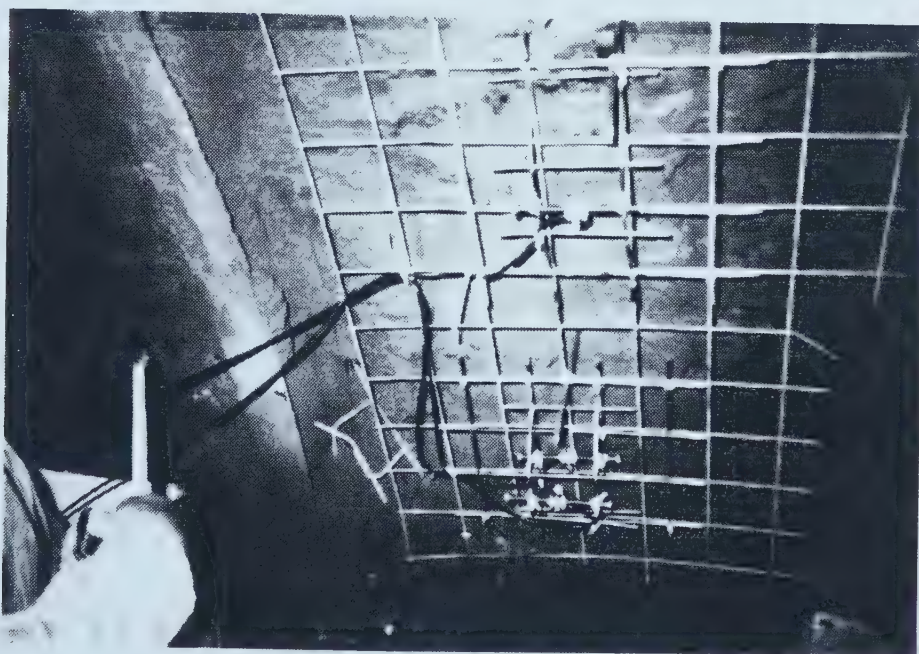


Plate 2.6 View of Resistance Strain Gages Bonded to Steel Ribs

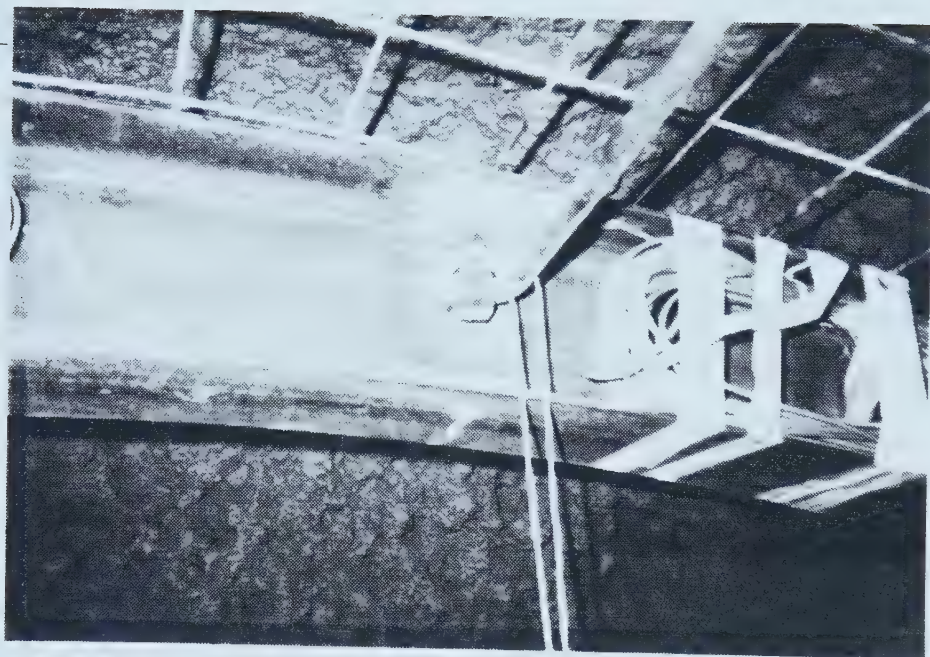


Plate 2.7 Installation of Vibrating Wire Strain Gages

3. FLAT JACK TEST

3.1 Introduction

Due to the problems discussed in Chapter 2, the lining instrumentation using embedded strain and stress gages was not able to provide enough information to determine the stresses in the shotcrete lining¹. Several techniques for load measurements in tunnel lining have been described in the literature, such as the measuring device by Baumann (1985), by Gloetzi hydraulic pressure cells (Voort, 1976) or by the closed system hydraulic cushion embedded in the shotcrete (Benecz et al., 1977). However, reliability of these instruments is highly dependent on the installation procedure, as discussed by Sauer and Sharma (1977), Heinz (1984) and Negro (1988).

An alternate measuring technique was investigated. The following characteristics were desired:

1. Short duration to perform;
2. High repeatability;
3. Economical compared to other techniques.

A test which appears to conform to these requirements is the flat jack test. It is a technique which has been traditionally used in the field of rock mechanics (Rocha, 1968). More recently, the flat jack test has been used in diagnostic analyses of masonry tunnel linings and historical buildings (Rossi et al., 1982; Maier et al., 1983). As far as it is known this is the first use of the flat jack test in shotcrete lining. Moreover, due to the special conditions in the project, modifications were introduced to the conventional test procedure.

3.2 Tests Using Conventional Procedure

¹Only using the available data at the end of the instrumentation program. Later, using results of an extensive laboratory investigation on the shotcrete properties, it was possible to estimate the stresses.

3.2.1 Brief Review of Current Practice

The flat jack test for stress determination is a two step procedure. Firstly, the material under stress is cut creating a slot. This induces displacements which are measured at some reference points. Secondly, a flat jack is inserted in the slot and it is pressurized until the initial displacements are restored. This pressure is related to the normal stress acting perpendicularly to the slot plane.

At early stages of the development of the flat jack test, the slots were made by diamond drilling along a line, with a partial overlapping (Alexander, 1960). Later Rocha et al. (1966) at the Laboratorio Nacional de Engenharia Civil (LNEC) in Portugal, introduced the diamond disk saw to create the slot, which resulted in faster and cleaner cuts and reduced the rock mass disturbance. Associated with this cutting technique, the flat jack has changed from a rectangular to a circular segment shape. Figure 3.1

illustrates the typical LNEC test arrangement which can be briefly described as follows:

1. On the surface of the material under stress, apply pairs of measuring base points A', A'', B' and B''. LNEC procedure used a 20 cm long extensometer with a 0.001 mm sensitivity dial gage developed at their research center (Rocha et al., 1966; Martins and Sousa, 1987).
2. Take initial readings which are the distances between the base points A'-A'', B'-B'', A''-A'' and B''-B''.
3. With a sawing machine and a circular disk saw, 60 cm diameter and 5 mm thick diamond-edge, open a slot between the bases. This will cause a stress relief and, as a result, relative displacements between base points.
4. Insert a flat jack with a geometry fitting the slot shape and apply pressurized oil in the jack. This is done by increasing the pressure in steps until the initial readings have been restored. The pressure at this condition (cancelling pressure) is related to the mean normal stress acting on the slot plane before the cutting operation.

Details of the LNEC test procedure can be found in Rocha et al. (1966) and an improved test interpretation in Bonvallet and Dejean (1977), Borsetto et al. (1983) and Martins and Sousa (1987).

Due to the efficiency and accumulated experience of the LNEC procedure, the stress measurement on the shotcrete lining in this research project followed the guidelines of this method.

3.2.2 Application of the LNEC Test Procedure

An attempt was made to apply the flat jack test using the LNEC procedure with a smaller jack, but it resulted in unreliable measurements. A brief description of the preparation procedures adopted as well as the problems encountered during three tests performed in NATM tunnels follows.

The tunnels were at the SLRT South Extension project in Edmonton, described in Chapter 2. The specified minimum shotcrete lining thickness was 18 cm close to the ribs and 14 cm mid way between them as shown in Figure 3.2. The distance between steel ribs was typically 1 m but reduced to 60 cm in critical sections. These geometrical conditions led to two problems in applying the conventional LNEC procedure:

1. The dimensions and shape of the slot were not appropriate for the tunnel lining. The construction procedure resulted in a slight curvature in the longitudinal direction of the tunnel, as illustrated in Figure 3.2. The curvature was basically a function of the steel rib spacing and local irregularities due to construction imperfections. This is a source of incompatibility between the slot and the jack, since the former is curved at the shotcrete surface while the latter presents a straight edge. It was not advantageous to make this edge curved either, as an attempt to provide complete contact between jack and slot, because the shotcrete curvature was not always the same. The usual LNEC slot depths (Rocha et al., 1966) are 10.5, 17 and 24 cm, which produce roughly 46, 55 and 59 cm wide

slots at the surface. It is clear that smaller flat jacks would conform better to these curvatures.

2. The depth of the slot should be minimized due to lining thickness limitations.

Rocha et al. (1966) observed that jack pressure was not entirely transmitted to the testing material in the neighborhood of the welded edges of the jack. This pressure transmission deficiency increased as the depth to radius ratio of the slot decreased. Since the shotcrete thickness was a limitation, the solution to keep this ratio at reasonable values was to reduce the cutting radius.

While these two problems required reducing the test scale, the size of coarse aggregate in the shotcrete and the extensometer accuracy required a bigger test scale. The scale of the flat jack illustrated in Figure 3.3 represents a compromise solution of these requirements and the adequacy of these dimensions will be verified in the next sections.

Due to the deficient transmission of the pressure described above, a correction factor has to be determined in the laboratory (Rocha et al., 1966; Bonvallet and Dejean, 1977; Martins and Sousa, 1987). Plates 3.1 and 3.2, respectively, show the stress application system and the flat jack and the circular saw used for this purpose. A concrete prism 60.8 cm long, 50.5 cm wide and 17.5 cm high was submitted to a known uniaxial state of stress and the relative displacement measurements were taken using an extensometer with a 127 mm (5 in.) base and a 0.00254 mm (10^{-4} in.) sensitivity dial gage. Although the extensometer dial gage was 2.54 times less precise and the test scale was 1.69 times smaller than the one described by Rocha et al. (op.cit.), an agreement between imposed and measured pressures within 20% was expected, based on the good repeatability that was achieved during laboratory tests not presented herein.

Plate 3.3 shows a typical arrangement of the first series of tests in tunnel, illustrating the electric saw machine assemblage and the measurement point locations. Plate 3.4 shows a detail of the latter with the flat jack already installed and the untreated shotcrete surface irregularities. It was not possible to obtain a smooth surface finishing

even with application of an electric concrete grinder. Consequently, it was very difficult to properly install the measurement points and the resulting repeatability of the readings was extremely poor. The surface irregularities caused rotation of the steel disk pair gage points for the conical tip type extensometer. It was difficult to reproduce the same positioning of the extensometer under site conditions, as opposed to the plane and smooth concrete tested under laboratory conditions.

In order to ensure the same positioning and to apply the same force during the reading of the extensometer (avoiding the errors noticed in the former tests), a holding structure for this instrument was used in later tests. Initially, this frame was supposed to be fixed to the steel ribs through a group of six magnet grip devices but this proved to be inadequate due to the irregular rib surface. Plate 3.5 shows an improved version of that frame which was fixed to the structure where the cutting saw machine would be assembled. In this particular case, one can observe the installation of three pairs of measurement points. The same frame used for the steel disk installation device, was used to fix the base disk points and to provide a better plane alignment between them. This modification improved the extensometer reading accuracy but still the overall results were considered inadequate. Firstly, the extensometer repeatability was only 27% of the maximum displacement during the slot cutting. It was estimated that a repeatability of the order of 0.00762 mm (3×10^{-4} in.) of the extensometer readings could be achieved, compared with a displacement of 0.02794 mm (1.1×10^{-3} in.) measured after the stress relief in a location close to the tunnel floor. This particular test yielded a pressure of 1050 kPa, which can be considered compatible with the magnitude of the expected normal stress level in this shotcrete lining. Secondly, the holding frame was adequate only for tests close to the floor. Under this condition, the weight of the extensometer provided a suitable force to hold itself in place. At higher locations along the tunnel perimeter, weight compensation would be necessary to the load application system of the holding frame, since variations beyond a narrow range resulted in unreliable readings.

Thirdly, to achieve the accuracy described above, a very careful and time consuming procedure was necessary. For measurement of each three pairs of points, in one pressure stage application, it was necessary to take at least five readings. The total time spent to restore the initial reading was around two hours. On the other hand, as pointed out by Bonvallet and Dejean (1977), the measurements had to be carried out quickly in order to avoid creep and delayed distortion. Although this recommendation was stated for tests in rock, the results of tests in shotcrete given in Chapter 4 show that similar strict requirements are to be considered in shotcrete lining measurements, depending on the shotcrete age.

Though the third problem described can be minimized by changing the measurement sequence, the remaining ones cannot and they demonstrate the inadequacy of this type of extensometer. Therefore, it was decided to change the displacement measuring device to a vibrating wire strain gage. Laboratory tests, as well as, in situ tests were conducted to evaluate the applicability of this type of gage. Plate 3.6 illustrates the gage installation used during in situ tests. This instrument had 1×10^{-6} m/m nominal accuracy with 152.4 mm (6 in.) active gage length, which was potentially 60 times more accurate than the extensometer used before. However, as the vibrating wire strain gages must be fixed during the cutting of the slot, the measuring points must be changed from A-A position to A-B (Figure 3.1). Rocha et al (1966) showed that during the measurements in flat jack test, the relative displacement Δ_{AA} is about three times larger than Δ_{AB} . Therefore, the substitution of the extensometer by the vibrating wire strain gage will provide an increase of displacement measurement accuracy of about 20 times. The results of the test series using this modification were encouraging and details of the investigations conducted to study this method is described in the following sections.

3.3 Characteristics of the Mini Flat Jack Test

3.3.1 Equipment Description

Figure 3.3 shows the physical dimension of the mini flat jack. As described in Section 3.2.2 its dimensions represent a compromise solution required by the restrictions imposed on the test. This jack comprised a 0.15 mm thick stainless steel sheet on each face, which were welded to a 5 mm wide steel collar around the perimeter (Figure 3.3). The latter was necessitated by welding strength requirements and its width and thickness were maintained to a minimum. There was one inlet steel tubing for hydraulic pressure application and another for air drainage. Both of them passed through a protective flap placed to guard against possible operator injuries caused by projection of oil under high velocity in case of sudden failure of the jack (Rocha et al., 1966). The flap was connected to the straight side of the circular segment shape jack by using three 4 mm diameter bolts. Plate 3.4 shows a top view of this detail and Plate 3.2 illustrates its use to place the jack into the slot.

The hydraulic system was composed of a conventional manual oil pump with a pressure dial gage connected to its outlet. The same gage was used throughout all test series, and calibration checks (repeated before and after each test series) indicated repeatability within 6.9 kPa (1 PSI) while setting a predetermined pressure.

The slot was made with an electrical circular saw machine powered by a 1/3 HP and 1725 rpm engine using a pulley-belt transmission to rotate a 1.5 mm thick and 35.6 cm diameter (14 in.) diamond blade (Plates 3.2, 3.3 and 3.6). Plate 3.7 shows the cutting system assembled in a location at the tunnel crown and one can observe the cooling system tubing leading to the disk protection structure and a valve to control the amount of flow. Water was circulated at site air temperature using a submersible electrical pump. In the laboratory tests, the saw machine was attached to the steel rods of the load application system (Plate 3.1) while at the site, it was fixed to the lining itself. In order to ensure precise positioning of the cutting system at site, the installation was done in two steps, described below:

1. Installation of the holding frame. Plate 3.6 shows this frame in a front view and one should observe that it was attached, in this case, to the shotcrete by three steel clamps. These clamps had a hole close to the center, where 12.7 mm (0.5 in.) diameter expandable bolts were used to fix them. A 15.8 mm (5/8 in.) diameter bit with an impact drill was used to make 10 cm deep holes to fit the bolts and a distance of 158 mm (10 diameter) from any edge to the vibrating wire gage was considered the minimum requirement to avoid interference with the test². Since the frame could be fixed using just three clamps (Plate 3.6), the usual distance was of the order of 25 diameters. Another feature of the frame is the use of steel flaps close to each edge which holds four 15.8 mm (5/8 in.) bolts. These bolts were used to adjust the frame into a suitable cutting position and a detail of their use can be seen in Plate 3.7.

2. Fix the cutting saw machine to the holding frame. This machine was assembled in a steel axle which had a screw in one of its ends. The cuts were made by rotatory movement around the axle and adjustments using the screw permitted translation of the system to obtain parallel cuts.

After the assemblage was completed, the saw was placed in contact with the shotcrete in a cutting position and final measurements were taken for proper installation of the vibrating wires gages. These vibrating wire strain gages were, in most cases, of the same model (Geokon, type VCE4200) used in the tunnel lining instrumentation and are described in Chapter 2 .

3.3.2 Test Procedure Investigations

3.3.2.1 Jack Calibration

²Applying an analytical solution (Kirsch, 1898), the disturbance caused by the stress relief due to a hole execution is negligible for distances beyond two diameters. More space was required due to the saw machine weight and the drilling technique used.

During the investigation of the flat jacks behavior, Rocha et al. (1966) performed a test that was described as follows:

"... In order to calibrate the jacks, they were applied in pairs between the plates of a testing machine, which were kept at a fixed distance of about 5 mm while the oil pressure in the jacks increased . . ."

Similar tests were conducted using a compression testing machine controlled by a micro computer. The latter, with features described in detail in Chapter 4, maintained the distance between the plates within 0.05 mm at four measuring points. The equipment alignment was critical to obtain parallelism and a constant adjustment of the load applied by the machine was necessary to compensate for the frame deformation due to the pressure increase in the jack.

The force required to achieve this condition as well as the hydraulic pressure applied to the jacks were recorded and the result are shown in Figure 3.4. The ordinate represents the hydraulic pressure applied to the flat jacks and the abscissa, the applied force divided by the area of the undeformed jacks in a plan view (which represents the pressure transmitted by a 'perfect' jack). Also presented are the values obtained by Rocha et al. (1966) for the flat jack with an almost identical ratio f/R (Figure 3.1: $f/R=0.567$ and Figure 3.3: $f/R=0.562$). From Figure 3.4, it is clear that for a given jack, as the gap between plates is increased, the influence of the welded edges increases, reducing the efficiency of the jack pressure transmission. It is also evident that a higher efficiency was reported by Rocha et al. (op.cit.) for jacks 1.69 times bigger than used in the present research. Since the area ratio between those jacks was 2.88, a reduction of the width of the welded edges (for the smaller jacks) would be necessary to maintain the same level of efficiency. Unfortunately this was not possible due to manufacturing limitations.

The pressure necessary to expand the 6.8 mm thick jack itself, may be considered negligible, since by applying a pressure of 6.9 kPa (minimum pressure value that can be read by the hydraulic system), the typical deformed shape of the unconstrained jack was

18.2 mm at the center area and 8.5 mm near the welded edges. Therefore, it seems that the area of the jack which is actually in contact with the plates played the major role in the pressure transmission mechanism of this device.

3.3.2.2 Laboratory simulation

The first aspect to be investigated in the laboratory was the technique to fix the vibrating wire strain gages to the concrete. Methods which require drilling holes were disregarded in order to avoid stress field disturbance in the measurement region. Also, the installation procedure had to be flexible enough to adapt to the irregularities at the shotcrete surface (Plate 3.4). Moreover, it had to be completed in a reasonable time, as the test can interfere with tunnel construction activities.

In order to meet these requirements, the installation procedure used a quick-setting commercial pre-mixed mortar (known as 'Water Plug'). Made of hydraulic cement and an expansive additive, water plug sets in 5 minutes and ensures good contact. The installation layout is presented in Figure 3.6a and its execution was as follows:

1. Locate and put marks at points A and B where measurements will be taken.
Draw the auxiliary lines a, b, c, d, i, j and k;
2. Wet the concrete around points A and B and apply, in each point, approximately 8 cm³ of previously mixed mortar;
3. Put the strain gage in position using the lines i, j and k and add enough mortar to cover all the flanges. After applying some pressure and vibration to ensure good contact, the mortar should have approximately, the shape under the surfaces α and β indicated in Figure 3.6a;
4. Using a spatula and a ruler, remove the excess mortar beyond the lines a-b and c-d.

Using this technique, the points A and B and the lines a, b, c and d can be located within 2 mm of accuracy. Although precise control of the surfaces α and β was not done,

they should follow approximately the shape indicated in Figure 3.6a. As the mortar was a quick-setting type, when an excessive amount (around 3 times the volume indicated) was applied, cracks developed due to the exothermic nature of the curing process. The heat caused fluctuations in the gage readings during the curing of the mortar capsule and a criterium had to be established for ensuring consistent measurements: strain readings to be within the nominal precision of the instrument (1×10^{-6} m/m) for at least 10 minute interval.

This installation procedure was later improved but applied only in the last series of in situ tests. The vibrating wire strain gages were changed from model VCE4200 to VSM4000 (same manufacturer). The latter has metallic blocks at the instruments heads, and was approximately 2% shorter than the former. The installation procedure followed the same guidelines as presented above and is illustrated in Figure 3.6b. Further details are given in the presentation of the in situ test results. The installation procedure discussed hereafter refers to the first type (Fig 3.6a), unless otherwise stated.

In order to evaluate the installation procedure, laboratory tests were conducted and two typical results are presented in Figure 3.5. The vibrating wire (VW) strain gages were fixed on the surface of 45 cm high and 15 cm diameter concrete cylinders along the vertical direction. Also, a conventional strain meter device³ was assembled to these cylinders which could take measurements from points 30 cm apart within 0.5×10^{-6} m/m strain accuracy. The cylinders were then submitted to load in a testing machine and readings from this strain meter and vibrating wire (VW) gages were recorded. The measurements taken by the strain meter were considered the 'nominal correct values' and they are represented as the abscissa in Figure 3.5. Test CLVWVG represents a typical 'very good' installation test, where the VW gages readings follow the same strain pattern for the three cycles of load which were applied. The average deviation for this test was 0.5×10^{-6} m/m with three readings showing poor agreement between 2.5 and 3×10^{-6}

³A modified ASTM C469 compressometer as described, in Chapter 4.

m/m. Test CLVWAV represents a typical average installation behavior where a shift of the readings was observed. Three loading cycles were also applied to this test and between the first and second loadings a shift of the order of 2.5×10^{-6} m/m was recorded. After this, the deviations were maintained in the order of 1×10^{-6} m/m.

It was not possible to identify the reasons for these different trends either by taking careful measurements of the distances between lines a-b and c-d (Figure 3.6a) or by comparing the weights of the mortar capsules after disassembling the tests. Therefore, using the worst case, an error of 4×10^{-6} m/m for a single reading was estimated while a 2×10^{-6} m/m average deviation should be expected. If yielding in the mortar capsule around the gage flanges was considered, this effect would be minimized during the flat jack test, because in this procedure, the gages are under tension most of the time. Under this condition, the mortar capsule will only resist the force due to the wire stiffness of the strain gage, whereas under compression, the steel tubing will restrain the deformations. It will be shown later in this chapter that hysteresis was not observed during the situ tests, suggesting the absence of plasticity. It was also observed that the strain reading deviations were of the same order of magnitude as estimated in the laboratory (i.e., 2×10^{-6} m/m).

The tests and discussions presented so far, have tried to isolate each feature of the mini flat jack test that could influence measurement. In order to assess the global behavior of the method under laboratory conditions, three tests were conducted. These tests were conducted in concrete blocks (60.8 cm long, 50.8 cm wide and 17 cm thick), under known uniaxial stress, similar to those already illustrated in Plates 3.1 and 3.2. The difference was the use of the vibrating strain gages instead of the conventional dial gages extensometers. The relative positions of the vibrating wire gages to the slot are presented in Table 3.1, according to the parameters (X, Y) shown in Figure 3.7. The thickness of the concrete block was close to that of the shotcrete tunnel lining, and the other dimensions were limited by the size of the load application system. This system was the

same as shown in Plate 3.1 and used a load distribution apparatus originally developed by Brandt (1985) and further modified by Costalonga (1988). This flexible load application system was used to ensure uniform stress distribution. A rigid plate application system, as used by Rocha et al. (1966), was avoided due to its well known tendency to concentrate stress in case of either poor contact or insufficient stiffness of the plates.

Rocha et al. (1966) have used a 55 cm long, 55 cm wide and 100 cm thick block to make similar tests using flat jacks 69 % bigger than those under study⁴. Considering scale correction, in the present test, the length L (Figure 3.7) was slightly longer than that used by those authors (2.8 %) while the width W was 56 % longer. As the boundary Λ was closer to point B (Figure 3.7) than in the configuration used by Rocha et al. (1966), it was considered necessary to locate the slot 7.5 cm from the horizontal center line (Figure 3.7) in order to reduce the influence of the boundary on the displacements at point B.

The shorter length at the lower portion seems to have a small influence on the measurements to be done at the upper section. Rocha et al. (1966), using a heavily instrumented physical model, have noticed that beyond one radius R from the slot, the strain and stress disturbance was hardly felt. For the smaller thickness of the present tests (about one third of the blocks used by Rocha et al. (1966), considering the flat jack scale correction) this distance should be longer. However, the distance between the lower boundary Λ and the slot being $1.29 R$, together with the use of a flexible load application system should minimize this effect, leading to better results than those obtained when accepting the proximity of the boundary to the region where the measurements will be taken.

Table 3.1 shows the concrete properties measured using cylinders cast with the same concrete used for the blocks. In each flat jack test two vibrating wire strain gages

⁴Notice that the flat jack pressure correction factor determined by Rocha et al., 1966, using the mentioned blocks, is still being used at LNEC (Martins and Sousa, 1987), indicating their confidence in the determination.

were installed, but in the case of VW 2 gage, for test CLMR2, installation problems were detected and its data were disregarded. Tests CLMR1 and CLMR2 were performed under an air condition of 100% RH (relative humidity), at 4.5 °C, inside a moisture room, whereas CLNRH was run under normal laboratory conditions (52% RH and 18 °C). For the latter, the vibrating wire strain gages were thermally insulated over and around the measurement region. The use and necessity of this protection is discussed later in this chapter.

These tests, as well as others which will be described, used 7.5 mm wide slots in order to allow smooth installation of the jack within an acceptable pressure transmission efficiency (Figure 3.4). Since the diamond saw was 1.5 mm thick, it was necessary to complete the slot by making two parallel cuts followed by removal of material in between. After the first cut was finished, one of its faces was used to hold a spacer which guided the saw for the second cut. The concrete left between the two cuts was first chipped off and the remaining irregularities levelled by sawing (this operation is hereafter referred to as the 'cleaning' procedure). Using this technique, the slot width was obtained within 0.3 mm. The floor of the slot was levelled by translating the saw under rotation, from the position of the first cut to the position of the second one. The results shown in Figure 3.4 suggests that the 0.3 mm deviation would be negligible in terms of the jack pressure transmission efficiency.

Figure 3.8 summarizes the results of these three tests, for the displacement measurements that were taken during the first cutting. It presents the data in terms of the usual non dimensional parameters to represent the depth of cutting (f/R) and the relative displacements between the reference points $\left[\frac{E\Delta_{AB}}{R\sigma} \right]$ where R is the radius of the cutting saw (same as the flat jack), f is the depth of the cutting (Fig 3.1), σ is the uniaxial stress applied to the concrete block (Figure 3.7), E is the Young's Modulus (Table 3.1) and Δ_{AB} is the relative displacements between the points A-B. The last parameter is the main

difference between the present procedure and that of LNEC: the former uses the deformations between the points A-B, while the latter has traditionally used the points A-A (Figure 3.1). Rocha et al. (1966) favored A-A points for ordinary tests because they produce larger relative displacements, although they also took measurements between the points A-B, at the physical model measurement at LNEC. In the case of the present research, the instruments were stationary during the test and the only way to avoid the cutting line of the saw was to use the reference line A-B. Figure 3.8 also presents the measurements taken by Rocha et al. (1966) for the points A-B.

The measurements presented in Figure 3.8 for the values of f/R from zero to approximately 0.3 were subjected to higher deviation than noticed during the previously reported installation test of the gages. In the initial stages of cutting, the vibrations induced by the saw oscillated the readings within order of 2 to 3×10^{-6} m/m, as opposed to stable readings observed throughout the other test. The measurements of the cutting depth (f) had an estimated error of 1 mm and were taken with a conventional scale.

Figure 3.8 shows higher gradients close to the end of the cutting ($f/R=0.562$) than the data obtained by Rocha et al. (op. cit.). This reflects a fundamental difference between these tests: in the Rocha et al. model, an infinitely thick mass was under consideration while in the present case, the thickness of the block test simulated the expected shotcrete lining. Once the slot depth was 30.9% of the total thickness of the block in the first case, compared to 95.6% for the second case, a higher gradient of relative displacements should be expected as compared to the ratio f/R for the latter (since in this case, the cut almost penetrated through the block). Another difference was the relative positioning of the measurement points to the slot, and the longer distance between points A and B for the present studies.

Approximately 10% to 20% of the maximum deformation recorded during the first cut occurred in the subsequent second cut and cleaning stage. As the enlargement of the width was small compared to the other dimensions of the slot, the associated stress

relief did not seem to be the cause for such observations. It seemed that the time dependent behavior of the concrete also contributed to these deformations as was reported by Bonvallet and Dejean (1977) for flat jack tests in rocks. To solve this kind of problem, Bonvallet and Dejean suggested a short test duration in order to avoid creep and delayed distortion or wait for these deformations to occur and then apply suitable corrections. As the latter would potentially introduce indeterminacy into the test interpretation, the former approach was chosen. Therefore, the in situ stress interpretation for the mini flat jack was assumed equal to the cancellation pressure necessary to restore the relative displacements observed at the end of the first cutting. On the average, each cut took 8 minutes to complete and 10 minutes for the removal of the concrete between the cuts. Approximately 45 minutes after the initial reading was taken, the jack was inserted for the beginning of the test.

The mini flat jack test loading stage was done in three cycles, each of which took approximately 3 minutes. The relative displacement presented the same magnitude of reading deviations observed in the gage installation tests done in concrete cylinders (Figure 3.5). For the test interpretation, the relative displacement difference values were taken with reference to the zero load condition of the flat jack, at the beginning of each stage. Figure 3.9 illustrates a typical result of this procedure for the case of test CLNRH (all the results are presented in Appendix C) where the three loading cycles were superimposed and a linear regression was applied. The relative displacements were normalized in the same way as previously mentioned and the flat jack pressure was normalized by the stress applied to the concrete block. Figure 3.9 also illustrates the procedure to determine the hydraulic pressure necessary to restore the relative displacements observed at the end of the first cut of the slot.

The same procedure was applied to the other tests and the results are summarized in Table 3.2. The column of the normalized pressure actually represents a correction factor (CF) that should be applied to the hydraulic 'cancelling pressure' in order to obtain

the in situ stress. As pointed out by Martins and Sousa (1987), this 'cancelling pressure' can be expected to have a small variation depending on the location of the measurement points, due to the non uniform transmission of pressure by the flat jack. Despite this effect, during the tests, a refined assessment of this factor was not possible because it was believed that the experimental measurement errors were of the same order of magnitude as this effect. For this reason, the correction factor was taken as the average of all tests performed: $CF=1.289$. This 29% correction may be compared to the 62% obtained on the test carried out on an isolated jack, between rigid plates (Figure 3.4 for gap=7.5 mm).

Rocha et al. (1966) have noticed similar response and suggested 50% of the factor derived from the test done with the jack between rigid plates. Although the displacement field of the plate test and the slot in an actual test should be slightly different, it seemed that this factor was not significant enough to produce such deviations. It is believed that some eccentricity in pressure application was responsible for this observation and in order to test this hypothesis, a simplified model was used. Consider the elements I and J in Figure 3.10, on the jack surface, with t_i and t_j representing tensions that will be created when the jack is pressurized, as the result of the restriction imposed by the curved boundary ξ . As element I is further from this boundary than J, the t_i component constraining the steel sheet displacement in the z direction is smaller than t_j . Therefore the upper region of the jack, close to the straight welded contour (ζ), will displace more easily than the region along the curved boundary(ξ). This phenomenon which was visually observed during the parallel plate tests, resulted in larger areas with deficient pressure transmission, around the neighborhood of the curved boundary ξ , than the straight one. Consequently the flat jack pressure transmission deficiency is not symmetrical in the xy plane, leading to a slight eccentricity. Also, recognizing that in the plane xy, regions closer to the boundary ξ represent larger moments ($y' \times \Delta A$), it seems that 1 mm to 2 mm of eccentricity may easily occur. If one considers a 2 mm eccentric load in a 10 cm high beam (the same value as the slot depth), the difference between the

stresses on the upper and lower surfaces will be 24% of the average normal stresses. Since in the flat jack test the equivalent load was displaced towards the surface, which represents also a 'softer' region due to the cut, it is evident that even a small eccentricity may cause those differences observed. Therefore, despite the fact that the effective area of the jack transmission pressure may be established through the parallel rigid plate test (Figure 3.4), the eccentricity partially compensates this deficiency and the overall correction factor for the test was smaller than that established previously. The latter seems to be a function of the jack manufacturing procedure and it might be reflected in the slightly different ratio between these factors obtained for the mini jacks to those used by Rocha et al. (1966). These authors suggested an overall factor of 1.08 while Bonvallet and Dejean (1977) using jacks with identical geometry had suggested a factor in based on 'effective surface' correction in the order of 1.21. Although the latter values were close to those presented in Table 3.2, it is clear that this correction factor should be determined in the laboratory on an individual basis.

3.3.2.3 Test Procedure Deviations

The laboratory tests presented, considered the mini flat jack in situ stress measurement done under uniaxial loading under high relative humidity (RH close to 100%), except for the case of test CLNRH. The deviations that may occur, if these conditions are varied, will be discussed shortly.

Figure 3.11 shows the arrangement of test FLDV , done to investigate temperature changes during the slot cutting procedure under low relative humidity conditions. The concrete block was the same size as those described before, and nine measuring points were monitored. Five resistance temperature device (RTD) instruments were installed 1 cm deep from the block surface. Four vibrating wire strain gages including a thermistor for temperature readings were installed. Two were left unprotected and two received thermal and moisture insulation protections (a Styrofoam cover fixed in

place by a layer of paraffin). Although in the field the washout water used for cutting usually did not spill all over the area where displacement measurements were taken, all the surface was kept wet by sprinkling water periodically. This procedure was used to simulate the worst condition possible, in case of performing the cutting under low relative humidity condition. Only one cutting was done, and the time for its execution was increased by decreasing the load applied to the circular saw. This would simulate the case of a test where cutting was difficult and the total time expended in test FLDV was approximately 30 minutes. The concrete block was subjected to a uniaxial stress of 200 kPa under 52% relative humidity at 18 °C; the results are shown in Figures 3.12 and 3.13. The former shows no significant variation in the concrete temperature readings close to the surface. Due to the measuring system that was used, the maximum accuracy should be 0.3 °C. These small temperature variations are in agreement with the observations made by Rocha et al.(1966).

Figure 3.13 shows variation of the order of 3 °C for the unprotected gages after 20 minutes. This can be explained by the temperature depression of 5.5 °C for a wet state expected by applying a psychrometric table (Hudson, 1974: 213) to the test environment. The total amount of cooling was not observed because the air flow caused by the saw was stopped during the cutting procedure and also, due to the air temperature water periodically sprinkled over the gages. Nevertheless, the variation observed may cause a shift of approximately 20×10^{-6} m/m in the strain gage readings, considering the thermal coefficient of expansion (-6.6×10^{-6} m/m/°C) presented in Chapter 2, for these instruments. This value is of the same order of magnitude as the readings obtained for the first cutting deformations for the tests presented before. Therefore, despite the observation that the concrete itself did not experience much temperature variation, the changes that occurred in the strain gages may invalidate any attempt to perform the test under low relative humidity, under unprotected condition. Figure 3.13 shows the good performance of the protection that was used in terms of temperature control, and for this

reason, it was used in test CLNRH which was performed to check the validity of the discussion presented above. One should notice that this kind of protection will also efficiently prevent the air temperature change effect and moisture content variation at the shotcrete surface during the test.

Concerning the uniaxial stress evaluation, Rocha et al.(1966) have shown that the flat jack test can provide good estimates of the stress normal to the slot, even if the pressure was not applied parallel to the principal axis. This test was done in a block subjected to a uniaxial stress and the slot was cut at 45° to the load direction. The observed average error of 15% was considered sufficient for practical purposes. Tunnel linings may also be subjected to considerable bending moments or higher gradients of stress in relation to the lining thickness, as opposed to a smoother stress transition in the case of a rock mass (traditional application of the flat jack test). Abdunur (1985) presented some results of flat jack test during the cutting stage for a plate subjected to bending moment. Unfortunately he focused on the stress relief condition and did not present results for the pressurization stage of the test. In order to evaluate the applicability of the tests under such a condition (bending moment), a test was made. The test was assembled using the same equipment and the concrete block was the same size as those used before. In order to simulate bending moment, the load application system was relocated at an eccentricity of 1.9 cm towards the upper surface, where the strain gages would be applied. This test, ELNRH, was conducted under normal laboratory conditions, with thermal protection applied on the gages. The stress level, concrete properties and measurement locations are presented in Table 3.3.

The first difference between this test and the previous ones (CLMR1 , CLMR2 and CLNRH) was observed during the cutting procedure. Although the average normal stresses applied to these tests were very similar, the eccentricity employed in the test ELNRH caused higher stress level close to the surface. Under this circumstance, as the cutting progressed, the faces converged towards the disk saw and imposed a friction not

observed in the other tests. As this friction eventually gripped the saw and impeded its rotation, it was necessary to execute the cut by a series of up and down movements. As a result, the execution of the first cut lasted 16 minutes and it was observed that the strain measurement readings were subjected to the saw vibration until the end of the cutting. Figure 3.14 shows the results of this stage of test and Figure 3.15 presents the readings obtained during the jack pressurization. The test interpretation was done using the procedure presented before, except for the value of the parameter σ . Here, σ was considered as the average normal stress acting on the cutting area (the stress field, inferred considering the imposed eccentricity by the load application system, was integrated over the slot area and the resulting force was divided by the same area). The results are presented in Table 3.3 for the two strain gages used during this test. Comparing the normalized cancelling pressures for this case to those of the previous tests (Table 3.1), it may be observed that the average of the previous ones were within the error range of the latter.

The increases in the readings, between the end of the first cutting and the beginning of the jack pressurization, in all of these tests, were between 10% and 20% of the reading related to the first cut. Four combined factors may have caused these deformations: the enlargement of the slot width, time dependent behavior of the concrete, deformations related to the concrete moisture content variations and temperature changes. A compensation for the last one is very difficult because a complex transient heat flow was established during the test. As the temperature of the gage steel tube changes faster than the temperature of the wire, any correction will depend on this gradient. Considering a decrease of 0.2 °C for the thermally protected instruments, in Figure 3.13, one may expect an increase of the order of 2×10^{-6} m/m in the gage reading, considering that only the steel tube had contracted (this value will reduce as the wire also contracts). This value represents typically 10% of the first cutting readings for the flat jack tests. In order to minimize this effect as well as the time dependent and moisture

content related deformation of the concrete, the test must be performed as fast as possible. Since the cutting stage constituted a time limitation, the solution was to perform the test interpretation using the deformations caused by the first cut. It is recognized that this solution will introduce a slight stiffness inconsistency, as the width of the slot will not be the same for the cutting phase and the pressurization stage. The results using this procedure however, have shown consistent measurements, suggesting that either the influence of those differences be negligible or incorporated into the overall correction factor used to adjust the cancelling pressure. In any case, the mini flat jack procedure provided a suitable stress evaluation for practical use.

For the reasons described above, one should expect more deviations in tests like ELNRH than in CLMR 1, CLMR 2 and CLNRH, because the cutting of the former lasted twice as long as the others.

3.4 In Situ Measurements

3.4.1 Foreword

The developments of the flat jack test described above were intended to be used in the tunnel described in Chapter 2 (North bound NATM tunnel, Figure 2.4). In situ stress measurements were not initially considered during instrumentation planning, but the results have shown that they could be helpful. Unfortunately, at the time the test procedure and equipment were ready, the north bound tunnel had already received the final lining. As the scope of this research was limited to the behavior of the primary lining, the mini flat jack tests were conducted in other tunnels.

The results presented so far in this Chapter, did not follow a chronological sequence but are organized on the basis of technical similarity. In fact most of the laboratory results presented were done to investigate difficulties encountered at site. The site tests were done in four different periods and tunnel locations, and they were always done in primary shotcrete linings. After each series of site tests, the results were analyzed

and the problems were investigated in laboratory through simulated conditions. The findings were then applied to improve the test procedure for the subsequent series; for this reason, the execution of each series of site tests was slightly different from the previous one. Or in other words, each test series was an improved version of the former tests.

In situ tests were performed in four tunnels, and two of which were part of the SLRT project: the Tail Track NATM tunnel and the South Bound NATM tunnel (Figure 2.1a). Tests using the LNEC procedure were done at the Tail Track tunnel, but produced unreliable results and are not presented. Modifications were then introduced and the vibrating wire strain gages were used for the first time at the South Bound NATM site where nine tests were performed. Unexpected readings of the instruments were detected in some of these tests, and required more laboratory investigations (tests CLNRH, ELNRH and FLDV). By the time the source of these anomalies were identified and a solution found, the shotcrete primary lining of the SLRT project had already been permanently lined (cast in place concrete). These improvements were then finally applied in two tunnels located at São Paulo, Brazil.

3.4.2 Tests at SLRT South Bound Tunnel

Nine in situ stress measurements were performed at this site, using the vibrating wire strain gage installation shown in Figure 3.6a. General information as well as the results are presented in Table 3.4. Figure 3.16 shows the relative spatial positions of the tests referred to in this table. Seven tests were performed to determine radial stresses σ_r , while the other two were carried out to estimate the longitudinal stresses σ_l . For the radial stress determination tests, the slot cuttings were parallel to the tunnel alignment, while in the longitudinal stress tests, the cuttings were executed transversely to it.

Four tests (IST1/1, IST1/2, IST2/1 and IST2/2) showed similar behavior to those performed in the laboratory and, a typical result for the relative displacements during

first cutting is illustrated in Figure 3.17 (results are shown in Appendix C). It represents test IST2/2, where the vibrating wire strain gages were equidistant from the axis y (Figure 3.7). Although an effort was made to set all the gages in this symmetrical configuration after cutting, they were usually out of position by 1 cm to 2 cm. It was difficult to predict the slot position accurately, because the cut was done by rotating the cutting machine around an axle, under variable height of the holding frame and slightly different curvature of the lining, at each site. Since laboratory tests showed that the determination of stress in flat jack tests was fairly independent of the measurement position for practical purpose (Table 3.2), the alignment deviations were considered negligible.

Tests IST1/1 and IST1/2 were executed close to the springline, near the tunnel face where the shotcrete was 12 and 15 hours old, respectively. The laboratory test results that will be shown in Chapter 4 indicate that creep deformations, at these ages, were approximately ten times larger than those observed for shotcrete older than 24 hours. Therefore, it is believed that the results of tests IST1/1 and IST1/2 were affected, to some degree, by this kind of deformation. The in situ stresses were probably lower than those measured because the creep deformations increased the readings of the relative displacements during the first cut. It is believed that the stresses would not be lower than 30% of the measurements because the increase of the deformations during the second cut, and cleaning procedure were of the order of 30% to 35% of the first cut (compared to 10% to 20% observed in the laboratory tests for well cured concrete block).

The behavior during tests IST2/1 and IST2/2 were very similar to those carried out in the laboratory and they were considered the most reliable. In test IST2/1, strain gage installation problems were detected in VW2; therefore, its data were disregarded.

Tests IST1/3 and IST2/3 showed compressive straining during the first cutting as opposed to tensile straining usually observed in this stage. This could be an indication of tensile stress, due to bending moment on the opposite side of that applied in test ELNRH

(Table 3.3). As no laboratory tests were conducted to investigate this situation, interpretation of the in situ measurement will not be given and the problem will remain open to further investigation.

Test series IST3 led to unusual pattern during cuts (Appendix C) and the interpretation considered only the values of the readings at the end of the first cut. Although the temperature measurements during test FLDV and the results of test CLNRH were presented earlier in this Chapter, they were actually performed after these in situ tests, in order to study the deviations observed in test series IST3. Until that point, temperatures were checked before and after each cutting stage. As the temperature changes were negligible during tests performed in the laboratory, it was sufficient to take readings at the beginning and at the end of the tests, as a control procedure for the site readings. After comparing the laboratory tests CLMR 1, CLMR 2 and in situ test series IST1 and IST2 to the series IST3, it was verified that the main difference was the relative humidity (RH). The relative humidity in the laboratory tests was 100%, 95-97% in test series IST1 and IST2 and 70% in IST3. The last series were designed to measure the stresses acting close to the tunnel floor. As the construction technique required a soil fill at the bottom region, it was necessary to wait until the excavation was completed. Afterwards the fill was removed and it was possible to access the floor and perform the test. At the time, the tunnel had already arrived at Corona Station and the air flow from the operating section of the SLRT system decreased the relative humidity. Figure 3.18 shows the results for the test IST3/1 and illustrates the worst case among the tests in this series. It may be observed that the relative displacements do not follow the same pattern observed before and for this reason, test FLDV was performed to evaluate the possible cause for the deviation. Temperature measurements were shown in Figures 3.12 and 3.13, while Figure 3.19 shows the readings obtained by the strain gages installed at positions 7 and 10 (Figure 3.11). During test FLDV water was sprinkled over the concrete block area while during test series IST3, the shotcrete was already wet due to

water accumulated at the tunnel floor. In test IST3/1, the saw was pinched as in test ELNRH and, the first cut was done by moving the cutting machine up and down. During this procedure, a considerable amount of water spilled over the strain gages. The results obtained in tests FLDV (Figure 3.19) and CLNRH (Table 3.2) partially explain the deviations observed in test series IST3: temperature fluctuations (Figure 3.13) had considerably affected the gage readings. Although the temperature changes in gage VW 7, do not proportionally follow the trend of strain readings in Figure 3.19, it is believed that the time delay response of the thermistor was partially responsible for the observations. The temperature variations however, do not explain the negative relative displacements (compression) observed in test IST3/1.

In tests IST3/2 and IST3/3, the behavior during cutting was similar to that presented in Figure 3.19 for VW 7. Although in these tests the water was not spilled as in the case of test IST3/1, it seemed that the shotcrete was wet enough to interfere with the test results. Whatever the cause of disturbance, with greater effect on test IST3/1, these test series were considered unreliable because the tests did not follow the pattern observed in laboratory. Therefore, the results should be considered only as a qualitative index of the stress state. Nevertheless, tests performed under low relative humidity (RH=52%, tests CLNRH and ELNRH) have shown a behavior compatible with tests under moisture room conditions (RH=100%, tests CLMR 1 and CLMR 2). This indicates that the problem can be easily avoided by applying a thermal protection. For relative humidity around 95% to 97% (like in test series IST1 and IST2), this protection was not necessary. The temperature depression, using a psychrometric table for this range (Strock, 1948), is of the order of 0.5 °C. Although the value obtained from this table was used in a simplified way, as a potential temperature change in the previous analysis, it is actually an over estimation of the real value. The psychrometric thermal depression, in fact refers to the 'adiabatic saturation temperature' (McQuiston and Parker, 1988: 522), which is a hypothetical thermodynamic parameter. Threlkeld (1970) has shown that for

idealized conditions, similar to tests IST1 and IST2, in a steady state equilibrium, the wet bulb temperature depression is lower than the 'adiabatic saturation temperature' by approximately 0.27 °C. Since the temperature had not yet equilibrated (Figure 3.13) and the gages were not totally wet, the temperature depression should not be higher than 0.2 °C. Therefore, the temperature changes in the strain gages, for those conditions, may be considered negligible.

3.4.3 Complementary Tests

Although the laboratory test FLDV pointed to the probable sources of error observed in some of the in situ tests done at SLRT South Bound tunnel, full scale tests were conducted to verify the results. At the time test FLDV was completed, the NATM tunnels of the SLRT project had already received permanent linings. For this reason, complementary in situ tests were conducted in two NATM tunnels located in São Paulo, Brazil. Figure 3.20 shows the cross sections and the locations of two of the tests conducted in these sites. The construction of these large cross section tunnels did not follow the conventional NATM tunnel construction sequence, and hence in situ tests were considered useful in those projects. The stress analysis of the lining of these tunnels was considered out of the scope of the present thesis, and only the results showing factors that improves the accuracy of the flat jack test will be discussed.

Tests ISIG and ISJK (Figure 3.20) were performed using a technique similar to the one described before, the flat jack itself was the same as used before and the hydraulic system was assembled using the same type of pump and gage. The differences were the following:

1. model of the strain gages. The model VSM-4000 (Plate 3.8 and Figure 3.6) was used instead of the gage VCE-4200 (Geokon). The geometry and precision of these gages are similar, but the latter had proven to be easier to handle during

installation and more convenient during disassembling. It required less mortar, and hence, smaller amount of temperature changes.

2. use of the thermal protection, Plate 3.9 (first time at in situ tests).
3. different cutting machine (Plate 3.9). It had the same characteristics as that used in the previous tests, and the differences were only a result of the equipment and parts available locally.
4. an area of approximately 1 m² around the test location was protected by a silicon based water repellent product. This precaution was intended to avoid expansion of the shotcrete due to increase of the moisture content (data to be presented in Chapter 4).

The two vibrating wire strain gages used in each of these tests were assembled 4.5 cm apart (Plate 3.8) using the technique illustrated in Figure 3.6b, covered by thermal protection made from a block of Styrofoam. In the laboratory, this kind of protection was fixed using paraffin which provided impermeability at the Styrofoam-shotcrete interface. At the site, the Styrofoam block was fixed using rubber bands (Plate 3.9) and the contact was treated using a commercial sealant product known locally as 'Vedacite' (Plate 3.10)

Test ISIG can be considered as an example of a standard test, while test ISJK presented deviations and was subjected to experimentation to check some of the procedural details. The results of these tests were separated in four stages: thermal equalization, first cutting, second cutting, slot cleaning and finally pressurization stage.

Figures 3.21 and 3.22 present the relative displacements and temperature reading variations observed during the thermal equalization period. In the tests presented earlier, it was mentioned that the mortar capsule (Figure 3.6a) generated some heat as a result of which the temperature had risen and then dropped to a stabilizing level (air temperature) inducing some thermal strains. In order to avoid errors due to this effect, it was necessary to wait until the readings stabilized. The time necessary for this thermal equalization period was around 30 minutes and for this reason, the readings for this stage at test ISJK

were taken to 30 minutes. The results in Figures 3.21 and 3.22 show that this interval was not sufficient for stabilization and the strain development was different from those observed before.

The strain readings in these tests had monotonically increased instead of dropping to a peak value and then rising to a stable level, as it was observed at the other tests. The change of the gage VCE-4200 to VSM-4000 had considerably reduced the amount of mortar necessary to install the gages (Figure 3.6). The heat generated by the mortar in the case of VSM-4000 was not sufficient to heat the vibrating wire strain gages, which should reduce the decreasing trend observed for VCE-4200. The decrease of the temperature readings observed in tests ISIG and ISJK (VSM-4000) was attributed to the installation of the thermal protection. This protection had insulated the vibrating wire strain gages from the air temperature and equilibrium was established with the temperature of the shotcrete. The temperature of the instruments, being higher than the shotcrete, dropped during the thermal equalization period.

Figure 3.23 and 3.24 show respectively the relative displacements and temperature reading variations observed during the first cuttings. The readings of test ISIG, done at the lining at the Cohab Tunnel, presented a pattern similar to those observed in the tests (presented before) the data of which were considered reliable. Note that the temperature readings were very stable in this test (variation of ISIG/VW1 in Figure 3.24 is within of the precision the measuring equipment), showing the efficiency of the thermal protection.

Test ISJK presented a compressive straining pattern, as observed in tests IST1/3 and IST2/3 (Table 3.4), and quantitative interpretation was not possible. The major difference in the case of test ISJK, was the heavily steel reinforced lining used at the tunnel under Pinheiros River. In this test, the slot cutting had crossed three steel bars ($\phi=1$ cm) spaced at 10 cm, located 2.5 to 3 cm from the surface (Figure 3.25). Note that no reinforcement was used in the laboratory tests as well as the Cohab Tunnel lining

which was constructed with no mesh but in the SLRT tunnel linings very light steel mesh was used (Figure 2.2). As the cuttings in the lining of the SLRT tunnels did not cross the steel mesh, the only test which cut reinforcement was the test ISJK.

Figure 3.25 shows schematically the plan view through the slot at the test ISJK, illustrating a cutting front passing approximately through the center of BAR 2 and another one passing through BAR 1 and BAR 3. Note that the cutting front does not approach the final depth in a straight line, instead, it describes a rotational movement resulted from the radius of the cutting machine assemblage (Plate 3.9 and Figure 3.26). Figure 3.25 shows that the saw was about 2.5 cm deep ($f/R=0.14$) when it passed through the center of BAR 2. Due to the limited number of readings at the beginning of cutting (Figure 3.23), it is not possible to isolate the deformations resulting from the stress relieve generated by the cut of BAR 2. On the other hand, there is a clear sudden change of the deformation pattern (Figure 3.23) when the saw passes through BAR 1 and BAR 3, approximately at a depth of 5.8 cm or $f/R=0.33$ (Figure 3.25). The readings show a compressive straining of the gages during this event, suggesting that the bars were under tensile stress. This observation should be taken with caution, since the temperature readings started to rise around $f/R=0.33$ (Figure 3.24). It seems that due to the higher thermal conductivity of the bars, they could become a temperature dissipator when heat was generated during the cut. This would spread the heat to the concrete along the length of the bars, increasing the temperature of the concrete and the air under the thermal protection. The expansion trend observed in Figure 3.23 after $f/R=0.33$, for the small increase of the air temperature observed (Figure 3.24 and 3.28), supports this hypothesis.

Figures 3.27 and 3.28 show the measurements during the second cutting and cleaning procedure, which ideally should display constant temperature readings and small variation in relative displacements. Tests ISIG presented constant temperature readings (within the precision of the measuring instruments) and the relative displacements were about 10% of those observed during the first cut. These

displacements, as pointed before, could be caused by delayed deformation (Bonvallet and Dejean, 1977) or to some degree by the widening of the slot. The influence of the latter seems to be very small, as shown by the almost constant readings during the second cutting for test ISIG (Figure 3.27). During the cleaning period, most of the relative displacement readings had shown expansive straining. Note that these variations took place between 10 to 15 minutes and for the remaining 20 minutes of this stage, the readings were almost constant. Therefore, it seems that no time dependent process could be responsible for these deformations; either delayed deformations due to stress relief or volume change due to moisture change caused by the water used during cutting.

The results of test ISJK, during the second cutting and slot cleaning stage, are helpful in understanding the observations above and also illustrate some other details. As in the case of test ISIG, test ISJK shows almost constant readings during the second cutting (Figure 3.27), which can be interpreted as an indication of absence of time dependent or stress dependent deformations. Note that the deformations observed during the slot widening stage also happened during cleaning period. It is believed that the variation of the relative displacement readings observed during the cleaning was resulted from 'relaxation' of the strain gages. This 'relaxation' could be induced by the impacts and vibration generated when the saw ripped the concrete between the cuts. Note that test CLVWAV (Figure 3.5), test of vibrating wire installation, was repeatable to about 2.5×10^{-6} m/m or $2.1 \times 10^{-6} \left[\frac{\Delta_{AB}}{R} \right]$, which corresponds to the same order of magnitude observed during cleaning (Figure 3.27).

In test ISJK, after finishing cleaning, the saw machine was disassembled in order to check the possible influence of its weight on the test result. It can be observed (Figure 3.27) that the weight of the saw had produced much smaller changes in the relative displacement than those observed during cleaning. After disassembling the saw machine, the thermal protection was removed at test ISJK. This showed that a temperature

variation of the order of a degree Celsius (Figure 3.28) can induce variation of relative displacement readings of the same order of magnitude observed during first cutting (Figure 3.27 and 3.23). Turning the air ventilation of the tunnel on or off or a spot light close to the test, could induce the same effect. Therefore, the thermal protection is regarded as the prime precautionary measure to ensure the accuracy of the test.

Figures 3.29 and 3.30 show the readings taken during the pressurization stage. Deviations in test ISJK are mainly due to the temperature variation, as indicated in Figure 3.30. For interpretation of test ISIG, one should take the pressure (σ) in Figure 3.29 to restore the relative displacements observed at the end of first cutting in Figure 3.23. This pressure should then be reduced by the correction factor ($CF=1.289$) presented earlier, in order to obtain the average in situ normal stress. Test ISJK cannot be interpreted due to the steel reinforcement in the shotcrete lining.

3.5 Summary and Conclusions

The investigations on the flat jack test presented in this Chapter were based on the LNEC procedure (Rocha et al., 1966), originally developed for measuring in situ stress in rock.

A scale reduction was necessary due to the geometric restrictions imposed by the special features of stress determination in a tunnel lining. LNEC flat jack test procedure using a smaller mini jack was then performed in the laboratory and at site. However, the results suggested that the displacement measurement device be changed. Vibrating wire strain gages were used and tests results confirmed their suitability.

In analyzing the laboratory results, as well as published data, it is believed that the flat jack manufacturing technique leads to a slight eccentric pressure application at the slot. It is caused by the welded edge pressure transmission imperfections; therefore, each individual of flat jack should be calibrated by a laboratory test. For the jacks used in this research, the applied hydraulic pressure should be divided by a factor of 1.289, to

obtain the in situ stress. As the eccentricity of the jacks may be a source of some deviation, further investigation is recommended in this area. It seems that application of more advanced manufacturing procedures, like composite material technology, may reduce the edge pressure transmission imperfection to a negligible value. Also, this technology would produce thinner flat jacks, which in turn, would reduce the time required to perform the test.

Thermal protection must be provided for the strain gages, specially if the test is performed under low relative humidity environment. Laboratory test FLDV has shown that for this condition, the psychrometric thermal depression induces considerable changes on the strain gage readings that invalidate the test results. In situ test ISJK showed that by simply removing the thermal protection (Figures 3.27 and 3.28), relative displacement reading deviations of the same order of magnitude can be observed. The thermal protection (to the vibrating wire strain gages) is regarded as the prime precautionary measure to ensure the accuracy of the test.

Figure 3.31 presents the stress concentration from linear elastic analysis around an unlined tunnel, typical of the LNEC flat jack test. As the radius of tunnels are typically of order of meters and the flat jack is at the order of decimeters, it seems reasonable to neglect the stress variations across the flat jack in tests within vicinity of a tunnel boundary (note that if one consider the more realistic case of non linearity and plastic deformation, the stress concentration is smaller than shown in Figure 3.31). In fact, this is the common assumption used in the interpretation of the flat jack tests in unlined tunnel. The same is not always true for the case of test performed in shotcrete lining of tunnel excavated in soil, where the stress gradient might be much higher or where the lining might be subjected to bending moment.

The laboratory test ELNRH indicated that the mini flat jack test can be used to evaluate the average stress acting on the slot, even if considerable bending moment was applied to the concrete block. In this particular case, the compressive stresses were higher

at the surface where the strain gages were installed. At the present stage, however, it is not possible to identify or evaluate the magnitude of this bending moment.

It is suggested that an investigation into the possibility of changing the test procedure using slots (and associated jack) at different depths be conducted. Variations of the 'average' stress may indicate bending moment and the difference of their values probably will furnish its magnitude. It was suggested, during interpretation of in situ test results, that bending moment might occur in a direction opposite to the one applied in the laboratory test (ELNRH), resulting a condition where the test was not checked in laboratory. Data obtained are not conclusive and further investigation is necessary.

Another suggestion to analyze tests done in linings subjected to bending moment is an interpretation based on the stress relief stage. Figure 3.32 shows the relative displacement pattern for laboratory tests done in concrete plates by Abdunur (1985), which closely followed the test procedure by Rocha et al., 1966 (Figure 3.1). It seems that the distinct pattern followed by these tests may be used for a quantitative evaluation of the bending moment. Note that Abdunur's tests as well as the ordinary test setup uses the reference points A'-A' ($\Delta_{A'A'}$, Figure 3.1), which would require the removal of the cutting saw for each reading. The test procedure used in the present investigation takes measurements between points A-B ($\Delta_{A''B''}$, Figure 3.1), which renders it suitable to the interpretation of the relief stage as the readings can be taken continuously. However, this approach still will face considerable difficulty since the patterns (as shown in Figure 3.32) will be a function of average stress, bending moment, Young's modulus, position of the gages, thickness of the lining and cutting pattern (Figure 3.26). Besides these factors, based on the deviations observed in the in situ tests, it seems necessary to improve the accuracy of the readings at least ten times in order to allow the evaluation of the bending moment.

For this type of lining, it is suggested that a study of the test under bending moment should include steel reinforcement. The presence of the steel might require more

thermal protection, since the results of the in situ test ISJK indicated temperature-related deviations. In the case of bending under exclusively compressive stress, it seems that the first solution (tests at different depths) would provide the best results. In the case of tensile stresses, it seems that the second solution (interpretation of the strains which developed during the relief stage) would be more applicable.

The evaluation of Young's modulus using the results from the flat jack test was not included in the present investigation. However, due to the consistency and linearity of the readings observed during the pressurization stage, it is suggested that studies be done to obtain this parameter. Although Rocha et al. (1966), Rossi et al. (1982) and Abdunur (1985) had presented some results on the subject, due to the different test procedure and setup, further investigations are suggested in order to verify the accuracy of the Young's modulus determination for the present setup.

The mini flat jack test proved to be an economic, fast and reliable procedure to evaluate the in situ stress in tunnel linings. It can be performed by a trained crew in about two hours and the laboratory tests indicated an estimated error of the order of 10% (Table 3.2). In situ tests performed in shotcrete lining older than 2 days, indicated that deviations are of the same order of magnitude as those observed in laboratory tests. It is estimated that the in situ measurements can provide stresses within a 20% error. For tests performed in younger shotcretes, further studies are necessary to ascertain the estimated error.

Table 3.1 Test Conditions for Flat Jack Calibrations

TEST	Age (days)	Composition		Environment Conditions		Mechanical Properties	
		a/c	w/c	RH(%)	Temp(°C)	E(GPa)	f _c (MPa)
CLMR1	12	0.05	0.6	100	5	21.3	15.9
CLMR2	163	0.00	0.6	100	5	23.4	26.9
CLNRH	164	0.00	0.6	52	18	25.0	37.3

a/c accelerator cement ratio
w/c water cement ratio
RH relative humidity
E Young's modulus according to ASTM C469
f_c strength according to ASTM C39

Table 3.2 Calibration Factor for Flat Jack Test

Test	σ (kPa)	Gage	x(cm)	y(cm)	$100\left[\frac{E\Delta_{AB}}{R\sigma}\right]$	$\frac{\sigma_{FJ}}{\sigma}$ (CF)
CLMR1	824	VW1	0.8	5.5	42.6	1.380
		VW2	8.6	5.5	28.4	1.310
CLMR2	845	VW1	3.8	4.0	32.6	1.251
		VW2	11.3	4.0	-	-
CLNRH	844	VW1	2.5	7.0	28.8	1.230
		VW2	7.5	7.0	16.5	1.274
						1.289 (average)

σ stress applied to the concrete block
x, y relative position of the strain gage to the slot (Figure 3.7)
σ_{FJ} hydraulic pressure in the flat jack
E Young's Modulus (Table 3.1)
Δ_{AB} relative displacements between the monitoring points (Figure 3.7)
R radius of the cutting saw
σ_{FJ} / σ ratio corresponding to the Flat Jack Correction Factor (CF)

Table 3.3 Calibration Factor for Eccentric Loading, Test ELNRH

Aver. Stress σ (kPa) (1)	E (GPa) (2)	f_c (MPa) (3)	Gage	x (cm)	y (cm)	$100 \left[\frac{E \Delta_{AB}}{R \sigma} \right]$	$\frac{\sigma_{FJ}}{\sigma}$ (CF)
1.33	28.2	36.7	VW1	7.7	7.5	35.8	1.336
			VW2	2.5	7.5	50.1	1.396

(1) according to procedure described in text (eccentricity=1.9 cm)

(2) according to ASTM C469

(3) according to ASTM C39

$\frac{\sigma_{FJ}}{\sigma}$ ratio corresponding to the Flat Jack Correction Factor (CF)

Table 3.4 Summary of In Situ Tests, SLRT/NATM South Bound Tunnel

Test	L_t (m)	D_t (m)	D_{bt} (m)	Age (hours)	t_1 (cm)	α_t (degree)	DIR.	θ_t (min)	Gage	$10^{-6} \left[\frac{\Delta_{AB}}{R} \right]$	Stress (kPa)
IST1/1	5	0.5	4.4	12	15	199	(R)	6	VW1	14.7	750
									VW2	17.4	741
IST1/2	5	1.5	4.4	15	16	199	(L)	4	VW1	17.4	423
									VW2	21.6	417
IST1/3	5	12.5	3.4	72	13	195	(R)	8	VW1	-13.2	-
									VW2	-13.9	-
IST2/1	3	14.5	5.5	107	13	101	(R)	9	VW1	16.9	836
									VW2	-	-
IST2/2	3	14.5	5.5	108	10	137	(R)	10	VW1	15.3	759
									VW2	15.3	759
IST2/3	3	14.5	5.5	110	14	198	(R)	8	VW1	-13.2	-
									VW2	-11.1	-
IST3/1	-	62.8	3.1	462	19	255	(R)	26	VW1	12.5	1219
									VW2	8.3	978
IST3/2	-	62.8	3.1	465	23	288	(R)	8	VW1	6.6	361
									VW2	8.3	455
IST3/3	-	62.8	3.1	467	20	255	(L)	17	VW1	1.4	~0
									VW2	-0.3	~0

$L_t, D_t, D_{bt}, t_1, \alpha_t$ according to Figure 3.16

DIR. Direction of the test: (R)=radial test; (L)=longitudinal test

θ_t time to execute the first cutting

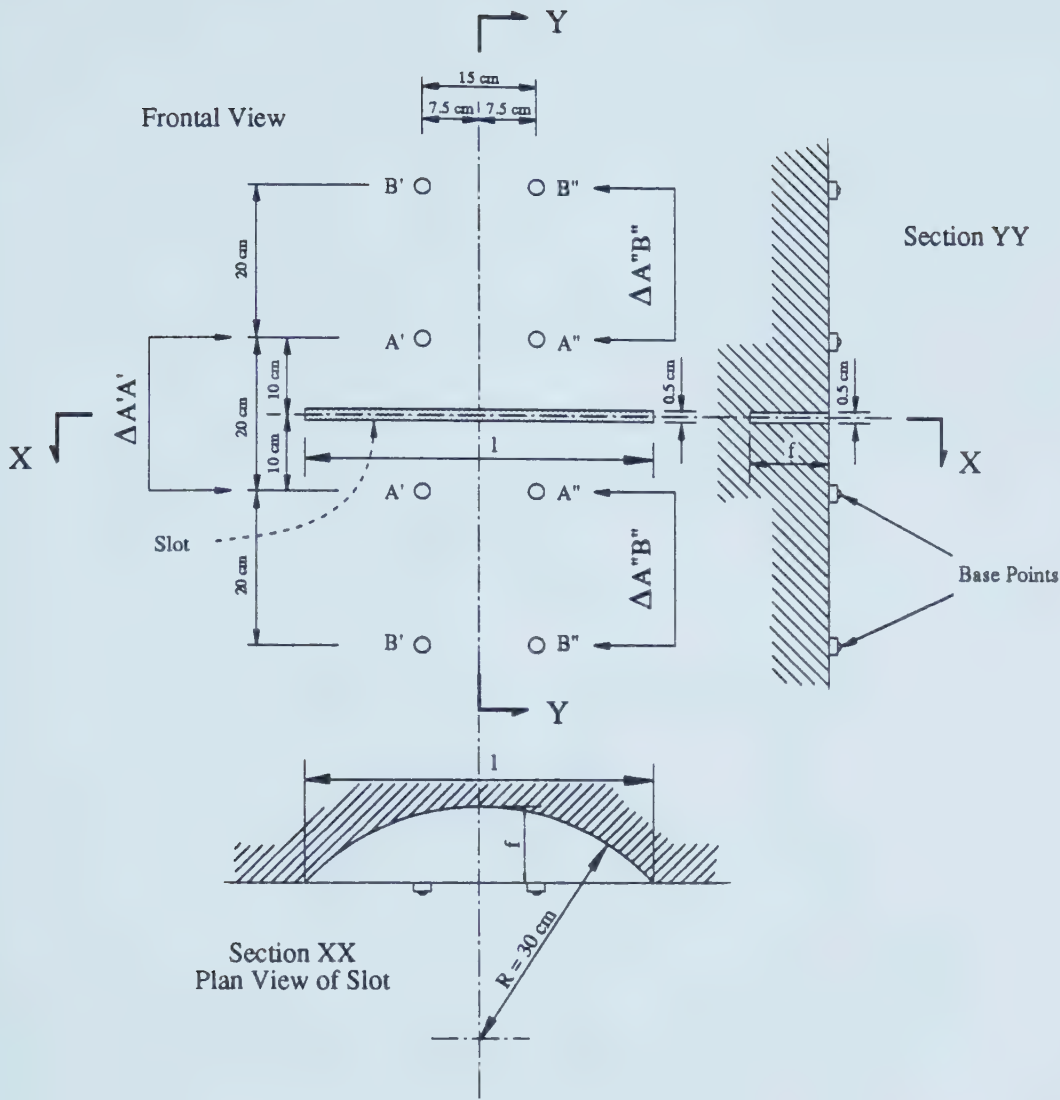


Figure 3.1 Layout of LNEC Flat Jack Test (modified from Rocha et al., 1966)

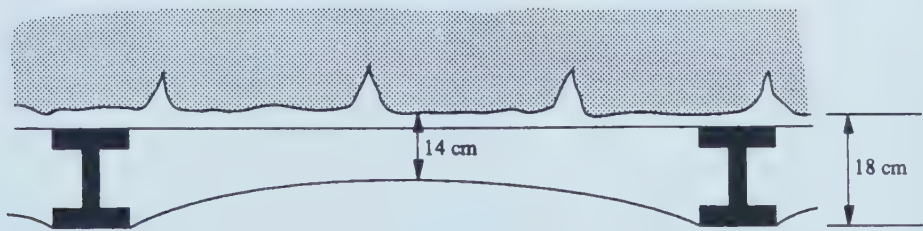


Figure 3.2 Longitudinal Cross Section of SLRT Lining, NATM Tunnels

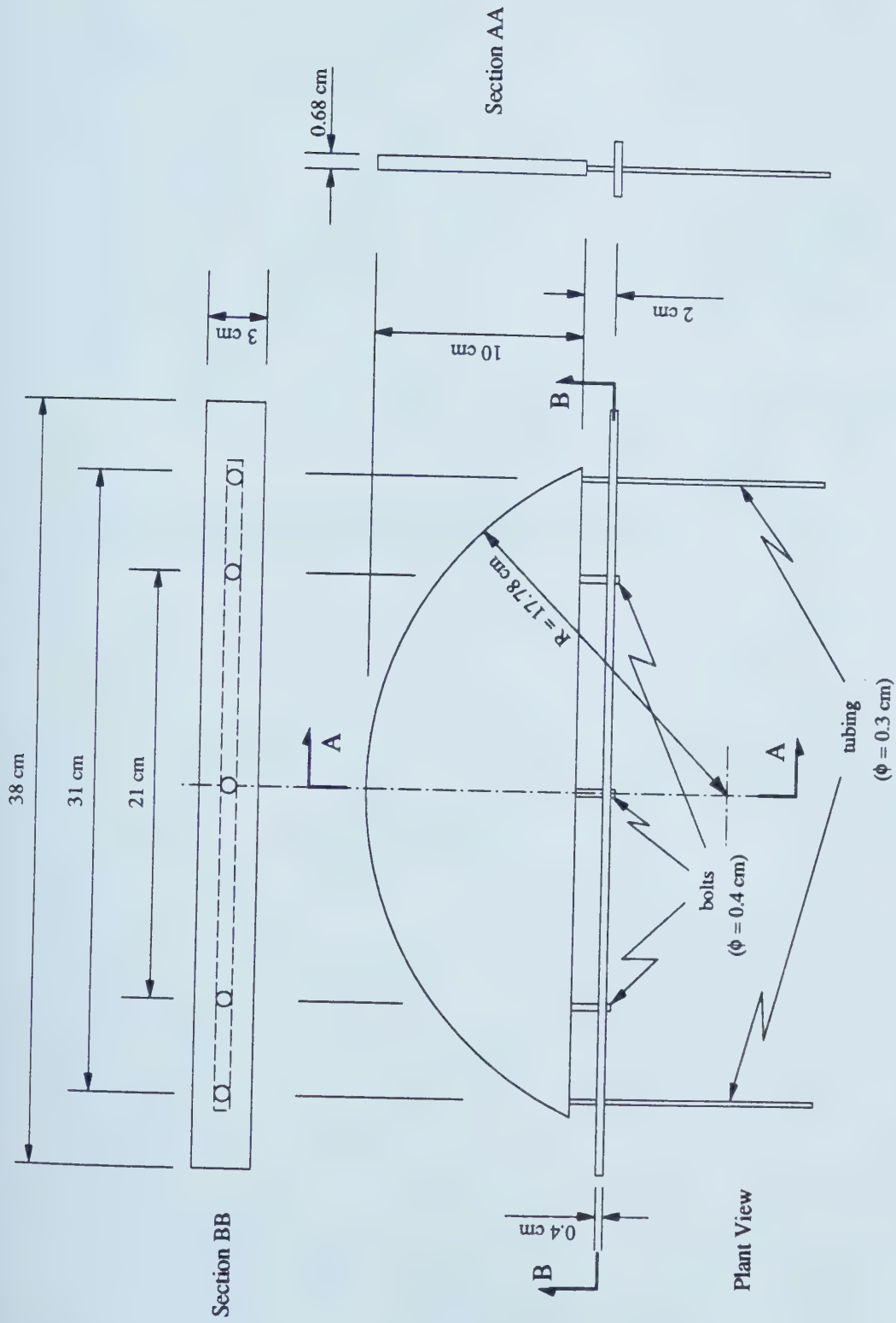


Figure 3.3 Layout of Mini Flat Jack

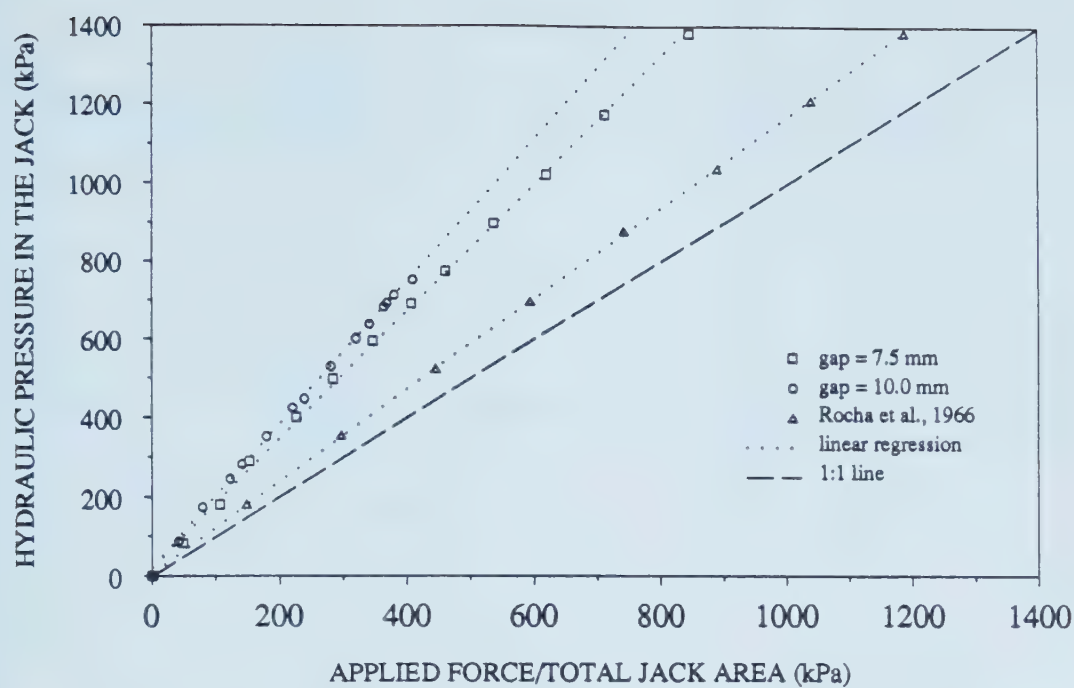


Figure 3.4 Load Transmission Characteristics of Flat Jack

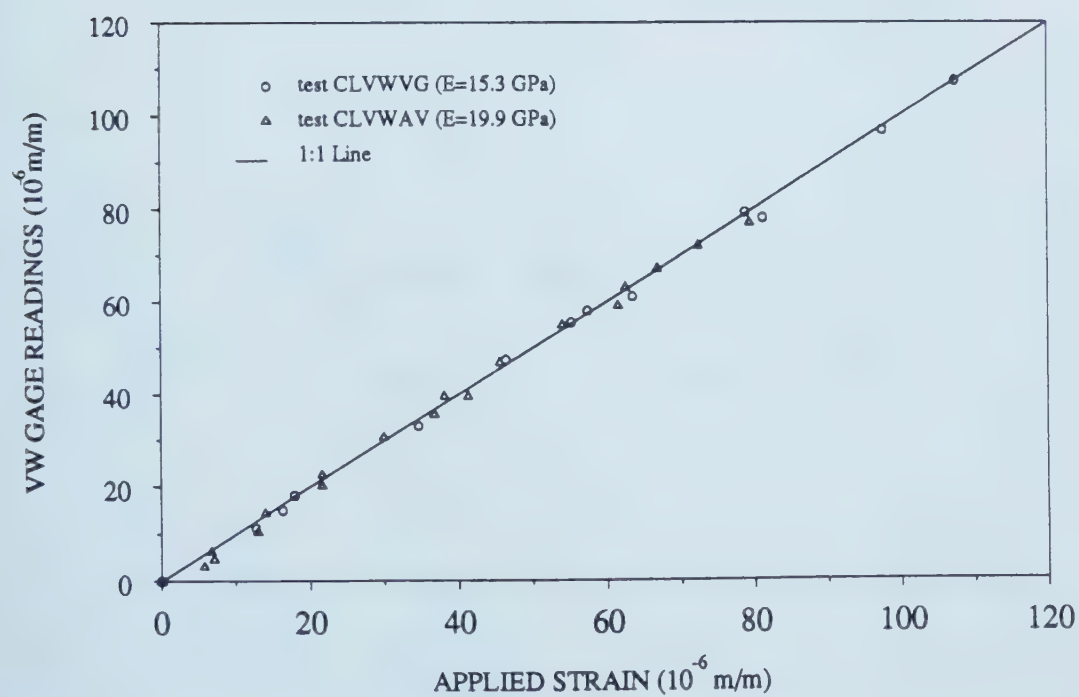
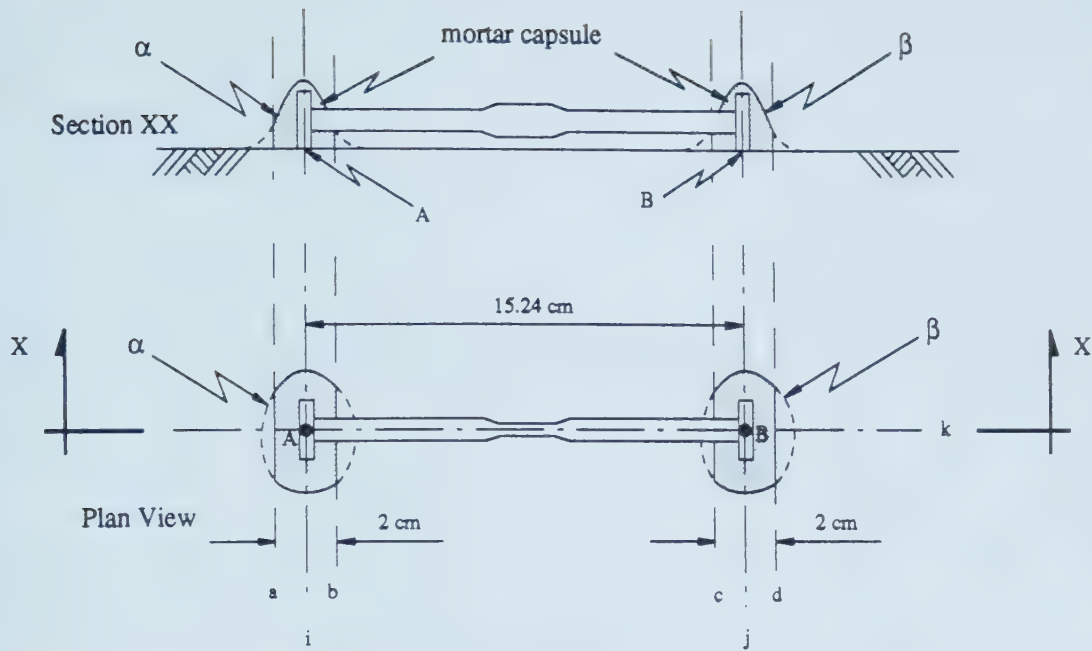
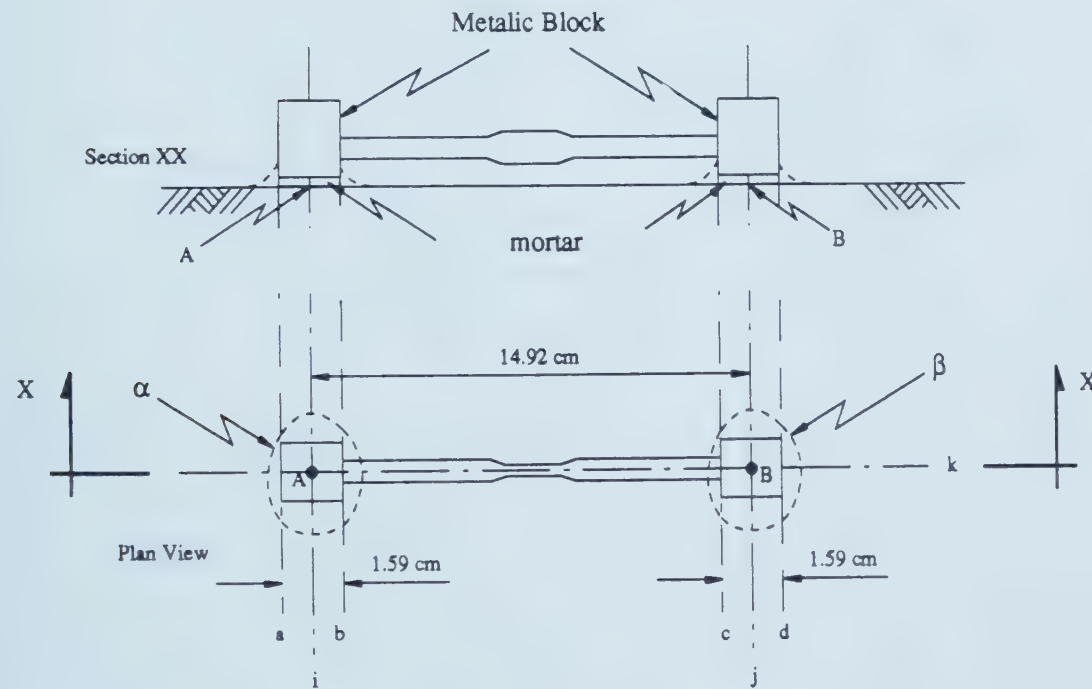


Figure 3.5 Tests of Installation of Vibrating Wire Strain Gages (VW) on Concrete Cylinders



a) Installation of Vibrating Wire VCE-4200 (Laboratory and SLRT Tunnels Tests)



b) Installation of Vibrating Wire VSM-4000 (Complementary In Situ Tests)

Figure 3.6 Layout of Installation of Vibrating Wire Strain Gages

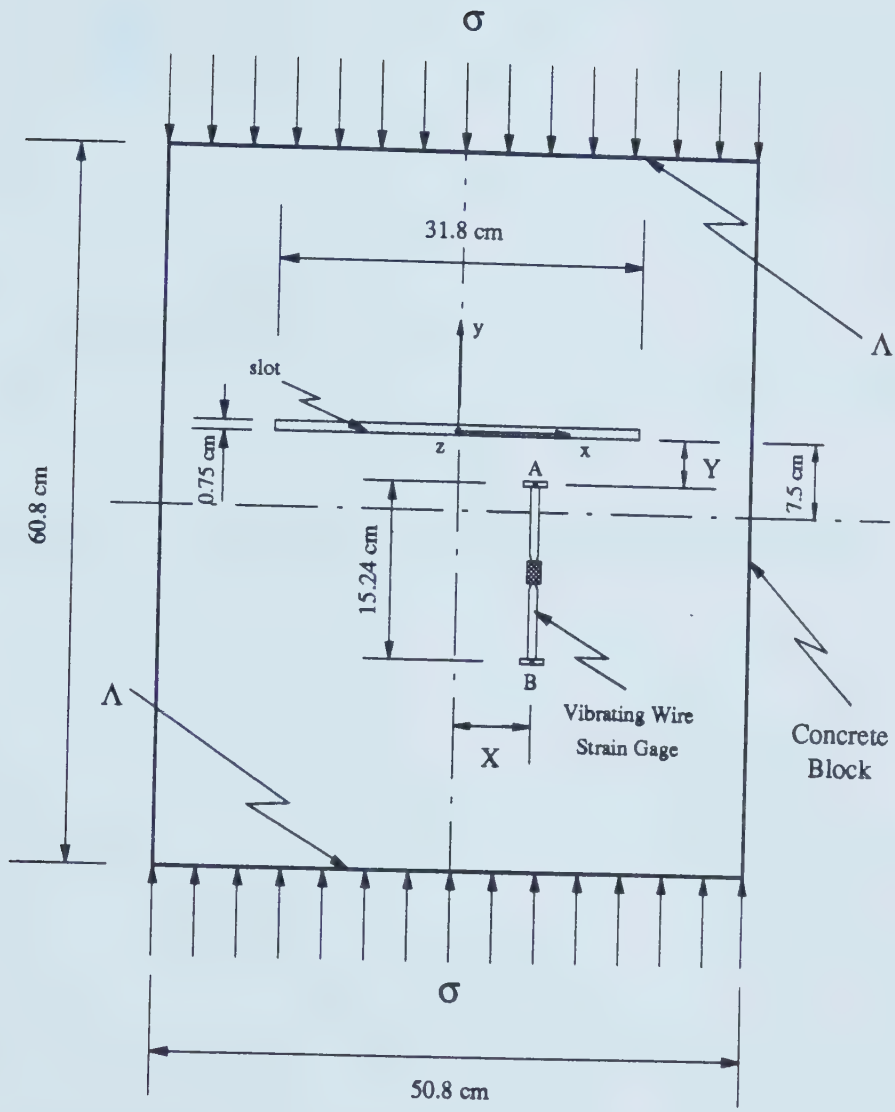


Figure 3.7 Layout of Laboratory Mini Flat Jack Test

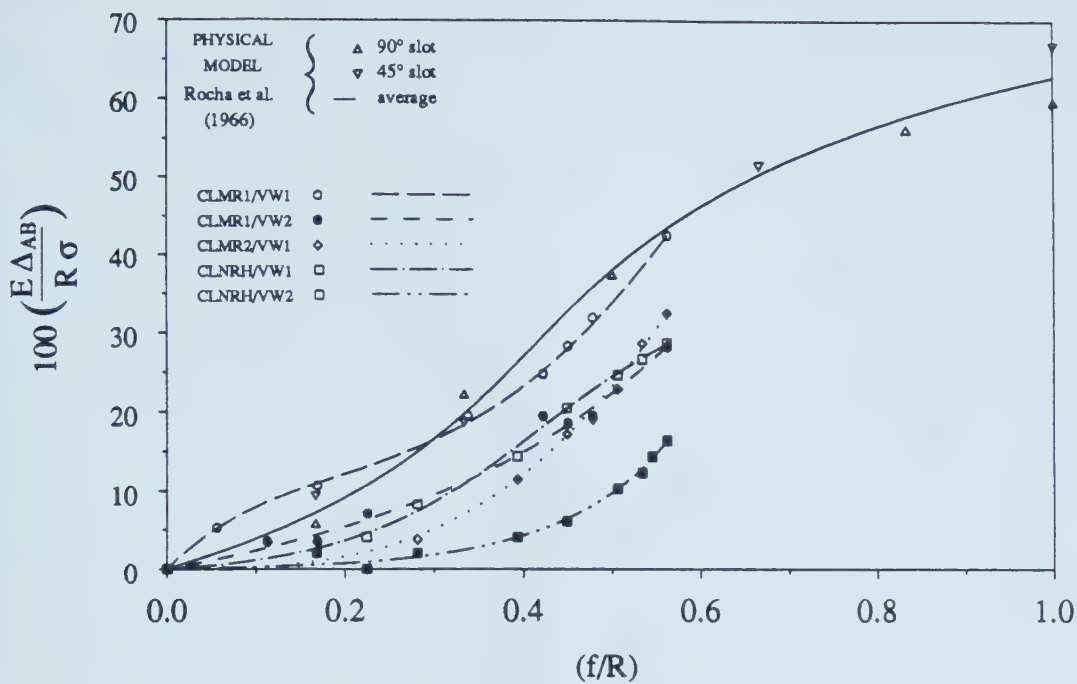


Figure 3.8 Relative Displacements during the First Cutting, Laboratory Tests

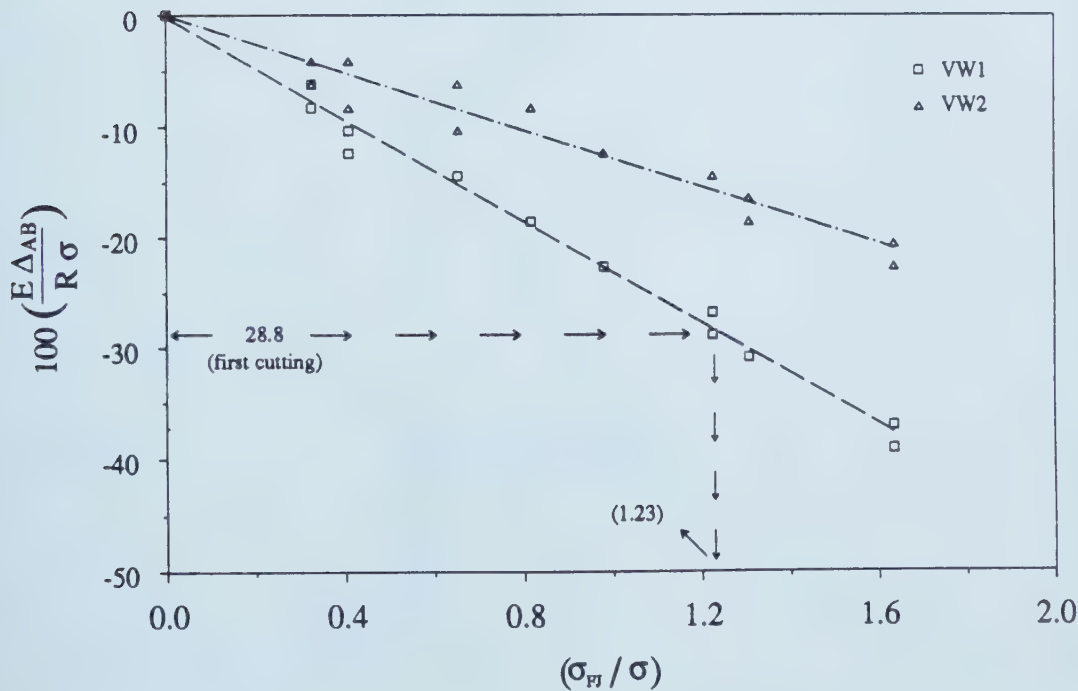


Figure 3.9 Relative Displacements during Jack Pressurization Stage, Test CLNRH

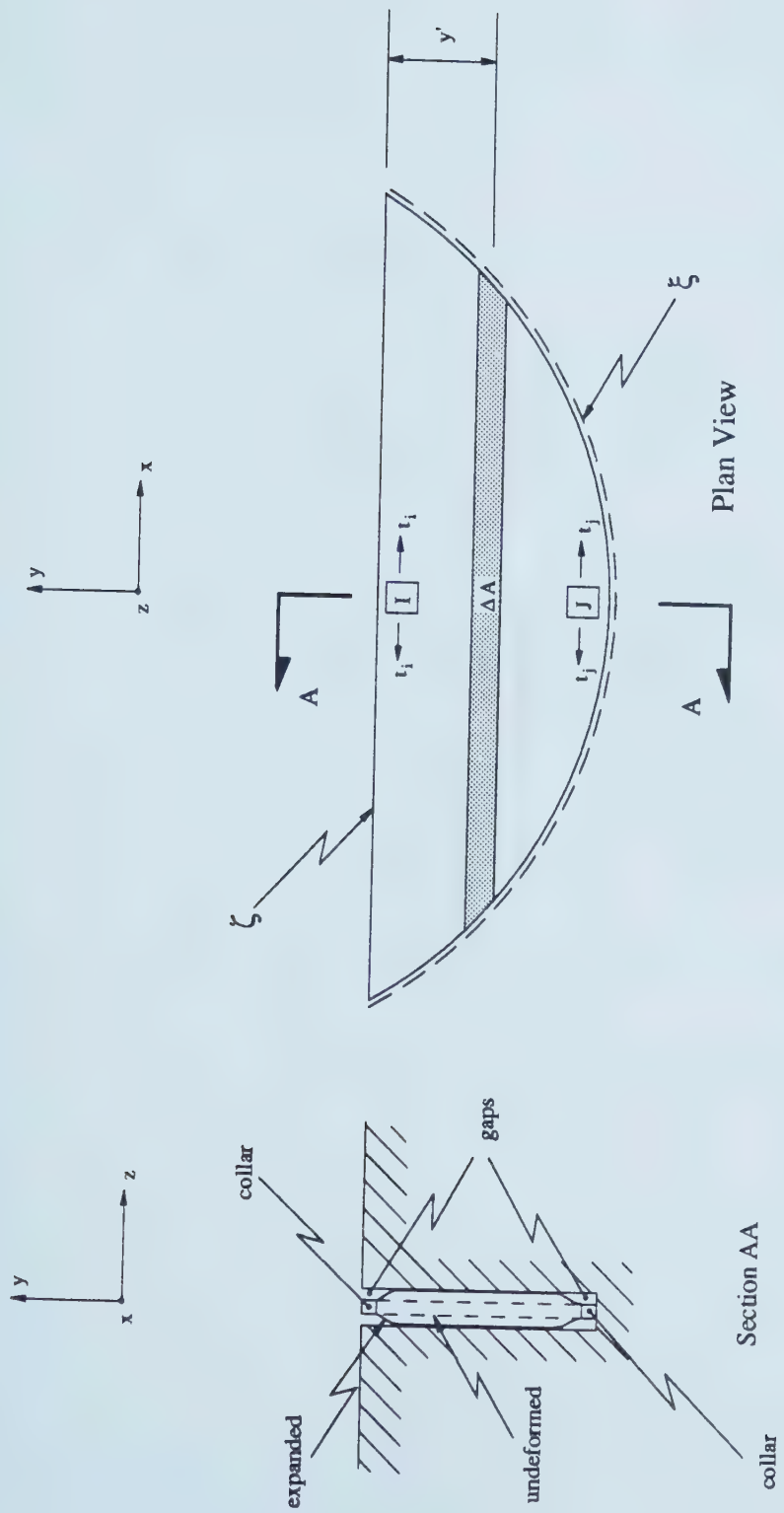


Figure 3.10 Illustration of Pressure Transmission Deficiency

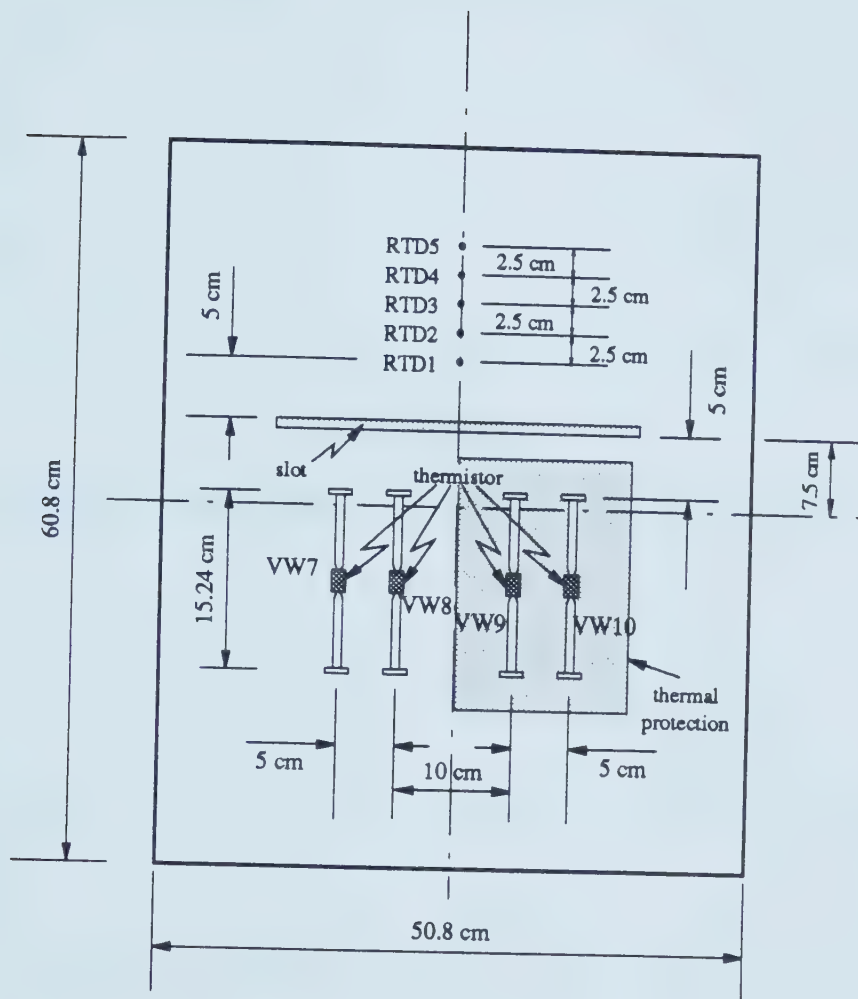


Figure 3.11 Layout of Test FLDV

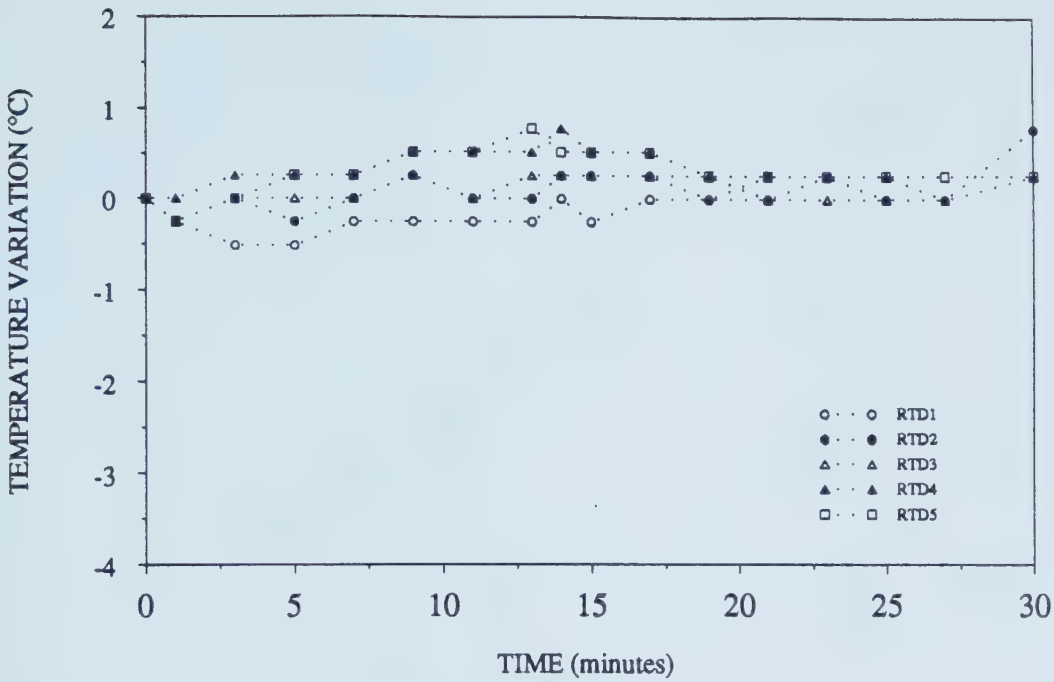


Figure 3.12 Temperature Readings taken by RTDs during Cutting, Test FLDV

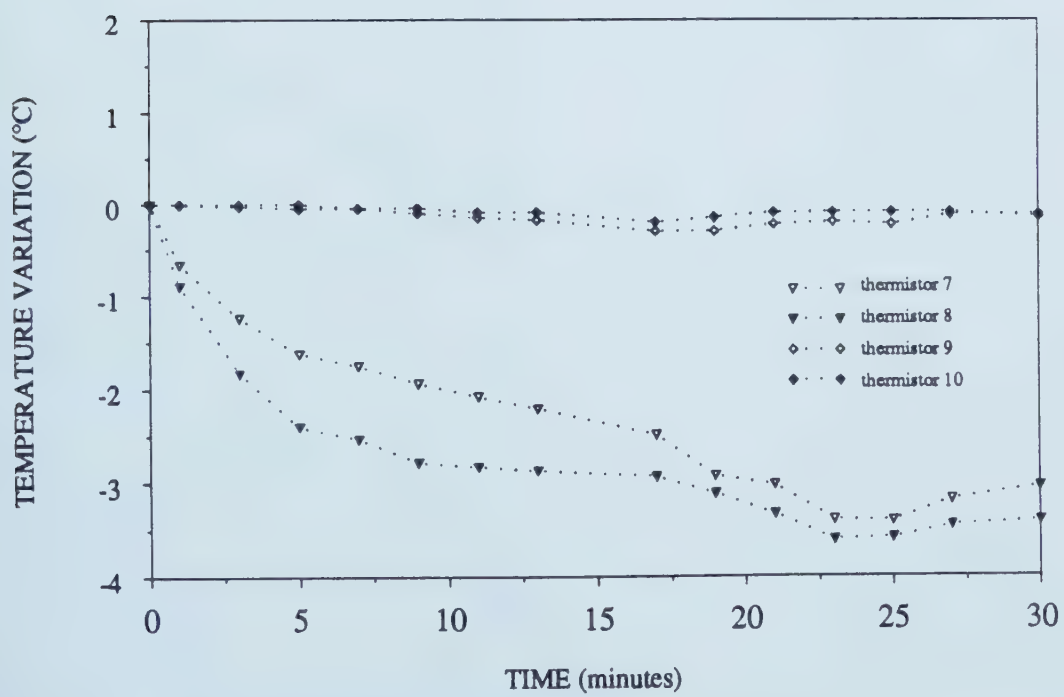


Figure 3.13 Temperature Readings taken by Thermistors during Cutting, Test FLDV

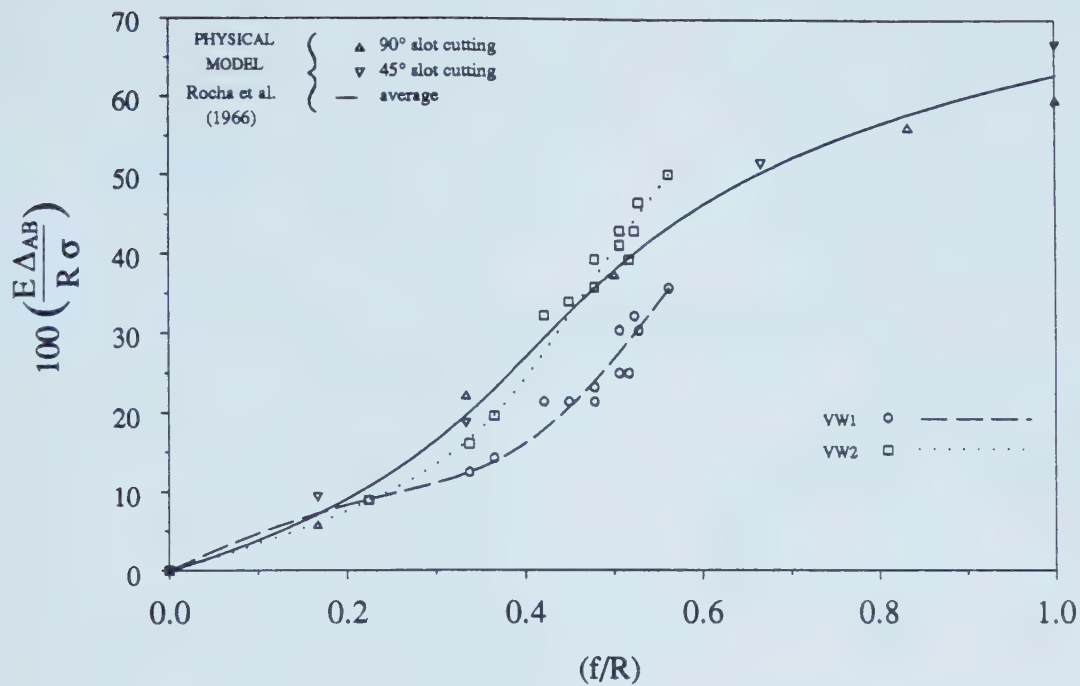


Figure 3.14 Relative Displacements during the First Cutting, Test ELNRH

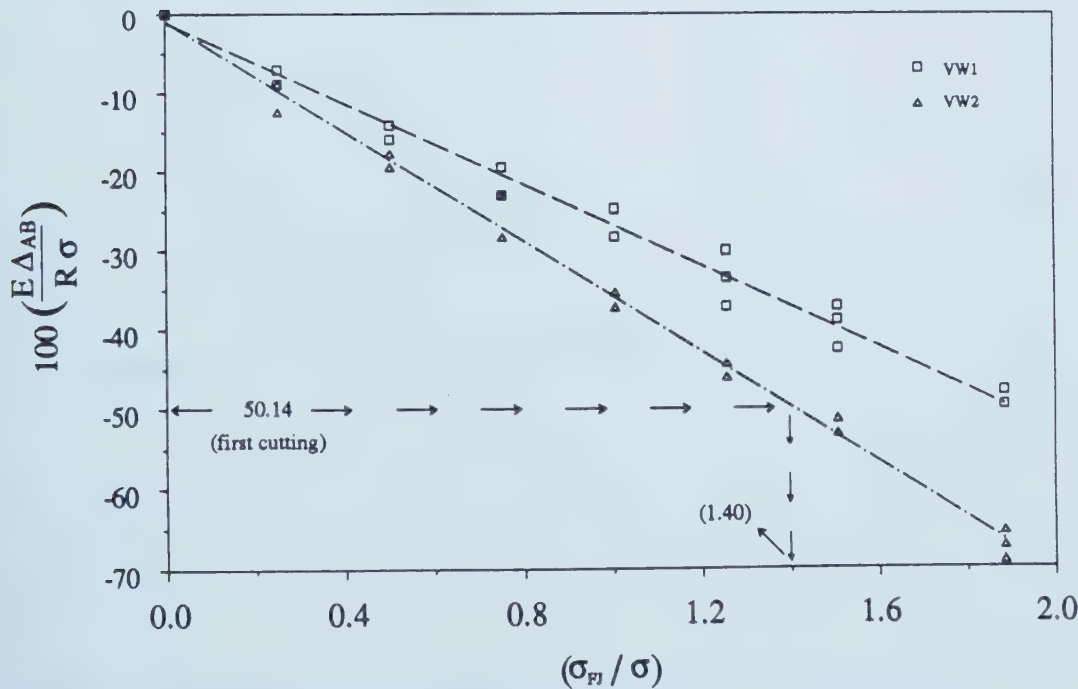


Figure 3.15 Relative Displacements during Jack Pressurization Stage, Test ELNRH

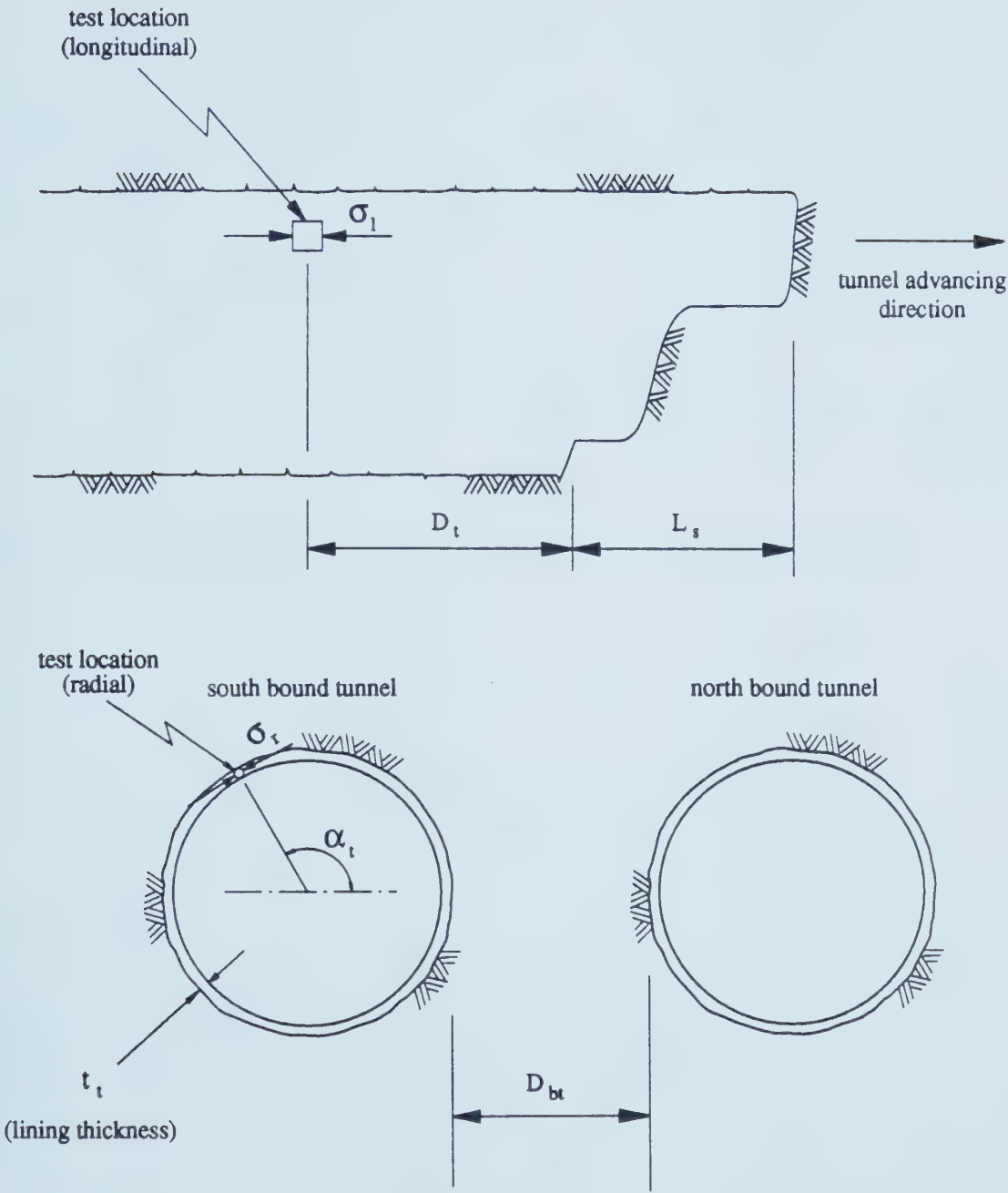


Figure 3.16 Geometrical Parameters used to describe In Situ Test Location SLRT, South Bound Tunnel

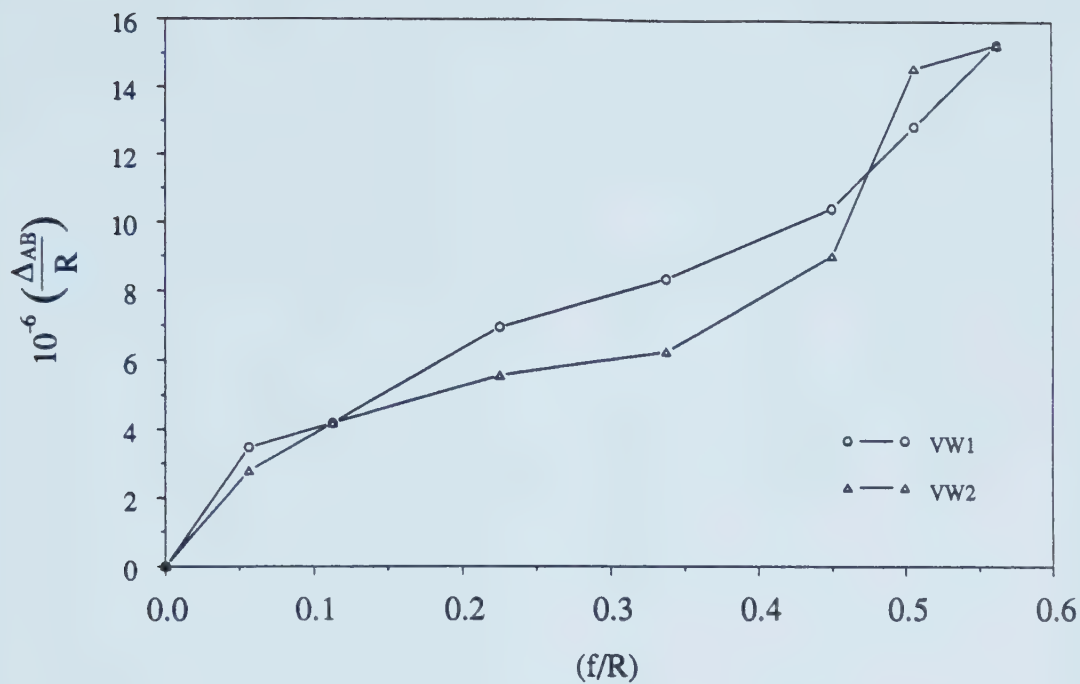


Figure 3.17 Relative Displacements during the First Cutting, In Situ Test IST2/2

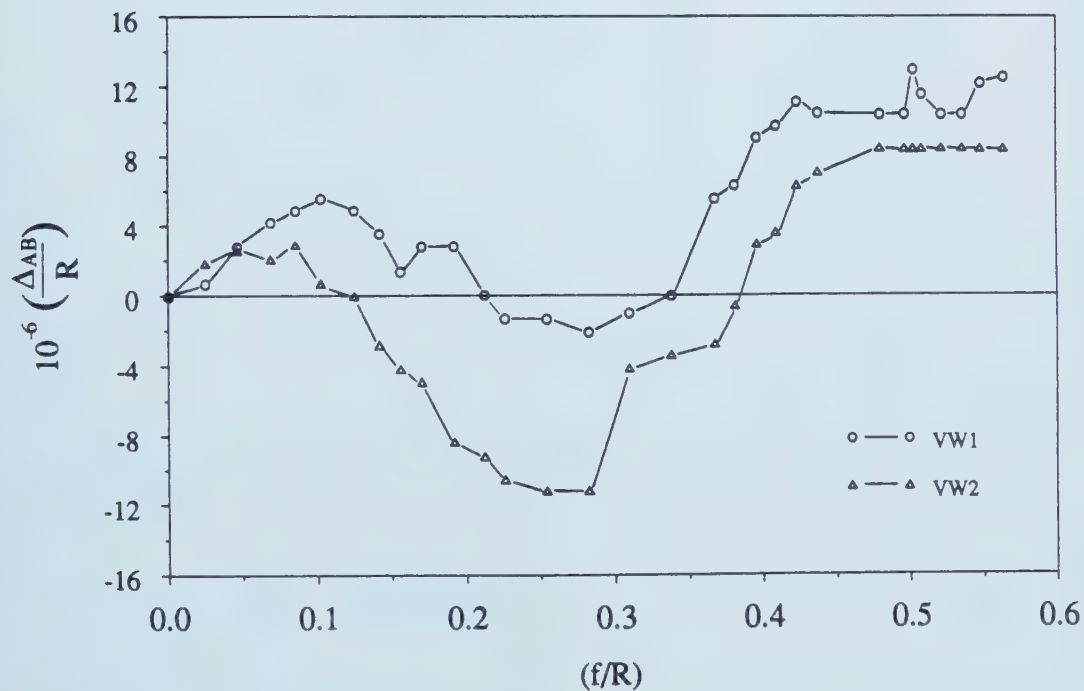


Figure 3.18 Relative Displacements during Jack Pressurization Stage, In Situ Test IST3/1

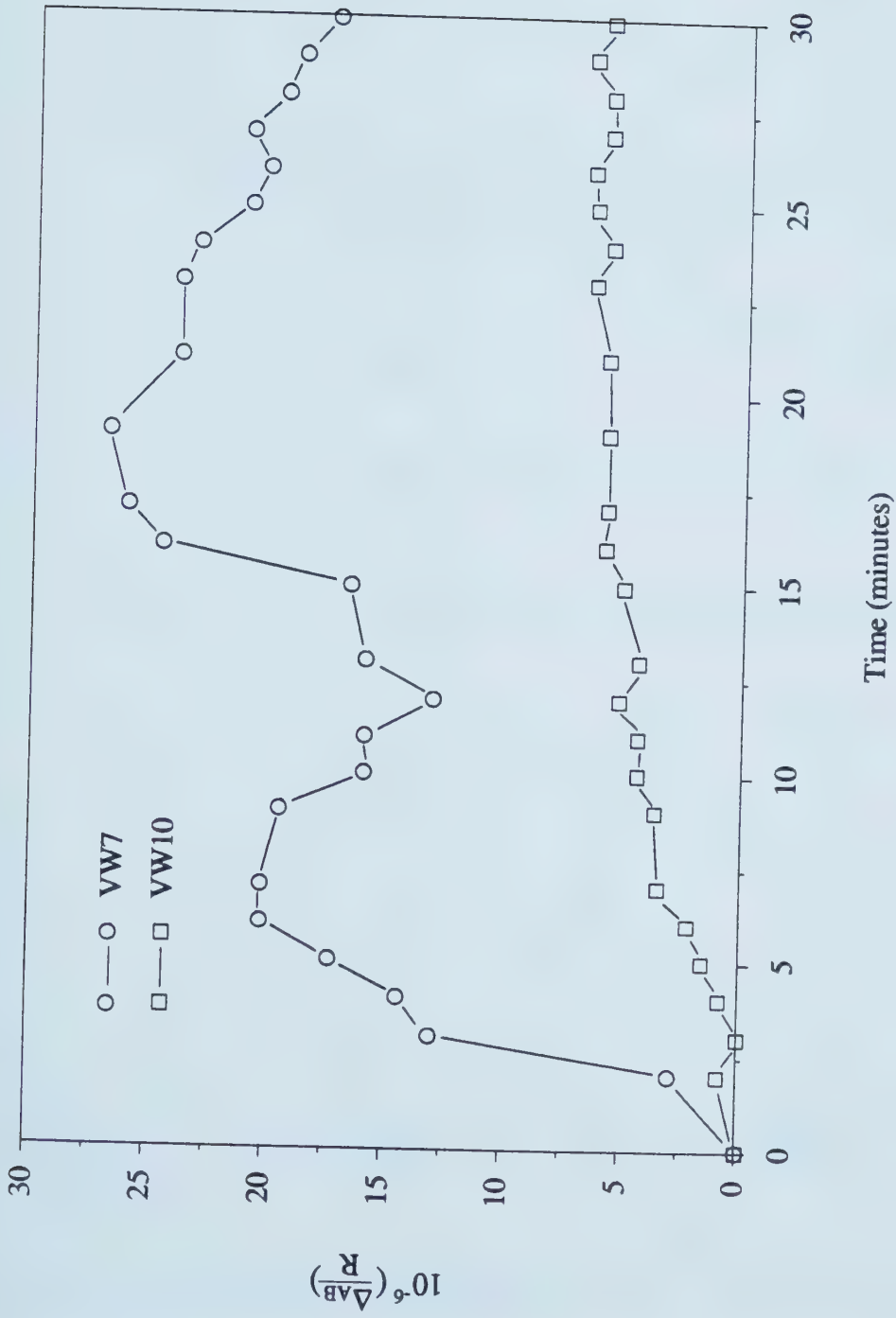
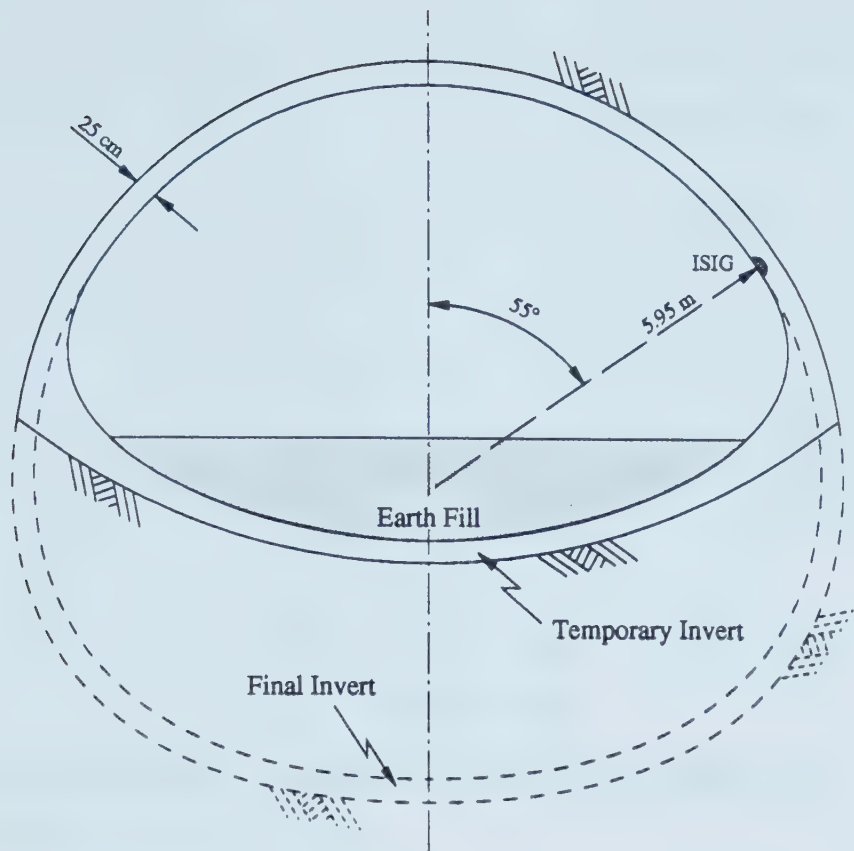
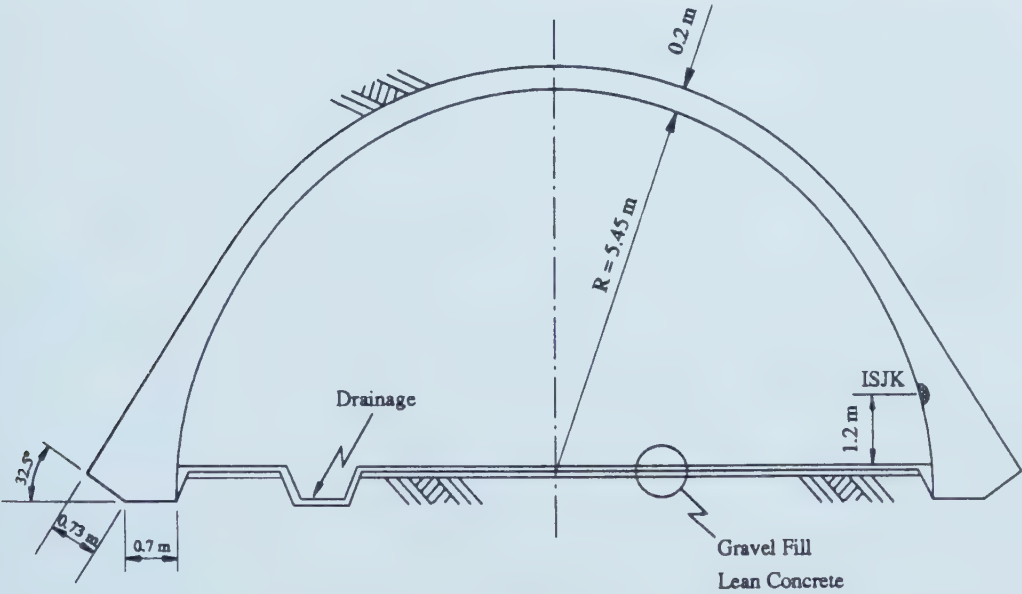


Figure 3.19 Relative Displacement Readings recorded by Thermally Protected Gage VW10 and for Unprotected VW7, during Cutting, Test FLDV



a) Cohab Tunnel, Line East-West, Itaquera/Guaianazes, Sao Paulo Metro System, Brazil, TEST ISIG



b) Tunnel under Pinheiros River, Viario Juscelino Kubistchek, Sao Paulo, Brazil, TEST ISJK

Figure 3.20 Cross Section of Tunnels where Complementary In Situ Tests were Performed

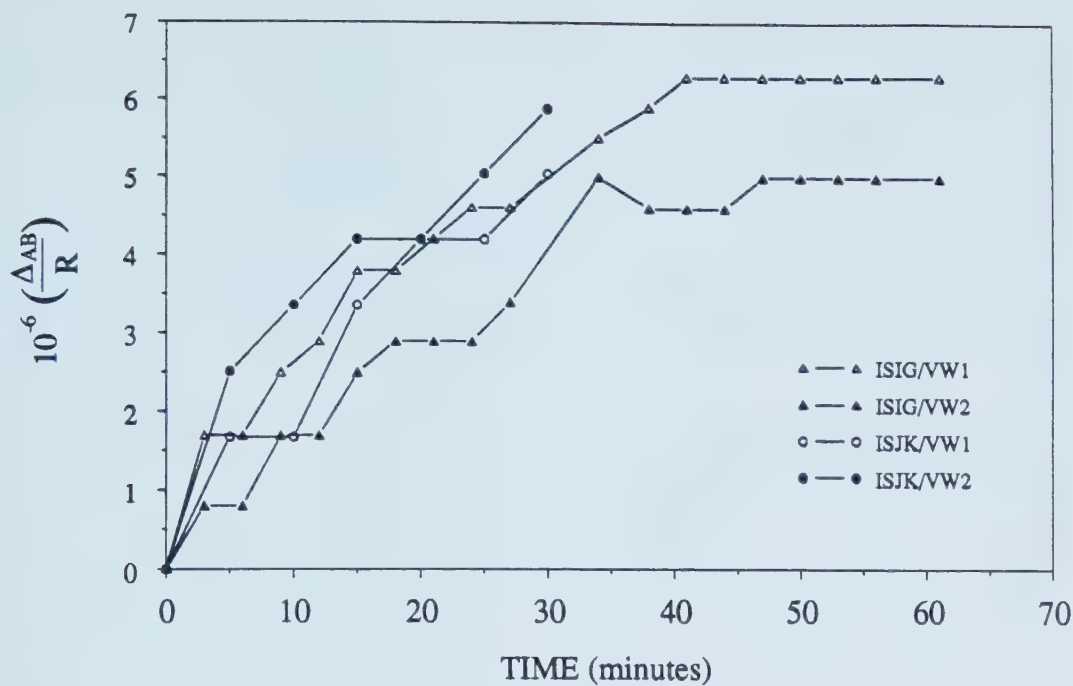


Figure 3.21 Relative Displacement Readings during Thermal Equalization, Complementary In Situ Tests

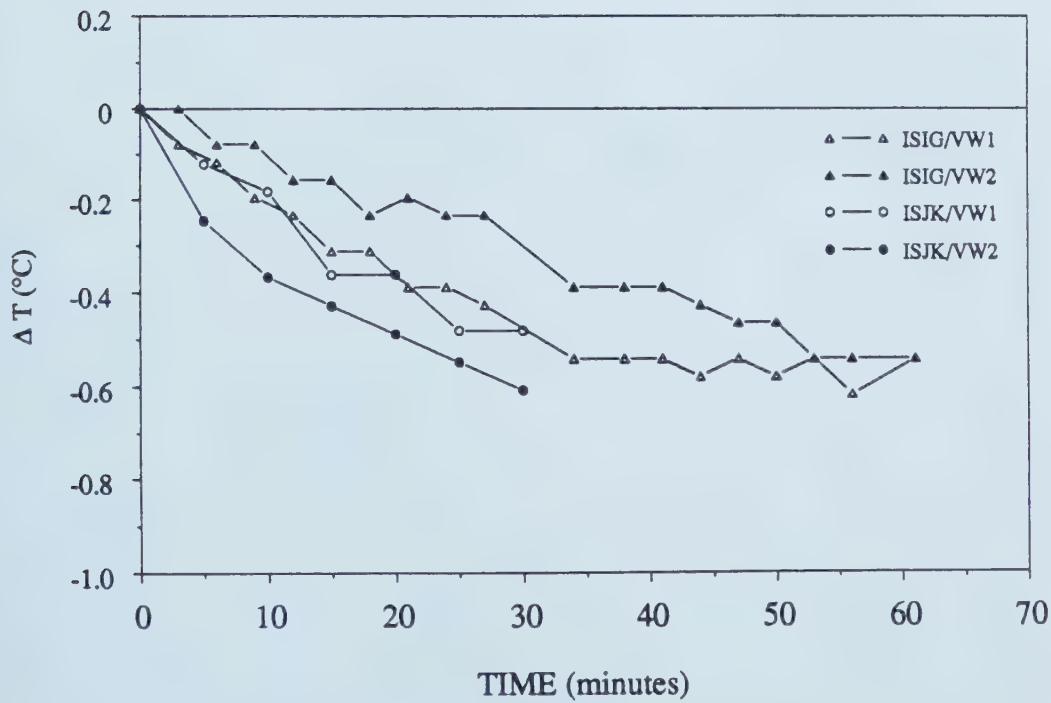


Figure 3.22 Temperature Reading Variation during Thermal Equalization, Complementary In Situ Tests

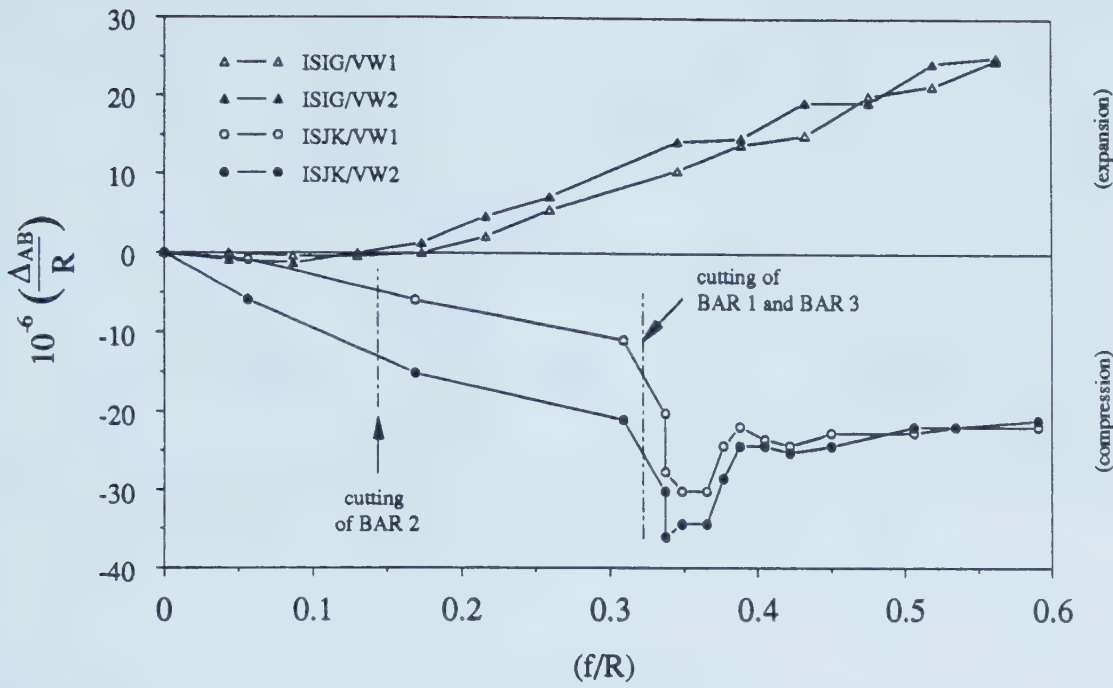


Figure 3.23 Relative Displacement Readings during the First Cutting, Complementary In Situ Tests

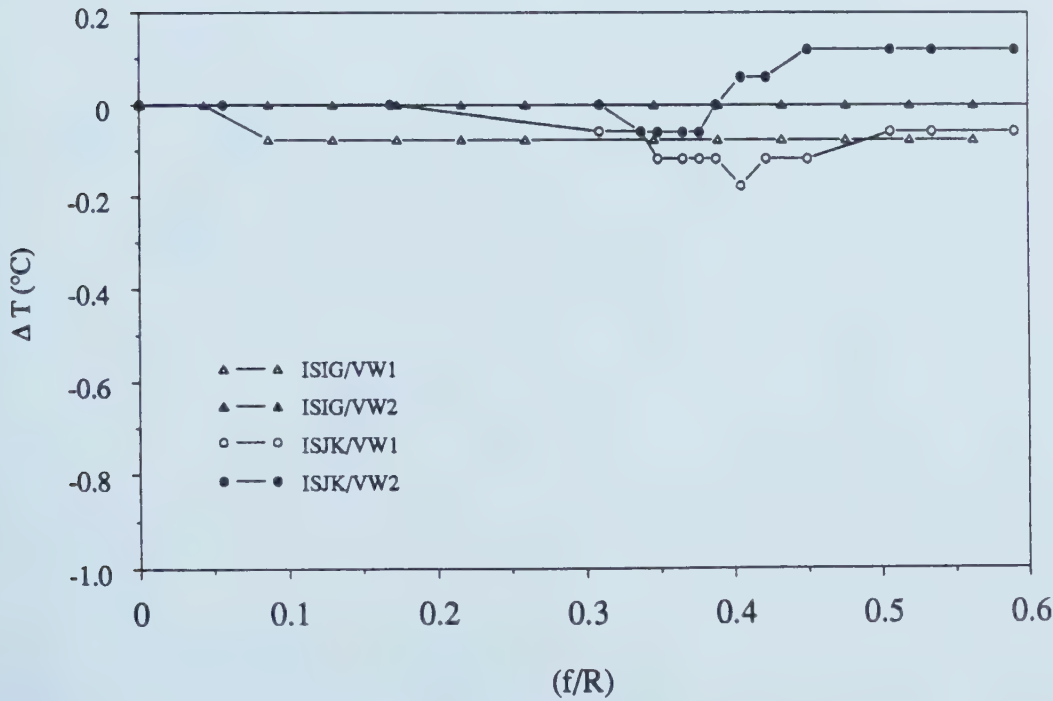


Figure 3.24 Temperature Reading Variation during the First Cutting, Complementary In Situ Tests

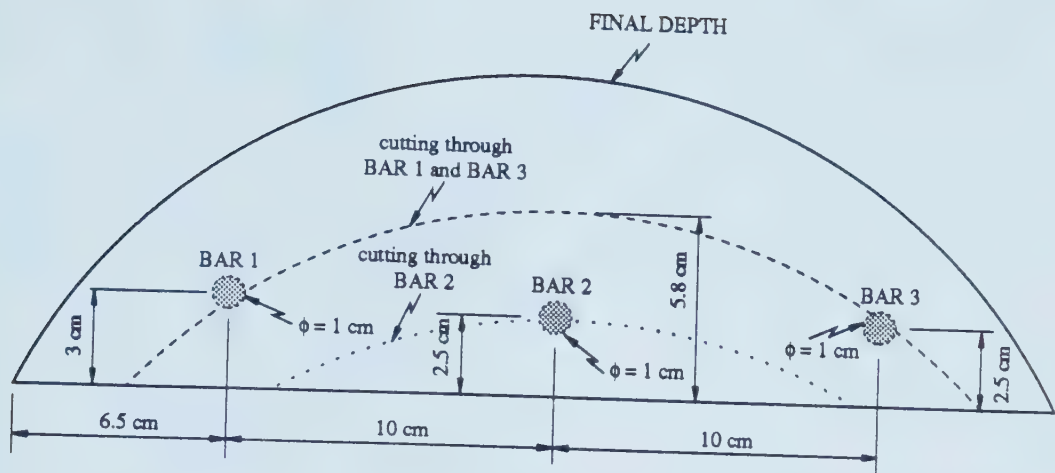


Figure 3.25 Lay Out of the Cutting Plane of Test ISJK

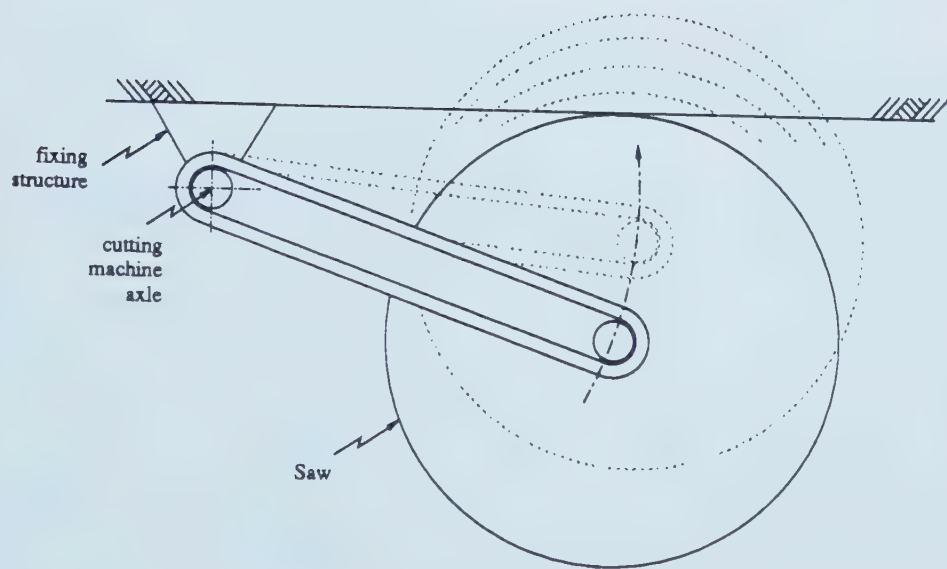


Figure 3.26 Scheme of Curved Path of Cutting Front

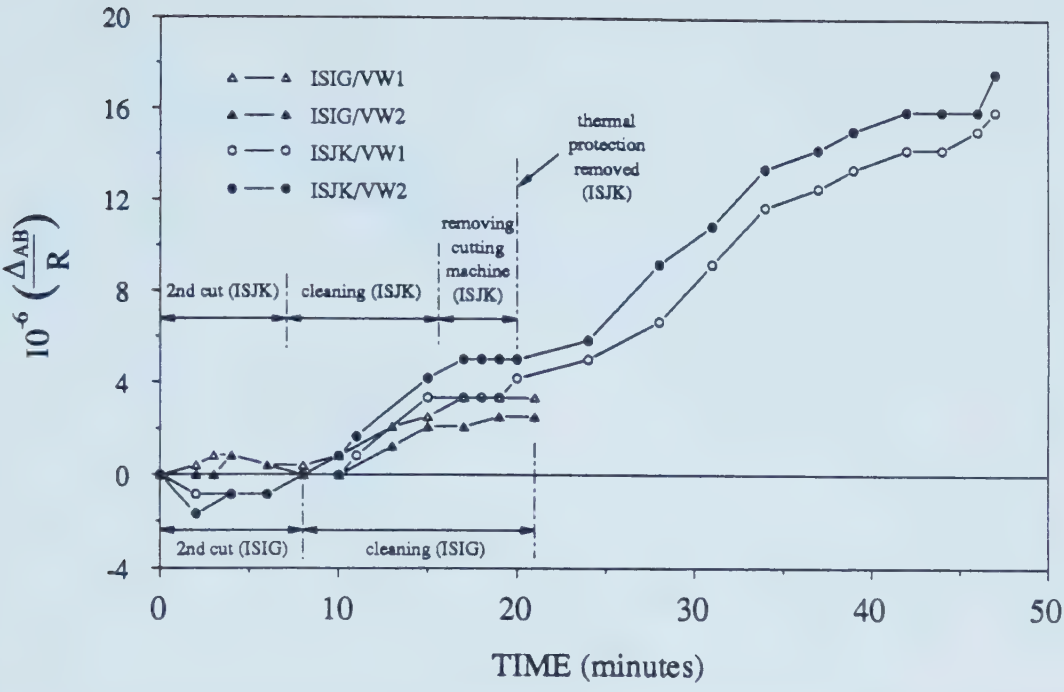


Figure 3.27 Relative Displacement Readings during Second Cutting and Slot Cleaning, Complementary In Situ Tests

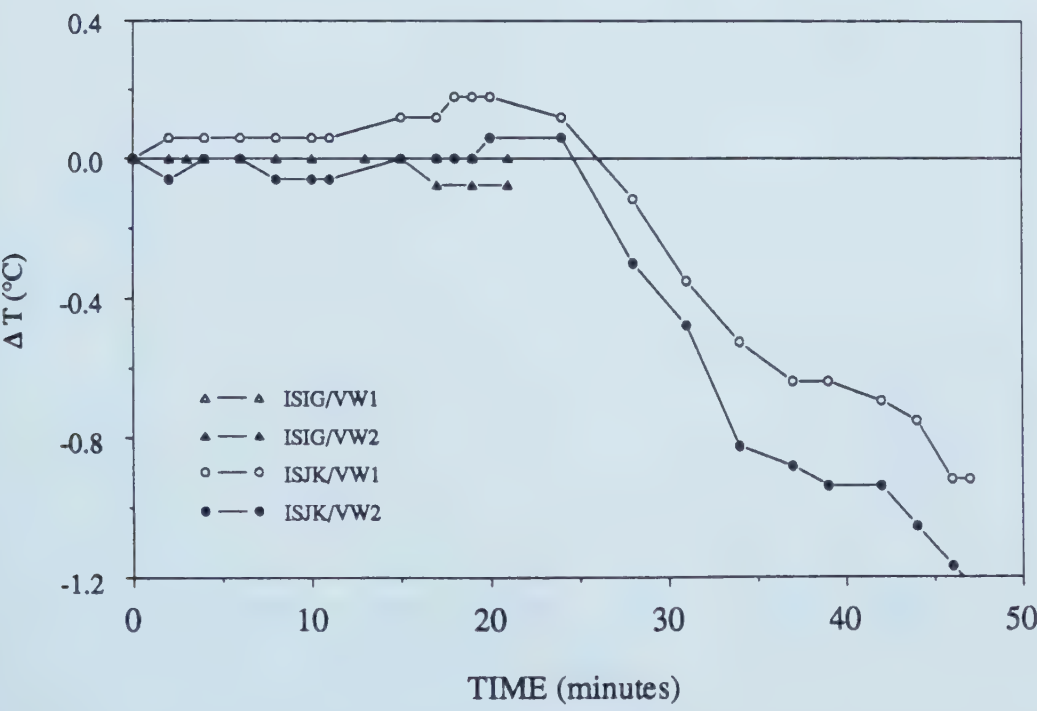


Figure 3.28 Temperature Reading Variation during Second Cutting and Slot Cleaning, Complementary In Situ Tests

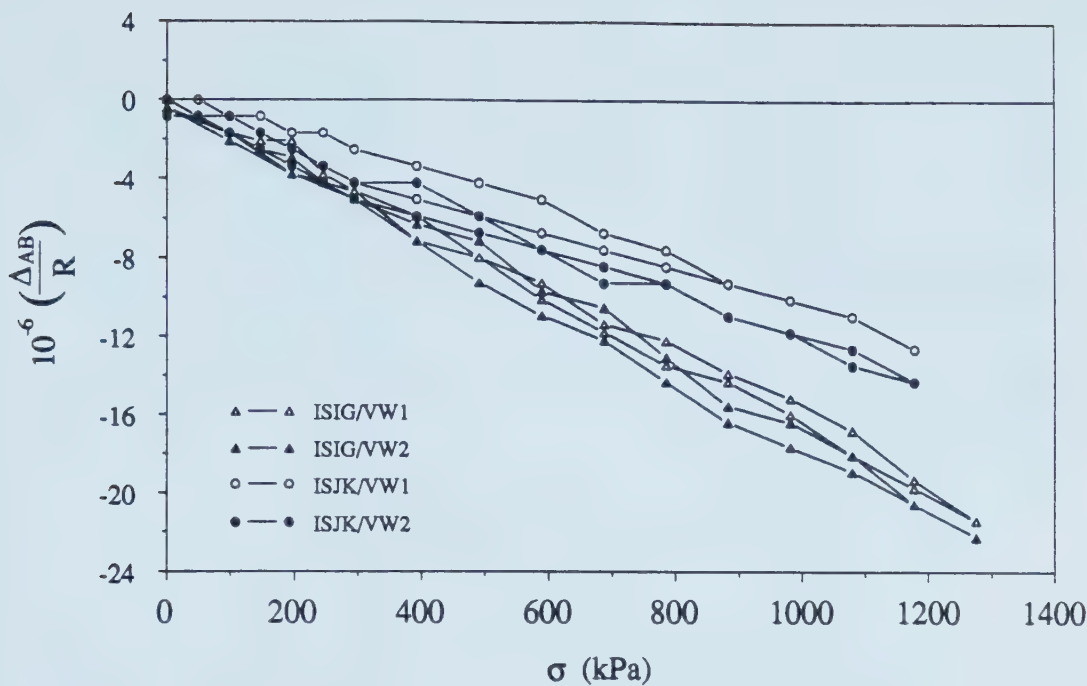


Figure 3.29 Relative Displacement Readings during Pressurization Stage, Complementary In Situ Tests

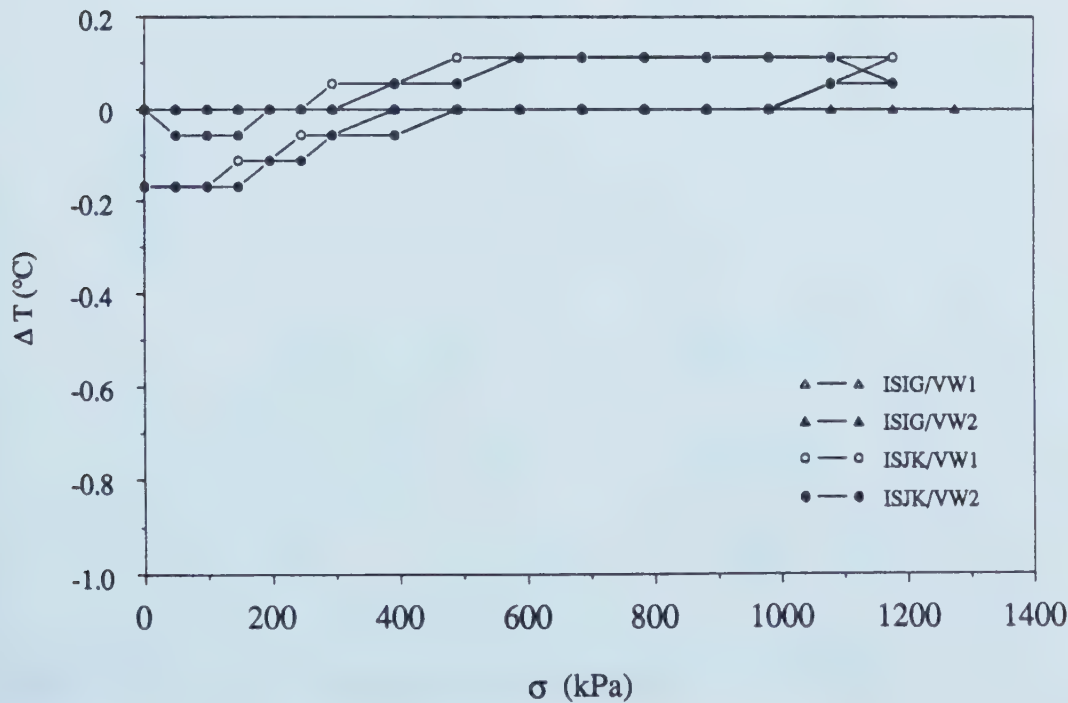


Figure 3.30 Temperature Reading Variation during Pressurization Stage, Complementary In Situ Tests

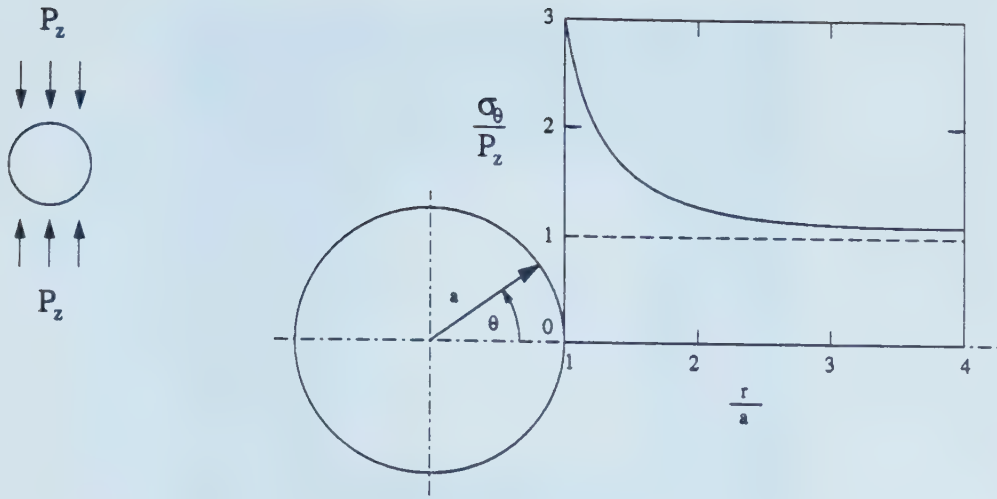


Figure 3.31 Stress Concentration around a Tunnel, Elastic Solution

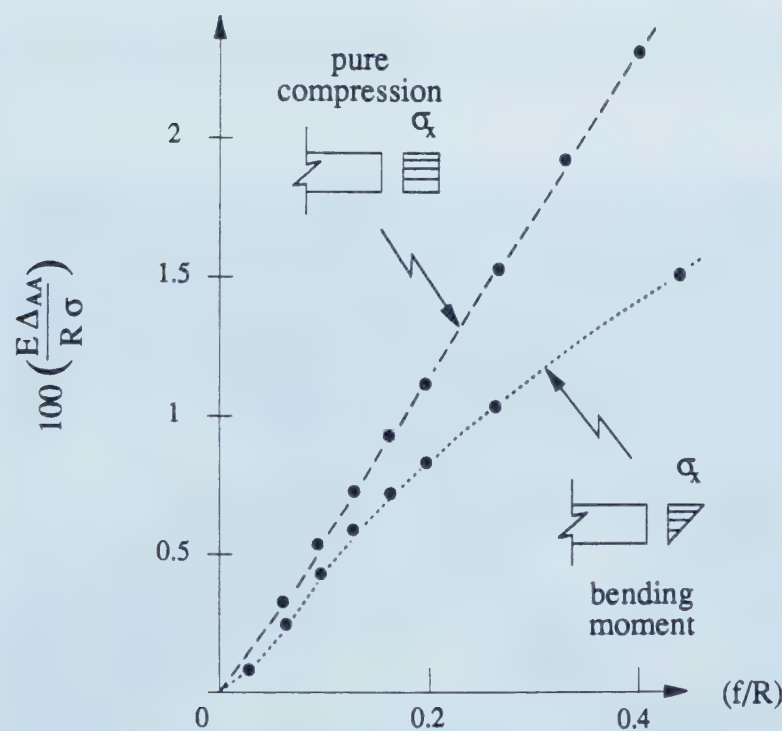


Figure 3.32 Relative Displacements during Cutting, Laboratory Tests (modified from Abdunur, 1985)

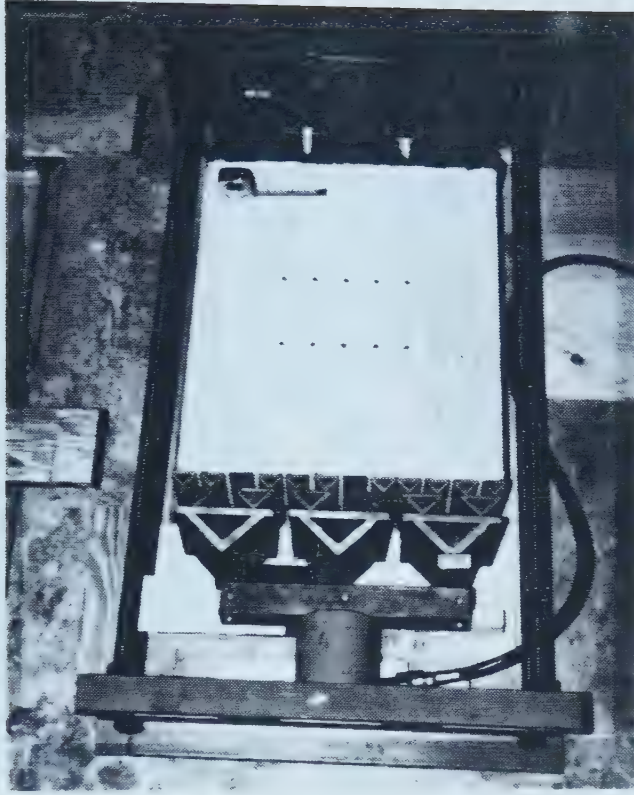


Plate 3.1 Stress Application System used in Mini Flat Jack Tests Performed in Laboratory

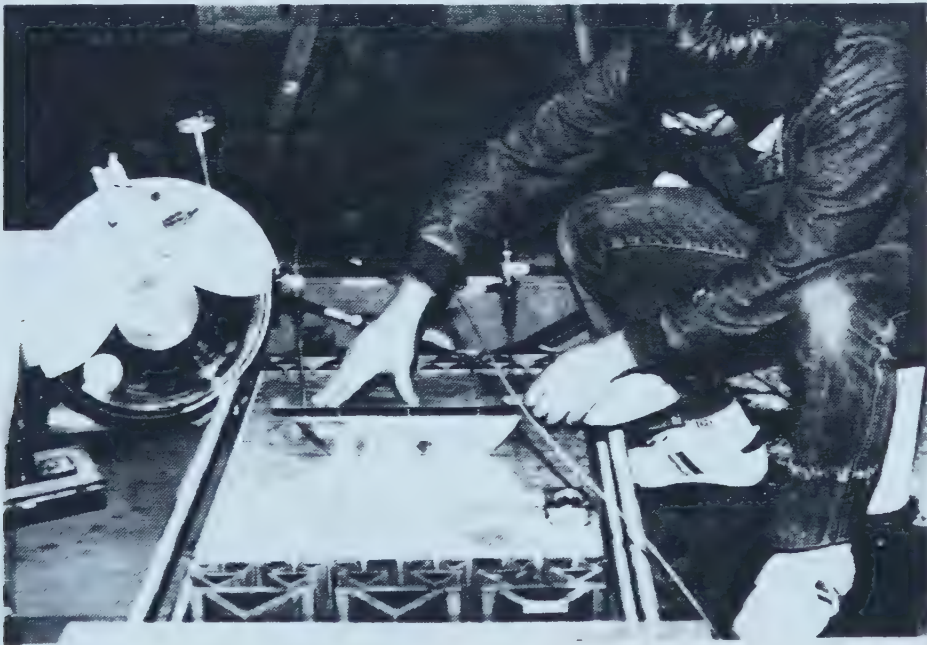


Plate 3.2 Insertion of Mini Flat Jack into Slot during Laboratory Tests

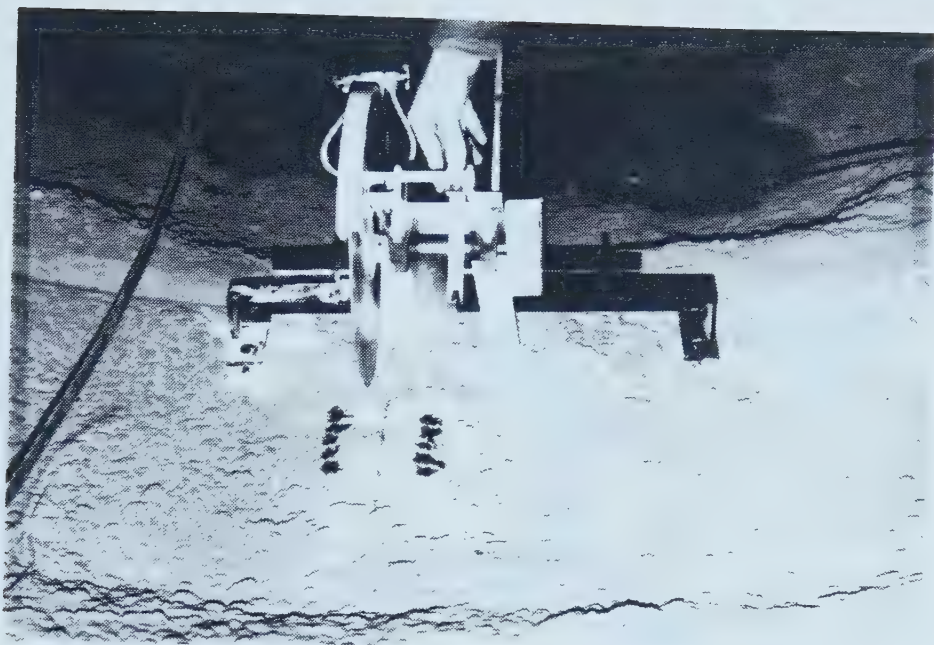


Plate 3.3 In Situ Trial Test using LNEC's Procedure

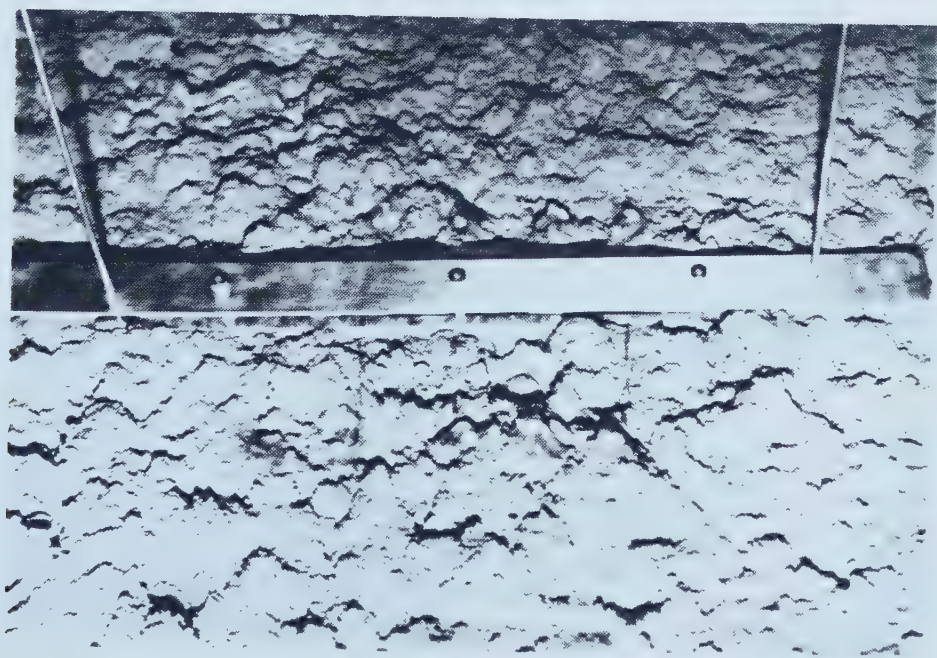


Plate 3.4 Detail of Shotcrete Surface Irregularities

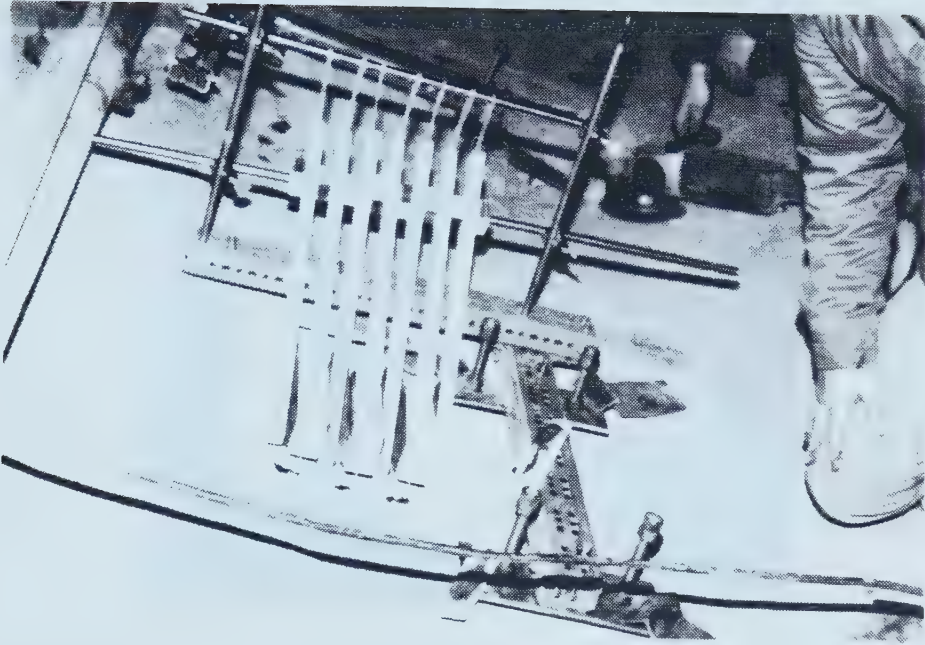


Plate 3.5 Installation of Gage Points using Holding Frame

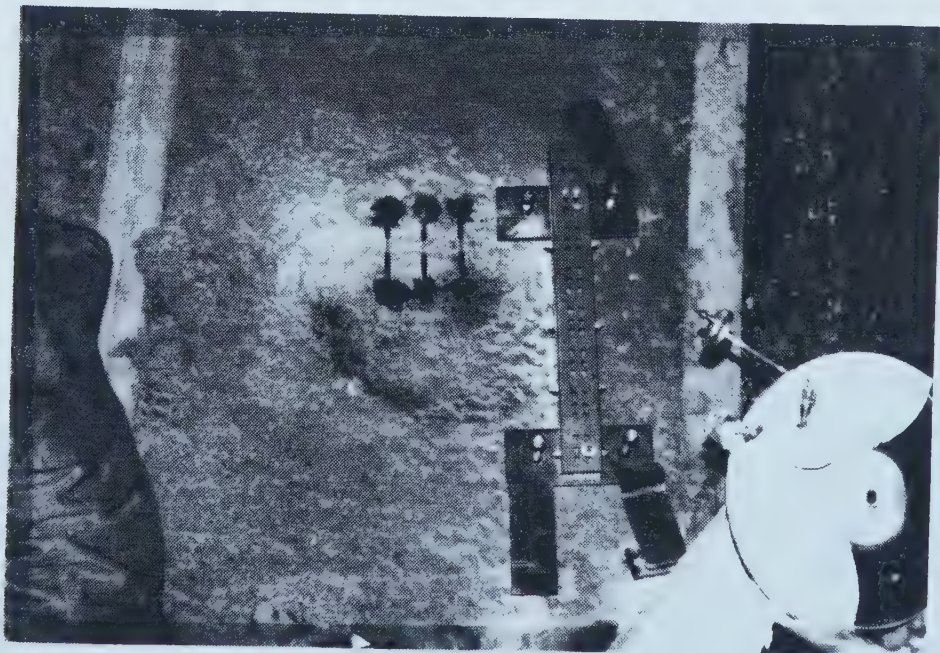


Plate 3.6 Installation of Vibrating Wire Strain Gages for Mini Flat Jack Test



Plate 3.7 Cutting Saw Assembled at Tunnel Crown and in Position for Cutting the Shotcrete

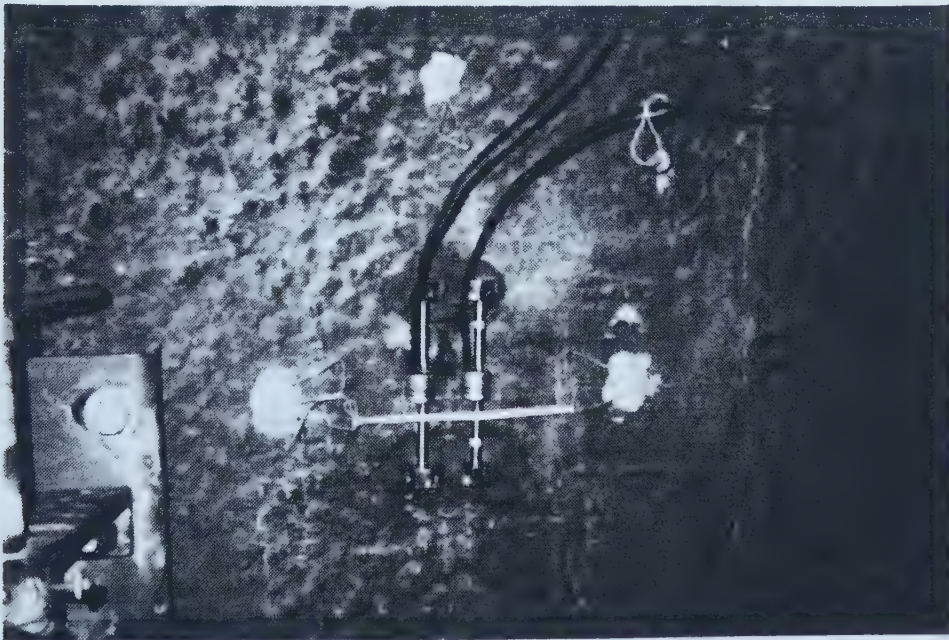


Plate 3.8 Installation of Vibrating Wire Strain Gages model VSM-4000

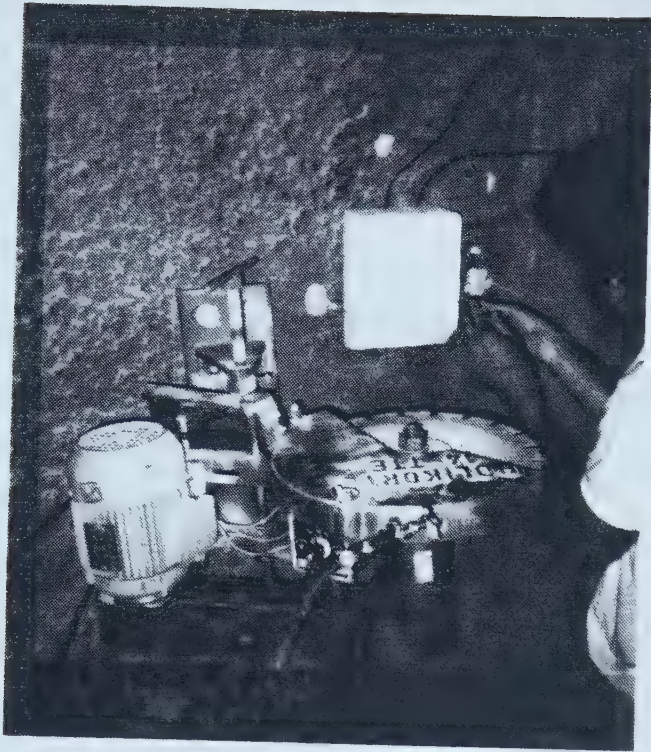


Plate 3.9 Installation of Thermal Protection on Strain Gages in Mini Flat Jack Test

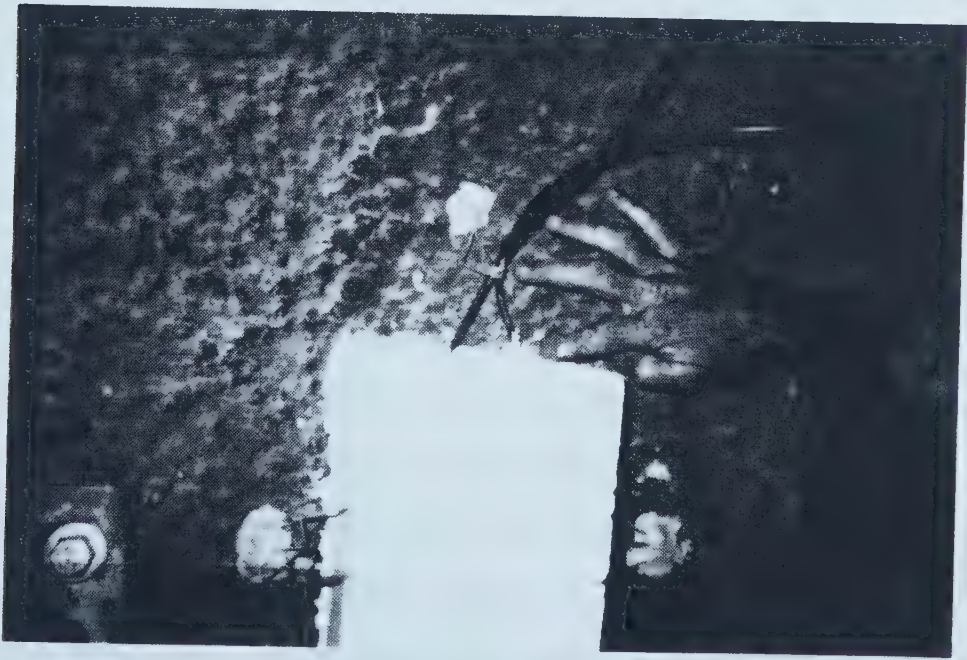


Plate 3.10 Detail of Sealing Application in Thermal Protection to the Strain Gages

4. EARLY AGE PROPERTIES OF THE SHOTCRETE

4.1 Introduction

The term shotcrete used in this thesis follows the terminology proposed by Mahar et al.(1975: 1-3):

" . . . The term shotcrete . . . is compatible with the definition by ACI (1966) and refers to any pneumatically applied concrete or mortar placed directly onto a surface. This definition is used to distinguish shotcrete from pneumatically placed concrete in which all or some of the material must be moved into position after it is extruded from the nozzle. Gunitite is shotcrete which contains primarily sand-size aggregate . . ."

This definition is not universally accepted and some institutions have differentiated shotcrete from gunitite (e.g., Concrete Society, 1979; ABNT, 1986). The shotcrete technology seems to have been first used in 1907 by Carl E. Akely (McIntyre Porcupine, 1957), the curator of the Chicago Field Museum at the time. In 1909, the process was patented by the Allentown Cement Company (Manson and Manson, 1982) and "Gunitite" became a trade name for a mixture of sand and cement applied by pneumatic pressure with a machine manufactured under the trade name "Cement Gun". The first underground application of this technique was credited to George Rice, chief engineer of the Pittsburgh Bureau of Mines, at the Brucetown experimental mine in 1914 (Littlejohn, 1988).

The shotcrete technology was traditionally applied in tunnels driven in rocks. Its first application in soils was in Frankfurt, at the end of 1960's.

Throughout these years, this method experienced substantial technological advances (e.g., ACI, 1966; ACI, 1973; ACI, 1976) and it has been used for a wide range of applications (e.g., Cipriani, 1985). The technological aspects of the shotcrete application were considered out of the scope of the present study and therefore, only a brief review will be given. The main purpose of this chapter is to investigate the early

age mechanical properties of the shotcrete used at the SLRT system tunnels, in Edmonton. General recommendations of shotcrete practice have been given by many organizations around the world (e.g., U.S. Army, 1974; AFTES, 1975; U.S. Army, 1976; ACI-506, 1977; ACI-506, 1978; DIN, 1979; Concrete Society, 1979; U.S. Corps of Engineers, 1982; ABNT, 1986) and they presented the basic concepts and technological control for utilization of this procedure. The application of the method in underground construction is also documented by many authors (e.g., Deere et al., 1969; Mahar et al., 1975; Manson and Manson, 1982; Brux, 1983; Littlejohn, 1988) and one can find the general recommendations. Other authors have investigated the method under conditions limited by the requirements of specific tunnel construction projects (e.g., Brierley, 1975; Parker, 1975; Jones, 1976; Ward and Hills, 1976; Simondi et al., 1982) and one can find among other information, strength, elastic modulus and technological control parameters. Investigation has been carried out on the influence of the type of equipment, shotcrete composition, accelerators, fibers, application details, etc. (e.g., ACI, 1966; ACI, 1973; Parker, op. cit.; ACI, 1976; Simondi et al., op. cit.; Castelo Branco, 1985; Cipriani, 1985; Silva and Kuperman, 1985; Jones, 1985; Morgan et al., 1989). Equipments with high capacity of production (e.g., Putzmeister, 1985), the use of shotcrete associated with TBM excavation (e.g., Hatakeyama et al., 1987) and NATM tunnels with compressed air have also been reported (e.g., Krischke, 1987).

The behavior of the shotcrete lining for tunnels in rock seems to be, in many cases, connected with features like discontinuities, joints, wedges (e.g., Parker, 1975; Brierley and Cording, 1976; Jones, 1976; Ward and Hills, 1976), which results in more non-uniform load distribution than one would expect in tunnels in soil. Due to this characteristic, and also to the stress independent deformations, as will be seen later, the strain development in linings of tunnels driven in rock and in soil usually results in considerably different patterns. Many design recommendation for shotcrete lining for tunnels in rock are available (e.g., Deere et al., 1969; Mahar et al., 1975; Schneider and

Reeh, 1984) and the support system is usually associated with other ground control techniques (e.g., Cording and Deere, 1972; Brierley, 1975; Ward, 1978; Hoek and Brown, 1980).

There are many design methods for tunnels in soil and extensive reviews of them can be found in Branco, 1981; Heinz, 1984; Duddeck and Erdmann, 1985 and Negro, 1988. The present investigation was not intended to provide a completely new design method. Instead, effort was concentrated on the early age behavior of a shotcrete lining, making use of an available design method. In this author's opinion, the method proposed by Negro (1988) is the most complete and consistent for tunnels in soil. His method couples the calculation of the soil deformations with the development of loads in the lining, as opposed to the usual design routine where they are calculated independently and sometimes with conflicting hypotheses. Moreover, Negro's method takes into account the non linearity of the soil and provides a complete load distribution in the lining and the displacement field of the soil. It is also capable of checking the stability of the tunnel and does not ignore the effect of the water seepage and pore pressure relief induced by construction operations. Therefore, it is clear that the lining behavior is just one factor, among many others that should be considered.

It is not reasonable to propose a completely new design method to include the behavior of the shotcrete at early ages, and neglect all the experience accumulated related to other aspects of the design. The method proposed by Negro (1988), which has been extensively tested and validated through analyses of case histories, numerical and analytical models, is used as a framework in the present investigation. Modifications are suggested wherever necessary. Negro (op. cit.) has applied the method to many tunnels constructed by the NATM technique, i.e., shotcrete lining, and the engineering judgment used to consider the deformation parameters in terms of design would be helpful in illustrating the complexity of this type of problem. Negro (1989) used an equivalent

Young's modulus of the shotcrete in the order of 10 GPa, for design, and it was justified by the following:

- 1-Good agreement between results of back analyses of the ABV tunnels using a non linear elastic finite element simulation (Negro, 1988: 591, 595 and 597), with $E = 9$ GPa for the shotcrete lining, and the overall instrumentation results.
- 2-In examining Erdmann (1983: 193-205) and Negro (1988: 387-388) it was verified that the effect of the elastic modulus development according to the distance to the face, i.e., shotcrete with different ages, was almost equivalent to adopting a constant modulus, considering in the method (Negro, op. cit.) a delay of the lining activation, as discussed in Chapter 2.
- 3-When adopting $E = 10$ GPa and considering that the lining was just activated when the invert was closed (usually one diameter behind the tunnel face), the design method (Negro, 1988) could successfully forecast the tunnel behavior during construction for a number of case histories.
- 4-The elastic modulus referred to in the previous item was approximately the same as shotcrete of 4 to 6 hours of age. This time is related to half of the working shift following the application of the shotcrete in the invert, when the tunnel advances (usually at the heading).

Although these considerations might appear to be an oversimplification of the problem, the method has been successfully applied in practice, and Table 4.1 shows the good agreement obtained in a recent project at the Paraiso tunnel in the Metro-São Paulo, Brazil (Negro, 1989). In this case, not only was the convergence of the tunnel wall predicted accurately by the method, but also the displacement field of the soil mass. Notice that a NATM tunnel is usually excavated in stages (e.g., Heinz, 1988: 61), and in the reasoning above, the lining was considered to be activated only after the ring was closed. The rate of tunnel advancing became an important factor, since it defined the age at which the lining was loaded. These aspects will be discussed in more detail in Chapters

5 and 6, but it should be recognized here some of the factors that define the soil-lining load transfer process: the construction sequence, the rate of the tunnel construction advancing and the development of the shotcrete properties with age.

Many investigations have been carried out (e.g., Kubetsky, 1970; Vollstedt and Duddeck, 1977; Yuen, 1979; Ito and Hisatake, 1981; Erdmann, 1983; Pottler, 1985) in order to evaluate the influence due to lining parameters like creep, aging and the advance velocity of a tunnel on the load distribution. Most of them were only limited to a parametric analysis using an analytical or numerical solution and usually no comparison of the results with a real case history was presented, specially in terms of the loads in the shotcrete lining. Also, the importance of the early age behavior of the lining, as regards thermally induced deformations and shrinkage have been recognized (e.g., Heilbrunner, 1980; Paul et al., 1983: 149). The difficulty to obtain stress from strain measurements in concrete lining is well known (e.g., Shepherd and Wilson, 1960; England and Illston, 1965; Hornby and Noltingk, 1973; Brierley and Cording, 1976; Jones, 1976: 138; Schubert, 1988), and usually the difficulties are worsened in case of short term behavior, by the very limited information available on the early age properties of concrete (Byfors, 1980: 7). For shotcrete, it is even worse, and most of the published data present only strength properties (e.g., Ward and Hills, 1976; Simondi et al., 1982; Babendererde and Wirtz, 1986; Brameshuber and Kottas, 1987). Further information is available in literature, like: Parker (1976) who presented strain-stress curves and moment-trust tests in shotcrete beams, Rokahr and Lux (1987) who did a rheological study of shotcrete using laboratory tests and numerical simulations and Wind and Kern (1987) who presented temperature and elastic modulus development with time. Gais et al. (1986) presented temperature evolution data and proposed an interpretation of stress using strain measured in shotcrete lining by making assumptions related to the elastic modulus and applying German standard DIN 4227 to deformations due to shrinkage and creep. By using creep test results, Weigler and Karl (1981) showed that this standard for

prestressed concrete (DIN 4227 - part 1), does not correctly describe the behavior at early age. Schubert (1988) adapted, for shotcrete, the method originally proposed by England and Illston (1965) for concrete. This method accounts for the time dependent deformations, shrinkage and thermal strains, and will be discussed in Chapter 6.

A complete set of test results that could provide a full description of the shotcrete behavior was not found so it was necessary to perform an extensive test program in the laboratory to characterize the shotcrete used in the SLRT tunnels. The results would be useful in interpreting the lining instrumentation presented in Chapter 2 and to characterize and recognize the mechanisms that occur during the soil-shotcrete interaction in tunnels close to the face, i.e. short term behavior. The latter is of increasing importance as the use of shotcrete as a permanent lining becomes widespread in practice (e.g., Selmer-Olsen, 1976; Cruz et al., 1982; Simondi et al., 1982; Onuma et al., 1985). The test results will also be used for a more realistic parametric analysis using the analytical solution to be presented in Chapter 5.

4.2 Laboratory Tests Organization

As mentioned earlier, the main purpose of the present chapter is to characterize the behavior of the shotcrete at early ages. The definition of the term 'early age', however, is not well established and its use may be a function of the type of structure, the composition of the concrete, the relevant curing conditions and the objective to be achieved (Byfors, 1980: 21). Negro (1988) carried out an extensive investigation of case histories of tunnels constructed in soil and numerical analyses and concluded (Negro, op. cit.: 174) that for linings activated one diameter (D) behind the face, non-plane strain conditions had prevailed in the regions $1D$ to $2D$ ahead and $2D$ behind the face. A 'plane strain' condition may be understood in this case, as a situation where the tunnel face advance does not affect the stress and strain distribution in the lining. Therefore, it seems reasonable to assume that most of the 'short term' load transfer from the soil to the lining

is completed approximately 2D behind the face, i.e., when plane strain condition is achieved. By using these reasonings, 'early age' for the shotcrete is defined as the time necessary for the tunnel to advance 2D. Considering a typical construction rate of 1.8 m per 8 hour shift, and a typical 6 m diameter tunnel, the 'short term' loading of the shotcrete will vary between 2.2 days (3 shifts/day) and 6.7 days (1 shift/day). Although these values may be considered the common range found in practice, most of the laboratory tests were carried out beyond the upper limit, in order to be at the safe side and also try to establish some criteria to extrapolate the results for the long term behavior.

In tunnel construction, as in any other geotechnical problem of load transfer (e.g., retaining wall, deep pile foundation, geogrid reinforcement), the amount of energy exchanged between the soil and lining, depends on the relative stiffness between them. It is evident, therefore, that deformation parameters of the shotcrete should be investigated. The complexity of concrete behavior at early age is well known and was pointed out by Byfors (1980: 3):

" . . . an inventory of the literature showed that very little was known of the properties of concrete at this early age, probably partly due to the difficulties involved in finding suitable testing method . . . "

This author was referring to plain concrete, where the amount of knowledge available is considerably larger than in the case of shotcrete. The lack of standard testing procedures and interpretation were one of the biggest problems encountered during the present research. Tests were carried out by adapting available methods whenever possible, or applying standard laboratory procedures. Ideally, the laboratory test results should provide time-dependent deformations for the many different conditions (shotcrete composition, curing and drying environmental condition, temperature effect, etc.) found in practice, as in the methods available for concrete structures (e.g., Rush et al., 1973; CEB-FIP, 1978; Bazant and Panula, 1978-1979; Byfors, 1980; ACI Committee 209,

1982), where these variables are considered. However, this goal could not be reached due to constraints on the extension of such laboratory testing program, and a compromise was necessary in setting the limits of test conditions. As a result, it was decided to reduce the number of parameters under investigation, and to perform the tests under SLRT tunnel conditions that were readily reproducible: the same shotcrete composition and similar environmental conditions. The results of the present investigation are limited to such features and since only compression tests were performed, flexural and tensile behavior had to be evaluated indirectly (e.g., Parker, 1975; Byfors, 1980).

The laboratory tests which were run to evaluate the early age properties of the shotcrete may be divided into six groups:

1. Control and strength tests
2. Tests for evaluation of the elastic parameters
3. Short term creep tests
4. Tests for evaluation of the stress independent deformations
5. Stress controlled tests
6. Strain controlled tests

The tests in the first group were aimed at investigating the best method to reproduce "shotcrete" in the laboratory. Tests were initially intended to be done on samples obtained from an actual shotcrete equipment, but this plan was abandoned as investigation progressed. Just to execute the creep tests, 18 months were necessary and most of the laboratory investigation were done in two years. Keeping the equipment and hiring the necessary specialized crew (e.g., ACI, 1966; Mahar et al., 1975: 7-1; ABNT, 1986) for the length of time mentioned was cost prohibitive. The option of taking the samples from a construction's site or at the contractor yard faced two problems. At the time the test began, equipment and specialized operators were not readily available in the Edmonton area, and continuity of the research could be at a high risk. Preliminary analysis (Brandt, 1987) of construction control tests indicated that disturbance caused by

the transportation of a shotcrete panel from the tunnel site to a laboratory affected strength results. Due to these problems, the compromise solution was to reproduce the shotcrete under laboratory conditions. The tests performed and methods developed to reproduce laboratory specimens of 'simulated' shotcrete were gathered in the first group. Also, in the same group, strength tests are presented.

The second group of tests was carried out to evaluate the elastic parameters of the shotcrete at different ages. Most of the tests were run using conventional compression test procedures, but due to the impossibility to measuring those parameters within the first four hours using conventional techniques, the ultrasonic method also was used. In the third group, the short term creep tests were performed using the conventional procedure, i.e., the creep was taken as the difference between the deformation of a constant loaded specimen and the deformation of an 'identical' unloaded specimen (dummy). The fourth group of tests was designed to measure stress independent deformations in laboratory specimens exposed to environmental conditions similar to the SLRT site. The last two groups of tests were carried out in order to evaluate the shotcrete behavior under stress and strain paths similar to those expected in the tunnel lining.

4.3 Control and Strength Tests

The reproduction of shotcrete in the laboratory faced two main problems: the knowledge of the exact composition of the shotcrete used at the tunnel site and the difficulties in mixing and casting the concrete in laboratory. The first problem was related to the well known rebound losses of the shotcrete (e.g., Kobler, 1966; Parker, 1975; Parker et al., 1976; Ward and Hills, 1976; Simondi et al., 1982; Mason and Mason, 1982; Cipriani, 1985), i.e., when the shotcrete is sprayed, part of it is lost due to reflection. A systematic control of the rebound was not possible in the present project, because it would have interfered in the excavation operations which immediately followed shotcrete application. Parker (op. cit.), Ward and Hills (op. cit.) and Cipriani

(op. cit.) have shown that for dry mix process not only the concrete composition affected the rebound, but also operation procedures and equipment details (e.g., position of water inlet in the nozzle, length of the nozzle, impact velocity, pressure of the compressed air, nature of the sprayed surface, etc.). Parker (op. cit.) and Parker et al. (op. cit.) emphasized that the sprayed thickness has a strong influence on the rebound losses and Cipriani (op. cit.) showed that the position where the shotcrete was applied (e.g., crown, springline, floor) also affected the reflection. The results presented by Ward and Hills (op. cit.) indicated that the deposited material had finer grain distribution than the sprayed one, while Parker (op. cit.: 245) mentioned that it should not be coarser and suggested that it could be finer. Parker et al. (op. cit.) also pointed out that in order to obtain actual rebound losses, the test should simulate all the actual shotcrete production conditions. Since site measurements were not possible and the exact composition of the shotcrete could not be predicted accurately, it was decided to use the same input mix composition used at site, i.e., no significant grain size variation related to rebound was assumed.

The second problem in reproducing shotcrete under laboratory conditions was mixing and casting the specimen. This difficulty was directly related to the water-cement ratio (w/c) and the short setting time of the concrete. The latter was a result of the accelerator normally added to the shotcrete composition. The w/c at SLRT tunnels was around 0.4 and 0.5, depending on the nozzleman operation (Brandt, 1987). An accelerator-cement ratio (a/c) of 0.05, was kept constant at site by an electronic controller. Comparing this w/c to those reported by different authors summarized in Table 4.2, it is noted that the 0.05 lies in the upper range. Caution should be exercised in using these values, since the influence of the grain size distribution of the mix on the w/c ratio was not isolated, i.e., the finer the components, the higher the values of w/c .

Many trials were done in the laboratory to obtain a cylindrical specimen of concrete using $w/c=0.4$ and $a/c=0.05$ and all of them resulted in specimens of poor

quality. Using this composition, it was not possible to ensure a homogeneous mix. Initially, all the dry components were mixed in an electrical mixer, and then two alternatives were tried. In the first trial, water was added and the components were left mixing until homogeneity was reached (approximately 5 minutes) and after this, the accelerator was added. In the second case, water and accelerator were previously mixed in a container and then the solution was poured into the mixer. In both cases, approximately 30 seconds after the accelerator was added, the mixture gained a considerable cohesion. Under this condition, lumps were formed in the concrete mass and no further mixing took place. Manual mixing was also tried, but the results were even worse. Considering that some degree inhomogeneity could be accepted, an attempt was made to use the concrete prepared as described above, to obtain a cylindrical specimen. Five techniques were tried: simple vibration, vibration with dead load, dynamic compaction using either Modified Proctor or Marshall hammers and static compaction using a compression testing machine. All of these attempts proved to be inefficient, since in all of them, macro pockets of air were formed inside the specimens. The dynamic compaction, using Modified Proctor hammer, proved to be the most efficient but, it was subjected to time related problems. The concrete mass was placed in layers. Although the results of the initial layers compaction were considered acceptable, approximately 3 minutes after the accelerator was added the concrete became inadequate to be compacted. The layers deposited after this time were defective, and probably the previous ones had poor quality due to disturbance caused by hammer impacts. In conclusion, the impossibility of obtaining good quality specimen using $w/c=0.4$ and $a/c=0.05$ led to a different concrete composition.

To obtain a good quality specimen, it was found necessary to increase the w/c ratio. The increase of this ratio proved to be effective in terms of mixing and casting procedure, for values above approximately $w/c=0.5$. One should observe that this value was the upper limit of the w/c expected at site, and therefore, tests for the rest of the

range would be missing. In order to obtain the properties for $w/c < 0.5$, it became necessary to use the results of higher ratios ($w/c = 0.5$ and 0.6) and extrapolate the results.

Figure 4.1 shows the grain size distribution of the gravel and the sand used in the production of the shotcrete, for samples collected at the SLRT construction site. Also shown in the same figure is the sand used in the laboratory test specimens. The gravel used in the tests was composed in the laboratory, using the sieve series shown in Figure 4.1 for a material with similar geological composition as the one used at the site. The amount of cement the shotcrete mix at the site was not constant, and values of 350, 380 and 400 kg/m^3 were applied to different sections. Since 350 kg/m^3 was used throughout of the main instrumented sections of the SLRT lining, this value was used for the laboratory tests. The cement was Type 50 (sulfate resistant) and the accelerator, (Dynagunit 721), used at the site was offered by the manufacturer, Dynamit Nobel of America, in liquid form. The ingredients of the latter include potassium hydroxide, water and other unknown substances (patent protection). Table 4.3 summarizes the compositions of the simulated shotcrete used for the laboratory tests.

Based on the experience accumulated during the trial tests in mixing and casting the shotcrete specimens under different conditions, the following steps were considered the best procedure possible under the equipment restrictions found in laboratory, for batches around 25 to 50 kg:

- 1-In an electrical mixer, add cement to gravel and mix them for about 30 seconds,
- 2-Add 80% of the water and mix the components for 2 minutes,
- 3-Add the sand and mix the components for 3 more minutes,
- 4-Add a solution formed by the remaining water and the accelerator, then mix the concrete for 1 minute,
- 5-Cast the concrete in a cylindrical mold assembled in a vibrating table. This procedure should be finished in 3 minutes after the accelerator is added. If this limit is exceeded, vibration becomes ineffective. The vibration should be done in

stages and each one should not exceed 5 seconds, in order to avoid segregation of the aggregates. The interval between each stage is about 15 seconds, which is the time necessary to take about 1 kg of concrete mass from the mixer and pour it into the cylinder mold. In order words, the specimen is cast in layers and each layer is vibrated for at least 5 seconds,

6-The specimen is then sealed in plastic bags to avoid moisture losses

The first stage in evaluating the manufacturing procedure of the 'laboratory' shotcrete was a comparison between unit weights. Figure 4.2 presents a bar diagram which shows the unit weights of the specimens cast in the laboratory (series STA and STB) and those measured in cores collected at the site. Table 4.4 shows the composition of the concrete, the w/c ratio, total number of observations, the mean value and standard deviation of the tests presented in Figure 4.2. All the results of cores shown in this section were based on the tests done to control the SLRT tunnels construction (Brandt, 1987). The specimens were obtained either by coring straight from the tunnel lining or by shotcreting panels and then sampling. From now on, the first will be referred to as 'in situ' and the last as 'panel'. The data presented in Figure 4.2 and Table 4.4 show a clear agreement of the results of the in situ, panel and series STB measurements. The latter used w/c=0.6, while the series STA, which used w/c=0.5, had lower unit weights than the previous ones. All the specimens used in the laboratory were carefully crushed after the measurements were taken, in order to detect any macro pockets of air inside of the concrete, and in none of them was this kind of defect found. No clear explanation was found for the lower unit weights obtained for the specimens in series STA (w/c=0.5), although their values were very close to those reported by Ward and Hills (1976). These authors made tests in cores taken from shotcreted panels using an actual shotcrete equipment for w/c ranging from 0.45 to 0.65. They verified that the unit weights were lower than what should be expected for a well compacted concrete with similar cement and water contents.

Figures 4.3 and 4.4 show the increase of strength with time for the tunnel construction control tests (shown in Figure 4.2) which were carried out for panel and in situ evaluation, respectively. Since the specimens had different length to diameter ratios, correction factors recommended by ASTM C42-82 were applied. In order to compare these results to the laboratory tests in conventional cylinder specimen, the core strength values were multiplied by a factor of 1.08, according to recommendations by McIntyre (1987: 37). However, these corrections didn't have any significant influence on the results because when comparing their mean values and standard deviations to the same parameters of the raw data, the differences were negligible. The curve fitting based on the equations proposed by Byfors (1980: 119-120) are also shown in these figures. This author verified that the compressive strength development, including the early age effect, could be described as follows:

$$H = \frac{A_1 t^{B_1}}{1 + \frac{A_1}{A_2} t^{(A_1 - B_2)}} (\%) \quad [4.1]$$

where

$$H = \frac{f_{cc}^t}{f_{cc}^{28d}} 100 (\%)$$

t = age in hours

f_{cc}^t = strength at age t

f_{cc}^{28d} = strength at 28 days

A_i, B_i = constants

Byfors (1980: 119) showed that parameter A_2 was a function of B_2 , and it could be represented by:

$$A_2 = \frac{100}{t_0^{B_2}} \quad [4.2]$$

where

$$t_0=672 \text{ h (or 28 days)}$$

As Equation 4.1 expresses the percentage of the 28 day strength at time t , it is clear that for time $t=28$ days, H should be equal to 100%. For this condition, however, Equation 4.2 is not algebraically correct. The correct expression for A_2 should be:

$$A_2 = \frac{-(100) 672^{(B_1-B_2)A_1}}{100 - 672^{A_1 B_1}} \quad [4.3]$$

For the range of values of the parameters B_1 , B_2 and A_1 obtained by Byfors (op. cit.: 120), Equation 4.2 may be considered as a good approximation of Equation 4.3. Byfors(op. cit.) probably used graphical methods to obtain the parameters of Equation 4.1, and since the simplified expression made this task easier, it was believed that this was the reason for the simplification in Equation 4.2. Huang et al. (1986) have shown that for pressuremeter test interpretation, where multiple parameter regression is necessary, the use of a Simplex algorithm (Marquardt, 1963) reduced the errors from the adjustment procedures. This method has also been applied successfully in back analyses of geotechnical problems (e.g., Gioda, 1985; Nguyen, 1985) and the main feature of the algorithm is that it never diverges. Since the curve fitting problem for the expression presented above and the pressuremeter test interpretation are similar from a parameter adjustment point of view, the Simplex algorithm was applied to the present problem. A program was implemented in a microcomputer for this purpose and it was based the source code and flow chart published by Caceci and Cacheris (1984). In order to obtain the constants A_1 , A_2 , B_1 and B_2 using this numerical method, the consistency between the equations was necessary. Hence, Equation 4.2 was disregarded and the Equation 4.3 was used in its place. As a result, the curves presented in Figures 4.3 and 4.4 were based on the following expression:

$$f_{cc} = \frac{(A_1 t^{B_1})}{\left[1 + \frac{A_1}{A_2} t^{(B_1 - B_2)}\right]} \frac{f_{cc}^{28d}}{100} \quad [4.4]$$

It should be noted that A_2 is not an independent parameter and is given by the Equation 4.3. For the in situ core tests, curve fitting was not performed since its results would not be reliable due to the limited data available. In Figure 4.4, if the in situ core tests results were compared with the curve fitting results obtained for the panel tests, it may be observed that they follow similar trends within the range of data presented. Figure 4.5 shows the results of the laboratory test series STA and STB and a summary in terms of best fit, mean values and standard deviation bars of the tunnel construction control tests. In order to analyze these results, one should consider Figure 4.6, which represents, schematically, Equation 4.1. In this expression, A_1 and B_1 represents respectively the value of H when $t=1$ (or $\log(t)=0$) and the slope of line 1 for a log-log chart, while A_2 and B_2 have the equivalent meaning for line 2. Byfors (1980: 120-122) verified that for specimens with the same composition but different water cement ratios (w/c), the parameters A_2 , B_1 and B_2 remain constant while A_1 varies. Figure 4.7 illustrates this behavior and it indicates that line 1 translates with the same slope (parallel) to the right while w/c increases.

Figure 4.8 shows the results obtained in the present investigation for the normalized (H) strength. One can observe the same trend suggested by Byfors (1980) for plain concrete. Table 4.5 presents the parameters of the Equation 4.1 for these tests and also the values reported by Byfors (op. cit.). Figure 4.9 shows the variation of the parameter A_1 as function of w/c . It can be observed that there is a considerable disagreement between the values for the shotcrete values and those for plain concrete, presented by Byfors (op. cit.: 122). Since A_1 represents the percentile strength at $t=1$ hour, it is clear that the use of accelerators in the shotcrete will increase the values of this

parameter. In other words, A_1 is related to the origin of line 1, which represents the gain of strength during the very early ages. The addition of the accelerator decreases the time necessary to complete this stage and the higher values of A_1 reflected this effect.

Table 4.5 shows that for the remaining parameters (A_2 , B_1 and B_2), the values were of the same order of magnitude. The difference was probably affected slightly by the influence of the concrete composition, while the main reason was attributed to strength evolution differences: the shotcrete had much higher strength during the early age and lower value for 28 days. Low value of the 28 day strength, for series STA, is also noticeable. Under normal conditions, for $w/c=0.5$, one should expect strength values between those corresponding to the site ($w/c=0.4$ to 0.5) and to the series STB ($w/c=0.6$). The lower values of the unit weights for the series STA shown in Figure 4.2 can explain this deviation, since lower unit weights are related to lower strength (e.g., Seabrook, 1976; Byfors, 1980: 73-74; Brameshuber and Kottas, 1985).

Figure 4.10 compares the results presented in Figure 4.5 to those reported by other authors. Effort was spent in choosing cases where the shotcrete composition was similar to the one used in the SLRT tunnels. Their main features are summarized in Table 4.6. A direct quantitative evaluation of these data cannot be done accurately, because, as reported by Simondi et al. (1982), the compatibility between the cement and accelerator could have a major effect of the strength development of the shotcrete. These authors tested four different cements with three types of accelerators, and observed distinct behavior even among mixes using the same accelerator and the same cement type but the cement manufactured by different companies. Nevertheless, the data presented in Figure 4.10 show that Equation 4.1 proposed by Byfors (op. cit.: 120) for plain concrete at early age, could be adapted for shotcrete. Most of the results followed the same trend presented in Figure 4.6, although some deviation can be observed in the first hours. Also, it can be seen that the results of the present research lie within the scatter of the data

reported by the other authors, suggesting that the present shotcrete may be considered as a typical one in terms of strength.

4.4 Determination of Elastic Parameters

The specimens of the test series STA and STB described above were also used to determine the elastic parameters under conventional static loadings and ultrasonic pulse measurements. The results of these tests are summarized in Table 4.7 and discussion on the techniques of execution and interpretation will be subsequently given. The specimens were the standard 15.24 mm (6") diameter and 30.48 mm (12") high cylinders and the stress-strain curves for the static loadings were obtained observing the recommendations of the standard test method ASTM C469-87a. Figures 4.11 and 4.12 show the data for these tests for the series STA and STB respectively, and also the curves fitted according to the equation (4.5) suggested by Saenz (1964). Byfors (1980: 153) pointed out the deviations from linearity of the stress-strain relation for concrete and the difficulties to define an elastic modulus for the early age (Byfors, op. cit.: 155) because of the markedly non-linear development, even at low stress levels. This author also verified that the ratio between the initial tangent and the conventional secant modulus (e.g., ASTM C469-87a) is not constant during the early ages (Byfors, op. cit.: 162), for compressive strength below about 200 kPa. In order to obtain better characterization of such a kind of material, in spite of taking the conventional secant intersection for stress level at the order of 30% to 50% of the strength, the present investigation will use a non-linear relation to describe the stress-strain behavior. In this way, a secant modulus can be determined not only for the conventional stress level, but also for any other suitable value. Saenz (op. cit.) has proposed the following relation to represent the stress-strain curve for concrete, which also describes post failure behavior:

$$\sigma = \frac{\epsilon}{A+B\epsilon+C\epsilon^2+D\epsilon^3} \quad [4.5]$$

where the conditions to be fulfilled are:

For $\epsilon=0$, $\sigma=0$ or point of origin

For $\epsilon=\epsilon_0$, $\sigma=\sigma_0$ or point of maximum stress

For $\epsilon=0$, $d\sigma/d\epsilon=E_{it}$ or value of the initial tangent modulus

For $\epsilon=\epsilon_0$, $d\sigma/d\epsilon=0$ or maximum of the curve

The same author also reported that the above equation can be simplified to describe only the ascending branch of the stress-strain curve in compression as:

$$\sigma = \frac{\epsilon}{A+B\epsilon+C\epsilon^2} \quad [4.6]$$

where:

$$A = \frac{1}{E_{it}} \quad [4.7]$$

$$B = \frac{1}{\sigma_0} - \frac{2}{E_{it} \epsilon_0} \quad [4.8]$$

$$C = \frac{1}{E_{it} \epsilon_0^2} \quad [4.9]$$

or:

$$\sigma = \frac{E_{it}\epsilon}{1 + \left(\frac{E_{it}}{E_s} - 2 \right) \frac{\epsilon}{\epsilon_0} + \left(\frac{\epsilon}{\epsilon_0} \right)^2} \quad [4.10]$$

where:

$E_s=\sigma_0/\epsilon_0$ or secant modulus for $\epsilon=\epsilon_0$

Since post failure behavior was not measured, Equation 4.5 was disregarded for curve fitting and the other relations were used. Two options were possible in fitting the data presented in Figures 4.11 and 4.12:

1 - Direct application of Equation 4.6 and adjusting the parameters A, B and C

2 - Substituting the strength values evaluated in laboratory tests ($\sigma_0 = f_{cc}$) for parameter B (Eq. 4.8), and adjusting E and ϵ_0 by replacing Equations 4.7, 4.8 and 4.9 into 4.6

Curve fitting using option 1 proved to be inadequate because in many cases, the results presented negative values for the parameter C (specially for specimens tested before 10 hours). In order to maintain the physical meaning of the parameters in Equation 4.10, option 2 was taken. One should observe that this solution eliminates one degree of freedom in the equation to be fitted. The curve fittings were performed using a microcomputer program for the Simplex algorithm referred to previously and the results are shown in Table 4.7.

Figure 4.13 shows the development with age of the initial tangent modulus using the values obtained from the regression for the series STA and STB. Also shown in the same figure is the elastic modulus for shotcrete reported by other authors (see Table 4.6) using conventional methods (e.g., ASTM C469-87). Despite the scatter of data around the first 10 hours, the data follow similar overall trends. For comparison, the values proposed by Gartung et al. (1979) for numerical simulations are shown in the same figure. It can be observed that these values are lower than any other measured ones, probably to compensate for the creep deformations not considered in the numerical model. This aspect will be explored in Chapter 6 and the results of the elastic modulus obtained from creep tests, also shown in Figure 4.13, will be discussed later in this chapter.

The specimens in series STB were subjected to ultrasonic pulses before the static tests were carried out, and the results are also presented in Figure 4.13. In the case of the specimens STB/10 and STB/11, continuous readings were taken. Brameshuber and Kottas (1987) proposed the use of this method to obtain deformation and strength parameters for shotcrete and presented correlations between compression wave velocities and these parameters. The same approach was proposed by Teodoru (1986) to obtain

strength for concrete at early age. On the other hand, a direct determination of elastic parameters is possible by applying an analytical solution, as has been used in rock mechanics (e.g., Jaeger and Cook, 1979; ASTM D2845-83). Although elastic modulus interpretation is possible using only compression wave velocities, an estimation of Poisson's ratio is necessary (e.g., Heinz, 1988: 183-186). However, Byfors (op. cit.: 172) and Anson (1966) showed that Poisson's ratio is a function of the age for the concrete at early stages (see Figure 4.15). In order to overcome this problem, a standard method developed for rocks (ASTM D2845-83) was applied to the shotcrete. This procedure uses measurements of compression and shear wave velocities, leading to the calculation of the Poisson's ratio. No problems were anticipated by adapting a method for rock to shotcrete, since the equations used for the test interpretation were derived using linear elastic theory (e.g., Jaeger, 1969: 132). Also, as one of the conditional factors of the test procedure is a function of the grain size of the rock sample (ASTM D2845-83), the recommendations seem to be applicable to the shotcrete. Notice that the grain size of the coarse aggregates of the shotcrete are of the same order of magnitude of, for instance, coarse grained granite or potash evaporite.

Figure 4.14 shows the Poisson's ratio obtained for the series STB and the specimens STB/10 and STB/11 using two different pairs of piezophones. The results for STB/11 for the first 10 hours were not considered reliable because the determination of the compressive wave velocities was affected by the sensitivity of the piezophones used in this test. Below 10 hours, there was high attenuation of the ultrasonic pulses due to the low stiffness of the concrete (e.g., Teodoru, 1986), and as a result, the signal amplitude was not high enough to take an accurate measurement. Better transducers were used in the other cases, and the problem above was not observed in the test for specimen STB/10. Recommendations to improve the sensitivity of the testing apparatus can be found in ASTM D2845-83. Figure 4.14 shows that the results for the series STB and STB/10 tests follow the general trend proposed by Anson (1966) for dynamic Poisson's

ratio and confirms the suspicion of unreliable measurements for the STB/11 during the first 10 hours.

The dispersion observed in Figure 4.13 may be attributed to the different concrete compositions, specimen shapes and evaluation methods used to obtain the elastic modulus. In order to estimate the influence of the latter, Figures 4.16 and 4.17 were prepared. The elastic modulus obtained using the recommendations of ASTM C469 will be referred to as E_c (conventional modulus), the one resulting from curve fitting using Equation 4.10 as E_{it} (initial tangent modulus) and the one using ASTM D2845 method as E_{us} (ultrasonic modulus). Since E_c is the most common parameter used in practice, it was used as a reference value. Figure 4.16 shows the ratio E_{it}/E_c for different ages obtained in the test series STA and STB. It can be observed that this ratio varies from approximately 1.6 at very early age to around 1.2 at 28 days. These values agree with the ones suggested by Byfors (1980: 156-157) for plain concrete, and it indicates the pronounced non linearity at very early ages. Figure 4.17 shows the ratio E_{us}/E_{it} for different ages, which theoretically should be constant and equal to 1. Since E_{it} is defined as $d\sigma/d\varepsilon$ for $\varepsilon=0$ (see Equation 4.6), i.e., tangent modulus for zero strain, it should equal E_{us} , which is obtained at very small strains. The abnormal results shown in Figure 4.17 can be explained by the restrictions recommended by ASTM D2845-83 to obtain reliable results:

$$D \geq 5 \left(\frac{V_p}{f} \right) \geq 15 \text{ d} \quad [4.11]$$

where:

D =minimum lateral dimensions of test specimen

V_p =velocity of the compressive wave

d =average grain size of the specimen

f =natural resonance frequency of transducers

The relation 4.11 represents the specimen geometrical requirements to ensure accurate measurements. Table 4.8 shows the values of these parameters for the data presented in Figure 4.17. Although the specimen dimensions were suitable for the average stiffness of the concrete, it can be observed that $5(V_p/f)$ values were below the lower limit (15 d) for low values of f_{cc} , and above the upper limit for higher values of f_{cc} . Therefore, the measurements associated with these ranges were not reliable and their results should be used just as qualitative indications. Only the middle portion may be considered accurate and for this condition, the ratio E_{us}/E_{ii} gets close to 1 (Figure 4.17).

The shotcrete elastic modulus is usually not available for tunnel lining design. Moreover, tests cannot be performed frequently because of the difficulties found in practice in obtaining specimens large enough to allow measurements of deformations. An alternative often used by practitioners is the use of relations of the elastic modulus as a function of strength (see Table 4.9). This approach is very convenient since the strength values are either well known or can be easily obtained by performing tests on cores. Figure 4.18 was prepared to evaluate the application of those relations for shotcrete at early age. The elastic moduli presented for the test series STA and STB were interpreted according to the recommendation of ASTM C469 (see Table 4.7). The results reported by Brierley (1975: 111) and Parker (1976: 464) followed the same interpretation but the specimens were prismatic (see Table 4.6) and taken from shotcrete panels. The results published for plain concrete at early age (see Table 4.10), summarized by Byfors (1980: 154), were also included in Figure 4.18. It can be observed that the relations proposed for shotcrete (Table 4.9) overestimate the values of the elastic moduli at early age. Brierley (1975: 109) noticed this aspect and suggested that for strengths below 20.7 MPa (3000 psi), the elastic moduli be considerably lower than those estimated using the ACI (1971) relation. All the relations proposed for shotcrete, shown in Table 4.9, were based on square root relations (namely ACI, 1971; NBR 6118: ABNT, 1980 and Pauw, 1960) and followed the same patterns. The CEB-FIP (1978) recommendation, that uses a cubic root

relation was also presented for comparison purposes, and one can observe that the disagreement remains.

Since the data for shotcrete and plain concrete follow the same trend, the relation proposed by Byfors (1980: 161) for the latter will be applied to the former:

$$E_c = \frac{c_1 f_{cc}^{d_1}}{1 + \frac{c_1}{c_2} f_{cc}^{(d_1+d_2)}} \quad [4.12]$$

It can be observed that this relation is similar to Equation 4.1 and its parameters have the same geometrical meaning as in Figure 4.6. Curve fitting was performed using all the data shown for shotcrete and the results by Haugland et al. (1976) for plain concrete. Since the results reported by Brierley (1975: 111) and Parker (1976: 464) were from specimens with non conventional shapes, the strength values could be subject to some deviation in relation to those taken using standard procedures. Notice a lack of data for the shotcrete in the region where the curve changes slope (approximately between 1.5 to 7 MPa of strength in Figure 4.18). The data in this region are crucial to obtaining an acceptable curve fit, and for this reason more data were considered necessary. The results presented by Haugland et al. (op. cit.) for plain concrete were selected because of the large number of data, the same trend as those of the shotcrete results and the tests were carried out in conventional cylindrical specimens. The curve fitting result using the data described above is shown in Figure 4.18 and the parameters for Equation 4.12 can be found in Table 4.11. The values obtained by Byfors (1980: 160) are also in this table and the author commented that his results led to higher values of Young's moduli than those reported by other authors. Byfors (op. cit.: 156) attributed this deviation to the higher loading rate used in the tests (see Table 4.10). In conclusion, the relation proposed herein is applicable for strength obtained from cylindrical specimens and the elastic modulus defined in a conventional way (e.g., ASTM C469; stress level of 1/3 of the compressive

strength - see Table 4.10) and the results represent the average behavior either for plain concrete or shotcrete. It can be observed in Figure 4.18 that the proposed relation leads to elastic moduli very close to the ACI (1977) for strength above 10 MPa (as opposed to 20.7 MPa suggested by Brierley, 1975: 109). Notice also that the relation obtained by Byfors (op. cit.) furnished results almost equal to the NBR 6118 (ABNT, 1980) recommendation for values of strength above 2 MPa, and it seems that the former relation could be applied as an upper limit estimation for the elastic moduli of shotcrete.

4.5 Short Term Creep Tests

4.5.1 Introduction

The necessity to consider the deformations associated to creep in tunnel linings constructed with shotcrete has been reported by many authors (e.g., Brierley and Cording, 1976; Heinz, 1984: 42; Gais et al., 1986; Rokahr and Lux, 1987; Schubert, 1988), but as mentioned earlier in this chapter, the fundamental parameters in describing this kind of behavior were rarely published. In the following, the tests performed to characterize the short term creep at early age, using specimens prepared in the same way as described in the previous section will be presented.

The definition of the creep parameters at early age for the shotcrete is not a simple task: the creep phenomenon follows an exponential type of behavior, i.e., it ceases theoretically at infinite time. Also, different mechanisms have been reported for short term creep, as related in the long term to cement pastes (e.g., Schwarzl, 1969; Sellevold, 1970; Sellevold and Richards, 1972).

Byfors (1980: 177) hasn't defined any suitable period of time to study creep. On the other hand, most of the results presented by this author were carried out for up to 100 hours. It has been previously shown, that for a typical tunnel, the maximum duration for the short term soil-lining load transfer is around 160 hours. The present investigations were carried out bearing this value in mind, and limitations on the results caused by this

choice will be discussed later, in this section. An extensive investigation of creep properties carried out on shotcrete specimens can be found in Litvin and Shideler (1966). These tests started at the age of 7 days or later, and lasted around 360 days. These results will be used in Chapter 6 to investigate the effect of the long term creep in the soil-lining transfer development.

4.5.2 Testing Procedures

The short-term creep tests were carried out using the 'traditional' technique (Byfors, 1980: 185; Neville, 1981: 396; Horrigmoe, 1985), i.e., creep was taken as the difference between the deformation of a constant loaded specimen and the deformation of an identical, unloaded companion specimen. The latter was used to compensate the stress-independent deformations and the thermal deformation of the strain measurement device. The specimens were cylindrical, 150 mm diameter and 450 mm high. Each pair was cast simultaneously using the same mix and the same preparation procedures. The mix was the same presented in Table 4.3, and the water cement ratio was set at 0.6, since at this content, better quality specimens could be obtained. One should notice that for ordinary concrete, the creep is "sensibly independent of the water/cement ratio" (Neville, 1981: 403), and the same characteristics were also verified for the early ages tests (Byfors, 1980: 192).

The specimens received sulfur caps (ASTM C617-1987) at around three hours of age, followed by a moisture protection seal composed of ten parts of paraffin for one of mineral grease. The content of the latter was kept high in order to avoid contraction cracks and also to make the mixture ductile enough to accommodate the concrete deformations. The paraffin was applied using a brush, at a temperature close to the melting point, and the thickness was about 2 mm. This technique is the same are used in soil mechanics, and Hvorslev (1948) has shown that this method can provide efficient protection for up to one month of storage out of the moisture room.

The effects of the temperature evolution caused by this procedure will be discussed in the next section, but for now, it can be stated that the temperature of the specimens in laboratory followed a similar path to those observed in the SLRT lining instrumentation. After the paraffin seal was applied, a compressometer, as described in ASTM C469-87a, was attached to the specimens. The compressometer was like that used in the previous sections and it was adapted to have a 30 cm distance between the yokes. This modification was intended to improve the strain measurement accuracy. In order to avoid the boundary confinement effect at the edges, the height of the specimen was increased from the conventional 30 cm, to 45 cm. The compressometer was assembled around the specimen by compressing the fixing rods against the surface of the cylinder. Since this procedure usually broke the paraffin seal, heat was applied around these areas to restore protection.

Plate 4.1 shows the twin specimens with the compressometers already installed and Plate 4.2 shows the creep test assembled for load application. The deformations were monitored using LVDT gages and the load was applied using a hydraulic system that can be seen on the left side of Plate 4.2. The latter was controlled by a microcomputer, and it was able to supply a constant hydraulic pressure to the jack, which could be observed at the upper portion of the loading frame. The stress level of the test was checked by using a load cell between the jack and the specimen (see Plates 4.3 and 4.4).

4.5.3 Interpretation through Rheological Models

Eight conventional creep tests were performed, at loading ages varying between 4 hours and 168 hours, and their interpretation will be discussed.

Since these test results are intended to be applied to soil-lining interaction problem, i.e., deformation dependent loads, a rheological approach was the most logical choice. Neville (1970: 394-430) presented an extensive review of rheological models proposed by many authors with varying complexity. Although some variation exists, they

are generally composed of two basic models, known as a Kelvin (or Voigt) model and Maxwell model (see Figure 4.19). As an example, Figure 4.20 illustrates how complex a model can be in order to simulate accurately the behavior of the concrete, for a wide range of conditions. In this case, the Freudenthal and Roll's model (1958) was developed for long term behavior, under reversible high compressive stresses. Interpretation of laboratory tests using this kind of model is a relatively easy task, but implementing it into a soil-lining interaction model for tunnel design is not realistic for ordinary projects. In fact, Muir Wood (1975), Curtis (1976), Schmidt (1984) and Negro (1988: 8) among others have suggested that simple models, if used properly, could be able to provide suitable accuracy for the design of tunnel linings. Negro (op. cit.: 9) also pointed out that although simplicity is necessary, the design procedure would have to be based on a consistent theoretical background to avoid the usual shortcomings of the existing empirical methods. Accordingly, the use of a rheological model constituted by a spring and a Kelvin cell, shown in Figure 4.21, is proposed in this research. This model will be used for the analytical solution of the soil-lining interaction in Chapter 5, and it will be shown that it can reasonably accommodate the laboratory data. All the elements in this model will be considered linear, and the accuracy of this simplification will be checked later on in this chapter by a series of stress controlled and strain controlled tests. The use of this model for tunnel lining design is not original. For example, Curtis (1976) proposed a simplified adaptation in Muir Wood's solution (1975) in order to consider the creep of the ground and lining. Yuen (1979) also used this viscoelastic model, and derived an analytical solution for application in deep tunnels under high horizontal stress.

The model shown in Figure 4.21 can be decomposed in two parts: the left represents the immediate (or elastic) response while the right is the time dependent component. For interpretation of the creep tests, only the time dependent response will be of interest. The stress components (see Figure 4.21) can be written as:

$$\sigma' = E_t \epsilon_c \quad [4.13a]$$

$$\sigma'' = \eta \dot{\epsilon}_c \quad [4.13b]$$

where

ϵ_c =creep deformation

E_t and η are the parameters for the time dependent deformation

$$\dot{\epsilon}_c = \frac{d\epsilon_c}{dt'}$$

t' =time after load application

These expressions show that the stress acting on the spring is linearly proportional to the strain (Eq. 4.13a), i.e., linear elastic, while the stress on the dashpot is linearly proportional to the time rate of the strain (Eq. 4.13b). The total stress will be:

$$\sigma = \sigma' + \sigma'' = E_t \epsilon_c + \eta \dot{\epsilon}_c \quad [4.14]$$

For a constant load $\sigma=\sigma_0$, the previous equation has the following solution (e.g., Flugge, 1967: 8):

$$\epsilon_c(t') = \frac{\sigma_0}{E_t} (1 - e^{-\lambda t'}) \quad [4.15]$$

where

$$\lambda = E_t / \eta$$

The expression above shows a linear relation between creep and the applied stress level. This linearity is generally accepted for ordinary evaluation of the creep deformations below a limited stress/strength ratio. Neville (1981: 401) has reported that the upper limit of this ratio was not well defined, suggesting however that it could be

between 0.3 and 0.6. Neville (op. cit.) also reported a possible deviation of this linearity for the concrete at the early ages. On the other hand, in a research performed specifically to define the behavior of plain concrete at early age, Byfors (1980) proposed linear creeping up to the stress/strength ratio of 0.3 to 0.4 (Byfors, op. cit.: 179). The same author also suggested (Byfors, op. cit.: 182) that the concrete behavior deviations at early age compared to well cured samples be reduced when rapid-hardening mixes are used. Although the data available up till now are not conclusive, it seems that if deviation exists, it will be reduced in the case of the rapid-hardening shotcrete. For the creep test interpretation, it was assumed the linearity shown in the Equation 4.15 and the data were treated in terms of the specific strain, i.e., strain per unit stress. For this purpose, Equation 4.15 can be written:

$$\frac{\epsilon_c(t')}{\sigma_0} = \frac{1}{E_t} \left[1 - e^{-(E_t/\eta) t'} \right] \quad [4.16]$$

where $(1/E_t)$ and (E_t/η) are the coefficients to be determined from creep test results.

Figures 4.22 to 4.29 show the creep tests results and the curve fittings performed, while Table 4.12 shows the conditions imposed in each test. As mentioned previously, a simple rheological model was deliberately selected in order to meet the usual restrictions of time and/or budget imposed by ordinary projects. Therefore, some deviations should be expected between the actual behavior of the shotcrete and the predictions given by the model. In order to minimize these deviations, the definition of the parameters used in the model were obtained though a parametric analysis during the curve fitting procedures, followed by engineering judgement.

Table 4.12 shows the age of the shotcrete when the tests began, and the time spent to apply the load. Although the latter should be ideally zero, i.e., no creep

deformations during load application, this condition could not be matched due to the restrictions imposed by the hydraulic system used in the tests. However, it will be shown later that the load was applied fast enough to consider the creep during this stage (loading) negligible in terms of test interpretations. Curve fittings were performed for the constant load stage, by applying the Simplex algorithm to Equation 4.16. As the rheological model cannot be well adapted to data throughout the tests, the fitting technique was applied using data of different intervals of time. Taking for instance Figure 4.25, it can be observed that if only the data for the first 2 hours of the test were considered ($\Delta t'=2$ hours), the adjusted curve would agree well with the initial portion of the test, but creep would be underestimated afterwards. If the curve fitting were performed using the data up to the end of the test ($\Delta t'=49$ hours), reasonable agreement would be obtained between 2 and 49 hours, but at the earlier stages, creep would be underestimated. Considering data for intervals of between (4, 8, 16, 32, 72 hours and end of test), creep deformations would be underestimated at the early and final stages. Since this effect was observed in most of the tests (CRSG4H to CRSG168H), it was necessary to establish some criteria to choose the most suitable interval of time to interpret the creep tests, for the purposes of the present application. Figures 4.30 and 4.31 show the parameters $1/E_t$ and E_v/η obtained for each of the tests, though the Simplex algorithm considered the data for different time intervals. The first parameter ($1/E_t$) can be understood as the final specific creep, i.e., the strain per unit stress at the end of the creep, while the second is related to the viscous behavior (E_v/η) and it indicates how 'fast' the creep deformation would develop. Those figures indicate that both of the creep parameters converge approximately at the same values for age at loads greater than about 10 hours, independent of the time interval considered for model fitting. These results suggest that although the creep presents a sharp age dependency for the very early ages, around about 10 hours, and after this point, an age independent model could be applied.

The above partial results, however, should be used with some caution. Observing Figures 4.22 to 4.29, the results suggest that just for age at loading up to 8 hours, the strain rate, or strain per unit time, have already drastically reduced the age by about 40 hours. Therefore, it is reasonable to assume that creep had already stabilized in these tests. On the other hand, in tests CRSG12H to CRSG168H, the strain rate didn't show any clear indication of reduction. As a result, curve fitting presented for these tests underestimated deformations for the long term.

The main objective of the present investigation was to define the parameters of shotcrete for the short term load transfer of soil-lining system in tunnel construction. The interpretation of the tests should be compatible to this criterion. It was already mentioned that for the usual case, this 'short term' could be represented by the range 2.2 to 6.7 days, or 53 to 160 hours. As an example, Figure 4.32 shows the strain and stress development that one could expect for the case of the upper limit, i.e., most of the load was transferred to the lining within about 6.7 days. This figure shows the strains measured at the inner and outer fibers of the lining at the Langen tunnel, and the stresses were interpreted by Schubert (1988), using a method adapted from that developed by England and Illston (1965). The shotcrete properties were obtained from investigations performed at the Montan University, Leoben. This model will be discussed later in this thesis, but for now, the results will be used as a reference for the creep test interpretations. The stress evolution in Figure 4.32 shows that approximately 80% of the load was applied to the lining in about half of the total time to the short term load transfer process, i.e. of the order of 3.2 days. Therefore, it seems reasonable to assume that the stress-strain behavior of the short term load transfer mechanism of a tunnel construction will mainly be a function of the properties of the shotcrete in the first half of this period. Since this criterion is somewhat arbitrary, as it was based on limited data presented by Schubert (1988), it will be checked later in this chapter through stress controlled and strain

controlled tests, by a parametric analysis using an analytical solution in Chapter 5, and the interpretation of the case history monitoring in Chapter 6.

According to the criteria stated above, for the lower limit of the short term load transfer period of 53 hours, the properties of the shotcrete corresponding to the first 27 hours will dominate the overall behavior. For the upper limit of 160 hours, the first 80 hours should be considered. One should notice also, that although in the tests CRSG36H and CRSG78H, the strain rate did not show any clear reduction trend, the total time covered by these tests was approximately the upper limit, i.e., 160 hours. In the case of the test CRSG78H, the regression in the interval of 72 hours seems best represent the behavior for the upper limit condition. Considering the average short term load transfer interval of 107 hours¹, it seems that the parameter values proposed and shown in Figures 4.30 and 4.31 would be most adequate to analyze a typical case of tunnel construction. For the lower limit, i.e., 53 hours, the average parameter of the shotcrete for age after 10 hours could probably be better represented by shifting the previous values towards the analysis done for the 32 hour interval. This would avoid excessive underestimation of creep at very early ages by assuming lower viscosity (see Figure 4.30). If parameters were chosen for short intervals, for example 16 hours, the very early age deformations would be better estimated, but the final values would be excessively underestimated (see Figures 4.22 to 4.27). For the upper limit (160 hours), it seems that the parameters obtained for curve fitting using the data up to the end of test are the most suitable. Considering particularly the test CRSG78H, the parameters coming from an interval of 72 hours are probably the best estimation. However, if these parameters are used as average values, the rate of creep would be underestimated for the early stages (see Figure 4.31). In any case, it seems that creep parameters would lie between the curve fittings performed for data using the first 32 hours and the end of test. For the case of the lower

¹average of the lower limit, 53 hours and upper limit, 160 hours.

limit (53 hours), the time dependency of creep in the first 10 hours could be potentially more significant. For the limited time interval considered in this investigation, the results suggest that the total amount of creep was reasonably constant after 10 hours of age (Figure 4.30), while their rate drop considerably after 78 hours.

As mentioned earlier, the load during creep tests was not applied instantaneously and the analyses were carried out to evaluate this effect on the test interpretations. The load was applied under constant rate until the desired value was reached and then, it was kept constant. The solution of the strain development under this type of loading will be given later in this chapter (see Equations 4.24 and 4.25), and it was used to perform the curve fittings. This solution included the creep that occurred during the constant rate loading, as opposed to the interpretation of the test based on Equation 4.16. The results are shown in Figures 4.30 and 4.31. The curve fittings were conducted using the data up to the end of the tests. A good agreement can be observed between these results and the conventional interpretation procedures. Therefore, for the present application, one may consider that the load was applied instantaneously. The results of these analysis for each test are shown in Appendix D and the parameters obtained are presented in Table 4.13. Note that at test CRSG4H, Figure D.2 in Appendix D, that the load was not perfectly constant. Due to the higher stresses necessary for the older specimens, these variations were within the maximum accuracy given by the load application system. Figure 4.30 also shows the ratio E_t/E obtained using Equations 4.24 and 4.25, can be understood as the ratio between the elastic strain and the short term creep. On the average, it shows that after 10 hours, the elastic deformations are about twice as large as the creep ones. In order words, the short term creep represents approximately one third of the stress dependent deformations. Therefore, although assuming that average values of the creep parameters will induce some error, especially for loads applied after about 40 hours, it will potentially represent 33% of the total deformations. Considering that almost 80% of the total load had already been applied at that time, the deviations would eventually be

kept in an acceptable level in terms of design. All statements related to creep up till now are still at a speculative level, but their validity will be checked throughout this thesis.

Figure 4.33 compares the present investigation results to those conducted by Byfors (1980) for the early age behavior of plain concrete. It is well known that accelerated concrete (or shotcrete) presents higher strength at very early ages in comparison to ordinary concretes, while for older ages, the strength of the former is lower than the latter. Although just two sets of tests results were presented, it seems that a similar trend, observed in Figure 4.33, may be applied in terms of short term creep. At ages up to about 20 hours, the creep of accelerated concrete (or shotcrete) is lower than the ordinary one, while the reverse is true for older ages. In the same figure, the predictions using the average parameters presented in Figures 4.30 and 4.31 (i.e., $E=15$ GPa, $1/E_t=0.03$ 1/GPa and $E_t/\eta=0.003$ 1/min) were shown. It can be observed that up to 1 hour, the model clearly underestimated creep, but afterwards a reasonable agreement was achieved. Note that the interval of analysis of these results was compatible to the short term soil-lining load transfer. For longer analysis, the parameters suggested above will clearly underestimate creep, because none of the presented tests (e.g., see Figure 4.33), specimens older than 24 hours presented any indication of strain rate decrease. This aspect will be discussed in Chapter 6.

4.6 Stress Independent Deformations

4.6.1 Introduction

In the creep tests presented above, stress-independent deformations were compensated by using twin dummy specimens. This section presents the investigations carried out to evaluate strains. They are commonly associated with three factors: temperature changes, shrinkage and autogeneous volumetric change. All tests were carried out in specimens with identical composition to those which were used for the creep tests.

The strains associated with temperature changes are the first aspect to be analyzed.

In Chapter 2, when the temperature correction factor for the vibrating wire strain gages was presented, the difficulties to determine that parameter at very early ages was discussed. The reason is that between 3 and 20 hours, the internal heat generated inside the shotcrete specimen dictates the temperature evolution. Any attempt to control this temperature to levels suitable for taking measurements, for evaluation of the correction factor under the limitations of the laboratory monitoring equipment, caused unacceptable temperature gradient within the specimen. For the same reason, the coefficient of thermal expansion was evaluated under temperature changes resulting from the cement curing process. It was also pointed out in Chapter 2, that as the curing process takes place, a gradient of temperature occurs between the specimen and the air. It was shown however, that when the temperature of the specimen begins to drop, the gradient between a point at the center and another close to the surface, remains almost constant and below 0.3°C . Under this condition, although not ideal, the coefficient of thermal expansion can be determined with acceptable accuracy.

4.6.2 Testing Procedure

Three tests were performed (TEMP1, TEMP2 and TEMP3) and followed a similar setup used for the creep tests, i.e., the specimens had the same dimensions, the same paraffin seal was applied and the strains were measured using the same ASTM C469-87a type compressometer. The only difference in this case was that the RTD (Resistance Temperature Device) was placed 5 cm from the bottom of the cylinders. This instrument was incorporated in the specimens during the casting procedure. Figure 4.34 shows the strain variation with temperature change for these tests, and Figures 4.35 and 4.36 show the temperature variation with time. One can notice that the readings started about 4 hours after the specimens were cast. The reason, as in the case of the creep tests,

was the impossibility to manipulate the specimens earlier, for seal application and test assembling due to the low strength at the very early stages. Byfors (1980: 272) has compiled data of thermal expansion coefficient available for concrete at early age, which are shown in Figure 4.37, and one can see the high values measured at very early ages. During this period, plastic shrinkage may have taken place (see Figure 4.38) and/or autogenous volume change (e.g., Andriolo, 1984: 185; Dunicliff and Green, 1988: 316). Plastic shrinkage occurs before actual hardening of the concrete takes place (Byfors, op.cit.:275) and it can be associated with high capillary pressure or suction development (Wittmann, 1976). Using a thermodynamic approach (e.g., Kuwajima, 1985), it is possible to demonstrate that high values of suction may be generated by the chemical changes of the cement. Therefore, the concrete matrix may change volume similarly to the plastic shrinkage, even if a seal is applied to avoid water losses. The autogenous volume changes occur due to the hydration processes of the concrete, resulted by the reaction and formation of chemical components (Andriolo, op.cit.). In other words, the volume occupied by the cement varies. Using ordinary laboratory equipment, the isolation of each volume change component, at the very early ages, was extremely difficult, and for this reason, approximations were made.

Figure 4.34 shows that the strain vs. temperature relation is linear after the peak value. Moreover, in Figure 4.36 one can see that the linearity is valid after 10 hours of age. Figure 4.37 suggests that the coefficient of thermal expansion would likely be constant after the same period, while Figure 4.38 shows that most of the very short term shrinkage may have already taken place. It is reasonable to assume that only deformations related to temperature took place in the specimen after 10 hours of age. Notice that the ordinary shrinkage was avoided by protecting the specimen with the paraffin seal. Therefore, the coefficient of thermal expansion (α_T) can be taken as the average of the values shown in Figure 4.34, i.e., $\alpha_T=8.25 \times 10^{-6}$ (m/m)/°C, regarding that it is only valid after 10 hours of age. Since these thermal strains may produce a

considerable impact on the soil-lining interaction, prior estimation of such values are useful for tunnel design. Schubert (1988), using the expression developed at the Montan University, Leoben, suggested the following for shotcrete linings:

$$\epsilon_T = (-\cos (A_T t^{0.25}) + 1) B_T \tag{4.17}$$

where

ϵ_T =temperature related deformations (10^{-6} m/m)

t =age in days

$A_T=250$

$B_T=30$

(cosine in degrees)

Considering that the coefficient of thermal expansion estimated above is valid also for the period 0 to 10 hours, it is possible to rewrite Equation 4.17 as a function of temperature change:

$$\Delta T = (-\cos (A_T t^{0.25}) + 1) \frac{B_T}{\alpha_T} \tag{4.18}$$

where

$\Delta T = T - T_0$

T =temperature at age t

T_0 =reference temperature (for $t=0$ or $t=+\infty$)

α_T =coefficient of thermal expansion

Figures 4.35 and 4.36 show the development of temperature using Equation 4.18¹ by considering the reference temperature $T_0=24^{\circ}\text{C}$ (laboratory temperature) and the $\alpha_T=8.25 \times 10^{-6}$ (m/m)/ $^{\circ}\text{C}$. It can be observed that although the peak value was reasonably estimated, there was a considerable disagreement of its evolution with time.

¹ Notice that this equation (as well as 4.17) should not be applied after approximately 100 hours, because after this period, the temperature indicated by the equation starts to increase again (cossine function).

Figures 4.39 to 4.42 show the same kind of comparison for the typical development of temperature measured with instruments installed in the SLRT tunnel lining. Details of installation and exact location of these instruments can be found in Chapter 2 and Appendix B. Figure 4.39 shows the temperature development for the dummy gages installed in the compensating panels. One can observe that there is a better agreement of temperature evolution with Schubert's results than with results in Figure 4.36, despite the greater deviation at peak. The reference temperature (T_0) in this case was 20°C (average temperature inside the tunnel), which was also applied in the case of Figure 4.40. Here, the instruments located close to the tunnel floor are shown. Moreover, Equation 4.18 provides a reasonable estimate of the temperature evolution.

Figure 4.41 shows the data for instruments located at the springline region, and the reference temperature (T_0) was set as 21°C. Observe that this value was 1°C higher than that of the previous case.

Figure 4.42 shows the results of the instruments located close to the tunnel crown and displays a considerable dispersion of the data. The reference temperature was set as 24°C, and it indicates that in the upper regions of the tunnel, the air temperature was higher than in the lower ones. In fact, by analyzing the temperature records for the instruments located close to the crown with the tunnel in operation, it was observed that whenever the tunnel construction stopped, the temperature dropped about 4°C and almost full recovery was achieved after construction was resumed. Similar temperature fluctuations were also observed by Heinz (1989) in a recent instrumentation of NATM tunnel in São Paulo. The shotcrete curing process and diesel-propelled machinery produced heat which caused a temperature gradient in the vertical direction. Also a gradient existed in the tunnel axis direction because the heat was generated mainly close to the face. The instruments at the floor did not indicate considerable temperature fluctuation because it was thermally protected by the soil fill that covered the region. Smaller fluctuation was observed at the springline than at the crown because the air

temperature in this region was closer to the one established when the tunnel construction stopped.

The air temperature fluctuation is only one factor among others that controls the shotcrete temperature evolution. Tests series RHS and TEMP4 were performed to investigate some of those factors. Four specimens were cast for the series RHS: two cylindrical (15 cm diameter and 45 cm high) and two prismatic (10 cm high x 15 cm wide x 20 cm long) specimens. One cylinder (RHS/2) was sealed with paraffin, while the other (RHS/4) was unprotected. One of the prisms (RHS/1) was cast over a soil layer 15 cm thick, and both the soil and concrete received a paraffin protection, but left the top surface of the concrete prism exposed to the air. The other prism (RHS/3) was also cast over a soil layer (15 cm), received another soil layer (15 cm) at the top, and all the exposed surface was sealed with paraffin. The soil had the same moisture content (18%) as the samples taken from the tunnel face, the area where the lining instrumentation was installed. The specimens RHS/1, RHS/2 and RHS/3 were left curing for 3.5 hours inside plastic bags, until the paraffin was applied. The specimen RHS/4 was left curing for 4 hours inside plastic bags until the mold was removed. All of them were cast with the same batch of concrete, and after the preparation stages were placed in a chamber having the same relative humidity observed in the tunnel ($RH=95\%$). Series TEMP4 were composed of two specimens cast in conventional paper-paraffin cylinders. One was 7.5 cm diameter and 15 cm high (TEMP4/1) and the other was 15 cm diameter and 30 cm high (TEMP4/2). After casting, the specimens were immediately transferred to the same chamber used in test series RHS leaving the specimens inside the cylindrical mold in all tests. This chamber was kept at the same air temperature as that in the laboratory, i.e., around 24 °C. Figure 4.35 shows the results and Figure 4.36 presents the details of the temperature evolution during the first 40 hours.

Series TEMP4 was designed to investigate specimen size effect on the development of temperature. The larger specimen TEMP4/2 (Figure 4.36) attained

considerably higher temperature. The same effect, related to the thickness of the lining, may be observed in Figure 4.42 for the instruments C1U/VW1 and C1U/VW2. These instruments were installed under a region where the over cut was of the order of 42 cm. From the region just above instruments C2IIU/VW40 and C2IIU/VW41, a soil block, measuring about 30 cm high, fell on top of the steel mesh where these instruments had been tied. The space was then filled with shotcrete, increasing the thickness of the lining in this region. Moreover, part of the temperature development differences may be attributed to local variations in lining thickness.

Comparing the results of the test TEMP4/2 to tests TEMP1, TEMP2, TEMP3 and RHS/2, (Figures 4.35 and 4.36), it seems that the paraffin application didn't produce any significant influence on the temperature evolution. The first test received no paraffin protection, while all others were sealed. Test TEMP4/2 reproduced the conditions of the specimens in which the strength and elastic modulus were evaluated and the other conditions of the specimens used in the creep tests. Figure 4.13 (creep test curves) shows that the elastic modulus also did not present any significant deviation due to the paraffin application and for this reason, this effect was neglected in the interpretation of the tests. The faster decrease in temperature observed in all laboratory tests (Figure 4.36), compared to field measurements (Figures 4.39 to 4.42), may be attributed to a 'shape' factor. In all laboratory tests, the specimens had higher specific area exposed to heat flow, therefore, the heat transmission process was faster than in the field. For the instruments at the crown (Figure 4.42), temperature also dropped considerably faster than predicted by Equation 4.18, probably as result of the higher speed of the air flow in this region. Observe that, in the SLRT tunnel, the ventilation was achieved by injecting air through a conduit installed at the crown, with the outlet located 1 to 3 diameter behind the face. A similar effect, but with smaller magnitude, can be observed for the springline (Figure 4.41). Another effect observed only in the laboratory tests, probably due to the higher specific area, was the lower peak temperature values when the concrete was

directly exposed to air. Figure 4.36 shows lower values for RHS/1 compared to RHS/3 and RHS/4 compared to RHS/2. This effect can be attributed to the greater amount of heat transferred from the concrete to the air due to water evaporation from the surface of the specimens.

Temperature development is a complex thermodynamic process and depends on many factors. Some of them are investigated keeping the concrete composition constant. The influence of the shotcrete composition and application condition on the temperature development were investigated to some extent by Parker (1976). Equation 4.18 gives a reasonable estimation, despite the dispersion observed, specially for the instruments located close to the floor. Better results are obtained if one adjusts the parameters A_T and B_T for each specific case. Examples of the use of curve fitting techniques to adjust the temperature development will be given in the section of strain controlled tests. In the case of incorporating this type of temperature estimation in the tunnel lining design routine, extra caution is recommended. Readings taken at SLRT tunnels indicated deviation of about 4°C in many cases, with maximum values reaching up to 14°C . If one adopts a coefficient of thermal expansion $\alpha_T = 8.25 \times 10^{-6} \text{ (m/m)/}^\circ\text{C}$, the thermal strain for 4°C will be of the order of $33 \times 10^{-6} \text{ m/m}$. This value represents about 15% to 25% of the strains measured in the SLRT tunnel lining (see Chapter 2 or Appendix B). The measurement of temperature is essential when calculating stresses from strains measured in shotcrete linings. More details on the results presented above will be given in Chapter 6 through parametric analysis and interpretation of the strains measured in the SLRT tunnel lining.

Due to the varied and complex processes present during the period between 0 and 10 hours, it was not possible to isolate each strain component. Temperature changes observed during this period caused thermal expansion (α_T could not also be evaluated) and cement hydration related to the latter, generated volume changes. These deformations, as will be seen in Chapter 6, have small significance in terms of stress

development and soil-lining interaction. In this period, the elastic modulus is low (Figure 4.13) and the creep deformations are high and fast (Figure 4.29 and 4.30). It is possible, however, to obtain an estimate of the strain in this period. Figure 4.43 shows the strain evolution measured at the dummy samples in the creep tests (zero load) and also the measurements taken during test series RHS. The strains in the latter were measured using embedded vibrating wire strain gages, similar to those used in the tunnel instrumentation. These vibrating wire gages were compensated by the temperature correction factor of $-6.6 \times 10^{-6} \text{ (m/m)/}^{\circ}\text{C}$, according to the test results presented in Chapter 2. None of the tests shown in Figure 4.43 presented readings before 4 hours, the time necessary to assemble the test. In absence of further data, Figures 4.37 and 4.38 provide some guidelines on the 'total' stress independent deformations in this period. Figure 4.36 shows a relative small temperature variation for the interval between 7 to 10 hours, close to peak value. For this reason all the strains presented in Figure 4.43 had the zero reference set at 7 hours. Therefore, the strains presented between 7 and 10 hours had reduced influence of the temperature changes. In this interval, a reasonable agreement among the measurements, regardless the specimens curing conditions can be observed. Ideally, RHS/1 represented the curing conditions of the shotcrete of the lining above the fill line at the floor, i.e., soil on one side of the shotcrete and air at RH=95% on the other. RHS/3 represented the shotcrete at the floor (soil on both sides), RHS/4 simulated the dummy panels used at the tunnel instrumentation (surround by air at RH=95%) and RHS/2 had the same conditions as the creep tests (completely sealed by paraffin). Although the curing conditions did not show any significant influence on the strain development between 7 and 10 hours, the same was not true between 4 and 7 hours. Between 7 and 10 hours, the temperature remained fairly constant, while between 4 and 7 hours the temperature development was considerably different among the specimens. Considering that the temperature change causes thermal expansion and volume changes related to the cement hydration reactions, it seems reasonable to relate the temperature difference to the strain difference at this

period. Figure 4.44 presents the temperature difference between 7 and 4 hours versus the strain difference between 4 and 7 hours. These values include some degree of approximation because the readings were not taken exactly at 4 and 7 hours. Values which were taken very close to these hours are shown in Figure 4.43.

Figure 4.44 shows that for temperature differences higher than 6 °C, small variation exists between the strain readings at 4 and 7 hours. In these cases, volume contraction related to hydration probably had been compensated by the thermal expansion. For the tests RHS/1 and RHS/4, a considerable strain difference was observed. These results should be taken with caution, because lower temperature changes were related to higher heat transfer permitted in these tests. One face of the concrete prism was left exposed in test RHS/1 while the specimen in RHS/4 did not receive any protection, therefore, shrinkage was intensified. Different results should be expected if the lower temperature development was related to the size effect. Another aspect to be noticed is the different behavior observed between RHS/2 and the creep tests in Figure 4.43. All these tests were prepared under identical procedure, but in the case of RHS/2, the strains were measured by vibrating wire gages while during creep tests, the ASTM-C469 type compressometers were used. The different strain pattern observed could be caused by a gradient of temperature within the specimen and/or temperature compensation problems in the vibrating wire strain gages. The gradient of temperature, as mentioned in Chapter 2, was higher when the temperature was increasing than when it was decreasing. This was caused by the higher rate of the former with time than the latter, as one can observe in Figure 4.36. Since in test RHS/2 the strains were taken at the center of the specimen and during creep tests they were measured at the external surface, part of the strain difference may be caused by the temperature gradient. Also, one should notice that the temperature compensation factor for the vibrating wire strain gages presented in Chapter 2, is valid only when the temperature of the specimen decreases. For the ascending portion, the stiffness of the shotcrete should be very low, compared to

the steel-made VW gages, therefore, inducing thermal stresses high enough to interfere in the readings.

The thermal expansion ($\alpha_T=8.25 \times 10^{-6}$ m/m/°C) can be applied after 10 hours of age, therefore, it is possible to isolate the shrinkage deformation then. Figure 4.45 shows the temperature compensated strain (i.e., considering the temperature correction factor on the strain readings of the vibrating wire gages and the thermal expansion coefficient of the shotcrete) development for the specimens of the test series RHS. It can be observed that for the specimens RHS/1, RHS/2 and RHS/3, the shrinkage was negligible and their values were considered zero within experimental error. Notice that RHS/2, a sealed specimen, presented strain values in the same order of magnitude as the specimens that were in contact with soil (RHS/1 and RHS/3). The tests were carried out for about 130 hours (same order of magnitude as the upper limit of the short term load transfer defined earlier, 160 hours). Specimen RHS/4 which was left unprotected under an environment of RH=95%, presented considerable shrinkage although the bi-linear pattern was not the expected behavior.

Figures 4.46 to 4.48 show the temperature compensated strain, similarly calculated, for some of the strain gages used in the tunnel lining instrumentation. Figure 4.46 show the strain development for the instruments installed in the compensating panels. In Chapter 2, it was mentioned that these panels were accidentally submerged in slurry on the tunnel floor. The inversion of trend from contraction to expansion, shown in Figure 4.46, corresponds to the time this incident occurred.

Figures 4.47 and 4.48 show the strain development for the instruments installed in the longitudinal direction of the tunnel (for detailed information of these instruments, see Chapter 2 and Appendix B). Since the compensating panels were subjected to an unexpected condition, the results of the longitudinal instruments will be used as guidelines to evaluate the shrinkage development at the shotcrete lining. As the tunnel advances, only a small value of stress should be expected in the longitudinal direction,

since the load (gravitational) is applied essentially in the vertical direction. Also, the heading is always the first region to advance and to receive the shotcrete lining. Therefore, longitudinal stresses would be more significant at the heading, since impact of the excavation unloading would be felt first in this area, which also has higher stiffness than the rest of the lining in the closed ring, near the face. Figure 4.47 shows the readings taken from the instruments located close to the tunnel floor. The instruments C2IIB/VW4 and C2IIB/VW6 were placed close to the surface line of the soil fill and the others at the very bottom. These instruments showed a strain development similar to the panels (see Figure 4.46) after they were submerged in slurry. The exception was the instrument C1IB/VW8, which showed irregular readings around 40 hours (data not shown). After this, the strain development of this instrument was almost parallel to the other instruments located at the floor. The difference noticed between the strain measured with these instruments and those measured in the laboratory to simulate the same condition (RHS/3, cast between two layers of soil), could have two sources: the amount of water available in the soil layers in the test RHS/3 was not enough to generate expansion and/or the soil in contact with the shotcrete had higher moisture content than that used in laboratory. In fact, during the installation of the instruments located at the invert, some water accumulated on the floor, before the shotcrete application. Although the amount of infiltrated water was small, it was always present in the instrumented sections. Therefore, the soil in contact with the shotcrete, either the natural soil remaining at the bottom of the excavation or the fill placed above, had contact or was mixed with free water. As a result, the moisture content of the soil close to the shotcrete contact at the site could be higher than the soil layers used in the laboratory simulation. The instruments C2IIB/VW4 and C2IIB/VW6, located around the intersection of the fill surface and the tunnel lining, presented lower values of shotcrete expansion. In this case, the water supply was limited due to this boundary condition, and as a consequence, the expansion was minimized.

In order to check the shotcrete expansion when water was available, another test was performed. Two specimens were cast similarly to RHS/4, i.e., without paraffin seal. The first one (RHIM/1) was left curing at an environment of RH=95% until the end of the test. The second one (RHIM/2) was left at the same condition and at around 30 hours of age, it was submerged in water. The results shown in Figure 4.45, confirmed the expansion tendency shown by the instruments installed at the tunnel floor. The specimen RHIM/1 presented the same linear trend as the shrinkage observed in RHS/4 under laboratory conditions, as opposed to the exponential one observed at the site (dummy panels, Figure 4.46).

Figure 4.48 shows the strains measured in the longitudinal direction of the tunnel at the springline (C2IB/VW5 and C2IB/VW10) and at the crown (C2IU/VW1, C2IU/VW2, C2IU/VW3 and C2IU/VW7). Similar to the temperature measurements, these instruments showed cyclic oscillation according to the tunnel construction operation. This effect can be observed more clearly in Figure 4.49, showing the same instruments for a longer period. As observed in Figure 4.42, the temperature dropped faster at the crown than on the floor. The same effect was observed at the springline (Figure 4.41), but in reduced scale. This higher rate of temperature decrease was related to the faster rate of moisture loss from the shotcrete, and it was considered a consequence of water evaporation from the lining surface, enhanced by the air ventilation. Test RHS/1 was intended to simulate the shotcrete at the crown and springline regions, i.e., exposed to the air at one side and in contact with soil at the other. However, the air flow was not simulated in the laboratory, therefore, this condition induced lower values of shrinkage. This air flow had two contributing effects in generating higher values of shrinkage at site than in the laboratory simulation: the velocity of the air flow itself and lower values of relative humidity of the air that was injected for ventilation. Notice that inside the tunnel the RH was around 95% and the air injected from the surface had RH around 50%. This condition creates a peculiar shrinkage regime for the tunnel lining problem, compared to

the conventional case of concrete structures. The soil became a source of moisture, discharged at the shotcrete surface and carried out by the air flow. A dynamic water diffusion in non saturated porous media (mathematical formulation of this kind of problem can be found in Taylor, 1972) is established and the flow is controlled by the properties of the air stream. Figure 4.49 shows that expansion was observed whenever the construction was stopped, and contraction whenever it was resumed. It indicates that these two conditions could establish different diffusion regimes, inducing different moisture content levels, which were measured indirectly by the volume change of the shotcrete. The discussion that follows is an attempt to explain the mechanism that could take place in the shotcrete lining. When construction was stopped, there was no air flow and the relative humidity of the air became high. Under this condition, the soil was able to supply enough water to increase the moisture content of the shotcrete, inducing the expansion. When the construction was resumed, the air flow restarted with lower relative humidity. These two factors increased the rate of the water taken from the surface of the shotcrete, inducing a new diffusion regime. Under this condition, the moisture content of the shotcrete could drop, causing contraction. Notice that the data presented in Figure 4.49 were already compensated for thermal expansion factor. Also, Figure 4.45 shows that water can produce volume changes in very short period of time (RHIM/2), compatible to the period of stopping and resuming of tunnel construction. The missing information to substantiate the mechanism described above is the relation between the moisture content and the suction in the shotcrete. However, if one accepts that this relation can be similar to the experimental results observed in soils (e.g., Kuwajima, 1985), the mechanism is justified. Nevertheless, considering the average values of strain fluctuations shown in Figure 4.49, it can be observed that the mean value of the shrinkage during the time did not increase considerably. This confirms the results shown in the test RHS/1 (Figure 4.45) indicating a negligible shrinkage for a 'constant' environment condition of $RH=95\%$, with the shotcrete in contact with the soil.

The 'wind effect' is probably the most significant factor which controls the magnitude of the shrinkage at the crown and the springline. Most of the strains presented in the Figures 4.47 to 4.49 can be attributed to moisture fluctuations, therefore, it seems reasonable to assume that the longitudinal load at the tunnel lining could be considered negligible in terms of strain generation. As a result, those strains can be used as a guideline to estimate the shrinkage for interpretation of the instrumentation of the SLRT tunnel lining. Also, one should observe that none of the instruments installed in the longitudinal direction presented shrinkage evolution as high as the ones observed by the dummy gages in the panels (Figure 4.46) or the test RHS/4 (Figure 4.45), where the specimen was left unprotected in the same environmental condition ($RH=95\%$) found in the tunnel. Therefore, shrinkage estimation based only in terms of the relative moisture content of the air, as has been conventionally proposed (e.g., Gais et al., 1986), cannot provide an accurate estimation in the case of NATM tunnels excavated in soils. The moisture provided by the soil plays a major role in the shrinkage process. It induces expansion at the invert region of the lining, and reduces the shrinkage at the other areas. At the crown and springline, the temperature dropping rate and the strain fluctuations at the longitudinal strain gages, are indications that the moisture losses of the shotcrete were related to the air ventilation. The latter induced higher values of shrinkage at the site than those observed in the laboratory, test (RHS/1) with air at rest. When the construction was stopped, i.e., no air flow, the rate of the shotcrete moisture loss dropped, and the water supplied by the soil was sufficient to reverse shrinkage to expansion.

4.7 Stress Controlled Tests

The results of creep tests and their interpretation through a simple viscoelastic model was presented in section 4.5. In order to test the accuracy of this rheological model, six stress controlled tests were carried out, and they will be discussed in this section.

These tests were identical to the creep ones, in terms of specimen preparation, load application system and measurement instruments (see Plates 4.1 and 4.2). The dummy specimens were also used, in order to isolate the stress dependent deformations. The stress independent deformations will be explored in the next section under strain controlled tests. Therefore, the only difference between the creep tests and the present ones was the way the load was applied. During the former, the load was kept constant with time, while during the latter, the tests followed the functions shown in Figure 4.50. The load was applied in steps in four tests (CRMST1 to CRMST4), while in the other two (CRSLP1 and CRSLP2), they followed a constant slope until a certain value was reached, and then the stress level was maintained. These tests had the same problems as those observed in creep test CRSG4H (see Figure D.2, Appendix D) for the lower stress levels: the load application system could not keep the stress constant. Figure 4.51 shows a detail of the stress values in this region and Figure 4.52 shows typical relative errors, presenting as an example, for test CRSLP2. The peak values should not be considered as stress variations, because it was verified that they were electrical noise in the load cell readings. The relative errors presented in Figure 4.52 were defined as the expected values of the stress minus the measured one for a specific time, divided by the first. It can be observed that during the first few hours, the load presented an error of about 10% and afterwards, the error was kept below 1 %.

The stress-time functions for the present set of tests (see Figure 4.50), can be represented by a combination of the following functions:

$$\sigma(t') = \frac{\sigma_1}{t_1} t' \quad \text{for } 0 \leq t' \leq t_1 \quad [4.19]$$

$$\sigma(t') = \sigma_1 \quad \text{for } t' > t_1$$

where:

$$t = \text{age}$$

$$t' = t - t_0$$

σ_1 , t_0 are constants for each step

Table 4.14 shows the values of σ_1 and t_1 for each stage of the tests, and t_0 represents the age at which a particular load stage started. For example, in the test CRMST3, the fourth stage of loading started at 15.8 hours of age, the stress increment was 147.4 kPa and was applied at constant rate during 7.5 minutes. At the end of this period, the specimen was subjected to the stress increment of 147.4 kPa, plus the increments of the three previous stages, i.e., an accumulated stress of 486.2 kPa.

The basic equation 4.15, used to perform the creep tests interpretation, can be rewritten as:

$$\varepsilon(t') = \sigma_0 J(t') \quad [4.20]$$

where:

$$J(t') = \frac{1}{E_t} (1 - e^{-\lambda t'})$$

$t' = t - t_0$ time after load application

Equation 4.20 represents creep deformations (excluding elastic strain) for an instantaneous application of stress at constant level, considering the viscoelastic model represented in Figure 4.21. The relation $J(t')$ is different for each viscoelastic model considered for a particular material, and it is called compliance (Flugge, 1967: 22). The compliance, as shown in Equation 4.20, represents the common form to represent the creep used in design or conventional test interpretation, i.e., under constant load. This is a special case of the compliance representation, and it is not suitable for the soil-lining interaction problem, because in this case, the load is a function of time. For the more general load application condition, using the property of linear superposition of the viscoelastic model (Flugge, op.cit.: 25), one can represent the strain as:

$$\varepsilon(t') = \sigma_0 J(t') + \int_0^{t'} J(t'-t'') \frac{d\sigma''}{dt''} dt'' \quad [4.21]$$

where:

σ_0 = stress at $t'=0$

The equation above shows that the strain at any given time depends on the entire stress history $\sigma(t'')$, $t'' < t'$, until that moment. Equation 4.21 is known as hereditary integral. It can be integrated by parts, and after some algebraic manipulation, Equation 4.21 can be rewritten as (Flugge, op.cit.: 26):

$$\varepsilon(t') = \sigma(t') J_0 + \int_0^{t'} \sigma(t'') \frac{dJ(t'-t'')}{d(t'-t'')} dt'' \quad [4.22]$$

Equation 4.22 is a more convenient form of the hereditary integral, for the present application. Notice that the compliance presented in Equation 4.20 did not include the elastic component, since in that case, only the creep deformations were of interest. Now, the load is a function of time, therefore, the compliance should be considered (Flugge, op.cit.: 16) for the viscoelastic model shown in Figure 4.21, in its complete form:

$$J(t') = \frac{p_1}{q_1} e^{-\lambda t'} + \frac{1}{q_0} (1 - e^{-\lambda t'}) \quad [4.23]$$

where:

$$p_1 = \frac{\eta}{E+E_t}$$

$$q_0 = \frac{EE_t}{E+E_t}$$

$$q_1 = \frac{E\eta}{E+E_t}$$

$$\lambda = \frac{q_0}{q_1}$$

For the stress function like that represented by the Equation 4.19, considering the viscoelastic model mentioned above, the strain can be evaluated by substituting the

compliance represented by Equation 4.23 into Equation 4.22. After integration, one would obtain:

$$\varepsilon(t') = \frac{\sigma_1 p_1}{t_1 q_1} t' + \frac{\sigma_1}{t_1} \left(\frac{1}{q_0} - \frac{p_1}{q_1} \right) \left[t' - \frac{1}{\lambda} (1 - e^{-\lambda t'}) \right] \quad [4.24]$$

$$\text{for } 0 \leq t' \leq t_1$$

and

$$\varepsilon(t') = \frac{\sigma_1}{q_0} t' + \sigma_1 \left(\frac{1}{q_0} - \frac{p_1}{q_1} \right) \left[\frac{1}{\lambda t_1} (1 - e^{-\lambda t'}) \right] e^{-\lambda t'} \quad [4.25]$$

$$\text{for } t' > t_1$$

where:

$$t' = t - t_0$$

Equation 4.24 represents the strains when the stress is increasing at a constant rate, while Equation 4.25 represents the strains after the stress is kept constant. These functions are shown in Figure 4.53, for a fictitious case, and one should notice the coordinate transformation used for the time parameter. Age (t) was used as a global reference, while $t' = t - t_0$ was the local coordinate to calculate creep deformations. The above equations were applied for the interpretation of creep tests (series CRSG), and the strain evolution with time can be found in Appendix D.

By adopting a viscoelastic representation of the shotcrete at early age, linearity of the model was assumed implicitly and, as a consequence, superposition of the events is valid.

The present set of tests will give the opportunity to check the adequacy of this assumption. Also, the accuracy of a strain analysis using the average values of the viscoelastic parameters proposed earlier, will be evaluated. These values are shown in Figures 4.30 and 4.31 ($E = 15 \text{ GPa}$, $1/E_t = 0.03 \text{ 1/GPa}$, $E_t/\eta = 0.003 \text{ 1/min.}$), and are recommended for the early stages, after 10 hours of age, only. The stresses applied to the

specimens, for the tests under consideration in this section, can be decomposed into a series of functions like the one represented by Equation 4.19. Figure 4.54 shows the stress and strain functions, equivalent to the one presented in Figure 4.53, for two stress increments. It will be used to illustrate the strain calculation procedure.

Considering for instance the test CRMST2 (see Table 4.14), the first stress increment, $\sigma_1=66.43$ kPa, was applied at 4.6 hours of age (t_0) at a constant rate which lasted 4.93 minutes (t_1). Applying Equations 4.24 and 4.25, one obtains the strains like the one indicated in Figure 4.54 for the stage 1. The second stress increment was 125.6 kPa (σ_1 , second stage) which started at 6.03 hours of age (t_0 , second stage) and was applied at a constant rate for 6.25 minutes (t_1 , second stage). At the end of this period, the specimen was subjected to a total of 192.06 kPa (66.43 kPa of the first stage plus 125.6 kPa of the second one). Figure 4.54 illustrates each of the two stress increments, as well as the total stress applied on the specimen. Notice that the time dependent strains resulting from the application of the first stress increment did not cease at the starting time of the second increment. Therefore, the creep deformations of the first stage (as well as in any other stage) should be carried out up to the end of the period of analysis. Accordingly, the strains represented in Figure 4.54 (first and second stages) were evaluated up to the end of the calculation period. The total strain at any moment will be the addition of the deformation (elastic and time dependent) induced by all the previous stress increments. The result, for the case of two incremental stages, is presented in terms of the global reference of time, i.e., in terms of the shotcrete age. The tests presented in Table 4.14 followed these calculations sequence, and the results will be discussed in the following.

In order to evaluate the strains in tests CRMST1 to CRMST4, the following calculation assumptions were used (Table 4.15):

- MSTa-for each stress increment stage, the viscoelastic parameters were estimated according to the values obtained using the creep test results (Table

4.13). The values of the parameters used for this assumption are shown in Table 4.14.

-MSTb-the viscoelastic parameters were set as the average values proposed earlier ($E=15$ GPa, $1/E_t=0.03$ 1/GPa, $E_v/\eta=0.003$ 1/min.). Notice that the average values are not suitable to be applied before 10 hours of age, and for this reason, the viscoelastic parameters were kept identical to the assumption MSTa for $t_0 < 10$ hours.

-MSTc-the same deformation parameters as the assumption MSTb were used, except for considering $\eta=0$. This assumption considered that short term 'creep' deformations occurred instantaneously. This assumption will be useful to evaluate the possibility of applying a linear elastic model for the shotcrete at early age¹.

Assumptions MSTa and MSTb were calculated using the values obtained through curve fitting, σ_1 and t_1 of the Equation 4.19, as presented in Table 4.14, while assumption MSTc is calculated using the stresses actually measured by the load cell (see Table 4.15). Figure 4.52 showed that small stress fluctuations occurred up to 10 hours of age, after which time these variations became negligible.

Test CRMST1 was designed to represent approximately the stresses imposed on the tunnel lining, in the case of tunnels advancing at a fast rate. At this rate and for the typical tunnel construction, the load in the lining would be imposed within 60 hours, 80% of which would occur in the first 30 hours.

Figure 4.55 shows the results of the strain measured in this test and the ones calculated by using the assumptions above. It can be observed in this figure, that the calculated strain path contained large error for the first stress increment and then they continued almost parallel to the measured strain path. This initial error was not surprising

¹ Notice that the condition $\eta=0$ is equivalent to neglect the dashpot in the model shown in Figure 4.21. In this case, the model will have a linear elastic response, with an equivalent elastic modulus of $E_{eq}=(EE_t)/(E+E_t)$.

since at this age, larger dispersion of the shotcrete properties was expected (e.g., Figures 4.10 and 4.13). Notice that for the first stage (around 4 hours), the specific elastic strain ($1/E$) was about ten times the value at the second stage, and the specific creep ($1/E_t$) was about fifty times at the same stage. As a consequence, a variation of 30% in the viscoelastic parameters, for the first stage, will result in a variation of about 300% in the deformations of the second stage, if the same stress increment is applied. Therefore, high values of absolute error in the strain estimation during the first stage (or for load applied around 4 hours of age) should always be expected. The oscillation of the strains in assumption MSTc during the first stage is a consequence of the load variation as already shown in Figure 4.51. Figure 4.56 shows the difference between the calculated strains and the ones actually measured. If one disregards the deformations that occurred during the first stress increment, it can be observed (Figure 4.55) that the difference of strain at the beginning of the second increment and at 60 hours was of the order of 400×10^{-6} m/m. For the same interval, the strain difference was of the order of 30×10^{-6} m/m for the assumption MSTa, 25×10^{-6} m/m for the assumption MSTb and 30×10^{-6} m/m for the assumption MSTc. This represents a relative error of about 7% for the period 4 to 60 hours, if the strain analysis had started at the second stress increment. The decrease of the strain difference in Figure 4.56 after 60 hours was an indication that the creep deformations were underestimated for a longer period of time. This fact was predicted when the creep parameter values were discussed in an earlier section. The peak values of the strain difference presented by assumption MSTc between about 10 to 30 hours, represents the error of assuming an instantaneous 'creep', i.e., a linear elastic behavior. It can be seen (Figure 4.56) that this simplification introduced a small error, compared to the strain difference variation in the interval under consideration, for the particular stress increment sequence used in the present test.

The tests CRMST2, CRMST3 and CRMST4 represent approximately the stress evolution for the case of the typical tunnel construction at a slow rate of advance. In

other words, the load transfer is completed in 160 hours, with 80% of the stress applied in 80 hours. The magnitude and length of the stress increments were slightly different among these tests, but they all followed a similar trend. The strain calculation followed the same procedure described for the test CRMST1, and the viscoelastic parameters for the assumption MSTa are presented in Table 4.14. Figures 4.57, 4.59 and 4.61 present the strains measured and calculated for the tests CRMST2, CRMST3 and CRMST4, respectively. It can be observed, as expected, that the calculated strains during the first stage (around 4 hours) were subjected to a considerable absolute error. Figures 4.58, 4.60 and 4.62 show the strain difference, as was done for the tests CRMST1, CRMST2, CRMST3 and CRMST4 respectively. Disregarding the strains associated with the first stress increment and evaluating the relative error, as defined in the test CRMST1, for the tests CRMST2, CRMST3 and CRMST4 the relative errors were of the order of 18%, 8% and 8%, respectively. It can be observed that in the case of test CRMST2 (Figure 4.58), the higher value of the relative error was induced by the evaluation of strain at the second stress increment (8.03 to 12 hours). In all of the tests (CRMST1 to CRMST4), there was no considerable difference in the relative errors between the assumption MSTa and MSTb. This indicates that the average value of the viscoelastic parameters proposed at the creep test section can be applied without compromising the accuracy of the strain analysis. Assumption MSTc presented higher relative errors in tests CRMST2 to CRMST4 than in test CRMST1, but they were within acceptable limits.

Test CRSLP1 was subjected to a single stress increment, starting at 4.28 hours of age (t_0). The load was applied at a constant rate for 70.9 hours (t_1), and at the end of this period, the specimen was subjected to 2404.5 kPa (σ_1). This test followed the same general stress pattern of the tests CRMST2 to CRMST4 (see Figure 4.50), and it was also an approximation of the conditions of the typical tunnel construction under a slow rate of advance. Although the stress was applied in a single increment, the strain analysis was divided into two stages. This was an approximation to consider the variation of the

viscoelastic properties at the very early stages, as shown in Figures 4.30 and 4.31. The first stress increment, in terms of the strain analysis, started at the age of 4.28 hours and at 12.03 hours the stress reached a constant level. The viscoelastic properties for this period were taken as the ones for a shotcrete at the age at the midpoint of this interval, i.e., approximately 8 hours. Therefore this assumption will underestimate the deformation for the first half, but overestimate for the second one (see Figure 4.30).

The second stress increment, in terms of strain analysis, started at 12.03 hours and used the average values of the viscoelastic properties proposed earlier. Notice that this simplified strain analysis considered one set of the viscoelastic parameter for the interval 4 to 10 hours where the properties change drastically (see Figures 4.30 and 4.31) and, another set ('average' values) for the rest of the test. It should be clear that the superposition of the two 'artificial' stress increments would result in the total stress applied on the specimen. The parameters used for the strain evaluation of this test are shown in Table 4.14, and the results are presented in Figure 4.63. The assumption SLPa (see Table 4.15) in this case, used the viscoelastic parameters as described above. The assumption SLPb was similar to the assumption MSTc used for the tests CRMST1 to CRMST4, i.e., 'creep' deformations occurred instantaneously. Figure 4.64 presents the strain difference as it was defined for the previous tests. Disregarding the deformations of the first stage, and using the same definition used before, the relative error was around 16%. The dummy specimen in this test presented an unusual behavior which seemed to be the major source of error at the very early deformations. Figure 4.63 shows the strain development for the dummy specimens used in the tests CRSLP1 and CRSLP2. The latter represents the typical evolution of the deformations, as shown in Figure 4.43 for the dummy specimens of the creep tests: a slight trend of contraction during the first hours. On the other hand, dummy CRSLP1 presented expansion for the same period. Also, the inflection of the compensated strains around 25 hours contradict the trend expected by considering the development of viscoelastic properties (Figures 4.30 and

4.31): one should expect higher strain rates at the beginning, reducing monotonically with time. These facts are indications that the dummy specimens in this test had introduced error, at least in the first 25 hours. If one consider the strains of the loaded specimen, with compensation by the more typical behavior of dummy CRSLP2, a better agreement can be obtained for the first 30 hours. In this case, the relative error would drop to about 10%.

Test CRSLP2 was equivalent to test CRMST1, i.e., tunnel construction at fast advancing rate in this case, however, the main stress increment started later, at 12.1 hours of age. The stress increment of the first stage, a real one in this case, was very small compared to the second increment. The parameters used for the strain analysis are shown in Table 4.14. Two calculation assumptions were used in this test, and they were identical to the one used for test CRSLP1. The results are shown in Figures 4.65 and 4.66. In the first figure, the influence of the viscoelastic properties on the very early ages during the strain evolution, can be observed clearly. Although the first stress increment was only 3% of the second one (see Figure 4.50), the strain of the former was about 200% larger than the latter one. It indicates the importance of the very early age in strain development, although it could be neglected regarding stress analyses and depending on the loading sequence. Using the same concepts presented before, the relative error for the second stage was around 12% during the first 60 hours. Similar to what happened in test CRMST1, the strain difference continued to drop after 60 hours, indicating the underestimation of creep for long term analyses.

4.8 Strain Controlled Tests

In the previous section, the viscoelastic model was tested against the superposition of stresses. The validity of strain superposition assumed implicitly, that the stress independent deformations were compensated by the dummy specimens. The strain superposition will be checked in this section, by using three strain controlled tests. The

dummy specimens were not used in these tests, and stress analyses were conducted by compensating the stress independent deformations, based on the investigation presented in this chapter. Two out of the strain controlled tests (CRSCO1 and CRSCO2) followed the pattern presented by the vibrating wire (VW) strain gage 41, installed close to the tunnel crown. The other test (CRSCO3), followed the pattern presented by two instruments, VW18 and VW36, located at the springline and at the floor, respectively. Details of these instruments and complete set of readings can be found in Chapter 2 and Appendix D.

Figure 4.67 shows that for these VW gages, the strains occurred after 4 hours of age. This change of reference, i.e., set zero reference at 4 hours of age, was chosen to be compatible to the minimum time necessary to assemble the tests. The readings of the VW gages were corrected by the temperature correction factor of the instrument (presented in Chapter 2), i.e., the thermal expansion of the shotcrete was not compensated. A reading at 4.58 hours for gage VW41 was set as the reference. Two readings were taken from gages VW18 and VW36: the initial reading and at 7.9 hours, therefore, strain at 4 hours of age was estimated by interpolation. The strain pattern of these instruments can be described by the following equation:

$$\varepsilon(t') = a (1 - e^{-bt'}) \quad [4.26]$$

where:

$$t' = t - t_0$$

$$t = \text{age}$$

$$t_0 = \text{reference age}$$

$$a, b = \text{constants}$$

Curve fitting was performed using the Simplex algorithm already described. These results can be seen in Figure 4.67 and the coefficient values can be found in Table 4.16. Notice that despite the fact that the above equation is similar to Equation 4.15, the

physical meaning is completely different. The former considers the 'total' strain of the shotcrete, while the latter was derived by isolating just the creep deformations, i.e., only the time dependent component was considered.

The specimens used in the strain controlled tests had the same dimensions, mix composition, preparation procedures and paraffin seal as those in the creep tests. The strain measurement device, the steel frame and hydraulic jack were also the same as those for the creep tests and, they can be seen in detail at Plate 4.4. The assemblage of the strain controlled tests had two differences as related to the creep and stress controlled tests: the system which controlled the hydraulic pressure and the double flat jacks placed at the bottom of the specimen. The hydraulic pressure was operated under a system originally developed by this author, in order to perform stress path tests in soil. The hydraulic controller system used in the previous tests was not flexible enough to be applied to the present tests, because it could provide either constant rate of pressure increment or constant rate of oil volume injection. In order to follow the strain path like the one represented by Equation 4.26 (see Figures 4.67 and 4.68), a system would require more complex capabilities. One should notice that even if a constant rate of strain was intended, the former system would not be able to complete the required function. A constant rate of oil injection, cannot ensure constant rate of strain in the specimen due to the non linear deformation characteristic of the tubing-jack-frame system. This feature was also aggravated by plastic shrinkage, autogeneous volume change and thermal expansion exhibited by the specimen at very early ages. Therefore, a suitable hydraulic system would require a continuous feed back of the deformations undergone by the specimen, in order to constantly adjust the pressure to follow the required strain path. The system shown in Plate 4.3 was capable of performing this function.

This system was composed of an IBM PC compatible microcomputer, connected to another microcomputer developed and constructed at the Department of Civil Engineering, University of Alberta. The first one (right side at Plate 4.3) was used to take

the readings of all the instruments used in the test, perform calculations, make decisions and send instructions to the second one. This second microcomputer was able to set and maintain constant, pressure level in any of the three independent hydraulic systems. Each system was composed of an electrical oil pump, a pressure gage and an output line. The pressure was monitored at the exit of the pump by the second microcomputer, which could take decisions by itself and propel an electrical motor to maintain constant pressure. This microcomputer, which had three control panels and three digital displays, can be seen on the left side of Plate 4.3 with the three electrical pumps behind it. Each hydraulic line was limited to a pressure of 2 MPa and a volume of 200 cm³. Due to these restrictions, it was necessary to use the setup shown in Plate 4.4, i.e., the cylindrical jack at the top of the specimen and double flat jack at the bottom. Due to the area ratio between the cylindrical jack and the specimen cross section, the system could only apply stresses around 300 kPa on the specimen. The flat jacks at the bottom were assembled in the same way as the calibration tests in Chapter 3, i.e., two flat jacks placed symmetrically, with the curved boundary facing each other. This set up was satisfactory in terms of area ratio, or potentially could apply high levels of stress, but had very limited displacement allowance. At the early stages of the test, considerable displacement of the jacks was necessary to compensate the assemblage accommodation and the frame deformations. To solve these problems, the cylindrical jack was operated by one line at the beginning of the test until the pressure or volume limit was reached. At this moment, this line was shut down and the two remaining pumps started to operate the flat jacks. All these actions and the monitoring of the pumps limits was done by the PC microcomputer, which sent commands to activate and change lines to the second microcomputer.

In order to ensure the alignment of the load application system, each test was preceded by a specimen positioning routine. The pressures in the two flat jacks were always balanced, since they were connected to the two pumps by sharing a single hydraulic line. A pressure of 5 kPa was applied to the flat jacks, at the beginning of each

alignment test. This value represented the minimum pressurization necessary for the flat jacks to avoid inflation delays during the actual test. The alignment test had used a well cured concrete specimen, which had two VW strain gages installed on its surface, at the middle height and diametrically opposite. They were installed according to the technique described in Chapter 3 and illustrated in Figure 3.14. The flat jacks were assembled (See Plate 4.4) between two 1 cm thick wooden plates, and a 5 cm thick steel plate was placed over them. The specimen was placed on a 3.5 cm thick steel disk, with a 0.5 cm thick wooden disk between them. This wooden disk was also used in the creep and stress controlled tests, and it was necessary to provide a thermal insulation to the specimens edges. At the top of the specimens, the same type of disks was used, and a load cell was placed between the steel plate and the cylindrical jack. The load applied by the cylindrical jack was transmitted to the top of the load cell, through an articulated bearing system, as recommended by the ASTM C39-86. The alignment tests were carried out by assembling the specimen as described and applying a small load to ensure full contact between parts. At this point, the two pumps that were connected to the flat jacks were shut down and initial readings of the two VW strain gages were taken. The concrete specimen were assembled in such a way that each of these strain gages was placed direct over each flat jack. Increments of 50 kPa axial stress were applied by the upper jack, recording the VW gage readings for each step of load, until 250 kPa was reached. At this point the upper jack was shut down and the flat jacks were pressurized. Increments of 50 kPa were again applied until the stress on the specimen reached 500 kPa. The readings of the VW strain gages were then verified, and in the case of any difference between them being higher than 4×10^{-6} m/m, the test assemblage was realigned and the procedure repeated. The allowance of 4×10^{-6} m/m represented the 1×10^{-6} m/m reading precision of each instrument plus a 2×10^{-6} m/m of error, accepted as deviation of alignment. When this condition was achieved, marks were put on the disks and plates, in order to permit the reproduction of the assemblage. The distances between the specimen surface and the

steel rods of the loading frame (see Plate 4.4) were also recorded and they were also used to help correct the specimen position. This procedure proved to be very efficient and the results of the realignment tests after replacing the specimen were always within the assumed deviation. This routine was followed before each strain controlled test and also, whenever the flat jacks were moved from their aligned position.

The IBM PC compatible microcomputer was the main controller of the tests in this section, while the second was used only for setting the pressure in specific hydraulic lines. Using the PC microcomputer, the synchronization of the decisions was possible by accessing the internal clock of the machine. When the test started, the microcomputer took the initial readings of each instrument (temperature of the air and the specimen, strain and load of the specimen, pressure in each of the three hydraulic lines) and initialized the time. The temperature in the specimen was measured using RTD gages, installed using the same procedures of the tests TEMP1, TEMP2 and TEMP3. Using the time register, it was possible at any time to compare the reading of the strain in the specimen to the one given by Equation 4.26. If these values were different, the microcomputer calculated the relative differences and used this value as a correction factor to adjust the present hydraulic pressure. At the beginning of the test, the absolute values of the strain are low and the relative error may become very high, and can potentially produce an unstable condition. For instance, consider at moment 'i', a relative error of the strain (or correction factor of the hydraulic pressure) with a high positive number. The microcomputer would react by increasing the present hydraulic pressure by this high factor. As a result, the stress in the specimen would become too high and the strain would be much higher than that given by Equation 4.26. Therefore, at moment 'i+1', the relative error of the strain would assume a high negative value. The system would then react by decreasing the pressure by a high value, and at the moment 'i+2', the factor might have a high positive value again, and so on. This oscillation could converge, diverge or become stable, depending on the system characteristics. In order to avoid this

kind of behavior, the hydraulic pressure should converge monotonically to the achieve correct value. To ensure this condition, also known as super critic dumping system, concerning dynamic relaxation problems (e.g., Kuwajima et.al., 1987), the correction factor of the hydraulic pressure was kept within the range of -0.95 to +0.95. In other words, if the correction factor value happened to be below -0.95 or above +0.95, it was set to -0.95 or +0.95, respectively.

The readings of the PC microcomputer were taken using a special card known as DASH8-PGA. This hardware was capable of reading 8 channels, conditioning the signal by setting suitable gain values through software and converting the analog signal into a digital one. However, this card did not comprise analog filters, as expected in a conventional data logging system. For this reason, it was necessary to filter the signal of each instrument by using a digital technique (e.g., Aguiar et. al., 1985). In the present investigation, a combined 'band'-statistical digital¹ filter was used.

The analog signal provided by any gage, usually measured in Volts, has a continuous spectrum. In other words, it can assume an infinite number of values, even between two points very close to each other. To simulate this condition perfectly, the equipment that takes the signal and converts it to the computer would require an infinite amount of memory. Since this is not feasible, the conversion is made by assuming discrete values in bits, or digitally. In the case of the present equipment, the analog-digital (AD) conversion was done in so called '12 bit' bases. It means that any analog value was converted in a scale of integer numbers limited by 2^{12} . In other words, if the gain was set for an analogue range of -5 V to +5 V, it would correspond to a digital range of -2047 to +2047. As a result, the resolution of this conversion would be $5/(2^{12})\text{V}$ or 1.22 mV. The electronic noise in the readings may be generated at the AD conversion

¹ Notice that this was just an informal designation for the calculation procedure to treat the readings of instruments during the strain controlled tests. Formally, a 'band' filter implies a cutting of frequency out of a predefined range. In the present case, 'band' should be understood as an error allowance assumed for the analog-digital conversion.

and/or come from the analog signal itself. In order to minimize the error coming from the AD conversion, a 3 unit resolution was assumed. It means, for instance that, if a digital reading of 100 was taken, the actual reading could be any of a 'band' of values between 97 to 103. All instruments used in the tests had shown a random type of noise in the analog signal. In order to treat this problem, each instrument was read 1000 times and stored in the microcomputer memory. Considering the 3 unit bands, for each of the 1000 readings, a statistical distribution spectrum was calculated. The highest frequency of the digital reading was taken as the representative value for the interval in which the 1000 readings were taken. The time used to read all the instruments, perform calculations for each, evaluate the strains, take the decision and send the instruction was about 12 seconds. Therefore, the strain comparisons and pressure corrections were done with a resolution of 12 seconds. Comparative measurements of the same instruments, at the same time, showed that the results of readings, using this filter by the microcomputer, had an accuracy compatible with the ones taken by a conventional data logging system.

The accuracy of the strain readings was of the order of 0.5×10^{-6} m/m and for this reason, when the difference between the measured value and the calculated one (Equation 4.26) was below 0.5×10^{-6} m/m, no action was taken by the hydraulic system. This procedure avoided the stress fluctuation in the specimen, that could be induced by the inaccuracy of the strain readings. Figures 4.68 to 4.71 show the results of the tests CRSCO1, CRSCO2 and CRSCO3, in terms of strain, stress and also the temperatures of the specimen and air. In Figure 4.68, one can see that the control system followed successfully the patterns given by Equation 4.26. Although the difference between the strain calculated using Equation 4.26 and the measured one was below 0.5×10^{-6} m/m in most of the time, this accuracy was lost due to the air temperature fluctuations (see Figure 4.71). Later, it will be seen shown that these small fluctuations, with amplitude around 0.15°C , were able to introduce errors of reading around 4.6×10^{-6} m/m. The

thermal expansion of the compressometer frame was responsible for this observation, and its effect produced considerable deviations in the results of the test CRSCO3.

In the previous section, the stress history was known and the strain could be calculated by applying the hereditary integral (Equation 4.22). In the present case, the strain history is known and the stress has to be calculated. It can be proved (Flugge, 1967: 27) that for the condition:

$$\sigma(t') = \epsilon(t') Y(0) + \int_0^{t'} \epsilon(t'') \frac{dY(t'-t'')}{d(t'-t'')} dt'' \quad [4.27]$$

where:

$$t' = t - t_0$$

$$t = \text{age}$$

$$t_0 = \text{reference age}$$

$$Y(t') = \text{relaxation modulus,}$$

the function $Y(t')$ is a function of the constitutive relation assumed for the material, similar to the compliance $J(t')$. In the case of the viscoelastic model assumed in this chapter, the relaxation modulus can be represented by (Flugge, op. cit.: 17):

$$Y(t') = \frac{q_1}{p_1} e^{-t'/p_1} + q_0 (1 - e^{-t'/p_1}) \quad [4.28]$$

where:

$$p_1, q_0, q_1 \text{ are the same as in Equation 4.23}$$

The deformation values shown in Figure 4.68 were not compensated by dummy specimens, as was done in the creep and stress controlled tests. They included stress independent deformations, and therefore should be compensated in order to obtain a proper stress analysis. During the investigation of the stress independent deformations presented earlier, it was not possible to isolate the thermal expansion coefficient for the first 10 hours of age. For this reason, the analysis done during this period was

compensated by a 'total' stress independent deformation taken as average values (see Figure 4.43) from the dummy specimens of the creep tests. After 10 hours, the thermal expansion coefficient could be estimated, and the stress analysis made use of it accordingly.

Figure 4.72 shows the strains measured in test CRSCO1, up to 10 hours of age, and also the compensation of the stress independent deformations estimated from Figure 4.43. Since the latter considered 7 hours of age as an arbitrary reference point, the compensation should be done in relative terms and the reference, in this case, taken at the beginning of the test. For the first 10 hours of age, an approximate compensating assumption was used, while a more correct one, in terms of the viscoelastic model, will be presented for the remaining period. The simplified compensation considered a straight subtraction of the measured strains from the stress independent deformation (obtained by the Figure 4.43), as the strains caused by the load applied on the specimen. The strains calculated according to these considerations were presented as 'compensated (4-10 hours)' in Figure 4.72. Notice that in this figure, the stress independent deformations are presented with negative sign and had the references reset at the beginning of the test. This compensated strain development can be approximately described by Equation 4.26. The result of curve fitting is presented in Figure 4.72 and the coefficients are shown in Table 4.17. Substituting Equation 4.26 into Equation 4.27, and performing the integral, follows:

$$\sigma(t') = a \frac{q_1}{p_1} (1 - e^{-bt'}) + \frac{a (p_1 q_0 - q_1)}{p_1 (bp_1 - 1)} \left[e^{-bt'} - (bp_1 e^{-t'/p_1} + 1 - bp_1) \right] \quad [4.29]$$

The expression above represents the stress evolution for the viscoelastic material submitted to a strain history described by Equation 4.26. The first of four assumptions (see Table 4.18) used to perform stress analysis for the period 4 to 10 hours, assumed the viscoelastic parameter obtained in the creep tests at 8 hours of age (see Table 4.13) as an

average value of the present interval. The second assumption considered the same parameters, except in $\eta=0$, i.e., creep deformations occurred instantaneously. Same type of assumption used in the strain analysis of the stress controlled tests. The condition $\eta=0$ is equivalent to neglect the dashpot from the model shown in Figure 4.21. In this case, the model will have a linear elastic response, with an equivalent elastic modulus $E_{eq}=(EE_t)/(E+E_t)$. The first assumption (CO1Ia) was calculated according to the Equation 4.29, using the regression of the compensated strains. The second (CO1Ib) was a linear elastic case, and used directly the compensated strains (regression was not used). The results of the stresses which were calculated using these assumptions are presented in Figure 4.73 and the difference between these values and the measured ones are shown in Figure 4.74. It is clear that the overestimation of the stresses was generated around the first two hours of the analysis. This was the consequence of assuming the average deformation moduli for the period, as those estimated for 8 hours of age. In Figure 4.30 the sharp variation of the deformation parameters at the very early ages, has already been shown. Considering that around 4 and 5 hours of age, these deformation moduli are about one order of magnitude smaller than during the rest of the period, and also that the strains followed a continuous, monotonic and smooth function, it is reasonable to assume that the strains occurring around 4 and 5 hours of age had produced a negligible amount of stress. These small values of stress can be observed in the Figure 4.73. Disregarding the deformation occurring before approximately 6 hours of age, one obtains the strains indicated in Figure 4.72 as 'compensated (6-10 hours)'. It can also be approached by Equation 4.26. The result of a regression is shown in Figure 4.72 and, the coefficients are presented in Table 4.17. Reevaluating the stress under assumption CO1Ic and CO1Id (see Table 4.18), similar to assumption CO1Ia and CO1Ib, respectively, adapted to neglect the strains at the first two hours, the results can be seen in Figures 4.73 and 4.74. It can be observed that the error for these cases, was limited to about 20% of the load at 10 hours. Notice that the above discussion for the period before 10 hours of age would not be

necessary if a more complete model was used, i.e., a model that could describe the time dependency of the deformation parameters. It was necessary to neglect the strain that occurred before 6 hours due to the simple model assumed to perform the stress analysis. However, as will be seen in Chapter 6, the stresses generated before 10 hours of age are usually insignificant for the typical tunnel construction considered in this thesis. For this reason, a simplified calculation procedure in terms of average properties has been presented, and was intended only to provide the order of magnitude of the stresses.

Figure 4.75 shows the strains that occurred after 10 hours in the test CRSCO1. The temperature compensation shown in this figure was calculated by taking the temperature variation (Figure 4.70) and applying the thermal expansion coefficient ($\alpha_T = 8.25 \times 10^{-6} \text{ (m/m)/}^\circ\text{C}$) determined earlier. The thermally compensated strains were the differences between the measured and the thermal strains. These compensated deformations can be described by the expression:

$$\epsilon(t') = c t' \quad [4.30]$$

where:

$c = \text{constant}$

$t' = t - t_0$

$t = \text{age}$

$t_0 = \text{reference age}$

Linear regression (Equation 4.30) was applied to the experimental data. The results are presented in Figure 4.75 and the coefficients in Table 4.17. Substituting Equation 4.30 into 4.27, one obtains the stress evolution resulting from the application of a constant rate of strain:

$$\sigma(t') = c \frac{q_1}{p_1} t' + c \left(\frac{q_0}{p_1} - \frac{q_1}{p_1^2} \right) \left(p_1^2 e^{-t'/p_1} - p_1 (p_1 - t') \right) \quad [4.31]$$

where the coefficients are the same ones presented above.

Applying the expression above and considering the average viscoelastic parameter proposed for shotcrete older than 10 hours (see Table 4.18), one would obtain the stresses as shown in Figure 4.76 (assumption CO1Fa). This calculation procedure used the same assumption applied for the period before 10 hours, i.e., the stress independent deformations were compensated for by a straight subtraction. Notice that in the case of the period 4 to 10 hours, shrinkage, plastic shrinkage and/or autogenous volume changes and thermal compensation were all included implicitly, since estimations based on Figure 4.43 had included all these components. For the period after 10 hours of age, only thermal compensation was applied because the plastic shrinkage and/or autogenous volume changes were unlikely to have occurred for the period under analysis (see Figure 4.38) and conventional shrinkage was avoided by the paraffin seal. The calculation procedure made by this straight subtraction of the strain components is, however, theoretically incorrect in terms of the viscoelastic model. A correct routine should take a function that can describe the 'total' measured strain evolution and substitute it in Equation 4.27 to obtain the 'total' stress development. The compensation of the stress independent deformations should also be applied in the Equation 4.27, to obtain the 'compensating' stress, because in the viscoelastic model, there is always a delay between stress and strain developments. Therefore, the 'net' stresses should be the values of the 'total' minus the 'compensating' stresses. This procedure was applied for the test CRSCO1, for the period after 10 hours of age. The 'total' measured strain and thermal ones can both be described by Equation 4.26. The regression results are shown in Figure 4.75 and the coefficients in Table 4.17. Notice that the thermal strain had already been presented with a negative sign. Figure 4.76 shows the stresses related to the 'total' measured strain, the 'thermal' compensation term and the 'net' values for this theoretically correct solution (CO1Fb). The viscoelastic parameters were the average values proposed for shotcrete older than 10 hours and they are presented in Table 4.18. One more stress evaluation was performed by using the same deformation modulus of the previous

assumption and the instantaneous 'creep' ($\eta=0$, see Table 4.18). This linear elastic assumption (CO1Fc) was applied to the experimental thermally compensated strains (no regression of strain was used) and the results are shown in Figure 4.76. The differences between the calculated stress and the measured ones is shown in Figure 4.77. Notice that in these analyses, the whole test period was divided in two intervals: before and after 10 hours. To obtain the 'total' stresses for the second period, the values of both intervals should be added. This procedure, again, is not theoretically correct because it neglects the time dependent deformations. However, the viscosity of the first period is about one order of magnitude smaller than that of the second one, and the error introduced by this simplification can be considered negligible.

Test CRSCO2 followed the strain path of VW41 (Table 4.15), which was identical to the one used in test CRSCO1. The stress analysis in the period, before 10 hours of age, was performed using the same assumptions of the previous test, and the results are presented in the Figures 4.78 to 4.80. It can be observed that these results are very similar to those shown for the test CRSCO1 (Figures 4.72 to 4.74). The parameters and assumptions (CO2Ia, CO2Ib, CO2Ic and CO2Id) used for the stress analysis in test CRSCO2 are shown in Tables 4.19 and 4.20, respectively. Test CRSCO1 was stopped while strain was still increasing, while test CRSCO2 was carried out until the strains were close to stabilizing (see Figure 4.68). For this reason, the equation used to describe the compensated strains that occurred after 10 hours of age in test CRSCO1 was not appropriate for test CRSCO2. In Figure 4.81, it can be observed that Equation 4.30, which was used to describe the thermally compensated strains in test CRSCO1, was capable of following the strains of test CRSCO2 up to around 20 hours. In order to describe the compensated strain development until the end of the test (around 130 hours), the following expression would be necessary:

$$\epsilon(t') = f (1 - e^{-gt'}) (1 - e^{-ht'}) \quad [4.32]$$

where:

f, g, h are constants

$t' = t - t_0$

Curve fitting for the expression above was performed using the Simplex algorithm. The results can be seen in Figure 4.81 and the coefficients are presented in Table 4.19. Substituting Equation 4.32 into the Equation 4.27 and evaluating the integral, one should get:

$$\begin{aligned} \sigma(t') = & f \frac{q_1}{p_1} (1 - e^{-gt'}) (1 - e^{-ht'}) + \\ & + f \left[\frac{q_0}{p_1} - \frac{q_1}{p_1^2} \right] \left[- \frac{p_1 e^{-(g+h)t'}}{p_1(g+h) - 1} + \frac{p_1 e^{-gt'}}{gp_1 - 1} + \frac{p_1 e^{-ht'}}{hp_1 - 1} - \frac{ghp_1^3 (gp_1 + hp_1 - 2) e^{-t'/p_1}}{(gp_1 - 1)(gp_1 + hp_1 - 1)(hp_1 - 1)} + p_1 \right] \end{aligned} \quad [4.33]$$

The expression above represents the stress evolution for the viscoelastic model submitted to a thermally compensated strain as shown in Figure 4.81 and, described by Equation 4.32. Applying the average viscoelastic parameters for shotcrete older than 10 hours (Table 4.20, assumption CO2Fa) in Equation 4.33, one would obtain the stresses presented in Figure 4.82. As mentioned earlier, this procedure is not correct, but an acceptable simplification. The theoretically correct solution should apply Equation 4.27 to the 'total' measured strains and perform the thermal compensation by applying the same equation to the thermal strains. The measured deformations can be described by Equation 4.26. Figure 4.81 shows the results of curve fitting, while Table 4.19 presents the coefficients. On the other hand, the thermal strains in this case can be described by the following expression:

$$\epsilon(t') = k (1 - e^{-mt'}) (1 + e^{-nt'}) \quad [4.34]$$

where:

k, m, n are constants

Curve fitting using the expression above is presented in Figure 4.81 and the coefficients are shown in Table 4.19. Substituting the equation above into Equation 4.27 and performing the integral, one could obtain:

$$\begin{aligned} \sigma(t') = & k \frac{q_1}{p_1} (1 - e^{-mt'}) (1 + e^{-nt'}) + \\ & + k \left[\frac{q_0}{p_1} - \frac{q_1}{p_1^2} \right] \left[\frac{p_1 e^{-(m+n)t'}}{p_1(m+n) - 1} + \frac{p_1 e^{-mt'}}{mp_1 - 1} - \frac{p_1 e^{-nt'}}{np_1 - 1} - \frac{mp_1^2 (mp_1 (np_1 - 2) + n^2 p_1^2 - 2np_1 + 2) e^{-t'/p_1}}{(mp_1 - 1)(mp_1 + np_1 - 1)(np_1 - 1)} + p_1 \right] \end{aligned} \quad [4.35]$$

Adopting the viscoelastic parameters shown in Table 4.20 for Equations 4.33 and 4.35, the 'total', thermal and 'net' stresses would be as shown in Figure 4.82 (assumption CO2Fb). Also shown in this figure are the results using the same assumption as in test CRSCO1, for $\eta=0$ (Table 4.20, assumption CO2Fc) or considering an instantaneous 'creep'. The differences between the calculated and measured stresses are shown in Figure 4.83. Again, the stresses calculated in the period after 10 hours, should be added to the results obtained at the previous interval.

Test CRSCO3 followed the strain path of the vibrating wire strain gages VW18 and VW36. The coefficients of Equation 4.26, for these instruments, are presented in Table 4.15. The present test started at 4.65 hours of age, therefore, the parameter t_0 was reset at 4.65 hours. Test CRSCO3 was subjected to considerable smaller strains than in tests CRSCO1 and CRSCO2, as can be seen in Figure 4.68. This condition led to different behavior in the present tests, compared to the previous ones, in the early stages of the test. In order to discuss the reactions of test CRSCO3, it was divided into three periods: 4.65 to 10 hours of age, 10 to 18 hours and 18 hours to the end of the test. The first period used the same type of compensation as for tests CRSCO1 and CRSCO2, i.e., a 'total' stress independent deformation according to Figure 4.43 was used to correct the strains. Figure 4.84 shows these strains and also the measured ones. It can be observed

that during the first hour of the test, the measured strains were larger than those expected (Equation 4.26). The specimen had contracted without any load, as is shown by the stress independent deformations. During this period, the load was close to zero, as shown in Figure 4.85. Notice that the negative values correspond to the relaxation of the small load, around 5 kPa, applied at the beginning of the test to ensure full contact during the alignment routine of the specimen. The compensated strains can be described by the Equation 4.26. The curve fitting is shown in Figure 4.84 and the coefficients, in Table 4.21. Since, almost all compensated strains had occurred between 6 to 7 hours of age, the viscoelastic parameters were estimated for 6 hours of age. Table 4.13 shows the values for approximately 4 and 8 hours, and the parameters for 6 hours were taken as the average of these values. Applying these values in Equation 4.29, one should obtain the stresses shown in Figure 4.85 (see Table 4.22, assumption CO3Ia). The disagreement between these values and the observed ones was considerably high in relative terms. One can observe that the hydraulic system had reacted properly at the interval between 5.5 and 7.5 hours of age. During this period, the compensated strains were above those predicted by Equation 4.26, as can be seen in Figure 4.84. Therefore, some load was necessary to keep the strains in the correct path. Instability had occurred in the control system, between 7.5 and 8 hours and generated the oscillating path observed in Figure 4.85 between 8 to 10 hours. This instability in the hydraulic system led to incorrect strains shown in Figure 4.84. This period was the only one in which this kind of instability was observed among all three strain controlled tests. But, the system had stabilized on its own, around 11 hours of age.

Figure 4.86 shows the strain path that the test was supposed to follow for the period between 10 and 18 hours, according to Equation 4.26, and the strains actually measured. Observe that the latter were larger than those expected by Equation 4.26, in most of this period. The control system could not react in order to correct the strains, because as shown in Figure 4.87, the stresses in the specimen were close to zero and the

loading system could not apply tension in this period. The first point of measured strain presented in Figure 4.86 was considered as a reference value and the temperature induced deformations were calculated using the thermal expansion coefficient presented before ($\alpha_T = 8.25 \times 10^{-6} \text{ (m/m)/}^\circ\text{C}$). The result shows that the compressive strains were caused by the specimen cooling, as observed in Figure 4.70. Notice that the stress oscillation, shown in the first hour in Figure 4.87, was still a consequence of the instability of the control system. Therefore, for the second period of analysis, approximately between 10 to 18 hours, the load applied on the specimen was negligible, since the deformations in the period were caused by temperature changes.

Figure 4.88 shows the strains measured after 18 hours and the thermal strains for the same period. The thermally compensated strain can be described by Equation 4.26. The results of curve fitting are shown in Figure 4.88 and the coefficients in Table 4.21. Applying the average viscoelastic parameters (Table 4.22, assumption CO3Fa) in Equation 4.29, one should obtain the stress shown in Figure 4.89. Also presented in this figure, are the stresses calculated using the same deformation parameters, but considering $\eta=0$ (i.e., linear elastic model), and the experimental thermally compensated strains (assumption CO3Fb). One can observe that there is a considerable disagreement between the calculated and the measured stresses because the thermal strain in Figure 4.88 presented much higher relative oscillation than observed in tests CRSCO1 and CRSCO2. Temperature fluctuation could be responsible for this stress. In order to check this hypothesis, the thermal strains were investigated in more detail. These thermal strains are shown, in detail, in Figure 4.90. They can be better described by adding an exponential function like Equation 4.26 to a sinusoidal one as:

$$\epsilon(t') = q \sin[\omega(t'+r)] \quad [4.36]$$

where:

q, r, ω are constants

Applying the expression above in Equation 4.27 and performing the integral, one should obtain:

$$\sigma(t') = \frac{qp_1}{p_1^2\omega^2 + 1} \left\{ [p_1 \omega \cos(r\omega) - \sin(r\omega)] e^{-t'/p_1} - p_1 \omega \cos(r\omega + t'\omega) + \sin(r\omega + t'\omega) \right\} \quad [4.37]$$

The results of a regression, using simultaneously Equations 4.26 and 4.36 to fit the experimental data, are presented in Figure 4.90 and the coefficients are shown in Table 4.22. The 'total' measured strain can also be adjusted by Equation 4.26. The regression results and coefficients are presented in Figure 4.88 and Table 4.21, respectively. Using the average viscoelastic parameters (Table 4.22, assumption CO3Fc), the stress related to the 'total' measured strain can be evaluated by the Equation 4.29. This stress should be compensated for by the exponential component of the thermal strain (Equation 4.29) and the sinusoidal component (Equation 4.37). The results of these calculations are shown in Figure 4.89, and no considerable differences can be noticed between these values and those calculated before. It indicates that the specimen temperature variations could not lead to the observed deviations. Further investigations indicated that the variation of the air temperature in the laboratory (see Figure 4.71) was responsible for the unexpected results. These temperature variations had induced thermal expansion and contraction in the steel bars of the compressometer's frame. Adopting a coefficient of thermal expansion for steel of $\alpha=13.6 \times 10^{-6} (\text{m/m})/^{\circ}\text{C}$ (Hudson, 1974: 342) and considering the multiplying factor as 2.25 (geometrical characteristic of the compressometer), the strain corrections to the compressometer readings are shown in Figure 4.90. Considering that the specimen had the deformation modulus given by the average viscoelastic parameters (Table 4.22, same as assumption CO3Fb), with $\eta=0$ or linear elastic behavior, the stress compensation necessary due to strain correction of the compressometer is shown in Figure 4.91. Also shown in this figure are the stresses

calculated using the same deformation modulus on the thermally compensated strains (CO3Fb), and the values corrected by the compressometer compensation. Observing the results presented in Figure 4.91, it became clear that the air temperature fluctuations were the source of the stress oscillation. The same kind of comparison was performed for tests CRSCO1 and CRSCO2, and the results are shown in Figures 4.92 and 4.93, respectively. The air temperature fluctuations, in these cases, did not change the overall trend, especially in test CRSCO2 whose stress levels were considerably high. Notice that the stress correction induced by the compressometer was of the same order of magnitude as the stress differences between calculated and measured values for these tests (see Figures 4.77 and 4.83).

4.9 Summary and Conclusions

The tests performed in this chapter were necessary due to the lack of available information on shotcrete behavior at the early ages. This period (early age or short term) was defined pragmatically to attend to the necessity of analyzing a typical tunnel of 6 m of diameter, advancing 1.8 m per shift. Considering a typical construction of 1 shift/day to 3 shifts/day, the 'short term' would end at the range 2.2 days (53 hours) to 6.7 days (160 hours). All the analyses were carried out having these limits in mind. No phenomenological model was applied and the test interpretations were based almost exclusively on application of curve fitting techniques.

Specimens of shotcrete applied with the conventional equipment were impossible to obtain, therefore, the tests were performed on specimens of simulated shotcrete prepared in laboratory. Figures 4.2 and 4.10 showed that unit weight and strength, from laboratory specimens were in good agreement with those from tests performed either in cores taken in situ or taken from panels prepared at the site. All the laboratory tests were carried out using the same composition as the shotcrete used at the site (Table 4.3).

Strength tests were performed in specimens with the water-cement ratio (w/c) equal to 0.5 and 0.6. Also, using the results of in situ and panels cores, it was possible to estimate the strength development for a range of w/c between 0.4 and 0.6 (Figure 4.9). This can be done by applying Equation 4.4 once the strength of shotcrete at 28 days is known. Parameters A_2 , B_1 and B_2 can be taken as the average values, as shown in Table 4.5 (independent of w/c ratio) and A_1 can be estimated using Figure 4.9 according to w/c . This expression was compared to published data, which was well in agreement with Figure 4.10.

Elastic parameters (conventional) were evaluated using recommendations of the standard ASTM C469-87a. Due to the non-linearity at the early ages, the Equation 4.6 (Saenz, 1964) was used to describe the stress-strain relationship. The secant modulus is the most common parameter used in practice, therefore, the summary of results was presented in terms of this conventional Young's modulus. Ultrasonic measurements were carried out to cover the very early ages (0 to 4 hours) because, in this period, it was not possible to perform the conventional test. However, the accuracy of these measurements was compromised by the association of specimen size and frequency of resonance of the geophones (Table 4.8), as shown by the restrictions of ASTM 2845.

It is usually difficult to obtain the Young's modulus in practice. The use of strength-Young's modulus relationship has been suggested to solve this problem (Table 4.9), but the results in Figure 4.18 have shown considerable deviation, especially for the case of low strength values. The same expression reported by Byfors (1980) for plain concrete at early ages was proposed for shotcrete, in the same period. Equation 4.12 relates the conventional Young's modulus to the strength for the standard cylindrical specimen. Applying this relation, it is possible to obtain Young's modulus from strength tests performed in cores of shotcrete, for any specific time. It is suggested that suitable corrections (e.g., ASTM C42-82, McIntyre, 1987) be applied to the strength values of test in cores, to convert the values of standard tests, before applying Equation 4.12.

Notice also that it is possible to obtain the Young's modulus development with time if only the strength at 28 days is known: apply Equations 4.4 and 4.12, simultaneously. A higher degree of deviation should be expected in this case because each expression would introduce some inaccuracy.

Results shown in Figure 4.18 have suggested that the relationship between the conventional Young's modulus and the strength of the shotcrete is similar to that reported for plain concrete, at early ages. The parameters of this relationship (Equation 4.12) are shown in Table 4.11. The parameters reported by Byfors (1980) have presented similar values to those recommended by ABNT NBR 6118-1980 (Negro, 1989) for values of strength above 2 MPa, and the former relationship was suggested as upper bound to evaluate Young's modulus of shotcrete at early ages. The parameter presented in Table 4.11, for the present investigation, was taken as an average relation, for both shotcrete and plain concrete at early ages. The values obtained using these parameters have shown results close to the relation suggested by ACI-1971 (Brierley, 1975; Parker, 1976).

Short term creep tests were performed using conventional techniques and the interpretation used a three element viscoelastic model, as shown in Figure 4.21. Based on parametric analyses of curve fittings (Figures 4.30 and 4.31) and on partial data of stress-strain behavior expected in tunnel linings (Figure 4.32), average values were suggested for the parameters of the viscoelastic model:

$$E=15 \text{ GPa}$$

$$1/E_t=0.03 \text{ 1/GPa}$$

$$E_t/\eta=0.003 \text{ 1/min.}$$

These values were only suggested for shotcrete older than 10 hours, and for the earlier period, the value of these parameters should be taken according to Figures 4.30 and 4.31 or Table 4.13. It was shown that the short term creep represented approximately one third of the stress dependent deformations. The deformations at the very early stages (between 4 to 10 hours in these figures) may be very large, depending on the loading

function. The deformation parameters during this period were about one order of magnitude larger than those for the period after 10 hours. As an example, in test CRSLP2 a stress increment of 3% of the total load was applied between 4 to 12 hours of age, and it induced strains 200% larger than the deformations due to the subsequent loading (95% of the loading).

The evaluation of the stress independent deformations was done in terms of coefficient of thermal expansion and conventional shrinkage. The plastic shrinkage (Figure 4.38) and autogeneous volume change could not be isolated in the present investigation. They probably ceased before 10 hours of age, and occurred simultaneously with thermal expansion, which could also be age dependent during this period (Figure 4.37). Indication of the 'total' stress independent deformations for the period between 7 and 10 hours can be taken from Figure 4.43. The 'total' stress independent deformations between 4 to 7 hours can be evaluated approximately using the results presented in Figure 4.44.

A linear relation between strain and temperature variation was observed after 10 hours of age, and it was suggested that a coefficient of thermal expansion be taken as an average value of three tests ($\alpha_T = 8.25 \times 10^{-6} \text{ (m/m)/}^\circ\text{C}$). An expression to describe the temperature evolution (Equation 4.18) was also suggested, adapting a function reported by Schubert (1988), for use in shotcrete linings. Caution is advised in applying this equation, because temperatures measured in the SLRT tunnels had indicated wide fluctuations, depending on the position of the lining under consideration.

Shrinkage tests were performed trying to simulate in the laboratory, the environment found at SLRT site. Results had indicated that the conventional shrinkage evaluation based on relative moisture content of the air, as has been proposed for shotcrete linings (e.g., Gais et al., 1986), could not provide an accurate prediction. Using laboratory test results and measurements taken from instruments embedded in the shotcrete lining (SLRT), it was suggested that either the shrinkage be low at short term or

some expansion be experienced, depending on the position under consideration. An attempt mechanism to explain the cyclic expansion and contraction of the shotcrete (stress and temperature independent) observed in the SLRT tunnels, according to the tunnel construction operation, has been proposed. It seems that the moisture provided by the soil and the air circulation with relative humidity lower than that in the tunnel, could induce different diffusion regimes, depending on the construction operation. Associated with these regimes, variations of moisture content could occur in the shotcrete, inducing contraction or expansion.

Stress and strain controlled tests were performed and the adequacy of the viscoelastic model was verified through strain and stress analyses. Assuming the linear viscoelasticity, the linearity of the model was implicitly accepted (superposition of events was valid). The superposition of stresses was verified in the stress controlled tests, as the loading was applied in stages. The superposition of deformations was evaluated in the strain controlled tests, by applying the compensation of the stress independent deformations. Notice also that in the stress controlled tests, superposition of deformations was assumed because stress dependent deformations were obtained by compensation of a dummy specimen.

In order to perform strain and stress analyses, analytical solutions were presented and were applied by an extensive use of curve fitting technique to describe stress and strain evolutions. Due to the variability of the viscoelastic parameters during the first 10 hours of age, these analyses were always subdivided into two periods: before and after this age. The first period had a reduced importance for the present investigation, because this period has a small importance in the soil-lining interaction (more details in Chapter 6). The analysis carried out for periods up to 10 hours of age was intended to access the order of magnitude of strain and stress development only.

For the analysis of the period after 10 hours of age, the strain analysis performed in the stress controlled tests, the viscoelastic model presented error of the order of 10 %.

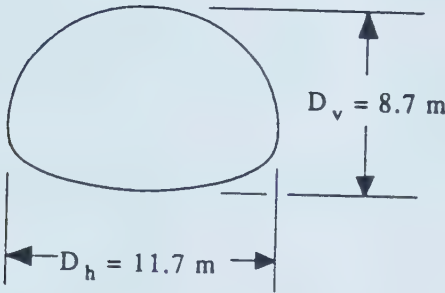
For the stress analysis performed in the strain controlled tests, the error was of the order of 15 %. It was observed, under a number of calculation assumptions and under different representative strain and stress paths expected in the tunnel lining, that the short creep deformations were very fast, compared to the rate of loading. In other words, the assumptions using $\eta=0$ (equivalent to linear elastic) had produced error on strain and stress evaluation of the same order of magnitude as the viscoelastic assumptions. This result opens the possibility of using an equivalent linear elastic model, to describe the short term behavior of the shotcrete. This partial result still requires more investigations, because the stress and strain imposed in these tests did not simulate the exact the environmental conditions, i.e., the stress independent deformations were not those that could happen at site. This aspect will be explored in Chapter 6.

The results of the strain and stress analyses for the period after 10 hours of age also demonstrated that the proposed average values for the viscoelastic parameter obtained in the short term creep tests (Figure 4.30 and 4.31) could be used without compromising the accuracy of the calculations. Notice that in the test series CRMST, the strains were evaluated either by the parameters obtained at different ages (Table 4.13) or by the average values. It should be pointed out, however, that the evaluation as done in the former was not theoretically correct: superposition was performed in bodies of different stiffness. As the viscosity was very low, compared to the rate of loading, this simplification was considered acceptable.

The results presented in this chapter were related only to the short term response of the shotcrete. The strain and stress analyses have shown that the parameters estimated for the short term behavior of the shotcrete had a tendency to underestimate the strains (or overestimate stresses) towards the end of the tests.

Table 4.1 Measured and Calculated Convergence at Paraiso Tunnels, São Paulo
(modified from Negro, 1989)

		Calculated	Measured
Date		10/27/88	12/12/88 to 01/18/89
Vert. convergence ΔD_v	(1)	21.6 mm	21.0 mm
Horiz. convergence ΔD_h	(1)	18.2 mm	15.0 mm
Young's modulus of Shotcrete		10 GPa	11.4 GPa (2)



(1) values measured after lining ring was closed
(2) values obtained by back analysis

Table 4.2 Water-Cement Ratio Reported in Literature for Shotcrete

w/c ratio	reference	notes
0.4	ABNT, 1986	value suggested for dry method
0.45-0.65	Ward and Hills, 1976	range suggested as obtained in practice for fine aggregate mix, dry method
0.20-0.70	Manson and Manson, 1982	-
0.26-0.37	Parker, 1976: 241	measured during rebound tests, dry method
0.34-0.50	Simondi et al., 1982	control tests in tunnel construction using dry method
0.28-0.43	Litvin and Shideler, 1966	measured in panels shotcreted by a number of contractors, maximum aggregate size between 0.95 cm to 1.9 cm

Table 4.3 Composition of the Shotcrete Simulated in Laboratory

G:S	cement content	w/c (3)	a/c (3)
1:1	350 kg/m ³ (1)	0.5 to 0.6	0.05 (2)

(1) cement type 50: sulfur resistant
 (2) accelerator based on potassium hydroxide
 (3) ratios in weight

Table 4.4 Summary of Compression Tests: Strength

Test	w/c	number of observations	Unit weight (kN/m ³)	
			mean value	standard deviation
STA	0.5	7	21.32	0.46
STB	0.6	11	22.64	0.17
insitu cores	0.4-0.5	20	22.69	0.26
panel cores	0.4-0.5	47	22.68	0.23

Table 4.5 Parameters for Strength Estimation According to Equation 4.1

Test	w/c	A ₁ (%)	A ₂ (%)	B ₁	B ₂	f _{cc} ^{28d} (MPa)
panel cores	0.4-0.5	0.300	29.446	2.676	0.188	29.022
STA	0.5	0.128	28.878	2.691	0.191	19.679
STB	0.6	0.040	30.335	2.670	0.183	22.906
Byfors (1980)	0.4-1.0	(2)	41.52	3.236	0.135	-

(1) parameters A₁, A₂, B₁ and B₂ valid for :
t in hours
H in %
f_{cc}^{28d} in MPa

(2) according to Figure 4.9

Table 4.6 Data Used for Comparison of Results in Figures 4.10 and 4.13

Author	Year	Type of specimen	a/c ratio	cement content (kg/m ³)	Notes
Babendererde and Wirtz	1986	N/A	0.05	N/A	NBS tunnel construction
Bortz et al.	1973	N/A	0.03	280-390	average values presented by Mahar et al., 1975: A2 and also by Parker, 1976: 365
Brierley	1975: 107, 110	prism took from panels 7.62 X 7.62 X 20.3 cm	0.02-0.03	420	Dupont Circle project, Washington tests conducted by Parker, 1973
Negro	1989	cores took from panels $\phi = 7.4 - 10.1$ cm $h = 6.1 - 15$ cm	0.03	425-435	tests for the construction control of the Paraiso tunnels, at Sao Paulo subways standard deviation available
Onuma et al.	1985	N/A	0.03	390	range presented by the authors as 'usual values' data presented was the average value of this range
Parker	1976: 377, 463	prism took from panels 7.62 X 7.62 X 17.8 cm	0.03	360	Dupont Circle project, Washington: same project of the data presented by Brierly, 1975
Radaelli	1983	N/A	(a)=0.03 powder (b)=1:3 liquid w:a	N/A	quoted by Cipriani, 1985
Simondi et al.	1982	coring in tunnel lining	0.03	405	Tunnel Eliana, Sao Paulo: average values
Jones	1976: 59, 60	according to ASTM C-469	0.03	420	Rock Creek tunnel Dupont Circle project, Washington
Fernandez- Delgado et al.	1975	N/A	0.03	390	quoted by Mahar et al., 1975: 4/46. average values
Gartung et al.	1979	-	-	-	values used in numerical analysis for comparison

Table 4.7 Summary of Test Series STA and STB

Specimen	w/c ratio	a/c ratio	AGE (hour)	γ (kN/m ³)	ASTM C39 f _c (MPa)	ASTM C469 E _c (GPa)	Saenz, (3) E _a (GPa)	1964 ϵ_0 (%)	V _p (m/s)	ASTM (4) V _s (m/s)	2845 E _u (GPa)	Poisson's ratio
STA/01	0.5	0.05	22.50	21.02	8.82	9.21	11.65	2.98	-	-	-	-
STA/02	0.5	0.05	33.78	21.03	9.64	10.17	12.24	2.52	-	-	-	-
STA/03	0.5	0.05	66.28	21.48	13.50	12.62	14.94	2.72	-	-	-	-
STA/04 (1)	0.5	0.05	44.50	20.75	11.02	-	-	-	-	-	-	-
STA/05	0.5	0.05	10.55	22.13	7.44	7.68	11.49	7.41	-	-	-	-
STA/06	0.5	0.05	3.87	21.59	0.72	0.94	1.48	9.79	-	-	-	-
STA/07 (1)	0.5	0.05	8.85	21.25	6.61	-	-	-	-	-	-	-
STB/01	0.6	0.05	96.98	22.56	17.87	17.80	22.55	3.13	4023.43	2127.47	27.19	0.31
STB/02	0.6	0.05	5.55	22.69	1.45	0.58	0.78	9.70	2049.19	773.28	3.92	0.42
STB/03	0.6	0.05	21.05	22.46	8.27	9.24	12.99	4.38	2991.11	1382.72	11.94	0.36
STB/04	0.6	0.05	123.42	22.89	13.16	14.71	20.95	4.73	3641.63	1891.52	21.96	0.32
STB/05	0.6	0.05	1060.33	22.84	22.97	18.37	22.89	3.69	3920.67	2188.12	28.40	0.27
STB/06	0.6	0.05	53.85	22.58	15.36	16.05	20.53	3.09	3641.63	1802.67	20.02	0.34
STB/07	0.6	0.05	6.80	22.65	1.23	0.60	0.82	8.80	2120.54	714.45	3.38	0.44
STB/08	0.6	0.05	4.30	22.55	0.56	0.14	0.22	52.48	1721.79	592.32	2.31	0.43
STB/09	0.6	0.05	197.63	22.38	18.71	18.99	25.11	3.60	3812.90	2048.87	24.84	0.30
STB/10 (2)	0.6	0.05	969.63	22.82	26.88	19.25	22.81	3.56	4364.83	2377.20	33.90	0.29
STB/11 (2)	0.6	0.05	179.13	22.71	17.59	16.81	21.93	3.63	3709.35	2083.57	25.51	0.27

(1) specimen submitted only in strength tests
 (2) specimen also submitted to continuous ultrasonic tests
 (3) curve fitting using Equation 4.6 assuming $\sigma_0=f_c$
 (4) see restrictions according to Equation 4.11, Table 4.8

E_c : conventional elastic modulus
 E_a : curve fit
 E_u : ultrasonic test

Table 4.8 Geometric Restriction to Obtain Reliable Measurement, According to ASTM 2845 (relation 4.11)

f_{cc} (MPa)	D (1) (m)	$5(V_p/f)$ (2) (m)	15 d (3) (m)
0.56	0.15	0.07	0.11
1.23	0.15	0.09	0.11
1.45	0.15	0.09	0.11
8.27	0.15	0.12	0.11
13.16	0.15	0.15	0.11
15.36	0.15	0.15	0.11
17.59	0.15	0.15	0.11
17.87	0.15	0.17	0.11
18.71	0.15	0.16	0.11
22.97	0.15	0.16	0.11
26.88	0.15	0.18	0.11

- (1) D=diameter of the specimen
- (2) $f= 120000$ kHz (resonance frequency)
- (3) $d= 7.5$ mm (average grain size, assumed as D_{10} of the concrete mix)

Table 4.9 Relations between Young's Modulus and Strength Used for Shotcrete

Author	Year	Relation (1)	Used by
ACI	1971	$E = 4.733 \sqrt{f_{cc}}$	Parker, 1976: 464 Brierley, 1975: 111
ABNT NBR 6118	1980	$E = 6.577 \sqrt{f_{cc}}$	Negro, 1989
Pauw	1960	$E = 5.581 \sqrt{f_{cc}}$	Brameshuber and Kottas, 1987
CEB-FIP	1978	$E = 9.5 \sqrt[3]{f_{cc} + 8}$	for comparison

(1) E in GPa and f_{cc} in MPa

Table 4.10 Summary of Data Used in Figure 4.18 (Modified after Byfors, 1980)

Author	Year	W/C	cement type	curing temp. (°C)	type of specimen	Notes
Hansen	1956	0.53	I	20	cylinder 15 X 30 cm l ₀ =30 cm	-
Gunzler	1970	0.47	SUZ300	N/A	N/A	-
Wierig	1971	0.50	PZ 275	20	prism 20 X 20 X 40 cm l ₀ =20 cm	loading time = 150 s
Haugland et al.	1976	0.4-0.85	6 types	2-20	cylinder 10 X 28 cm	-
Lew et al.	1978	N/A	I	1.7-22.8	cylinder 15 X 30 cm	loading time = 180 s
Byfors	1980	0.4-1.0	ordinary Portland cement	8-20	prism 10 X 10 X 40 cm	loading time = 30-60 s

Table 4.11 Parameters of Equation 4.12

	c ₁	d ₁	c ₂	d ₂
Byfors, 1980: 161	9930	2.675	7250	0.471
present investigation	1306	1.920	7194	0.363

(*) parameter valid for:
f_{cc} in MPa
E_c in GPa

Table 4.12 Summary of Creep Tests Coefficients (Eq. 4.16) Obtained by Curve Fittings for Different Time Intervals ($\Delta t'$), Series CRSG

test	age at loading (hours)	loading time (min.)	σ (kPa)	σ/f_{cc} (1)	duration of test (hours)	coefficients		$\Delta t'$ (hours)					
								2	4	8	16	32	72
CRSG4H	4.2	4	129.67	0.323	36.7	$1/E_t$ (2)	E_t/η (3)	2.1211	2.3047	2.4196	2.4491	2.4445	-
CRSG8H	8.1	6	618.63	0.315	40.1	$1/E_t$ (2)	E_t/η (3)	0.0657	0.0728	0.0750	0.0757	0.0753	-
						$1/E_t$ (2)	E_t/η (3)	0.0452	0.0350	0.0323	0.0315	0.0319	-
CRSG12H	11.9	9	1973.98	0.471	35.0	$1/E_t$ (2)	E_t/η (3)	0.0201	0.0247	0.0293	0.0331	0.0393	-
						$1/E_t$ (2)	E_t/η (3)	0.0569	0.0281	0.0149	0.0093	0.0048	-
CRSG16H	16.1	8	1966.70	0.299	48.8	$1/E_t$ (2)	E_t/η (3)	0.0148	0.0182	0.0216	0.0263	0.0326	-
						$1/E_t$ (2)	E_t/η (3)	0.0594	0.0311	0.0162	0.0087	0.0047	-
CRSG24H	24.3	8	1967.72	0.201	39.1	$1/E_t$ (2)	E_t/η (3)	0.0143	0.0166	0.0194	0.0248	0.0286	-
						$1/E_t$ (2)	E_t/η (3)	0.0672	0.0479	0.0310	0.0088	0.0043	-
CRSG36H	35.9	8	1971.84	0.162	67.6	$1/E_t$ (2)	E_t/η (3)	0.0104	0.0117	0.0137	0.0183	0.0223	-
						$1/E_t$ (2)	E_t/η (3)	0.0710	0.0485	0.0212	0.0078	0.0047	-
CRSG78H	77.7	9	2303.22	0.152	135.0	$1/E_t$ (2)	E_t/η (3)	0.0082	0.0102	0.0133	0.0161	0.0196	0.0253
						$1/E_t$ (2)	E_t/η (3)	0.2151	0.0621	0.0140	0.0070	0.0036	0.0018
CRSG168H	168.0	24	2464.06	0.141	156.7	$1/E_t$ (2)	E_t/η (3)	-	0.0068	0.0081	0.0101	0.0148	0.0206
						$1/E_t$ (2)	E_t/η (3)	-	0.0227	0.0167	0.0092	0.0023	0.0009

(1) f_{cc} based on regression of the series STB: Table 4.5
(2) in 1/GPa
(3) in 1/min.

Table 4.13 Summary of Curve Fittings, Series CRSG, According to Equations 4.24 and 4.25

test	s_1 (1) (kPa)	t_1 (1) (min.)	$1/E$ (1/GPa)	$1/E_t$ (1/GPa)	E/η (1/min.)
CRSG4H	127.4	4.00	1.6073	3.2134	0.1152
CRSG8H	617.5	6.50	0.1491	0.0843	0.0324
CRSG12H	1973.2	8.57	0.0998	0.0424	0.0041
CRSG16H	1966.4	8.43	0.0864	0.0381	0.0035
CRSG24H	1967.7	8.25	0.0753	0.0327	0.0031
CRSG36H	1971.9	8.75	0.0605	0.0276	0.0028
CRSG78H	2303.9	9.50	0.0504	0.0318	0.0014
CRSG168H	2464.1	24.25	0.0467	0.0282	0.0008

(1) according to Equation 4.19

Table 4.15 Assumptions Used in Strain Analysis of the Stress Controlled Tests

assumption	parameters	stress history	calculation
MSTa	viscoelastic parameters estimated for the beginning of each stress increment, according to the results presented in Table 4.13 (series CRSG). Values presented in Table 4.14	Equation 4.19 (regression) values of σ_1 & t_1 in Table 4.14	Equations 4.24 & 4.25
MSTb	for $t < 10$ hours, the same viscoelastic parameters used in MSTa for $t > 10$ hours, 'average values' according to Figures 4.30 & 4.31 $E = 15 \text{ GPa}$ $1/E_t = 0.03 \text{ 1/GPa}$ $E_t/\eta = 0.003 \text{ 1/min.}$	Equation 4.19 (regression) values of σ_1 & t_1 in Table 4.14	Equations 4.24 & 4.25
MSTc	same deformation parameters used in MSTb but $\eta=0 \Rightarrow$ linear elastic $\Rightarrow E_{eq} = (E E_t)/(E+E_t)$	actually measured (σ_{meas})	$\varepsilon = \sigma_{meas} / E_{eq}$
SPLa	1st. stress increment : viscoelastic parameters estimated for 8 hours of age. according to series CRSG (Table 4.13) 2nd. stress increment : 'average values' according to Figures 4.30 & 4.31 $E = 15 \text{ GPa}$ $1/E_t = 0.03 \text{ 1/GPa}$ $E_t/\eta = 0.003 \text{ 1/min.}$	Equation 4.19 (regression) values of σ_1 & t_1 in Table 4.14	Equations 4.24 & 4.25
SPLb	same deformation parameters used in SPLa but $\eta=0 \Rightarrow$ linear elastic $\Rightarrow E_{eq} = (E E_t)/(E+E_t)$	actually measured (σ_{meas})	$\varepsilon = \sigma_{meas} / E_{eq}$

Table 4.16 Parameters of Equation 4.26 for the Deformations Imposed during Strain Controlled Tests

instruments	test	a (10^{-6} m/m)	b (1/min.)	t_0 (hours)
VW 41	CRSCO1 & CRSCO2	243.77	0.001091	4.583
VW 18 & VW 36	CRSCO3	119.19	0.000943	4

TABLE 4.17 Equations and Parameters Used to Describe Deformation for Stress Analysis of Test CRSCO1

interval (hours)	'type' of strain	Equation	coefficient	unit	value
4-10	thermally compensated (1)	Eq. 4.26	a	10^{-6} m/m	62
			b	1/min.	0.00833
			t_0	hours	4.91666
6-10	thermally compensated (1)	Eq. 4.26	a	10^{-6} m/m	37
			b	1/min.	0.01
			t_0	hours	5.91666
>10	thermally compensated (1)	Eq. 4.30	c	$(10^{-6}$ m/m)/min	0.08333
			t_0	hours	10.1666
>10	'total' measured	Eq. 4.26	a	10^{-6} m/m	169.759
			b	1/min.	0.00106
			t_0	hours	10.1666
>10	'thermal' strain	Eq. 4.26	a	10^{-6} m/m	-32.010
			b	1/min.	0.00385
			t_0	hours	10.1666

(1) thermally compensated strain = measured - $\Delta T \alpha_T$

Table 4.18 Assumptions Used to Perform Stress Analysis in Strain Controlled Test, CRSCO1

assumption	period (hours)	parameters	strain history	calculation
CO1Ia	4-10	viscoelastic parameters estimated for 8 hours of age: series CRSG-Tab.4.13	thermally compensated (1) Equation 4.26 (regression) values of a, b and t ₀ in Table 4.17	Equation 4.29
CO1Ib	4-10	same deformation parameters used in CO1Ia but $\eta=0 \Rightarrow$ linear elastic $\Rightarrow E_{eq} = (E E_d)/(E+E_d)$	thermally compensated (1) (no regression) $\Rightarrow \epsilon_{comp}$	$\sigma = \epsilon_{comp} E_{eq}$
CO1Ic	6-10	viscoelastic parameters estimated for 8 hours of age: series CRSG-Tab.4.13	thermally compensated (1) Equation 4.26 (regression) values of a, b and t ₀ in Table 4.17	Equation 4.29
CO1Id	6-10	same deformation parameters used in CO1Ic but $\eta=0 \Rightarrow$ linear elastic $\Rightarrow E_{eq} = (E E_d)/(E+E_d)$	thermally compensated (1) (no regression) $\Rightarrow \epsilon_{comp}$	$\sigma = \epsilon_{comp} E_{eq}$
CO1Fa	>10	'average values' according to Figures 4.30 & 4.31	thermally compensated (1) Equation 4.30 (regression) value of c and t ₀ in Table 4.17	Equation 4.31
CO1Fb	>10	'average values' according to Figures 4.30 & 4.31	'total' measured strain Equation 4.26 (regression)	'total' stress Equation 4.29 <i>minus</i>
CO1Fc	>10	same deformation parameters used in CO1Fa & CO1Fb but $\eta=0 \Rightarrow$ linear elastic $\Rightarrow E_{eq} = (E E_d)/(E+E_d)$	'thermal' strain Equation 4.26 (regression) values of a's, b's and t ₀ in Table 4.17	'thermal' stress Equation 4.29
CO1Fd	>10		thermally compensated (1) (no regression) $\Rightarrow \epsilon_{comp}$	$\sigma = \epsilon_{comp} E_{eq}$

(1) thermally compensated strain = measured - $\Delta T \alpha_T$

TABLE 4.19 Equations and Parameters Used to Describe Deformation for Stress Analysis of Test CRSCO2

interval (hours)	'type' of strain	Equation	coefficient	unit	value
4-10	thermally compensated (1)	Eq. 4.26	a	10^{-6} m/m	63
			b	1/min.	0.00915
			t_0	hours	4.91666
6-10	thermally compensated (1)	Eq. 4.26	a	10^{-6} m/m	37
			b	1/min.	0.011
			t_0	hours	6
>10	thermally compensated (1)	Eq. 4.32	f	10^{-6} m/m	125.935
			g	1/min.	0.00110
			h	1/min.	0.00278
			t_0	hours	10
>10	'total' measured	Eq. 4.26	a	10^{-6} m/m	171.000
			b	1/min.	0.00113
			t_0	hours	10
>10	'thermal' strain	Eq. 4.26	l	10^{-6} m/m	-44.075
			m	1/min.	0.00152
			n	1/min.	0.00240
			t_0	hours	10

(1) thermally compensated strain = measured - $\Delta T \alpha_T$

Table 4.20 Assumptions Used to Perform Stress Analysis in Strain Controlled Test, CRSCO2

assumption	period (hours)	parameters	strain history	calculation
CO2Ia	4-10	viscoelastic parameters estimated for 8 hours of age: series CRSG-Tab.4.13	thermally compensated (1) Equation 4.26 (regression) values of a, b and t_0 in Table 4.19	Equation 4.29
CO2Ib	4-10	same deformation parameters used in CO2Ia but $\eta=0 \Rightarrow$ linear elastic $\Rightarrow E_{eq} = (E E_L)/(E+E_L)$	thermally compensated (1) (no regression) $\Rightarrow \epsilon_{comp}$	$\sigma = \epsilon_{comp} E_{eq}$
CO2Ic	6-10	viscoelastic parameters estimated for 8 hours of age: series CRSG-Tab.4.13	thermally compensated (1) Equation 4.26 (regression) values of a, b and t_0 in Table 4.19	Equation 4.29
CO2Id	6-10	same deformation parameters used in CO2Ic but $h=0 \Rightarrow$ linear elastic $\Rightarrow E_{eq} = (E E_L)/(E+E_L)$	thermally compensated (1) (no regression) $\Rightarrow \epsilon_{comp}$	$\sigma = \epsilon_{comp} E_{eq}$
CO2Fa	>10	'average values' according to Figures 4.30 & 4.31	thermally compensated (1) Equation 4.32 (regression) value of f, g, h and t_0 in Table 4.19	Equation 4.33
CO2Fb	>10	'average values' according to Figures 4.30 & 4.31	'total' measured strain Equation 4.26 (regression) 'thermal' strain Equation 4.34 (regression)	'total' stress Equation 4.29 <i>minus</i> 'thermal' stress Equation 4.35
CO2Fc	>10	same deformation parameters used in CO2Fa & CO2Fb but $\eta=0 \Rightarrow$ linear elastic $\Rightarrow E_{eq} = (E E_L)/(E+E_L)$	values of a, b, l, m, n and t_0 in Table 4.19 thermally compensated (1) (no regression) $\Rightarrow \epsilon_{comp}$	$\sigma = \epsilon_{comp} E_{eq}$

(1) thermally compensated strain = measured - $\Delta T \alpha_T$

TABLE 4.21 Equations and Parameters Used to Describe Deformation for Stress Analysis of Test CRSCO3

interval (hours)	'type' of strain	Equation	coefficient	unit	value
4-10	thermally compensated (1)	Eq. 4.26	a	10^{-6} m/m	24
			b	1/min.	0.03
			t_0	hours	5.56666
>18	thermally compensated (1)	Eq. 4.26	a	10^{-6} m/m	44.5
			b	1/min.	0.0008
			t_0	hours	17.9833
>18	'total' measured	Eq. 4.26	a	10^{-6} m/m	55.75
			b	1/min.	0.00095
			t_0	hours	17.9833
>18	thermal strain exponential component	Eq. 4.26	a	10^{-6} m/m	-11.697
			b	1/min.	0.001426
			t_0	hours	17.9833
>10	thermal strain sinusoidal component	Eq. 4.36	q	10^{-6} m/m	-0.6442
			w	1/min.	0.00436
			r	min.	280.470
			t_0	hours	18.3166

(1) thermally compensated strain = measured - $\Delta T \alpha_T$

Table 4.22 Assumptions Used to Perform Stress Analysis in Strain Controlled Test, CRSCO3

assumption	period (hours)	parameters	strain history	calculation
CO3Ia	4-10	viscoelastic parameters estimated for 6 hours of age: series CRSG-Tab.4.13	thermally compensated Equation 4.26 (regression) values of a, b and t ₀ in Table 4.21	Equation 4.29
CO3Fa	>18	'average values' according to Figures 4.30 & 4.3	thermally compensated Equation 4.26 (regression) values of a, b and t ₀ in Table 4.21	Equation 4.29
CO3Fb	>18	same deformation parameters used in CO3Fa but $\eta=0 \Rightarrow$ linear elastic $\Rightarrow E_{eq} = (E E_0)/(E+E_0)$	thermally compensated (no regression) $\Rightarrow \epsilon_{comp}$ (1)	$\sigma = \epsilon_{comp} E_{eq}$
CO3Fc	>18	'average values' according to Figures 4.30 & 4.31	'total' measured strain Equation 4.26 (regression) 'thermal' strain exponential component Equation 4.26 (regression) 'thermal' strain sinusoidal component Equation 4.36 (regression)	'total' stress Equation 4.29 minus 'thermal' stress exponential component Equation 4.29 minus 'thermal' stress sinusoidal component Equation 4.37
values of the parameters in Table 4.21				Table

(1) thermally compensated strain = measured - $\Delta T \alpha_T$

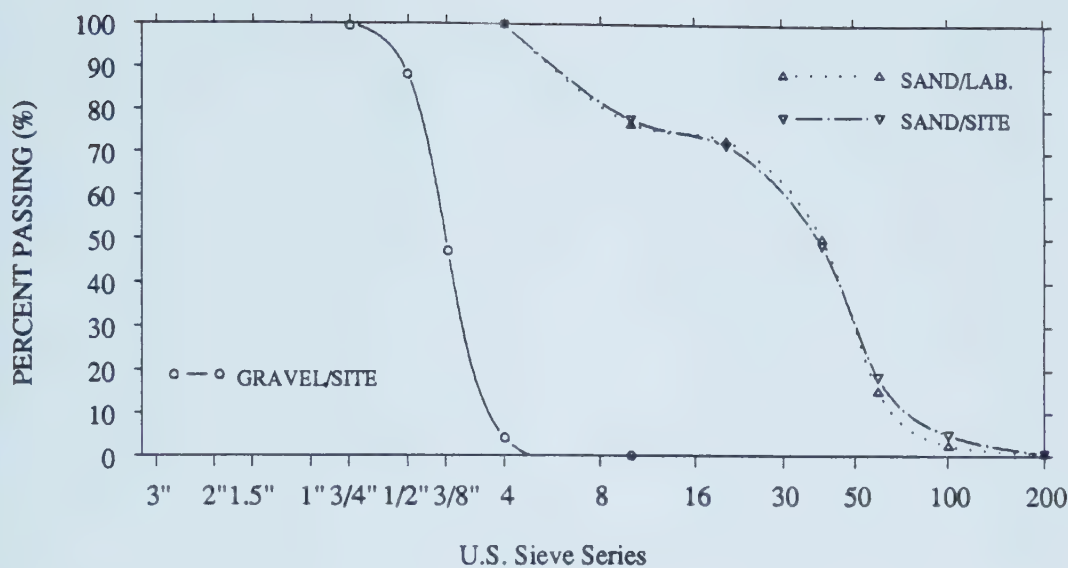


Figure 4.1 Grain Size Distribution of Gravel and Sands

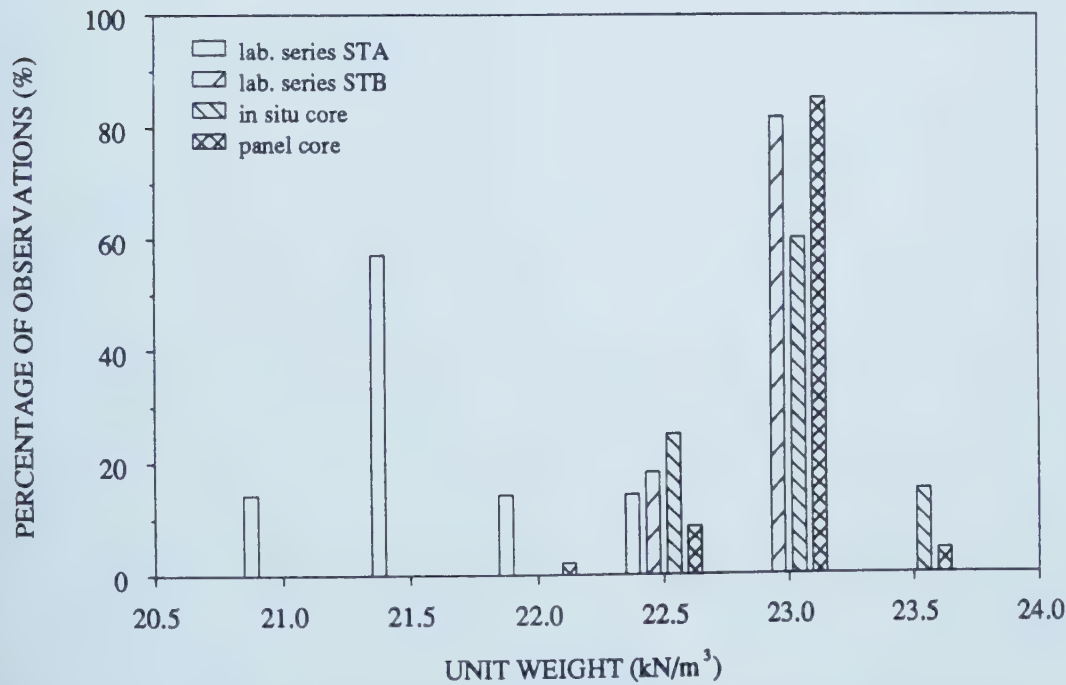


Figure 4.2 Histogram of Unit Weight Measured in Cores Taken at SLRT Site and Specimens Cast in Laboratory

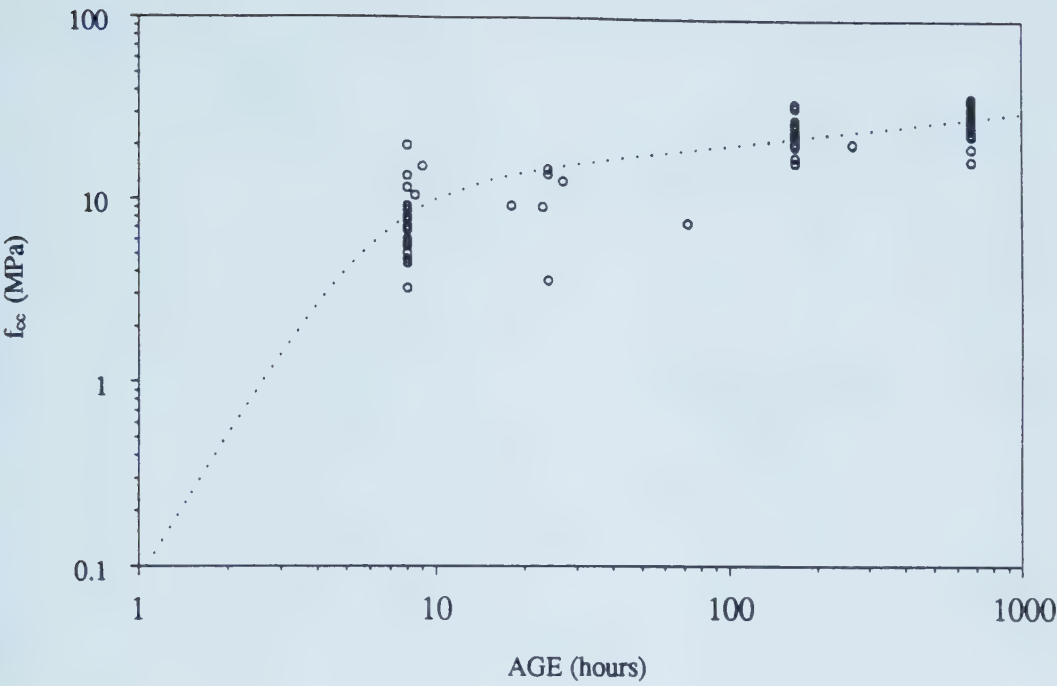


Figure 4.3 Strength Evaluated Using Cores Taken from Panels of Shotcrete Made at the SLRT Site

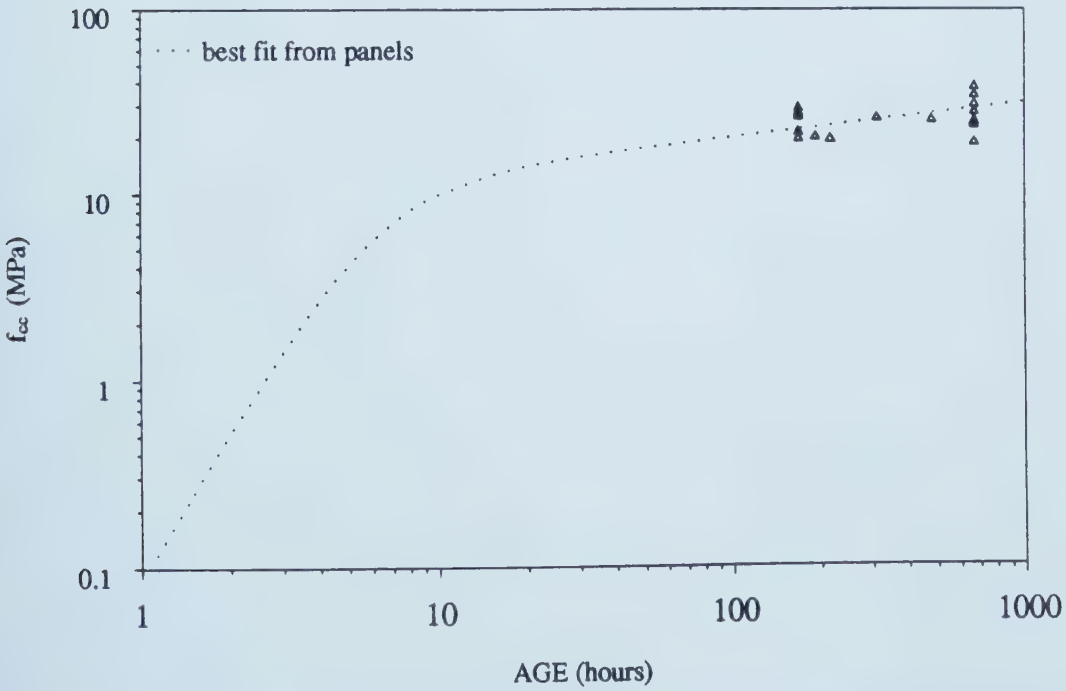


Figure 4.4 Strength Evaluated Using Cores Taken from SLRT Tunnels Lining

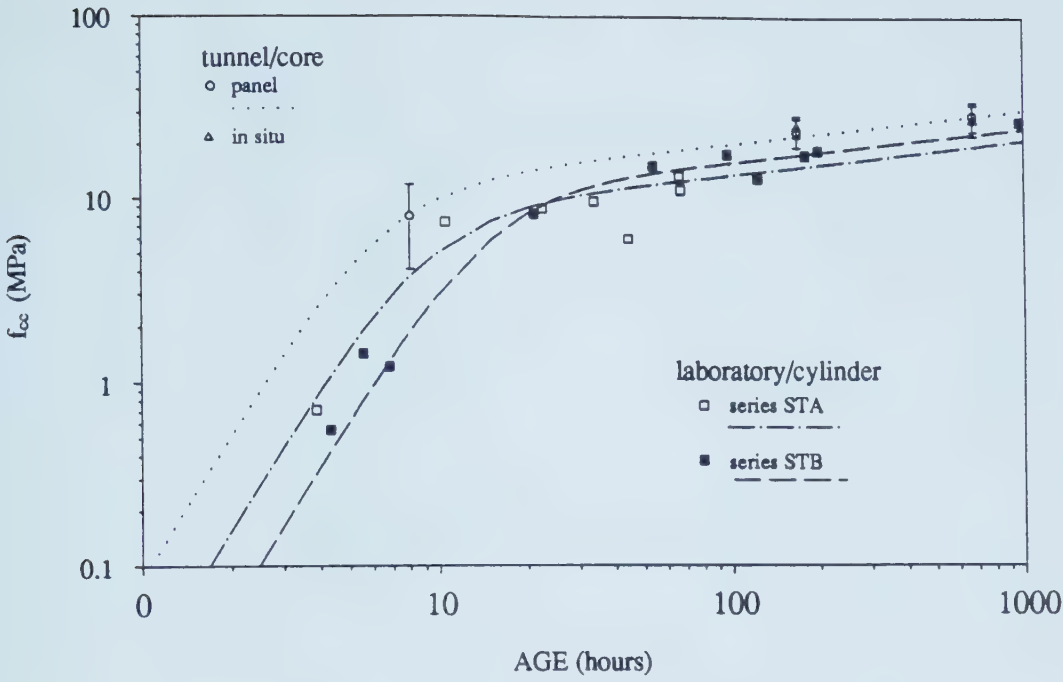


Figure 4.5 Strength Measured Using Specimens Cast in Laboratory

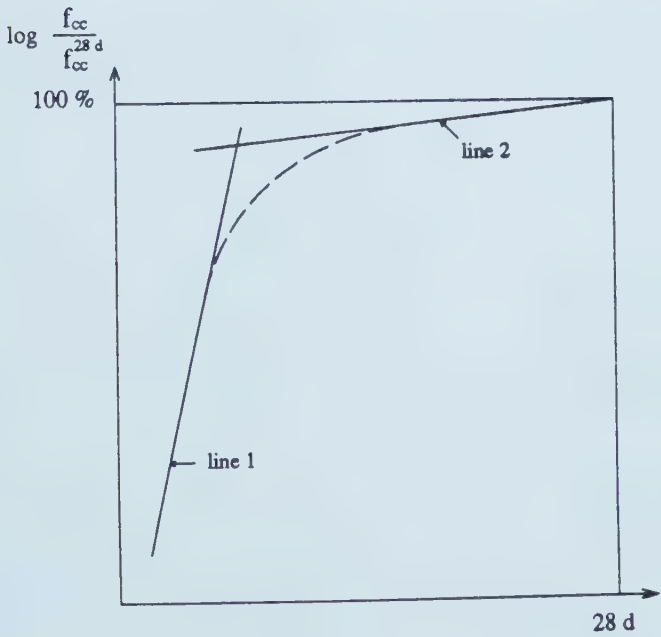


Figure 4.6 Basic Appearance of the Strength Gain in a Log-Log Chart (modified from Byfors, 1980)

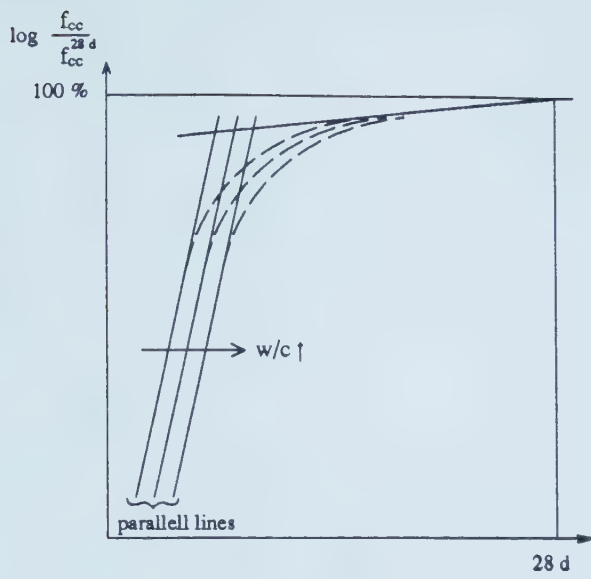


Figure 4.7 Schematic Effect of the w/c Ratio on the Relative Strength Gain (modified from Byfors, 1980)

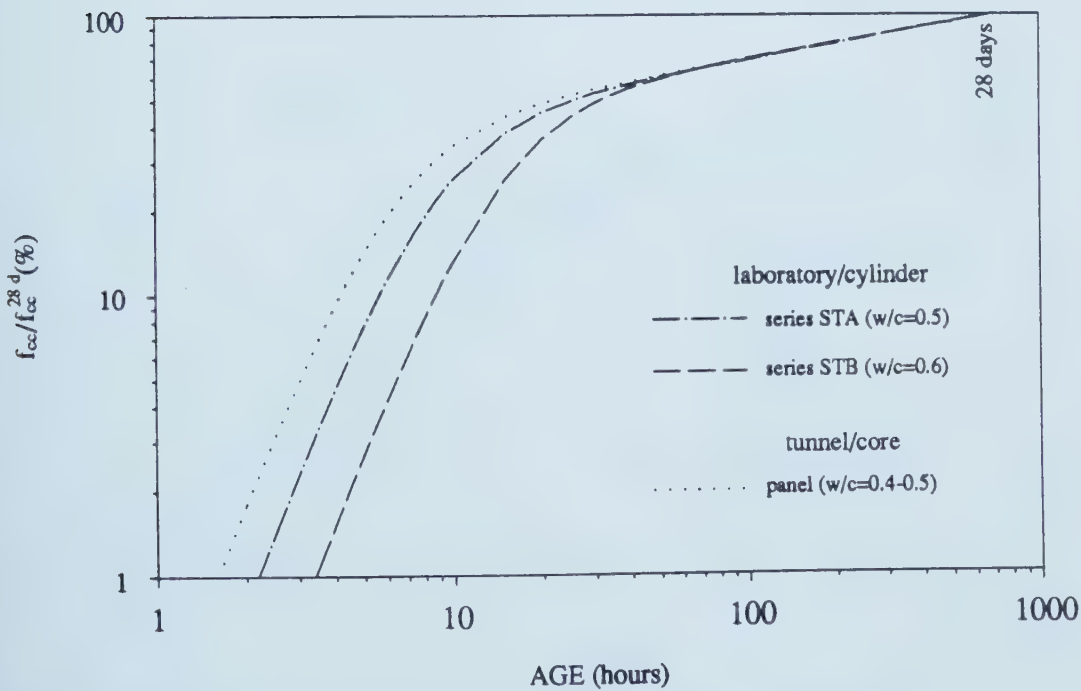


Figure 4.8 Effect of the w/c Ratio on the Relative Strength Development

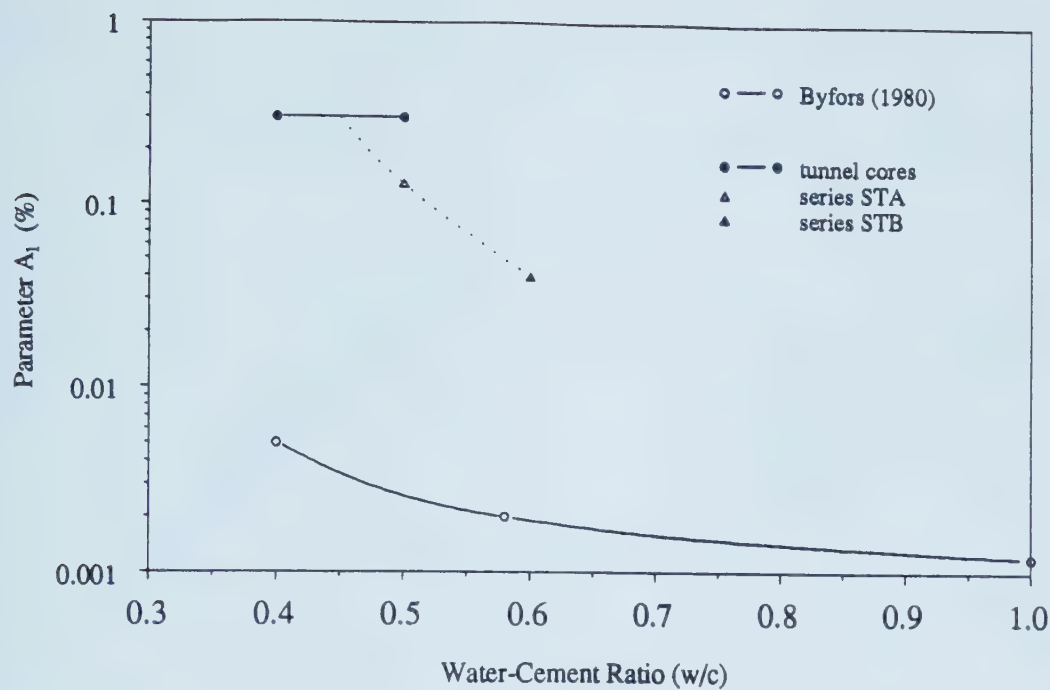


Figure 4.9 Influence of w/c Ratio on Parameter A_1 (Equation 4.4)

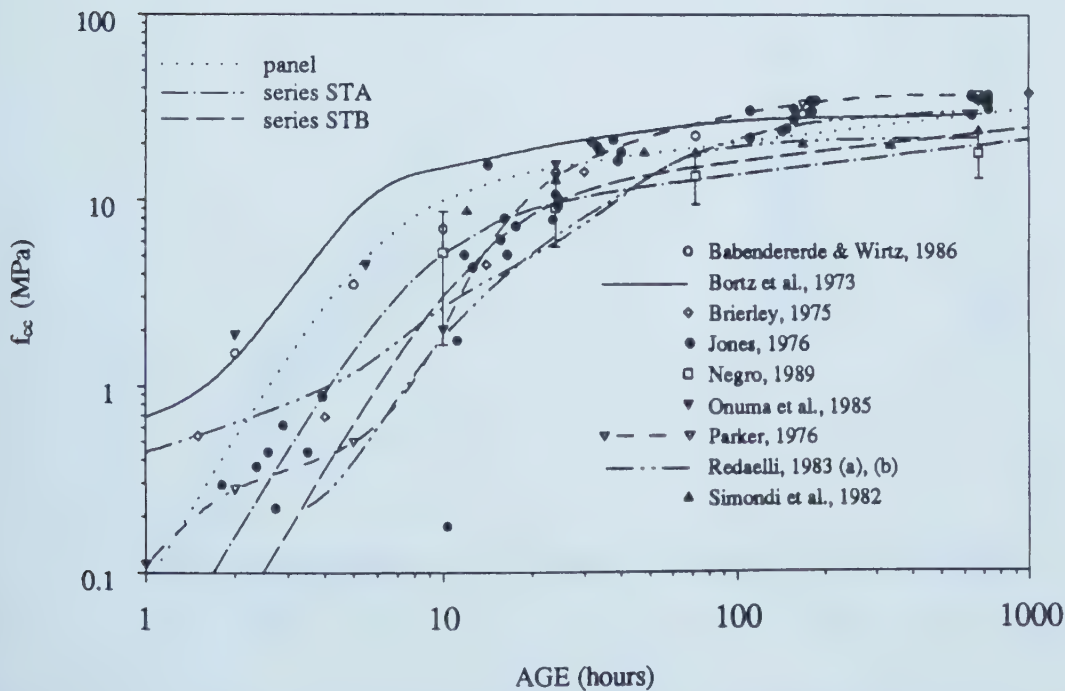


Figure 4.10 Comparison of Strength Development with Published Data

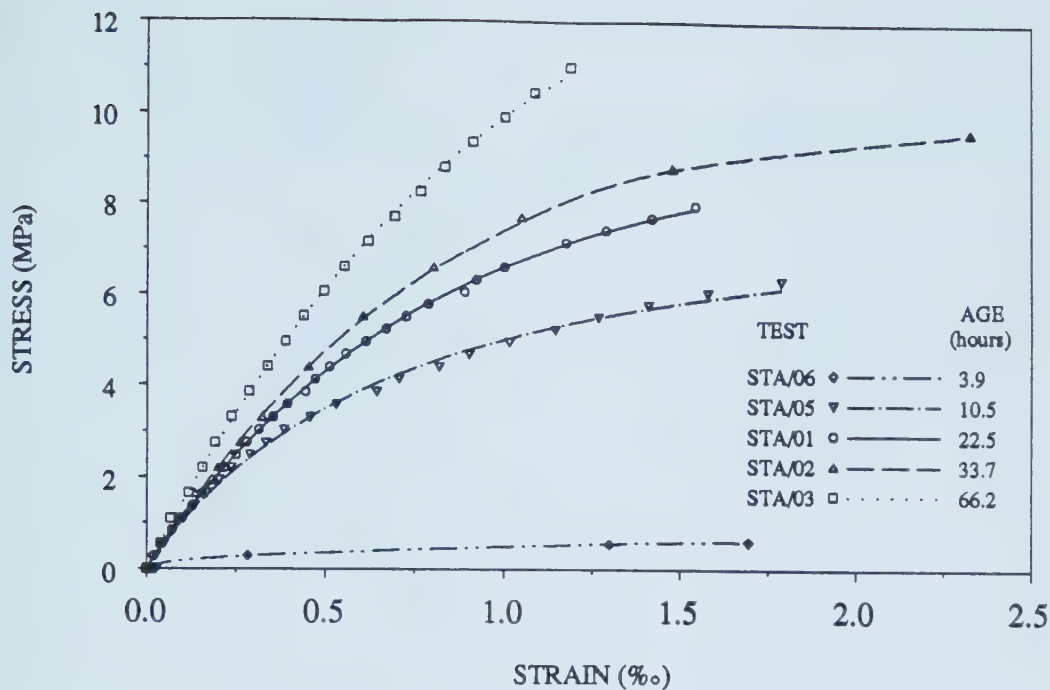


Figure 4.11 Stress-Strain Fittings and Measured Values During Compression Tests, Series STA

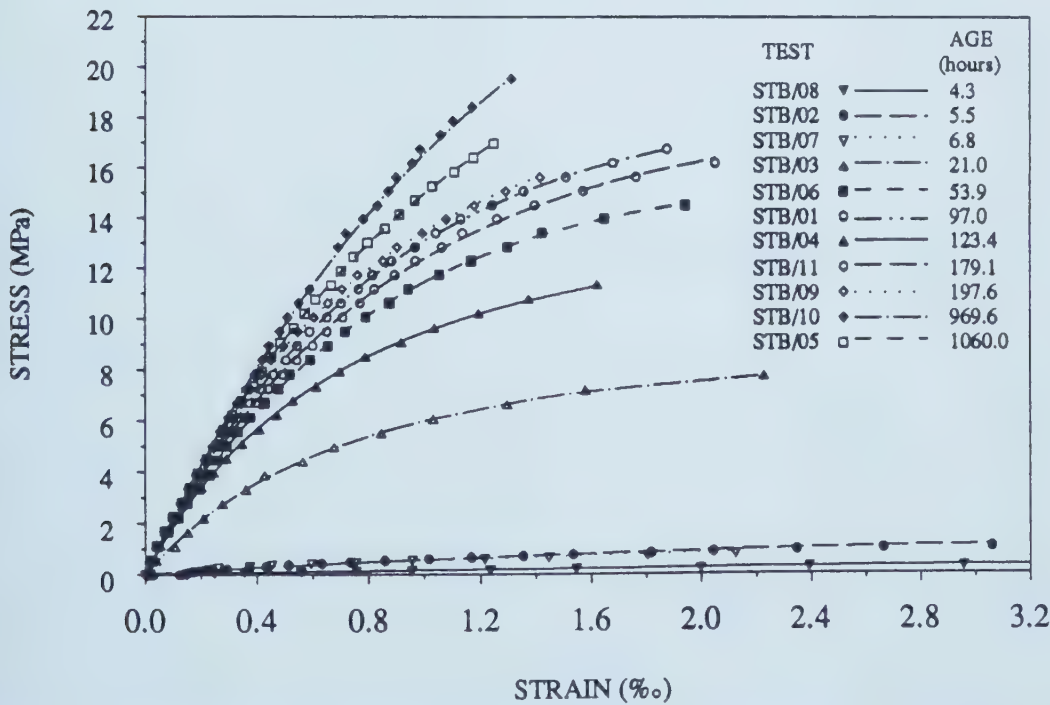


Figure 4.12 Stress-Strain Fittings and Measured Values During Compression Tests, Series STB

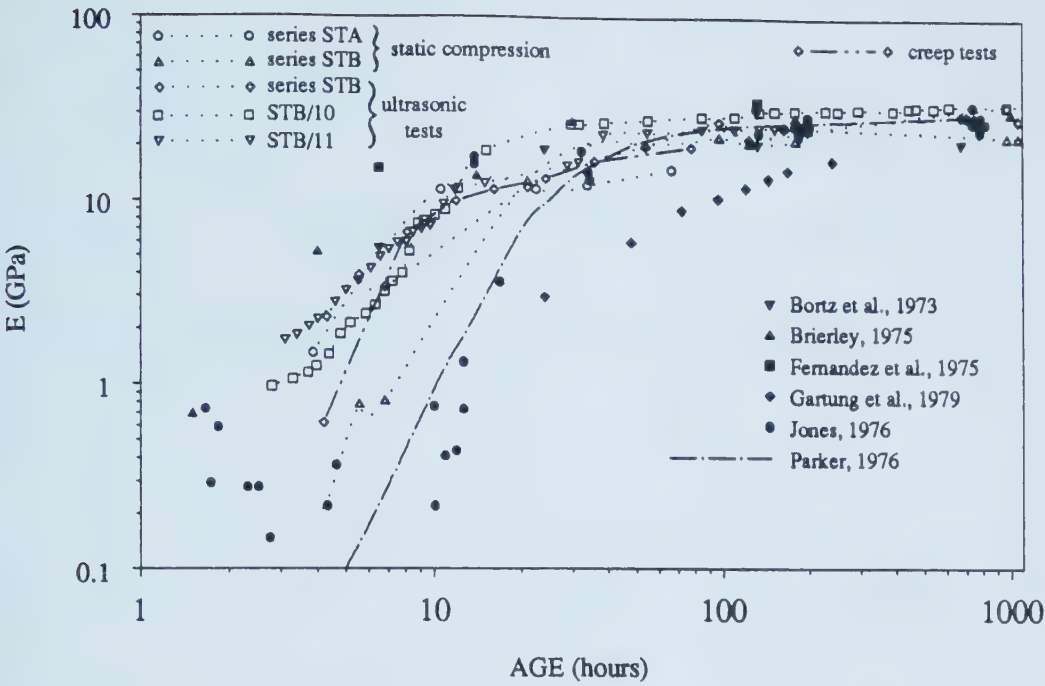


Figure 4.13 Elastic Modulus Development Measured by Different Procedures

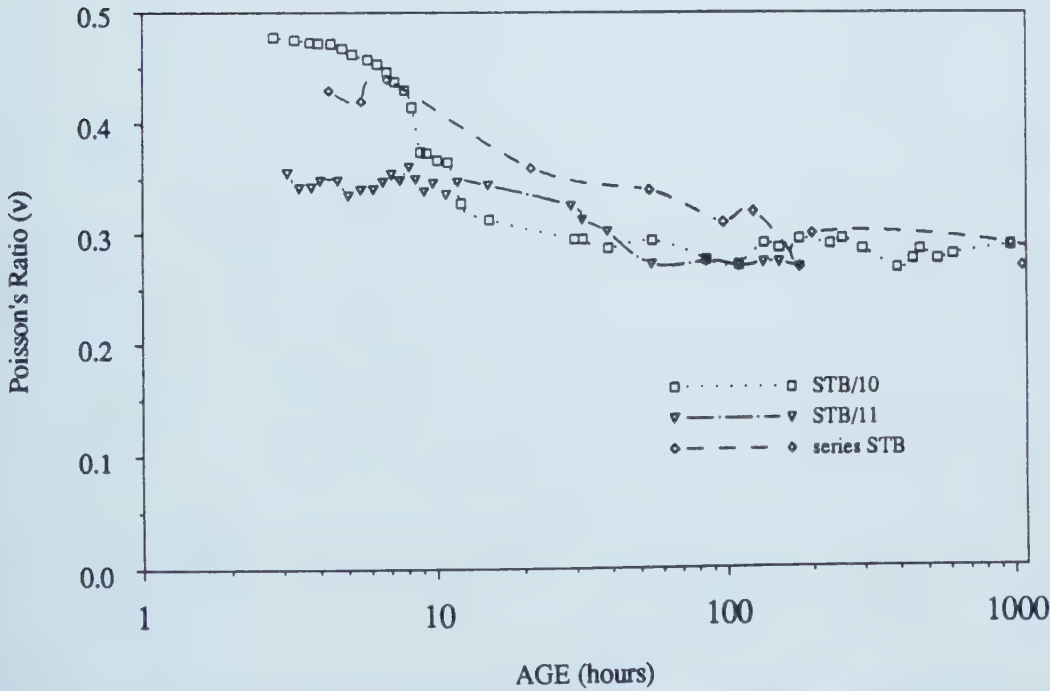


Figure 4.14 Poisson's Ratio Measured Using Ultrasonic Technique

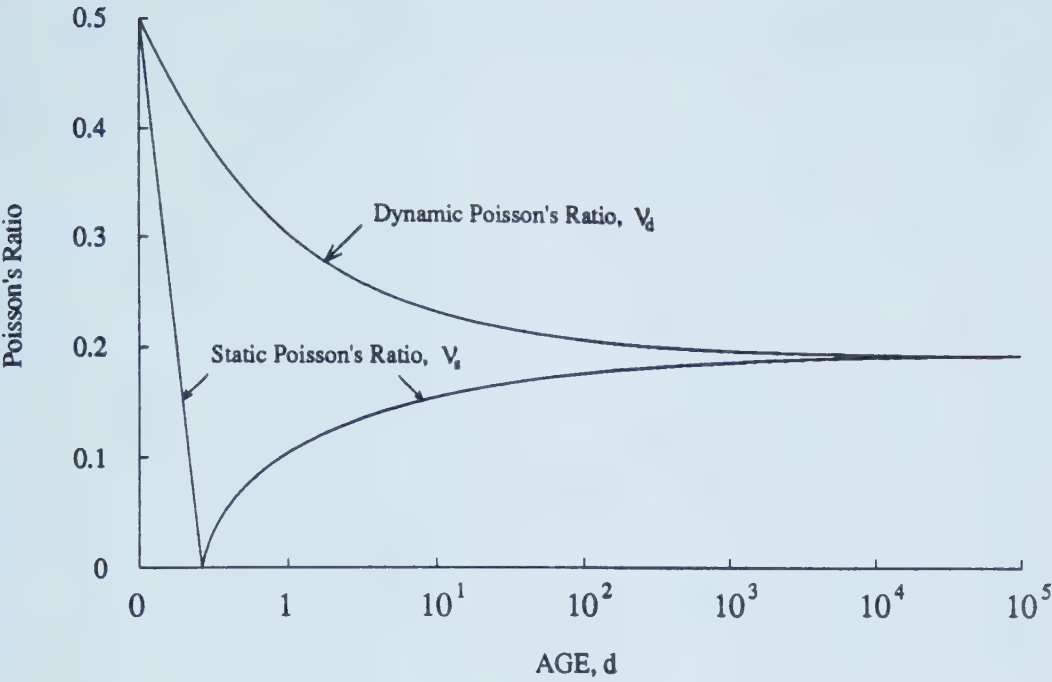


Figure 4.15 Development of Dynamic and Static Poisson's Ratio (modified from Anson, 1966)

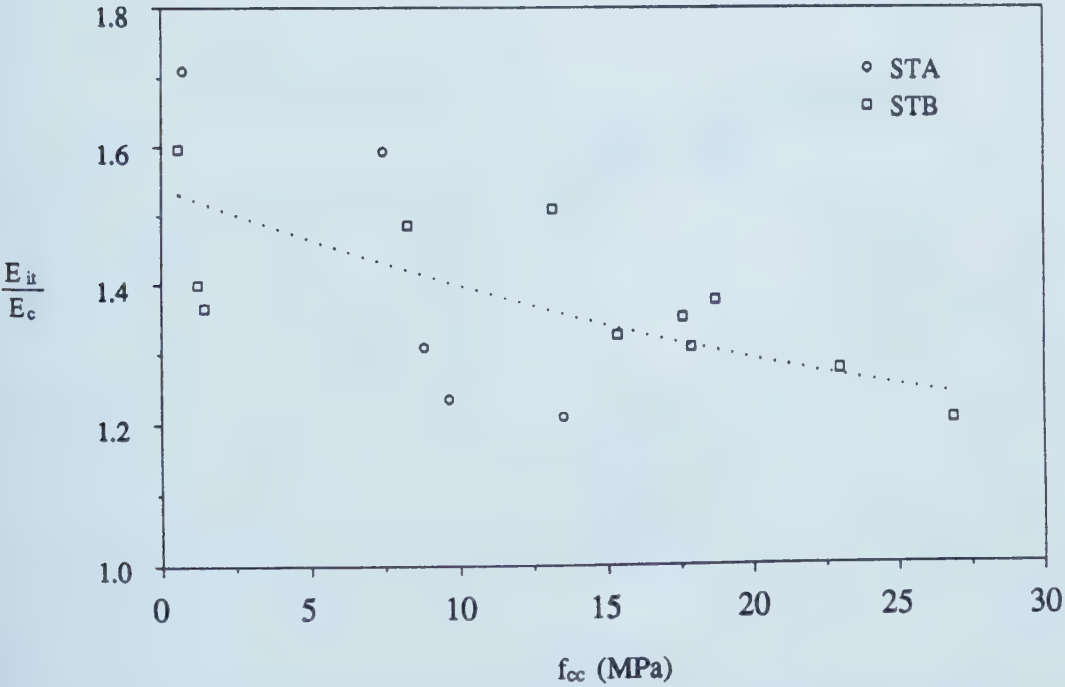


Figure 4.16 Ratio Between Conventional and Initial Tangent Modulus as Function of Strength

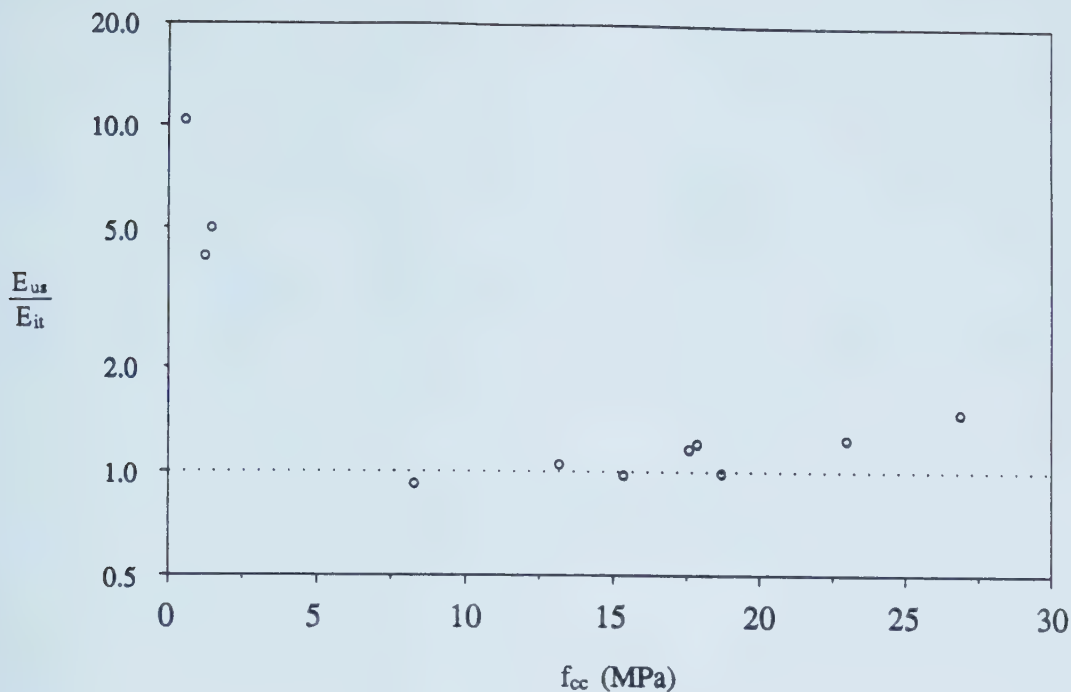


Figure 4.17 Ratio Between Initial Tangent Modulus Measured in Conventional and Ultrasonic Tests

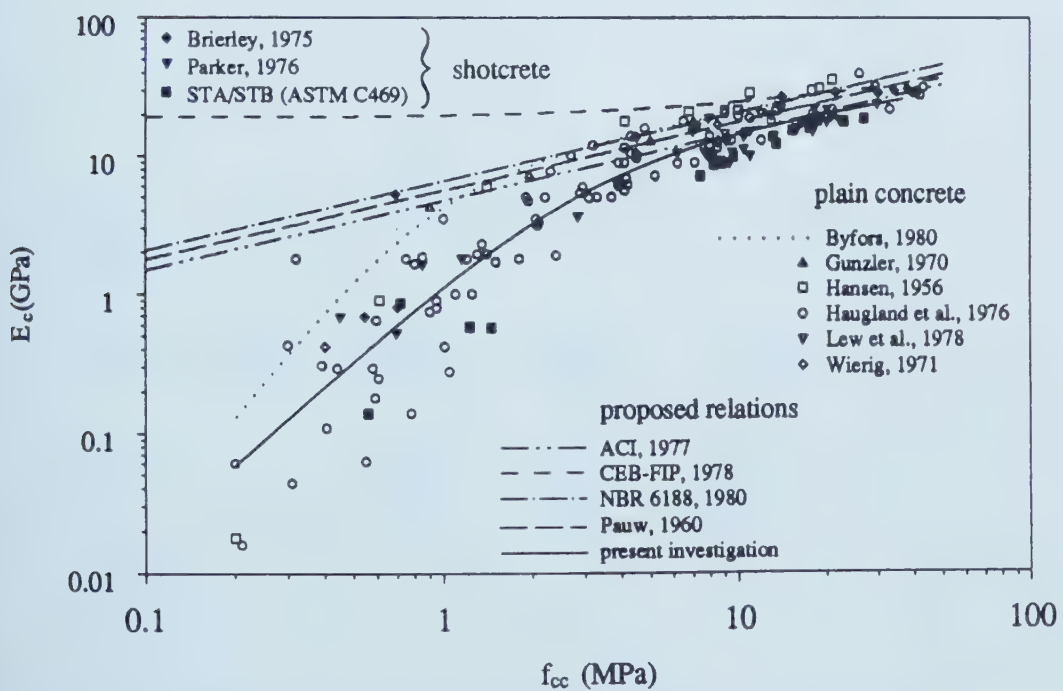


Figure 4.18 Measured and Calculated Relations between Conventional Young's Modulus and Strength

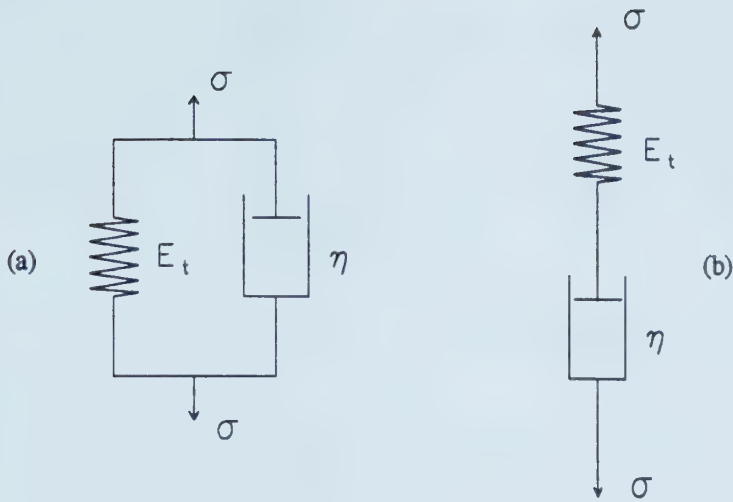


Figure 4.19 Basic Rheological Models: (a) Kelvin Model; (b) Maxwell Model (modified from Neville, 1970)

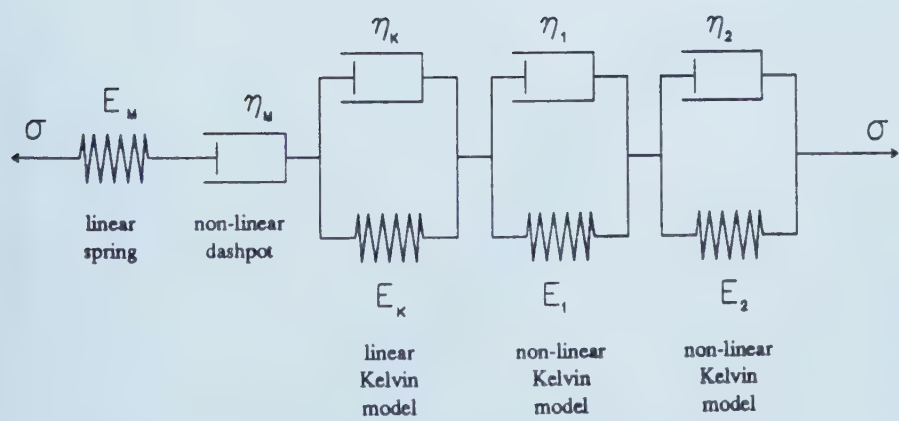


Figure 4.20 Freudenthal and Roll's Model (modified from Neville, 1970)

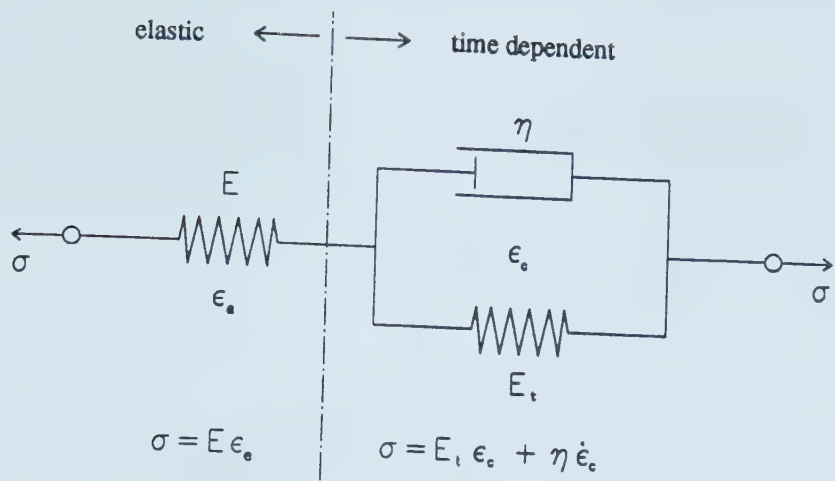


Figure 4.21 Three Elements Viscoelastic Model

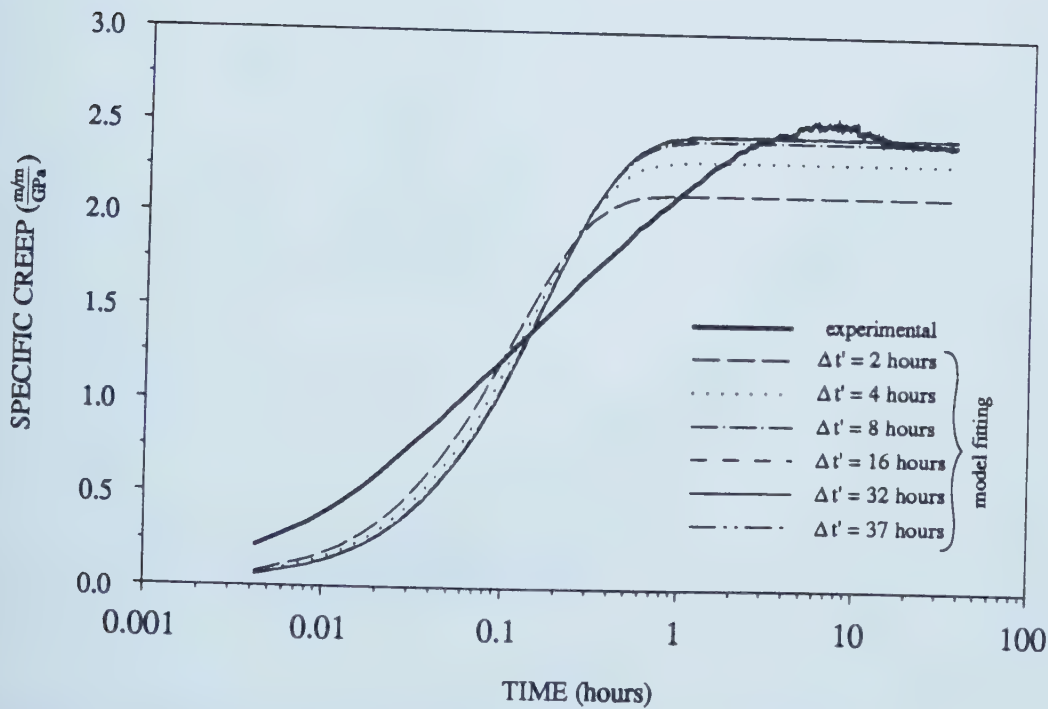


Figure 4.22 Measured and Calculated Values of Creep Test, CRS4H

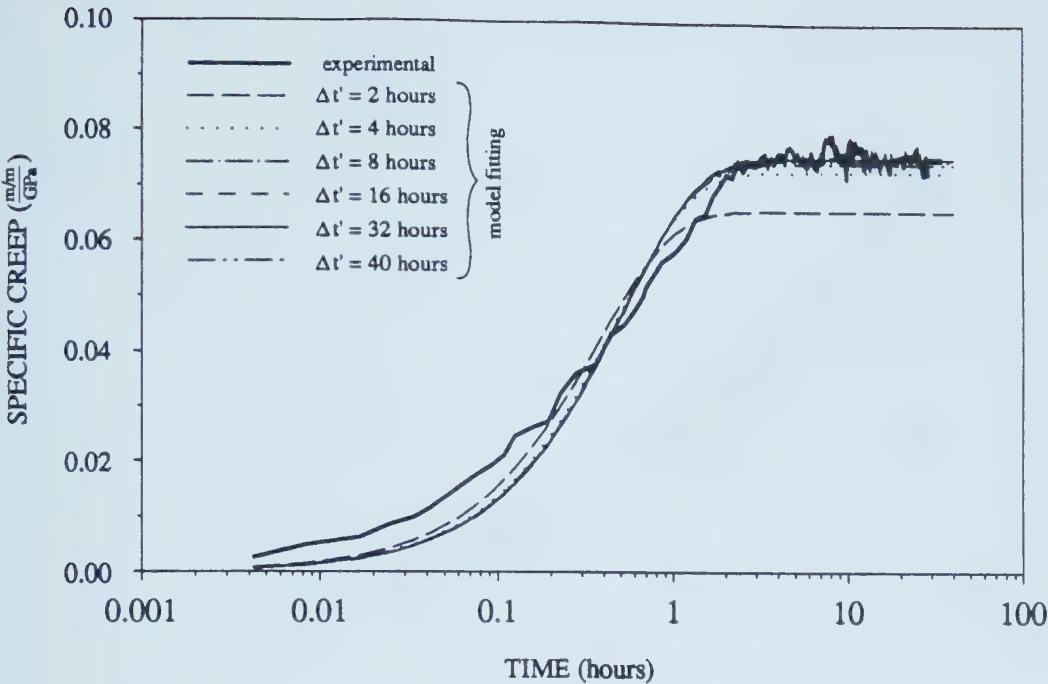


Figure 4.23 Measured and Calculated Values of Creep Test, CRSG8H

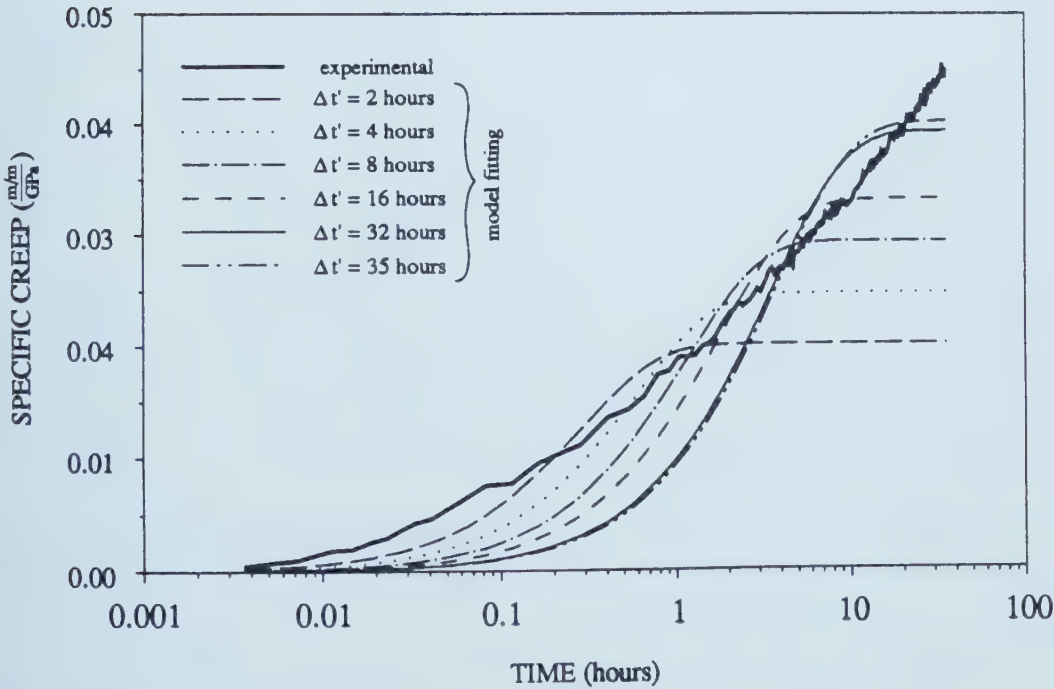


Figure 4.24 Measured and Calculated Values of Creep Test, CRSG12H

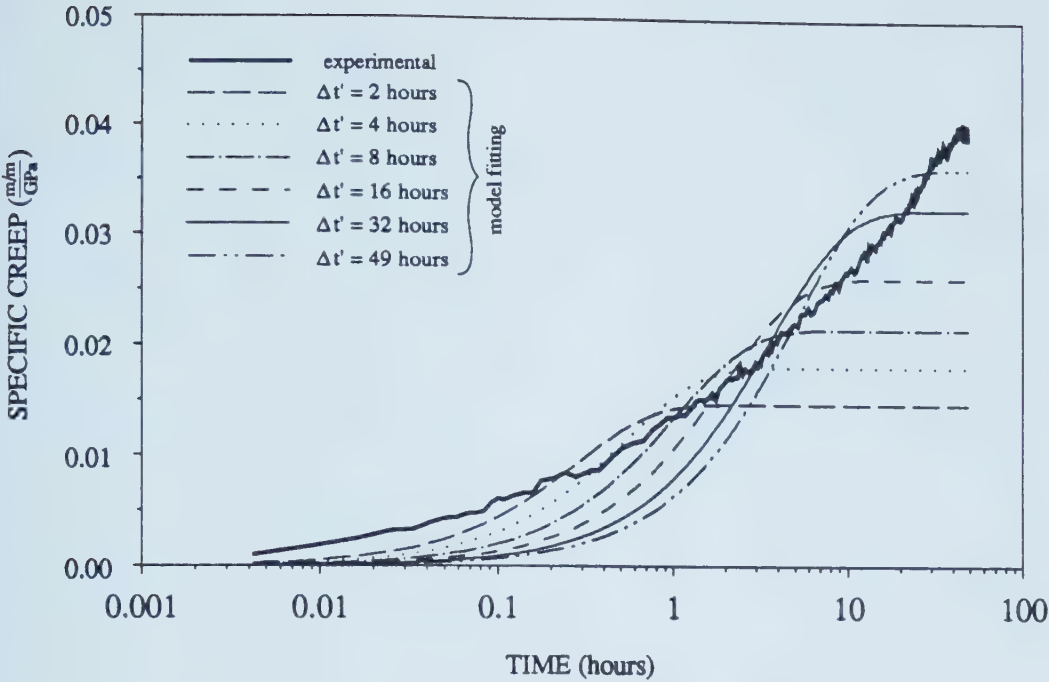


Figure 4.25 Measured and Calculated Values of Creep Test, CRSG16H

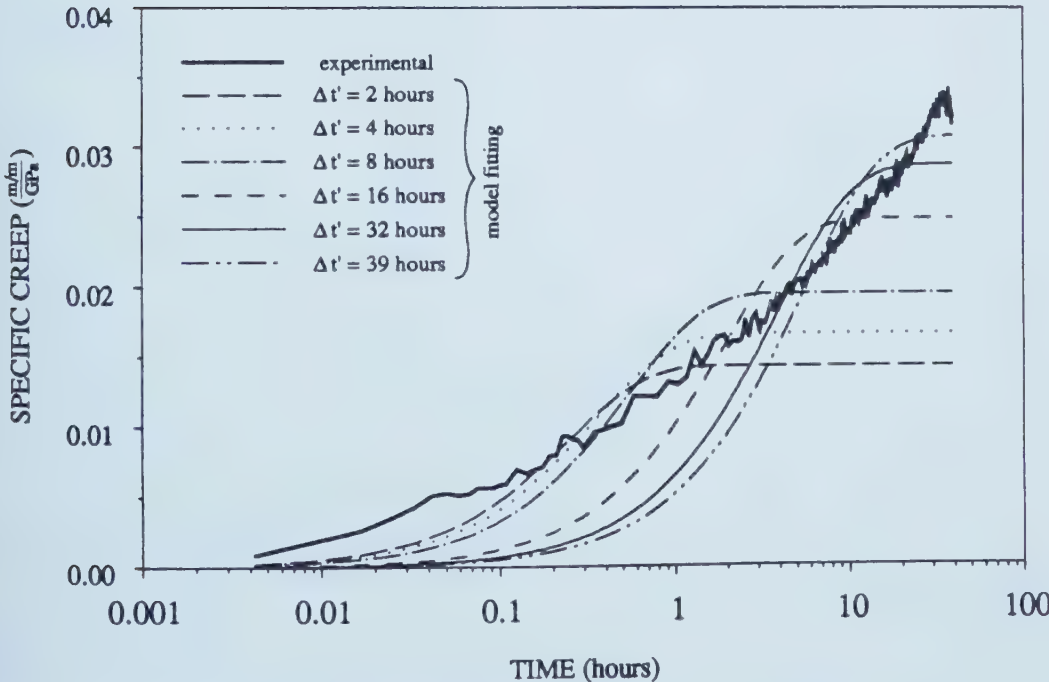


Figure 4.26 Measured and Calculated Values of Creep Test, CRSG24H

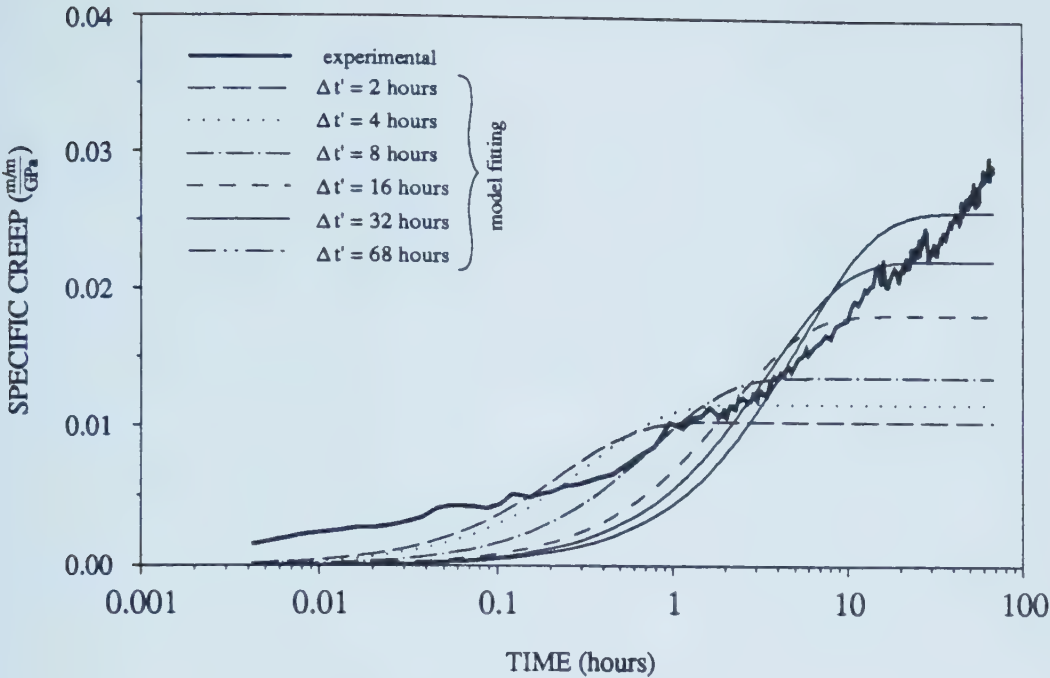


Figure 4.27 Measured and Calculated Values of Creep Test, CRSG36H

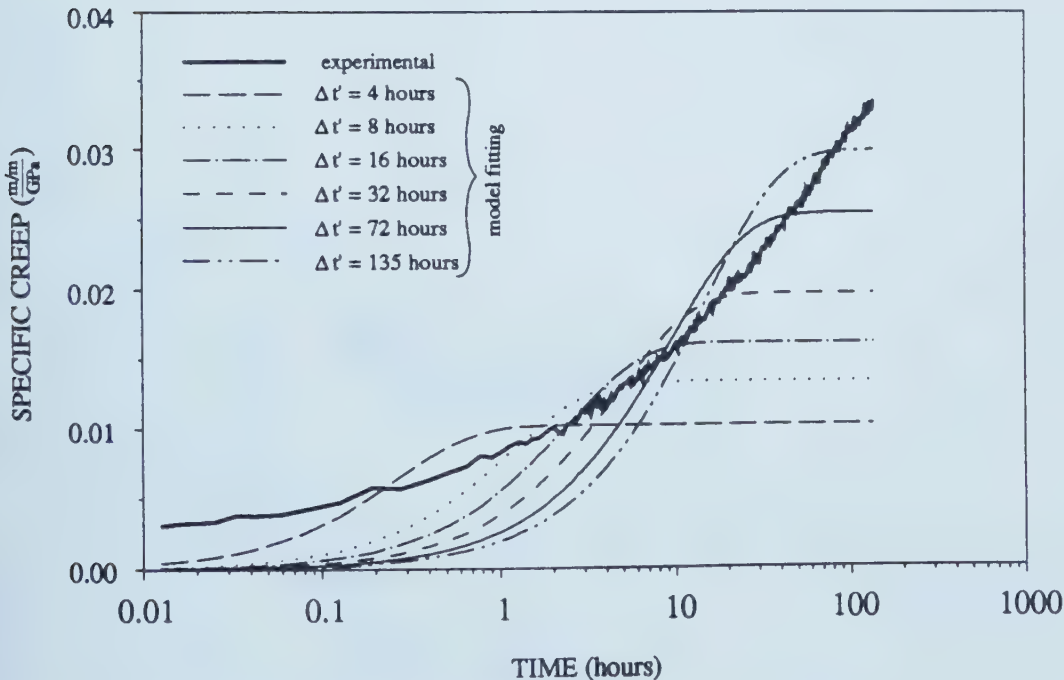


Figure 4.28 Measured and Calculated Values of Creep Test, CRSG78H

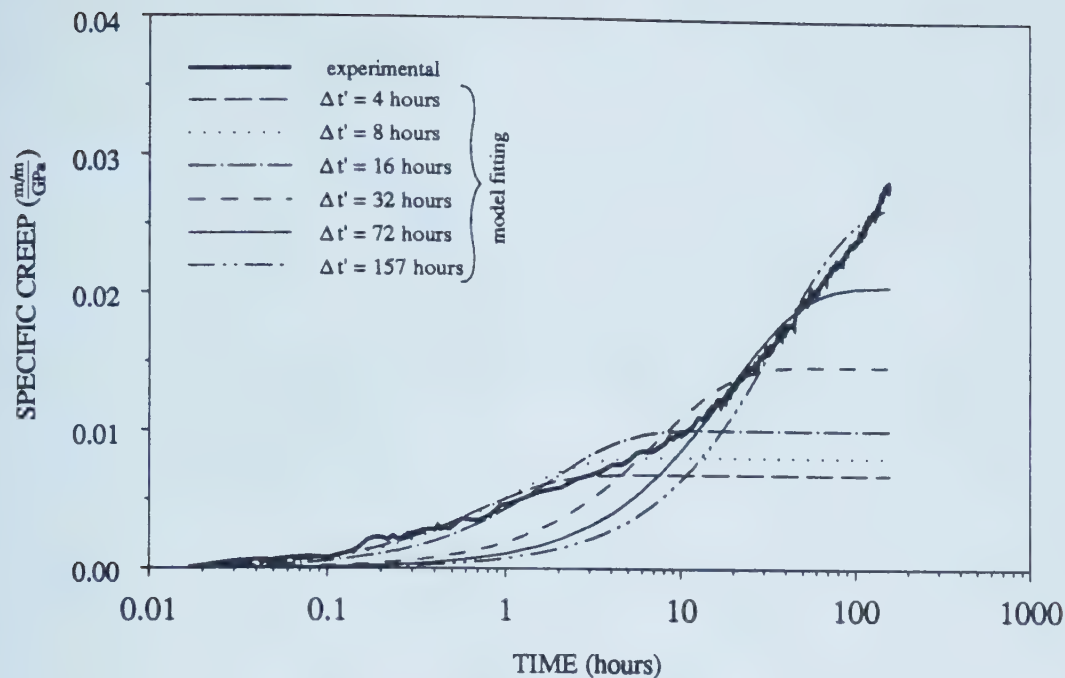


Figure 4.29 Measured and Calculated Values of Creep Test, CRS168H

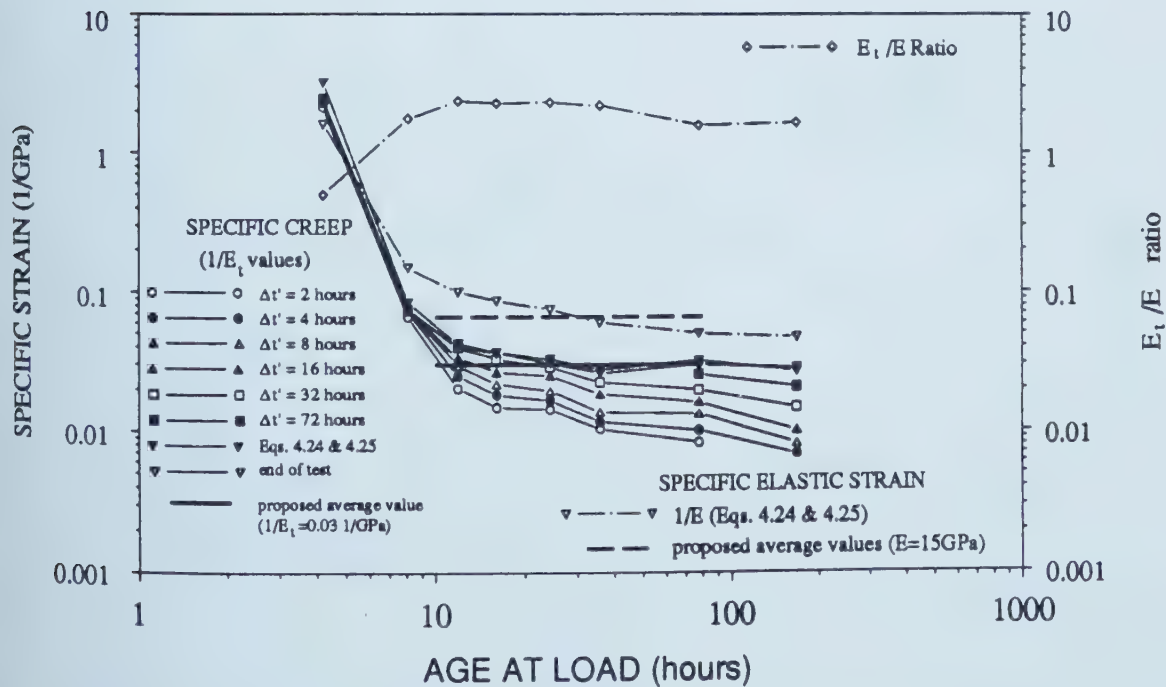


Figure 4.30 Summary of Specific Deformation Values, Creep Tests

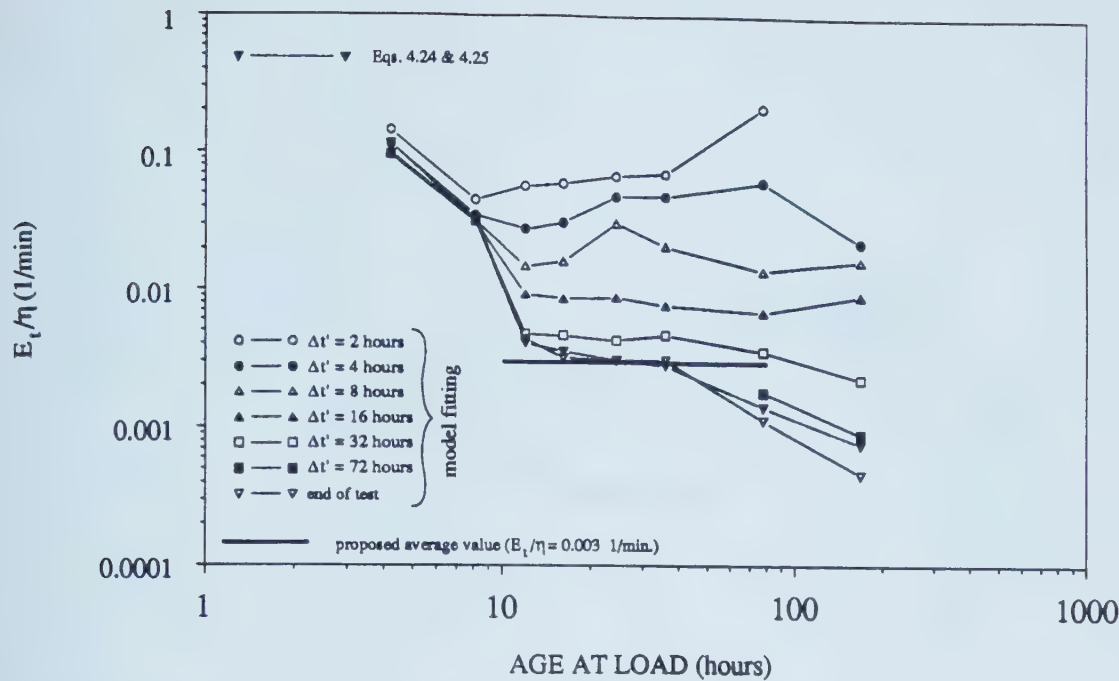


Figure 4.31 Summary of Viscosity Values, Creep Tests

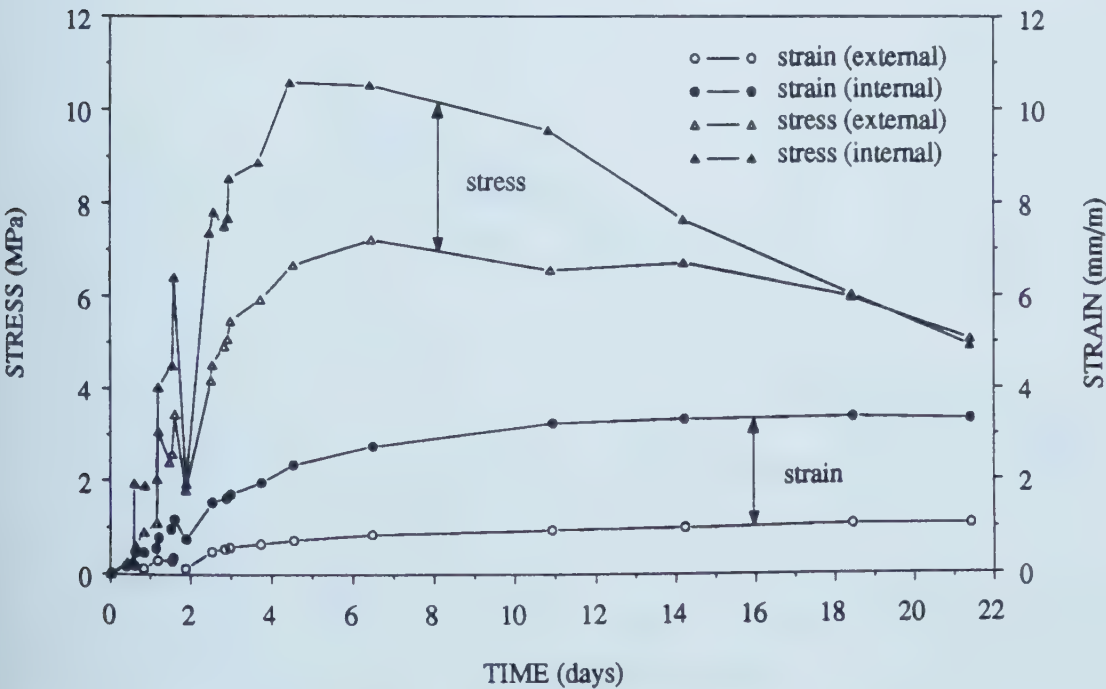


Figure 4.32 Strain Measured in the Lining of the Langener Tunnel and Calculated Stress (modified from Schubert, 1988)

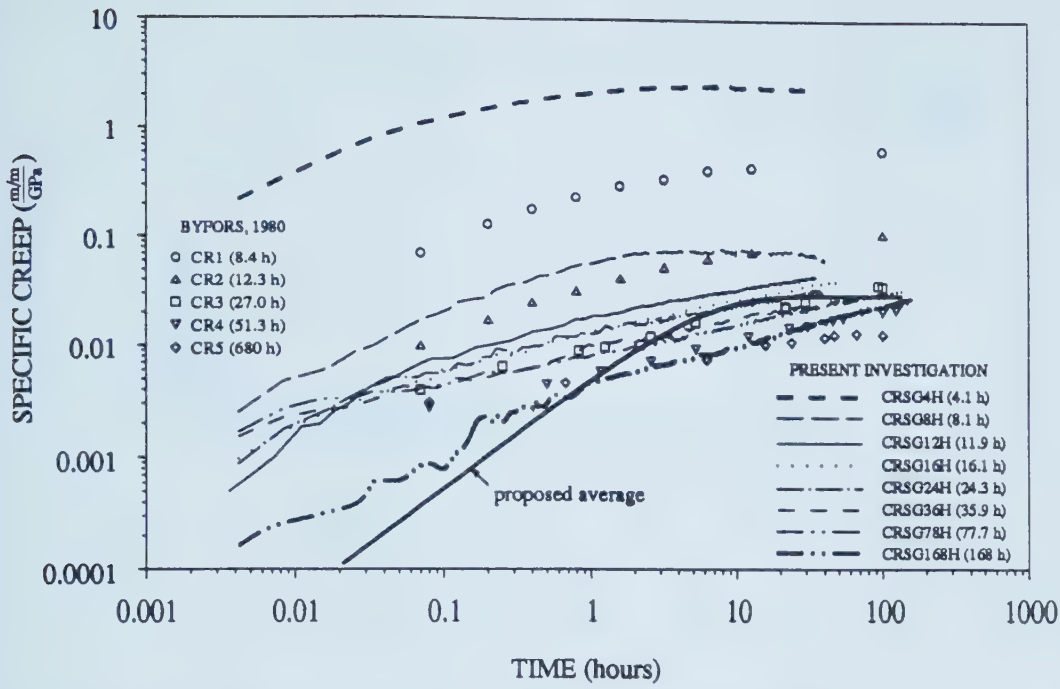


Figure 4.33 Comparison of Short Term Creep Tests with Published Data

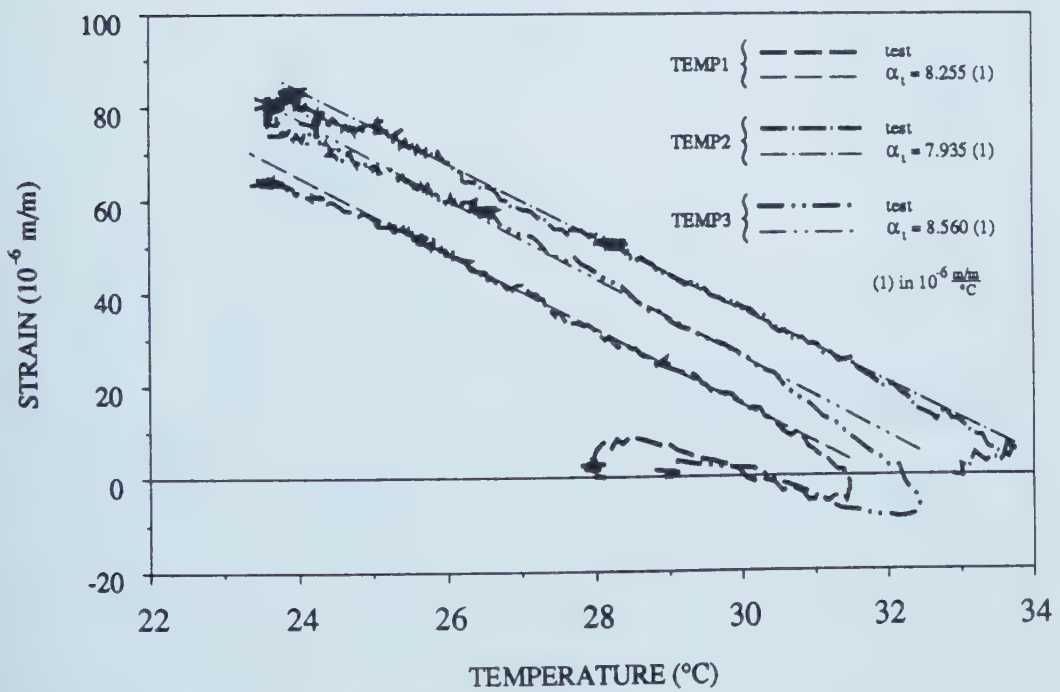


Figure 4.34 Evaluation of Thermal Coefficient of Expansion

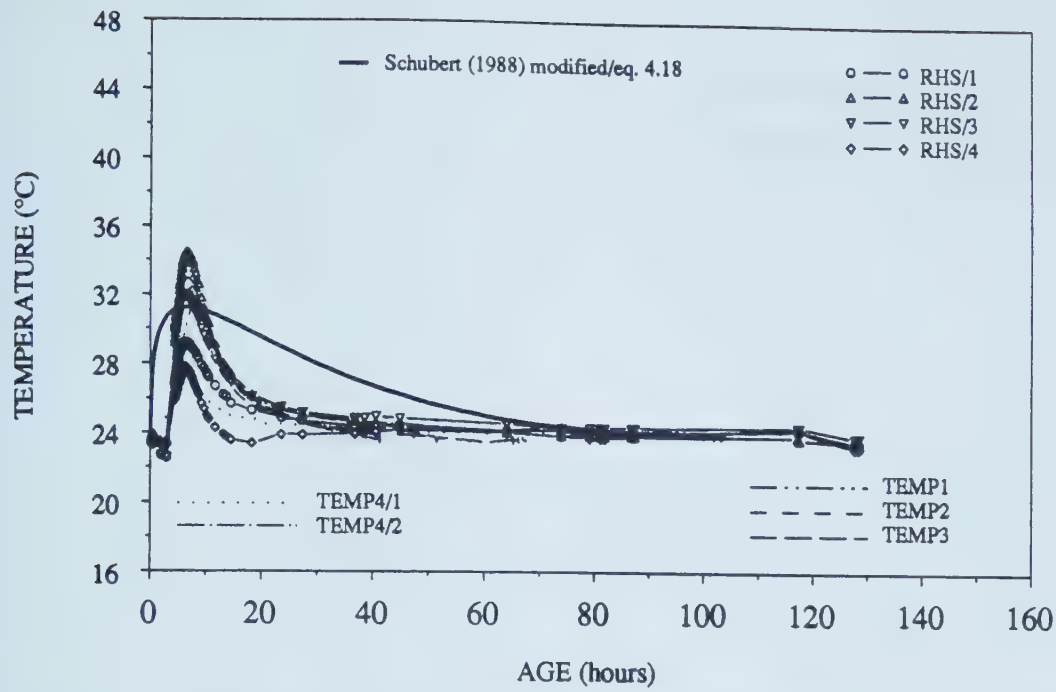


Figure 4.35 Temperature Development in Specimen Cast in Laboratory

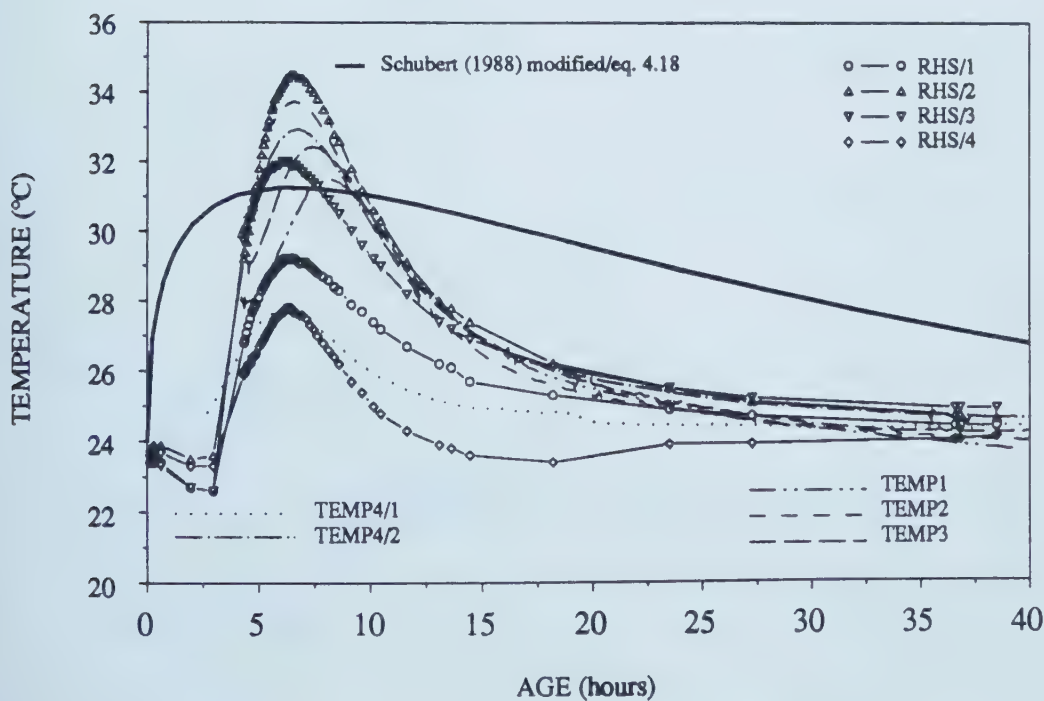


Figure 4.36 Temperature Development in Specimen Cast in Laboratory, Detail for the First Forty Hours

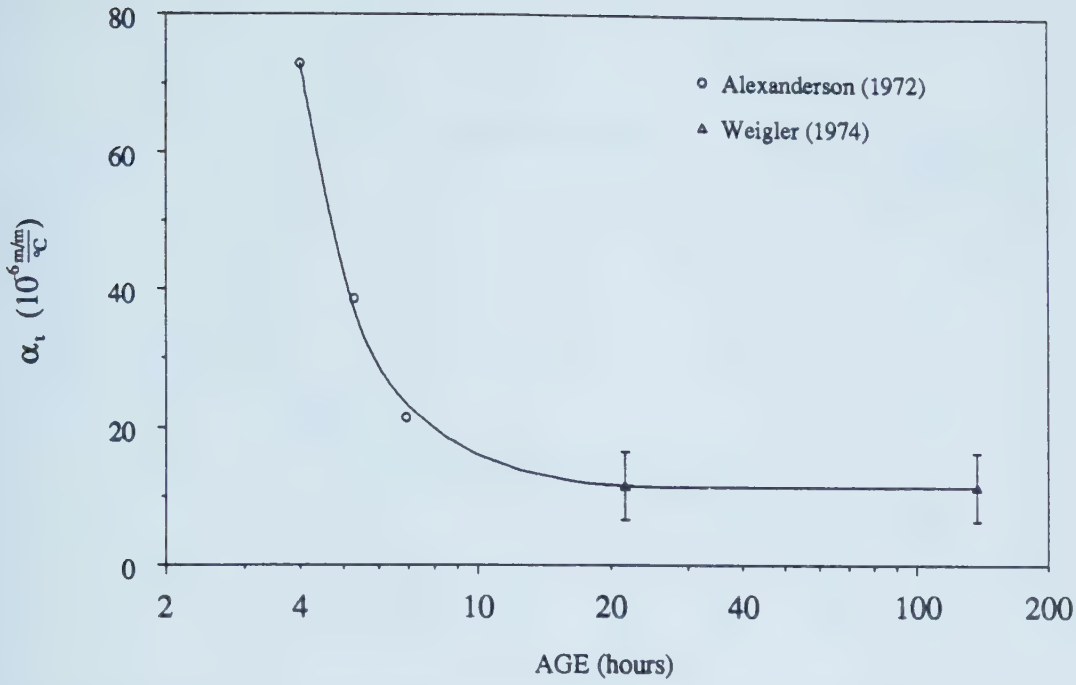


Figure 4.37 Age Dependency at Early Age for the Coefficient of Thermal Expansion Based on Data from Literature (modified from Byfors, 1980)

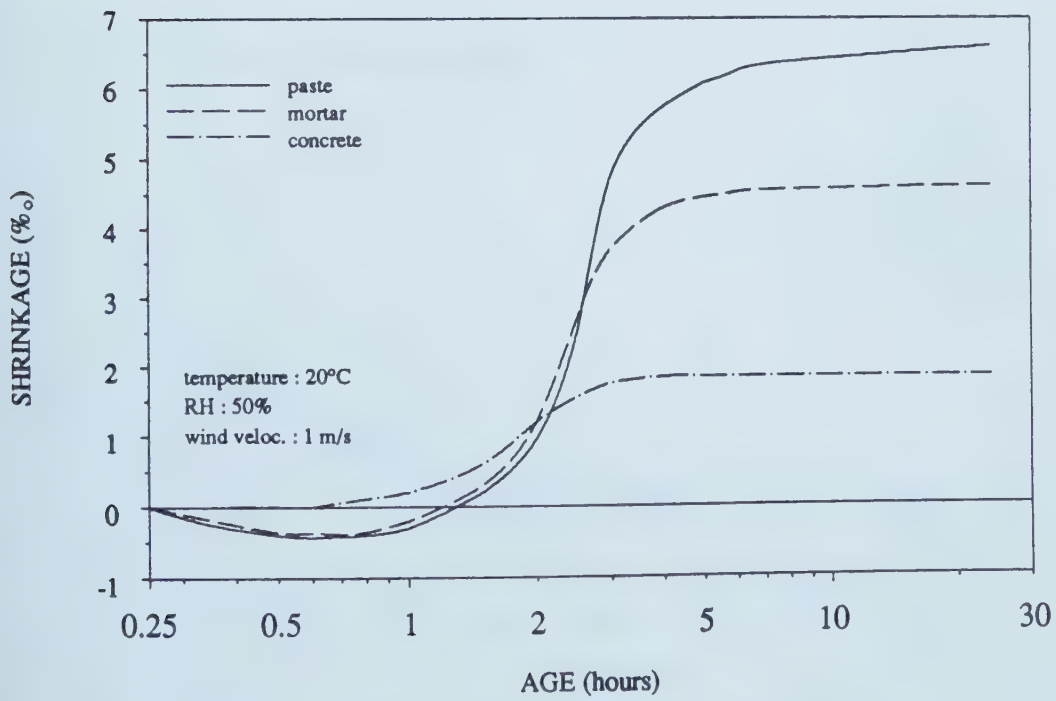


Figure 4.38 Plastic Shrinkage (modified from Vironnaud, 1960)

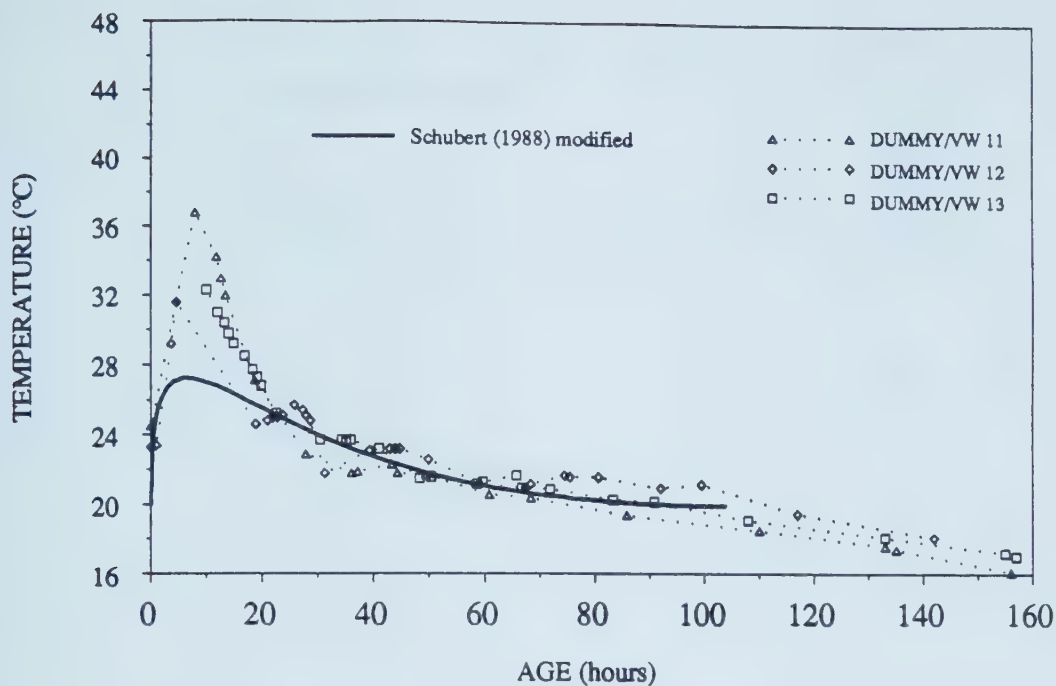


Figure 4.39 Temperature from Instruments Installed in Compensating Panels

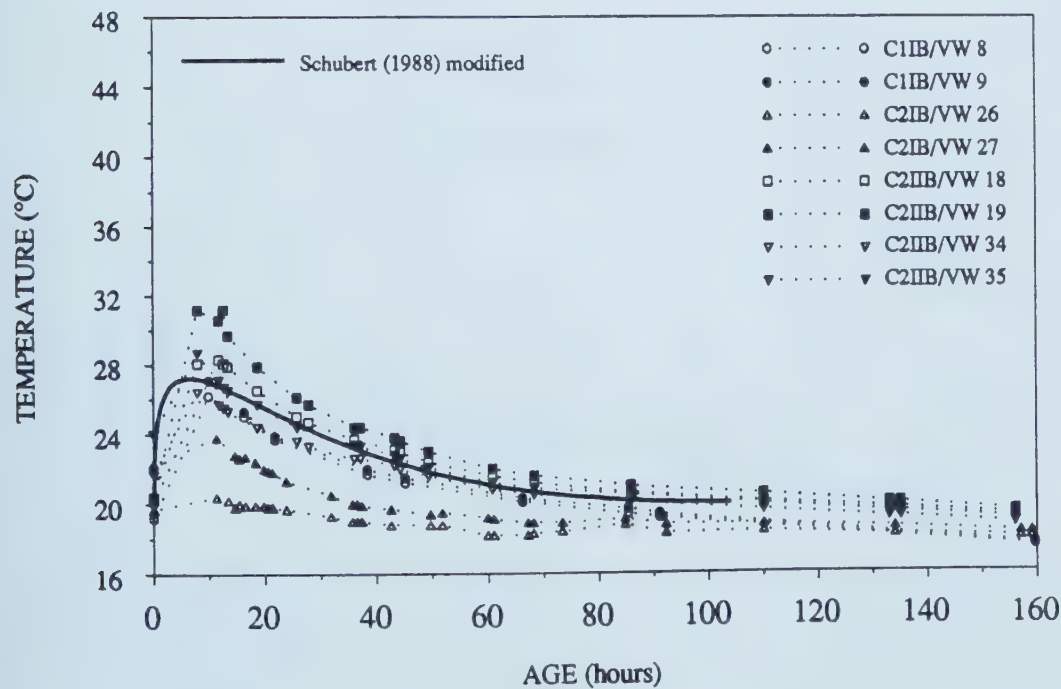


Figure 4.40 Temperature from Instruments Installed Close to the Tunnel Floor

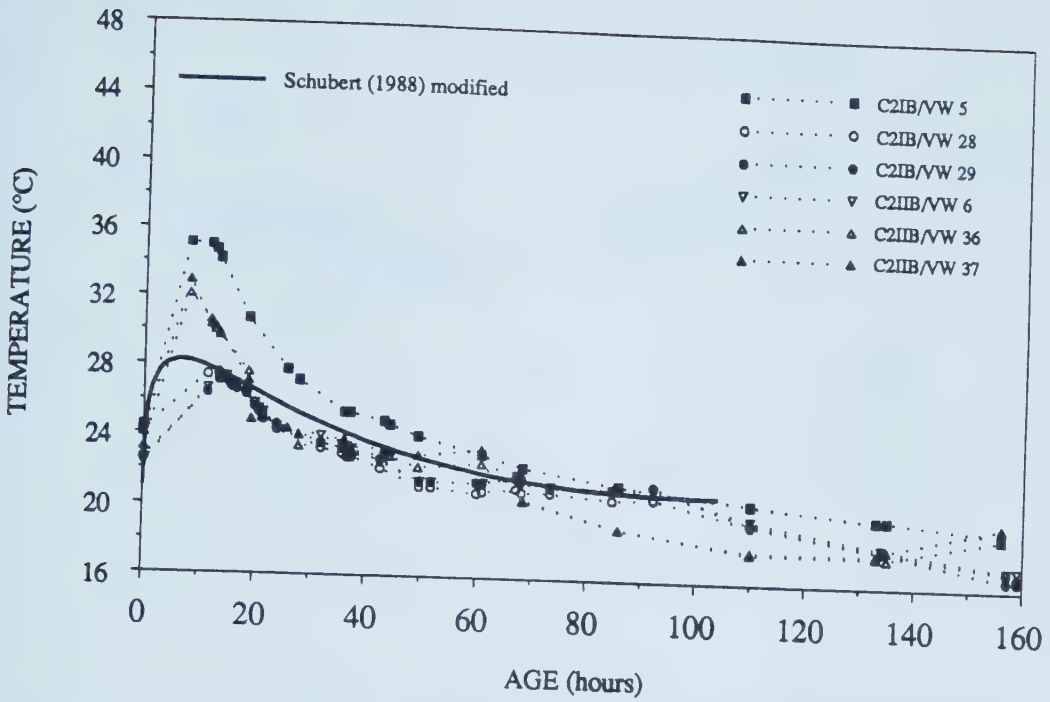


Figure 4.41 Temperature from Instruments Installed Close to the Tunnel Springline

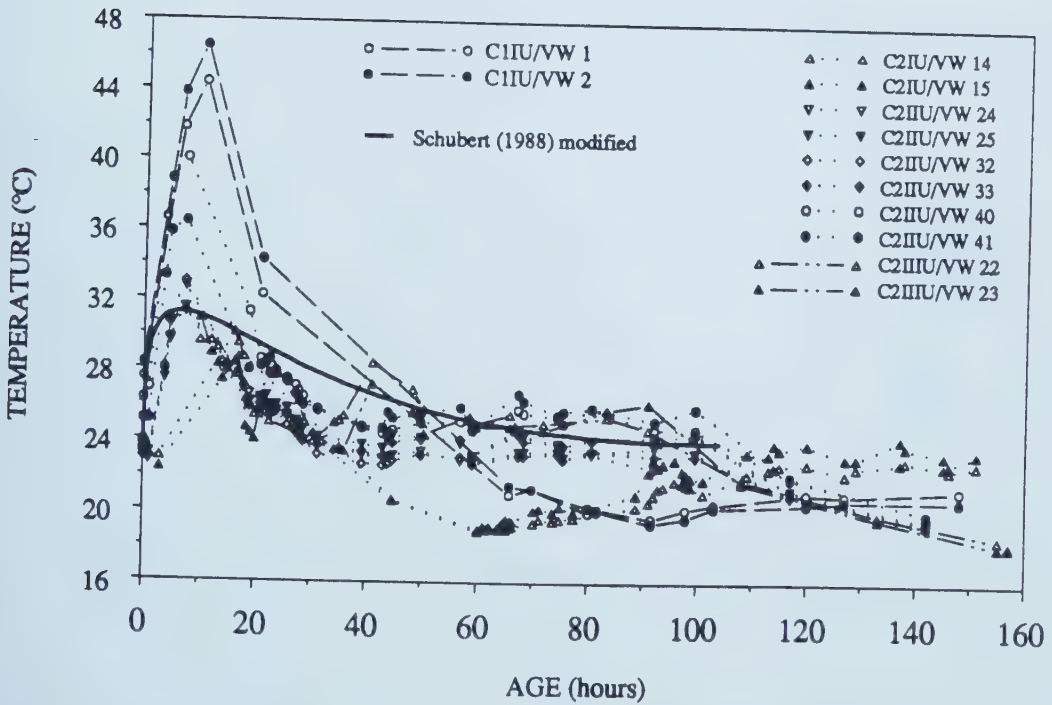


Figure 4.42 Temperature from Instruments Installed Close to the Tunnel Crown

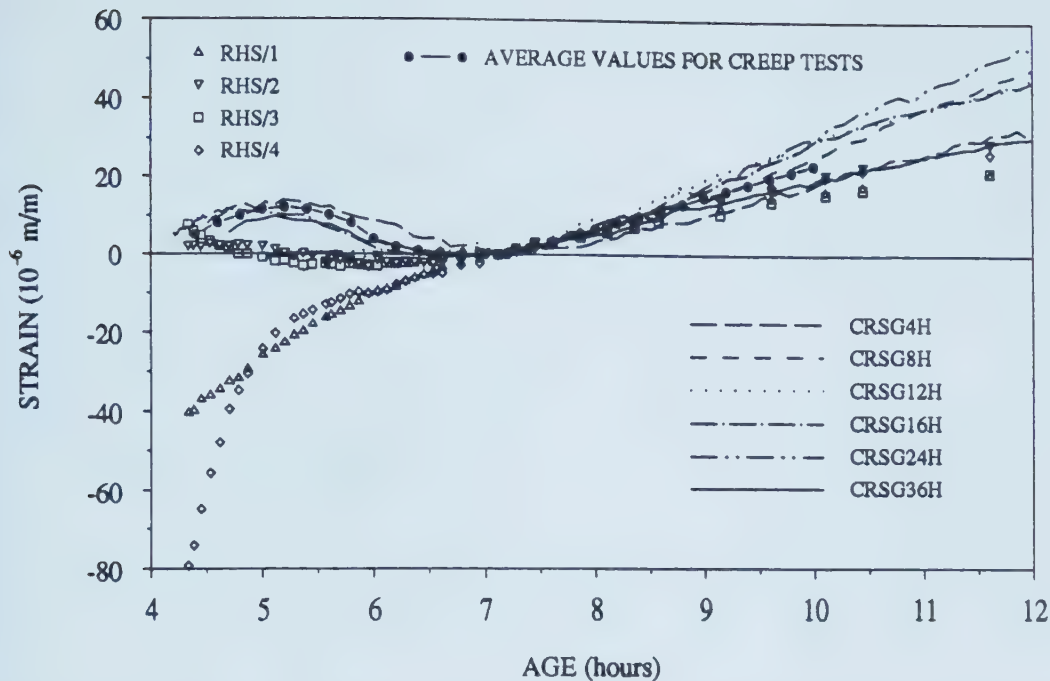


Figure 4.43 Deformation Development from Laboratory Specimens at Very Early Stages

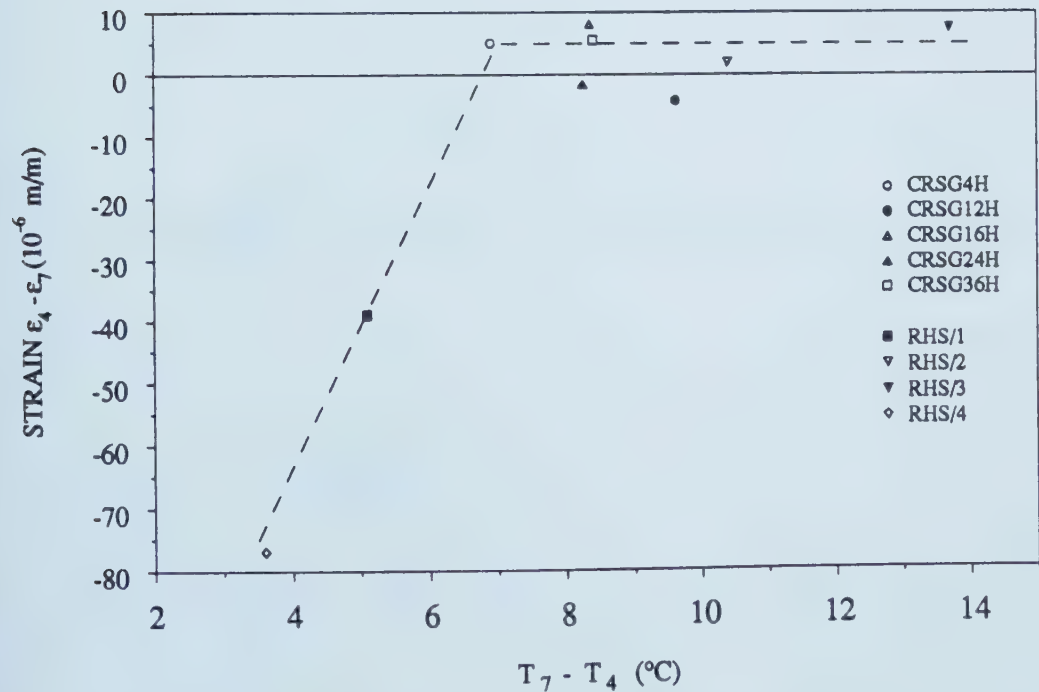


Figure 4.44 Estimation of Strain for the Interval 4 to 7 Hours Based on Temperature Difference

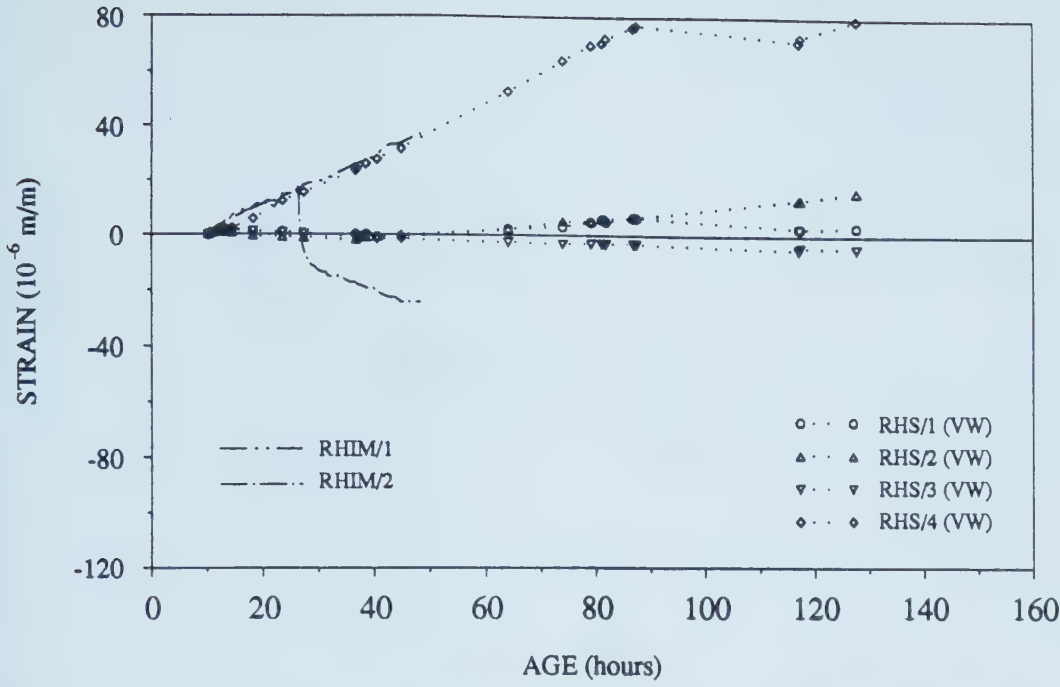


Figure 4.45 Shrinkage Measured in Laboratory for Specimens Subjected to Different Environmental Conditions

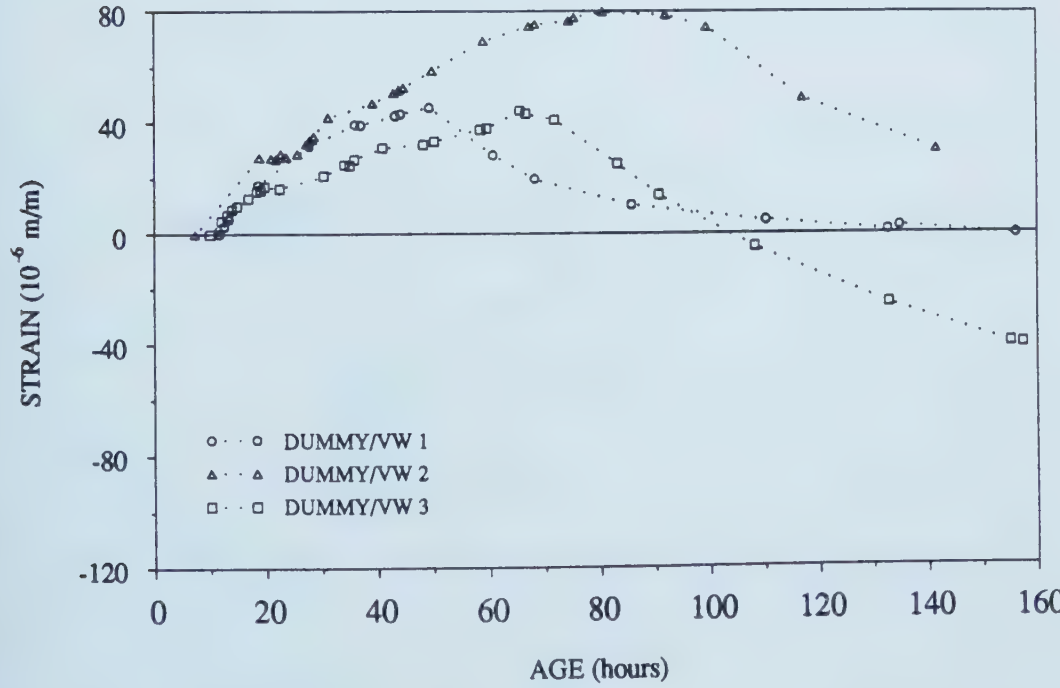


Figure 4.46 Shrinkage from Instruments Installed in Compensating Panels

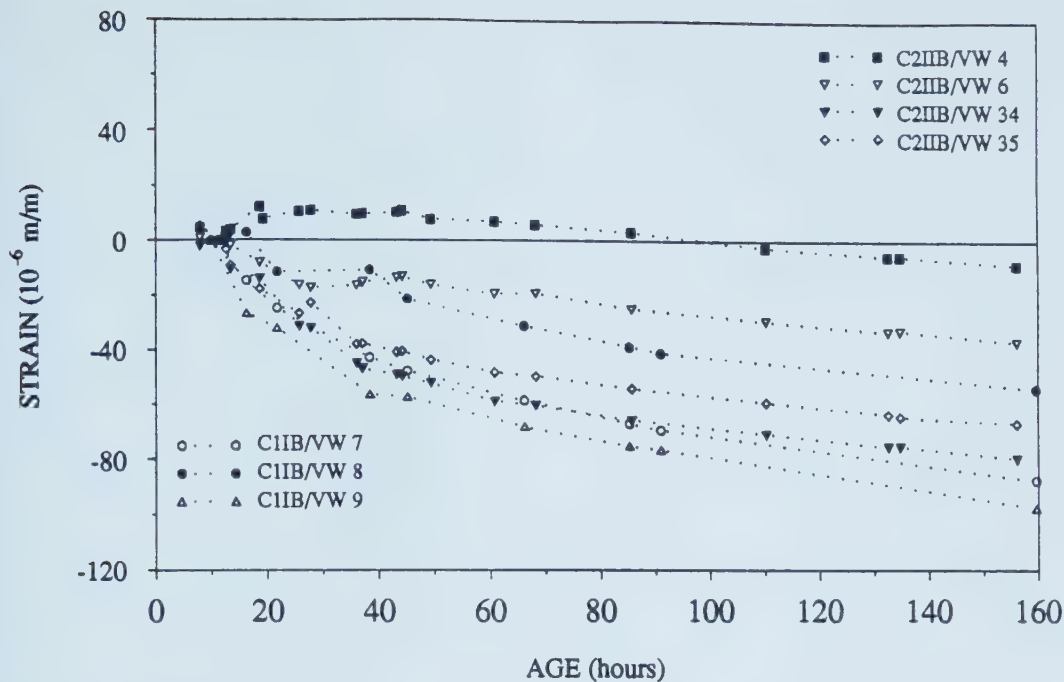


Figure 4.47 Shrinkage from Instruments Installed in Longitudinal Direction of the Tunnel, Close to the Floor

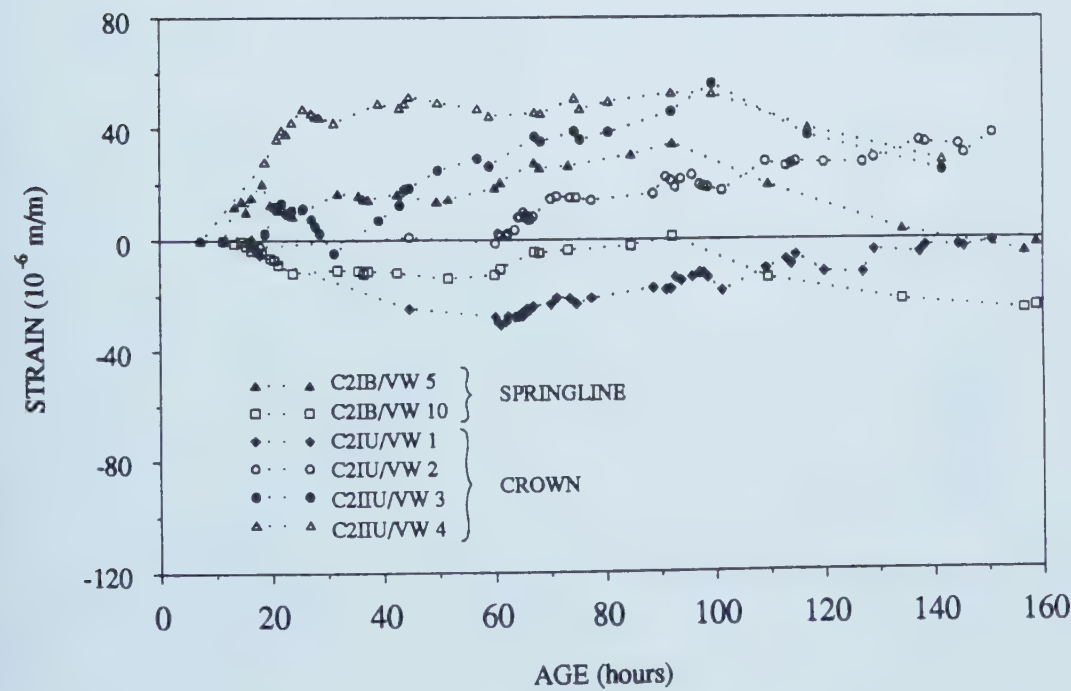


Figure 4.48 Shrinkage from Instruments Installed in Longitudinal Direction of the Tunnel, Close to the Springline and to the Crown

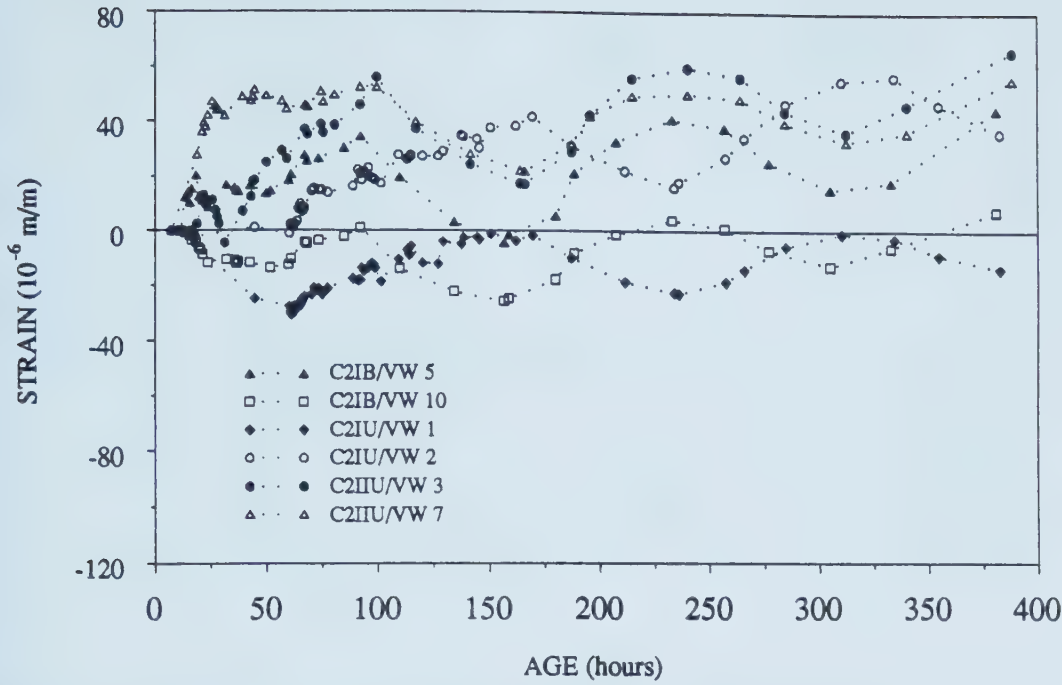


Figure 4.49 Shrinkage from Instruments Installed in Longitudinal Direction of the Tunnel, Close to the Springline and to Crown: Long Term Oscillation

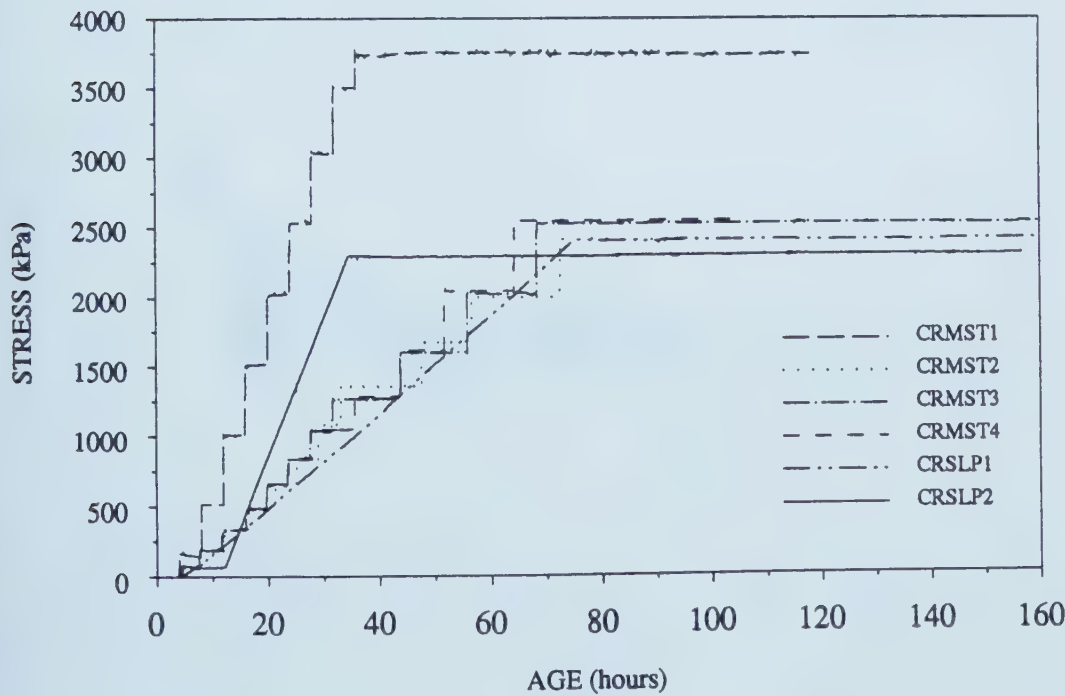


Figure 4.50 Load Path Applied in Stress Controlled Tests

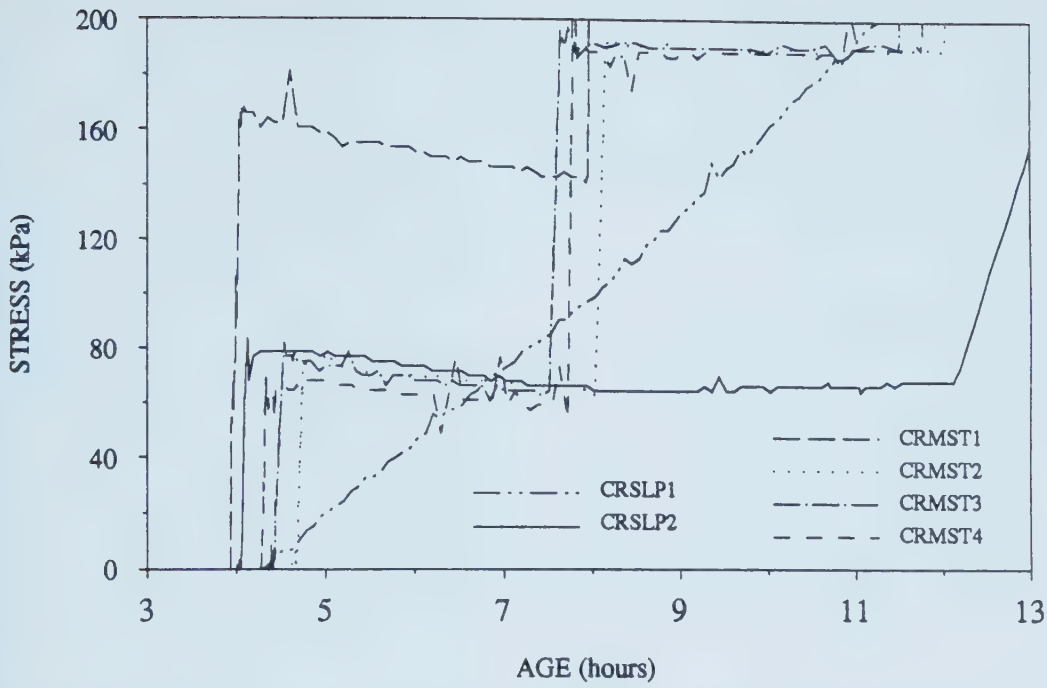


Figure 4.51 Load Deviations in Stress Controlled Tests at Early Stages

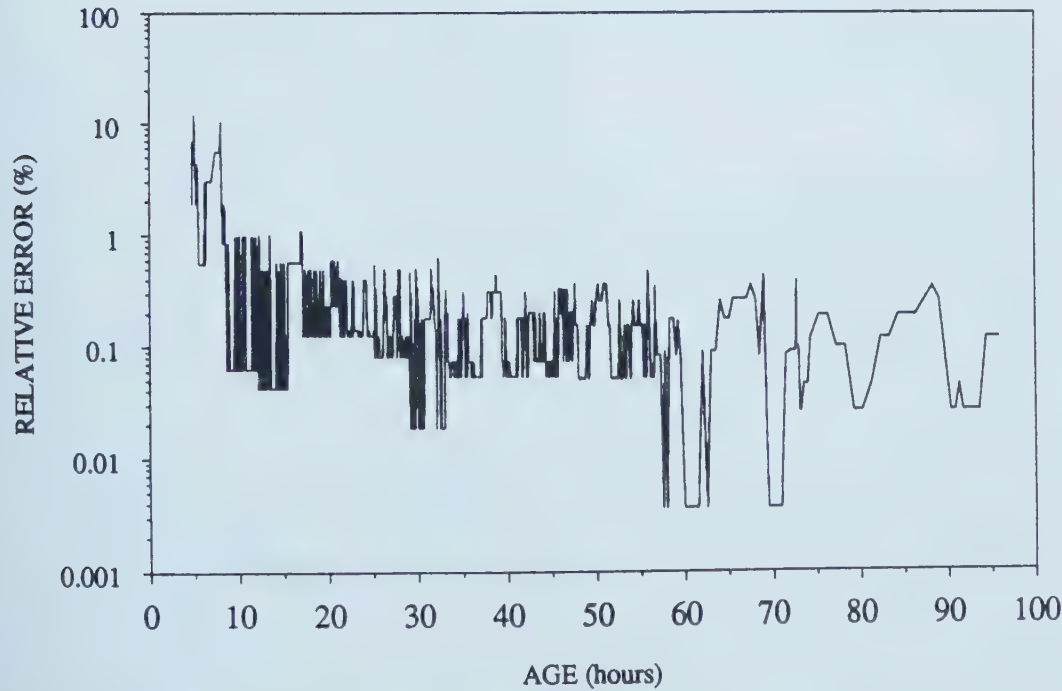


Figure 4.52 Relative Error of Applied Load, Test CRSLP2

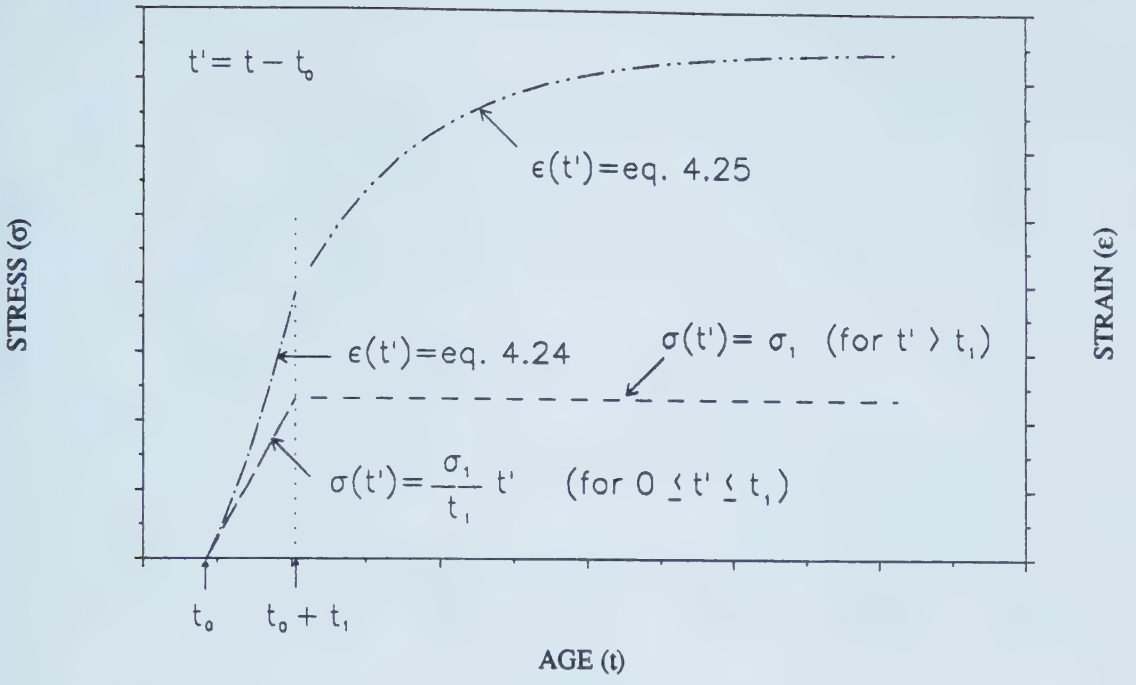


Figure 4.53 Strain Development for Load Applied According to Equation 4.19

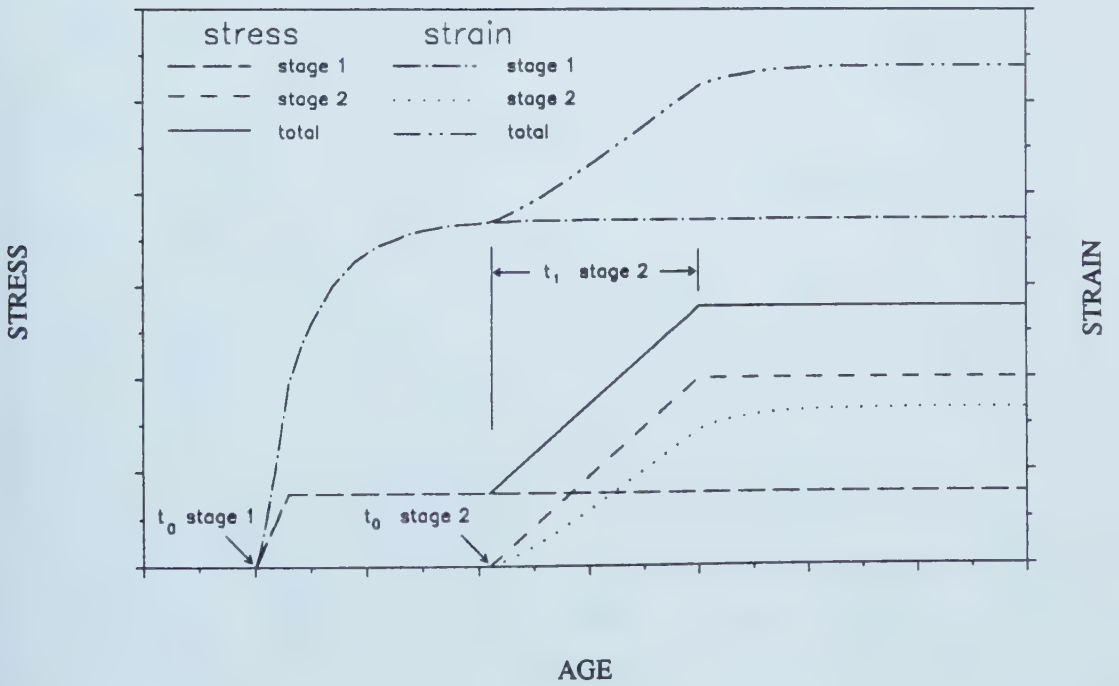


Figure 4.54 Superposition of Strains of Two Load Increments

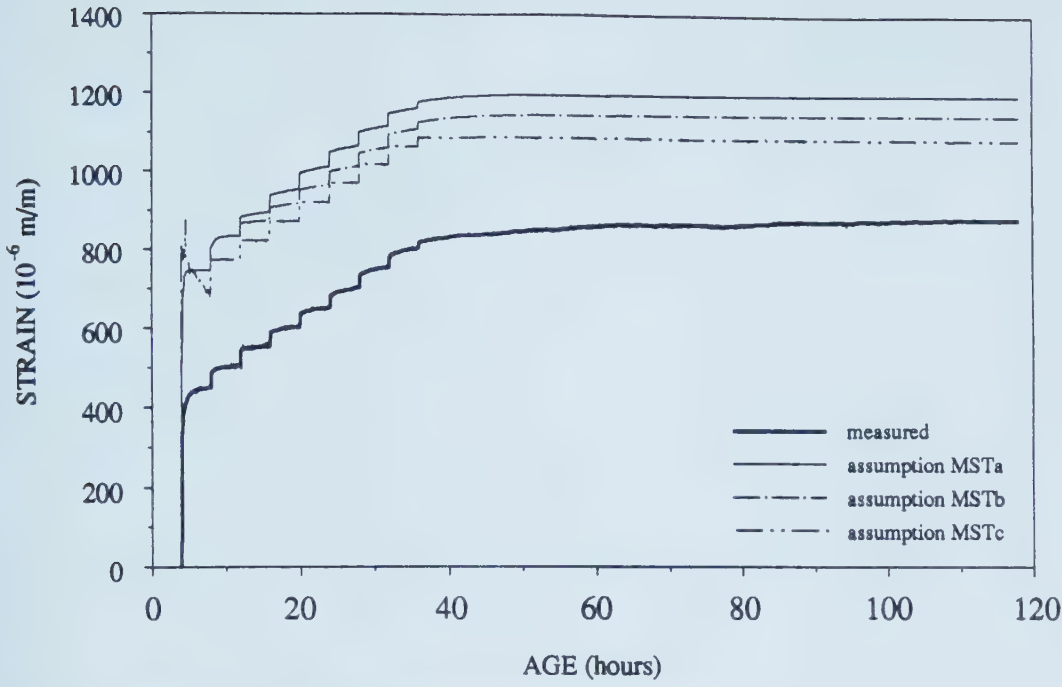


Figure 4.55 Measured and Calculated Strains, Test CRMST1

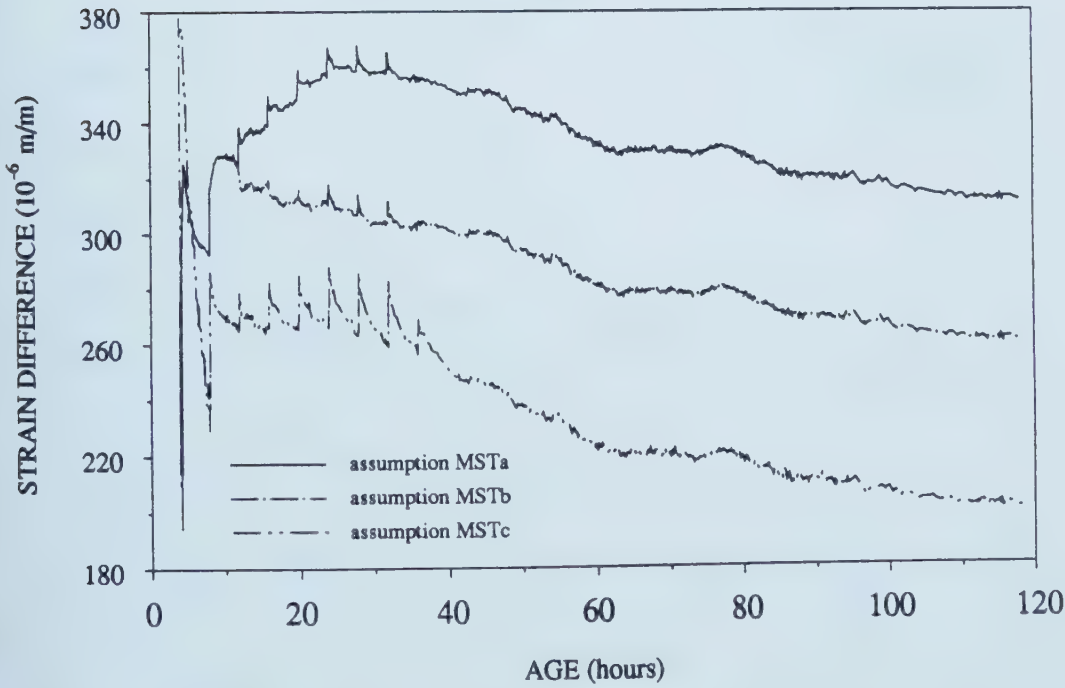


Figure 4.56 Difference of Measured and Calculated Strains, Test CRMST1

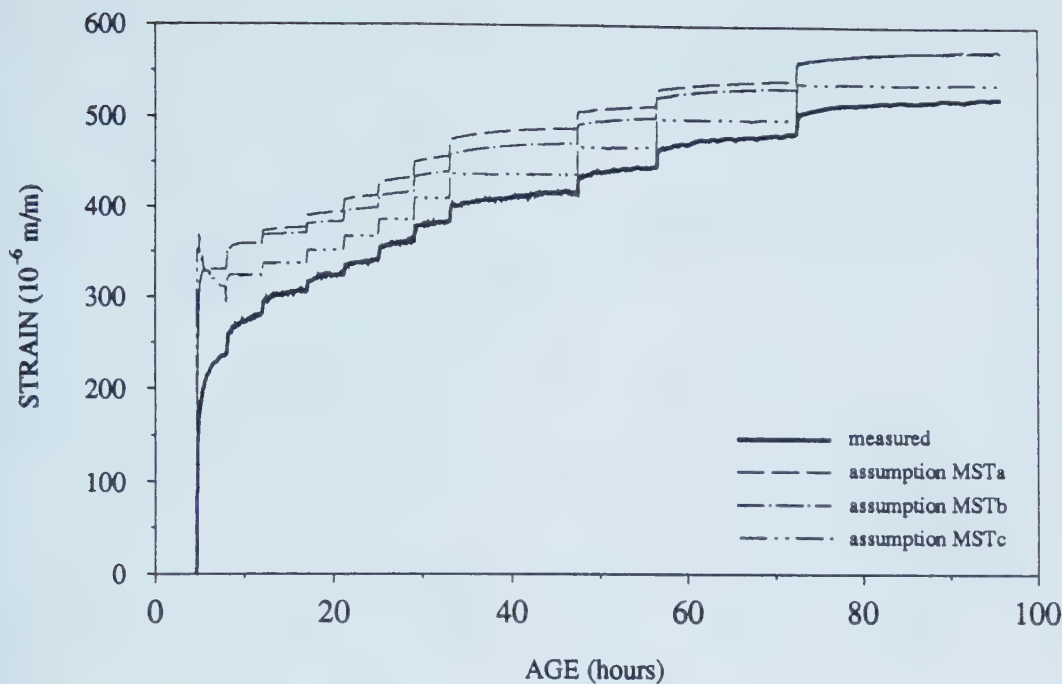


Figure 4.57 Measured and Calculated Strains, Test CRMST2

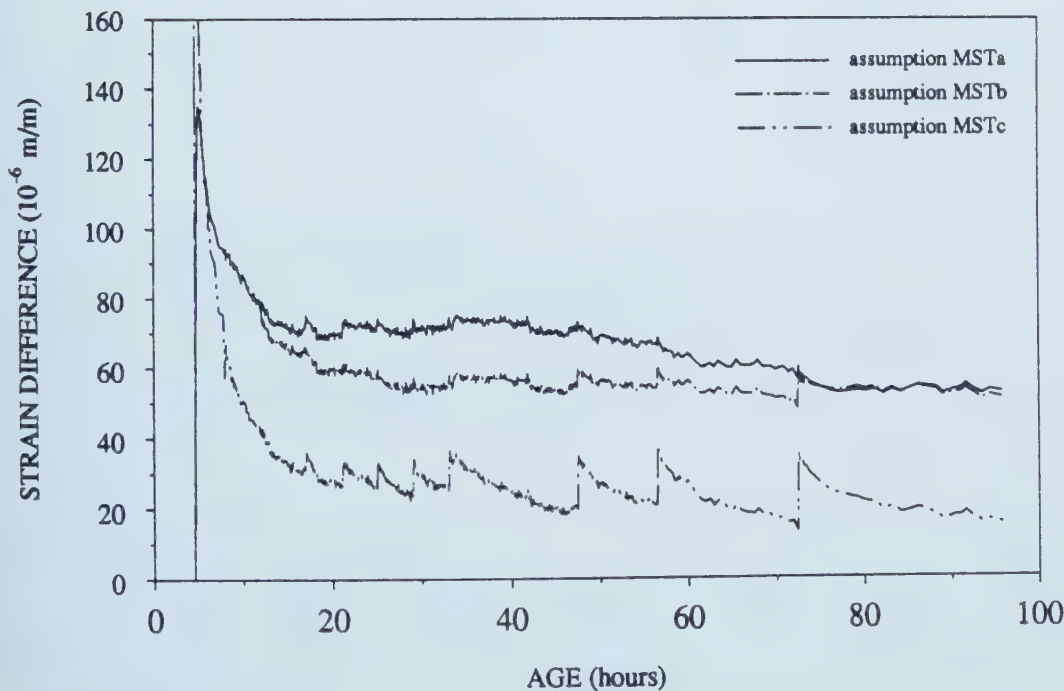


Figure 4.58 Difference of Measured and Calculated Strains, Test CRMST2

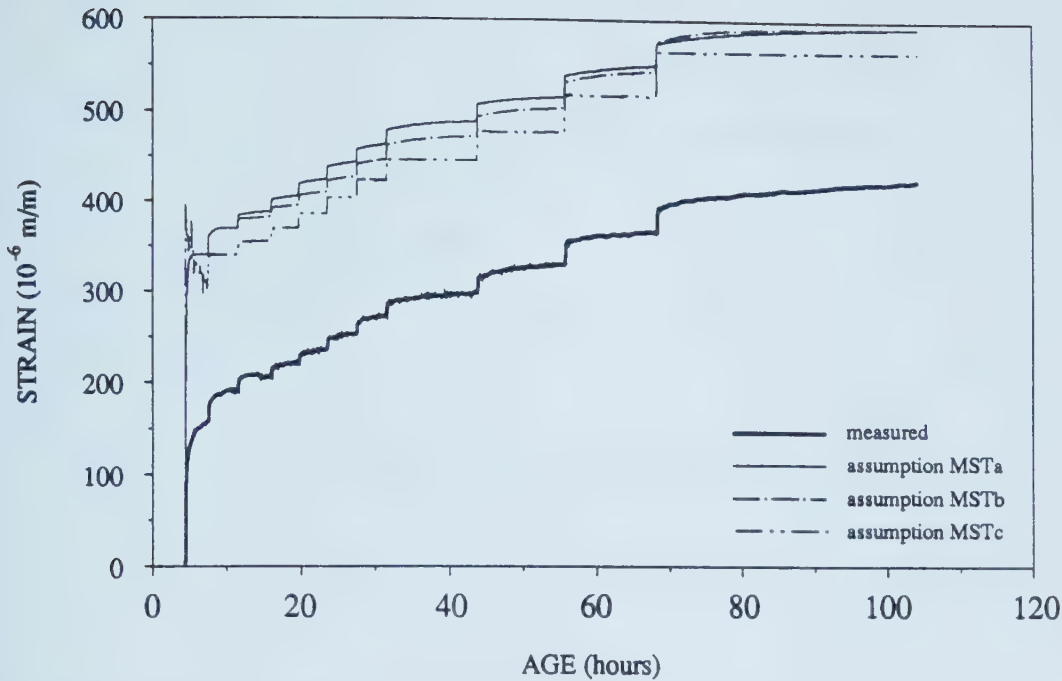


Figure 4.59 Measured and Calculated Strains, Test CRMST3

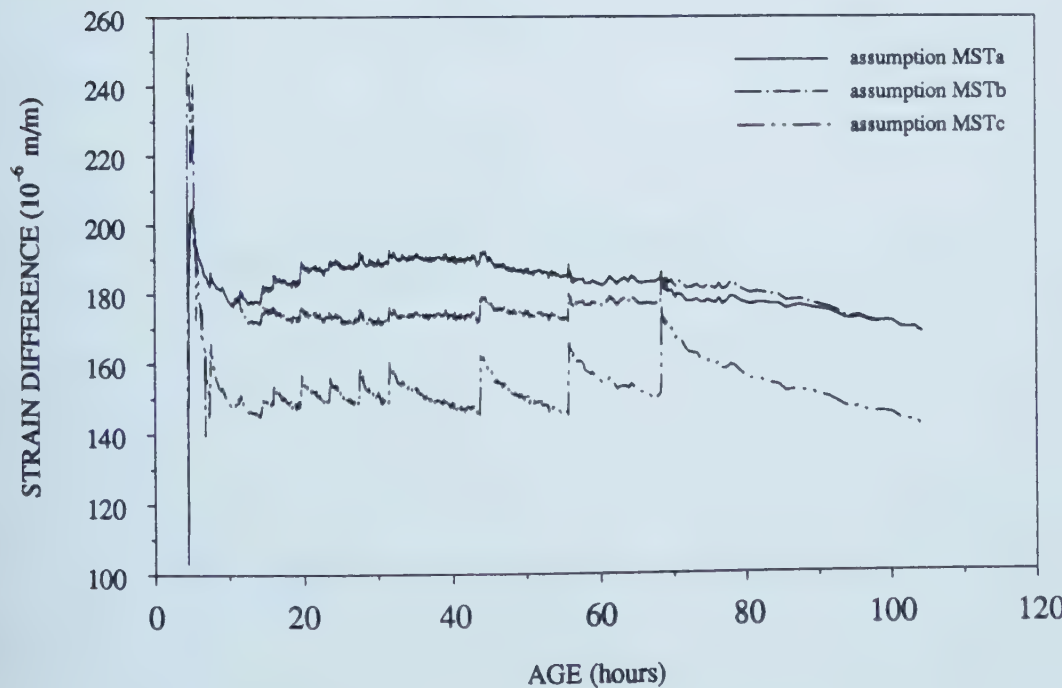


Figure 4.60 Difference of Measured and Calculated Strains, Test CRMST3

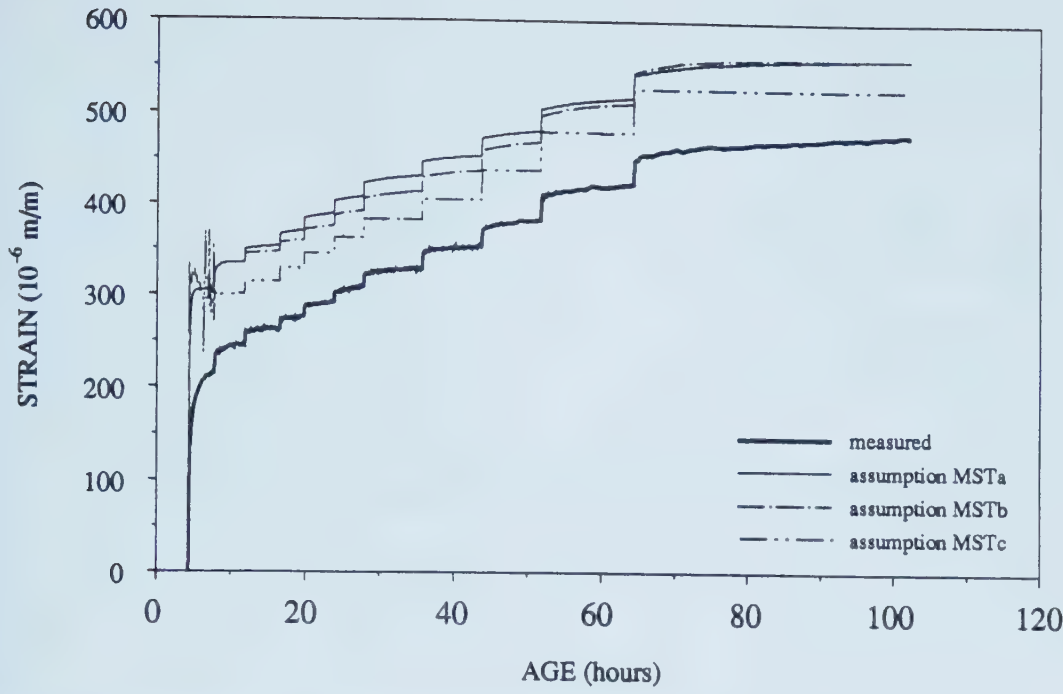


Figure 4.61 Measured and Calculated Strains, Test CRMST4

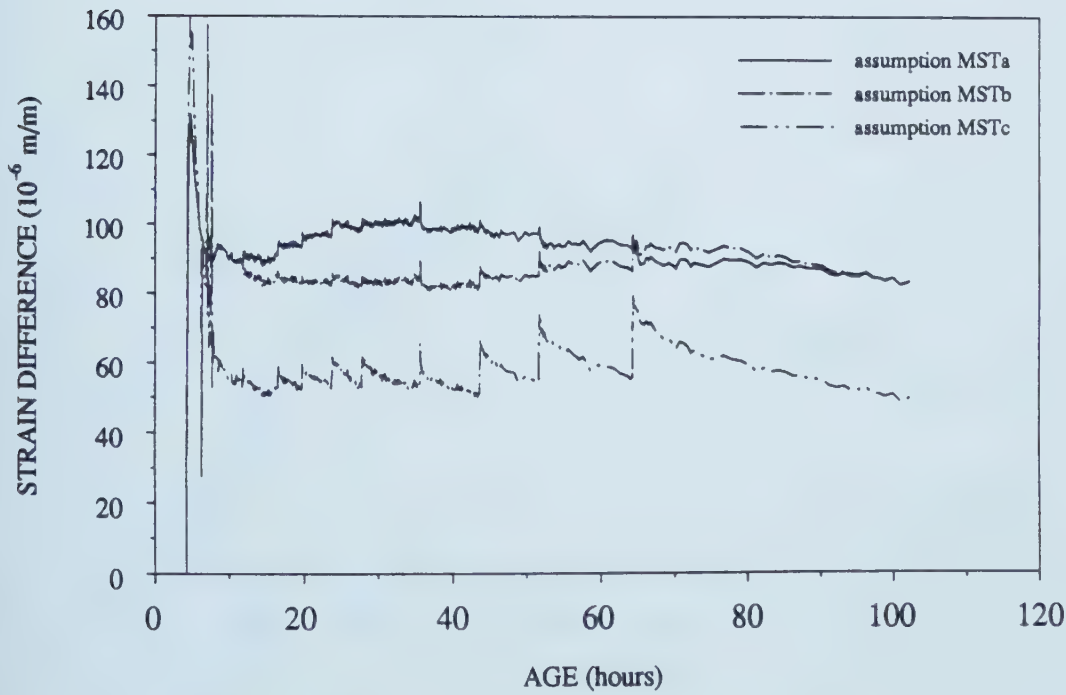


Figure 4.62 Difference of Measured and Calculated Strains, Test CRMST4

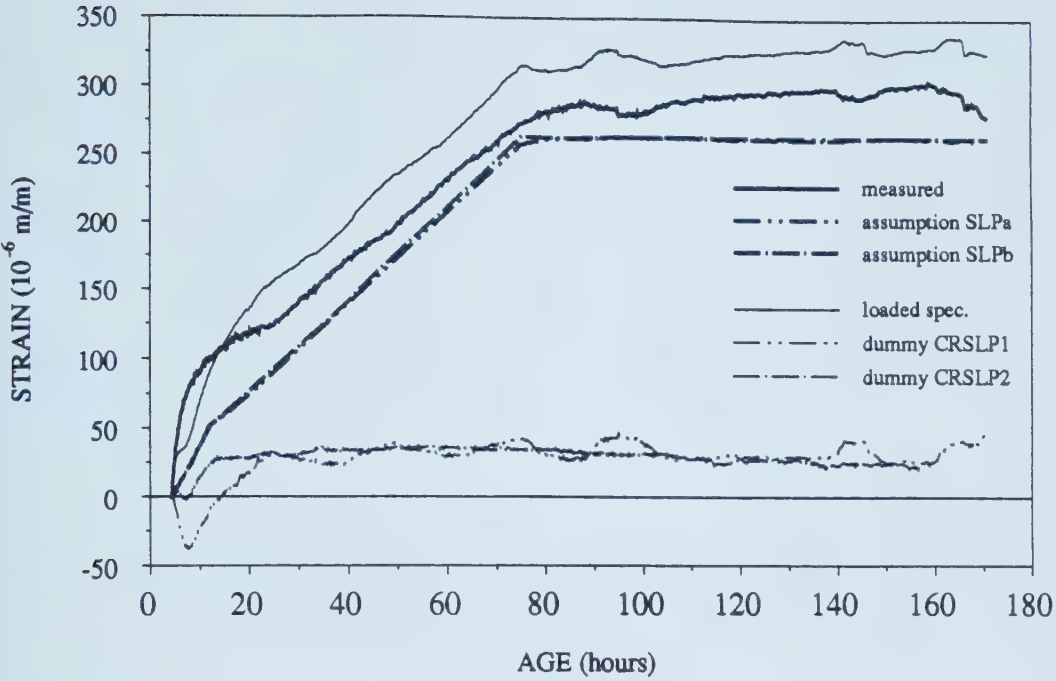


Figure 4.63 Measured and Calculated Strains, Test CRSLP1

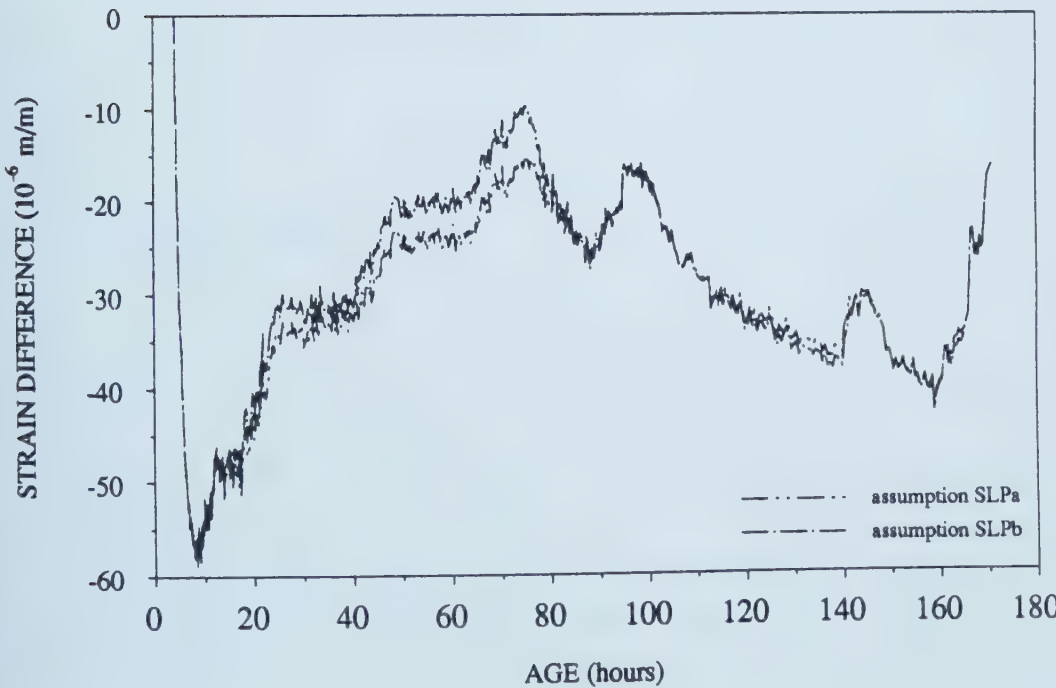


Figure 4.64 Difference of Measured and Calculated Strains, Test CRSLP1

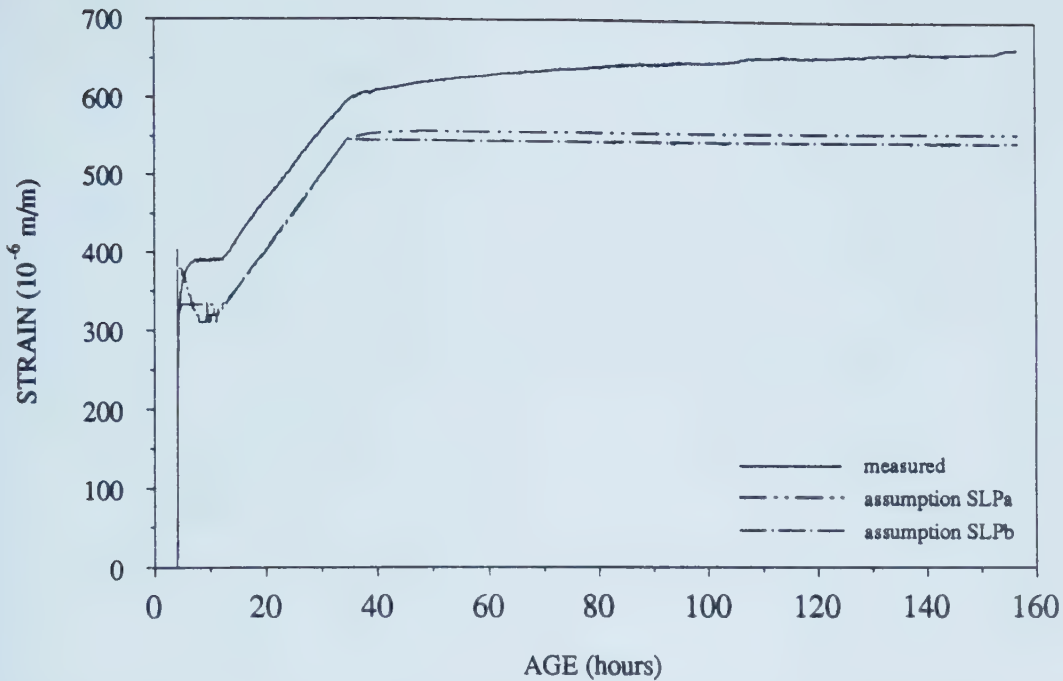


Figure 4.65 Measured and Calculated Strains, Test CRSLP2

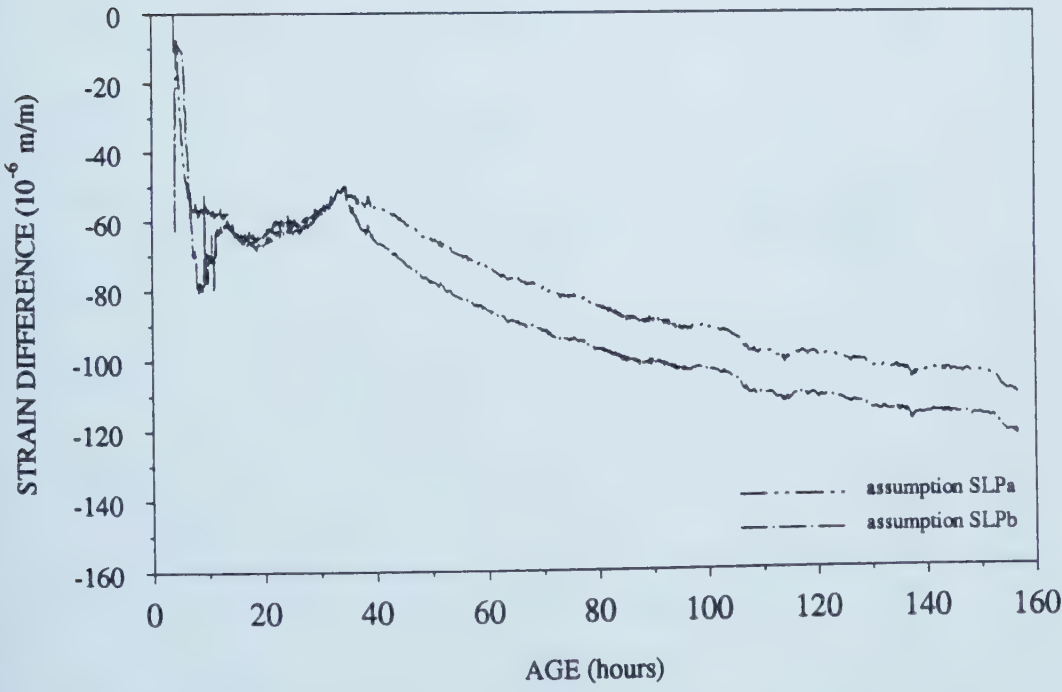


Figure 4.66 Difference of Measured and Calculated Strains, Test CRSLP2

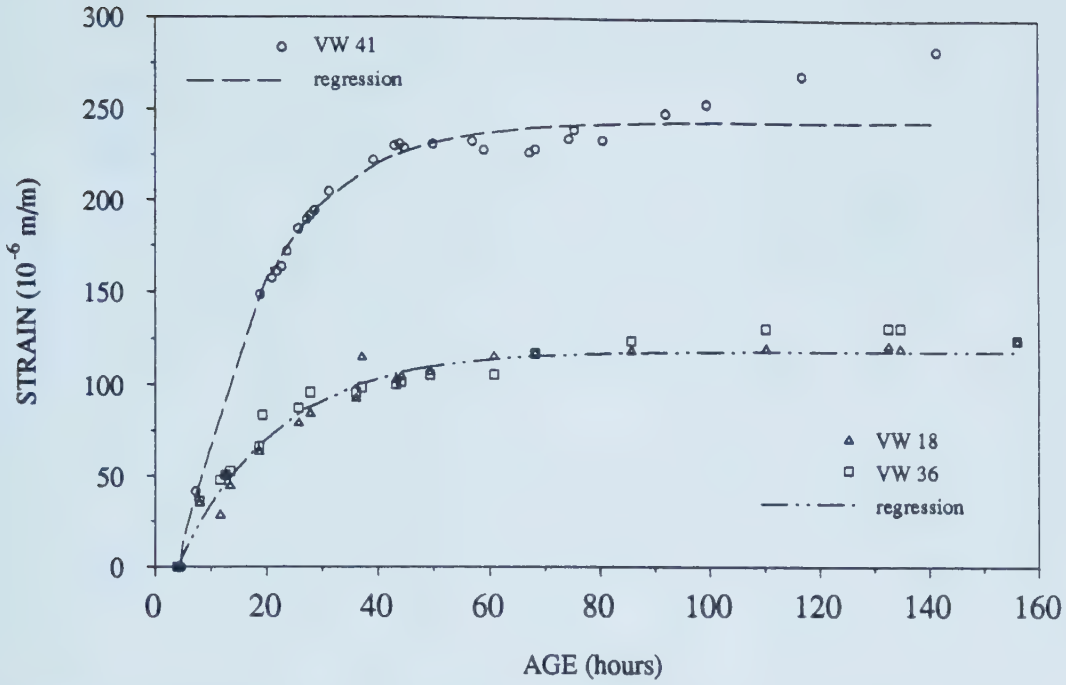


Figure 4.67 Typical Strain Development Observed in Instruments Installed in the Tunnel Lining and Applied in Strain Controlled Tests

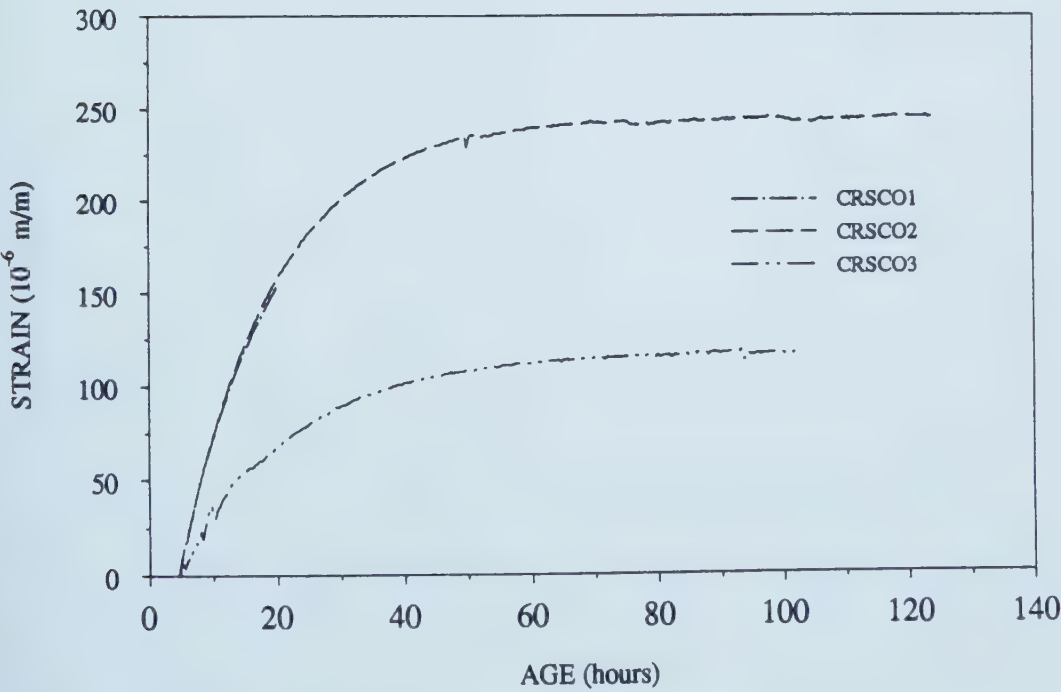


Figure 4.68 Deformations Measured in Strain Controlled Tests

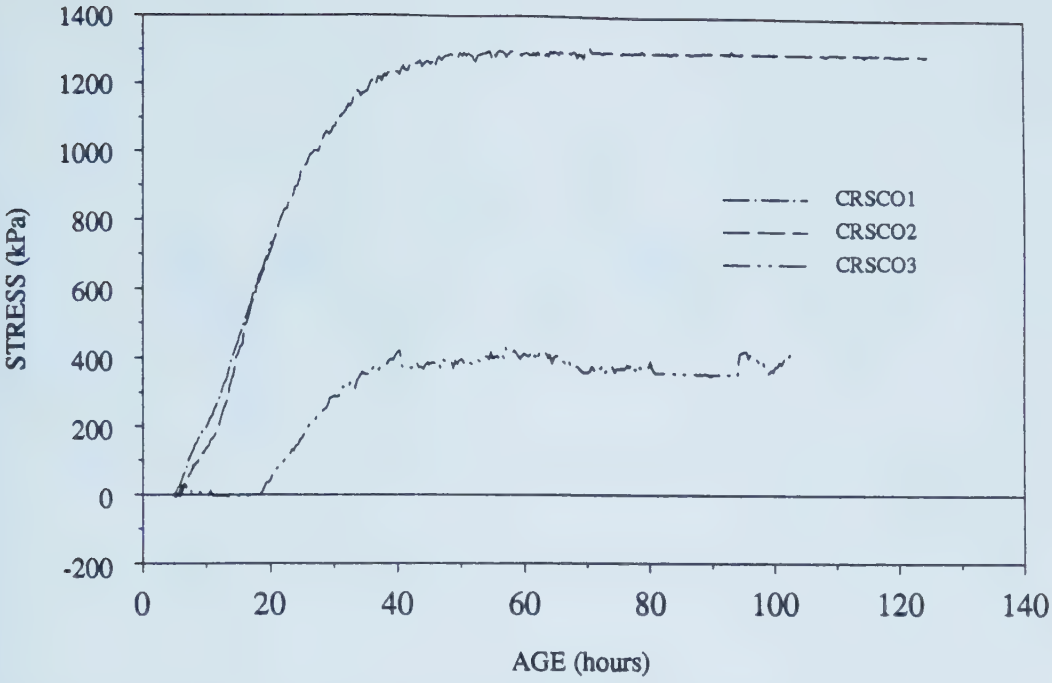


Figure 4.69 Stress Measured in Strain Controlled Tests

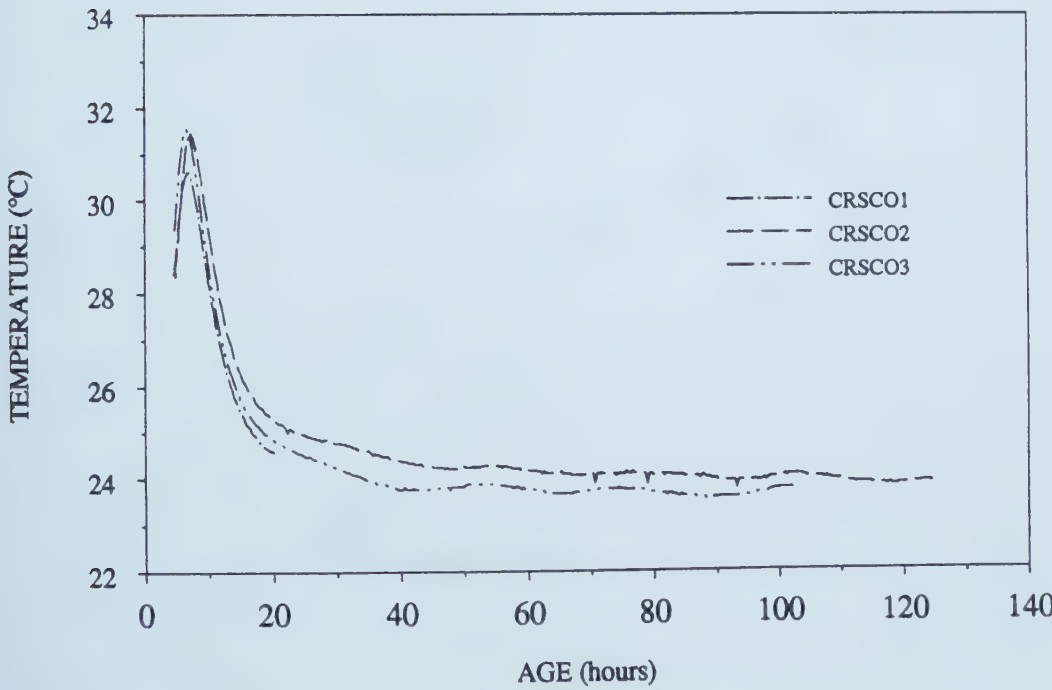


Figure 4.70 Temperature of the Specimens in Strain Controlled Tests

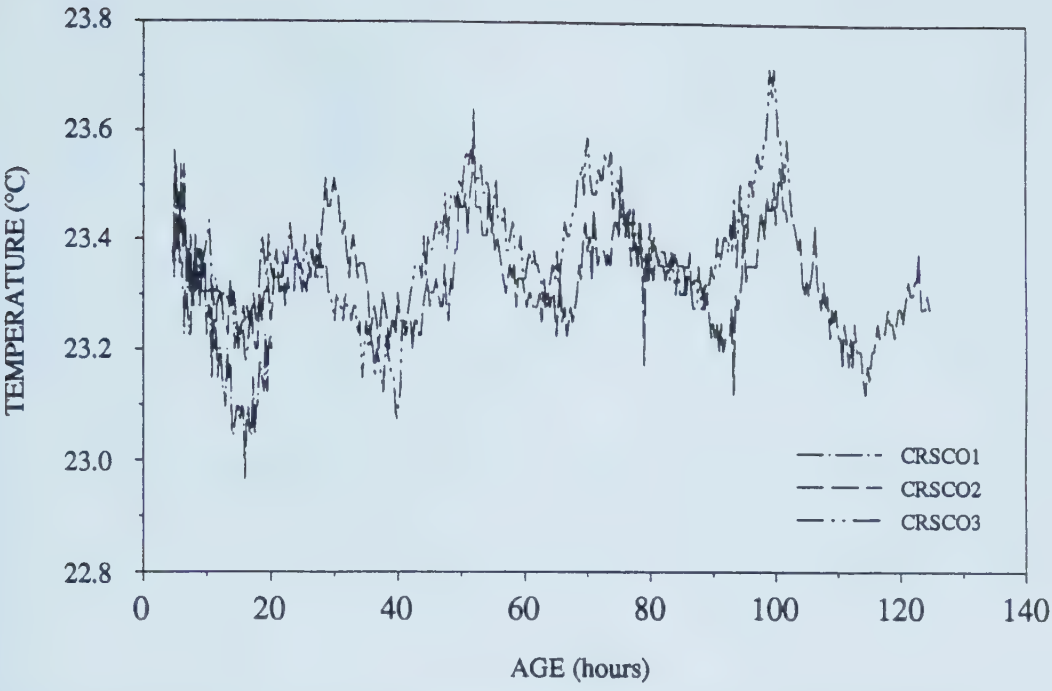


Figure 4.71 Temperature of the Air During Strain Controlled Tests

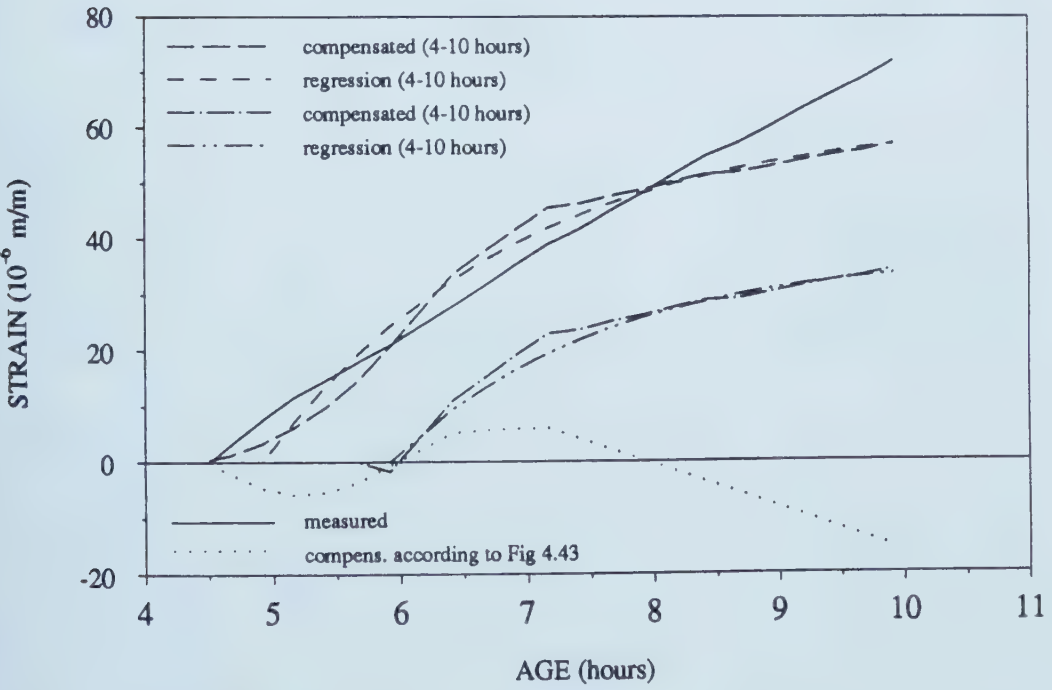


Figure 4.72 Measured and Assumed Strains before 10 Hours, Test CRSCO1

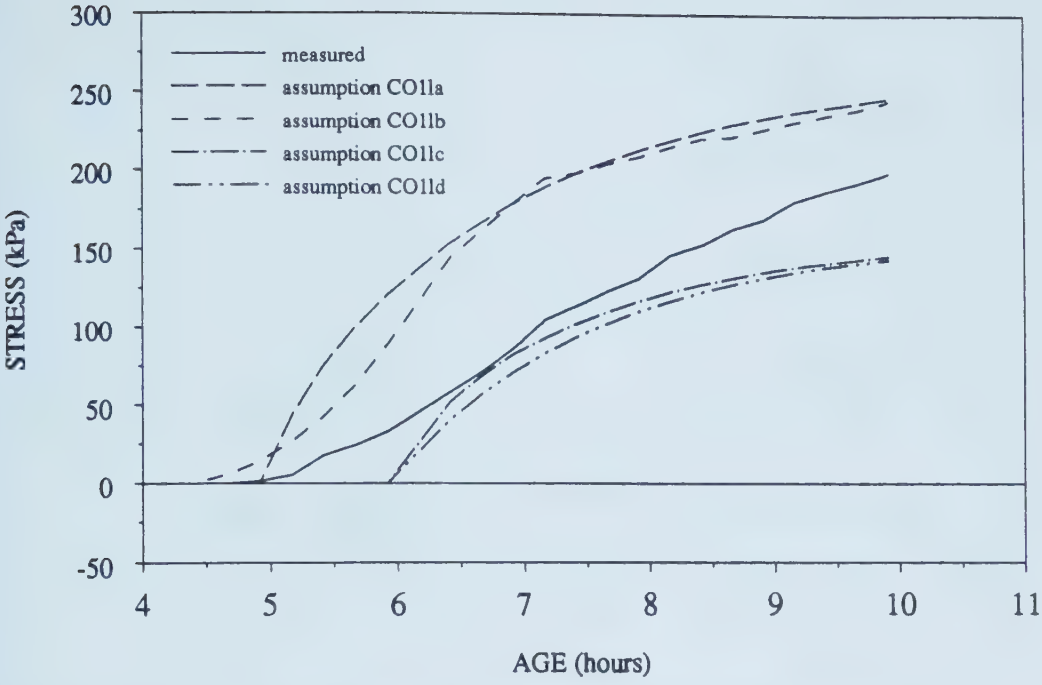


Figure 4.73 Measured and Calculated Stresses before 10 Hours, Test CRSCO1

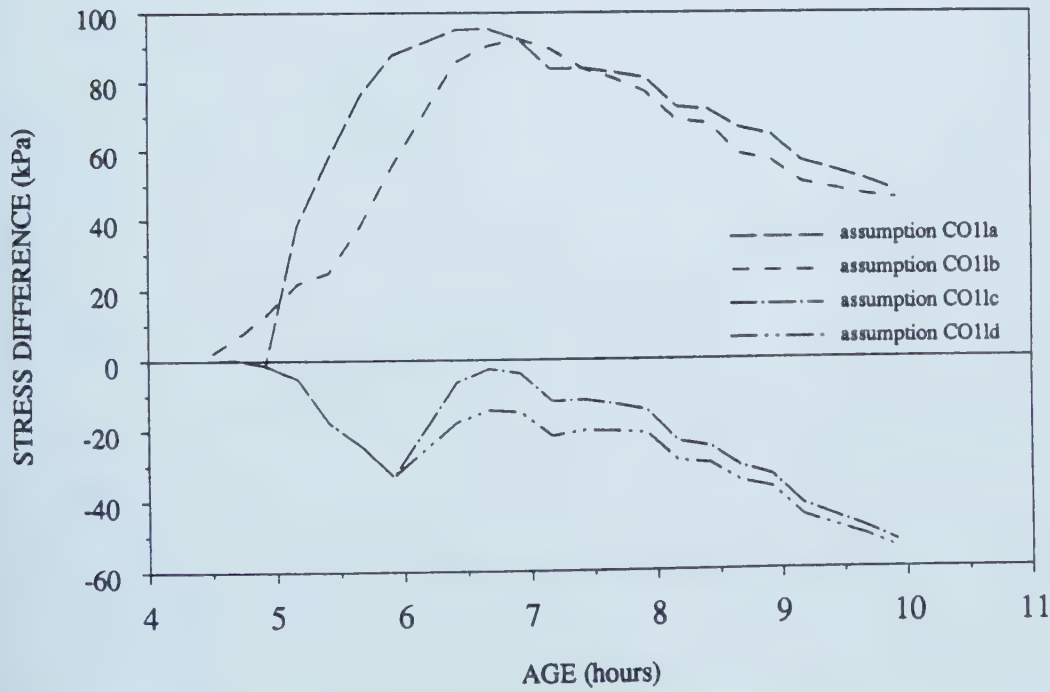


Figure 4.74 Difference of Measured and Calculated Stresses before 10 Hours, Test CRSCO1

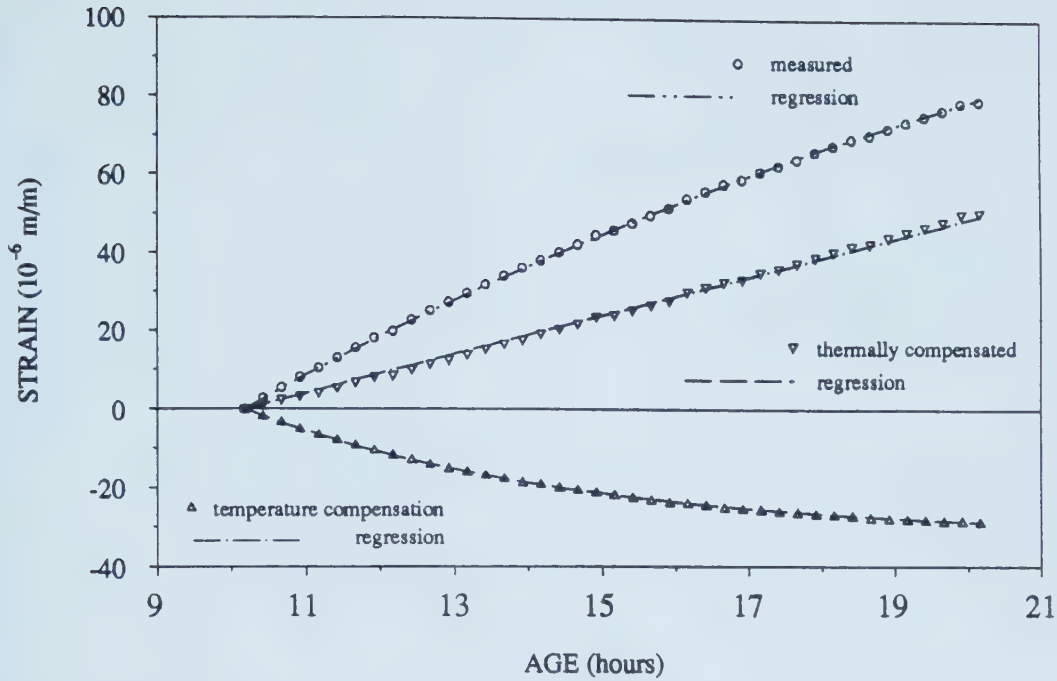


Figure 4.75 Measured and Assumed Strains after 10 Hours, Test CRSCO1

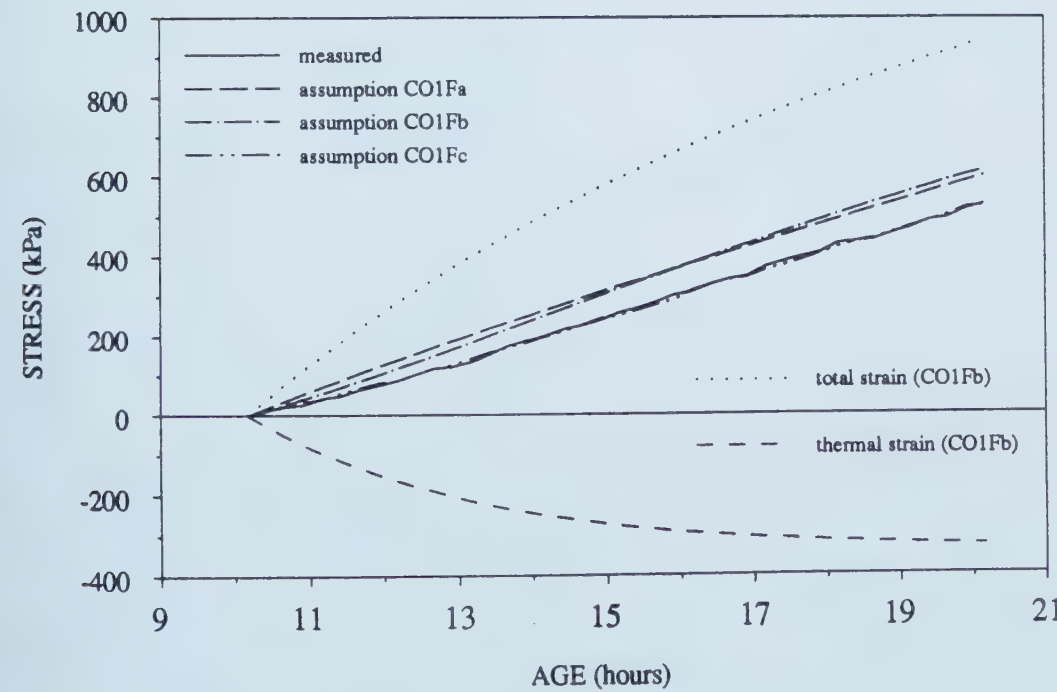


Figure 4.76 Measured and Calculated Stresses after 10 Hours, Test CRSCO1

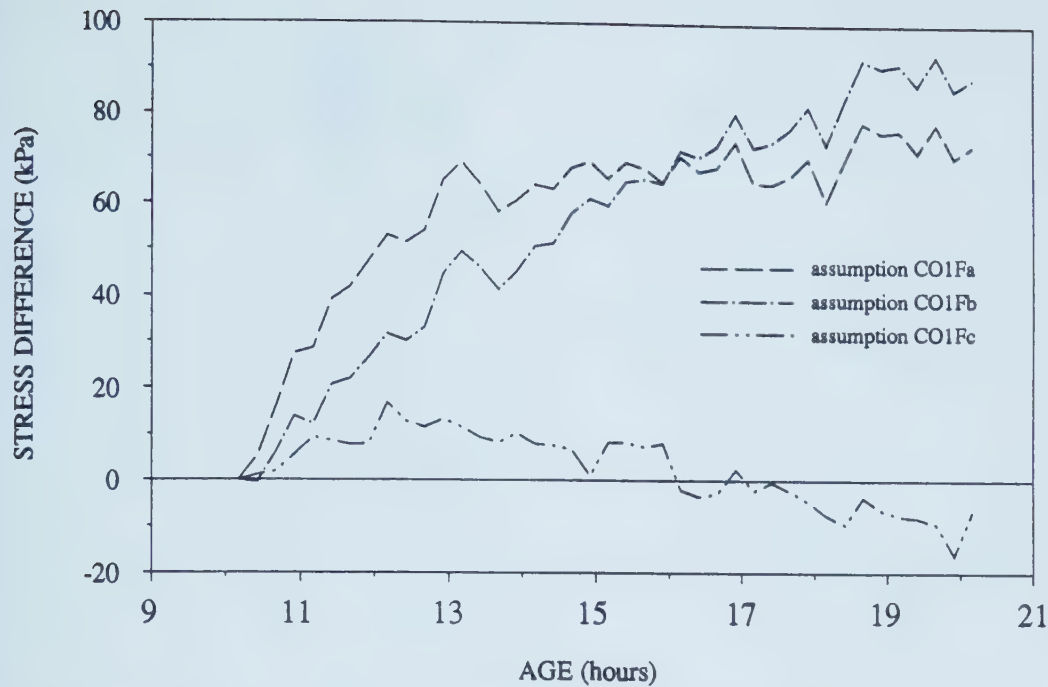


Figure 4.77 Difference of Measured and Calculated Stresses after 10 Hours, Test CRSCO1

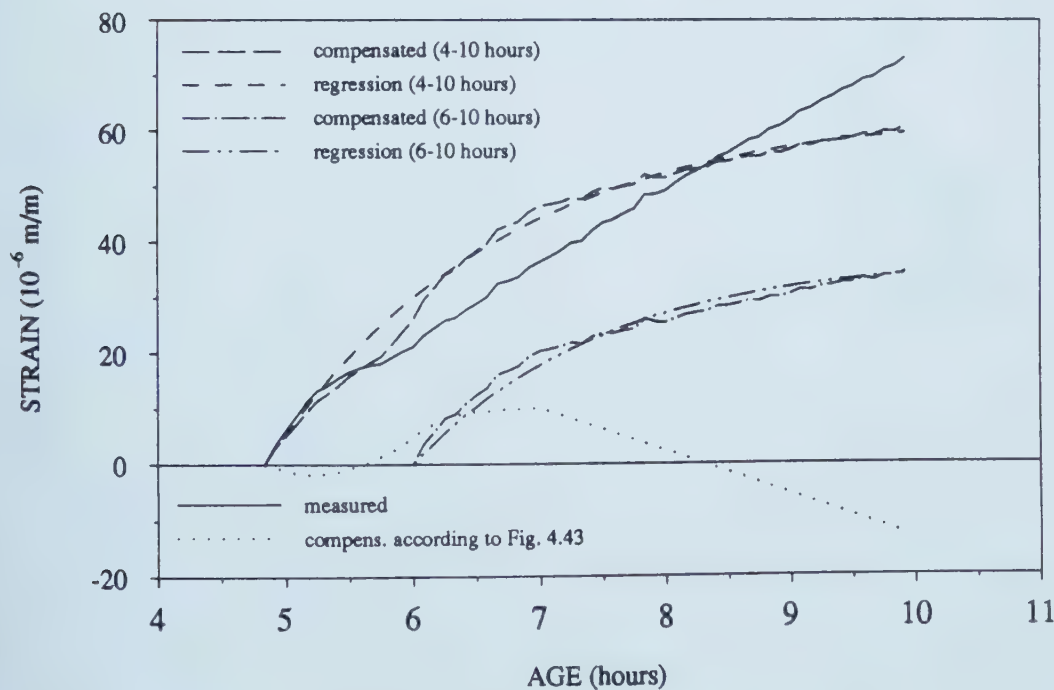


Figure 4.78 Measured and Assumed Strains before 10 Hours, Test CRSCO2

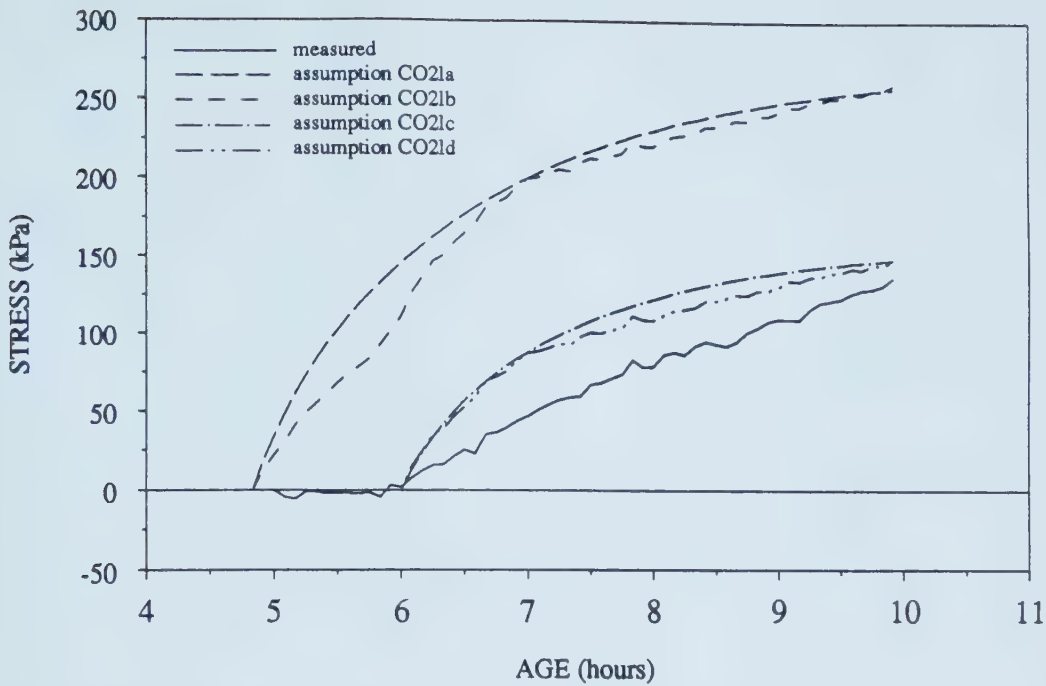


Figure 4.79 Measured and Calculated Stresses before 10 Hours, Test CRSCO2

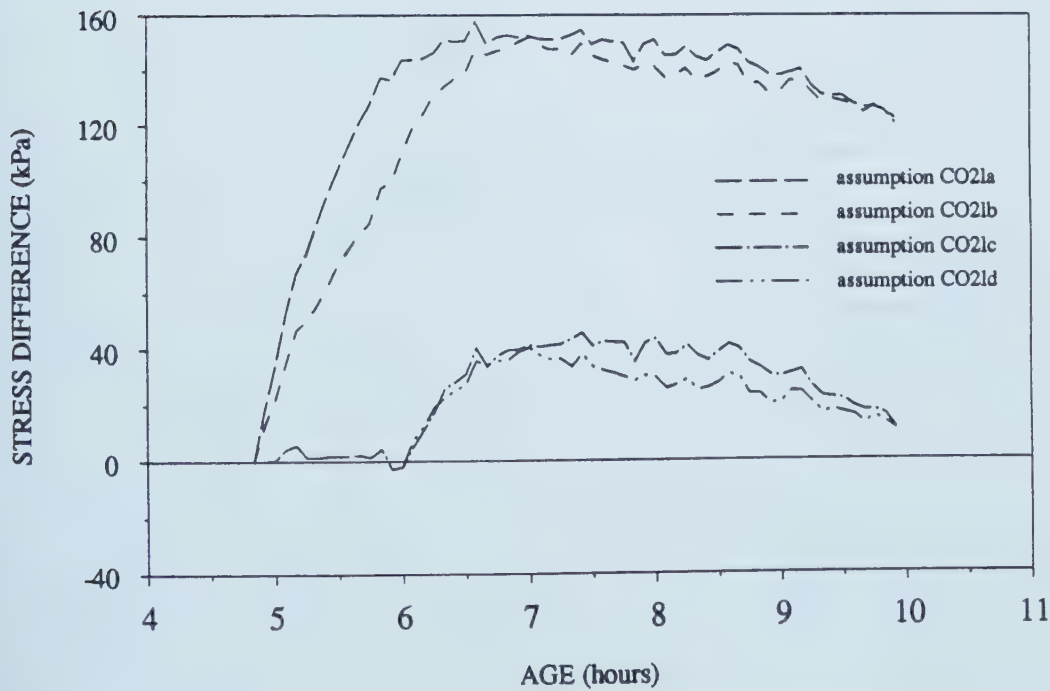


Figure 4.80 Difference of Measured and Calculated Stresses before 10 Hours, Test CRSCO2

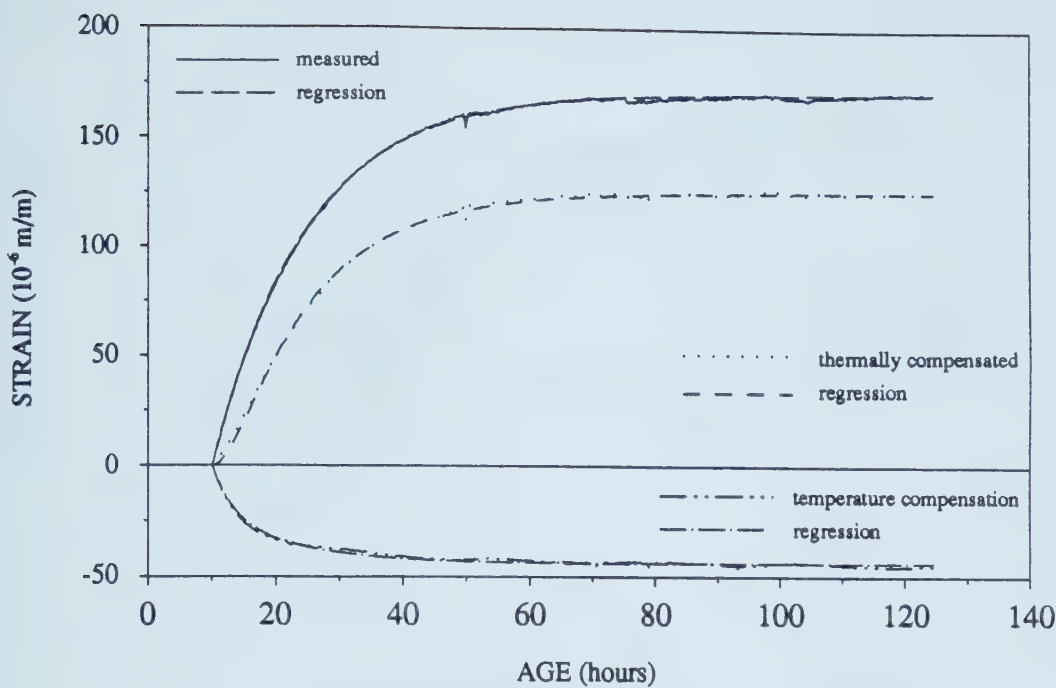


Figure 4.81 Measured and Assumed Strains after 10 Hours, Test CRSCO2

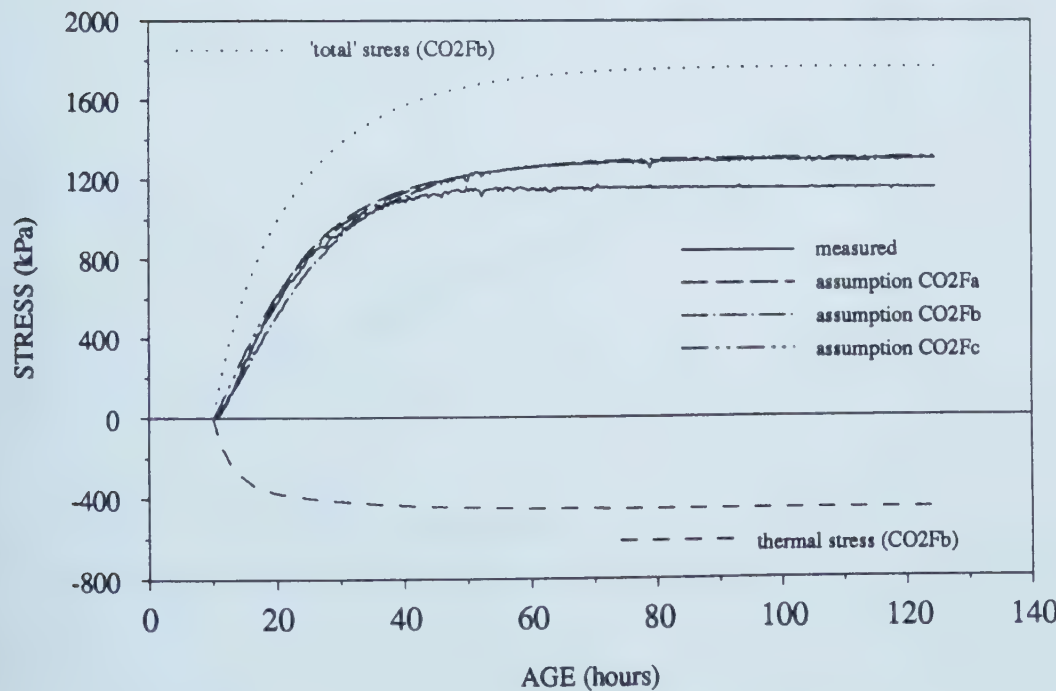


Figure 4.82 Measured and Calculated Stresses after 10 Hours, Test CRSCO2

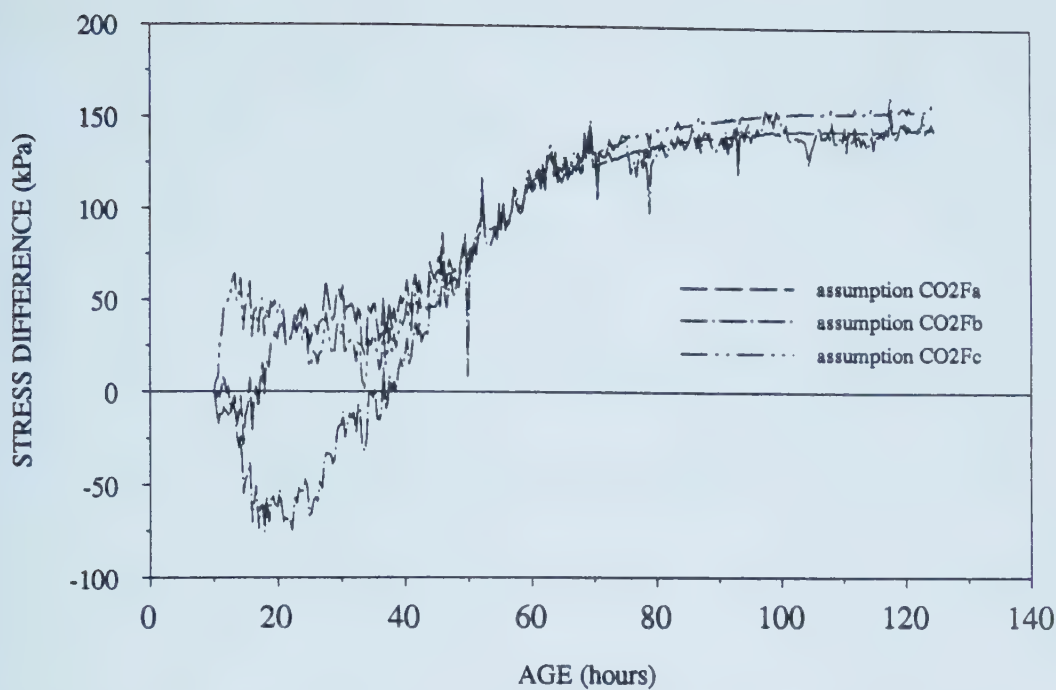


Figure 4.83 Difference of Measured and Calculated Stresses after 10 Hours, Test CRSCO2

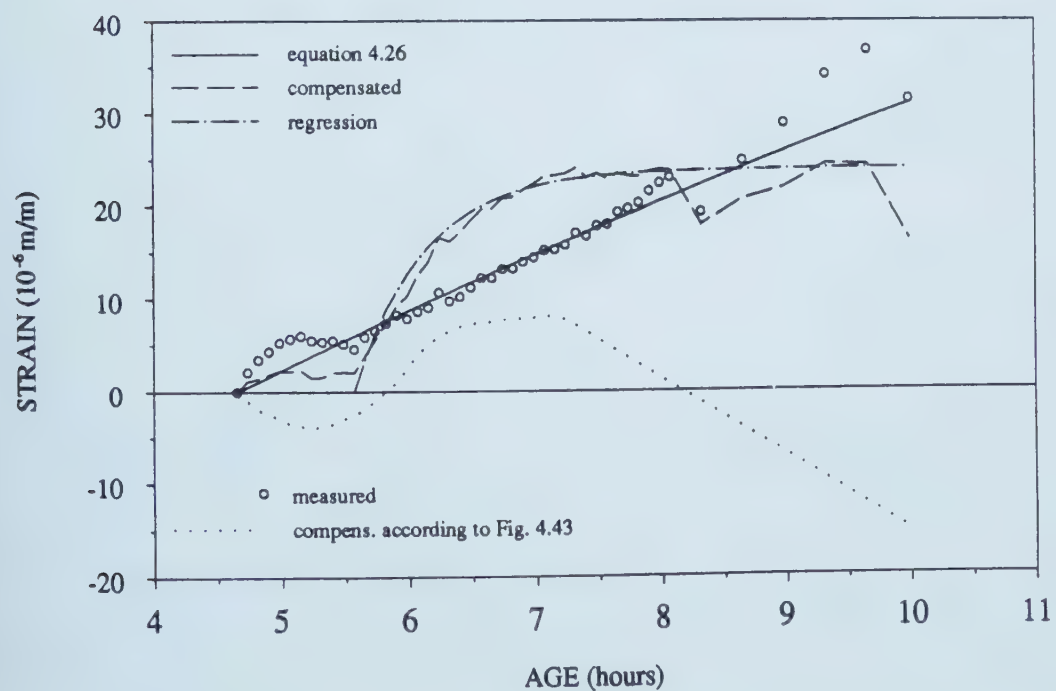


Figure 4.84 Measured and Assumed Strains before 10 Hours, Test CRSCO3

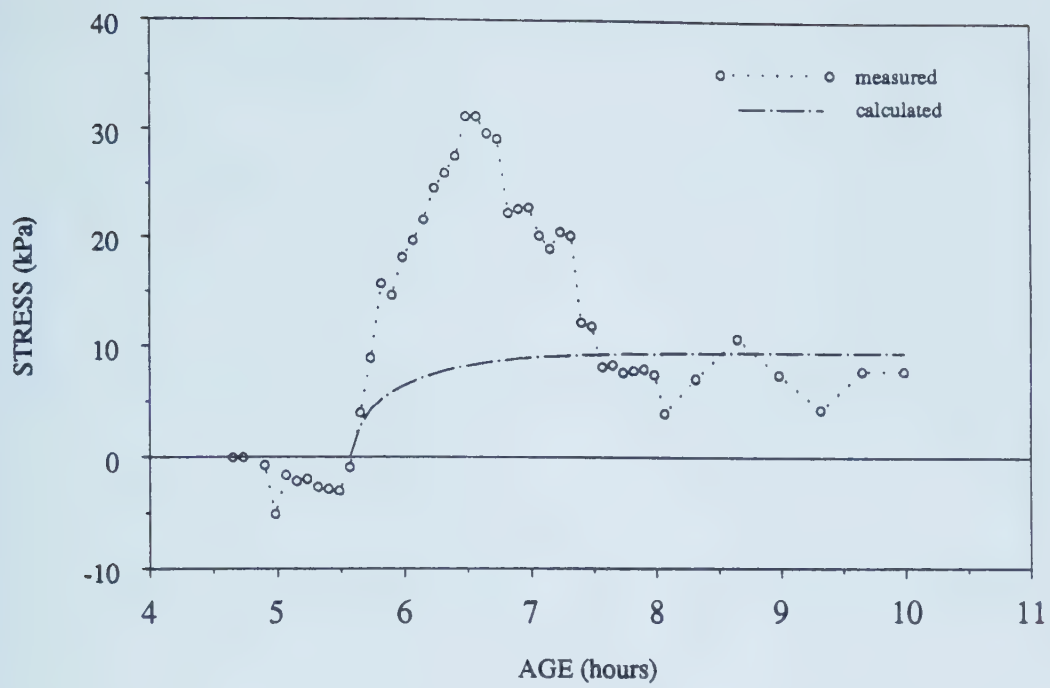


Figure 4.85 Measured and Calculated Stresses before 10 Hours, Test CRSCO3

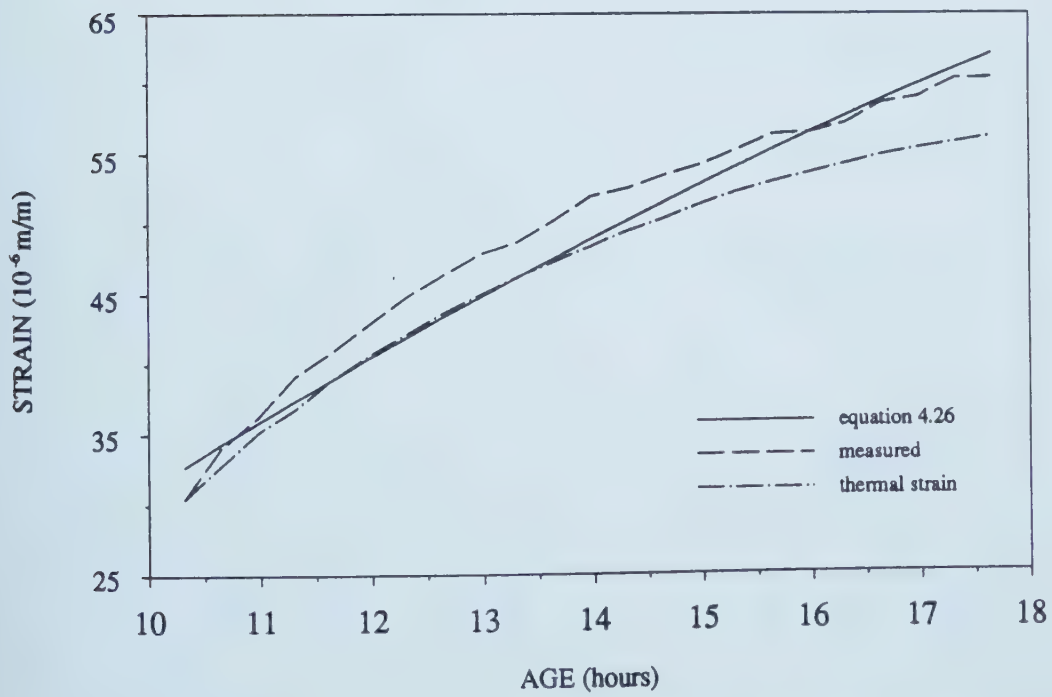


Figure 4.86 Measured and Calculated Strains between 10 to 18 Hours, Test CRSCO3

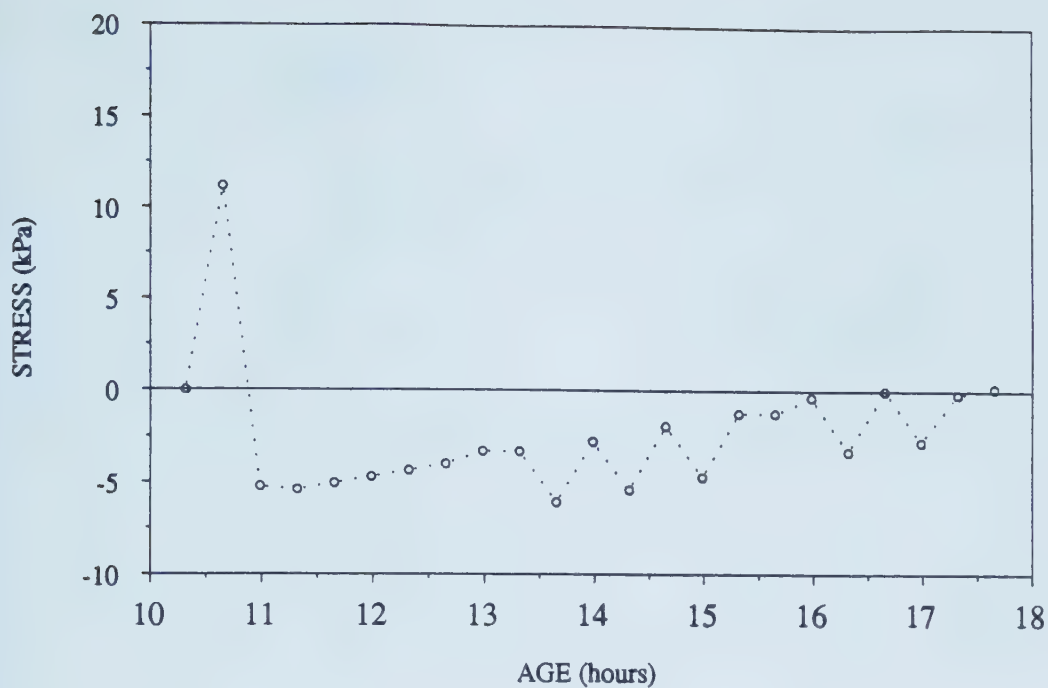


Figure 4.87 Measured Stress between 10 to 18 Hours, Test CRSCO3

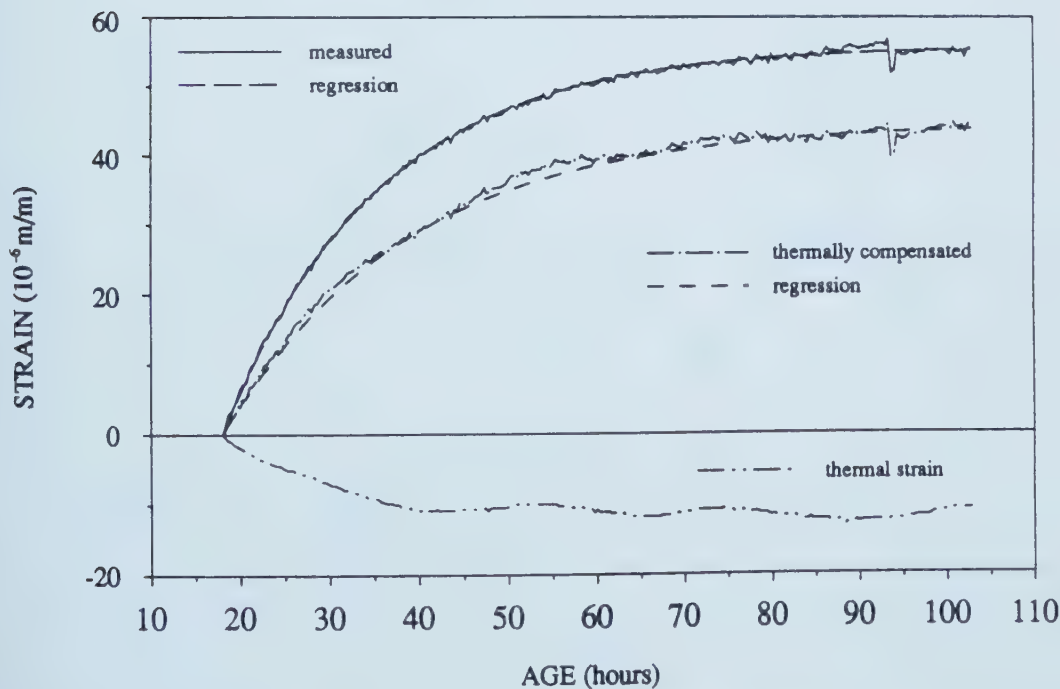


Figure 4.88 Measured and Assumed Strains after 18 Hours, Test CRSCO3

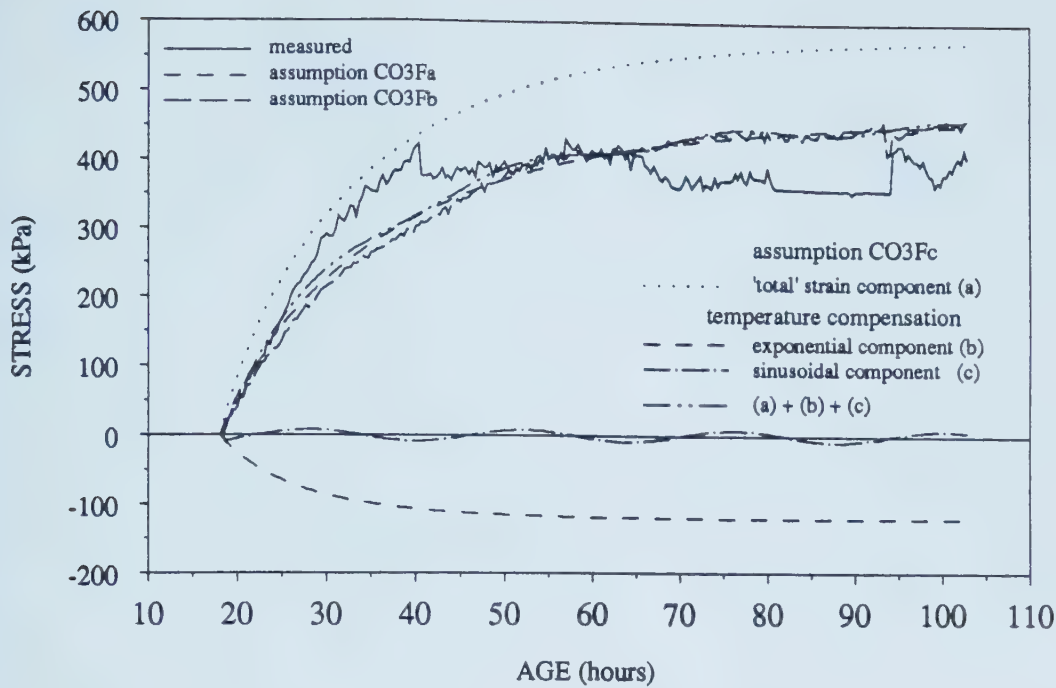


Figure 4.89 Measured and Calculated Stresses after 18 Hours, Test CRSCO3

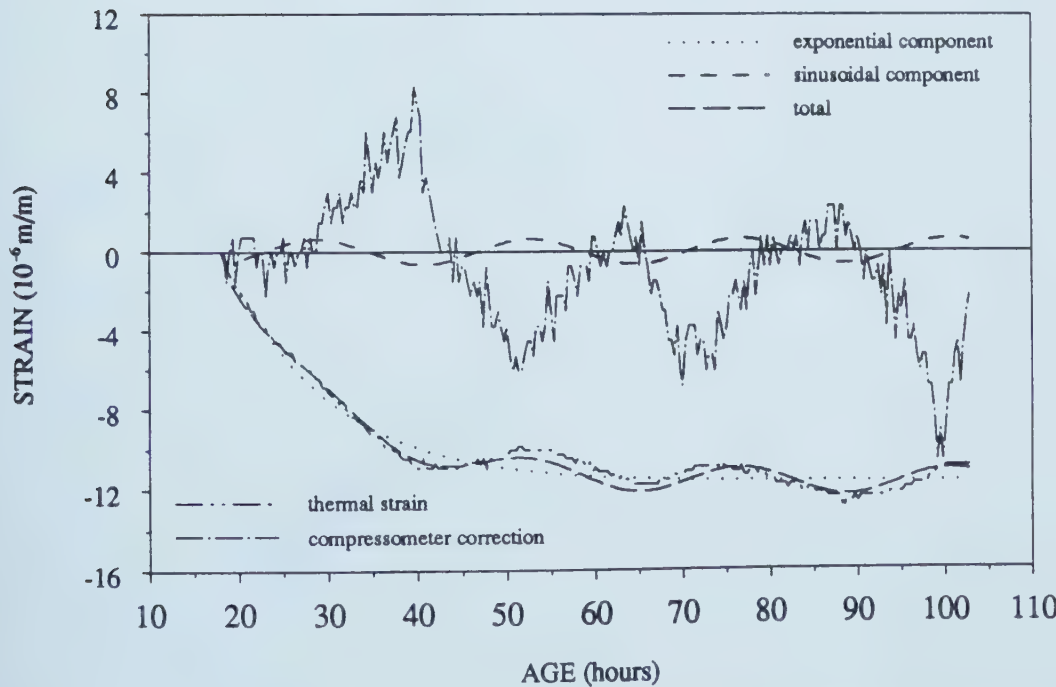


Figure 4.90 Measured and Calculated Thermal Strains after 18 Hours, Test CRSCO3

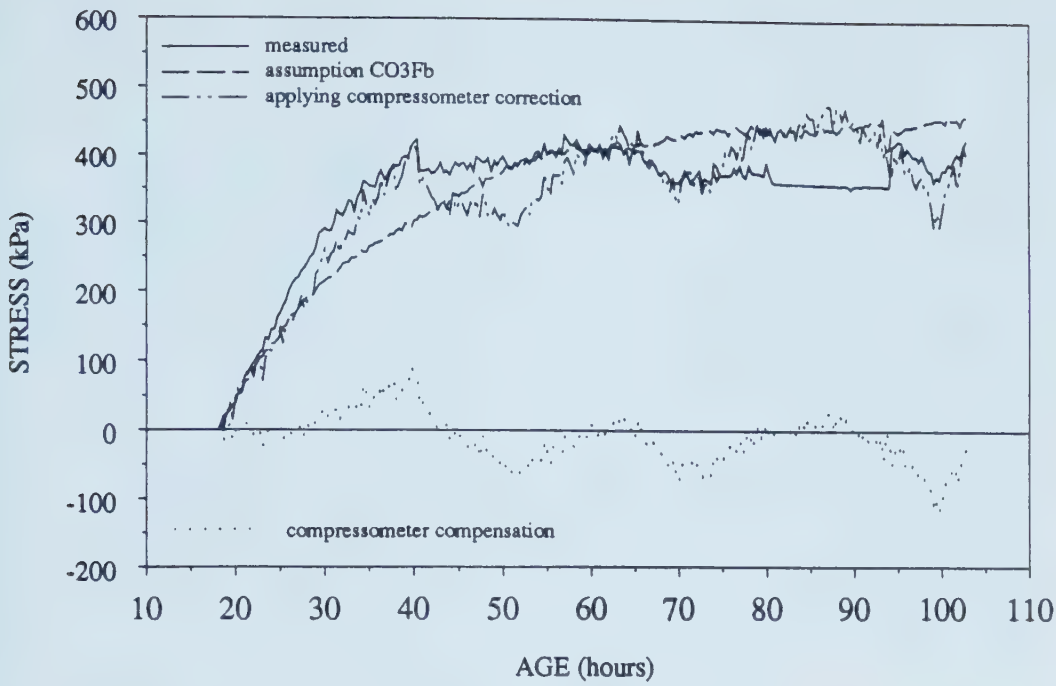


Figure 4.91 Stress Development Including the Compressometer Compensation, Test CRSCO3

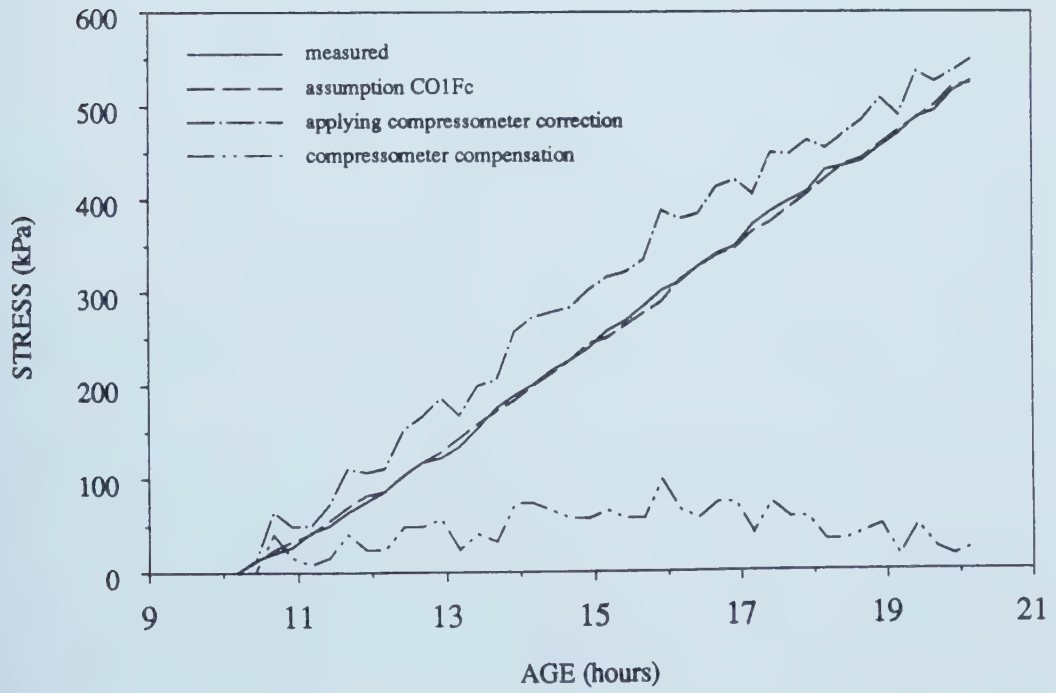


Figure 4.92 Stress Development Including the Compressometer Compensation, Test CRSCO1

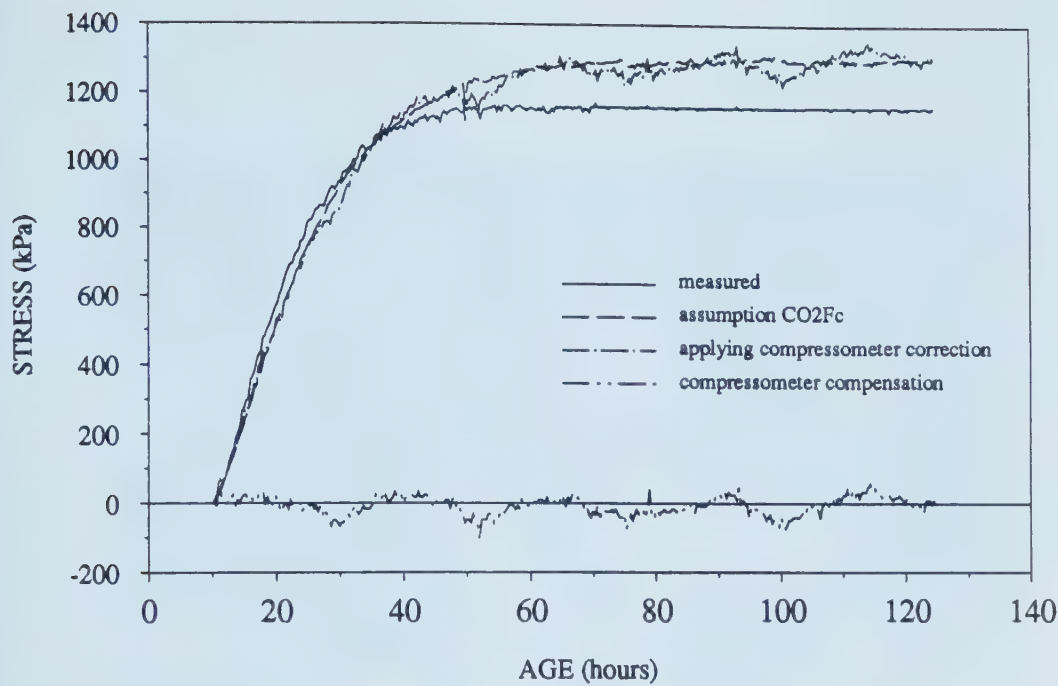


Figure 4.93 Stress Development Including the Compressometer Compensation, Test CRSCO2

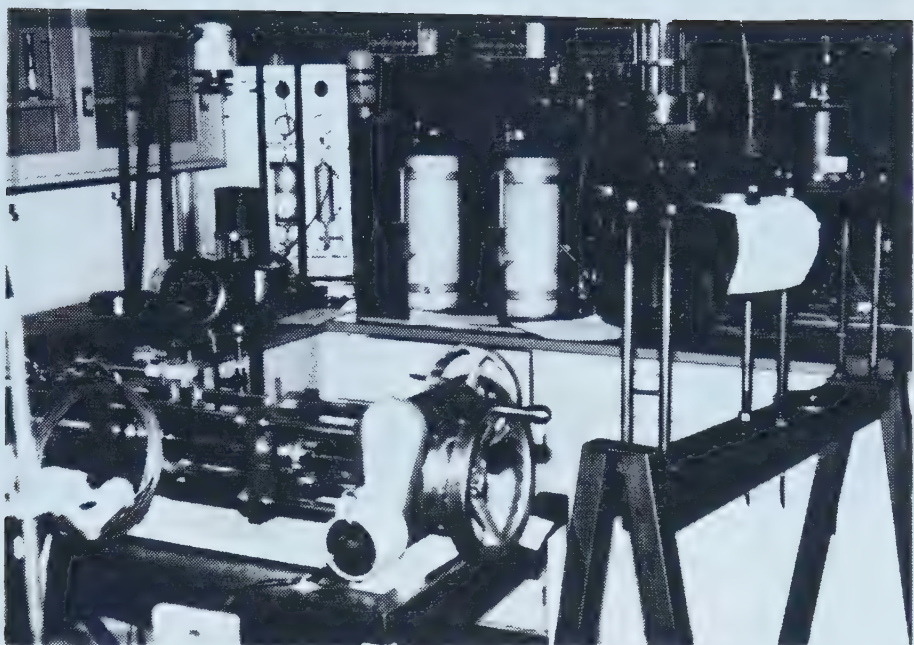


Plate 4.1 View of Hydraulic System and Twin Shotcrete Specimens used during Creep and Stress Controlled Tests

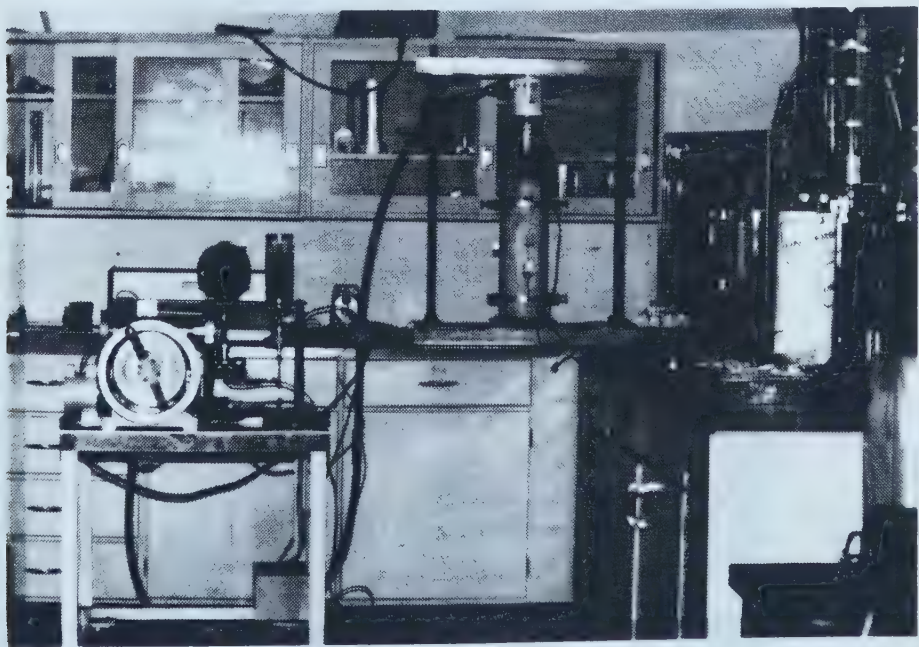


Plate 4.2 Shotcrete Specimen Assembled for Creep and Stress Controlled Test

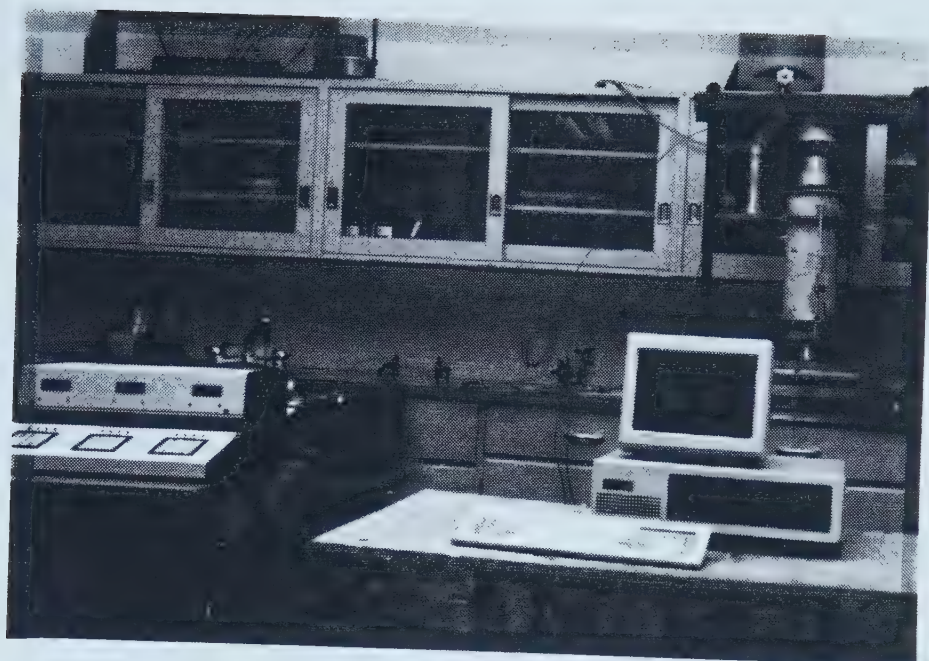


Plate 4.3 View of Equipments used for Strain Controlled Tests

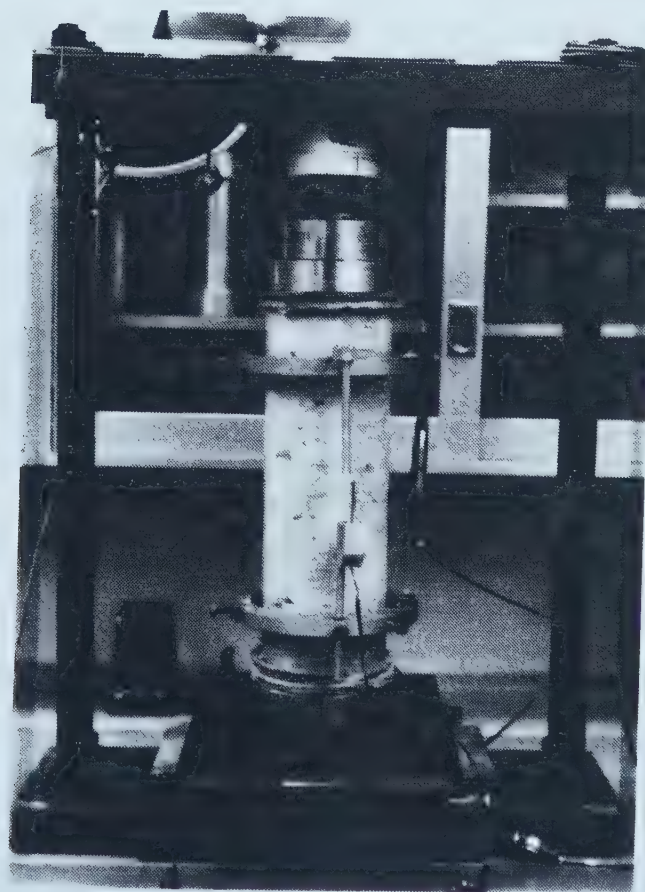


Plate 4.4 Shotcrete Specimen Assembled for Strain Controlled Test

5. EFFECT OF TUNNEL ADVANCING RATE ON LINING LOADING

5.1 Introduction

The purpose of this chapter is to present a simplified calculation procedure which takes into account the rate of tunnel construction advancing on lining loading estimation. The results of laboratory tests presented in the previous chapter showed clearly that the shotcrete properties depend on its age. This suggests that the load distribution in the lining would be affected by the tunnel construction rate. However, this aspect is not usually considered in routine designs.

In order to study this effect, one might ideally perform sophisticated finite element simulations taking into account the complex constitutive laws of the soil and the shotcrete under the true three dimensional nature of the problem. However, as mentioned earlier, this kind of procedure cannot usually be applied in routine calculations and the problem must be simplified for practical use.

The solution proposed here consists of an adaptation of a viscoelastic analytical solution (Yuen, 1979), modified through a parametric transformation to simulate the three dimensional effect of the load transfer process. This parametric transformation was meant to depict the same response of three dimensional finite element simulations presented by Hanafy and Emery (1980, 1982).

5.2 Analytical Approximation

5.2.1 Foreword

Conventional tunnel design uses the two-dimensional plane strain formulation to represent the actual three-dimensional nature of tunnel excavation. Usually, it is assumed that the 3D configuration can be represented reasonably by a succession of 2D plane strain transverse sections. This approach is not theoretically correct because, for example, it does not take into account the shear stresses between the 'plane strain' sections. Despite

this fact, the plane strain assumption has been used successfully in practice in many available design methods. Negro (1988) showed that this approximation is accurate enough for design purposes, including the case of ground exhibiting a non linear and stress sensitive behavior such as the hyperbolic model (Duncan and Chang, 1970).

In a 2D simulation technique the advancing of a tunnel face can be represented by forces applied inside the tunnel boundary to balance the initial insitu stresses and then gradually reduced to zero. This simulation procedure which was described in Chapter 2, is one of the most common and it has been used by many other authors. This procedure will be referred as 'ground stress reduction' technique and it is presented schematically in Figure 5.1a. The 'core stiffness reduction' technique, in which the tunnel is always 'filled' by a core as illustrated in Figure 5.1b, is another usual technique. Initially this core has a given stiffness representing the original in situ condition far from the tunnel face. As the face approaches, the stiffness of the core is reduced and eventually goes to zero when the construction has passed the section. As discussed in Chapter 2 with respect to the stress reduction technique, the core stiffness reduction procedure can also simulate the 3D load transfer process. The implementation of these techniques can be analytical, numerical, empirical or a combination of these, and a summary of representative approaches is shown in Negro (1988: 394-396). The third technique, shown in Figure 5.1c, represents the simulation proposed in this chapter. It is a simple procedure to evaluate the load on lining for different rates of tunnel construction by controlling the stiffness of the ground.

All the procedures discussed above are necessary due to the limitations of the plane strain modelling. An overview of these limitations can be done with the help of the arching concept as traditionally used in soil mechanics (e.g., Terzaghi and Peck, 1967: 267). Figure 5.2 presents the three-dimensional arching effect near the face of an advancing tunnel as shown by Eisenstein et. al. (1984). The transverse planes α_i 's in Figure 5.2 represent the sequence of 'plane strain' sections which are intended to be simulated by plane strain representation. Note, however, that the 2D plane strain model is

only capable to reproduce the transverse arching as shown in section 1-1 of Figure 5.2. The techniques discussed above (Figure 5.1) are efforts to model artificially the 3D longitudinal and horizontal arching in a 2D plane strain model. This subject will be discussed in the following.

5.2.2 Tunnel Advance Simulation using 2D Model

Figure 5.3 illustrates one of the analyses published (Ohnishi et al., 1982), using the core stiffness reduction method for tunnel construction simulation. It can be considered as a typical example of its application. These results were obtained by using a two-dimensional finite element code which was capable of making changes of stiffness in stages for the tunnel cross section core. This core at the initial stage of simulation was composed by many overlapping layers of elements and the stiffness reduction was obtained by the sequential removal of one layer for each stage. In this example, 7 layers (or construction stages) were simulated and their Young's moduli had the values E_1 to E_7 as shown in Figure 5.3a. The sum of their stiffness is equal to the stiffness of the original ground, indicated by E_R , which represents the original in situ condition before any excavation takes place. The tunnel face advancing in the actual 3D situation corresponds to the removal of the layers in the 2D model. At the final stage, all the layers will be removed representing the full release of the stresses due to the tunnel excavation. Therefore, the curve shown in Figure 5.3a is the core stiffness manipulation necessary to model the effect of the longitudinal and horizontal arching for sections close to the tunnel face, missing in the 2D model representation.

The initial and final conditions, i.e. long before and long after construction, are trivial because these cases can clearly be replaced by the 2D plane strain representation. Now, let us consider a transverse slice of the tunnel construction close to the face which requires normal stress σ_n and shear stresses τ_{xz} and τ_{yz} at the cutting planes in order to maintain equilibrium. On the other hand, note that a 2D plane strain representation

requires $\sigma_n = \nu (\sigma_x + \sigma_y)$, $\tau_{xz} = 0$ and $\tau_{yz} = 0$, for the case of linear elastic material. As the equilibrium stresses at the face of the 3D transverse slice do not match the stress conditions required by the plane strain assumption, some 'external agent' is necessary to approximate the 2D modelling to the actual 3D situation. This 'external agent' can be understood as an artifice used to compensate the interaction between the imaginary sequence of transverse sections missing in the 2D representation. The 'external agent' can be either an application of stress in the tunnel contour (ground stress reduction method) or a core placement (core stiffness reduction method). Note that this is an alternative explanation of the arching mechanism for the problem, in terms of the plane strain stress requirements or conditioning.

Figure 5.3a presents a normalized stiffness curve for an application of the core reduction method, as proposed in the above method. This curve relates the core stiffness and the distance from its transverse section to the tunnel face A_d normalized by its diameter D . Using this curve, one can relate the removal of each element layer represented by E_1 to E_7 , or tunnel core stiffness reduction, to the position of the tunnel face. This technique simulates the third dimension missing in the 2D plane strain model, by manipulating the stiffness of the tunnel core. The comparison of results using this technique with an axisymmetric simulation is presented in Figure 5.3b, showing reasonable agreement. Ohnishi et al. (1982) assumed that once the normalized stiffness curve is defined, for the unlined tunnel case, the same curve can be used for the case of a tunnel with lining. Applying this technique, it is possible to analyze different sequences of tunnel construction using a relatively simple and economical 2D plane strain model.

5.2.3 Simulation of Tunnel Advance Rate using 2D Model

The technique presented above can be considered a reasonable approximation for design and indeed it has been used by many authors to analyze construction sequence of tunnels (Negro 1988: 394-396). It is important to note again that the core stiffness

manipulation is used in this technique in order to artificially simulate the 3D effect in a 2D plane strain formulation. This concept of stiffness manipulation will be combined with an existing analytical solution (Yuen, 1979), and it will be shown that it is possible to obtain a solution which can reasonably simulate different rates of tunnel construction.

Figure 5.4 presents the results of an axisymmetric finite element method (FEM) simulation presented by Hanafy and Emery (1980), for a linear elastic material with the horizontal-vertical stress ratio $K_0=1$. The tunnel closure U was normalized as it was presented in Chapter 2 :

$$U = \frac{u_r E}{D \sigma_{r0}} \quad [5.1]$$

where

u_r is the radial tunnel displacement

E is the Young's modulus

D is the tunnel diameter

σ_{r0} is the initial radial insitu stress

and the other parameters in Figure 5.4 are:

U_f is the final closure

A_d is the distance from the given transverse section to the face

R is the tunnel radius

As mentioned earlier, the focus of this chapter is the evaluation of the load on the tunnel lining. As the lining is usually installed after the excavation takes place, the analysis from now on will consider the deformations after the face has passed the reference transverse section only. This condition corresponds to the positive portion of the abscissas for the curve presented in Figure 5.4. This figure shows that the positive portion of the tunnel closure curve can be approached by the following equation:

$$U\left(\frac{A_d}{R}\right) = U_f \left(1 - \kappa e^{-\frac{\omega}{R} A_d}\right) \quad [5.2]$$

where

$U\left(\frac{A_d}{R}\right)$ is the normalized radial displacement as a function of tunnel advancing

U_f is the final normalized radial displacement

and

$$\kappa = 0.629$$

$$\omega = 1.099$$

are constants obtained through curve fitting. Therefore, the tunnel convergence according to the face advancing can be reasonably represented by equation 5.2, for a linear elastic material and $K_0 = 1$.

Now, consider a tunnel excavated in a three element viscoelastic material such as that used in Chapter 4 (Figure 4.21). It can be shown that the plane strain solution for displacement of a tunnel excavated under constant load (Yuen, 1979: 191) is:

$$u(t) = u_{\text{elastic}} \times \vartheta_r(t) \quad [5.3]$$

where

$u(t)$ is the convergence evolution with time

u_{elastic} is the elastic or instantaneous convergence

$$\vartheta_g(t) = 1 + \frac{G_R}{G_{gt}} (1 - e^{-\lambda t})$$

$$G_g = \frac{E_g}{2(1 + \nu_g)}$$

$$G_{gt} = \frac{E_{gt}}{2(1 + \nu_g)}$$

$$\lambda_g = \frac{2 G_{gt}}{\eta_g}$$

E_g , E_{gt} , η_g and ν_g are the viscoelastic properties as introduced in Chapter 4 (Figure 4.21), for a three element viscoelastic material.

Applying Equation 5.3 the final convergence u_f for time $t = \infty$ is:

$$u_f = u(\infty) = u_{\text{elastic}} \frac{G_g + G_{gt}}{G_{gt}} \quad [5.4]$$

Substituting Equations 5.1 and 5.4 into 5.3:

$$U(t) = U_f \left[1 - \left(\frac{E_g}{E_{gt} + E_g} \right) e^{-\lambda_g t} \right] \quad [5.5]$$

Comparing Equation 5.2 with 5.5, one observes the similarity between these expressions. This similarity will be used to include the third dimension effect in a 2D plane strain solution in an analogous way as done for the core stiffness reduction technique described earlier. In the approximation proposed here, instead of manipulating the stiffness of the core, the stiffness of the ground will be variable. Equation 5.3 shows that:

when $t = 0$

$$\vartheta_g(0) = 1$$

$$u(0) = u_{\text{elastic}} \quad (\text{equivalent Young's modulus of ground is } E_g)$$

when $t \rightarrow \infty$

$$\vartheta_g(\infty) = \frac{E_{gt} + E_g}{E_{gt}}$$

$$u(\infty) = u(0) \frac{E_{gt} + E_g}{E_{gt}} \quad (\text{equivalent Young's modulus of ground is } \frac{E_{gt} E_g}{E_{gt} + E_g})$$

Therefore, the viscoelastic solution exhibits an equivalent Young's modulus of E_g at the moment zero and it is gradually reduced to $\frac{E_{gt} E_g}{E_{gt} + E_g}$ in the final equilibrium. Note that this reduction of stiffness potentially allows for simulation of the tunnel face advance (similar to the core stiffness reduction technique), and as the solution includes the time component, it potentially allows for simulation of different rates of construction advancing.

At this point, it should be clear that the viscoelastic model is intended to be used just as an artifice to manipulate the ground stiffness, as in the core stiffness reduction technique. The function $\vartheta_r(t)$ in Equation 5.3 plays the same role as in the stiffness curve of the core technique shown in Figure 5.3a. Therefore, all the viscoelastic parameters E_g , E_{gt} , η_g and ν_g presented before should be considered as artificial parameters (as E_1 to E_7 in the example of core stiffness technique) necessary to include the construction advancing effect in a 2D plane strain solution. The actual behavior of the ground is time independent and linearly elastic with the 'real' Young's modulus $E_{g_{\text{real}}}$. Moreover, in the case of the core stiffness reduction technique, both stress and displacement field of the ground can be evaluated. For the solution proposed here only the displacement field of

the ground can be used because the stress field of the ground will be affected due to the stiffness manipulation required by the solution.

In the core stiffness reduction technique, Figures 5.1b and 5.3, the core stiffness is reduced to zero which corresponds to the final condition when the problem approaches the 2D plane strain condition. Similarly, the ground modulus is reduced to $\frac{E_{gt} E_g}{E_{gt} + E_g}$, in the final condition in the viscoelastic solution (Equation 5.5). As this final condition actually represents the 2D condition, the relation between the artificial viscoelastic parameters and the real elastic modulus of the ground is:

$$E_{g_{real}} = \frac{E_{gt} E_g}{E_{gt} + E_g} \quad [5.6]$$

The equation above represents the first condition necessary to adapt a plane strain solution of a three element model, like that represented by Equation 5.5, in order to obtain the similar effect of the core reduction stiffness technique. In other words, Equation 5.6 represents the first requirement to artificially include the 'third' dimension in a two dimensional viscoelastic solution. Equation 5.2 is a curve fitting of the radial displacement development as a function of the construction advancing, for the case of an unlined tunnel in an axisymmetric linear elastic simulation. This curve can be used to adjust or 'calibrate' Equation 5.5, in order to present the similar radial displacement history of an actual 3D situation. Comparing Equation 5.2 with 5.5, this goal is achieved by making:

$$\kappa = \frac{E_g}{E_{gt} + E_g} \quad [5.7]$$

and

$$\omega \frac{A_d}{R} = \lambda_g t \quad [5.8]$$

Using Equations 5.6 and 5.7, it is possible to determine the values of the artificial parameters E_g and E_{gt} . Equation 5.8 can be rewritten as:

$$\lambda_g = \omega \frac{A_d}{R t} \quad [5.9]$$

Note that $\frac{A_d}{R t}$ represents the rate of tunnel advance in terms of radius per unit of time. Using the parametric transformations shown by Equations 5.6, 5.7 and 5.9 and introducing into 5.5, it is possible to reproduce the displacement history described by Equation 5.2. This solution will represent an unlined tunnel constructed in a time independent, linear elastic ground with Young's modulus of $E_{g_{real}}$ constructed with $\frac{A_d}{R t}$ rate of advance. Note also that the solution expressed by Equation 5.5 is a function of time t . As the rate of advance was defined during the parameter transformations, it is trivial to convert time into position of the tunnel face and *vice versa*. Figure 5.5 presents the results of this analytical approximation to describe the convergence history of an unlined tunnel, and a good agreement is found when compared with the axisymmetric simulation presented by Hanafy and Emery, 1980. In this figure, note that the convergence of the analytical approximation tends to the analytical closed form solution (Kirsch, 1898) for plane strain condition as the ratio $\frac{A_d}{D}$ tends to infinity.

As discussed previously, the primary interest of this chapter is the study of load on the lining as a function of different rates of tunnel advance and not just the displacement field of an unlined tunnel contour as provided by the solution presented above. In order to evaluate loads acting in the lining, an analytical solution derived by Yuen (1979) is used. This solution was originally developed for analysis of tunnel lining

in rock which takes into account the initial stress system, the time-dependent behavior of both the lining and the ground, and a time delay t_0 for the lining installation. Both the lining and ground are assumed to be homogeneous and isotropic. The solution was derived for the plane strain condition for either full slip or non slip conditions at the ground-lining interface and it provides expressions for stresses and displacements of the lining and ground.

Note that Equation 5.3 used earlier is only a portion of the complete solution derived by Yuen (1979). In the complete solution both lining and ground are assumed to behave according to the three element viscoelastic model such as that already mentioned (Figure 4.21), and for this reason, it becomes ideal for the present application. Using the parametric transformations for the ground and rate of tunnel advancing described by Equations 5.6, 5.7 and 5.9, one can obtain the artificial viscoelastic parameters to emulate the 3D effect of the construction. Applying the viscoelastic properties of the shotcrete as found in Chapter 4, the short term creep of the lining can be taken into account by the solution as well. Therefore, in Yuen's complete solution for the application proposed here, the viscoelastic properties of the ground will be artificial parameters and the viscoelastic properties of the shotcrete lining will be real ones.

The derivation of this solution is considered out of scope of this thesis and one should refer to Yuen (1979) to obtain this information. A summary of the solution presenting the main equations and their applications for three case histories can be found in Lo and Yuen (1981). Appendix E presents a source code of a program written in BASIC with self explaining comments, which shows explicitly all the expressions used by the solution. This program was translated from a FORTRAN code included in Yuen (1979: Appendix J) and was modified to incorporate the parametric transformation represented by Equations 5.6, 5.7 and 5.9. Some other modifications were also necessary to provide the proper output for the present problem, basically concerning the time lag of the result presentation, and they are indicated in the source code in Appendix E. This

program, to be referred from now on as ADVRATE, will require as input, the 'real' Young's modulus $E_{g_{real}}$ and Poisson's ratio ν_g of the ground, rate of the tunnel construction $\frac{A_d}{R t}$, the viscoelastic properties of the shotcrete (E_l , E_{lt} , η_l and ν_l), the lining thickness T and time delay t_0 of the lining installation. The program will present the thrust, bending moment and displacement of the lining. The analytical solution with the parametric transformation, the program ADVRATE, is the calculation procedure proposed to analyze the tunnel construction simulation in a linear elastic ground and a viscoelastic lining. Note that the viscoelastic model used in Chapter 4 for interpretation of the shotcrete tests was a simplified assumption to incorporate elastic and creep short term deformations. Note also that all the calculations using ADVRATE will assume the usual non slip condition at the shotcrete ground interface.

Note that the discussion above assumed that once the ground stiffness reduction was 'calibrated' for unlined tunnels, it would be valid in line tunnel simulations, as it is usually done in core stiffness reduction simulations. In order to check the validity of this assumption, two analyses were carried out. Figure 5.5 shows the comparison of lined tunnel convergence between the axisymmetric FEM simulations by Hanafy and Emery (1980) and the results from ADVRATE. The parameters of the tunnel simulated in these examples are shown in Table 5.1, and both ground and lining were assumed to be linear elastic, time independent materials. Figure 5.5 presents the results for two different cases, i.e, for the liner being placed at the face and for the liner being placed one radius ($1 R$) behind the face. Consider first the case of the liner being placed at the face of the tunnel. In this case, one observes that the analytical approximation underestimates the tunnel convergence. Besides the errors inherent to the numerical and analytical procedures, there is a difference in the construction simulation between them. In the numerical FEM procedure, the first step of the tunnel construction is the 'excavation' of the FEM mesh by the extent of a group of elements representing the actual excavation step. Then the stress

redistribution due to this procedure is calculated and the lining is finally placed. The simulation continues by repeating the same steps which closely resembles the actual construction sequence. Note that in the axisymmetric FEM simulation, in each excavation stage an extent of the tunnel close to the face will be unsupported. Or in other words, the lining is always placed after the stress redistribution takes place due to the ground relief of an excavation step. On the other hand, the analytical approximation had considered the liner being placed right at the tunnel face, and no unsupported tunnel extent was simulated. This difference of simulation led to the systematic underestimation of tunnel convergence by the analytical approximation. The convergence is smaller in the analytical approximation, but the load in the lining tends to be larger in the ADVRATE simulation, because the liner is placed right at the face. Although it is possible to define an equivalent delay of lining installation for the analytical approximation to simulate the unsupported stage, the higher load assumption was considered safer for design purpose, due to the simplified nature of the solution.

The other comparison shown in Figure 5.5 is the case of a lining placed one radius behind the face. Similarly to the previous case, the FEM simulation provides larger convergence than the analytical approximation, due to the stress redistribution in each excavation step. Note that for the FEM simulation, the installation delay has been considered as the distance between the tunnel face and the position of the lining just after its installation, i.e., after the stress redistribution and before the excavation of the next stage. In the ADVRATE, the delay of lining installation by one radius was simulated by converting this value into time delay t_0 . Note that Yuen's original solution was derived allowing delay of the lining installation. At initial time $t=0$, only the elastic or instantaneous component of the ground deformations had occurred and after this, the time dependent deformations start to develop. Yuen's solution permits the installation of the lining at any time delay t_0 , allowing time dependent deformation of the ground before the support activation. As the parametric transformation represented by Equations 5.6,

5.7 and 5.9 correlate time to face advancing, it is possible to convert the one radius delay of lining installation into a time delay t_0 , using the rate of face advancing. For this example, Table 5.1 shows that for radius $R = 5$ m and rate of advancing $A_d = 3$ m/day, resulting in a time delay of $t_0 = 5/3$ days. Therefore, due to the assumption of constant rate of the tunnel construction included in ADVRATE, the time delay of $t_0 = 5/3$ days, corresponds to a delay of installation of the lining one radius behind the face.

The tunnel convergence comparison of the three examples presented in Figure 5.5 shows a good agreement between an axisymmetric FEM simulation and the analytical simulation represented by the program ADVRATE. Although in the lined cases the analytical approximation presents smaller total tunnel convergence, it also tends to simulate larger convergence after the lining was installed because in the analytical approximation, the lining is simulated to be installed earlier, closer to the tunnel face. Consequently the analytical approximation tends to present, intentionally, larger values of load on the lining than an axisymmetric FEM simulation. Note again that the interest here is directed toward the loads in the lining, and some errors in the determination of the convergence are considered acceptable.

5.3 Limitations and Extensions of the Analytical Approximation

5.3.1 Simplifications in Yuen's (1979) Solution

During the derivation of his solution, Yuen (1979) divided the time dependent ground-lining interaction into two problems: the interaction under hydrostatic state of stress and the interaction under pure distortional state of stress. The solution for an arbitrary value of insitu horizontal to vertical stress ratio K_0 was obtained by the superposition of these two basic problems. Yuen (1979: 211) showed that the time dependent pressure $P_l(t)$ acting at the ground-lining interface due to the hydrostatic state of stress is given by:

$$P_1(t) = \frac{P_0}{f} \left[A_1 + A_2 e^{-\beta_1 t} + A_3 e^{-\beta_2 t} \right] \quad [5.10]$$

where

G_g, G_{gt}, ν_g and η_g are the viscoelastic parameters of the ground

(these are the artificial ground parameters in ADVRATE)

G_l, G_{lt}, ν_l and η_l are the viscoelastic parameters of the lining

R_1 and R_2 are respectively the internal and external radius of the lining

$$C_2 = \frac{(1 - 2\nu_l) R_2^2 + R_1^2}{R_2^2 + R_1^2}$$

$$p'_{1g} = \frac{\eta_g}{2(G_g + G_{gt})}$$

$$q'_{0g} = \frac{2 G_g G_{gt}}{G_g + G_{gt}}$$

$$q'_{1g} = \frac{G_g \eta_g}{G_g + G_{gt}}$$

$$p'_{1l} = \frac{\eta_l}{2(G_l + G_{lt})}$$

$$q'_{0l} = \frac{2 G_l G_{lt}}{G_l + G_{lt}}$$

$$q'_{1l} = \frac{G_l \eta_l}{G_l + G_{lt}}$$

$$a = q'_{0l}$$

$$b = p'_{1g} q'_{0l} + q'_{1l}$$

$$c = p'_{1g} q'_{1l}$$

$$d = q'_{0l} + C_2 q'_{0g}$$

$$e = p'_{1g} q'_{0l} + q'_{1l} + C_2 q'_{1g} + C_2 p'_{1l} q'_{0g}$$

$$f = p'_{1g} q'_{0l} + C_2 q'_{1g} p'_{1l}$$

$$d' = \frac{d}{f}$$

$$e' = \frac{e}{f}$$

$$\beta_2 = \frac{e' + \sqrt{e'^2 - 4d'}}{2}$$

$$\beta_1 = \frac{d'}{\beta_2}$$

$$A_1 = \frac{a}{\beta_1 \beta_2}$$

$$A_2 = c - A_1 - A_3$$

$$A_3 = \frac{b \beta_2 - c \beta_2^2 - a}{\beta_2 (\beta_1 - \beta_2)}$$

Yuen (1979) developed his solution bearing in mind the application for lined circular tunnels constructed in rock with high horizontal stress field, like the conditions found in cases located in Southern Ontario, Canada. Yuen (op. cit.) performed a numerical study on the terms of Equation 5.10, using reasonable ranges of parameters for the lining and the rock expected for that specific type of problem. It was found that the term $A_3 e^{-\beta_2 t}$ has little effect on Equation 5.10 for the first 20 days of analysis and no effect for then on. Yuen (op. cit.) considered that the term $A_3 e^{-\beta_2 t}$ was negligible for practical application (for the specific type of problem) and simplified Equation 5.10 to:

$$P_1(t) = \frac{P_0}{f} (A_1 + A_2 e^{-\beta_1 t}) \quad [5.11]$$

The question now is to evaluate whether this simplification is also valid for the expected range of parameters for the present application. Note however that the simplification presented above was made for the hydrostatic component of the problem only. Yuen's (op.cit.) derivation of the problem of ground-lining time dependent interaction under pure distortional state of stress presented shear stresses acting at the interface ground-structure with similar form of Equation 5.10. Yuen (1979: 239) assumed a simplification similar to the passage from Equation 5.10 to 5.11 for the shear stresses, by repeating the numerical evaluation as done for the case of hydrostatic state of stress. The shear stress equation also presented three terms, as in the hydrostatic case of Equation 5.10, and the third term vanished in the shear equation similarly to what was observed for the hydrostatic case. This equation will not be shown because the interest here is the evaluation of the simplifications mentioned above for the present application and it can be shown that both hydrostatic and pure distortional cases present similar limitations. Therefore, the verification here will be limited to the case of the hydrostatic case and the results can be assumed to be valid for the distortional case.

In order to evaluate the relative significance of the term $A_3 e^{-\beta_2 t}$ in Equation 5.10, the following ratio should be considered:

$$R_{A_3} = \frac{A_3 e^{-\beta_2 t}}{A_2 e^{-\beta_1 t}} \quad [5.12]$$

Yuen (1979: 211) suggested that the term $A_3 e^{-\beta_2 t}$ in Equation 5.10 can start to be neglected for the upper limit of R_{A_3} of the order of 0.1, for all practical purposes. Table 5.2 shows the ranges of parameters considered typical for the present application, which were used to evaluate the validity of the simplification in Yuen's solution based on the R_{A_3} value criterium. Substituting all the viscoelastic parameters and the tunnel geometry as shown in Equation 5.10 into Equation 5.12, one would find a highly complex and non linear expression. For this reason, it is not possible to establish a single trend or limiting criterium for the applicability of Yuen's complete solution, or the limitations of ADVRATE, due to the simplification as that used to substitute Equation 5.10 by 5.11. However, the numerical investigation on R_{A_3} for the ranges described in Table 5.2 has indicated that for softer ground and/or higher rate of advancing, R_{A_3} tends to be higher than 0.1, while for stiffer ground or lower rate of advancing, R_{A_3} tends to be lower than 0.1. Note that the critical values of R_{A_3} occur for small values of t . These observations indicate a potential compromise on the applicability of the analytical approximation ADVRATE, because the load on lining tends to be critical for soft ground under high rate of construction.

One option to avoid this problem, i.e. the limitation due to Yuen's simplification, is to assume high values of $\frac{E_u}{\eta_l}$ for the shotcrete. It can be shown that when $\frac{E_u}{\eta_l}$ tends to infinite R_{A_3} tends to zero, making it possible to apply the solution for all practical range of ground stiffness and rate of tunnel construction. Note that the condition of high values

of $\frac{E_d}{\eta_l}$ is equivalent to assume that the short term creep deformations of the shotcrete occur almost instantaneously. In order to investigate the consequences of such assumption, a simplified calculation will be shown because the ADVRATE cannot be used for this purpose due to the limitations that are discussed here. Figure 5.6 shows a typical curve fitting of strain history as measured in instruments embedded in shotcrete for the SLRT tunnel and presented in Chapter 4. Data presented in Figure 2.3 show that the rates of advance in this case were of the order of 4 m/day. Table 5.3 shows the rate of advance recorded in recent tunnel constructions in São Paulo, where the NATM construction is widely used, and these values will be taken as typical values for this method of construction. This information indicates the rate observed in SLRT case history lies at the upper limit of the typical range. Figure 5.5 indicates that the deformations of a tunnel stabilizes around 4 radius from the face, which corresponds to about 46 hours (rate = 4 m/day, Radius = 3 m) in Figure 5.6. These two figures show similar development and stabilizing trends of the deformations, which suggests similar rates of loading in both cases.

It was shown in Chapter 4 that the deformations as presented in Figure 5.6, imposed in a three element viscoelastic model, will produce stresses as described by Equation 4.29. This solution was used to study the influence of the 'viscosity' of short term creep observed in shotcrete, i.e. the term $\frac{E_d}{\eta_l}$, on the load build up in the lining. Figure 5.7 shows the stress development for value of $\frac{E_d}{\eta_l} = 0.003 \text{ min.}^{-1}$, which represents the average value recommended in Chapter 4, values for double and for half of the average value $\frac{E_d}{\eta_l}$ and for a high value $\frac{E_d}{\eta_l}$, which will represent the condition where creep occurs instantaneously. These results show clearly that the assumption of 'instantaneous' creep would produce small deviation on the load build up with a maximum value of the order of 10%. Note that the deformation shown in Figure 5.6 imposed in this test,

represents a fast rate of tunnel advancing. For this case, Figure 5.7 shows that the short term creep deformations of the shotcrete occurred much faster than the loading due to the construction rate, and for this reason the viscosity term could be neglected. Therefore, the results taken from Figure 5.7, i.e. the assumption of 'instantaneous' creep, can be used for slower rates of tunnel construction. In conclusion, in cases of R_{A_3} larger than 0.1 (usually for soft ground under high rate of construction), one should assume an 'instantaneous' short term creep of the shotcrete in order to be able to use ADVRATE. This assumption would not produce time-load deviation larger than 10% and no deviation for the final load (Figure 5.7).

5.3.2 Horizontal to Vertical Stress Ratio

The analytical approximation presented above was developed considering a simulation under axisymmetric condition, i.e., the horizontal to vertical stress ratio $K_0 = 1$. As Yuen's solution (1979) was derived for any value of K_0 , ADVRATE can potentially be applied for any value of horizontal to vertical stress ratio of the ground. In order to examine this possibility, the results from ADVRATE calculations will be compared with three dimensional (3D) FEM simulations by Hanafy and Emery (1982) and plane strain closed form analytical solution by Einstein and Schwartz (1979).

The results by Hanafy and Emery (1980 and 1982) were selected as reference because their analyses conditions are the closest to those of the ADVRATE analytical approximation: circular tunnel, linear elastic homogeneous isotropic ground, non gravitational stress field and absence of stress free surface. These conditions were required for a FEM analysis used to 'calibrate' ADVRATE, in order to avoid unknown factor of correction due to, for example, a non circular excavation or an elastoplastic analysis. The simulations by Hanafy and Emery (1982) for $K_0 \neq 1$ were based on an axisymmetric approach with Fourier series approximation to allow non-symmetric radial loading. As the non-symmetric radial loads were represented only by the first four

harmonic terms of the Fourier series, the results by Hanafy and Emery (1982) are not 'exact'. Note that this approximation will result in smaller magnitude and imperfect distribution of the loads. The parameters used in Hanafy and Emery (1982) simulations are shown in Table 5.4 and the results of unlined tunnels in terms of convergence are shown in Figures 5.8 and 5.9, for points located at the crown/floor and springline, respectively. For this reason, in order to compare the results of these simulations with the analytical approximation, it was necessary to estimate some adjustments of the input parameters. Using a linear elastic closed form solution (Kirsch, 1898), it was found that the vertical stress σ_v should be reduced from 1.7 MPa to 1.45 MPa (85% of original value) and the Poisson's ratio ν_g should be reduced from 0.4 to 0.3. These corrected parameters produce convergence values for K_0 of 0.75, 1.00 and 1.25, for Kirsch's closed form solution results equivalent to the FEM analyses from Hanafy and Emery (1982). Therefore, in ADVRATE calculations the corrected vertical stress σ_v was set as 1.45 MPa and ν_g was set as 0.3. Figures 5.8 and 5.9 show the results from ADVRATE and the convergence values agree well with the 3D FEM simulation by Hanafy and Emery (1982). Note however, that these results show poorer agreement than those shown in Figure 5.5 for unlined tunnel and $K_0 = 1$, even for the case of $K_0 = 1$ in Figures 5.8 and 5.9. These larger deviations can be attributed to the approximation in the 3D FEM formulation and also due to the adjustments done in σ_v and ν_g .

Figures 5.10 and 5.11 present the comparison of convergence of lined tunnels between the 3D FEM simulation by Hanafy and Emery (1982) and results from ADVRATE for points located at the crown/floor and springline. The parameters used in these analyses were the same used in the unlined simulation presented above and they are shown in Table 5.4. It can be observed that the agreement of the convergence development shown in Figures 5.10 and 5.11 is poorer than those shown in Figure 5.5, particularly close to the tunnel face. On the other hand, good agreement is observed for the final values of convergence. These results were expected as a consequence of the

deviations already observed in the unlined cases, resulting from the approximation in the 3D FEM simulation and the adjustments done for the analytical approximation ADVRATE. It is interesting to observe the different convergence development patterns: in the 3D FEM simulation the convergences show a smooth asymptotic trend while in ADVRATE the convergences show change of trends when the lining is installed, presenting in some cases inversion of the convergence trends. Note that this inversion of convergence trend, for $K_0 \neq 1$, has been observed during construction instrumentation (e.g. Branco, 1981: 111) and in 3D FEM simulations (e.g. Katzenbach, 1981: 65). The design method used in Chapter 2 also presented this trend, which can be observed for $K_0 < 1$ at the springline, as shown in Figures 2.16 and 2.17.

The effect of this different convergence development pattern on the load on the lining cannot be assessed directly because Hanafy and Emery (1982) presented displacement results only. An evaluation of the load results will be presented based on the well known plane strain analytical closed form solution developed by Einstein and Schwartz (1979), for linear elastic materials. As this solution assumes that the lining is installed simultaneously with the excavation of the lining, it requires adjustment to take into account the 3D effect and delay of the lining installation. One option would be the application of correction concept similar to that presented in Chapter 2 for Negro's (1988) method, which was developed for non linear ground with consideration of gravitational stress gradient. As the ground here is considered linear elastic, the stress release factor α as defined by Negro (1988), see Figure 2.15, can be redefined as:

$$\alpha = \frac{U}{U_f} \quad [5.13]$$

Substituting Equations 5.5 and 5.7 into 5.13, one will find:

$$\alpha = 1 - \kappa e^{-\lambda_g t} \quad [5.14]$$

Negro (1988) proposed reduction of unit weight by $\Sigma = 1 - \alpha$ in order to take into account the 3D and lining delay effects, as shown in Figure 2.15, for the analytical closed form solution by Hartmann (1970). Therefore, in the linear elastic ground, the reduction factor for the unit weight would be:

$$\Sigma = \kappa e^{-\lambda_g t} \quad [5.15]$$

For the axisymmetric analysis by Hanafy and Emery (1980) $\kappa = 0.629$ and $\omega = 1.099$ were found adequate for curve fitting of Equation 5.2. Considering a delay of one radius on lining installation, as in the cases of lined tunnels under investigation and applying Equation 5.9, one will find $\lambda_g t = \omega$. Substituting these values into Equation 5.15, one would find $\Sigma = 0.21$. Note that in Einstein and Schwartz's (1979) solution the insitu stress is an input value while in Hartmann's (1970) solution, the insitu vertical stress is calculated by multiplying the unit weight by the column of soil. For this reason, in the calculations performed using Einstein and Schwartz's (1979) solution, the factor Σ was applied to correct the insitu stress as shown in Table 5.4 ($\sigma_{v_{red}} = \sigma_v \Sigma$), maintaining the values of all the other parameters. As this solution was derived for plane strain condition, these results are presented as the asymptotic values in Figures 5.12 and 5.13. In these figures, T , $\bar{\sigma}$ and t correspond to thrust, average of insitu vertical and horizontal stresses and thickness of the lining, respectively. These figures also present the load development as calculated by ADVRATE, which final loads agree well with the results from Einstein and Schwartz's (1979) solution. The deviation of the results can be attributed to the different assumptions used to take into account the delay of lining installation in Einstein and Schwartz (1979) and ADVRATE. Nevertheless, these results show that the analytical approximation ADVRATE presents final loads compatible with

the corrected plane strain solution. It is believed that these results are within the practical range of load values because the correction applied in Einstein and Schwartz's solution using the Σ concept followed the same correction criteria as those used by Negro (1988) to correct Hartmann's solution, which was tested and approved by back analyzing several case histories.

5.3.3 Gravitational Stress Gradient

As mentioned above, ADVRATE does not include the gravitational stress gradient effect in the analytical approximation proposed here. Negro (1988: 26) concluded that in urban shallow tunnel design, for values of the cover/diameter ratio (H/D) greater than 1.5, the stress free boundary at the ground surface could be neglected, but the influence of the gravitational stress gradient should always be taken into consideration. Note also that the findings of this thesis are intended to be applied in connection with Negro's (1988) method, which is limited to tunnels with $H/D > 1.5$. For this reason, only the gravitational stress gradient will be investigated here.

As mentioned earlier, the main difference between the solutions by Einstein and Schwartz (1979) and Hartmann (1970) is the consideration of the gravitational stress gradient in the latter. Therefore, the comparison between the results of these solutions can be used to verify the effect of gravitational stress gradient on the load on the tunnel lining. Figures 5.14 and 5.15 present the calculated thrust and bending moments respectively, normalized as previously discussed in this chapter. In the normalization of results of Hartmann's solution, $\bar{\sigma}$ refers to the average of horizontal and vertical insitu stresses at a point at the center of the tunnel, and in Figure 5.15, M stands for bending moment. The parameters used in these analyses are shown in Table 5.5, where the ground represents a medium clay, the liner parameters are typical equivalent secant moduli of shotcrete as discussed in Chapter 4 and the radius of the tunnel is 3 m. In all

calculations, both in Einstein and Schwartz as well as in Hartmann's solution, the 'no slip' condition was assumed for the interface between the ground and shotcrete.

Figure 5.14 shows that the values of thrust in springline are the same for both solutions, while the Einstein and Schwartz's solution underestimates the thrust for the floor and overestimates it for the crown. Note that here, the deviations in Einstein and Schwartz's solution would be similar to those expected from ADVRATE, as both of them do not consider the gravitational stress gradient. Figure 5.15 shows similar deviations in bending moments as observed for thrust calculations, but in this case, one can observe a shift of values as opposed to the asymptotic trends shown in Figure 5.14. This deviation can be attributed to different derivation details for the bending moment evaluation equations. Hartmann (1970) did not neglect the derivatives of second order while Einstein and Schwartz (1979) did. For this reason, the asymptotic values of the Hartmann solution might be considered more accurate.

Observing Figures 5.14 and 5.15 for tunnels constructed with $H/D > 1.5$, the deviations expected in terms of thrust and bending moments are smaller than 15%, decreasing as H/D increases. Therefore, for fast calculations, the gravitational stress gradient can be neglected, and ADVRATE can be used without adjustments. However, for more careful calculations, a correction is suggested in the results from ADVRATE, proportionally to the differences observed in results shown in Figures 5.14 and 5.15, using the appropriate calculation parameters in Einstein and Schwartz's and Hartmann's solutions.

5.4 Applications

5.4.1 Tunneling Response for Different Rates of Construction

The analytical approximation ADVRATE presented so far, can take into account the short term creep of the liner by using the average viscoelastic parameters as suggested in Chapter 4, for shotcrete older than 10 hours. However, the linear viscoelastic model is

not able to simulate the changes of the shotcrete properties due to curing at the period between 0 to 10 hours of age. The shotcrete tests presented in Chapter 4, showed that the deformations at very early stages may be very large, depending on the loading function. The deformation parameters during this period were about one order of magnitude larger than those for the period after 10 hours. As an example, in test CRSLP2 a stress increment of 3% of the total load was applied between 4 to 12 hours of age, and it induced strains 200% larger than the deformations due to the subsequent loading (95% of the loading). These facts suggest that in terms of load build up, the presence of the lining can be neglected for the period before 10 hours age. Therefore, in calculations using ADVRATE, the 'total' delay of the lining installation will be considered as the 'physical' delay of the lining installation plus 10 hours necessary to harden the shotcrete enough to carry load.

Table 5.6 presents the parameters used to investigate the thrust and convergence development in lined tunnels for different rates of construction advancing using ADVRATE. It represents a typical tunnel with radius of 3 m constructed in stiff clayey ground with $K_0 = 1$ at depth of about 10 m. The shotcrete lining properties are taken as the average values of the viscoelastic model for the short term behavior, and the thickness is 15 cm. The rate of construction is within the typical range as shown in Table 5.3 and as discussed in Chapter 4 and the delay in the lining installation is one radius.

Figures 5.16 and 5.17 present the development of the convergence and thrust, respectively, according to the tunnel advancing, and using the same normalization as presented earlier. A striking feature that can be observed in these figures is that slower rate of advancing reduces the tunnel convergence and increases the thrust in the lining while faster rates produce the opposite reaction. Note that these effects are direct consequences of the minimum curing time necessary to harden the shotcrete enough to sustain load. This aspect can be observed in Figure 5.17, where the 'physical' delay of the lining installation is one radius for any of the rate of construction. However, according to

results from laboratory tests, additional 10 hours are necessary to harden the shotcrete. When different rates of advance are considered, these 10 hours will reflect as different additional delays of lining activation in terms of distance from the tunnel face. One can observe this effect in Figure 5.17 where different 'total' ('physical' plus 10 hours) delays of lining activation can be recognized by the points where the loads start to increase. Although these results are based on a simplified model where the curing effect was simulated by a single discrete step, i.e. during 0 to 10 hours the deformation properties were considered zero and afterwards they were non zero with constant values, a more realistic simulation considering a continuous curing of the shotcrete would produce similar effects. It is interesting to note that the variation on the convergence values due to the different rates of advancing are of the order of 10%, while the variation of the thrust values are of the order of 50%.

Figures 5.18 and 5.19 show the values of convergence and thrust for the same calculation presented above, but in these cases, the development is shown in terms of time. These figures show, as expected, that the stabilization of convergence and thrust occur in short time intervals for fast rate of construction, and *vice versa*. Figure 5.19 shows that the faster the construction rate, the smaller the final load. However, for the fast construction rates, the loads start to build up earlier, which also means lower strength of the shotcrete. For the range of parameters investigated in these examples, shown in Table 5.6, it can be shown that the strengths of the shotcrete are at least one order of magnitude larger than the thrust values, for any time, suggesting the strength would not be a problem in these cases. These results can be obtained using Equation 4.4 which describes the strength development with time, and using the parameters shown in Table 4.5. Note however, that these simplified calculations have neglected the ground-lining interaction for the period between 0 to 10 hours of age of shotcrete. For this period, stability problems can occur near the tunnel face, which is not taken into account in this calculation. The stability problems are considered out of scope of the present thesis and

one should refer to Heinz (1988: 81-126), who reviewed and compiled solutions for two and three dimensional problems. Therefore, in order to validate the calculations using ADVRATE, one should first ensure the stability of the tunnel construction, specially for the near face zone for the period 0 to 10 hours of age of shotcrete.

5.4.2 Adjustments for Non Linear Ground Response

The design method as proposed by Negro (1988) has been used as a reference calculation procedure for the practical application of the findings of the present thesis. This method considers the non linearity of the ground response, while the ADVRATE calculations, as presented earlier, assume the ground as linear elastic. The adaptation of ADVRATE to include the non linearity of the ground can be done in a similar way as Negro (op. cit.) adapted Hartmann's (1970) solution into the design method. As already discussed in Chapter 2, in Negro's method the ground-lining interaction stage of the calculation procedure can be approached by a linear elastic model. However, before calculating the ground-lining interaction using a linear elastic analytical solution it is necessary to provide adjustments to consider the amount of stress release and stiffness change at the moment of the lining activation. The factors used by this method are an artifice to take into account the delay of the lining installation to use in a plane strain simulation. The estimation of the stress release and stiffness change is based on prediction of the value of the convergence of a point at the tunnel crown. This convergence is evaluated using results from linear elastic three dimensional FEM calculations, which have simulated the ground surface and the gravitational stress gradients.

In order to include the non linear ground response in ADVRATE, it is proposed to reduce the ground stiffness following exactly the same procedure by Negro (op. cit.). The delay of lining installation in ADVRATE should follow the same simulation procedure as it was done in the examples presented earlier. Note that this a necessary

approximation since ADVRATE does not simulate the ground surface and gravitational stress gradient as included in Negro's (1988) method. Or in other words, the delay of lining installation as proposed in ADVRATE is based on a weightless linear elastic axisymmetric simulation by Hanafy and Emery (1980), while in Negro (op. cit.), the evaluation is based in linear elastic 3D FEM simulation which considered the gravitational stress distribution in the ground. For this reason, one should expected some deviation between the results of these two assumptions. If the method is applied for construction control, the measured displacement of the crown should be used, neglecting the estimation by the 3D FEM results. Accordingly, in ADVRATE, the delay of the lining installation may be adjusted to field measurement by finding the time t in Equation 5.15 that presents the average value of Σ that one would find applying the recommendation by Negro (op. cit.: 1177). Another feature in this method is the correction of the non linear response of the ground due to the ground-lining interaction stage. This was done interactively in Negro's method using Hartmann (1970), and it is possible to repeat this procedure using ADVRATE.

For quick calculations of the ground lining interaction, Negro (op. cit.: 1321) recommended 50% of reduction for both ground stiffness and insitu stresses, for either TBM or NATM construction techniques. For the case of NATM tunnels, the interest of the present thesis, these values are taken as the average values shown in Table 5.7 which shows all the NATM tunnels back analyzed by Negro (op. cit.).

A complete example of application of the corrections discussed in this section will be presented in the next chapter for the final interpretation of the SLRT instrumentation.

5.5 Summary and Conclusions

This chapter presented a simplified procedure which simulates different rates of tunnel construction. The procedure followed the same concept of stiffness manipulation

of the core stiffness reduction technique in order to simulate the 'third' dimension missing in a plane strain model. The analytical approximation proposed manipulates the ground stiffness instead of the core stiffness as in the previous techniques. The plane strain three element viscoelastic analytical solution for lined tunnels derived by Yuen (1979) was used to 'control' the stiffness of the ground as function of time, which permitted simulation of different rates of tunnel construction.

Using an axisymmetric linear elastic FEM simulation by Hanafy and Emery (1980) it was possible to calibrate the 'artificial' viscoelastic parameters of Yuen's solution in order to emulate the advancing of the tunnel construction of the 'real' linear elastic ground. This calibration is represented by parametric transformations which were introduced in Yuen's solution. The final result of this analytical approximation to solve the problem is presented in the form of a BASIC program (Appendix E) denominated ADVRATE. It was translated from a FORTRAN program by Yuen (op. cit.) with introduction of the parametric transformation and some other minor modifications. The viscoelastic properties of the liner in ADVRATE are suitable to describe the short term behavior of the shotcrete as presented in Chapter 4. Comparison between results from ADVRATE and axisymmetric simulations by Hanafy and Emery (1980) showed that the analytical approximation produced good estimation of convergence. Moreover, the delay of lining installation can be successfully simulated

Yuen (op. cit.) assumed a simplification during the derivation of the analytical solution, which is not valid for all ranges of parameters expected for shallow urban tunnels. This simplification tends to introduce errors for soft ground and/or high rate of construction. However, if one assumes that the short term creep of the shotcrete is 'instantaneous', this limitation vanishes. It was shown that this assumption would not produce time-load deviation larger than 10%, which is considered acceptable for practical purposes.

For values of $K_0 \neq 1$, the comparison between results of convergence developments from ADVRATE and the approximate 3D FEM simulation by Hanafy and Emery (1982) did not fully agree, although the final values were very close. It was noted that, as opposed to the FEM results, ADVRATE presented inversion of convergence trend when the lining is installed, as one would expect, for example, in the springline for $K_0 < 1$. Direct assessment of the impact of convergence deviations on the load development was not possible due to lack of data. Indirect assessment using the analytical solution by Einstein and Schwartz (1979) indicated that ADVRATE presented load at the magnitude one should expect from conventional design procedure.

ADVRATE does not take into consideration the gravitational stress gradient expected in shallow tunnel problems. In order to evaluate this effect, comparison between results of analytical solutions by Einstein and Schwartz (1979) and Hartmann (1970) were presented. The latter has included the gravitational stress gradient while the formers neglected it. Results indicated that ADVRATE would overestimate values of thrust and bending moment for points at the crown, underestimate them for points at the floor and make correct estimation for points at the springline. Deviations thrust and bending moments for a typical tunnel in medium clay with $H/D > 1.5$ would be limited to 15%. If this deviation is considered too large, it was suggested to correct the results obtained from ADVRATE proportionally to the difference from calculations using Einstein and Schwartz's (1979) and Hartmann's (1970) solutions.

Tunneling responses due to different rates of construction were investigated using ADVRATE and the parameters resulted from investigations on the shotcrete behavior presented in Chapter 4. The analyses simulated a typical tunnel of 3 m of radius, at 10 m depth, constructed in a stiff clay. The rates of advancing were 1/3, 2/3, 3/3 and 4/3 radius/day. It was observed that the variation on the rate of construction advance produced a variation of about 10% in the final value of convergences and about 50% in the final values of the lining thrust. The faster the construction rate, the larger the

convergence and the smaller the thrust. These results are the direct impact of the minimum time, set in these analyses as 10 hours necessary for the shotcrete to harden. Although the final thrusts are smaller in fast rate of construction, the loads start to build up earlier when the strength of the shotcrete tends to be smaller. Stability of the construction may be critical, specially in the 10 first hours neglected by ADVRATE. The stability calculation was considered out of the scope of this thesis and one should refer, for example, to the compilation done by Heinz (1988: 81-126). Also, a procedure based on Negro (1988) was suggested for a non linear ground response.

Table 5.1 Parameters Used in the Axisymmetric Simulations for Lined Tunnels Shown in Figure 5.5

	Young's Modulus	Poisson's Ratio	Complementary Informations
Ground	5×10^3 GPa	0.2	$K_0 = 1$ $\sigma_{insitu} = 8$ MPa
Liner	30×10^3 GPa	0.2	thickness = 0.6 m
Tunnel Construction	-	-	radius = 5 m (1) rate of advancing = 3 m/day

(1) rate of advancing required by ADVRATE simulation

(2) no slip condition assumed in ADVRATE

Table 5.2 Range of Values for the Parameters of Ground-Structure Interaction Problem Investigated to Evaluate the Applicability of Simplified Equation 5.11, for the present application

	Deformation Parameters	Complementary Informations
Ground (linear elastic)	$E_{greal} < 10$ MPa soft $E_{greal} \cong 50$ Mpa medium $E_{greal} > 120$ MPa stiff $\nu_g = 0.2$ to 0.4	typical values for clayey soils at 10m depth
Liner (viscoelastic)	$E_l = 15$ GPa $\frac{1}{E_d} = 0.03$ 1/GPa $\frac{E_d}{\eta_l} = 0.003$ 1/min. $\nu_l = 0.3$	viscoelastic parameters from results shown in Chapter 4 for short term behavior thickness = 0.18 m
Tunnel Construction	-	radius = 3 m range of rate of advancing = 1 to 6 m/day

Table 5.3 Rate of Advance of some Recent Urban Tunnels Built in São Paulo by the NATM (modified from Negro, 1989)

Tunnel	Approx. Extension (m)	Year of Construct.	Area of Excav. (m ²)	Excav. Scheme	Excav. Equipm.	Ground	Water Level	Rate of advance
ABV	70	1978	12.8	Heading & Bench	Jackhammer	dense clayey sand	below tunnel	1.2 m/day (8h/day)
Extension of N-S Line Double Track	200	1984	79	Head. & Bench (w. temporary invert)	Jackhammer & backhoe	stiff fissured clay	above tunnel	1.0 m/day (24h/day)
Paulista line Double Track Paraiso Tunnel	150	1988	80	Heading & Bench	Jackhammer & backhoe	soft porous clay & stiff variegated clay	at springline	1.5 m/day (24h/day)
Pinheiros 1 freeway	1000	1988	50	Head.&Bench (no invert)	Road Header w. conv. belt	hard fissured clay	above tunnel	4-6m/day (24h/day)
Pinheiros 2-freeways	1000	1988	50	Head.&Bench (no invert)	Jackhammer & backhoe	hard fissured clay	above tunnel	1-2m/day (24h/day)
Ibirapuera 1 freeway	1500	1988	50	Head.&Bench (no invert)	Jackhammer & backhoe	stiff fissured clay	above tunnel	1-2m/day (24h/day)
Ibirapuera 2 freeways	1500	1988	50	Head.&Bench (no invert)	Jackhammer & backhoe	stiff fissured clay	above tunnel	1-2m/day (24h/day)
Access tunnel to Consolacao Station (subway)	200	1989	49	Full face with central core	Jackhammer & backhoe	stiff to hard clay	above tunnel	1.2m/day (24h/day)

Table 5.4 Values for the Parameters in Hanafy and Emery (1982) Simulation used to Evaluate the Applicability of ADVRATE for Conditions of $K_0 \neq 1$

	Deformation Parameters	Complementary Informations
Ground (linear elastic)	$E_{greal} = 210 \text{ MPa}$ $\nu_{gor} = 0.4$: 'original' value $\nu_g = 0.3$: 'adjusted' value (1)	$K_0 = 0.75, 1.00 \text{ and } 1.25$ $\sigma_{vor} = 1.7 \text{ MPa}$: 'original' value $\sigma_v = 1.45 \text{ MPa}$: 'adjusted' value (1)
Liner (linear elastic)	$E_l = 21 \text{ GPa}$ $\nu_l = 0.2$	thickness = 0.17 m
Tunnel Construction	-	radius = 1.334 m delay of lining installation = 1 radius rate of advancing= 3 m/day (2)

(1) σ_v and ν_g adjusted to compensate FEM approximation (see text)

(2) rate of advancing necessary to simulation in ADVRATE

(3) no slip condition assumed in ADVRATE

Table 5.5 Values for the Parameters used to Evaluate the Influence of Gravitational Stress Gradient on Liner Loads

	Deformation Parameters	Complementary Informations
Ground (linear elastic)	$E_{ground} = 50 \text{ MPa}$ $\nu_{ground} = 0.3$ $\gamma_{ground} = 18 \text{ kN/m}^3$	$K_0 = 0.8$
Liner (linear elastic)	$E_l = 10 \text{ GPa}$ $\nu_l = 0.3$	thickness = 0.20 m
Tunnel Construction	-	radius = 3 m $0.5 \leq H/D \leq 8$

(1) no slip condition assumed for all calculations

Table 5.6 Parameters of Lined Tunnel Simulation using ADVRATE to Investigate Convergence and Thrust Developments for Different Rates of Construction Advancing

	Deformation Parameters	Complementary Informations
Ground (linear elastic)	$E_{greal} = 150 \text{ Mpa}$ $\nu_g = 0.3$	$K_0 = 1.0$ $\sigma_v = 170 \text{ kPa}$
Liner (viscoelastic)	$E_l = 15 \text{ GPa}$ $\nu_l = 0.3$ $\frac{1}{E_d} = 0.03 \text{ 1/GPa}$ $\frac{E_d}{\eta_l} = 0.003 \text{ 1/min.}$	viscoelastic parameters from results shown in Chapter 4 for short term behavior thickness = 0.15 m
Tunnel Construction	-	radius = 3 m range of rate of advancing = $\frac{1/3 \text{ } 2/3}{3/3 \text{ } 4/3}$ radius/day delay of lining installation = 1 radius

5.7 Results of the Application of Design Method for NATM Tunnels (modified from Negro, 1988)

Tunnel	ABV - S. Paulo	Romerberg-Frankfurt	Butterberg	Munich 5/9	Bochum	São Paulo - North Extension	Munich 8/1
Soil	Clayey-sand	Clay Marl	Sandy Gravel	Hard Marl	Heter. Marl	O.C. Clay	Hard Marl
H/D	1.550	1.775	1.183	2.880	1.351	1.138	3.184
Shape	non-circ.	circ.	non-circ.	non-circ.	non-circ.	non-circ.	non-circ.
K_0	0.8	0.8	0.5	1.0	0.8	0.9	1.0
Lining Activation	0.65	0.88	0.826	0.8	0.7	0.925	1.013
A_d/D							
Σ at L.A.	0.471	0.445	0.363	0.508	0.434	0.471	0.490
E_l/E_d at L.A.	0.445	0.448	0.542	0.511	0.537	0.409	0.488
E_l/E_d at Equil.	0.449	0.451	0.678	0.431	0.519	0.412	0.399
FS at L.A.	1.437	1.667	1.210	2.010	1.694	1.346	1.910

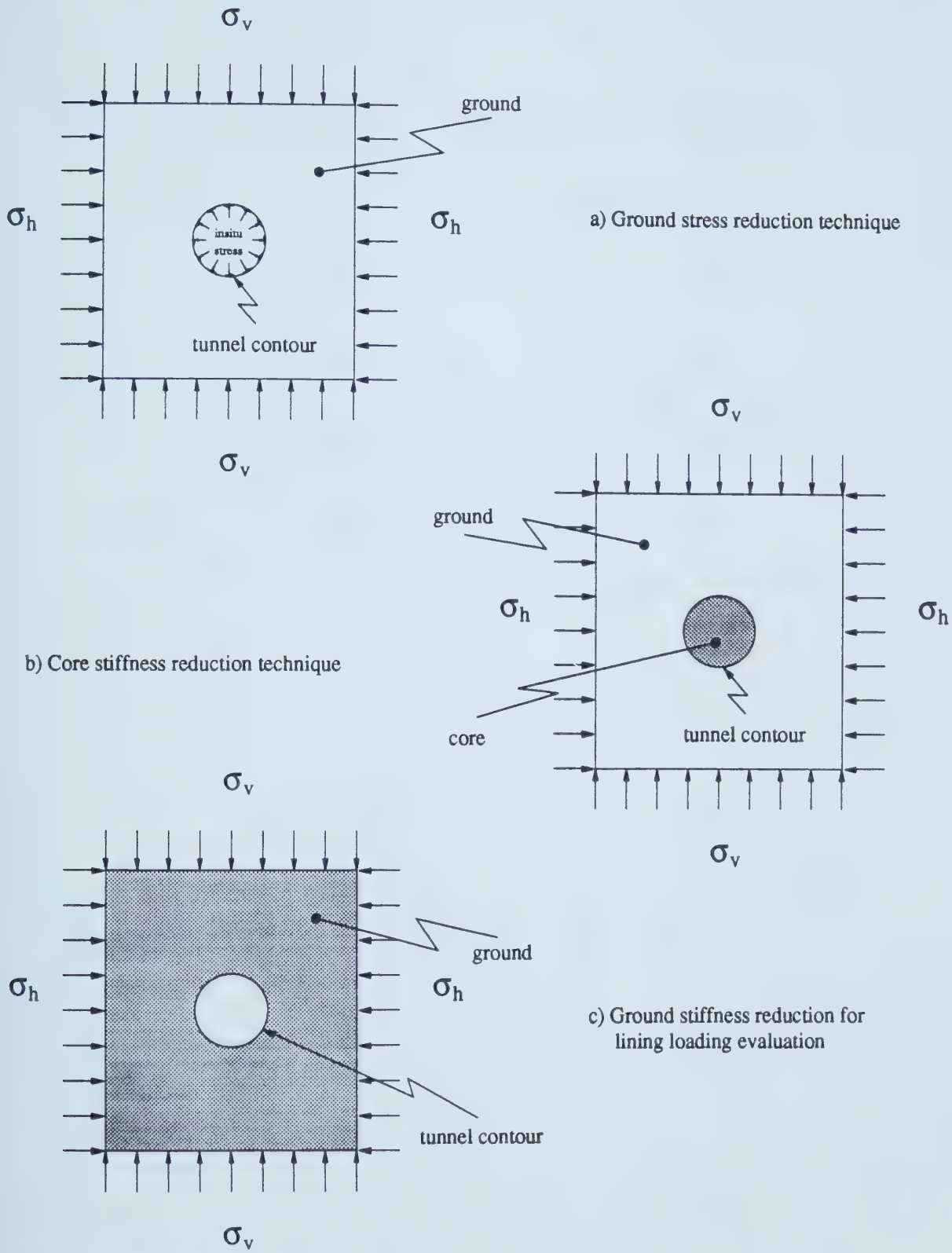
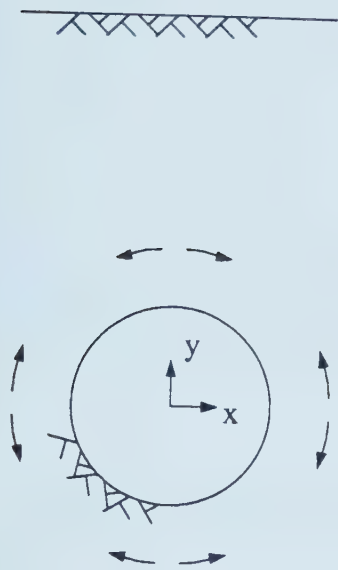


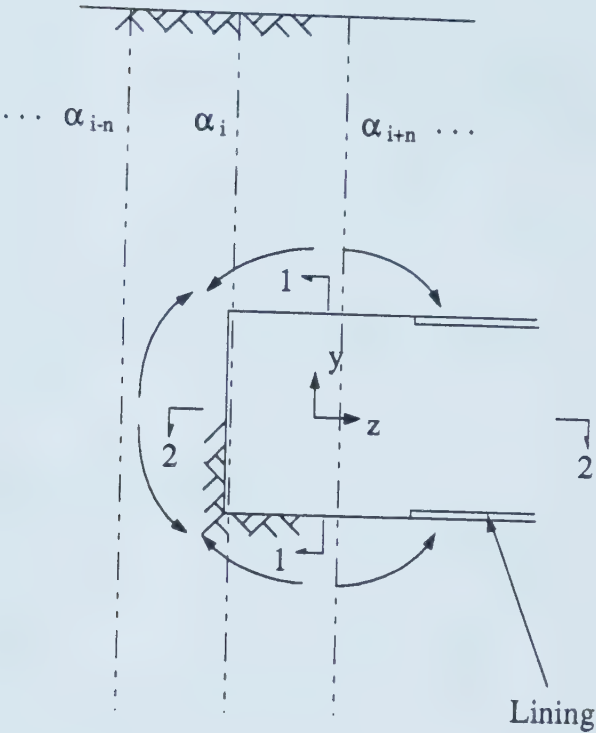
Figure 5.1 Techniques to Emulate Tunnel Advance Effect using Two Dimensional Model

TRANSVERSE ARCHING

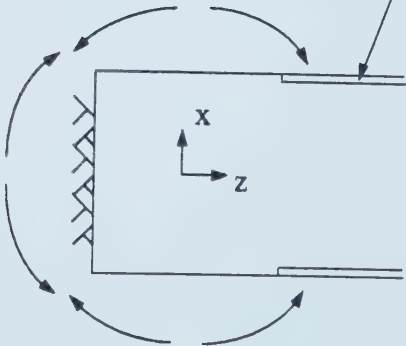


Section 1-1

LONGITUDINAL ARCHING

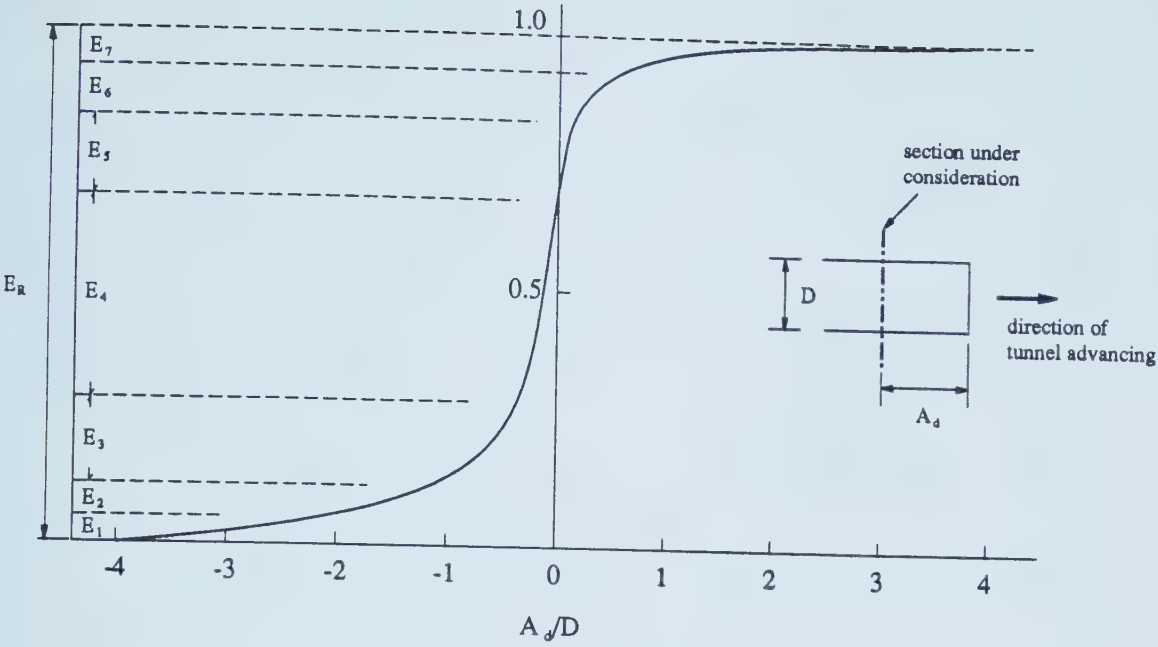


HORIZONTAL ARCHING

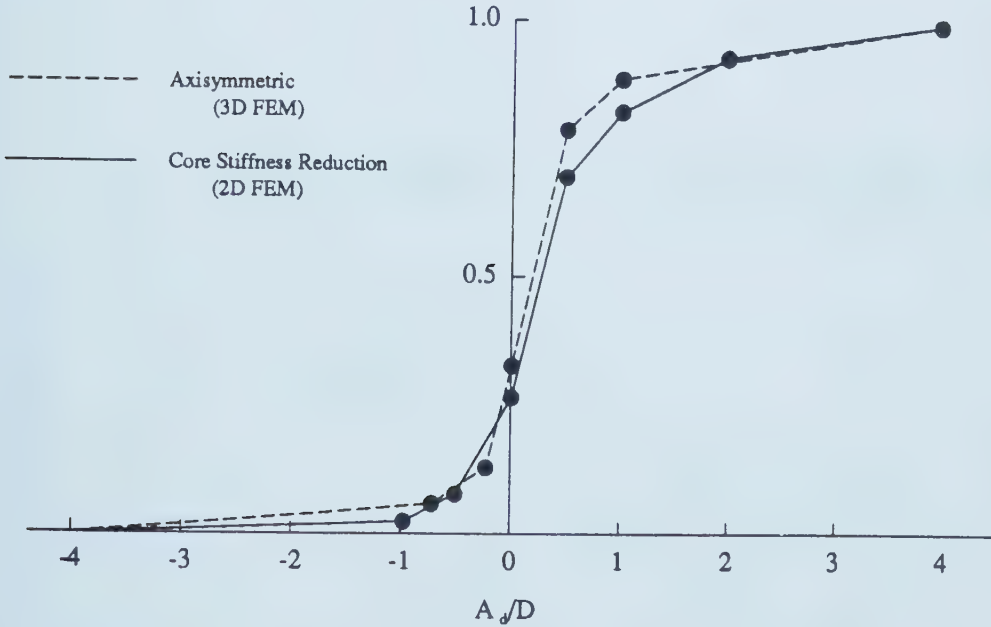


Section 2-2
(plan view)

Figure 5.2 Three-Dimensional Arching near the Face of an Advancing Tunnel
(modified from Eisenstein et.al., 1984)



a) Normalized Stiffness Curve according to Tunnel Advancing



b) Normalized Deformation in Progress of Tunnel

Figure 5.3 Analysis of Tunnel Advancing using Two-Dimensional F.E.M. Simulation (modified from Ohnishi et al., 1982)

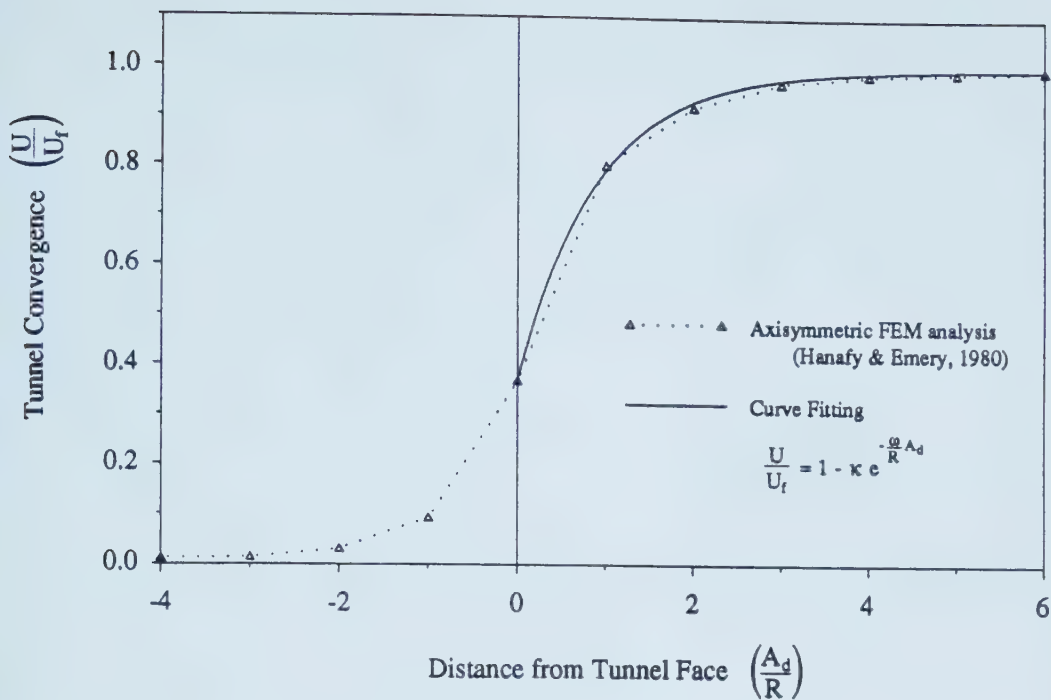


Figure 5.4 Curve Fitting of Tunnel Convergence versus Distance from Tunnel Face for $K_0 = 1$

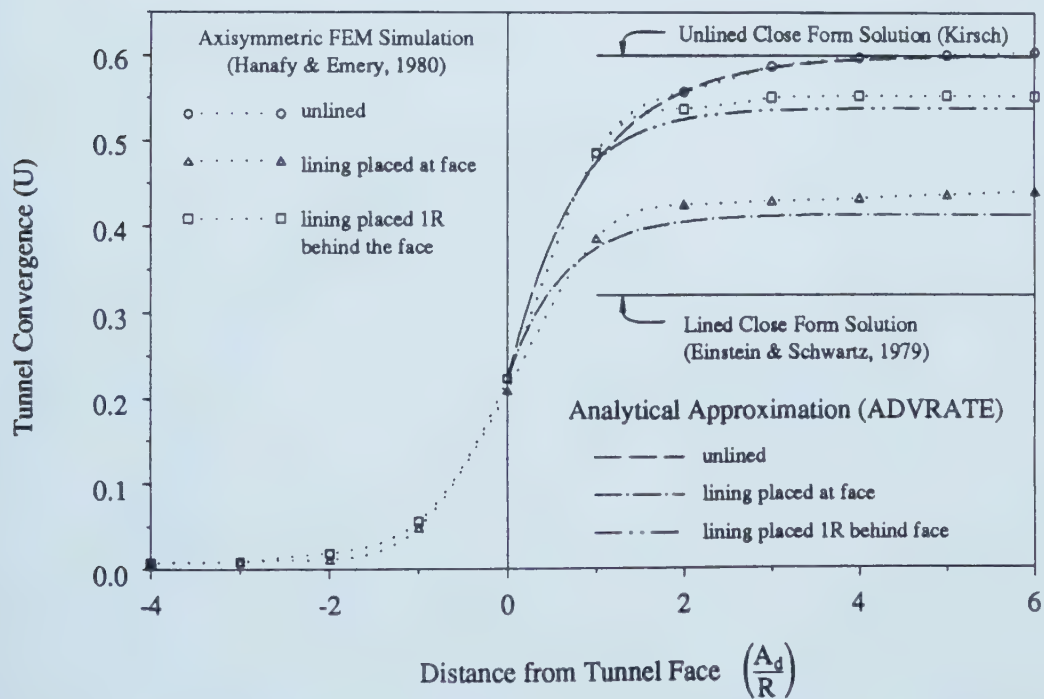


Figure 5.5 Comparison between axisymmetric FEM Simulation and Analytical Approximation for $K_0 = 1$

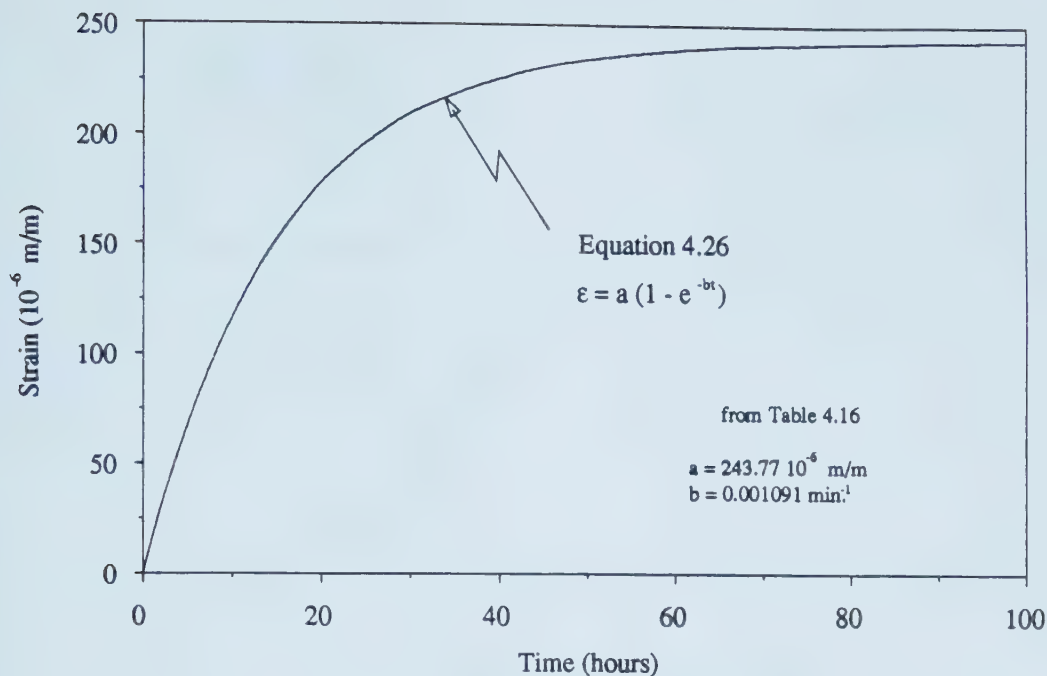


Figure 5.6 Strain Development as Fitted to Strain Readings in SLRT Shotcrete Lining, for Advancing Rate $A_d = 4$ m/day

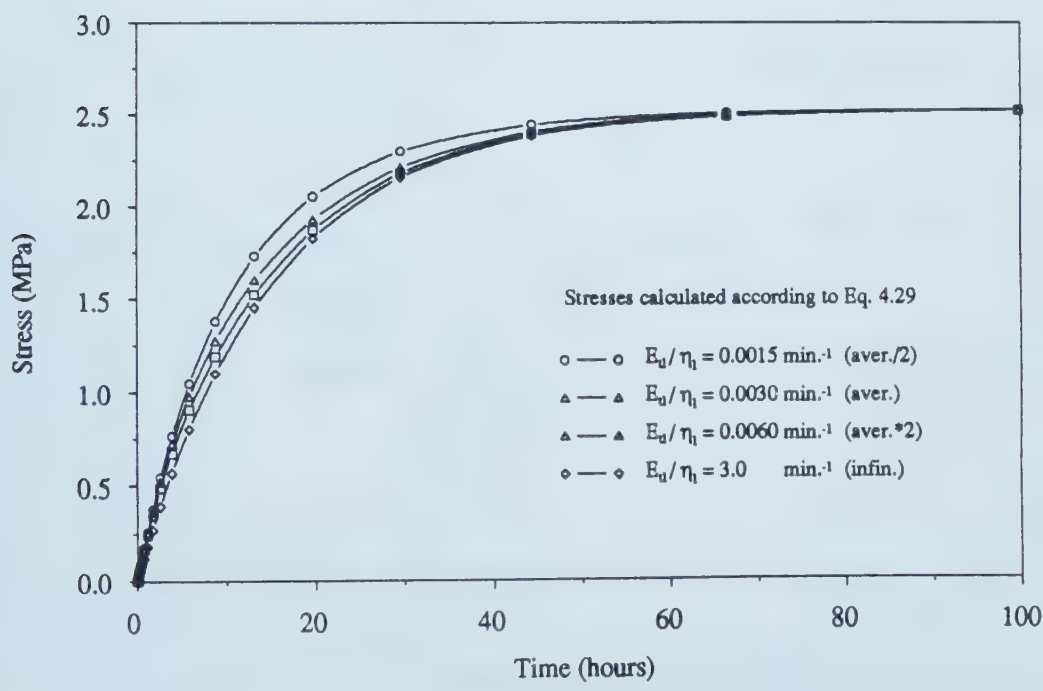


Figure 5.7 Stress Development for Strain Controlled Deformation as Measured in Typical Instrument in SLRT Tunnel, with Advancing Rate $A_d = 4$ m/day

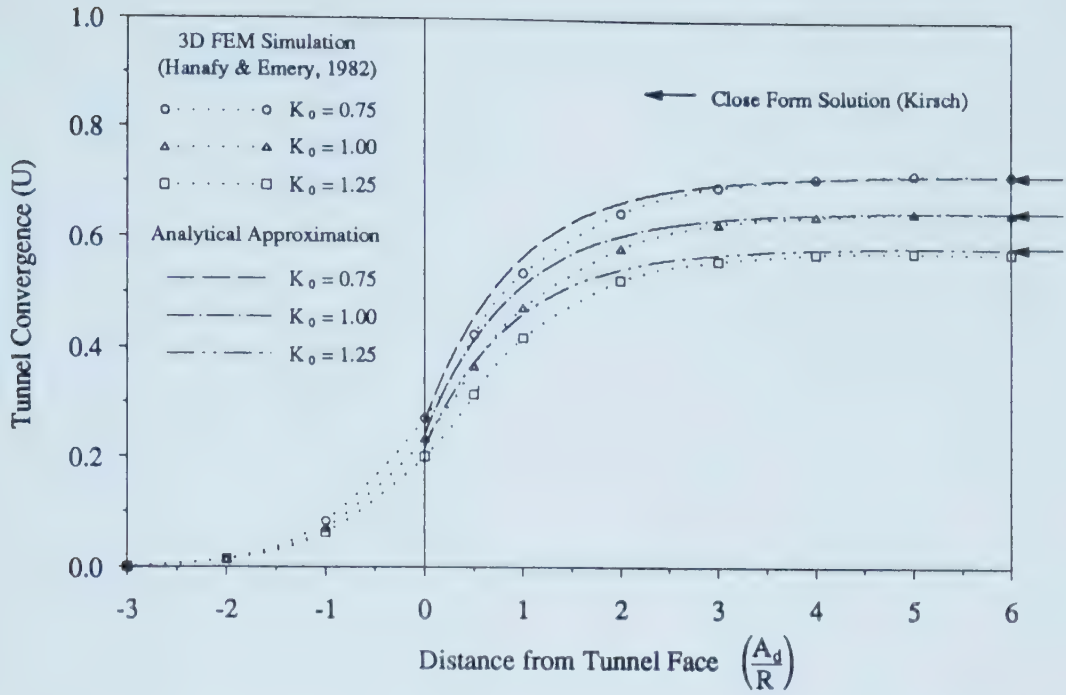


Figure 5.8 Comparison between Convergence Calculated by 3D FEM Simulation and Analytical Approximation for Points at Crown and Floor, Unlined Tunnel

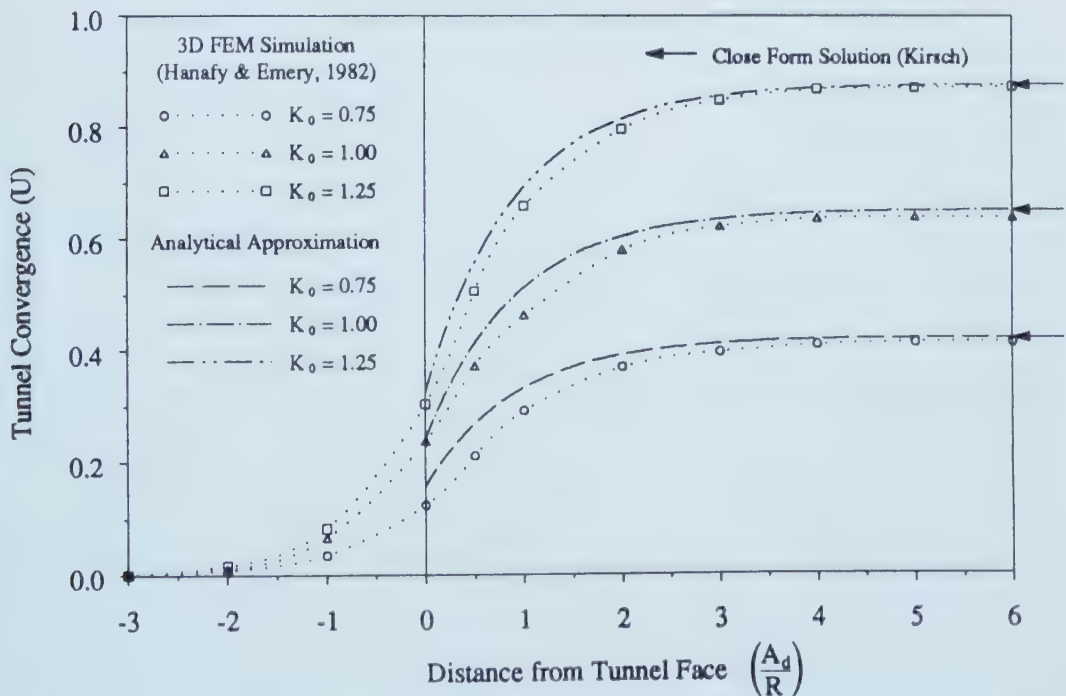


Figure 5.9 Comparison between Convergence Calculated by 3D FEM Simulation and Analytical Approximation for Points at Springline, Unlined Tunnel

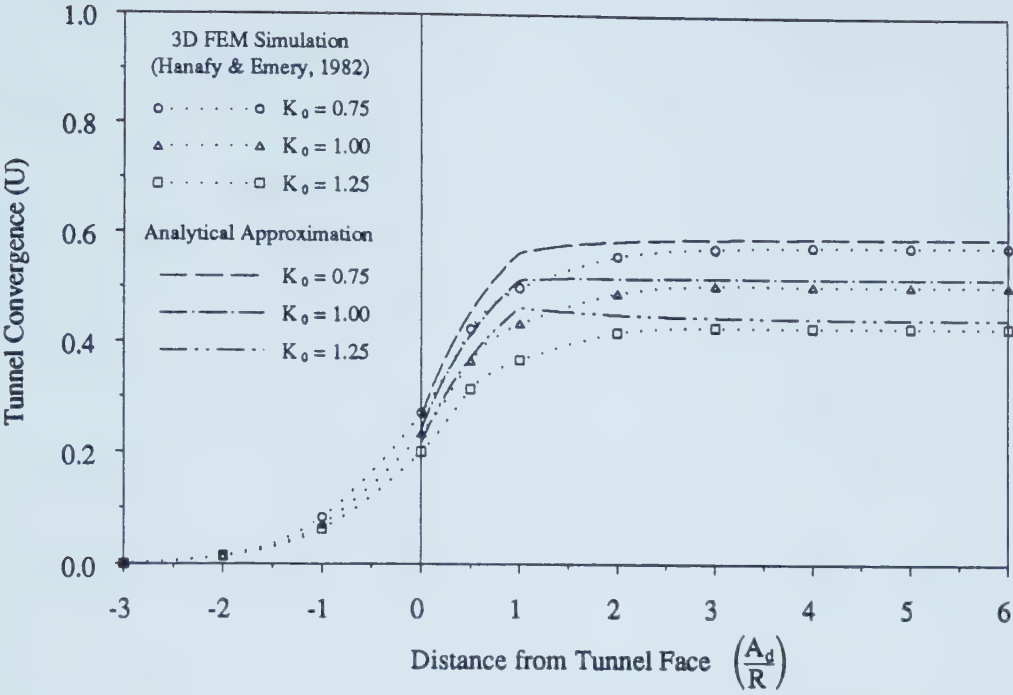


Figure 5.10 Comparison between Convergence Calculated by 3D FEM Simulation and Analytical Approximation for Points at Crown and Floor, Lined Tunnel

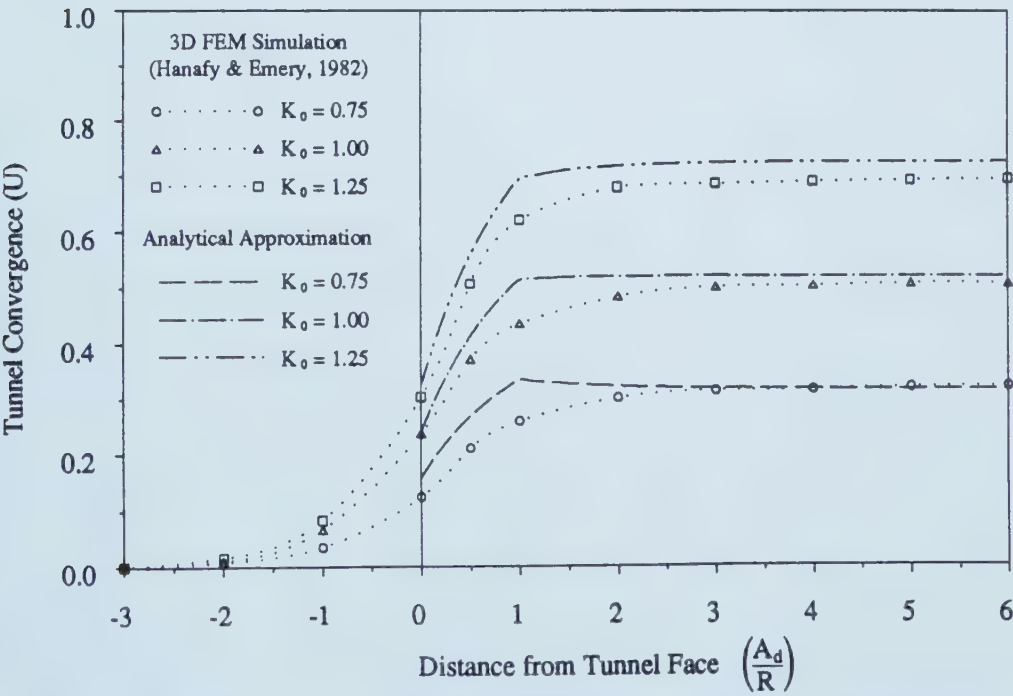


Figure 5.11 Comparison between Convergence Calculated by 3D FEM Simulation and Analytical Approximation for Points at Springline, Lined Tunnel

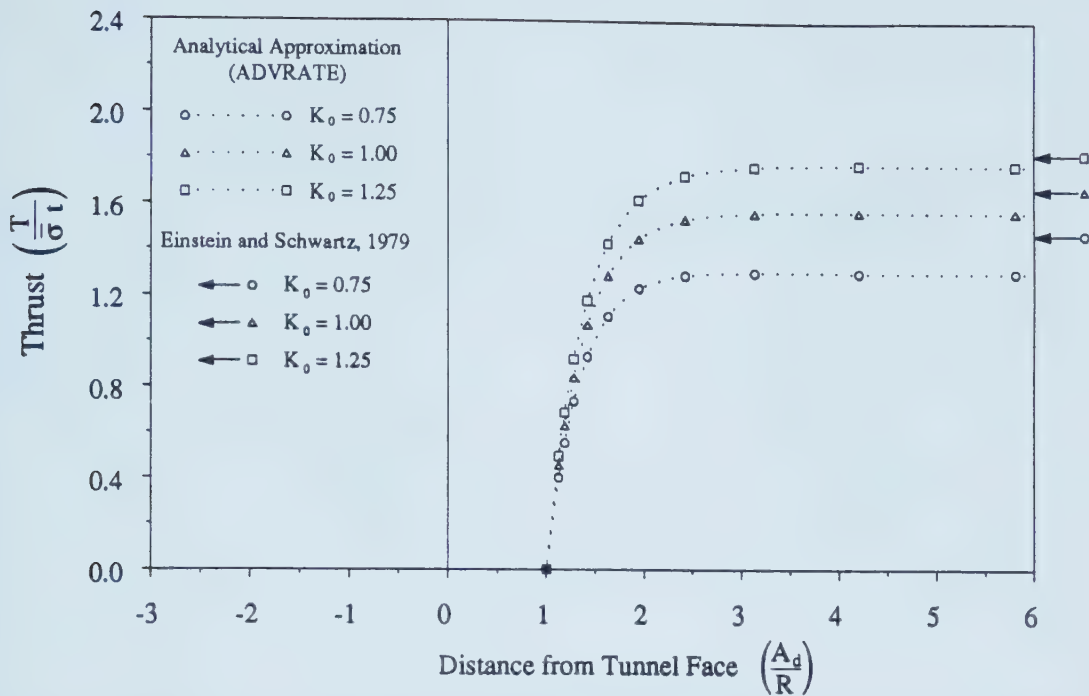


Figure 5.12 Comparison between Thrust Calculated by Analytical Approximation and Einstein and Schwartz (1979) Method for Points at Crown and Floor, Lined Tunnel

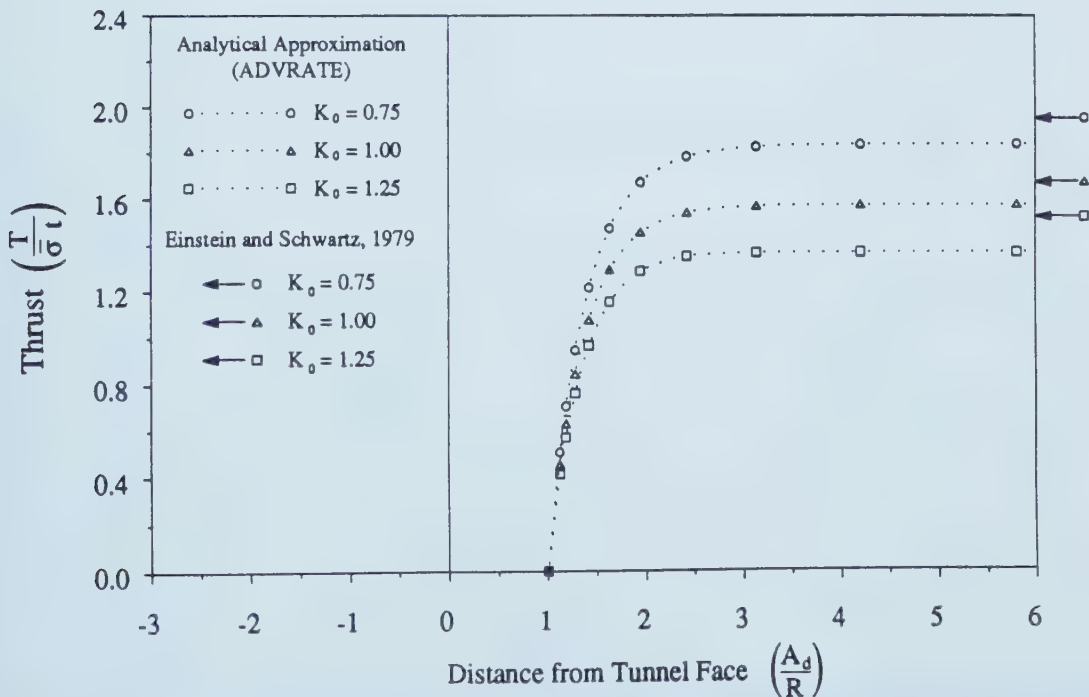


Figure 5.13 Comparison between Thrust Calculated by Analytical Approximation and Einstein and Schwartz (1979) for Points at Springline, Lined Tunnel

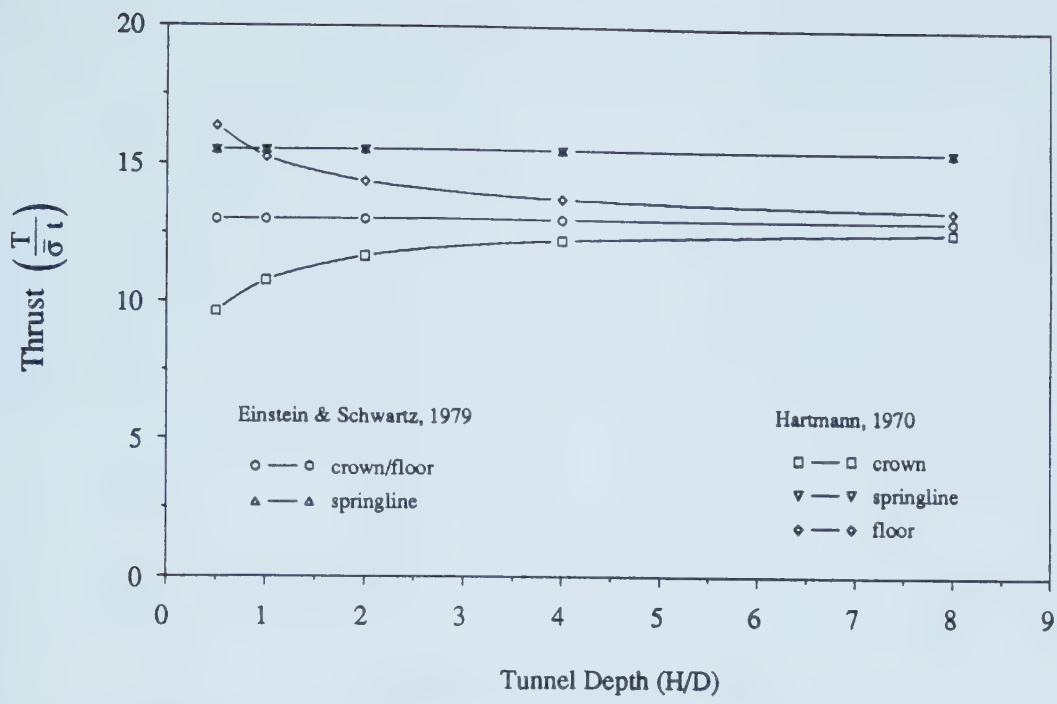


Figure 5.14 Effect of the Gravitational Stress Gradient on Thrust Calculated in Lining, for Tunnels at Different Depths

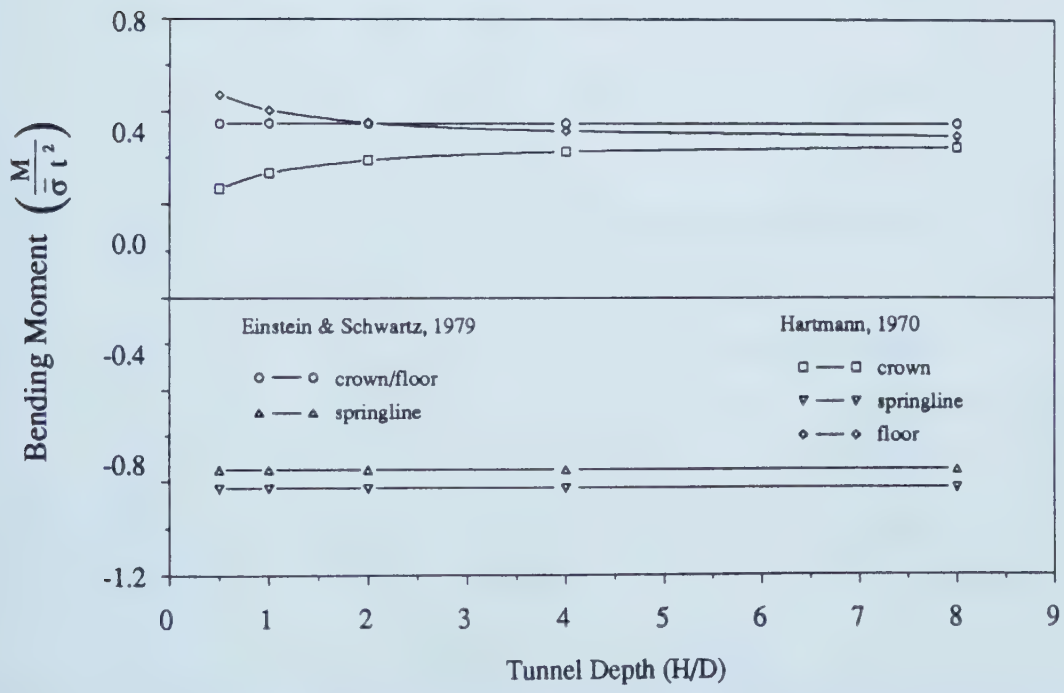


Figure 5.15 Effect of the Gravitational Stress Gradient on Bending Moment Calculated in Lining, for Tunnels at Different Depths

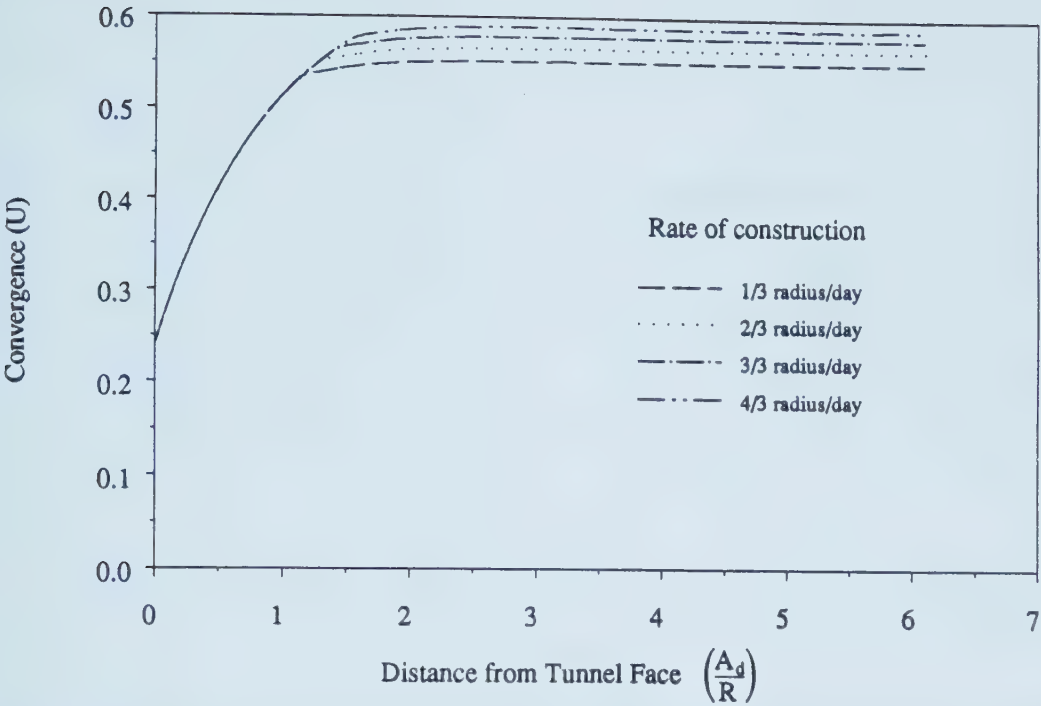


Figure 5.16 Development of Lined Tunnel Convergence with Tunnel Face Advancing, according to Results from ADVRATE Simulations

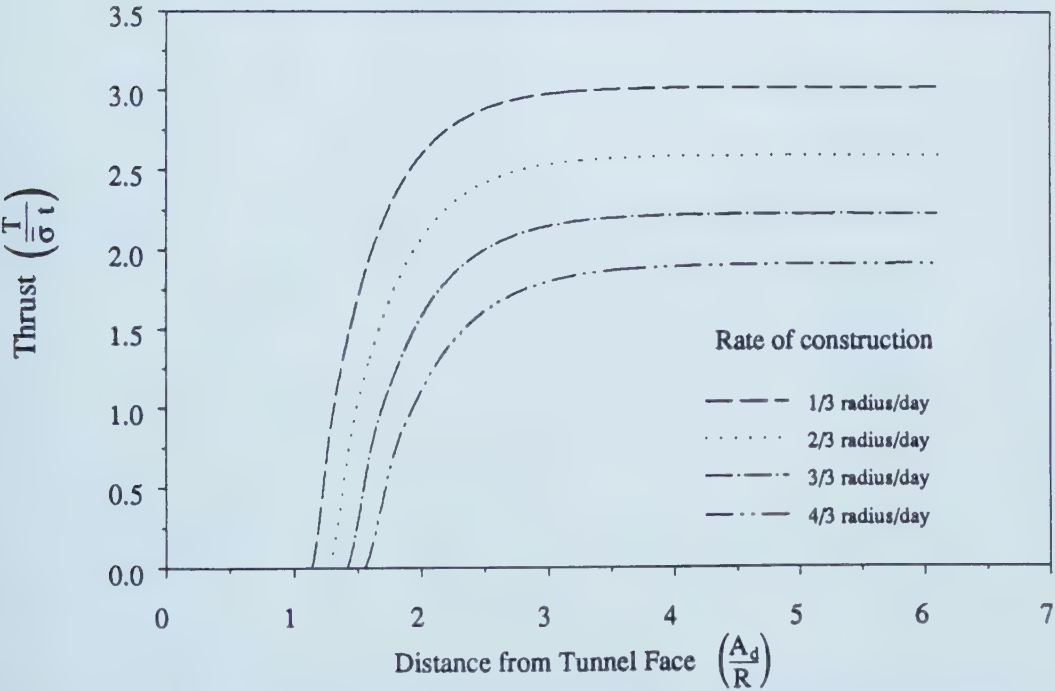


Figure 5.17 Development of Thrust in Lining with Tunnel Face Advancing, according to Results from ADVRATE Simulations

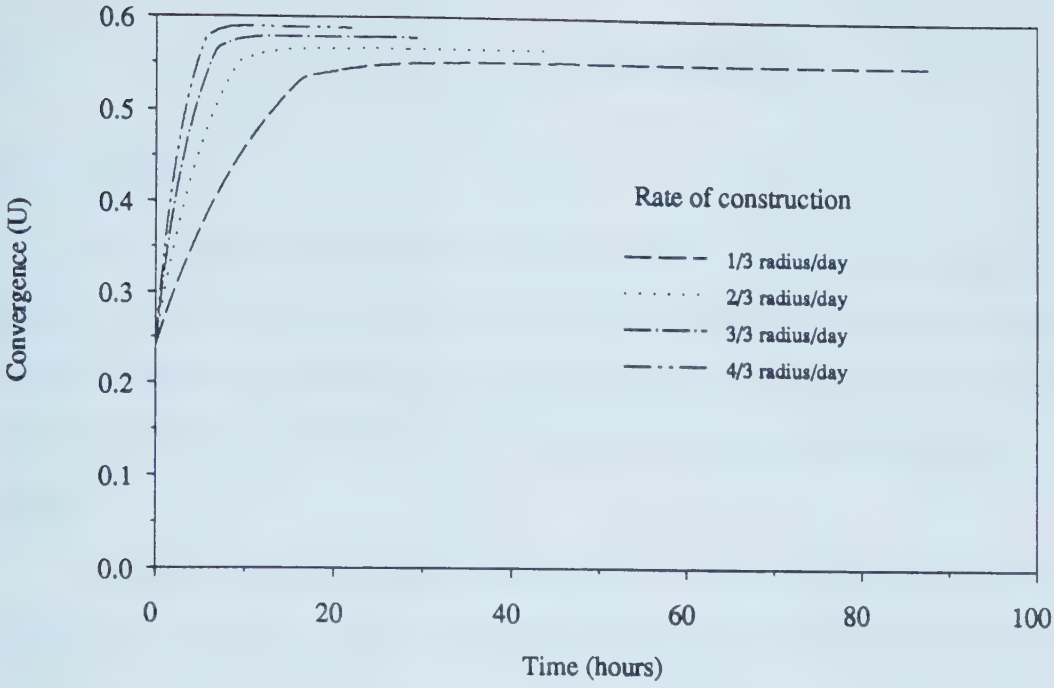


Figure 5.18 Development of Lined Tunnel Convergence with Time, according to Results from ADVRATE Simulations

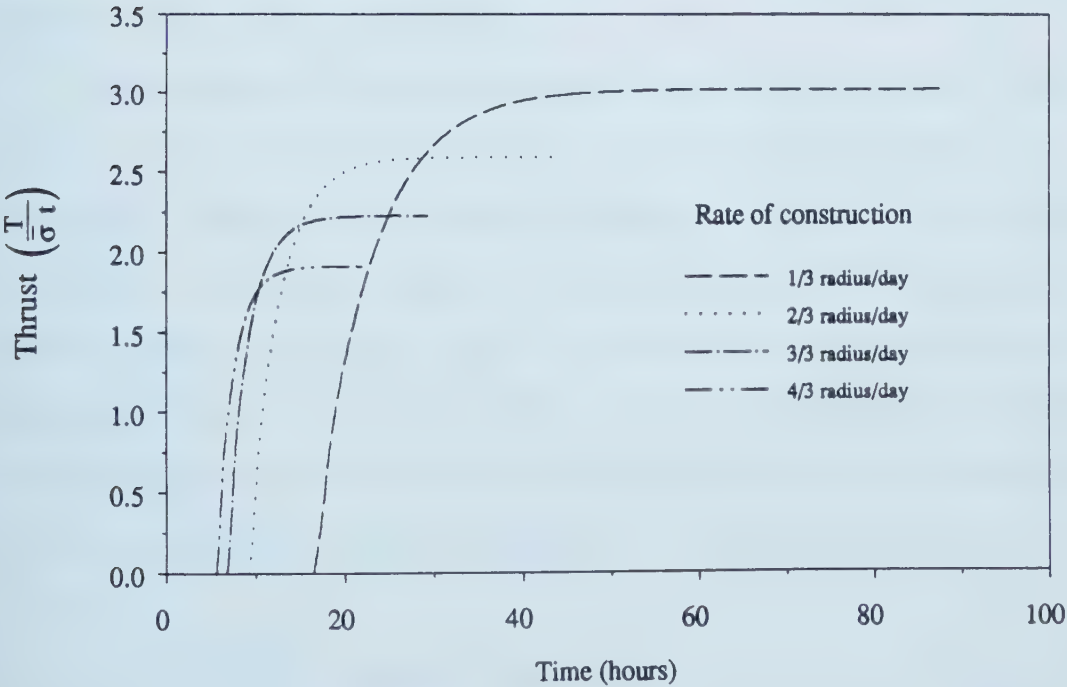


Figure 5.19 Development of Thrust in Lining with Time, according to Results from ADVRATE Simulations

6. PRACTICAL APPLICATIONS

6.1 Introduction

At the beginning of this thesis, the technical difficulties to study the ground-lining interaction in NATM tunnels for short term, where the shotcrete is loaded in the early ages were introduced. In order to allow a rational approach in dealing with the problem, site investigations and laboratory tests were performed and analytical tools were developed.

It is recognized that due to the highly complex nature of the problem, some aspects will remain unsolved and engineering judgment will be required to apply the results found in this thesis for practical applications. This chapter provides some guidelines to be used when engineering judgment is required either for design of or for interpretation of strain in shotcrete linings, using the SLRT lining data as framework.

6.2 Interpretation of Strain Measurements in SLRT Lining Instrumentation

6.2.1 Constitutive Relations of Shotcrete

The interpretation of the laboratory tests shown in Chapter 4 assumed a three element viscoelastic model for the short term behavior of the shotcrete. The interpretation of the lining instrumentation of shotcrete lining (NATM tunnels) using this model will now be compared with the evaluation proposed by Golser and co-workers (Schubert, 1988 and Golser et al., 1989). These authors adapted the method proposed by England and Illston (1965), where the strain measurements are evaluated by dividing the history of measured strain into finite time steps. For each time interval the stress level and elastic modulus are assumed to be constant, and the strain is given by:

$$\epsilon_2 = \epsilon_1 + \frac{(\sigma_2 - \sigma_1)}{E(t)} + \sigma_2 \Delta C(t) + \Delta \epsilon_d + \Delta \epsilon_{sh} \quad [6.1]$$

where:

- ϵ_2, σ_2 are strain and stress at time t_2
- ϵ_1, σ_1 are strain and stress at time t_1
- $E(t)$ elastic modulus at time t_1
- $\Delta C(t)$ change of specific flow between t_1 and t_2
- $\Delta \epsilon_d$ change of delayed elastic strain between t_1 and t_2
- $\Delta \epsilon_{sh}$ change of shrinkage between t_1 and t_2

Note that England and Illston (1965) originally denominated the parameter C presented above as a unit creep, which is analogous to the creep in the viscoelastic model used in Chapter 4, and represented by:

$$C = e^{(a + b A) d} \sqrt{T} \tag{6.2}$$

where:

- C = unit creep strain
- A = age at loading, in days
- T = time after loading, in days
- e = Napierian base
- a, b and d are constants

England and Illston (op. cit.) claimed that the results from Equation 6.2 were in good agreement with experimental results over the ranges of ages at loading from 8 to 120 days, and pointed out that it is likely to be inadequate for very young concrete. As the shotcrete is loaded at early ages, Golser et al. (1989) proposed a new relation for C , which they termed as 'specific flow', given by:

$$C(t) = A t^{1/3} e^{k\sigma} \tag{6.3}$$

where:

t = age, in days

A, k are constants

σ = stress

Golser et al. (op. cit.) claim that the expression above is used to take into account the nonlinear increase of flow with stress, which is necessary for stresses above 50% of the shotcrete compressive strength. Note that this limit is slightly higher than that discussed in Chapter 4, presented by Byfors (1980: 179) who proposed creep linearity up to the stress/strength ratio of 0.3 to 0.4. However, as pointed out by Golser et al. (op. cit.) this ratio rarely exceeds 0.1 in linings of shallow tunnels. Small values of stress/strength ratio were also observed in the SLRT project, presented subsequently in this chapter.

Therefore, the linearity of creep as a function of stress level, as assumed implicitly by the viscoelastic model, may be considered a good approximation for the case of shallow tunnels. Moreover, considerations of non linearity, as described by Equation 6.3 appear to be unnecessary. Note also that the viscoelastic model does not differentiate the creep deformations and the delayed elastic deformations as opposed to Equation 6.1. As the loads are expected to increase monotonically with time, the incorporation of creep and delayed elastic deformations under the same time dependent mechanism by the viscoelastic model can be considered a reasonable assumption. Therefore, in terms of concept for evaluation of stress dependent deformations, the viscoelastic model proposed in Chapter 4 and the usage of Equation 6.1 are equivalent, provided the load is increased monotonically.

Golser et al. (op. cit.) suggested that the elastic modulus development of the shotcrete can be well fit by the correlation suggested by CEB-FIP 1978:

$$E(t) = E_{28} \sqrt{\frac{t}{4.2 + 0.85 t}} \quad [6.4]$$

where:

E_{28} = elastic modulus at 28 days

t = age, in days

However, as shown in Chapter 4 (Figure 4.18), the relation between elastic modulus and strength proposed by CEB-FIP 1978 did not fit well the behavior of shotcrete at early ages. Figure 6.1 shows that Equation 6.4 presents considerable deviation for shotcrete younger than 10 hours, similarly to the deviations observed in Figure 4.18. Figure 6.1 also shows that better agreement can be obtained by using the procedure suggested in Chapter 4, i.e. applying Equations 4.4 and 4.12 with the parameters presented in Tables 4.5 and 4.11.

Note that in a stepwise calculation, as proposed by England and Illston (1965) represented by Equation 6.1, it is equivalent to the analysis performed for the multiple stress step test series CRMST presented in Chapter 4, using the calculation hypothesis MSTa shown in Table 4.15. However, the analysis of the laboratory tests of series CRMST and the strains controlled tests presented in Chapter 4 showed that using the average values of the viscoelastic parameters as shown in Figure 4.30 for the short term, good agreement was obtained between the calculated and measured values. Moreover, it was also shown that the assumption of instantaneous development of the short term creep deformations simplifies the calculation without compromising the accuracy. The same conclusion was achieved in the analysis of the shotcrete-ground interaction in Chapter 5, even considering the most critical case which corresponds to a high rate of tunnel construction. Therefore, for practical application, the behavior of the shotcrete for the short term, for the case of material with similar mix to that used in the SLRT project, can be taken as:

$$E_{eq} = \frac{E E_t}{E + E_t} = 10.33 \text{ GPa} \quad [6.5]$$

where:

E_{eq} = equivalent elastic modulus considering an instantaneous creep development

E = instantaneous or elastic modulus in the viscoelastic model = 15 MPa

$1/E_t$ = specific creep in the viscoelastic model = 0.03 1/GPa

which are the average values suggested for short term behavior of shotcrete presented in Figure 4.30. The value of E_{eq} is within the range proposed by many authors and it is close to the 10 GPa used in the preliminary interpretation presented in Chapter 2.

However that according to results of investigations shown in Chapter 4, the stresses in the shotcrete can be neglected, before 10 hours of age. Therefore, for design purposes, it seems reasonable to neglect the stiffness of the shotcrete in the first 10 hours, while in terms of stress interpretation of measured strains, the deformations of the first 10 hours should be disregarded.

6.2.2 Shrinkage Compensation

Golser et al. (1989) suggested that the law for shrinkage, as a function of age for the shotcrete, can be described by the relationship for ordinary concrete as recommended by ACI 1978:

$$\epsilon_{sh} = \epsilon_{sh\infty} \left[\frac{t}{B + t} \right] \quad [6.6]$$

where:

$\epsilon_{sh\infty}$ = final value of shrinkage

t = age, in days

B = constant

Note that these authors pointed out that the shrinkage was dependent on the location within the circumference of the tunnel lining. Also, as shown in Chapter 4, the shrinkage is highly dependent on moisture condition of the soil in contact with the shotcrete and on the fluctuation of the relative humidity of the air. These facts were also observed by Heinz and Rocha (1990) who suggested that the fluctuations in shrinkage strains are related to the operation of the air ventilation and the drainage conditions inside the tunnel.

Figure 4.48 shows that the deformations due to moisture fluctuations of the shotcrete may be very erratic and in a general case it does not follow Equation 6.6. Note also that the usage of compensating panels as described in Chapter 2 can only be effective if the panels are subjected to the same curing and drainage condition of the lining, i.e., contact with the same soil moisture, subject to the same change of relative humidity and in contact with the same amount of free water. Since the compensating panels used in the SLRT lining instrumentation failed to follow all these similarities, their data could not be used. Due to this lack of information, the shrinkage compensation will be done using the strain gages installed in the longitudinal direction of the tunnel, assuming zero stress in this direction. The mini flat jack test presented in Chapter 3 (Table 3.4) showed that this condition was achieved in the floor region but no reliable information was obtained for the springline or crown. Note that the results of the flat jack test IST1/2 which was run along the longitudinal direction for the springline position, shown in Table 3.4, were considered unreliable due to deviations resulted from the high amount of the short term creep for shotcrete at early ages. However, the total amount of deformations of the longitudinal strain gages located close to the springline and crown shown in Figure 4.48, are relatively small and of the same order of magnitude of the fluctuation observed during the period of instrument readings. These observations were interpreted as an indication of small amount of stress acting in these instruments. Considering that this assumption is valid, Figure 4.48 shows that shrinkage is not only a

function of the age and soil moisture content, but also a function of the operation of the air ventilation. Therefore, for the interpretation of the lining instrumentation, the usage of shrinkage law development, as presented in Equation 6.6 was disregarded, and the compensation was done using the strain gages installed in the shotcrete along the longitudinal direction.

6.2.3 Temperature Compensation

Schubert (1988) proposed a temperature development law for the shotcrete, which was presented in Chapter 4, Equation 4.17. Later, Golser et al. (1989) suggested that the temperature influences on strain at the shotcrete be insignificant and could therefore be neglected. The coefficient of thermal expansion measured for the shotcrete used in the SLRT project was $\alpha_T = 8.25 \times 10^{-6} \text{ (m/m)/}^\circ\text{C}$, for specimens older than 10 hours of age. Measurements presented in Appendix B for the embedded vibrating wire strain gages show that temperature variations can reach up to 15°C with a typical value of the order of 10°C , after 10 hours of age. As a result, temperature variation can potentially induce strain of $82.5 \times 10^{-6} \text{ m/m}$ which is at the same order of magnitude of the total measured strains in the SLRT project. Therefore, it is not reasonable to neglect the temperature influence on the strain measurements and the suggestion by Golser et al. (op. cit.) cannot be endorsed by the findings of the present work.

In order to make the thermal compensation of the strain measurements, one might consider two simple extreme cases: stress free compensation and strain free compensation. The first one would assume that the ground has negligible stiffness and the lining is free to expand due to the temperature variation. In other words, in terms of interpretation of strain measurements, one would assume that all the strains developed by the temperature variation would not cause any stress variation in the lining. Therefore, for the stress free compensation, the total strain measurement should be subtracted by the temperature variation times the coefficient of thermal expansion. In the other extreme,

the strain free compensation, one would assume that the ground has an extremely high stiffness which does not allow any movement of the lining due to the temperature variation. Therefore, in this case, the stresses in the lining should be compensated by the product of the temperature variation times the coefficient of thermal expansion times the elastic modulus.

In actual tunnels, the stiffness of the ground is neither zero nor infinite and therefore, part of the thermal expansion of the lining will be released due to the ground relaxation and part of it will be locked and cause the lining stresses to increase. In order to evaluate these terms, a simplified calculation procedure will be presented. This solution makes use of the solution of the classical problem of 'shrink fit' of two tubes which can be found in many text books (e.g. Hartog, 1959). This technique is normally used in manufacturing of guns, where two tubes are assembled one inside another in order to minimize plastification due to high internal pressure. The internal tube 2, as shown in Figure 6.2, has the external radius slightly larger than the internal radius of the external tube 1. The external tube 1 is expanded by heating and the two tubes are assembled together and as the temperature equalizes, internal stresses are generated. The solution of this problem is given by (Hartog, op. cit.: 151):

$$\frac{P r_1}{E_g} \left[\frac{r_0^2 + r_1^2}{r_0^2 - r_1^2} + \nu_g \right] + \frac{P r_1}{E_l} \left[\frac{r_1^2 + r_i^2}{r_1^2 - r_i^2} + \nu_l \right] = \delta \quad [6.7]$$

where:

r_0 , r_1 and r_i are the radii as shown in Figure 6.2

E_g and ν_g are the elastic properties of the outer tube

E_l and ν_l are the elastic properties of the inner tube

P is the pressure exerted by one tube on the other

δ is the difference between the external radius of the inner tube 1 and the internal radius of the outer tube 2.

If one takes r_0 large enough, the formulation above can be used for the thermal interaction of the lining-ground in tunnel problems. Disregarding the temperature gradient through the thickness of the shotcrete and the variation in circumference, i.e. assuming a single temperature variation ΔT for the entire lining, one can find a potential stress free thermal increment of the lining radius:

$$\delta = r_1 \alpha_T \Delta T \quad [6.8]$$

where

r_1 = external radius of the tunnel lining

α_T = coefficient of thermal expansion of the shotcrete

ΔT = temperature variation

Disregarding the temperature variation within the soil, substituting Equation 6.8 into 6.7 and taking the limit of the result for r_0 tending to infinite, one would find:

$$P = \frac{\alpha_T \Delta T}{\frac{1}{E_g} (1 + \nu_g) + \frac{1}{E_l} \left[\frac{r_1^2 + r_i^2}{r_1^2 - r_i^2} - \nu_l \right]} \quad [6.9]$$

and the tangential thermal stress σ_T in the lining will be given by (Hartog, 1959: 152):

$$\sigma_T = \frac{P r_1^2}{r_1^2 - r_i^2} \left(1 + \frac{r_i^2}{r^2} \right) \quad [6.10]$$

where:

$$r_i \geq r \geq r_1$$

Figure 6.3 shows the evaluation of Equation 6.10 for different values of temperature variation, calculated for a tunnel with the same geometry as the SLRT tunnels and a shotcrete with equivalent elastic modulus of 10.3 GPa, as proposed in item 6.2.1. One can note that for the ground modulus of 27 MPa for the SLRT case the thermal stresses for 10°C of variation are of the order of 20 to 30 kPa. As the peak of the temperature variation occurs in different times for the heading and for the invert, the actual thermal stresses are probably smaller. Therefore due to the low value expected for the thermal stresses, a free stress compensation will be applied to the SLRT case history. Note also that the deformations considered for the temperature variations are larger than the shrinkage strains discussed in the previous item. Therefore, the stress free compensation of the shrinkage was indeed reasonable. Figure 6.3 also shows that for stiffer ground, thermal stresses may be significant. If a ground with an elastic modulus of 1 GPa is considered under a variation of 10°C, a thermal stress of the order of 500 kPa may be generated. Therefore, in shallow tunnels constructed in stiff material, thermal stress may induce considerable relative variation on the loads acting in the lining. The same may be true for the stresses induced by the moisture variation of the shotcrete.

6.2.4 Evaluation of the Stress Dependent Strains

All the raw data related to the strain readings taken in the SLRT lining instrumentation were presented in Appendix B as a function of time. As shown in item 6.2.1, for practical purposes, the interpretation of shotcrete strain may be done by using an equivalent linear elastic modulus. In other words, the assumption of short term creep deformations occurring instantaneously seems to be accurate enough for all practical purposes and, therefore, a time dependent analysis of these deformations will not be presented. For this reason, the strain development with the suitable compensations will be presented in this section as a function of the tunnel face position.

In order to relate construction events to the strain response, all the deformations will be presented as a function of the same coordinate system. As the steel ribs were spaced by 1 m and numbered sequentially with the advancing, the rib number will be used as a reference value. Figure 6.4 presents the development of the SLRT tunnel construction with time in the area of interest, presenting the heading position and the invert installation as a function of the steel rib number. Note that the tunnel construction stopped for about 1 day when the heading was at rib 89 and about 3 days when the heading was at rib 111. Despite these periods of interruption, Figure 6.4 shows an almost constant construction rate averaging 3.7 m/day.

The purpose of this section is to isolate the portion of the measured strains in the shotcrete instrumentation, which was a direct result of load built up on the lining. Therefore, all the stress independent deformations are intended to be compensated. The result of these compensations would allow the interpretation of strain measurements to obtain the stress development in the tunnel lining. Investigations in Chapter 4 indicated the difficulties to obtain the thermal expansion coefficient, Poisson's ratio and shrinkage properties of the shotcrete for the first 10 hours of age. However, as discussed in item 6.2.1 and shown in the results of multiple step load tests and strain controlled tests presented in Chapter 4, for a range of strains measured in the SLRT tunnel lining for the first 10 hours, the stresses generated in this period are very small and can be neglected. For this reason, all the deformations measured in the shotcrete lining before 10 hours of age will be neglected.

It is interesting to observe that Golser et al. (1989) did not explicitly mention when their interpretation started, but as they used just shotcrete tests where the load was applied after 10 hours of age, one can assume that the first 10 hour period was also neglected by them. Unfortunately the importance of this period was not known at the time of the lining monitoring was carried out therefore no special attention was given to taking readings around 10 hours of age. The closest reading around 10 hours of age was

taken as a reference or an initial value for the compensation procedure. The age of the shotcrete at the beginning of the interpretation is indicated in Figures 6.5 to 6.8, for the vibrating wire strain gages embedded in the lining.

Item 6.2.2 pointed out the necessity to perform shrinkage compensations, which were functions of age, relative position in the circumference of the lining and operation of the tunnel ventilation. For this reason, it was necessary to perform the compensation using the vibrating wire strain gages installed along the longitudinal direction. As a consequence, only the gages installed close to the longitudinal gages could be compensated for shrinkage strains, as indicated in Table 6.1, and these are the instruments for which strains are presented in Figures 6.5 to 6.8. The interpretation for the other instruments will not be presented because the shrinkage compensations are substantial and at the present moment they are unpredictable.

Temperature compensations were also carried out using the readings of the instruments installed along the longitudinal direction. As indicated in item 6.2.3, both compensations were performed assuming stress free condition, which was evaluated by subtracting the reading of a given instrument from the reading of a longitudinal instrument close to it. The result of these strain compensations are presented in Figures 6.5 to 6.8, and the position of these instruments in the lining circumference can be found in Appendix B. Obviously, the readings of vibrating wire strain gages were corrected to compensate reading deviations caused by temperature variation, according to the coefficient presented in item 2.4.2.

Figures 6.5 and 6.6 present the compensated strains measured by vibrating wire strain gages embedded in the shotcrete at tunnel instrumentation section C2I, which was located between ribs 87 and 88. Figure 6.5 presents the results of two pairs of instruments, which were located close to the tunnel crown. Gages VW14 and VW15 present a small shift of readings during the initial stages followed by a relatively small strain development compared with gages VW16 and VW17. This small strain

development can be an indication of small amount of stress generated in that location or a flaw in the shotcrete around the gages heads. This latter option, however, seems to be improbable as both instruments VW14 and VW15 indicate similar and consistent pattern of strain developments.

It should be noted that the design analysis presented in Chapter 2 neglected the load development in the crown region, before the closure of the invert. Parametric analysis using an analytical approximation presented in Chapter 5 neglected the load development before 10 hours after the application of shotcrete at the invert. However, Figure 6.5 shows some strain development before the invert was closed when the heading was at rib 91, indicating some load development in this period.

It is also interesting to note that at rib 94, after the shotcrete at the invert reached more than 10 hours of age, inflections on the strain development curves can be observed. This suggests that when the invert reaches the age where it is able to carry load, the lining ring start to carry load in a higher rate. Figure 6.6 presents the compensated readings from strains for gages in section C2I installed close to the springline. The difference of strain development between instruments VW28 and VW29 is interpreted as an indication of bending moment development.

Figures 6.7 and 6.8 present the strain development in vibrating wire strain gages installed at the crown in the instrumented section C2II, between ribs 91 and 92. Comparing the response of instruments located in the crown region at section C2I, in Figure 6.5, with the response of the instruments located in the same region at section C2II, in Figure 6.7, one can observe a considerable difference on the development of their strains. Around rib 87, which corresponds to section C2I, the excavation proceeded by 1 m step, immediately followed by the installation of the steel rib and application of the shotcrete. However, when the tunnel heading was stopped at rib 95, the bench was excavated 2 meters in one single unsupported advancing step. The strain development which occurred in a few hours when the heading was stopped at rib 95, as presented in

Figure 6.7, shows the effect of the change in the construction sequence on loading response. The difference of strain development of pairs of gages presented in Figures 6.7 and 6.8 was considered as development of bending moments, similarly to what was presented before.

Figures 6.9 to 6.12 show the strain development measured in the steel ribs, also presented as a function of heading position in terms of the rib number. As mentioned in Chapter 2, these measurements were done using resistance strain gages installed with a full bridge configuration. Therefore, they were fully compensated for temperature variations which include compensations due to deviation induced by the gage itself and to thermal expansion of the steel.

Due to technical problems related to the setup of the read out box, all the readings of the resistance strain gages taken before the heading has reached rib 90, were considered unreliable. For this reason, part of the readings presented in Figure 6.9 is missing for instruments RS56 and RS57 located close to the crown, at section C2I. Figures 6.9 and 6.10 present the strain development in the ribs at section C2I, after the invert was closed. Comparing these results with those measured at sections C2II and C2III, one can observe again a considerable difference on the pattern of strain development. At the section C2I, where the invert was installed in 1 m step of construction, the strain tends to increase slowly within about 7 m of the tunnel advancing. On the other hand, at sections C2II and C2III where the excavation advanced 2 m in a single step, there was a sharp increase of deformation in the first 2 meters as shown in Figures 6.11 and 6.12.

Note that although the invert was closed when the heading was at rib 96, the shotcrete was already hard enough (10 hours of age) to carry some load only at rib 98. For this reason, during the first few meters of advancing, where a 2 meter section of the invert was 'soft', the load in the ribs increased quickly.

6.3 Load Evaluation based on SLRT Lining Instrumentation

6.3.1 Total Pressure Cells

As mentioned in Chapter 2, the readings of the total pressure cells were compensated for temperature changes applying a factor by which the readings were multiplied as recommended by the gage manufacturer. Note that this approach is clearly a simplification of the problem because the relative stiffness of the system shotcrete-soil-gage will affect the thermal stresses in a similar way as it was illustrated in item 6.2.3, for ground lining thermal interaction. This simplified temperature correction procedure was considered adequate for the present application as it would probably induce small deviations compared with other source of errors. One source of deviations was attributed to the imperfections occurred during the installation of these instruments due to the limited time available for this purpose. As a result, the contact between the pressure cell and the ground was not perfect, which has affected the reliability of these instruments as discussed for instance by Sauer and Sharma (1977). For this reason, the results presented in Figure 6.13 should be used with extra caution. Location of these instruments in the lining circumference is given in Appendix B and the total pressure cells are presented in terms of rib number, as before.

6.3.2 Loads in Shotcrete and Steel Ribs

Item 6.2.1 presented the considerations used to obtain the equivalent Young's modulus of 10.3 GPa for shotcrete with more than 10 hours of age. Stresses can be obtained by the straight application of this elastic modulus to the compensated strains presented in Figures 6.5 to 6.8. In order to obtain the thrust and bending moments acting in the shotcrete lining, some assumptions were necessary. Despite the effort spent to obtain direct measurements of the lining thickness, it was not possible to take readings at all points around the circumference of the instrumented sections, due to restrictions at the construction site. Measurements at the instrumented sections were only possible in the

north bound SLRT tunnel at the points accessible by a man standing up on the invert fill. Therefore, data taken from other tunnels of the same project, which was constructed by the same contractor with the same personal and same construction specifications, was used to estimate the typical thickness of shotcrete that was actually placed in the lining. There were 21 determinations of thickness, including those related to the flat jack tests (Table 3.4), which were taken at half way between steel ribs. This same longitudinal position was used for the vibrating wire strain gages installation and these measurements haven't indicated any trend of thickness difference along the circumferential position of the lining. Figure 6.14 presents the distribution of these measurements and 15 cm will be taken as a typical value for the calculation of loads in the shotcrete.

Load interpretation was performed only for the gages installed in pairs which strains were compensated as shown in Figures 6.5 to 6.8. These instruments were 11 cm apart according to the installation cage geometry and it was assumed that this cage was centered to the lining thickness. For the calculation of thrust and bending moments, the stresses were assumed to be linearly distributed between gages of a given pair. As the compressive and tensile strength values were never exceeded, no further correction was applied. Figures 6.15 to 6.20 present the results of these computations in terms of thrust and bending moments, for points located at crown, springline and floor.

The evaluation of the load in the steel was straightforward: the area and moment of inertia of the steel rib W 150x14 were taken according to standardized values and the Young's modulus was taken as 200 GPa. A linear distribution of stresses was also assumed and the results are presented in Figures 6.15 to 6.20 with the results obtained for the shotcrete instrumentation.

6.3.3 Load Share between Shotcrete and Steel Ribs

It was already suggested in Chapter 2 that the load share between shotcrete and steel ribs in terms of thrust would follow the ratio between the product of Young's

modulus versus the area (EA) of these structural elements. Note that this proportion was implicitly suggested by Heilbrunner and Gais (1981), for a calculation of load share in a NATM tunnel constructed in Munich. In order to check the validity of this proportion using the lining instrumentation, it is necessary to use instruments installed in a similar circumferential location and also at the same section, due to the irregular load distribution frequently observed along tunnel alignment, as in the SLRT case analyzed herein. The only instruments that meet these requirements are the gages VW16 and VW17 installed in the shotcrete and RS56 and RS57 installed in the steel ribs, both in the crown at section C2I.. The proportion between the thrusts measured by these instruments is about 16% from data presented in Figure 6.15 at pathamar level, which is in good agreement with the 18% of the ratio $\left[\frac{EA_{nb}}{EA_{shotcrete}} \right]$ for this case.

Load cells between the steel ribs similar to those described by Branco (1981: 136) were used in another instrumentation performed in Edmonton, for a NATM tunnel in an extension of the LRT system. The stresses in the shotcrete were measured using the flat jack test. The relation between the thrust in the steel rib taken from the load cell measurements and in the shotcrete was of the order of 11 % while the ratio $\left[\frac{EA_{nb}}{EA_{shotcrete}} \right]$ was 10%. Details of this analysis can be found in Eisenstein and Kuwajima (1990).

Aydan et al. (1988) did a three-dimensional FEM simulation of an advancing tunnel supported by forepoles, shotcrete, steel ribs and rockbolts. The ratio $\left[\frac{EA_{nb}}{EA_{shotcrete}} \right]$ in this analysis was 88.2 % and the relation between the thrust calculated in the rib and in the shotcrete was 77.7 %. These good results encourage the usage of this ratio as a simplified way to predict the load share between the shotcrete and rib in NATM tunnels.

A similar proportion can be obtained using a procedure recommended by Hoek and Brown (1980: 258). They suggest that when a combined support system be used, the

resulted equivalent stiffness be equal to the sum of the stiffness of the individual components:

$$k' = k_1 + k_2 \quad [6.11]$$

where:

k_1 = stiffness of the first system

k_2 = stiffness of the second system

As this approach assumes that both support systems deform equally and simultaneously, the proportion between the thrusts should be equal to the ratio between their stiffnesses. The stiffness of the shotcrete lining k_s in terms of support convergence characteristics is given by (Hoek and Brown, 1980: 253):

$$k_s = \frac{E_s (r_i^2 - (r_i - t_s)^2)}{(1 + \nu_s) ((1 - 2\nu_s) r_i^2 + (r_i - t_s)^2)} \quad [6.12]$$

where:

E_s = elastic modulus of shotcrete

ν_s = Poisson's ratio of shotcrete

r_i = tunnel radius

t_s = shotcrete thickness

The stiffness of the steel ribs k_r can be defined as:

$$k_r = \frac{E_r A_r}{S r_i} \quad [6.13]$$

where:

E_r = elastic modulus of the steel ribs

A_r = cross sectional area of steel ribs

S = spacing of ribs along length of tunnel

r_i = tunnel radius

Therefore the ratio between the thrust load in the steel ribs and shotcrete T_t is given by dividing Equation 6.13 by Equation 6.12:

$$T_t = \frac{k_r}{k_s} = \frac{E_r A_r (1 + \nu_s) ((1 - 2\nu_s) r_i^2 + (r_i - t_s)^2)}{S r_i E_s (r_i^2 - (r_i - t_s)^2)} \quad [6.14]$$

When the proportion of the thrust of the cases mentioned earlier using Equation 6.14 is recalculated, one would find a slightly lower value than that given by the ratio $\left(\frac{EA_{rib}}{EA_{shotcrete}} \right)$. As the relative differences between these two evaluations were smaller than 5%, the usage of ratio $\left(\frac{EA_{rib}}{EA_{shotcrete}} \right)$ is suggested due to its simplicity. Note also that both of these relations implicitly assumed the in situ stress ratio $K_0 = 1$. However, it seems that these equations can be applied for values of K_0 different from unit, since the case of the SLRT presented $K_0 = 0.8$, the case studied by Eisenstein and Kuwajima (1990) presented K_0 approximately equal to 2 and the numerical simulation by Aydan et al. (1988) presented a highly complex in situ stress condition.

6.4 Analysis of Results

6.4.1 Predicted Values for Design Purposes

Chapter 2 presented a type A prediction of SLRT tunnel behavior according to Lambe (1973) as indicated in Table 2.2. This was based only on information available before the tunnel was constructed. The main unknown parameters at that time were the behavioral properties of the shotcrete, particularly those at the early ages. Another unknown was the point of the lining activation, which may be viewed as the moment when the load starts to be carried by the lining, for design considerations. In the

preliminary calculation presented in Chapter 2 from Figures 2.14 to 2.18, the shotcrete was considered as a linear elastic material with Young's modulus equal to 10 GPa and the lining activation was assumed to occur when the invert was installed.

Results presented in Chapter 4 for the tests performed in shotcrete, with the reasoning discussed in that chapter and in item 6.2.1, indicated that the response of the shotcrete can be reasonably approached using an equivalent linear elastic modulus of shotcrete of 10.3 GPa, as indicated in Equation 6.5. Therefore, the Young's modulus of 10 GPa used in Chapter 2 was indeed a very good assumption.

However, some adjustment is still required as the behavior at very early ages, before 10 hours of age, must be considered. As one can observe in Figure 6.1, there is a sharp variation of the elastic modulus in the first 10 hours and also a similar variation of the creep properties in Figure 4.30. These variations are the reason for neglecting the shotcrete stiffness during the first 10 hours, as confirmed by the analysis of multiple step load and controlled strain tests presented in Chapter 4. For this reason, it seems reasonable to include this effect in the design of the shotcrete lining.

In terms of Negro's design method, used in Chapter 2, the 'inability' of the shotcrete to carry load before 10 hours of age can be introduced in the calculations by assuming a delay of 10 hours in the activation of the lining. Figure 2.14 shows that in the preliminary calculations, the activation of the lining was set as $X = 4$ m, which represents the actual distance from the heading to the invert at the instant of its installation. As the shotcrete freshly applied in the invert is too soft to carry load, and considering a period of 10 hours required for some cure to occur under the average rate of construction of 3.7 m/day (Figure 6.4), one would find a delay of 1.5 m for the lining activation. As the construction progressed in steps of 1 m, the delay of lining activation was assumed to be 2 m.

The calculations were repeated introducing this delay of lining activation and also correcting the value of the equivalent elastic modulus of the shotcrete. Note also that an

equivalent thickness of the lining was set as 18 cm, in order to take into account the contribution of the steel ribs. The calculation sheets are presented in Figures 6.21 to 6.25 and the results indicate an increase of about 7% on the tunnel convergence and also a decrease of about 7% on the stresses acting on the lining, compared with the calculations presented in Chapter 2. This difference is the response of the design method to the consideration of small stiffness of the shotcrete at very early ages, which was neglected during the first 10 hours of age. The surface displacements of the ground also increased by about 7% and good agreement between the measured and calculated transverse settlements can be observed in Figure 6.26.

Note that in the calculation presented in Figures 6.21 to 6.25 using Negro's (1988) method, only the final values of load and displacements can be obtained. Using the analytical approximation ADVRATE presented in Chapter 5, it is possible to evaluate the development of load and tunnel convergence as a function of the tunnel advance. Note that for design purposes, the procedure to consider the delay of lining installation in ADVRATE should be adapted in order to be consistent with the design calculation presented in Figures 6.21 to 6.25. In Chapter 5, the delay of lining installation was simulated in the linear viscoelastic approximation by imposing a time delay, an input in the computer program, equivalent to physical delay of the lining installation plus the 10 hours necessary for the shotcrete cure. However, in Negro's design method, the non linearity of the soil response, before and during the ground-lining interaction, is taken into consideration, as mentioned in Chapter 2. Therefore, in order to be consistent with the lining-ground interaction stage of the design method, the same amount of ground stiffness reduction and in situ stress release should be used.

The stiffness of the ground can be corrected simply by using the elastic modulus found in the last iteration of the lining-ground interaction stage, as presented in Figure 6.24. This procedure will produce equivalent response, as both Negro's and ADVRATE solutions were derived for linear elastic materials. In order to consider the

amount of in situ stress release before the lining activation, the parameter α , as defined in Equation 5.14, will be used. As demonstrated in Chapter 5, this in situ stress release parameter α and the parameter $\underline{\alpha}$, as defined by Negro (1988), are equivalent. Therefore, adjusting the parameter α to the value of $\underline{\alpha}$ found in the last iteration of the lining-ground interaction stage, as presented in Figure 6.24, ADVRATE would be adjusted for the non linearity of the ground response. Substituting Equation 5.9 into 5.14, one can find:

$$t = - \frac{\ln \left(\frac{1 - \alpha}{\kappa} \right)}{\omega \frac{A_d}{R t}} \quad [6.15]$$

where:

t = equivalent time delay for consideration of ground non linearity

κ, ω = constants defined in Equation 5.2

α = adjusted value of the in situ stress release parameter

$\frac{A_d}{R t}$ = rate of tunnel construction in terms of radius per unit of time

Using equivalent time delay t given by Equation 6.15 for the value of α adjusted for $\underline{\alpha}$ at the last iteration, loads and convergence development were calculated using ADVRATE. Using the recommendation discussed in item 5.3.3 for adjustments for the gravitational stress gradients, the final values of the load and convergence development were obtained. Thrust and bending moment developments are presented in Figure 6.15 to 6.20, where field measurements are also shown. Figure 6.27 presents the comparison between the calculated and measured settlements of a point close to the tunnel crown.

Figures 6.28 to 6.30 present respectively the final values, at the short term response of ground-lining interaction, of thrust, bending moment and radial pressure of the ground on the lining, for both calculated and measured values.

6.4.2 Comparison between Measured and Calculated Values

The first aspect one should consider before any comparison is made, is the high level of dispersion of the thrusts and bending moments obtained from lining instrumentation as illustrated in Figures 6.28 and 6.29 for the SLRT tunnel. Figure 6.31 presents the results from similar instrumentation as presented by Golser et al. (1989) for shallow NATM tunnel, showing a high level of irregularities on the load distribution.

Part of this variability can be directly attributed to the shotcrete lining thickness irregularities as shown in Figure 6.14 and also for the shotcrete mechanical properties variations. A histogram of strength distribution, for specimens with 7 days of age taken from panel and in situ core in the SLRT tunnels, is presented in Figure 6.32. Using the range of strength variation shown in this figure and applying Equation 4.12, one can estimate a variation of elastic modulus of the order of 30%. Note however that this variation should be larger for the period of 10 hours to approximately 80 hours of age, the period when the shotcrete is loaded in the present case history, as for younger ages the strength variations are large, as can be observed in Figure 4.2.

If the product of Young's modulus versus the thickness of the shotcrete is taken as an index of the lining stiffness, one would find a variation from 50% to 200% in the extreme cases, considering the range of variations described above. Note that this simple index is valid for estimation of thrust variation, as for bending moments the variations would be proportional to the cubic exponent of the lining thickness. Therefore, the variation on the bending moments in shotcrete linings should be larger than the range presented above.

One also should be aware that the introduction of a singularity in the lining, such as a gage, will likely of modify the stiffness locally. Therefore, the dispersions observed in Figures 6.28 to 6.31 do not come as a surprise.

Figures 6.15 and 6.16 present respectively the thrust and bending moment developments for points located close to the tunnel crown. The exact location of the instruments used in theses figures, along the tunnel circumference, are presented in Figure B.1, Appendix B. As shown in Table 6.1, vibrating wire strain gages VW40 and VW41 were compensated using the longitudinal gage VW3. Due to the distance between them and probable difference of shotcrete thickness, as VW40 and VW41 were installed at a location where large overbrake was recorded, the interpretation of these instruments may be subjected to some degree of error. At the design calculations presented earlier, the lining was assumed to be activated only 6 m behind the tunnel face, which results are shown in Figures 6.15 and 6.16. Note that in these design calculations, the tunnel was assumed to be excavated in full face and it was not possible to consider the difference of shotcrete stiffness between the heading and invert due to the difference of ages. Figure 6.15 shows that actually some thrust built up before the invert was installed and reached 10 hours of age, showing however that the final values are smaller than those predicted.

The higher rate of loading observed for VW40 and VW41, as mentioned earlier, seems to be related to the modification of construction sequence around the section C2II. Note also that instruments VW14/15 and VW16/17 at the section C2I, where the construction sequence was normal, presented an increasing on the loading rate after the point where the shotcrete in the invert reached 10 hours of age, i.e. at 6 m from the tunnel face. This is an indication that after this point, the lining starts to behave as a closed ring.

Figure 6.16 shows that most of the bending moments measured close to the tunnel crown developed before the shotcrete in the invert achieved 10 hours of age. Note that

the predicted values of bending moments were positive, according to convention shown in Figure 2.26, while the measured ones were negative. The positive value of bending moment at the crown is the expected response of a closed ring for a condition of in situ stress ratio K_0 smaller than 1. However, as the ring is not effectively closed before 6 m from the face, the bending moment becomes negative as shows the field data which are the expected responses for the opened ring. Note also that after the initial development of the bending moments, for few meters of tunnel advancing, their values maintain almost constant. The only measurements available for the springline were taken by the pair VW28/29, but due to the low values of these readings, shown in Figure 6.17 and to the limited data, the only comment for this point is that the bending moment for section C2I after the 10 hours of age (Figure 6.18) followed the direction expected for closed ring.

The values of thrust obtained for the gages installed in the steel ribs at springline and floor, as shown in Figures 6.17 to 6.20, suggest that thrust is generated after the installation of the invert and before the shotcrete achieves 10 hours of age. Thereafter, their values are maintained almost constant, while the bending moments are negligible throughout the measured period. Note that these instruments were installed at the section where the invert was excavated in a 2 m step without protection. Therefore, during the first meters of advancing, the loads were carried out by the steel ribs, as the shotcrete was not yet stiff. Figure 6.19 shows the thrust development for gages installed at the floor at section C2II, which presents a stabilization trend around 10 to 12 m from the tunnel face in agreement with the calculated values also presented in this figure. The bending moment in this point presented the highest value measured in the SLRT tunnel and almost meets the calculated values, as can be observed in Figure 6.20.

The thrusts and bending moments presented in Figures 6.15 to 6.20 and Figures 6.28 to 6.30 were calculated using an equivalent thickness for the shotcrete which would approximately take into account the longitudinal variation of lining thickness and the contribution of the steel ribs. Ideally one should add the loads measured

in the shotcrete and ribs in order to compare with the calculated values. However, the data available do not present good correspondence between the points measured in the shotcrete and in the ribs, in terms of instrumented section and circumferential positions. For this reason, the sum of the measured loads was not possible and individual data were compared with the calculated values.

Note also that all the measurements related to the shotcrete were taken at half way between the steel ribs. Observing Figure 3.2, one would easily recognize that this is a region of minimum stiffness in the tunnel lining along the longitudinal direction. Therefore, the measurements of loads in the shotcrete may be considered a lower bound approximation.

Figure 6.28 also included the measurements taken using the flat jack test in the South bound tunnel, constructed parallel to that used in the lining instrumentation. These two tunnels were about one radius apart, as described in Chapter 3, and due to this proximity, one should evaluate the interference of the construction of the first tunnel on the response of the second one. Ranken (1978: 194), using a linear elastic finite element simulation of simultaneous construction of parallel lined tunnels, studied shallow tunnels spaced as close as half of their radius and did not find considerable changes on the maximum values of thrust and bending moments. For spacing of one radius, as the SLRT case, the variation of thrust was of the order of 3% and the variation of bending moment of the order of 18 %. Note that the SLRT tunnels were neither constructed simultaneously nor the ground was linear elastic, which might introduce some deviations. However, as the measured settlements of the second tunnel are about 20% larger than those measured for the first tunnel, as shown in Figure 6.33, which results agree with the simulations by Ranken (op. cit.: 199), it is reasonable to assume that the relative deviations due to the linear elastic and simultaneous assumptions should not be very large.

Therefore the flat jack tests performed in the South bound tunnel can be used as a reasonable estimation for loads acting in the North bound tunnel. Figure 6.28 shows that the magnitude and variation of the thrust measured using the flat jack tests are similar to those obtained for the lining strain interpretation, suggesting that the compensations proposed for interpretation of gages embedded in shotcrete are reasonable. Note also that none of the measured values exceeds these calculated in Figure 6.28, indicating that the final values of calculated thrusts are on the safe side. Note also that the calculated values would induce stresses below 10% of the strength of the shotcrete (as shown in Figure 4.3) at the end of the short term interaction, which corresponds to about 80 hours. Figure 6.29 shows clearly that the bending moments in the crown region are controlled by the stage where the ring is not closed, and for this reason, they had opposite signs to the calculated ones.

6.5 Summary and Recommendations

This chapter presented the interpretation of the SLRT lining instrumentation performed using results taken from laboratory tests presented in Chapter 4 and from parametric analysis presented in Chapter 5. It was shown that the straining during the first 10 hours of age did not induce any significant amount of stress in the SLRT instrumentation and for this reason, the measurements in this period were disregarded.

The shrinkage and temperature variations induced considerable deformations in shotcrete linings, which required compensation on the readings. The compensations for these effects were performed assuming that they did not induce any stress variation. Using a simplified model, it was shown that in the case of the SLRT tunnels, this type of compensation is valid. For stiffer ground however, it might be necessary to evaluate the stress changes due to shrinkage and temperature variations.

According to results shown in the previous chapters, it was possible to define an equivalent Young's modulus for the shotcrete at short term as $E_{eq} = 10.3 \text{ GPa}$. Applying

this modulus to the compensated strains taken from the instrumentation, the development of thrust and bending moments in the shotcrete was evaluated assuming a typical thickness for the lining. The strain measurements in the steel ribs were taken using resistance strain gages in full bridge configuration, which implies compensation for both the gage reading deviations and steel expansion due to temperature variations. Assuming a Young's modulus of 200 GPa for the rib it was possible to calculate the developments of thrusts and bending moments. Using the SLRT instrumentation and some other published data, it was possible to confirm the suggestion given in Chapter 2 that the proportion of the thrust in the steel rib to the thrust in the shotcrete can be estimated by the ratio $\left(\frac{EA_{rib}}{EA_{shotcrete}} \right)$.

Calculation of final values of displacements in the ground and loads in the lining for the SLRT tunnel was performed using the design method by Negro (1988). As the modulus of the shotcrete was taken as $E_{eq} = 10.3$ GPa, these calculations represented the short term response. Extra delay on the lining activation, concerning the preliminary calculation presented in Chapter 2, was admitted due to the 10 hours necessary for the shotcrete at the invert to become stiff enough to carry load, and the results indicated an increase of 7% on the soil displacements and 7% decrease on the load in the lining. The developments of the convergence and loads at the ground-lining interaction during the tunnel advancing were calculated using the analytical approximation ADVRATE presented in Chapter 5.

Using the product of thickness versus the Young's modulus of the shotcrete as an index to evaluate the variation of the load in the lining, it was estimated that loads in SLRT tunnel could range from 50% to 200% of average values. The wide range of variation on load measurement obtained by the lining instrumentation was interpreted as a result of the shotcrete stiffness variability. Also, as the measurements were taken at the thinnest section along the longitudinal direction of the lining, the measured values should

be taken as a lower bound approximation, i.e. actual values should be higher. Results of flat jack tests performed in lining under similar loading conditions presented thrusts of the same order of magnitude and same range of variation obtained by the lining instrumentation, indicating that the strain interpretation provided reasonable values.

Besides the difference between the measured and the calculated values, which can be explained by the arguments above, the main deviation was detected on the behavior of the crown region. In the design calculations, the lining was assumed to be activated at the point where the shotcrete of the invert achieved 10 hours of age. In the design method, this implies that before this point, the lining does not exist and is then installed instantaneously, full-circle.

The lining instrumentation showed that thrust did indeed develop before the design activation point. Moreover, the measured bending moments developed in the opposite direction of those calculated. Also, at section C2I, it was observed that at the design activation point, higher rate of loading was observed indicating the point where the lining starts to behave as a closed ring. None of the measured values of thrust at the end of the short term interaction were above the calculated values, which corresponds to values of stresses below 10% of the shotcrete strength.

Soil monitoring is a common and effective instrument to control NATM tunnel construction procedure. On the other hand, monitoring of lining behavior is rarely used, but it is believed that a systematic monitoring of lining would provide a powerful tool for optimization of the NATM construction sequence. For practical application, the usage of embedded strain gages is not recommended due to the complexity and usual lack of knowledge on a particular shotcrete behavior. It is believed that a monitoring program based on the mini flat jack test would be a suitable way to evaluate the magnitude of loads in the lining. A lining instrumentation based on embedded strain gages seems to be more suitable for academic purposes where more detailed information on the lining response is required. This type of instrumentation will require a great knowledge on the

properties of the shotcrete and also knowledge on the response of the gages due to temperature changes. In order to enable shrinkage compensations, in each region around the tunnel perimeter and for each instrumented section, installation of compensating gages will be necessary. It is recommended that the compensating gages be installed along the longitudinal direction, protected by the so called 'no stress-strain' enclosure, which can be obtained from strain gage manufacturers. This enclosure is basically a box which involves the strain gages and isolates them from the acting stresses. For the shotcrete used in the SLRT tunnel, the strains measured before 10 hours of age were neglected for stress calculation purposes. This age, which also coincides with the peak of temperature and the stage when a sharp increase of deformation modulus is observed, is an important period for interpretation purposes and a careful monitoring during this period is recommended. Note that this value, 10 hours, was defined for the particular shotcrete with the particular mix used in the SLRT project. Some adjustment might be necessary from case to case.

The shotcrete deformation modulus is an important parameter in ground-lining interaction process, which usually is not available in practice. If no other information is available, the equivalent modulus $E_{eq} = 10 \text{ GPa}$ may be used for shallow tunnels as it agrees with the value suggested by Negro (1988) who successfully tested this value by backanalyzing many case histories. In order to obtain the design parameters of the shotcrete, one should ideally repeat a series of tests like the CRSG series presented in Table 4.12 and take the average values as shown in Figure 4.30. If it is not possible, based on the arguments presented in Chapter 4, a compression test done around 48 hours of age would provide a characteristic value of 'instantaneous' elastic modulus for a typical tunnel with 6 m of diameter and 3m/day of construction advancing rate.

By keeping the load constant for around 100 hours, a characteristic value of short term creep can be determined. The combination of these parameters would give an equivalent modulus as defined by Equation 6.5. Equations 4.4 and 4.12 applied for the

parameters shown in Tables 4.5 and 4.11 may also be helpful to obtain Young's modulus and strength of the shotcrete.

For considerations on the activation of the lining, in Negro's design method, it is suggested to consider the moment of the installation of the invert plus an extra delay of 10 hours to allow curing of the shotcrete. These assumptions are conservative in terms of soil deformation and non-conservative in terms of loads in the lining. Note that in shallow tunnels, the loads usually do not go beyond 10% of the maximum capacity of the lining, and therefore, problems to constraining the soil deformation usually will emerge before a problem of the lining capacity. Note also that the stability near the face, which is out of the scope of the present study, should be checked.

Field instrumentation showed that the bending moments in the crown region will develop before the invert is closed, and as a result, the usual 'full-circle' design calculations cannot predict their values. In case of $K_0 < 1$, the calculation will indicate bending moment in the opposite direction of the actual one. In case of $K_0 > 1$, the calculation will underestimate the actual values. As the values of bending moments are usually small in shallow soft ground tunnels, this deviation is not considered critical.

In the case of high rates of construction, long delays of the invert installation or high values of K_0 , high values of bending moments may be generated. In these cases, design precautions and careful monitoring programs are recommended.

Ideally, to analyze the problem approached in this thesis, a three dimensional finite element program would be necessary. However, a special plane strain code like that presented in Chapter 5 (Ohnishi et al., 1982) using the stiffness reduction technique may be helpful to define the magnitude of the problem. In any case, a field monitoring seems to be an invaluable source of feed back information to optimize the design and construction procedures.

Table 6.1 Instruments used for shrinkage and thermal strain compensations in SLRT lining instrumentation

Section	Region	Measurement	Compensation
C2I	Crown	VW14/VW15	VW1
C2I	Crown	VW16/VW17	VW2
C2I	Springline	VW9	VW10
C2I	Springline	VW28/VW29	VW5
C2II	Crown	VW25/VW40/VW41	VW3
C2II	Crown	VW32/VW33	VW7
C2II	Floor	VW18/VW19	VW34/VW35

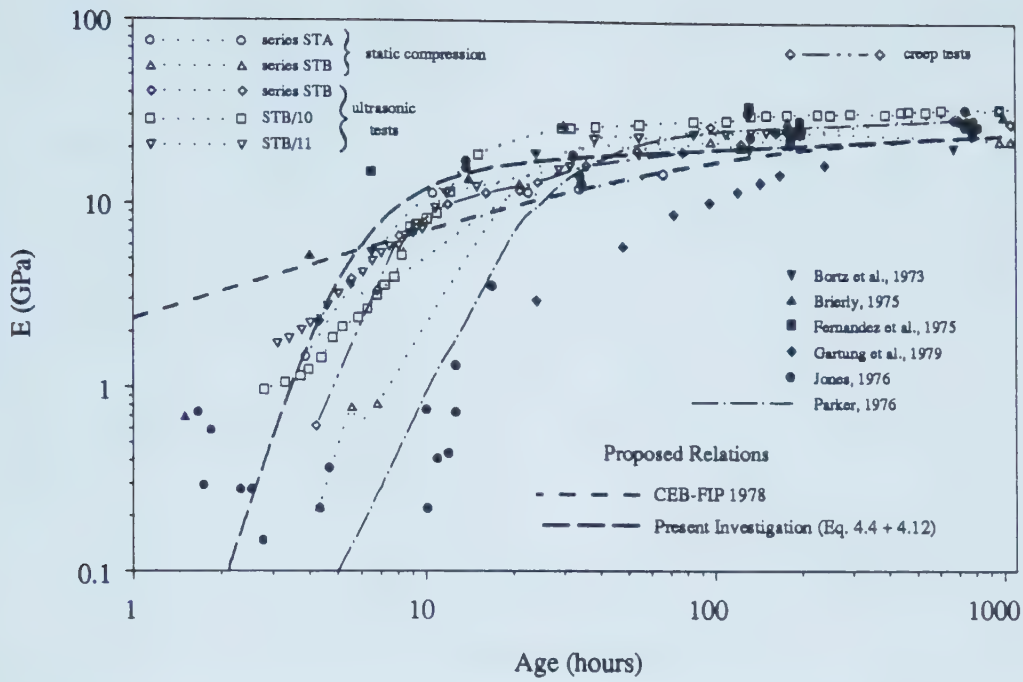


Figure 6.1 Elastic Modulus Development as a Function of Age

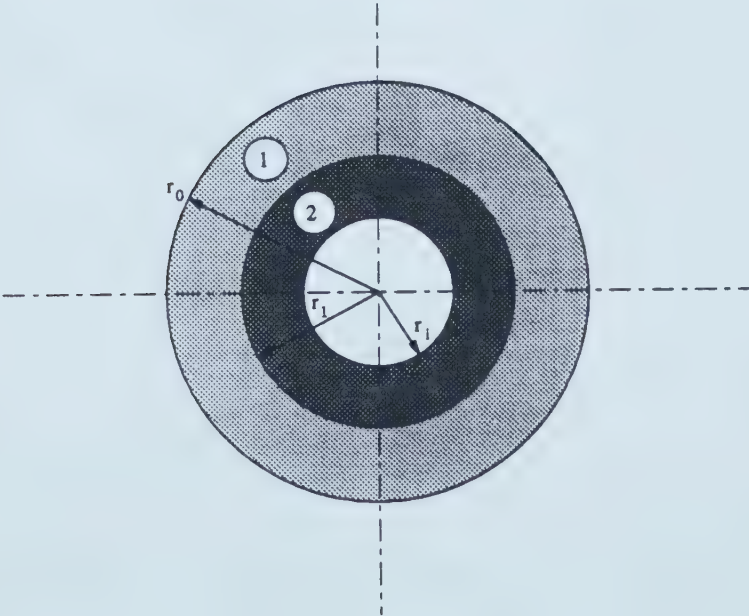


Figure 6.2 Shrink Fit of Composite Tube Assemblage

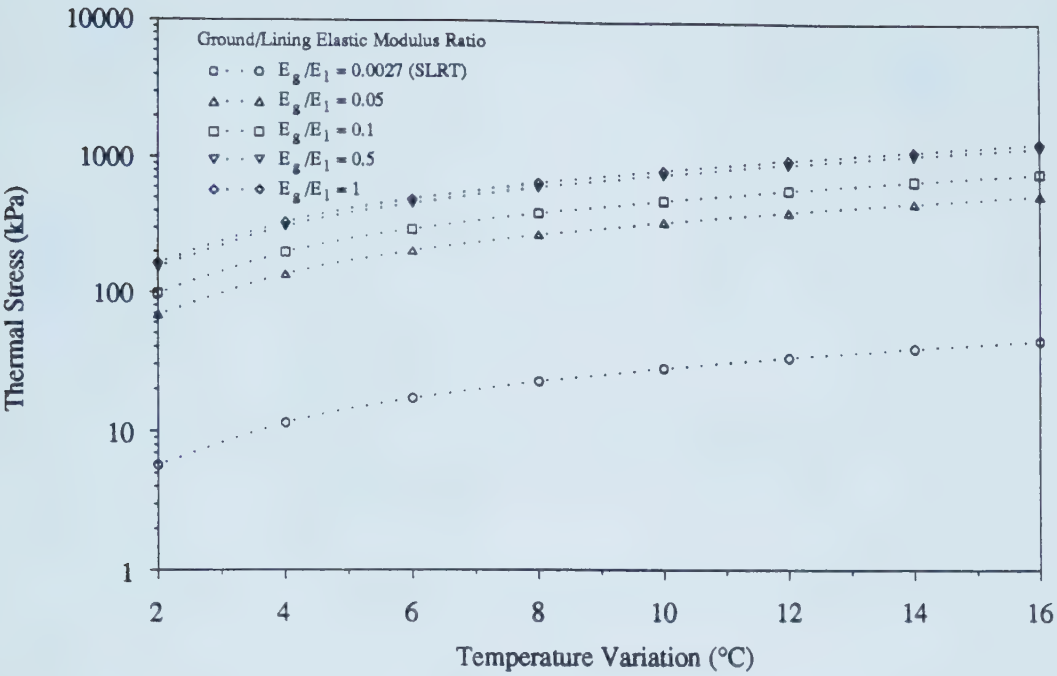


Figure 6.3 Simplified Evaluation of Thermal Stresses using Equation 6.10 for the SLRT Tunnel Geometry

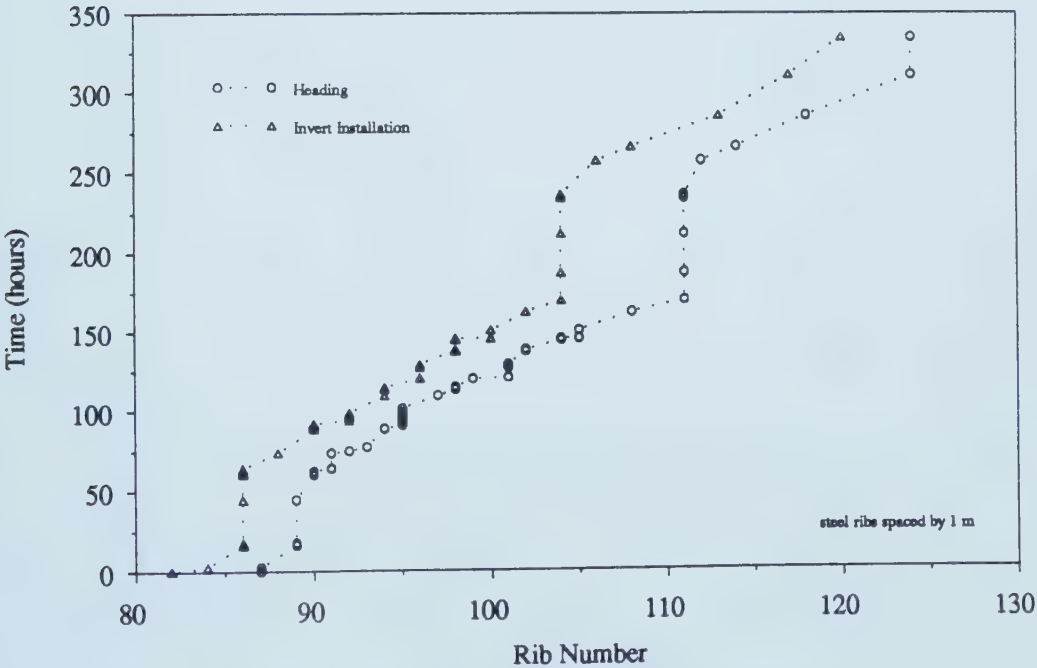


Figure 6.4 Construction Progress of the SLRT Northbound Tunnel close to the Lining Instrumentation

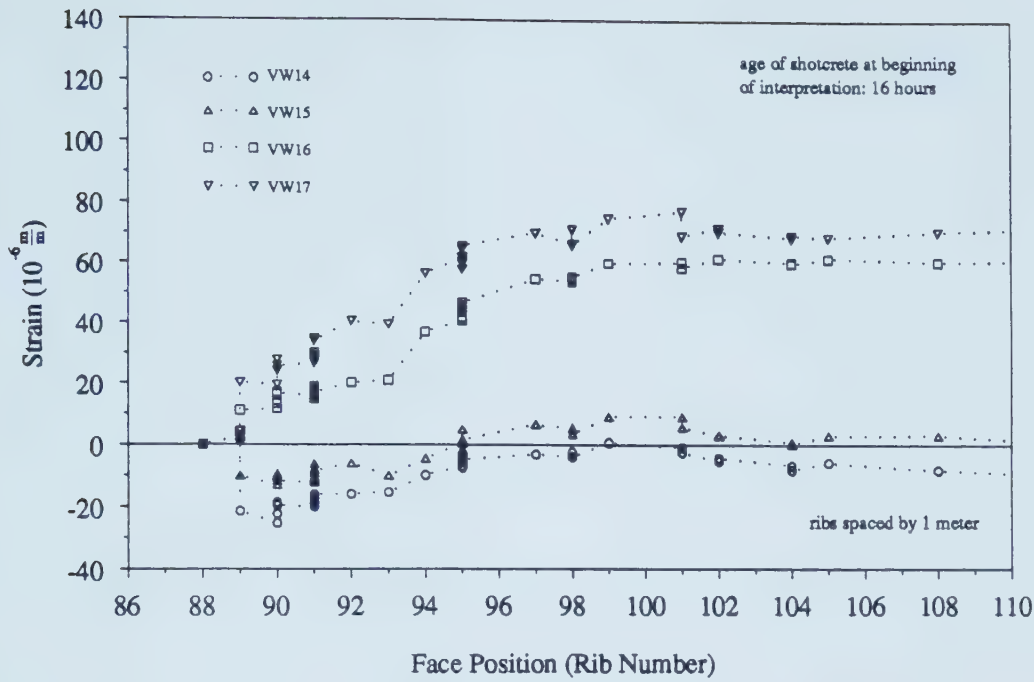


Figure 6.5 Compensated Measurements from Vibrating Wire Strain Gages Embedded in Crown Region, Section C2I

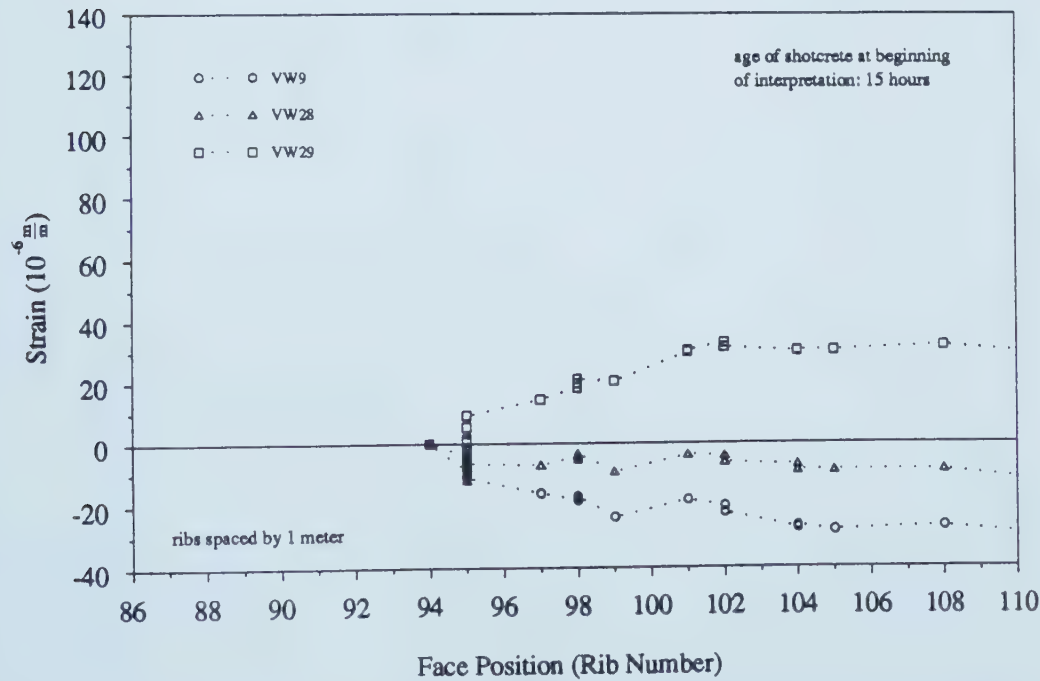


Figure 6.6 Compensated Measurements from Vibrating Wire Strain Gages Embedded in Springline Region, Section C2I

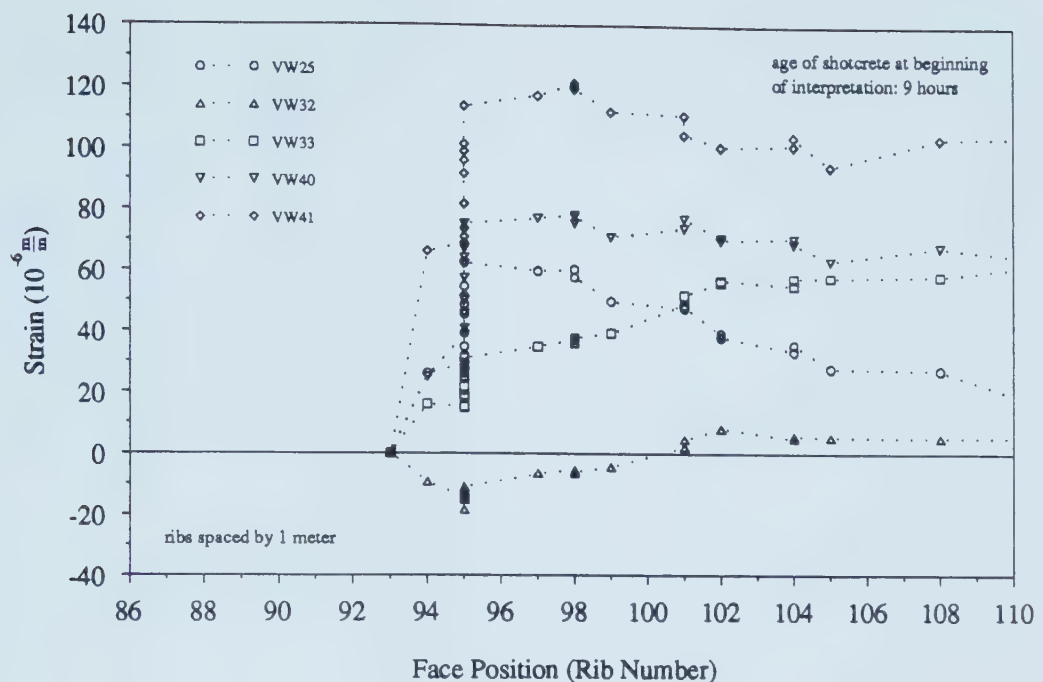


Figure 6.7 Compensated Measurements from Vibrating Wire Strain Gages Embedded in Crown Region, Section C2II

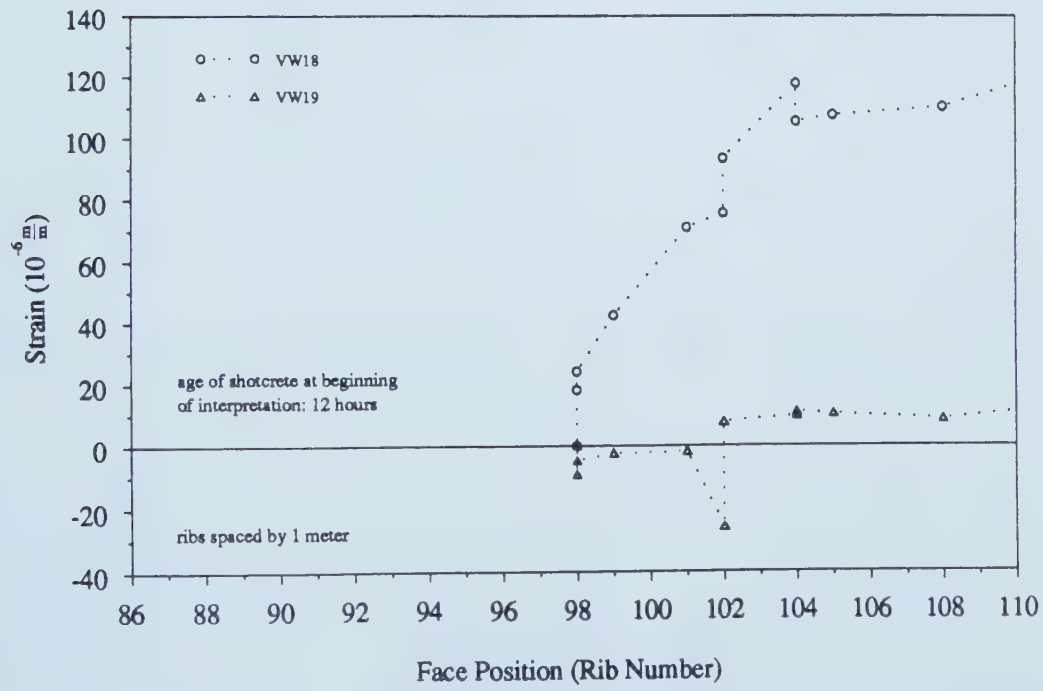


Figure 6.8 Compensated Measurements from Vibrating Wire Strain Gages Embedded in Floor Region, Section C2II

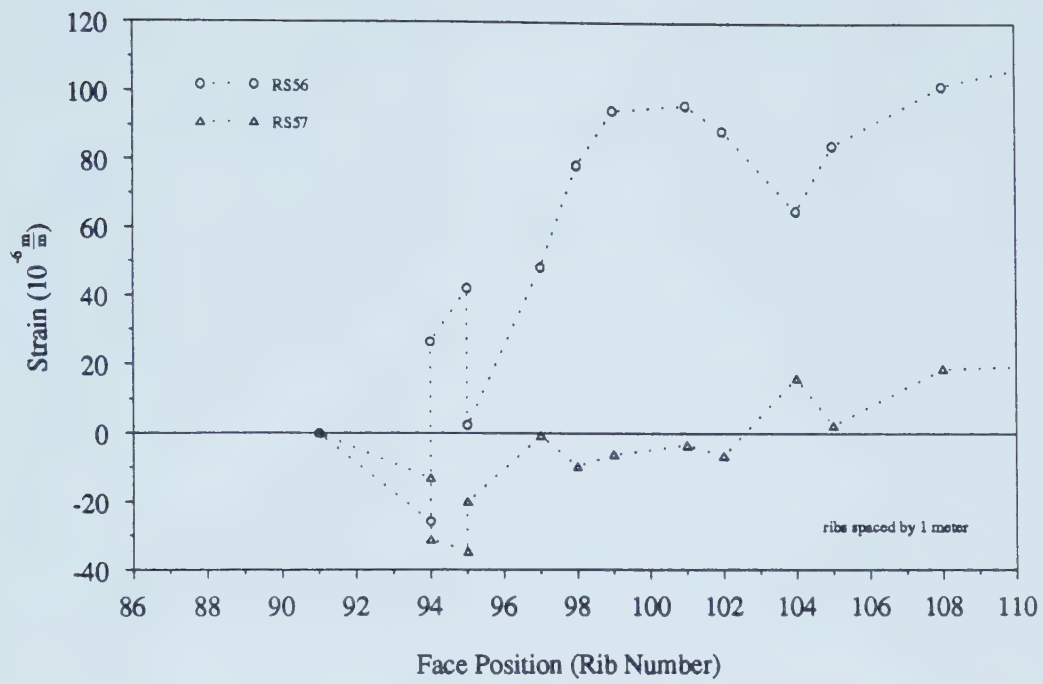


Figure 6.9 Strain Measured in Steel Rib in the Crown Region, Section C2I

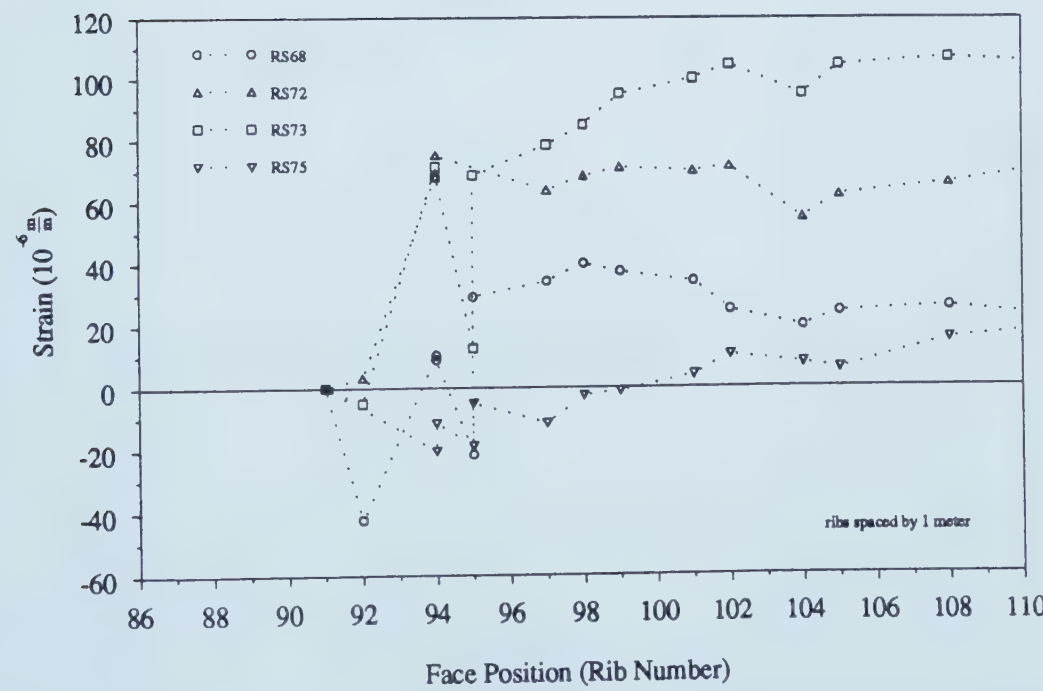


Figure 6.10 Strain Measured in Steel Rib in Springline and Floor Regions, Section C2I

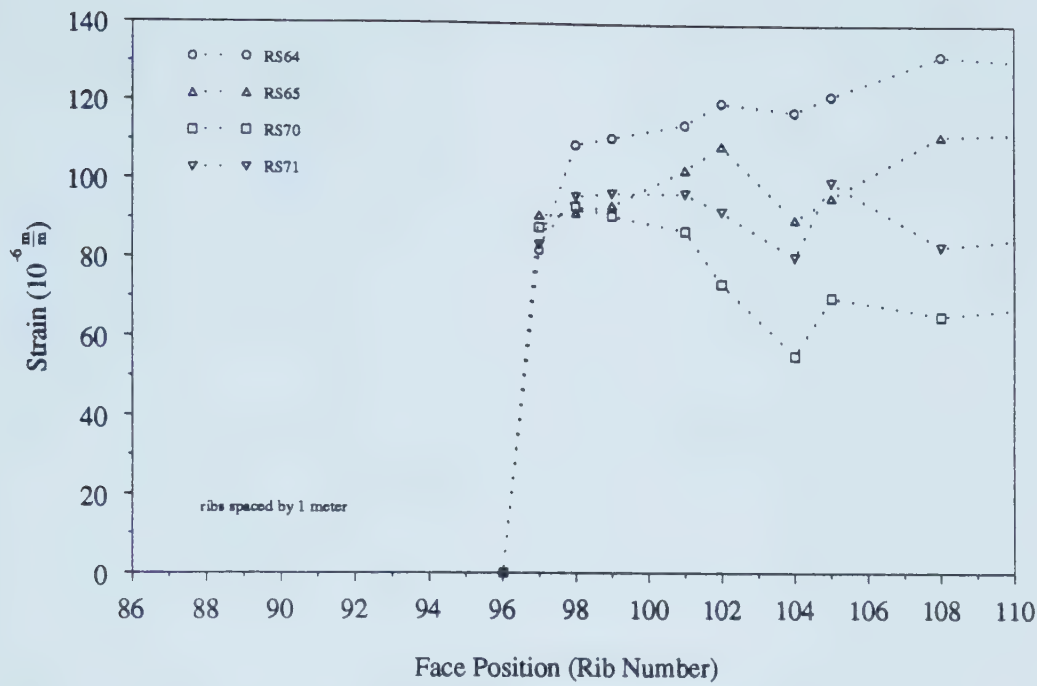


Figure 6.11 Strain Measured in Steel Rib in Springline and Floor Regions, Section C2II

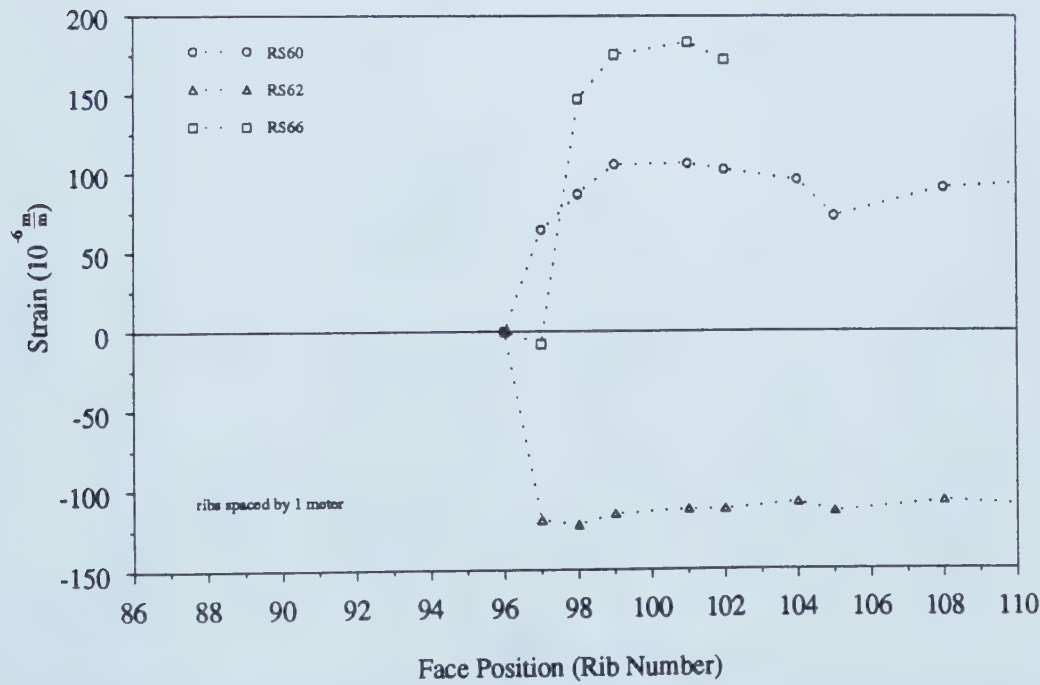


Figure 6.12 Strain Measured in Steel Rib in Springline and Floor Regions, Section C2III

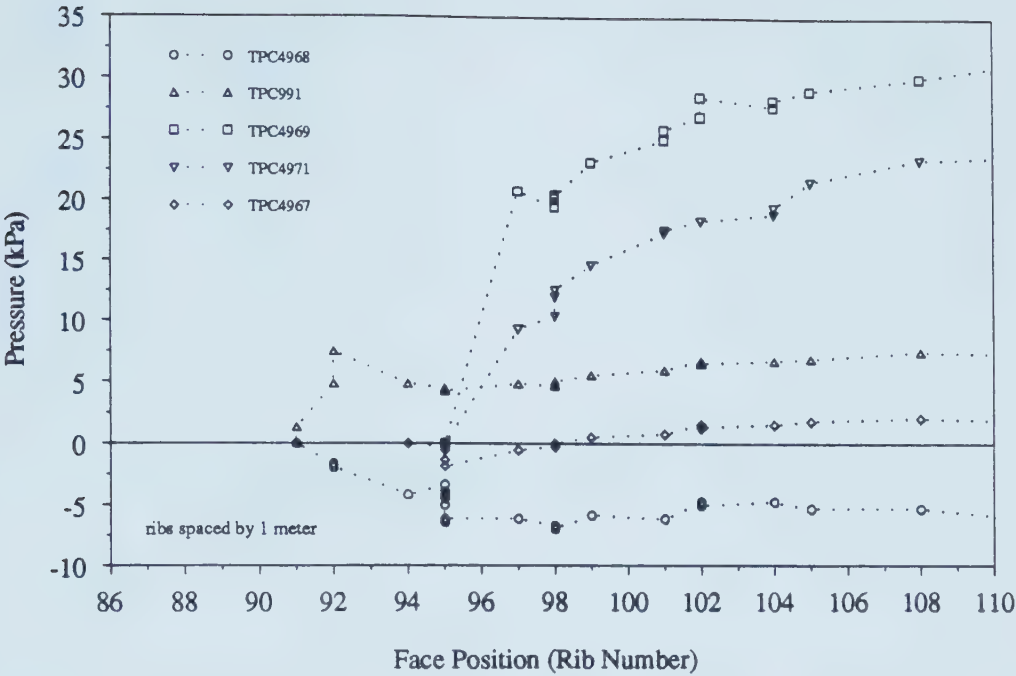


Figure 6.13 Compensated Measurements from Total Pressure Cell Installed at Soil-Lining Interface

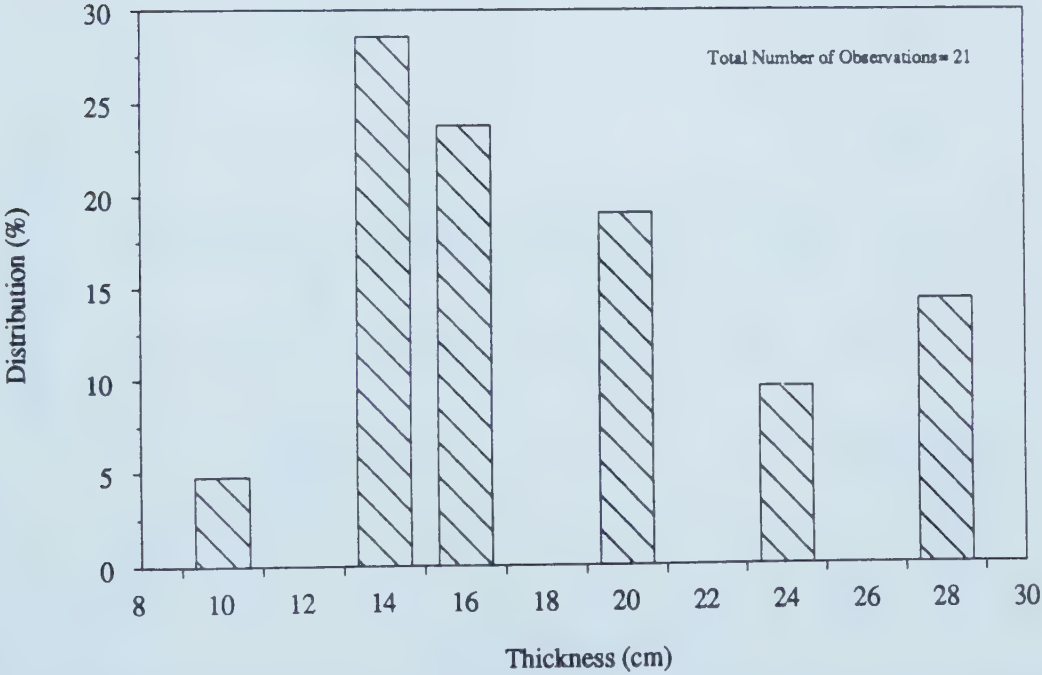


Figure 6.14 Distribution of Lining Thickness Measured in NATM Tunnels at SLRT Extension

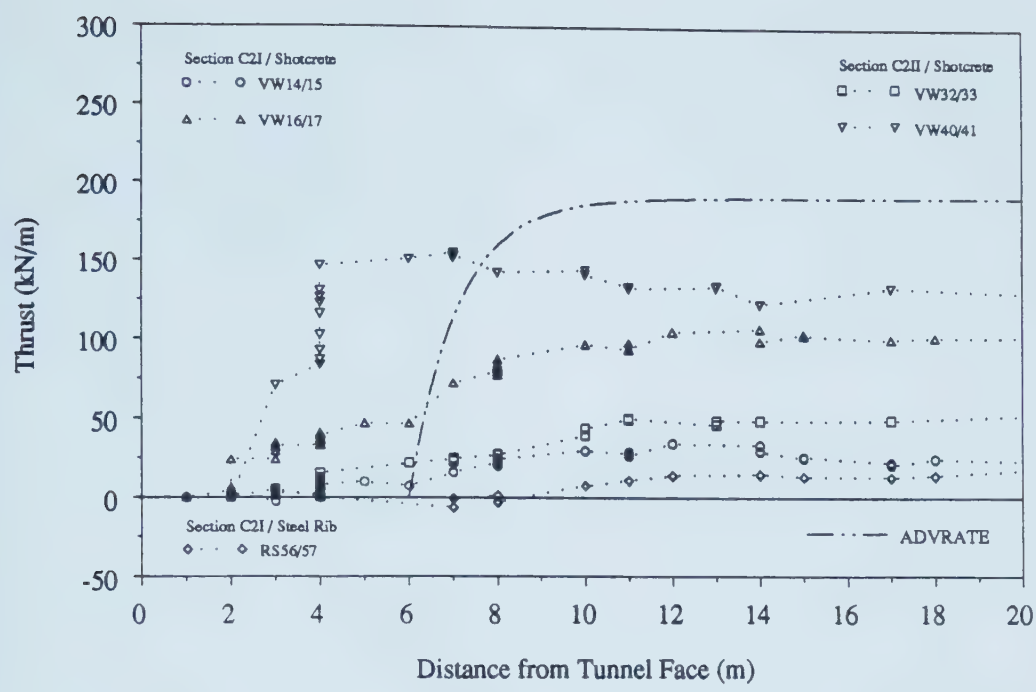


Figure 6.15 Calculated and Measured Thrusts in SLRT Tunnel Lining, for Points close to Crown

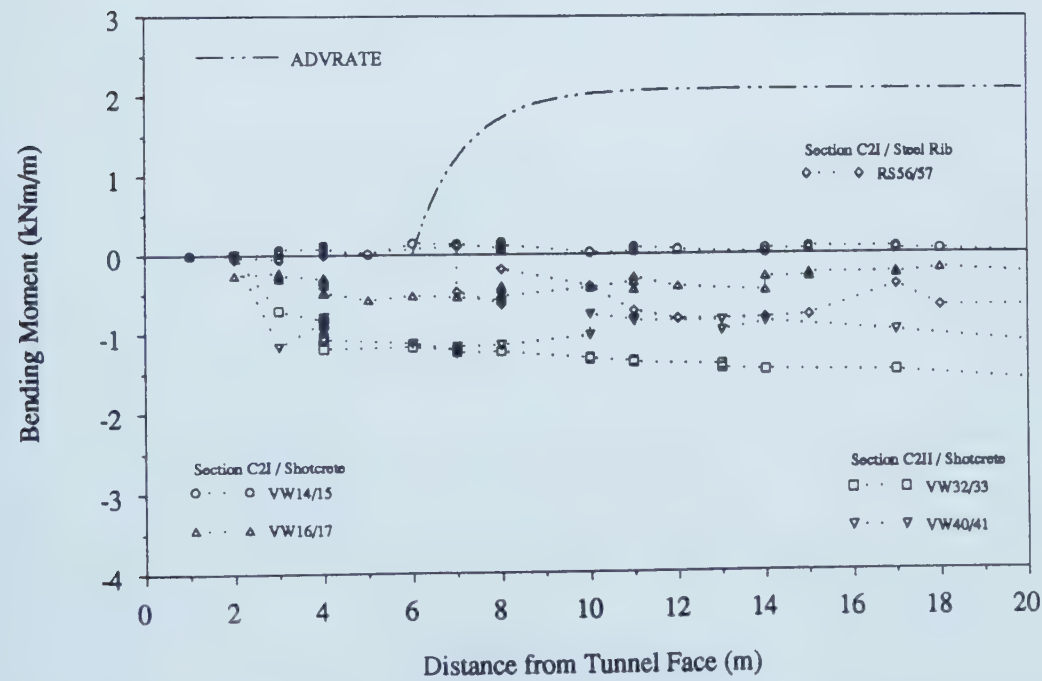


Figure 6.16 Calculated and Measured Bending Moments in SLRT Tunnel Lining, for Points close to Crown

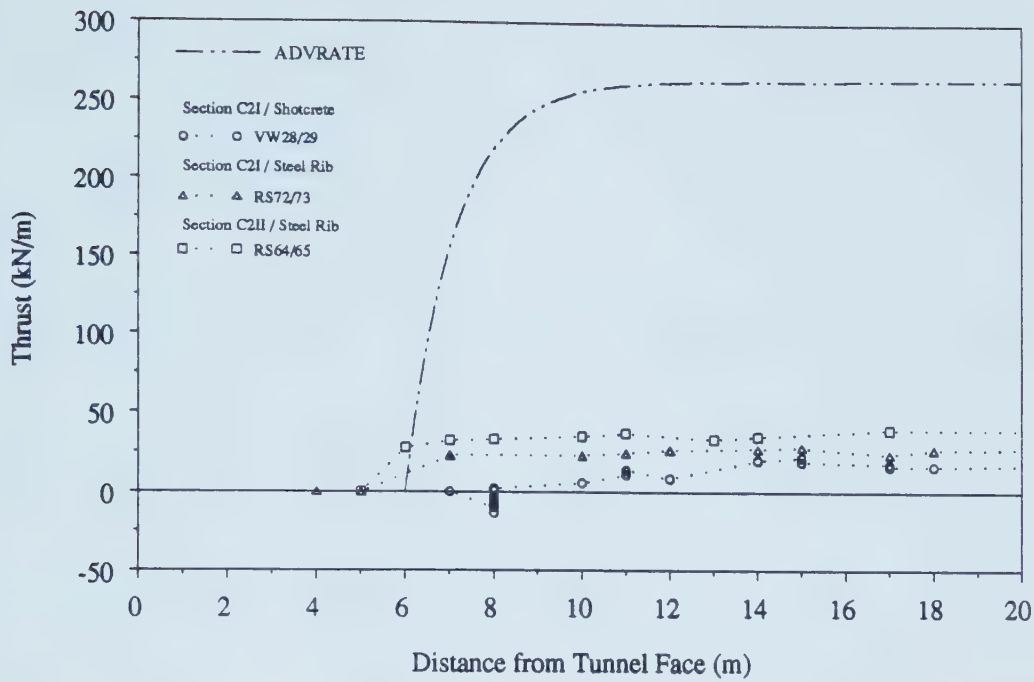


Figure 6.17 Calculated and Measured Thrusts in SLRT Tunnel Lining, for Points close to Springline

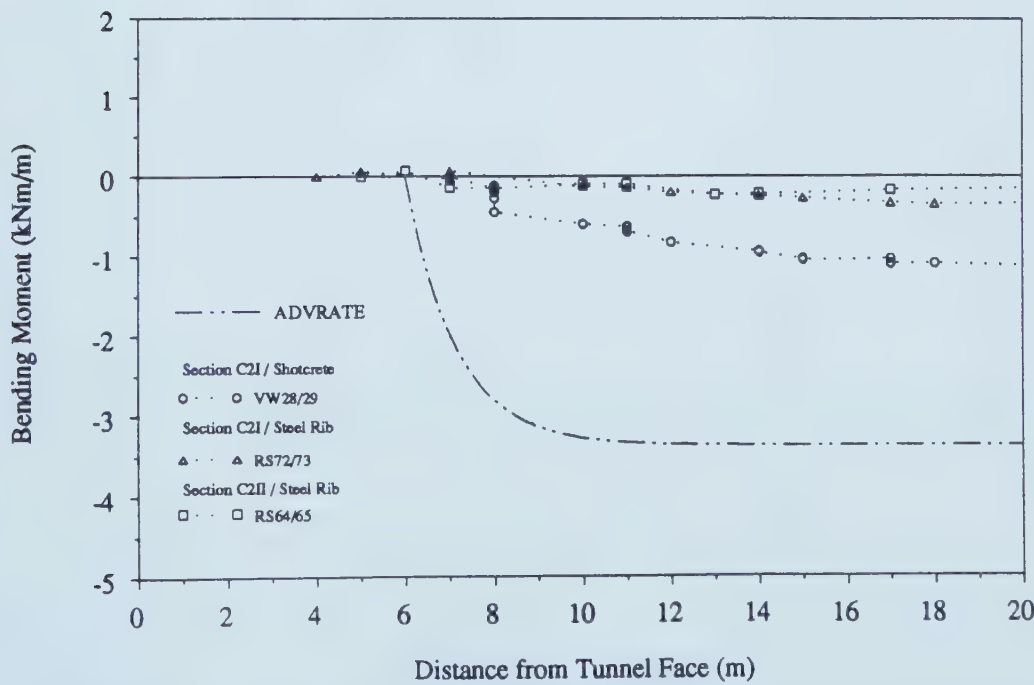


Figure 6.18 Calculated and Measured Bending Moments in SLRT Tunnel Lining, for Points close to Springline

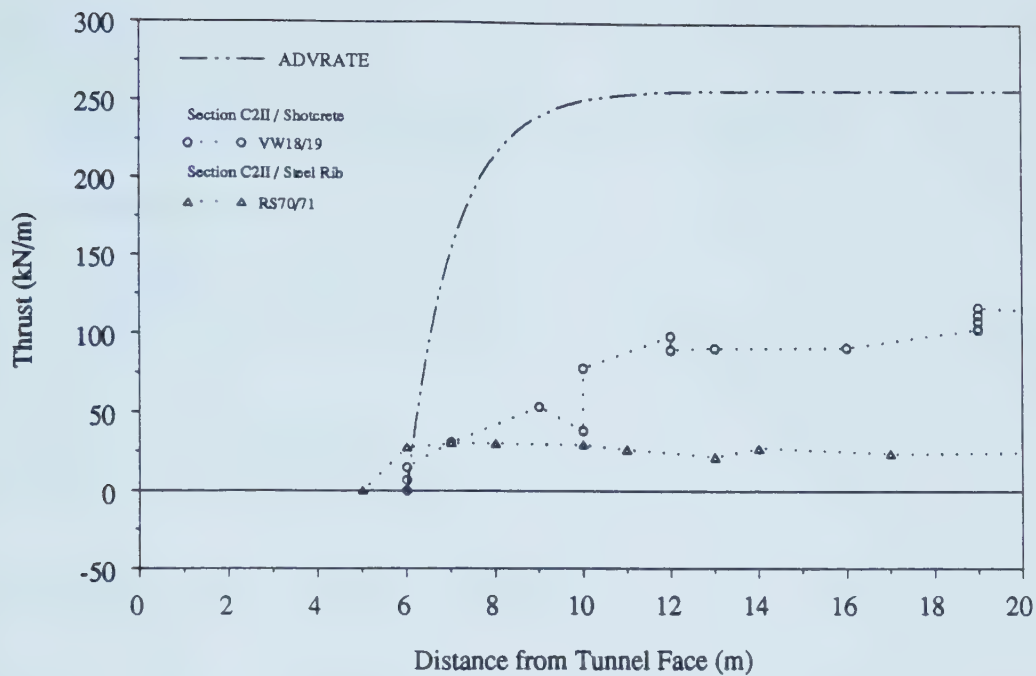


Figure 6.19 Calculated and Measured Thrusts in SLRT Tunnel Lining, for Points close to Floor

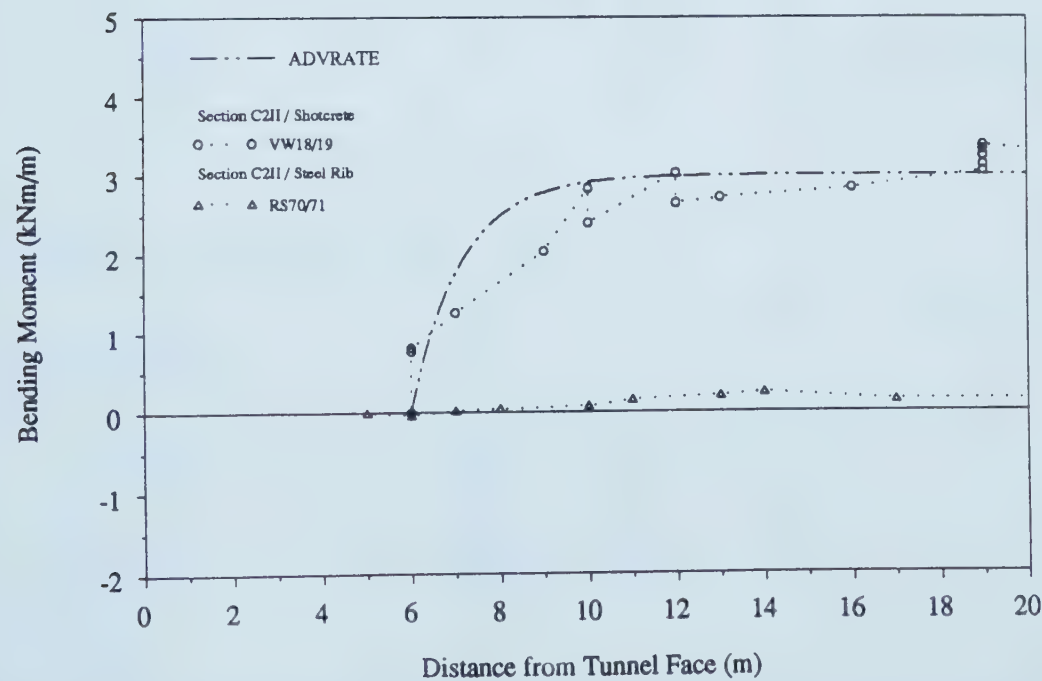


Figure 6.20 Calculated and Measured Bending Moments in SLRT Tunnel Lining, for Points close to Floor

1. GEOMETRY

$H =$
(crown to surface)

$D =$
(diameter of the tunnel)

$H/D =$

2. GROUND PROPERTIES

$\gamma =$

$K_0 =$

$(\sigma_3)_{\text{axis}} =$

$c =$

$\phi =$

$R_f =$

$\phi_a = \arcsin \left(\frac{1 + (\sigma_3/c) \tan (\phi)}{1 + (\sigma_3/c) \sec (\phi)} \right) =$

$\phi_o = \arcsin (1 - R_f + R_f \csc \phi_a)^{-1} =$

$(m-1) = \frac{2 \sin \phi_o}{1 - \sin \phi_o} =$

$K =$

$n =$

$p_a =$

$\mu =$

(Janbu's parameter, 1963)

$E_u = K p_a \left(\frac{\sigma_3}{p_a} \right)^n \left(1 - \frac{R_f (1 - \sin \phi) (\sigma_1 - \sigma_3)}{2 c \cos \phi + 2 \sigma_3 \sin \phi} \right)^2$

(Duncan and Chang, 1970)

Location	σ_3	σ_1	E_u (MPa)
1/2D above C	-	-	40
at S	-	-	69
1/2D below F	-	-	26

(from pressuremeter tests)
(Thurber, 1980: Figure 2.18))

3. TUNNEL CLOSURE AT LINING ACTIVATION

$X =$
(face to lining closure)

$X/D =$

$K_0 =$

$u_r = (D \sigma_{ro} / E_u) U$

Location	U	σ_{ro} (kPa)	$D \sigma_{ro} / E_u$	u_r (mm)
C	0.629	155.40	0.0245	15.4
S	0.500	174.72	0.0160	8.0
F	0.358	281.40	0.0682	24.4

(σ_{ro} : initial radial in situ stress)

Figure 6.21 Calculation Sheet with Geometric Ground Properties Data and Tunnel Closure at Lining Activation

4. REFERENCE VALUES

$H/D = 1.23$ $K_0 = 0.8$ $(m \cdot 1) = 2.82$

	$1 - \Sigma_{ref} = \alpha_{ref}$	α_{ref} / U_{ref}	U_{ref}
C	0.630	0.82	0.768
S	0.605	1.12	0.540
F	0.470	2.03	0.232

5. STRESS RELEASE AND STIFFNESS CHANGE AT LINING ACTIVATION

	U	U/U_{ref}	Beyond Limit?	λ	λ'
C	0.629	0.819	NO	0.125	0.69
S	0.500	0.926	NO	0.04	0.58
F	0.358	1.546	NO	-0.40	0.67

STRESSES : $\Sigma = 1 - (1 - \lambda) \alpha_{ref}$

	$(1 - \lambda)$	Σ
C	0.875	0.449
S	0.96	0.419
F	1.40	0.342

$\bar{\Sigma} = (\Sigma_C + 2\Sigma_S + \Sigma_F)/4 = 0.407$

$\bar{\alpha} = 1 - \bar{\Sigma} = 0.593$

$\gamma_{red} = \gamma \bar{\Sigma} = 8.15 \text{ kN/m}^3$

STIFFNESS : $E_t = (\lambda' / \lambda'_i) E_{ti}$

	λ'_i	E_{ti} / λ'_i	$E_t \text{ (MPa)}$
C	1.28	31.25	21.56
S	1.43	48.25	27.99
F	1.01	25.74	17.25

$\bar{E}_t = (E_{tC} + 2E_{tS} + E_{tF})/4 = 23.69 \text{ MPa}$

Figure 6.22 Calculation Sheet for Estimations of the Stress Release and Ground Stiffness at the Section the Lining is Activated

6. 2D STABILITY VERIFICATION

$\bar{\alpha} =$ $\bar{\sigma}_{\infty} = \frac{1+K_0}{2} \gamma \left(H + \frac{D}{2} \right) =$ $\phi =$ $c/\gamma D =$ $H/D =$

(approximation for calculation : $\phi = 30^\circ$, $c/\gamma D = 0$)

$\therefore P_1 / \gamma D =$ $P_1 =$ $\alpha_1 = 1 - P_1 / \bar{\sigma}_{\infty} =$

$FS = \frac{[(1 - K_0) (1 + K_0) + \alpha_1]}{[(1 - K_0) (1 + K_0 + \bar{\alpha})]} =$

7. LINING-GROUND INTERACTION

GEOMETRY : $Z_0 =$ $r_0 =$ $r_1 =$

SOIL : $\bar{E}_t =$ $\mu =$ $\gamma_{red} =$ $K_0 =$

LINING : $E_s =$ $\mu_s =$ $d =$ $I_s =$

ITERATION NO.: 1 $\bar{E}_t =$ $\alpha =$ $\beta =$

	u_r (mm)	Δu_r (mm)	$u_{rf} =$ $u_r + \Delta u_r + v_{\infty}$	U	U/U_{red}	λ'	E_t (MPa)	σ_r (kPa)
C	15.4	2.29	14.17	0.579	0.753	0.760	23.75	61.88
S	8.0	-1.67	6.30	0.395	0.731	0.750	36.19	82.90
F	24.4	2.57	30.51	0.447	1.932	0.575	14.80	84.13

$v_{\infty} = \frac{(1+\mu)(3-4\mu)}{4(1-\mu)} \gamma_{red} r_0^2 \ln \frac{r_0}{r_1} =$ $(\bar{E}_t)_{new} = (E_{tC} + 2E_{tS} + E_{tF})/4 =$

Figure 6.23 Calculation Sheet for 2D Stability Verification and Lining-Ground Interaction Analysis

ITERATION NO.: 2 $\bar{E}_t =$ 27.73 MPa $\alpha =$ 31.62 $\beta =$ $8.60 \cdot 10^{-3}$

	u_r (mm)	Δu_r (mm)	$u_{rf} =$ $u_r + \Delta u_r + v_{zo}^*$	U	U/U_{ref}	λ'	E_t (MPa)	σ_r (kPa)
C	15.4	2.02	14.41	0.589	0.766	0.755	23.59	61.48
S	8.0	-1.40	6.58	0.412	0.763	0.750	36.19	82.70
F	24.4	2.28	29.70	0.436	1.881	0.582	14.98	83.54

$$v_{zo}^* = \frac{(1+\mu)(3-4\mu)}{4(1-\mu)E_t} \gamma_{red} r_0^2 \ln \frac{r_0}{r_1} =$$
3.01 mm

$$(\bar{E}_t)_{new} = (E_{tc} + 2E_{ts} + E_{tf})/4 =$$
27.74 MPa

ITERATION NO.: 3 $\bar{E}_t =$ 27.74 MPa $\alpha =$ 31.62 $\beta =$ $8.60 \cdot 10^{-3}$

	u_r (mm)	Δu_r (mm)	$u_{rf} =$ $u_r + \Delta u_r + v_{zo}^*$	U	U/U_{ref}	λ'	E_t (MPa)	σ_r (kPa)
C	15.4	2.02	14.41	0.589	0.766	0.755	23.59	61.48
S	8.0	-1.40	6.58	0.412	0.763	0.750	36.19	82.70
F	24.4	2.28	29.70	0.436	1.881	0.582	14.98	83.54

$$v_{zo}^* = \frac{(1+\mu)(3-4\mu)}{4(1-\mu)E_t} \gamma_{red} r_0^2 \ln \frac{r_0}{r_1} =$$
3.01 mm

$$(\bar{E}_t)_{new} = (E_{tc} + 2E_{ts} + E_{tf})/4 =$$
27.74 MPa

$\bar{E}_t \equiv (\bar{E}_t)_{new} \Rightarrow$ end of iteration

ITERATION NO.: _ $\bar{E}_t =$ $\alpha =$ $\beta =$

	u_r (mm)	Δu_r (mm)	$u_{rf} =$ $u_r + \Delta u_r + v_{zo}^*$	U	U/U_{ref}	λ'	E_t (MPa)	σ_r (kPa)
C								
S								
F								

$$v_{zo}^* = \frac{(1+\mu)(3-4\mu)}{4(1-\mu)E_t} \gamma_{red} r_0^2 \ln \frac{r_0}{r_1} =$$

$$(\bar{E}_t)_{new} = (E_{tc} + 2E_{ts} + E_{tf})/4 =$$

Figure 6.24 Calculation Sheet for Iterative Analysis of the Lining-Ground Interaction

8. SUBSURFACE SETTLEMENTS

CROWN SETTL. = 14.41 mm

$U/U_{ref} = 0.766$

$\lambda_c = 0.18$

$\alpha_c = (1 - \lambda_c) \alpha_{ref} = 0.52$

$K_0 = 0.8$

$\phi = 33$

Depth Z (m)	Z/H	SETTLEMENT/CROWN SETTL.			SETTLEMENT NT (mm)
		H/D=1.5	H/D=3	H/D=1.23	
0	0	0.52	0.375	0.5461	7.87
2.59	0.333	0.59	0.44	0.617	8.89
4.53	0.583	0.665	0.5	0.6947	10.01
6.47	0.833	0.8	0.655	0.8261	11.91
7.12	0.916	0.875	0.765	0.8948	12.90
7.77	1	1	1	1	14.41

9. SURFACE SETTLEMENTS

$\alpha_c = 0.52$

$K_0 = 0.8$

$\phi = 33$

DIST. Y(m)		0	3.15	6.3	12.6	18.9
Y/D		0	0.5	1.0	2.0	3.0
SETTL.	H/D=1.50	0.52	0.46	0.365	0.21	0.13
CROWN	H/D=3.00	0.375	0.365	0.335	0.245	0.175
SETTL.	H/D=1.23	0.546	0.477	0.370	0.204	0.122
SETTL. (mm)		7.87	6.88	5.34	2.94	1.76

MAX. DISTR. : $\gamma_c = 1 : 2622$

Trough correction:

$$\gamma_{cc} = 1.4 \gamma_c \quad \Rightarrow \quad \gamma_{cc} = 1 : 1463$$
$$i = 0.606 \frac{s_{max}}{\gamma_{cc}}$$
$$s = s_{max} e^{-x^2/2i^2} \quad (\text{settlement trough : normal probability curve})$$

where s_{max} is the surface settlement as calculated for $Y/D=0$ in item 9

Figure 6.25 Calculation Sheets for Iterative Analysis of the Lining Ground Interaction and for Subsurface and Surface Settlements

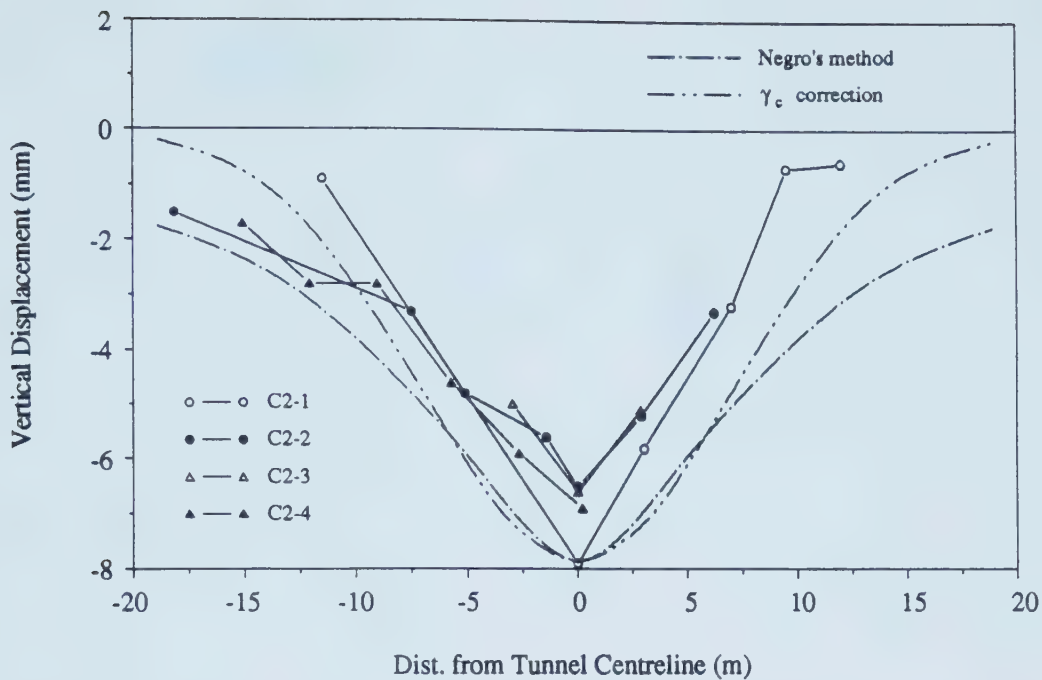


Figure 6.26 Measured and Calculated Transverse Settlement Distributions

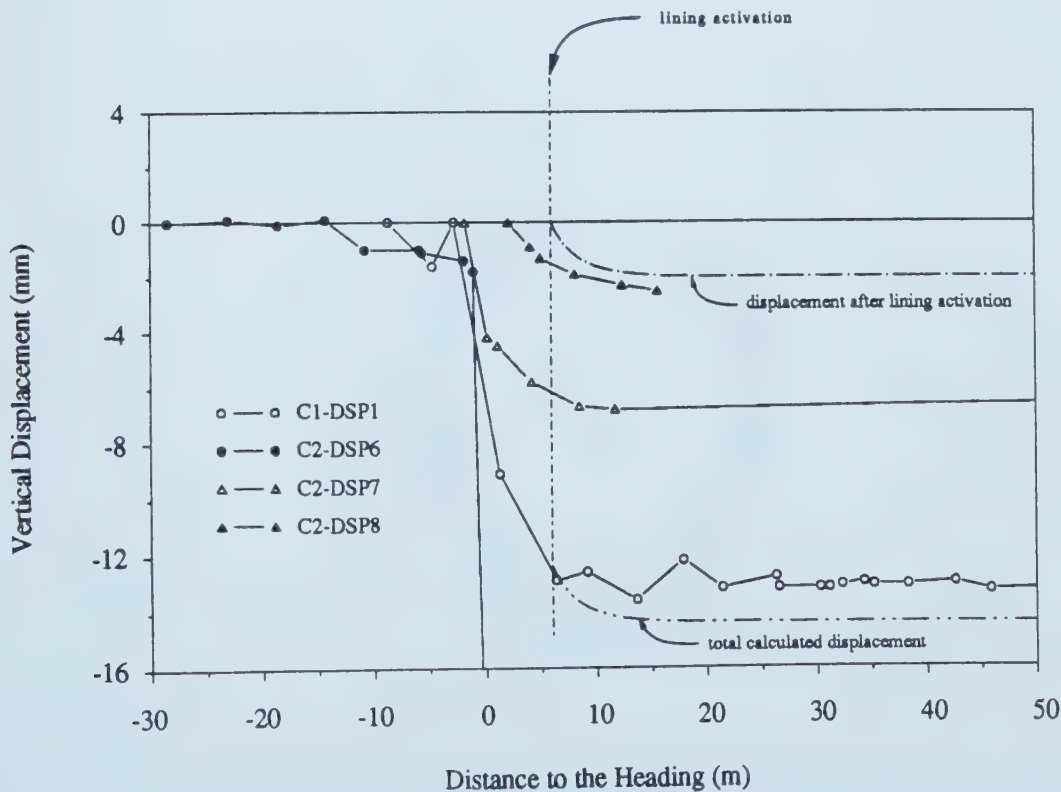


Figure 6.27 Measured and Calculated Settlements at Crown Region

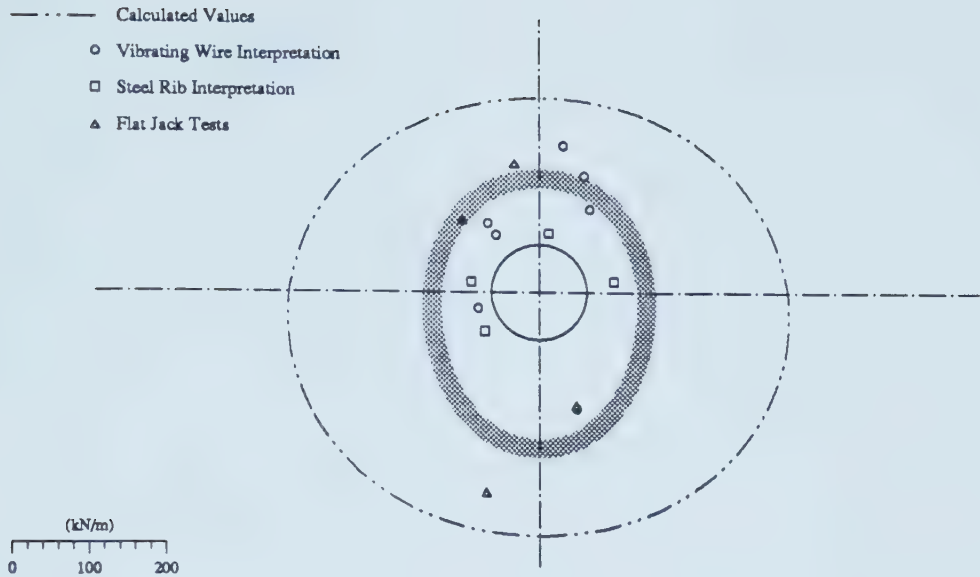


Figure 6.28 Comparison between Calculated and Measured Values of Thrust in SLRT Shotcrete Lining, using different Techniques

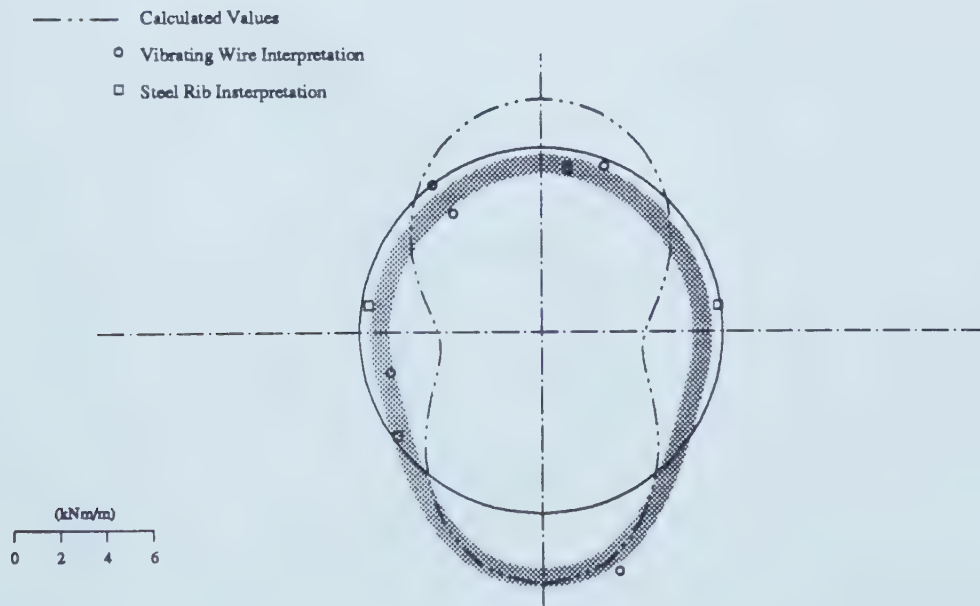


Figure 6.29 Comparison between Calculated and Measured Values of Bending Moment in SLRT Shotcrete Lining, using different Techniques

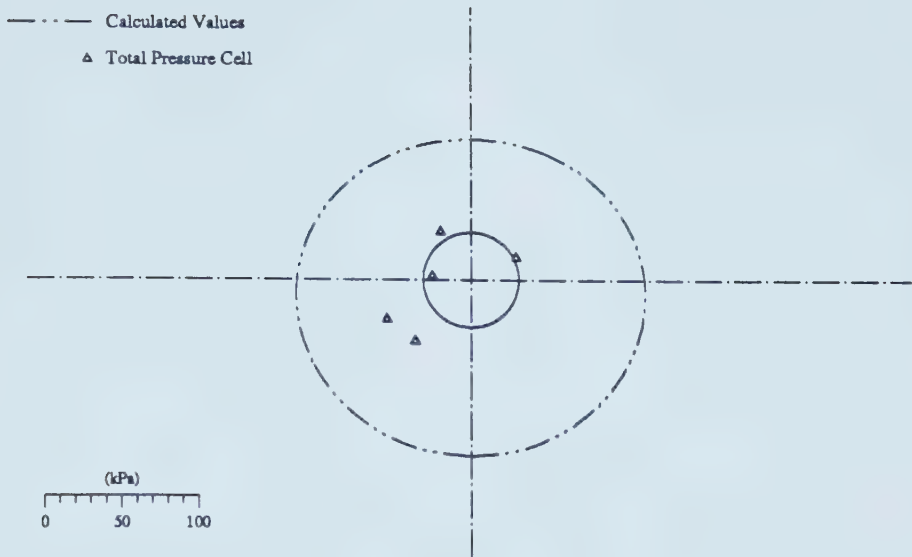


Figure 6.30 Comparison between Calculated and Measured Radial Pressures of Ground on SLRT Shotcrete Lining

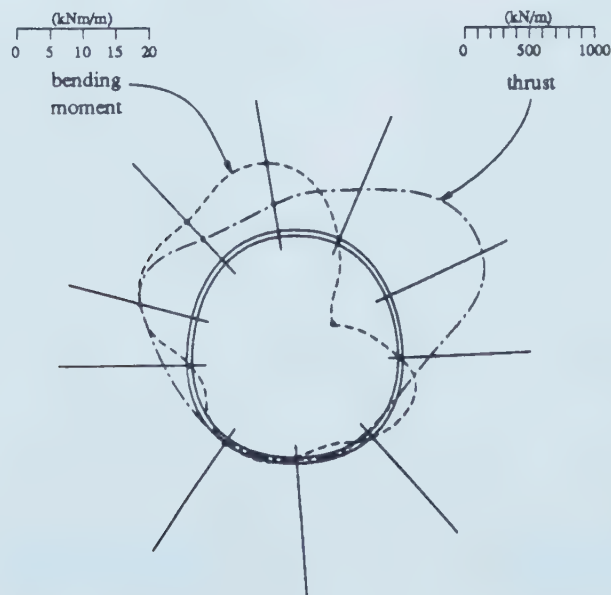


Figure 6.31 Bending Moments and Thrusts Measured in a Section of Subway in Vienna (modified from Golser et al, 1989)

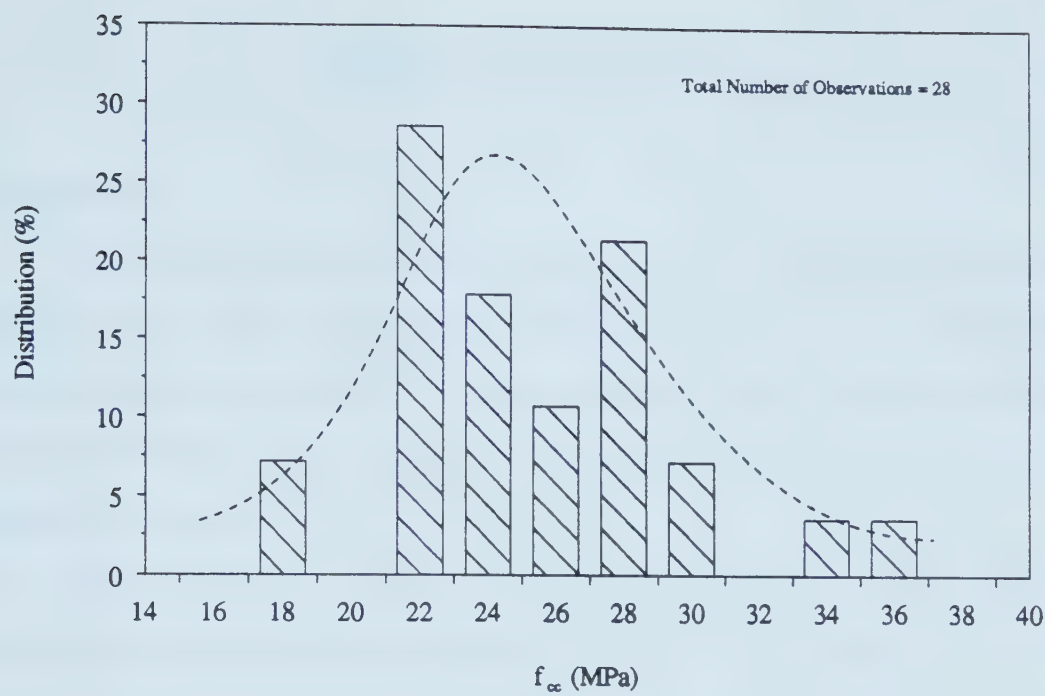


Figure 6.32 Distribution of Strength of Shotcrete Measured in Cores Taken from Panel and Tunnel Lining, South SLRT NATM Tunnel

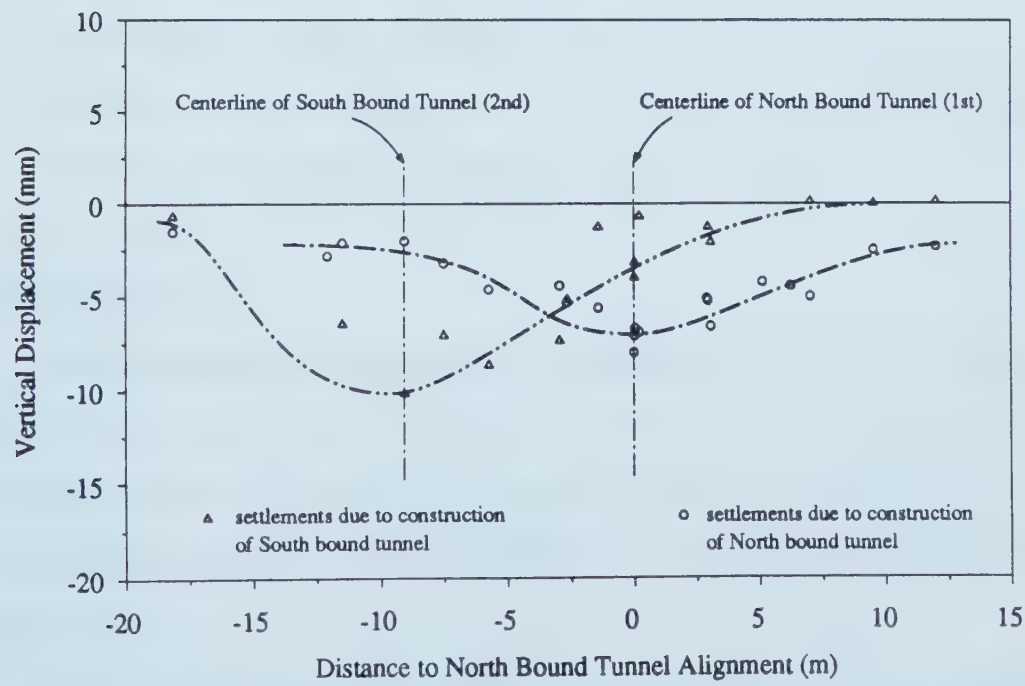


Figure 6.33 Surface Settlements Caused by the Construction of North Bound and South Bound NATM Tunnels

7. SUMMARY AND CONCLUSIONS

7.1 Introduction

This thesis focused on several aspects of the short term interaction between the ground and the shotcrete lining, in soft ground tunnels excavated by the NATM. In this method of construction, the shotcrete is loaded at early age and, therefore, the knowledge of its behavior in this period is essential for the assessment of the ground-lining interaction mechanism.

More specifically, the research was aimed at identifying the factors that play a role in the ground to lining load transfer process and to develop practical recommendations and tools for design purposes. As such, simplicity was consistently pursued in all stages of the work.

In order to achieve the proposed objectives, studies were carried out in three major aspects, namely:

1. field measurement of tunnelling response,
2. investigation of shotcrete behavior at the early ages,
3. development of an analytical procedure for estimating the evolution of internal loads in the lining taking into account the shotcrete behavior.

7.2 Field Measurements

The tunnel instrumentation program was conducted on the NATM 'Northbound Tunnel' of the South Light Rail Transit System (SLRT) in Edmonton. Soil and lining instrumentations were used to monitor the tunnel construction, but emphasis was given to the shotcrete instrumentation, due to the difficulty involved in the interpretation of the measurements.

In order to allow an evaluation of the various parameters involved in this type of problem, a prediction of the ground displacement and loads in the lining was carried out

using data available before the tunnel construction. These calculations were performed using the method developed by Negro (1988), which was described by showing a step by step procedure. The main assumptions of this method were discussed as well.

A preliminary assessment of the field data obtained was also carried out and allowed the identification of the main problems involved in design and interpretation of field instrumentation.

Due to the difficulties involved in monitoring loads in the shotcrete lining using embedded strain gages, the need was felt for the development of a reliable and economical in situ test. Such technique, termed the 'mini flat jack test', was an evolution from the procedure described by Rocha et al. (1966), which originally aimed at measuring stresses in rock.

A scale reduction was necessary due to the restrictions imposed by the thickness of a typical shotcrete lining. This scale reduction, associated with the relatively low stress magnitudes acting in shallow tunnel liners, led to some technical problems related to the accuracy of the measurements. For this reason, the mechanical extensometer used by Rocha et al. (1966) to monitor the displacements during the test, was replaced by a set of vibrating wire strain gages. This arrangement proved to be advantageous due to its higher sensitivity, and the net increase in accuracy, in displacement measurement, using the new system was about 20 times that of the original one. Due to the small magnitudes of these measurements, the strain gages had to be thermally protected in order to avoid temperature changes that would have induced unacceptable deviations.

The mini flat jack test performed in tunnel lining faces a condition not present in the usual application of rock mechanics: bending moments. In terms of stress distribution, the occurrence of bending moments can be understood as a high stress gradient across the slot executed during the test. A laboratory verification test indicated that the mini flat jack test could be used to evaluate the average stress acting in the slot. However, it was not possible to evaluate the magnitude of the bending moments. An

investigation on the possibility to modify the test procedure in order to include multiple stages, using slots (and associated jacks) with different depths at each stage is suggested for further studies. Variations on the 'average' stresses in each stage, or each depth, will indicate the occurrence of bending moments and the difference of the 'average' stresses can probably be used to obtain the bending moment magnitude.

The interpretation of the test using just the data taken during the cutting stage is another suggestion. Different patterns of the relative displacements during this stage may indicate bending moments and their magnitudes. Difficulties anticipated for this type of application were discussed in Chapter 3.

In cases where bending moments may be a problem, steel reinforcement is likely to be used as part of the lining. Future studies should investigate the effect of the steel reinforcements on the test results. One in situ test indicated problems of temperature development during the cutting of the steel reinforcement, and further investigation on the cooling and cutting techniques is also suggested.

The evaluation of the Young's modulus using results from the flat jack test was not attempted in the present investigation. However, due to the consistency and linearity of the readings observed during the pressurization stage, studies to obtain this parameter are suggested.

The mini flat jack test proved to be an economical, fast and reliable procedure to evaluate the in situ stresses in tunnel linings. The error for in situ tests performed in shotcrete lining older than 2 days was estimated to be of the order of 20%. Tests performed in younger shotcrete will require more studies, and they will probably face problems due to the short term creep deformations.

7.3 Shotcrete Behavior at the Early Ages

The mini flat jack test is a solution *a posteriori* as the loads in the lining are obtained after the construction of the tunnel. On the other hand, a designer needs to

obtain values *a priori*, i.e. estimates of the tunnel behavior prior to the construction. To meet these requirements, it is necessary to know the properties of the shotcrete. As most of the load develops during the early ages, investigations were carried out to obtain the properties of the shotcrete in this period. These investigations were presented in Chapter 4 and they were based on laboratory tests (including tunnel construction control tests), field measurements and data published by other authors.

The term early age or short term was defined pragmatically in order to analyze the construction of a typical 6 m diameter tunnel, advancing 1.8 m per shift. Considering a typical range of construction rate of 1 shift/day to 3 shift/day, the 'short term' would end between 53 and 160 hours.

All tests and analyses presented in Chapter 4 were carried out bearing this time limit in mind. The shotcrete specimens used in laboratory tests were prepared following a procedure developed to reproduce the same unit weight and strength development of the shotcrete placed in construction site.

Investigations on the strength of the shotcrete at the early ages showed that the strength development can be described by an equation originally developed by Byfors(1980) for plain concrete. Adaptations were introduced in the original formulation and the parameters for this 'new' equation (Equation 4.4), which describes the strength of the shotcrete as a function of age are given in Table 4.5.

It was also possible to evaluate the effect of the water-cement ratio (w/c) on the strength development for the range of $0.4 < w/c < 0.6$, but these results are restricted to the specific type and amount of accelerator and cement used in the SLRT project.

The development of Young's modulus was also investigated, and the data from compression tests were interpreted according to ASTM C469-87a. A marked non-linearity was observed at very early ages in compression tests performed in specimens older than 4 hours. In an attempt to measure the Young's modulus for ages of zero to 4 hours, ultrasonic tests were carried out but the accuracy was compromised due to

restrictions on the equipment available. Equation 4.12, also used in plain concrete (Byfors, 1980), was introduced and it relates the conventional Young's modulus to the strength for standard cylindrical specimens. Parameters of this equation for the shotcrete used in the SLRT project were presented in Table 4.11. Applying Equations 4.4 and 4.12, simultaneously, it was possible to describe the development of Young's modulus with age.

Short term creep tests were performed in shotcrete using a dummy specimen for compensation of temperature and shrinkage deformations, and the interpretation of these tests was performed using a three element linear viscoelastic model. Deformation parameters obtained from creep tests carried out on specimens of different ages are presented in Figures 4.30 and 4.31. For application on a typical tunnel construction, the following average values are suggested for the parameters of the viscoelastic model:

$$E = 15 \text{ GPa}$$

$$1/E_t = 0.03 \text{ 1/GPa}$$

$$E_t/\eta = 0.003 \text{ 1/min.}$$

These values are suggested for shotcrete older than 10 hours of age and, for earlier ages, it was suggested that the stiffness of the shotcrete may be neglected in terms of design. One should note that this reference age (10 hours) is affected by the composition of the shotcrete and may vary from tunnel to tunnel. The deformation parameters shown above indicates that the short term creep represents approximately one third of the stress dependent deformations.

The evaluation of stress independent deformations was performed in terms of the components due to thermal expansion and shrinkage. The coefficient of thermal expansion was taken as an average of three test results and was $\alpha_T = 8.25 \times 10^{-6} \text{ (m/m)/}^\circ\text{C}$. The temperature development in the shotcrete with age was estimated by Equation 4.18, modified from Schubert (1988), but it did not present good agreement with the field data.

Shrinkage tests were performed in order to simulate in laboratory the SLRT site environment. Results indicated that the conventional shrinkage estimations based on relative humidity of the air do not provide an accurate prediction. It was suggested that the shrinkage is a function of the soil moisture content in contact with the lining, the specific surface of this contact, air circulation condition, relative humidity of the air flow, among other parameters. It was also observed that points around the circumference of the tunnel lining present different shrinkage patterns.

Stress and strain controlled tests were performed and the adequacy of the viscoelastic model was verified through stress and strain analyses. Under the assumption of linear viscoelasticity, the linearity of the model is implicitly accepted, i.e. superposition of events is valid. The validity of the superposition of stresses was verified in the stress controlled tests, as the loading was applied in stages. The validity of the superposition of deformations was also verified in the strain controlled tests by applying the compensation of the stress independent deformations.

For shotcrete older than 10 hours, an analytical viscoelastic strain analysis compared with results of stress controlled tests presented error of the order of 10 % in the calculated strains values, while the stress analysis in the strain controlled tests, the error was of the order of 15 % in the calculated stresses. The results of the strain and stress analyses for the period after 10 hours of age also demonstrated that the proposed average values suggested for the viscoelastic parameters can be used without compromising the accuracy of the calculations.

The results presented in Chapter 4 were only related to the short term response of the shotcrete. The strain and stress analyses have shown that the parameters estimated for the short term behavior of the shotcrete tended to underestimate the strains (or overestimate the stresses) towards the end of the tests. This suggests that the use of these short term parameters for 'long term' estimation of stress in lining would be acceptable in terms of design.

7.4 Analytical Procedure

Chapter 5 presented a simplified procedure which simulates different rates of tunnel construction. This procedure is analogous to the core stiffness reduction technique used to simulate the face advancing in a plane strain representation.

The analytical approximation manipulates the ground stiffness, instead of the core stiffness. Using a parametric transformation, it was possible to use a plane strain viscoelastic analytical solution derived by Yuen (1979) to 'control' the stiffness of the ground. The adequacy of this approach was checked by comparing it with convergence of 'three dimensional' lined and unlined tunnel construction simulations (FEM) presented by Hanafy and Emery (1980 and 1982). This analytical procedure was termed ADVRATE and can simulate different rates of tunnel construction and different delays of the lining installation. The results are presented in terms of convergence, thrust and bending moments in the lining.

ADVRATE does not take into consideration the gravitational stress gradient expected in shallow tunnel problems. Deviations due to this simplification for a typical tunnel in medium clay with $H/D > 1.5$ were estimated to be a maximum of 15%. If this deviation is considered too large, it is recommended to correct the results obtained from ADVRATE proportionally to the difference from calculations using Einstein and Schwartz's (1979) and Hartmann's (1970) solutions.

ADVRATE was used to evaluate the tunnelling response due to different rates of construction, using the parameters from the investigations on the shotcrete behavior presented in Chapter 4. A parametric analysis was presented for a typical tunnel of 3 m of radius constructed in stiff clay at 10 m of depth, for rates of advancing of $1/3$, $2/3$, $3/3$ and $4/3$ radius/day. The results for this range of advancing rates indicated a variation of about 10% in the final convergences and about 50% in the final values of the lining

thrust. The faster the construction rates, the larger the convergences and the smaller the thrusts.

7.5 Practical Applications

Chapter 6 presented some practical applications for design and interpretation of instrumentation in NATM tunnel linings.

7.5.1 Interpretation of Lining Instrumentation

During the interpretation of the strain measurements taken from the embedded strain gages, it was shown that the readings during the first 10 hours of age of the shotcrete can be neglected because during this period, a small amount of stress is generated. Shrinkage and temperature variations induced considerable deformations in shotcrete linings and compensations for these effects were performed assuming that they did not induce any stress variation. It was shown that this type of compensation was valid for the SLRT tunnels in soft ground but, for stiffer materials, it might be necessary to evaluate the stress changes due to shrinkage and temperature variations.

Using the laboratory results presented in Chapter 4 and the results of parametric analyses presented in Chapter 5, it was possible to define an equivalent Young's modulus for the shotcrete during short term as $E_{eq} = 10 \text{ GPa}$, for the stress level expected in shallow tunnels like that in the SLRT project. This equivalent modulus is independent of the rate of the tunnel construction as the short term creep deformations develop much faster than the convergence for the practical range of construction rates. Note however, that for higher stress levels and/or deeper tunnels, the nonlinear creep might occur (Golser et al., 1989) and as a result, lower values of equivalent Young's modulus may be used (Pottler, 1990). Therefore, the short term value of equivalent Young's modulus $E_{eq} = 10 \text{ GPa}$ is recommended for stress/strength ratios below 0.3 to 0.4 only. For higher ratios, further studies are suggested.

Once the readings of strain gages embedded in shotcrete are compensated for temperature and shrinkage deformations, and using the equivalent Young's modulus of the shotcrete, it is possible to calculate the thrust and bending moments in the shotcrete assuming a typical lining thickness. Using the strain measurements of the steel ribs, which were fully compensated for temperature, and assuming a Young's modulus of 200 GPa for steel, it was possible to calculate the development of thrusts and bending moments in the steel ribs. Using these data and some other published results, it was suggested that for practical purposes, the proportion of the thrust between the steel ribs and the shotcrete can be estimated by the ratio $\left(\frac{EA_{rib}}{EA_{shotcrete}} \right)$.

7.5.2 Design

Chapter 5 presented the effect of construction rate on the ground-lining interaction for a linear elastic model. The extra 10 hour delay for the lining activation was one aspect that affected the interaction. It was used to allow for the invert shotcrete to become stiff enough to carry load.

Chapter 6 presented the calculations carried out to evaluate this 10 hour delay specifically for the SLRT tunnel using the design method by Negro (1988). The results indicated that the extra 10 hour delay induced a 7% increase on the soil displacements and 7% decrease of the loads in the lining. Therefore, this delay is conservative in terms of estimating soil deformation and non-conservative in terms of estimating loads in the lining.

It was suggested that in shallow tunnels, the loads usually do not go beyond 10% of the maximum capacity of the lining, therefore, problems concerned with constraining the soil deformations will usually emerge before any lining capacity is exceeded. For this reason, it is suggested, for design using Negro's (1988) method, that the lining activation should be considered as 10 hours after the invert installation.

7.5.3 Conclusions from SLRT Tunnel Analysis

Using the product of thickness versus the Young's modulus of the shotcrete as an index to evaluate the variation of the load in the lining, it is estimated that loads in SLRT tunnel could range from 50% to 200% of the average values. The wide range for load measurements obtained from the lining instrumentation is viewed as a consequence of the shotcrete stiffness variability. Also, as the measurements were taken at the thinnest section along the longitudinal direction of the tunnel, the measured values should be taken as lower bound approximations. Results of mini flat jack tests performed in lining under similar loading conditions presented thrusts of the same order of magnitude and same range of variation obtained by the lining instrumentation (strain gages) which is an indication that the strain interpretation provides reasonable values.

Besides the difference on the magnitude of the measured values as compared with the calculated ones, a major deviation was detected on the behavior of the crown region. In the design calculations performed using Negro's method, the earlier installation and curing of the crown region in relation to the invert at a given section, was disregarded. In other words, it was considered that the shotcrete around the circumference of the lining was placed at the moment of the invert installation.

The lining instrumentation showed that some thrust developed before the design activation point. Also, the measured bending moments developed in the opposite direction to those calculated. As the measured values of thrusts at the end of the short term interaction were below the calculated ones, and also because they usually do not go beyond 10% of the lining capacity, the deviations of the thrust are not considered a major concern. In the case of $K_0 < 1$, the calculation will indicate bending moments in the opposite direction to the actual one, while in case of $K_0 > 1$, the calculation will probably underestimate the actual values. As the values of bending moments are usually small in shallow tunnel constructed under usual conditions, this deviation is not critical.

In the case of high construction rates, long delays of the invert installation or high values of K_0 , high values of bending moments may be generated. In these cases, the design method used in this thesis will not be suitable. Either a three dimensional finite element code or a special plane strain code, like that presented in Chapter 5 (Ohnishi et al., 1982) using the core stiffness reduction technique, may be necessary to define the magnitude of the problem. In any case, a field monitoring program seems to be essential to optimize the construction procedure.

For practical applications, the employment of embedded strain gages is not recommended due to the complexity and lack of knowledge on the general shotcrete behavior. It is believed that a monitoring program based on the mini flat jack test would provide a better way to evaluate the magnitude of loads in the lining. A lining instrumentation with embedded strain gages seems to be more suitable for academic purposes, where more detailed information on the lining response is required. Recommendations to improve the accuracy on this type of instrumentation were presented in Chapters 2 and 6.

The tests presented in Chapter 4 investigated the short term (loads applied typically before 100 hours of age) behavior of the shotcrete for stresses below 30% of the strength for a fixed type and amount of accelerator and cement, varying the water-cement ratio from 0.4 to 0.6. Further studies of the effect of the shotcrete composition on its mechanical behavior at short term may provide useful technological information for practical applications.

Another aspect of interest is the evaluation of creep for stresses higher than 30% of the strength, possibly following the relationship suggested by Golser et al. (1989). This information seems to be useful for linings in deep tunnels or shallow tunnel with long delay of invert installation. Studies to convert the laboratory results into an equivalent Young's modulus, as presented in this thesis, are also recommended.

Results presented in Chapter 6 and measurements presented by Golser et al. (1989) indicated that in shallow tunnels, the load in the lining did not exceed 10% of its capacity. As this result was obtained for the short term response, further studies are recommended for the long term behavior. The final lining design may result considerably economical if low level of loading is confirmed for the long term behavior. Further studies are suggested for this subject by systematic measurements using the mini-flat jack tests in final linings of existing tunnels.

BIBLIOGRAPHY

- Abdunur, C., 1985. Mesure de contraintes sur ouvrages d'art par une methode de liberation miniaturisee. Bull. Haison Labo P. et Ch., Vol. 138, Jul.-Aug., Ref. 3010, pp. 5-14.
- ABNT, 1980. Projeto e execucao de obras de concreto armado. NBR-6118, Associacao Brasileira de Normas Tecnicas.
- ABNT, 1986. Argamassa e concreto projetado: especificacao. Draft of Brazilian standard for shotcrete specification, Texto Base 18.3.7, (from Kuperman, 1986).
- ACI, 1966. Shotcreting. Publication SP-14, American Concrete Institute, Detroit, 224 p.
- ACI Committee 506, 1966. ACI Standard, Recommended Practice for Shotcreting (ACI 506-66). ACI SP-14, pp. 196-217.
- ACI, 1971. ACI Standard building code requirement for reinforced concrete. ACI 318-63, Jun, 143 p.
- ACI, 1973. Use of shotcrete for underground structural support. Publication SP-45, ASCE and ACI, 467 p.
- ACI, 1976. Shotcrete for ground support. Publication SP-54, ASCE and ACI, 765 p.
- ACI Committee 506, 1977. Specification of materials, proportioning and application of shotcrete. American Concrete Institute.
- ACI Committee 506, 1978. Recommended practice for shotcreting. American Concrete Institute.
- ACI Committee 209, 1982. Prediction of creep, shrinkage and temperature effects in concrete structures. Design for Creep and Shrinkage in Concrete Structures, ACI, SP-76, pp. 193-300.
- AFTES, 1975. Beton projete. AFTES, texte provisoire.
- Aguiar, A.D., Kuwajima, F.K. and Preussler, E.S., 1985. Ensaio triaxiais dinamicos com registro a traves de microcomputador. Segundo Encontro Regional de Matematica Aplicada e Computacional da SBMAC, May, Sao Jose dos Campos.
- Alexander, L.G., 1960. Field and Laboratory Tests in Rock Mechanics. Proceedings, The Third Australia-New Zealand Conference on Soil Mechanics and Foundation Engineering, University of Sidney.

- Andriolo, F.R., 1984. Construcões de Concreto. Editora PINI, Sao Paulo.
- Anson, N., 1966. The effect of mix proportions and method of testing on Poisson's ratio for mortar and concretes. Magazine of Concrete Research Institute, Vol. 18, No. 56, pp. 115-130.
- ASTM, 1982. Method of obtaining and testing drilled cores and sawed beams of concrete. Standard Method, ASTM, C 42-82.
- ASTM, 1983. Laboratory determination of pulse velocities and ultrasonic elastic constants of rock. Standard Method, ASTM, D2845-83.
- ASTM, 1986. Standard test method for compressive strength of cylindrical concrete specimens. C 39-86.
- ASTM, 1987. Practice for capping cylindrical concrete specimens. Standard method, C617-87.
- ASTM, 1987. Standard test method for static modulus of elasticity and poisson's ratio of concrete in compression. C 469-87a.
- Atkinson, J.H., Brown, E.T. and Potts, D.M., 1975. Collapse of shallow unlined circular tunnels in dense sand. Tunnels and Tunnelling, May, pp. 81-87.
- Aydan, O., Kyoya, T., Ichikawa, Y. and Kawamoto, T., 1988. Three-dimensional simulation of an advancing tunnel supported with forepoles, shotcrete, steel ribs and rockbolts. Proceedings, Sixth International Conference on Numerical Methods in Geomechanics, Innsbruck, Apr., Edited by G. Swoboda, pp. 1481-1486.
- Babendererde, S., 1986. Extruded concrete lining. Proceedings, International Congress on Large Underground Openings, ITA, Firenze, Vol.I, pp. 607-611.
- Babendererde, S. and Wirtz, C., 1986. NBS tunnel construction in low mountain regions of Germany. Proceedings, International Congress on Large Underground Openings, Firenze, Vol. 1, pp. 29-38.
- Baumann, T., 1985. Messung der Beanspruchung von Tunnelschalen. Bauingenieur, No.60, pp.449-454.
- Bazant, Z.P. & Panula, L., 1978-1979. Practical prediction of time-dependent deformations of concrete, Material and Structures (RILEM, Paris), Part I, II, III and IV, I: 'Shrinkage', 11,65,307-316; II: 'Basic, Creep', 11,65,317-328; III: 'Drying creep', 11,66,415-424; IV: 'Temperature effect on basic creep', 11,65,424-434; V: 'Temperature effect on drying creep', 12,69,169-183.

- Benecz, I., Bodonyi, J., Nagy, B. and Szepesi, I., 1977. Measurements of loads acting on concrete linings. Proceedings, International Symposium on Field Measurements in Rock Mechanics, Zurich, April.
- Bonvallet, J. and Dejean, M., 1977. Flat jack test and determination of mechanical characteristics. Proceedings, International Symposium on Field Measurements in Rock Mechanics, Zurich, Apr., pp.361-374.
- Borsetto, M., Giuseppetti, G. and Manfredini, G., 1983. Recent advances in the interpretation of the flat jack test. Proceedings, International Congress on Rock Mechanics, Melbourne, Vol.1, pp.143-151.
- Bortz, S.A., Aleshin, E., Wade, T.B. and Chugh, Y.P., 1973. Evaluation of present shotcrete technology for improved coal mine ground control. IIT Research Institute, Bu. Mines Report OFR-54-73, 219 p.
- Brameshuber, W. and Kottas, R., 1987. Ein Verfahren zur Bestimmung der Fruhfestigkeitsentwicklung von Spritzbeton. Beton und Stahlbetonbau, No.10, pp.270-273.
- Branco, P., 1981. Behavior of a shallow tunnel in Till. M.Sc. Thesis, University of Alberta, Edmonton, 351 p.
- Brandt, J.R.T., 1985. Behaviour of soil concrete interfaces. Ph.D. Thesis, University of Alberta, Apr., 376 p.
- Brandt, J.R.T., 1987. Personal Communication.
- Brierley, G. S., 1975. The performance during construction of the liner for a large, shallow underground opening in rock. Ph.D. Thesis, University of Illinois at Urbana-Champaign, 318 p.
- Brierley, G.S. and Cording, E.J., 1976. The behaviour during construction of the Dupont circle subway station lining. ACI, Publication SP-54 : Shotcrete for Ground Support, Easton, Maryland, Oct., pp.675-712.
- Brown, E.T., 1981. Putting the NATM into perspective. Tunnels & Tunnelling, Nov., pp. 13-17.
- Brux, G., 1983. Shotcrete. Tunnel, No.1, pp.24-32.
- Byfors, J., 1980. Plain concrete at early ages. Research Report, Swedish Cement and Concrete Research Institute, ISSN 0346-6906, Department of Building, Royal Institute of Technology, Stockholm, 464 p.

- Caceci, M.S. and Cacheris, W.P., 1984. Fitting curves to data : the simplex algorithm is the answer. *Byte*, Vol.9, No.5, pp.339-360.
- Castelo Branco, J.E., 1985. Alguns topicos para pesquisa tecnologica com concreto projetado. *Proceedings, Segundo Simposio sobre Escavacoes Subterraneas, ABGE, Rio de Janeiro, Nov., Vol.1, pp.686-712.*
- CEB-FIP, 1978. Model Code for concrete structures. *Comite Euro-international du Beton, Paris.*
- Cipriani, J.C., 1985. Concreto projetado - usos e tecnologia no Brasil. *Proceedings, Segundo Simposio sobre Escavacoes Subterraneas, ABGE, Rio de Janeiro, Nov., Vol.1, pp.642-671.*
- Concrete Society, 1979. Specification for Sprayed Concrete. *The Concrete Society, Grosvenor Gardens, London.*
- Cording, E.J. and Deere, D.U., 1972. Rock tunnel supports and Field Measurements. *Proceedings, North American Rapid Excavation and Tunneling Conference, American Institute of Mining, Metallurgical and Petroleum Engineers.*
- Cording, E.J., Hendron, A.J., Hansmire, W.H., Mahar, J.W., MacPherson, H.H., Jones, R.A. and O'Rourke, T.D., 1975. Methods for Geotechnical Observations and Instrumentation in Tunnelling. *Rep. No. U1LU-E 75 2022, Department of Civil Engineering, University of Illinois, Urbana.*
- Costalonga, M.A.R., 1988. Geogrid pull-out test in clay. *M.Sc. Thesis, University of Alberta, 211 p.*
- Cruz, H.J.V., Couto, J.V.S., Hori, K., Salvoni, J.L. and Ferrari, O.A., 1982. Os tuneis do prolongamento norte - uma primeira avaliacao do NATM em area urbana. *Proceedings, Simposio sobre escavacoes subterraneas, Bras. Ass. of Engng. Geol., Rio de Janeiro, Nov.*
- Curtis, D.J., 1976. Discussion of paper 'The circular tunnel in elastic ground' by Wood, 1975. *Geotechnique*, Vol 26, No. 1, pp. 231-237.
- D'Escatha, Y. and Mandel, J., 1974. Stabilité d'une galerie peu profonde en terrain meuble. *Revue de L'Industrie Minérale*, Apr, pp. 45-53.
- Deere, D.U., Peck, R.B., Monsees, J.E. and Schmidt, B., 1969. Design of tunnel liners and support systems. *Final Report, Department of Civil Engineering, University of Illinois at Urbana, 288 p.*
- DIN, 1979. Spritzbeton. *Deutsche Norm, DIN 18551/79.*

- DIN, 1988. Spannbeton. DIN 4227, Bauteile aus Normalbeton mit beschränkter oder voller Vorspannung.
- Duddeck, H. and Erdmann, J., 1985. On structural design models for tunnels in soft soil. *Underground Space*, Vol.9, pp. 246-259.
- Duncan, J.M. and Chang, C.V., 1970. Nonlinear analysis of stress and strain in soils. *Journal of the Soil Mechanics and Foundations Division, American Society of Civil Engineers*, Vol. 96, pp. 1629-1653.
- Dunnicliff, J. and Green, G.E., 1988. *Geotechnical instrumentation for monitoring field performance*. John Wiley & Sons, 577 p.
- Einstein, H.H and Schwartz, C.W., 1979. Simplified analysis for tunnel supports. *Journal of the Geotechnical Engineering Division, American Society of Civil Engineers*, Vol. 106, pp. 499-518 (Discussion with corrections in July, 1980, pp. 853-838).
- Eisenstein, Z., Heinz, H. and Negro, A.Jr., 1984. On three-dimensional ground response to tunneling. *Proceedings, GEOTECH III '84, American Society of Civil Engineers* (edited by K.Y. Lo), Atlanta, Georgia, May, pp.107-127.
- Eisenstein, Z. and Sorensen, K.L., 1986. Tunneling for the south LRT extension in Edmonton, Alberta. *Proceedings, 6th Annual Canadian Tunnelling Conference*, Niagara Falls, Ontario, Oct.
- Eisenstein, Z. and Negro, A., 1990. Integrated design method for shallow tunnels in soft ground. *Proceedings, JTA Tunnel Symposium, Development of Utilization of Subsurface Space in Urban Area*, Tokyo, Mar.
- Eisenstein, Z. and Kuwajima, F.M., 1990. Stress measurements by flat jack method in the shotcrete lining of the SLRT south tunnel. *Report for The City of Edmonton and EBA engineering consultants Ltd.*, Aug., 18 p.
- El-Nahhas, F., 1977. Field measurements in two tunnels in the City of Edmonton. M.Sc. Thesis, Department of Civil Engineering, University of Alberta, Edmonton, Alberta, 85 p.
- England, G.L. and Illston, J.M., 1965. Methods of computing stress in concrete from a history of measured strain. *Civil Engineering and Public Works Review*, 60, Parts 1, 2 and 3, Apr., May and June, pp. 513-517, 692-694, 846- 847.
- Erdmann, J., 1983. Vergleich ebener und Entwicklung raumlicher Berechnungsverfahren für Tunnel. Bericht Nr. 83-40, Institut für Statik der Technischen Universität Braunschweig, 220 p.

- Fernandez-Delgado, G., Mahar, J. and Cording, E.J., 1974. Shotcrete, structural testing of thin lining. Report for Department of Transportation, Federal Railroad Administration, Washington, D.C., 219 p.
- Flugge, W., 1967. Viscoelasticity. Blaisdell Publishing, 127 p.
- Freudenthal, A.M. and Roll, F., 1958. Creep and creep recovery of concrete under high compressive stress. ACI Journal, Proc. 54, pp. 1111-1142.
- Gais, W.H., Harpf, R. and Herg, M., 1986. Hohlraumsicherung beim Nurnberger U-Bahnbau-Messergebnisse zum Tragverhalten. Forschung+Praxis 29, Alba Buchverlag, Dusseldorf, pp. 196-201.
- Gartung, E., Bauernfeind, P. and Bianchini, J.C., 1979. Three-dimensional finite element method study of a subway tunnel in Nurnberg. Proceedings, Rapid Excavation and Tunnelling Conference, Atlanta, Vol. 1, pp. 773-789.
- Gioda, G., 1985. Some remarks on back analysis and characterization problems in geomechanics. Proceedings, Fifth International Conference on Numerical Methods in Geomechanics, Nagoya, Apr., pp.47-61.
- Golser, J., 1979. Another view of the NATM. Tunnels & Tunnelling, Mar., pp. 41.
- Golser, J., Schubert, P. and Rabensteiner, K., 1989. A new concept for evaluation of loading in shotcrete linings. Proceedings, International Congress on Progress and Innovation in Tunnelling, Edited by K.Y. Lo, Toronto, Sept., pp. 79-85.
- Gunzler, J., 1970. Mechnische Eigenschaften von jungem Beton im Gleitbau. Bauplanung Bautechnik, Vol. 24, No. 8, pp. 372-375.
- Hanafy, E.A. and Emery, J.J., 1980. Advancing face simulation of tunnel excavations and lining placement. Proceedings, 13th Canadian Rock Mechanics Symposium, Toronto, May, CIM special volume 22, pp. 119-125.
- Hanafy, E.A. and Emery, J.J., 1982. Three-dimensional simulation of tunnel excavation in squeezing ground. Proceedings, The Fourth International Conference on Numerical Methods in Geomechanics, (edited by Z. Eisenstein), Edmonton, Canada, May, Vol. 3, pp. 1203-1209.
- Hanna, T.H., 1985. Field Instrumentation in Geotechnical Engineering. Trans Tech Publications, First Edition, 843 p.
- Hansen, P.G., 1956. Physical properties of concrete at early ages. School of Mines and Metallurgy of the University of Missouri, 140 p.

- Hardy Associates Ltd., 1986. Final Geotechnical Engineering Report South LRT Extension Corona Station to the North Bank of the North Saskatchewan River. Report to City of Edmonton, Aug.
- Hartmann, F., 1970. Elastizitätstheorie des ausgekleideten Tunnelhohlraumes und des eingebohrten kreisförmigen Rohres. *Strasse Brücke Tunnel* 22 (1970), Heft 8, 209-215, Heft 9, 241-246, und Jg. 24 (1972), Heft 1, 13-20, Heft 2, 39-45.
- Hartog, J. P., 1959. *Advanced Strength of Materials*. McGraw-Hill, New York, 505 p.
- Hatakeyama, O., Takeuchi, T. and Matsugaki, K., 1987. New shotcreting for ground support of TBM tunneling. *Proceedings, Sixth Australian Tunnelling Conference, AUCTA, Melbourne, Mar.*, pp. 153-159.
- Haugland, Hofsoy, Garborg, Fjeldstad, 1976. Tidligfastheter for betong. Sammandrag, Faltforsok, Laboratorieforsok, FCB, Trondheim, Rapport 76-1,2,3,4,5, quoted by Byfors, 1980.
- Heilbrunner, J., 1980. Bauablauf, Versuche und Messprogramm beim Bau des U-Bahn-Loses 8/1-5.1 in bergmannischer Bauweise. *U-Bahn für München, U-Bahn Linie 8.1*, pp. 209-261.
- Heilbrunner, J. and Gais, W.H., 1981. Neue Messergebnisse zum Tragverhalten von Verbaubogen und Spritzbeton bei der Hohlraumsicherung im U-Bahnbau. *Unterirdisches Bauen - Gegenwart und Zukunft, STUVA-TAGUNG '81, Berlin*, pp. 129-136.
- Heinz, H.K., 1984. Applications of the New Austrian Tunnelling Method in Urban Areas. M.Sc. Thesis, University of Alberta, Edmonton, 323 p.
- Heinz, H.K., 1988. Large cross section tunnels in soft ground. Ph.D. Thesis, Department of Civil Engineering, University of Alberta, 348 p.
- Heinz, H.K., 1989. Personal Communication.
- Heinz, H. and Rocha, R., 1990. Tensoes no Concreto Projetado em Tuneis. *Proceedings, SINGEO'90, Simposio sobre Instrumentacao Geotecnica de Campo, ABMS/ABGE, Rio de Janeiro, Abril*, pp. 221-230.
- Hochmuth, W., Krischke, A. and Weber, J., 1985. The construction methods used for the Munich underground: A review of developments over 20 years. *Tunnel*, No.4, pp. 206-218.
- Hoek, E. and Brown, E.T., 1980. *Underground excavations in rock*. The Institution of Mining and Metallurgy, London, 525 p.

- Hornby, I.W. and Noltingk B.E., 1973. The application of the vibrating-wire principle for the measurement of strain in concrete. Proceedings, 3rd SESA International Congress on Experimental Mechanics, Los Angeles, May, pp.167-172.
- Horrigmoe, G., 1985. Effect of pore water and its diffusion in concrete. Mechanics of Geomaterials, John Wiley & Sons, pp. 349-377.
- Huang, A.B., Chameau, J.L. and Holtz, R.D., 1986. Interpretation of pressuremeter data in cohesive soils by simplex algorithm. Geotechnique, Vol.36, No.4, pp.599-603.
- Hudson, R.G., 1974. Engineering Manual. Portuguese version.
- Hvorslev, J.M., 1948. Subsurface exploration and sampling of soil for civil engineering purposes. Waterways Experiment Station, Vicksburg, Miss., Nov.
- Ito, T. and Hisatake, M., 1981. Analytical Study of NATM. Proceedings, Tenth International Conference on Soil Mechanics and Foundation Engineering, Stockholm, Jun., Vol. 1, pp. 331-314.
- Jaeger, J.C., 1969. Elasticity, fracture and flow. 3rd. Ed.,Chapmann and Hall, London, 268 p.
- Jaeger, J.C. and Cook, N.G.W., 1979. Fundamentals of rock mechanics. 3rd. Ed., Chapman and Hall, London.
- Jones, M., 1985. Why add to shotcrete ?. Tunnels & Tunnelling, Jul., pp.53-58.
- Jones, R.A., 1976. A field investigation of the performance of shotcrete in underground construction. Ph.D. Thesis, University of Illinois at Urbana-Champaign, 354 p.
- Katzenbach, R., 1981. Entwicklungstendenzen beim Bau und der Berechnung oberflächennaher Tunnel in bebautem Stadtgebiet. Mitteilungen der Versuchsanstalt für Bodenmechanik und Grundbau der Technischen Hochschule, Darmstadt, Heft 24.
- Kirsh, G., 1898. Die Theorie der Elastizität und die Bedürfnisse der Festigkeitslehre. Ver. Deut. Ing., Vol.42, pp.797 (quoted in Hartog, 1958).
- Kobler, H.G., 1966. Dry-mix coarse-aggregate shotcrete as underground support. Shotcreting, Publication SP-14, ASCE/ACI, pp. 33-58.
- Krischke, A., 1987. Shotcreting methods with compressed air in Munich subway construction. Proceedings, Sixth Australian Tunnelling Conference, AUCTA, Melbourne, Mar., pp. 161-170.

- Kubetsky, V.L., 1970. Investigation of stresses in pressure tunnel linings with regard to creep of concrete and surrounding rock mass. *Proceedings, Second Congress of the International Society of Rock Mechanics, Beograd, Sept., Vol. 2, pp. 447-452.*
- Kuperman, S.C., 1986. Personal Communications.
- Kuwajima, F.M., 1985. Suction of a residual soil using low cost tensiometers. *Proceedings, First International Conference of Geomachanics in Tropical Lateritic and Saprolitic Soils, Brasilia, Vol. 1, 319-330.*
- Kuwajima, F.M., Eisenstein, Z., Gerber, G.E. and Harris, M.C., 1988. Tunnel instrumentation analysis using a microcomputer. *Proceedings, Seventh Annual Canadian Tunnelling Conference, Tunnelling for transportation and resource development, May, pp. 187-195.*
- Lambe, T.W., 1973. Predictions in soil engineering. 13th Rankine Lecture, *Geotechnique, Vol. 23, pp. 149-202.*
- Lew, Reichard, Clifton, 1976. Mechanical properties of concrete at early ages. National Bureau of Standards, Center for Building Technology, Institute for applied Technology, Washington D.C., 19 p., quoted by Byfors, 1980.
- Littlejohn, G.S., 1988. Sprayed concrete for underground support. *Proceedings, The Third International Conference on Underground Space and Earth Sheltered Buildings, Shaghai, China, Sept., pp. 234-240.*
- Litvin, A. and Shideler, J.J., 1966. Laboratory study of shotcrete. ACI SP-14, *Shotcreting, pp. 165-184.*
- Lo, K.Y. and Yuen, C.M.K., 1981. Design of tunnel lining in rock for long term time effects. *Canadian Geotechnical Journal, Vol. 18, pp. 24-39.*
- Loh, Y.C., 1951. Internal Stress Gauges for Cementitious Materials. Massachusetts Institute of Technology Report, Office of Naval Research, NR 064-331, July.
- Loh, Y.C., 1952. Internal stress gauges for cementitious materials. *Proceedings, Spring Meeting of the Society for Experimental Stress Analysis, Indianapolis, May, Vol. 9, No. 2, pp.13-28.*
- Mahar, J.W., Parker, H.W. and Wuellner, W.W., 1975. Shotcrete practice in underground construction. Report No. FRA-OR&D 75-90, Department of Civil Engineering, University of Illinois at Urbana-Champaign.
- Maier, L.B., Rossi, P.P and Landriani, G.S., 1983. Diagnostic analysis of masonry buildings. *Proceedings, IASBE Symposium, Venice, Sep., ISMES-189.*

- Manson, E.E. and Manson, R., 1982. Shotcrete. in Tunnel Engineering Handbook, Van Nostrand Reinhold Company, pp. 335-353.
- Marquardt, D.W., 1963. An algorithm for least-squares estimation of non-linear parameters. *Journal of the Society of Industrial and Applied Mathematics*, 11, 431.
- Martins, S.C. and Sousa, L.R., 1987. Recent advances in the interpretation of the small flat jack method. *Proceedings, International Congress on Rock Mechanics*, Montreal, pp.1241-1244.
- McIntyre Porcupine, 1957. Guniting at the McIntyre Porcupine Mines, Limited. *Proceedings, Sixth Commonwealth Mining and Metallurgical Congress*, pp. 349-355.
- McIntyre, M.B., 1987. Design strength for existing concrete structures. MEng. Report, Dept. Civil Engineering, University of Alberta.
- McQuiston, F.C. and Parker, J.D., 1988. Heating, ventilating, and air conditioning - Analysis and design. Third edition, John Wiley and sons.
- Morgan, D.R., McAskill, N., Richardson, B.W. and Zellers, R.C., 1989. A Comparative Evaluation of Plain, Polypropylene Fibre, Steel Fibre and Wire Mesh Reinforced Shotcrete. *Proceedings, Transportation Research Board Annual Meeting*, Washington, D.C., Copy from the authors.
- Muir Wood, A.M., 1975. The circular tunnel in elastic ground. *Geotechnique*, Vol. 25, No. 1, pp. 115-127.
- Muller, L., 1978. Removing misconceptions on the New Austrian Tunnelling Method. *Tunnel & Tunnelling*, Oct., pp.29-32.
- Negro, A. and Eisenstein, Z., 1981. Ground control techniques compared in three Brazilian water tunnels. Parts 1, 2 and 3, *Tunnels and Tunnelling*, Oct., Nov., Dec., pp. 11-14, 52-54, 48-50.
- Negro, A., 1987. Personal Communications.
- Negro, A.Jr., 1988. Design of shallow tunnels in soft ground. Ph.D. Thesis, Department of Civil Engineering, University of Alberta, Edmonton, 1480 p.
- Negro, A.Jr., 1989. Personal Communications.
- Neville, A.M., 1981. Properties of concrete. 3rd. Ed., Pitman, 779 p.

- Neville, A.M., 1970. Creep of concrete: plain, reinforced and prestressed. North-Holland Publishing, 622 p.
- Nguyen, V.U., 1985. Determination of critical slope failure surfaces. ASCE - GT2, Vol.111, pp.238-250.
- Ohnishi, Y., Nishigaki, Y., Kishimoto, H. and Tanaka, Y., 1982. Analysis of advancing tunnel by 2-dimensional F.E.M.. Proceedings, The Fourth International Conference on Numerical Methods in Geomechanics, (edited by Z. Eisenstein), Edmonton, Canada, May, pp. 571-578.
- Okada, H., Yamamoto, S. and Kita, K., 1989. Development of new type extruded concrete lining system. Proceedings, International Congress on Progress and Innovation in Tunnelling, Toronto, Sep., Vol. I, pp. 545-552.
- Onuma, N.T., Menezes, O.F., Scanduzzi, L., Castelo Branco, J.E.S. and Celestino, T.B., 1985. Propriedades do concreto projetado para aplicacao como revestimento definitivo de escavacoes subterraneas. Proceedings, Segundo Simposio sobre Escavacoes Subterraneas, ABGE, Rio de Janeiro, Nov., Vol.1, pp.592-603.
- Parker, H.W., 1975. Field-oriented investigation of conventional and experimental shotcrete for tunnels. Ph.D. Thesis, University of Illinois at Urbana-Champaign, 630 p.
- Parker, H.W., Fernandez-Delgado, G. and Lorig, L.J., 1976. A practical new approach to shotcrete rebound losses. ACI SP-54, Shotcrete for ground support, Maryland, pp. 149-187.
- Paul, S.L., Hendron, A.J., Cording, E.J., Sgouros, G.E. and Saha, P.K., 1983. Design recommendations for concrete tunnel lining. Volume II: Summary of research and proposed recommendations., Report UMTA-MA-06-0100 83-3, 174 p.
- Pauw, A., 1960. Static modulus of elasticity of concrete as affected by density. Title No. 57-32, Journal of the American Concrete Institute, Vol. 57, pp. 679-687.
- Peck, R.B., 1969. Advantages and limitation of the observational method in applied soil mechanics. Geotechnique, Vol.19, No.2, pp.171-187.
- Pottler, R., 1985. Ideeller Elastizitätsmodul zur Abschätzung der Spreibetonbeanspruchung bei Felshöhlraumbauten. Felsbau, No.3, pp.127-130.
- Pottler, R., 1990. Konsequenzen für die Tunnelstatik aufgrund des nichtlinearen Materialverhaltens von jungem Spritzbeton. Felsbau 8, Nr. 3, pp. 121-128.
- Putzmeister, 1985. Big shotcreters. Lining & Support, Tunnel and Tunnelling, Vol. 17, No. 8, pp. 37.

- Radaelli, L., 1983. Concreto Projetado. Associacao Brasileira de Geologia de Engenharia.
- Ranken, R. E., 1978. Analysis of ground-liner interaction for tunnels. Ph.D. Thesis, University of Illinois, Urbana-Champaign, 427 p.
- Rocha, M., 1968. New techniques for the determination of the deformability and state of stress in rock masses. Proceedings, International Symposium on Rock Mechanics, Madrid, Oct., pp.289-302.
- Rocha, M., Lopes, J.J.B. and da Silva, J.N., 1966. A new technique for applying the method of the flat jack in the determination of stresses inside rock masses. Proceedings, First Congress of the International Society of Rock Mechanics, Lisbon, Sept., Vol.2, pp.57-65.
- Rokahr, R.B. and Lux, K.H., 1987. Einfluss des rheologischen Verhaltens des Spritzbetons auf den Ausbauwiderstand. Felsbau 5, Nr. 1, pp. 11-18.
- Rossi, P.P, Peano,A. and Carabelli, E., 1982. Determinazione sperimentale delle caratteristiche meccaniche delle murature. Proceedings, AA.VV., Comportamento statico e sismico delle murature, Milano, ISMES-173.
- Rush, H., Jungwirth, D. and Hilsdorf, H., 1973. Kritische Sichtung der Verfahren zur Berücksichtigung der Einflüsse von Krieschen und Schwinden des Betons auf das Verhalten der Tragwerke. Parts 1, 2 and 3, Beton-und Stahlbetonbau, 68, pp. 49-60, 76-86 and 152-158.
- Saenz, L.P., 1964. Equation for the stress-strain curve of concrete. Written discussion, ACI Journal, Vol.61, No.9, pp.1227-1239.
- Sauer, G. and Sharma, B., 1977. A system for stress measurement in constructions in rock. Proceedings, International Symposium on Field Measurements in Rock Mechanics (edited by K. Kovari), Zurich, Vol. 1, pp. 317-329.
- Schmidt, B., 1984. Tunnel lining design - do the theories work ?. Proceedings, 4th Australia-New Zealand Conference on Geomechanics, Perth, May.
- Schneider, K.H. and Reeh, H., 1984. Zum statischen System bergmannisch vorgetriebener Tunnel. Beton-und Stahlbetonbau, No.7, pp. 179-183, No.8, pp. 214-217.
- Schubert, P., 1988. Beitrag zum rheologischen Verhalten von Spritzbeton. Felsbau 6, Nr. 3, pp. 150-153.

- Schwarzl, F.R., 1969. The numerical calculation of storage and loss compliance from creep data for linear viscoelastic materials. *Rheol. Acta*, Vol. 8, pp. 6-17.
- Seabrook, P.T., 1976. Properties of shotcrete on construction projects. ACI SP-54, Shotcrete for ground support, Maryland, pp. 29-44.
- Sellevold, E.J., 1970. Low frequency internal friction and short-time creep of hardened cement paste: and experimental correlation. *Proceedings, Conference on Hydraulic Cement Pastes: their Structure and Properties*, Sheffield, pp. 330-334.
- Sellevold, E.J. and Richards, C.W., 1972. Short-time creep transition for hardened cement paste. *J. Am. Ceram. Soc.*, Vol. 55, pp. 284-289.
- Selmer-Olsen, R., 1976. Examples of the behaviour of shotcrete linings underground. ACI, Publication SP-54: Shotcrete for Ground Support, Easton, Maryland, Oct., pp.722-733.
- Shepherd, R. and Wilson, A.H., 1960. The measurement of strain in concrete shaft and roadway linings. *Transactions, Institute of Mining Engineers*, Vol.119, pp.561-577.
- Silva, M.R. and Kuperman, S.C., 1985. Utilizacao de aditivos aceleradores de pega e cinza volante em concreto projetado. *Proceedings, Segundo Simposio sobre Escavacoes Subterraneas, ABGE, Rio de Janeiro, Nov., Vol.1, pp.578-591.*
- Simondi, S., Negro, A.Jr. and Kuperman, S.C., 1982. Utilizacao de concreto projetado como revestimento definitivo de tunel escavado em solo. *Instituto Brasileiro do Concreto, Coloquio sobre concreto em fundacoes e obras subterraneas*, 49 p.
- Taylor, S.A., 1972. *Physical edaphology*. W.H. Freeman and Company, San Francisco.
- Teodoru, G.V., 1986. Mechanical strength property of concrete at early age as reflected by Schmidt rebound number, ultrasonic pulse velocity and ultrasonic attenuation, ACI SP-95, *Concrete at early ages*, pp. 139-148.
- Terzaghi, K. and Peck, R.B., 1967. *Soil Mechanics in Engineering Practice*. Second Edition, John Wiley & Sons, 729 p.
- Thurber Consultants Ltda., 1980. South LRT Extension Geotechnical Report No. 5 Insitu Pressuremeter Tests 104th and 107th Street Stations. Report to Edmonton Transit, Jul.
- U.S. Army, 1974. *Investigation of Shotcrete*. U.S. Army Engineers Waterways Experiment Station.

- U.S. Army, 1976. State of the art review of shotcrete. U.S. Army Engineers Waterways Experiment Station.
- U.S. Corps of Engineers, 1982. Standard practice for shotcrete. U.S. Corps of Engineers.
- Vollstedt, H.W. and Duddeck, H., 1977. Time dependency and some other non-linearities in theoretical models for tunnels. Proceedings, Conference on Computer Methods in Tunnel Design, London, pp. 1-17.
- Voort, H.B., 1976. Tunnel instrumentation. ACI, Publication SP-54 : Shotcrete for Ground Support, Easton, Maryland, Oct., pp.713-721.
- Ward, W.H., 1978. Ground supports for tunnels in weak rock. Rankine Lecture, Geotechnique, Vol. 28, pp. 133-171.
- Ward, W.H. and Hills, D.L., 1976. Sprayed concrete : tunnel support requirements and the dry mix process. ACI, Publication SP-54 : Shotcrete for Ground Support, Easton, Maryland, Oct., pp.475-532.
- Weigler, H. and Karl, S., 1981. Creep of concrete under early age loading - influence of the rate of hardening of the cement. Betonwerk+Fertigteile-Technik, Sep., pp. 519-522.
- Wierig, H.J., 1971. Einige Beziehungen zwischen den Eigenschaften von grünen und jungen Betonen und denen des Festbetons. Parts 1 and 2, Beton, 11: pp. 445-448, 12: pp. 487-490.
- Wind, H. and Kern, E., 1987. Erprobung von Spritzbetontechniken und ihr Einfluss auf den Baufortschritt bei zwei Tunneln der DB-Neubaustrecke Hannover-Wurzburg. Forschung+Praxis 30, Alba Buchverlag, Düsseldorf, pp. 52-58.
- Wittebolle, R.J., 1983. The influence of microfabric on the engineering properties of glacial tills. M.Sc. Thesis, Department of Civil Engineering, University of Alberta, Edmonton, Alberta, 151 p.
- Wittmann, F.H., 1976. On the action of capillary pressure of fresh concrete. Cement and concrete research Vol. 6, No. 1, pp. 49-56.
- Wittmann, F.H., 1985. Deformation of concrete at variable moisture content. Mechanics of Geomaterials, John Wiley & Sons, pp. 425-459.
- Yuen, C.M., 1979. Rock-structure time interaction in lined circular tunnels in high horizontal stress field. Ph.D. Thesis, Faculty of Engineering Science, University of Western Ontario, London, 720 p.

APPENDIX A - Data from Soil Instrumentation of the SLRT Project

Table A.1 Location for Settlement Points

Instrument	Chainage (1) (400+...m)	Offset (2) (m)	Elevation (3) (m)	Transverse Section
C1-S1	206.770	3.710	664.386	C1
C1-S2	207.220	-0.180	664.453	C1
C1-S3	203.600	1.330	664.307	C1
C1-S4	207.990	-2.960	664.448	C1
C1-S5	215.400	-12.300	664.584	C1
C1-S6	199.500	-7.500	664.125	C1
C1-S7	197.600	-6.200	664.122	C1
C2-S1	182.162	12.016	664.079	C2-1
C2-S2	182.253	9.529	664.168	C2-1
C2-S3	182.162	7.006	664.045	C2-1
C2-S4	182.253	3.038	664.018	C2-1
C2-S5	182.291	0.000	663.920	C2-1
C2-S6	182.306	-11.505	664.110	C2-1
C2-S7	177.214	6.231	664.192	C2-2
C2-S8	177.085	2.935	663.983	C2-2
C2-S9	177.289	0.023	663.917	C2-2
C2-S10	177.247	-1.421	663.758	C2-2
C2-S11	177.247	-5.115	663.892	C2-2
C2-S12	177.220	-7.524	663.946	C2-2
C2-S13	177.225	-18.145	663.870	C2-2
C2-S14	174.000	2.884	664.153	C2-3
C2-S15	174.308	0.032	664.024	C2-3
C2-S16	173.975	-2.946	663.750	C2-3
C2-S17	171.473	0.209	664.156	C2-4
C2-S18	171.296	-2.662	664.036	C2-4
C2-S19	171.152	-5.738	663.814	C2-4
C2-S20	170.577	-9.060	663.739	C2-4
C2-S21	170.581	-12.091	663.792	C2-4
C2-S22	170.462	-15.102	663.706	C2-4
C1-DSP1	205.000	0.360	664.272	C1
C2-DSP6	172.803	0.145	664.178	C2-1
C2-DSP7	170.900	-0.300	664.152	C2-1
C2-DSP8	174.800	-0.700	663.978	C2-1
C2-B1	173.601	-23.336	664.272	C2

1. as shown at the alignment of Northbound tunnel in Fig. 2.2
2. <+> : leftside ; <-> : rightside (facing towards increase of chainage)
3. elevation of the top of the rod
4. S : shallow settlement point (rod length=2m)
5. DSP : deep settlement point (2 m above the tunnel crown)
6. B : bench mark (rod length=20 m)

Table A.2 Location of Multipoint Extensometers

Instrument	Chainage (400+... m)	Offset (m)	Elevation (1) (m)	No. Magnets	Magnets Depth (m)				
C1-M1	204.220	0.480	664.481	9	2.0	4.2	6.3	7.3	9.8
					12.8	15.3	17.1	23.8	
C1-M2	198.500	-6.500	664.167	9	2.0	4.2	6.3	7.3	9.8
					12.8	15.2	17.2	23.8	
C2-M1	177.743	7.815	664.343	8	2.4	4.6	6.6	10.0	13.1
					16.0	17.7	23.4		
C2-M2	178.720	3.943	663.919	8	2.1	4.6	6.5	9.7	13.0
					15.7	17.6	23.2		
C2-M3	175.007	4.427	664.259	8	2.0	4.4	6.4	9.8	13.0
					14.5	20.3	23.3		
C2-M4	175.098	0.739	664.040	10	2.2	4.6	6.5	8.3	10.2
					13.1	15.9	17.8	20.6	23.5
C2-M5	172.015	-4.484	663.676	8	2.1	4.6	6.7	10.1	13.1
					15.9	17.6	25.2		
C2-M6	182.106	-12.223	664.096	8	2.2	4.5	6.4	9.9	14.0
					15.7	17.6	23.4		
C2-M7	177.047	-18.890	664.090	8	2.2	4.6	6.6	9.8	12.9
					15.7	17.7	23.4		

1. Elevation at the top of the pipe

Table A.3 Location of Inclinometers and Piezometers

Instrument	Chainage (400+... m)	Offset (m)	Elevation (1) (m)	Depth (m)
C1-I1	198.482	-10.534	664.313	27.43
C2-I1	176.668	6.589	664.320	28.35
C2-I2	177.214	3.857	663.944	26.21
C2-I3	173.600	0.882	664.147	23.16
C2-I4	170.262	-4.631	663.930	26.21
C1-P1	178.752	-5.234	664.330	6.5
C2-P1	168.050	-5.038	664.087	9.7
H85-1-P	171.5	0.1	664.4	14.1

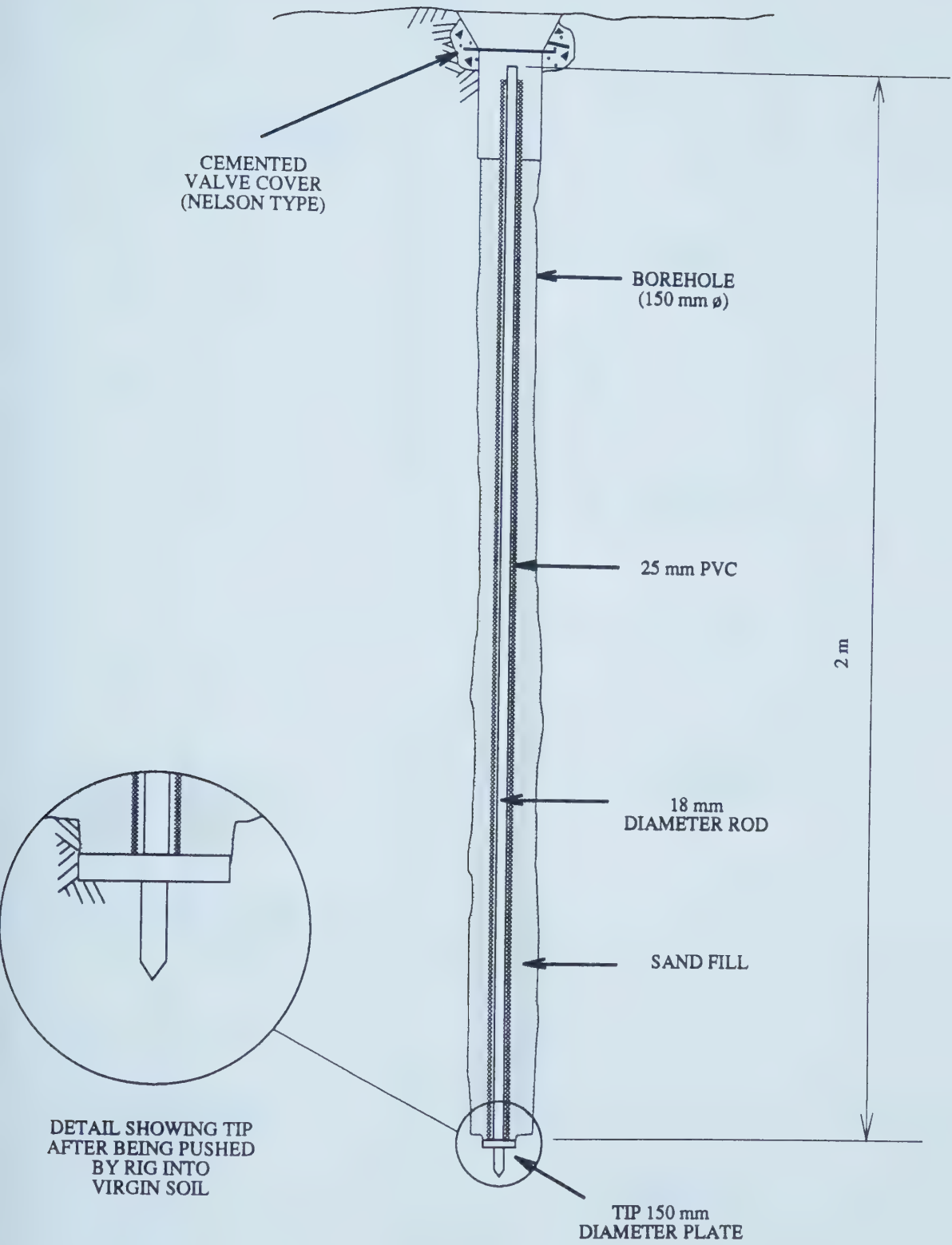


Figure A.1 Installation Details for Shallow Settlement Point

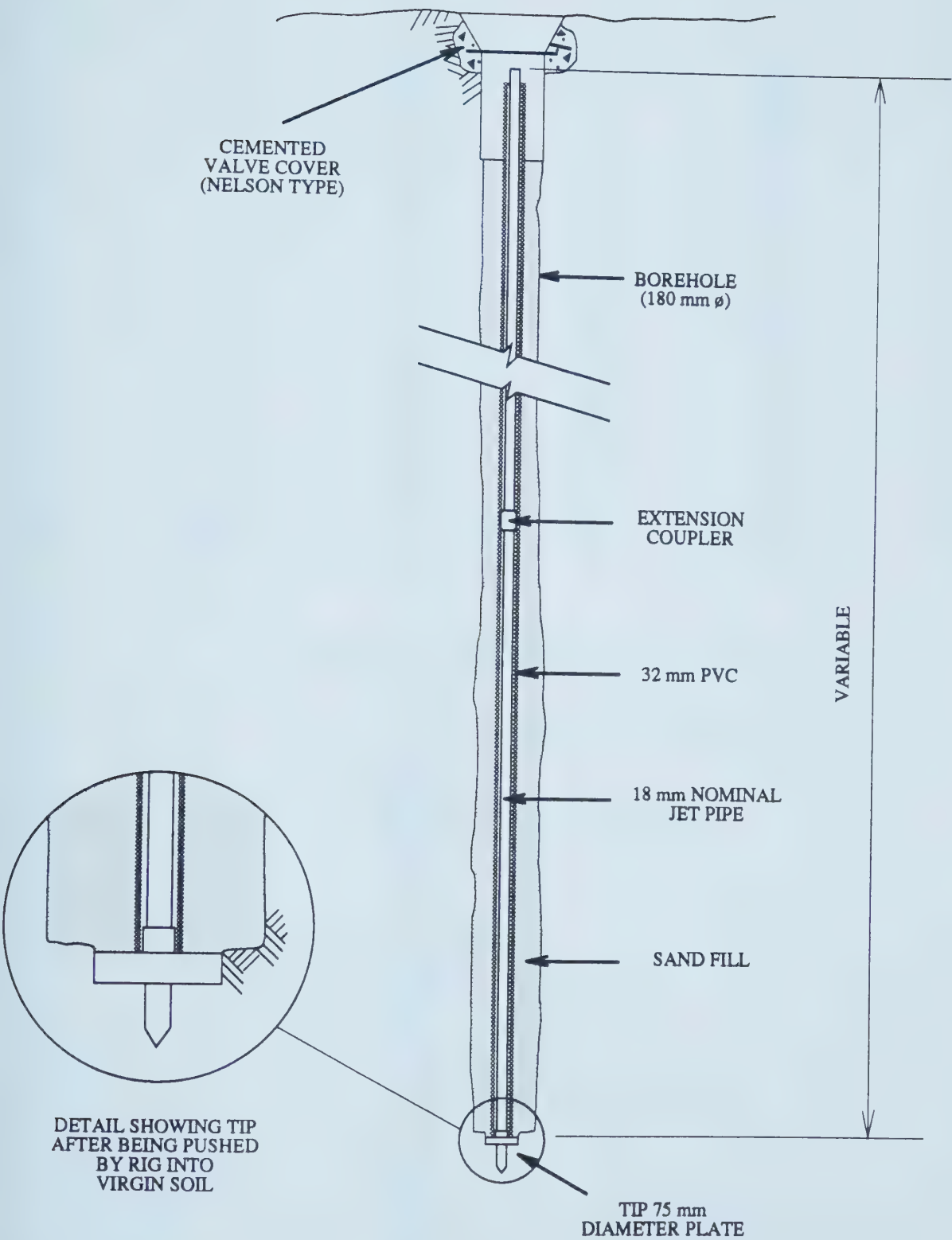


Figure A.2 Installation Details for Deep Settlement Point and Bench Mark

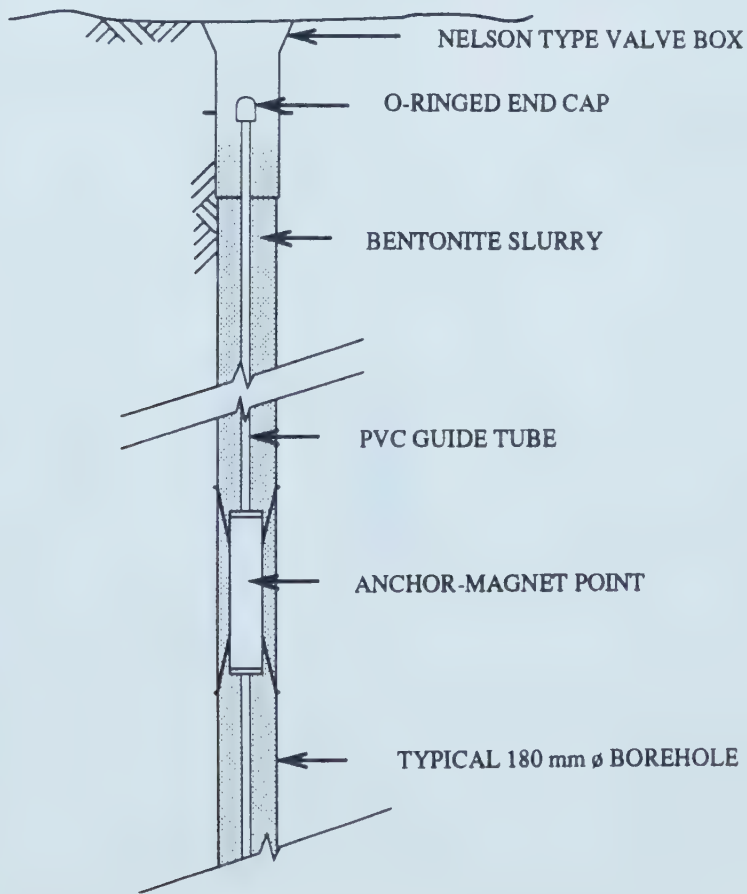
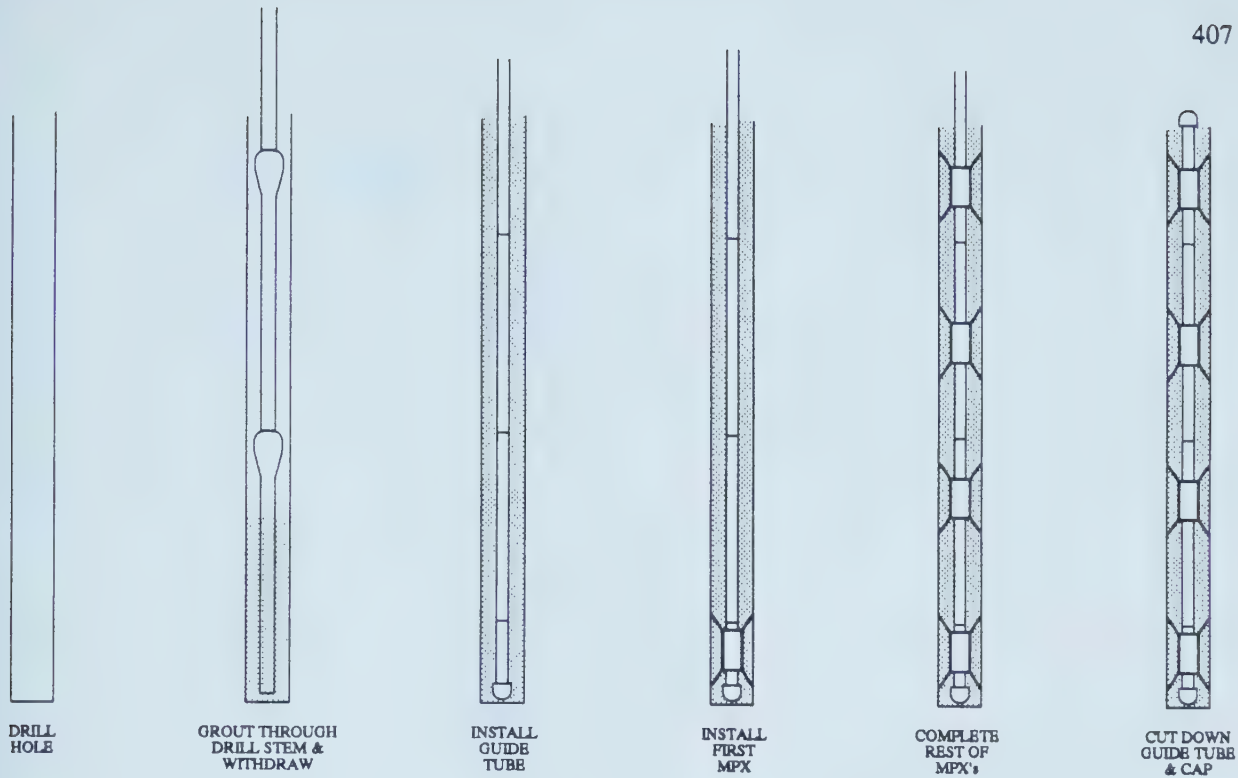


Figure A.3 Installation Details for Multipoint Extensometer

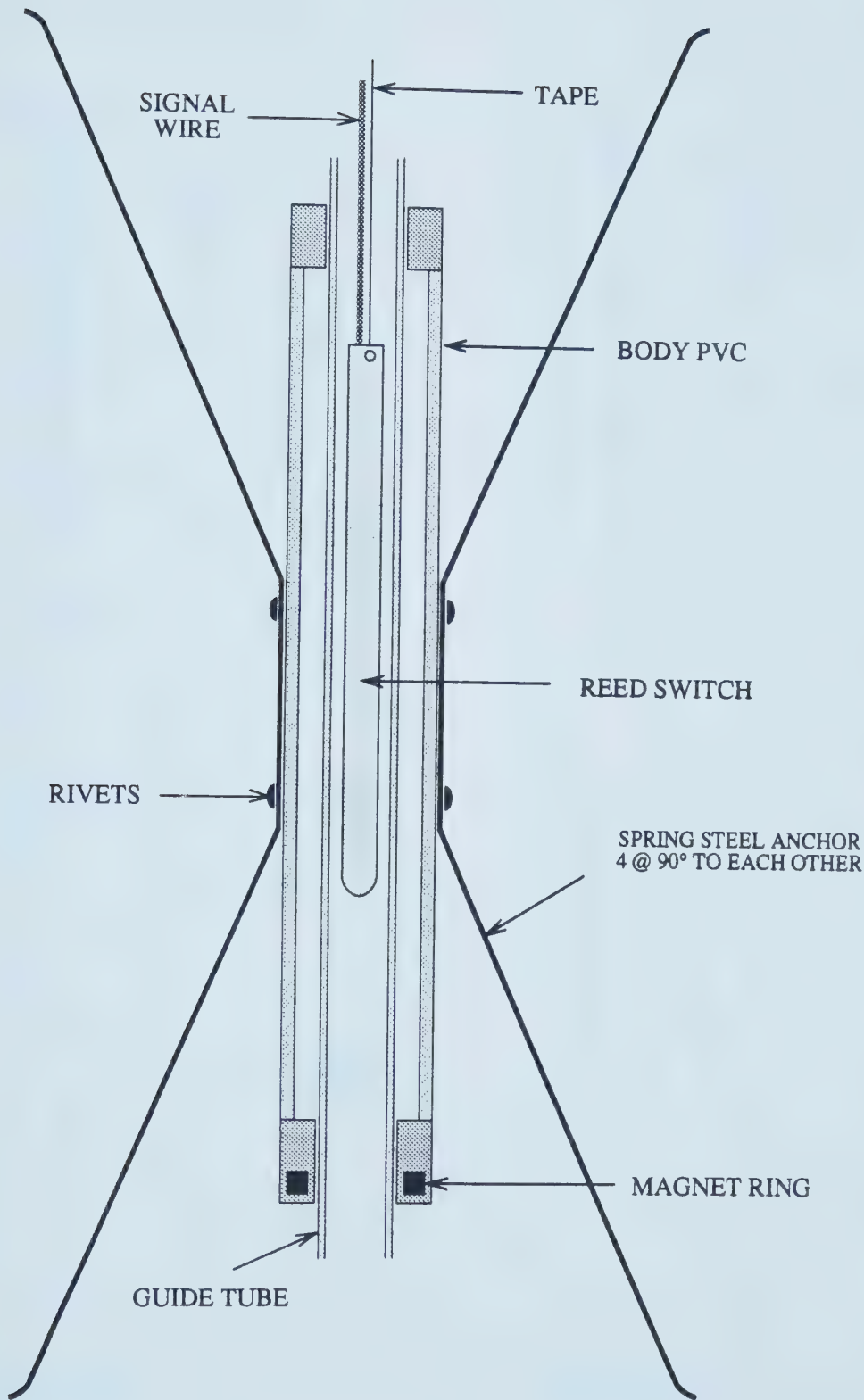


Figure A.4 Anchor Assembly Detail of Multipoint Extensometer U. of A. Type

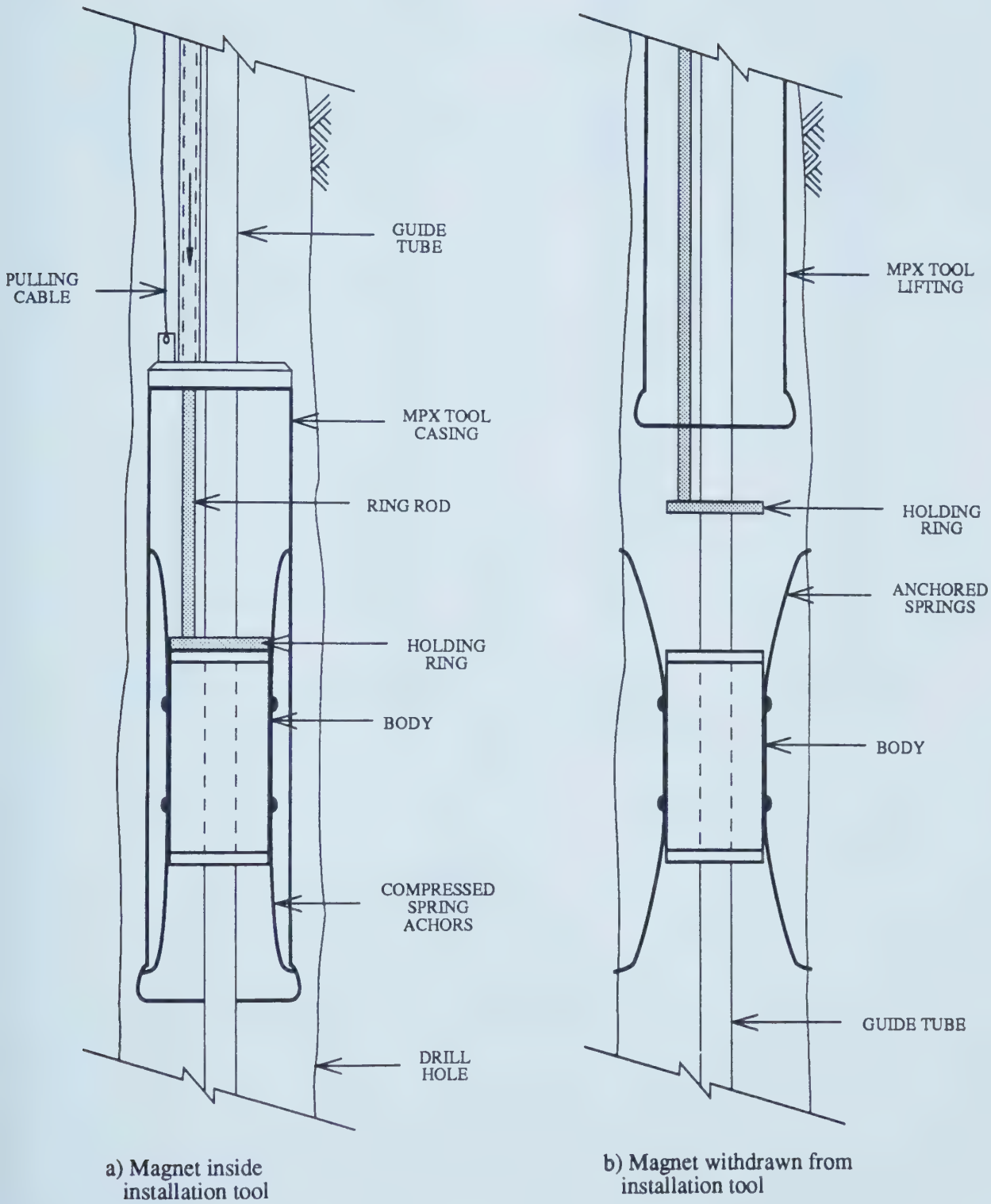


Figure A.5 Installation Details of Anchor Assembly for Multipoint Extensometer

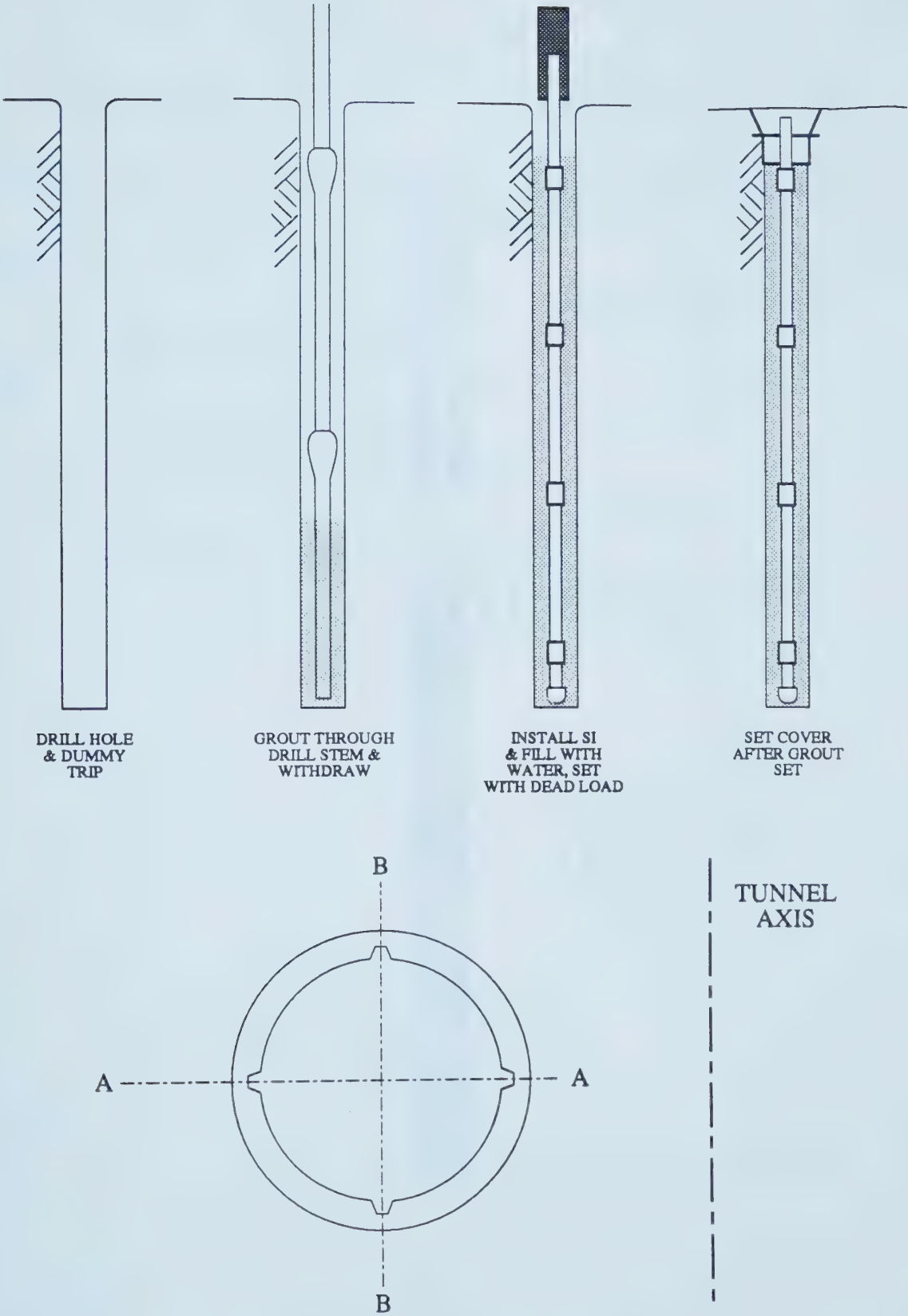


Figure A.6 Inclinometer Installation Details

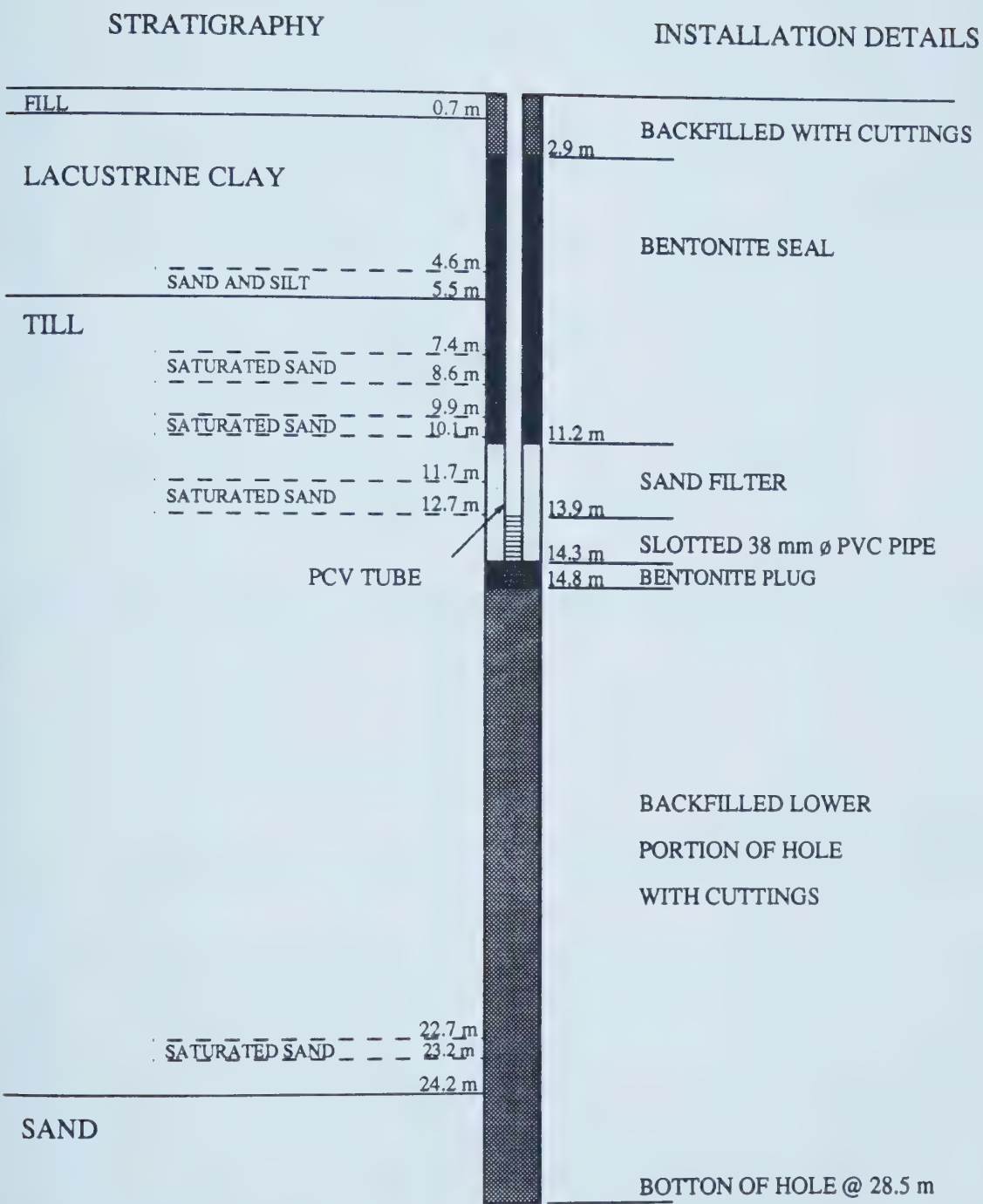


Figure A.7 Installation Procedure for Standpipe Piezometer H85-1
(modified from Hardy, 1985)

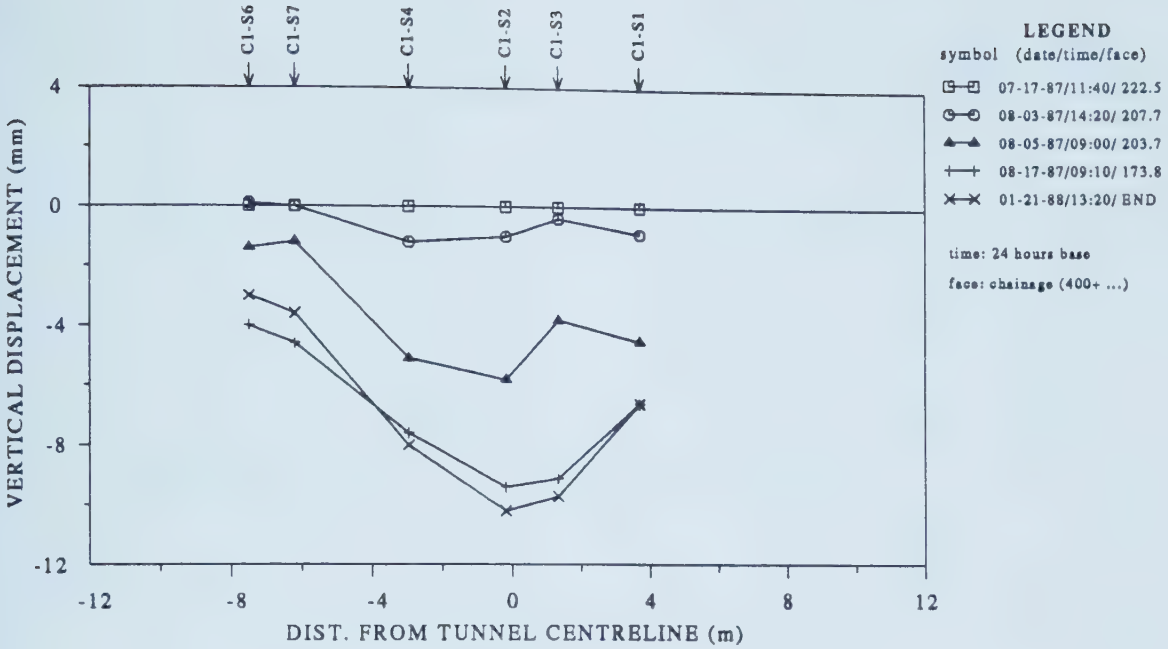


Figure A.8 Transverse Settlement Distribution. Early Warning Section (C1) Shallow Settlement Points

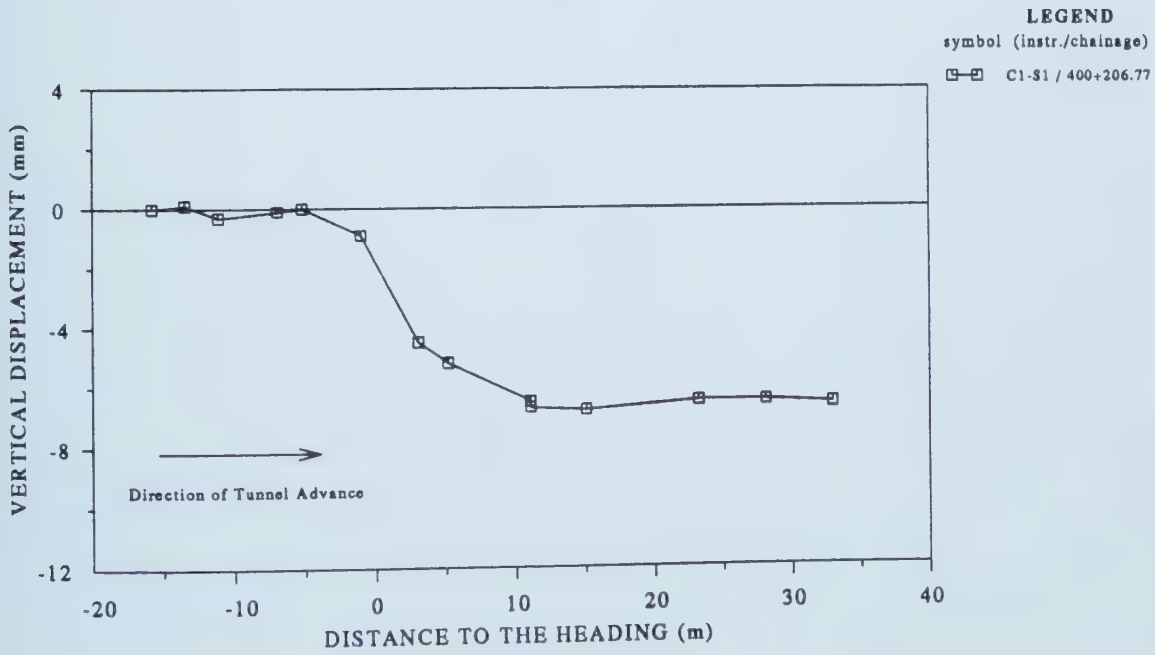


Figure A.9 Measured Vertical Displacements with Tunnel Heading Advancing, C1-S1

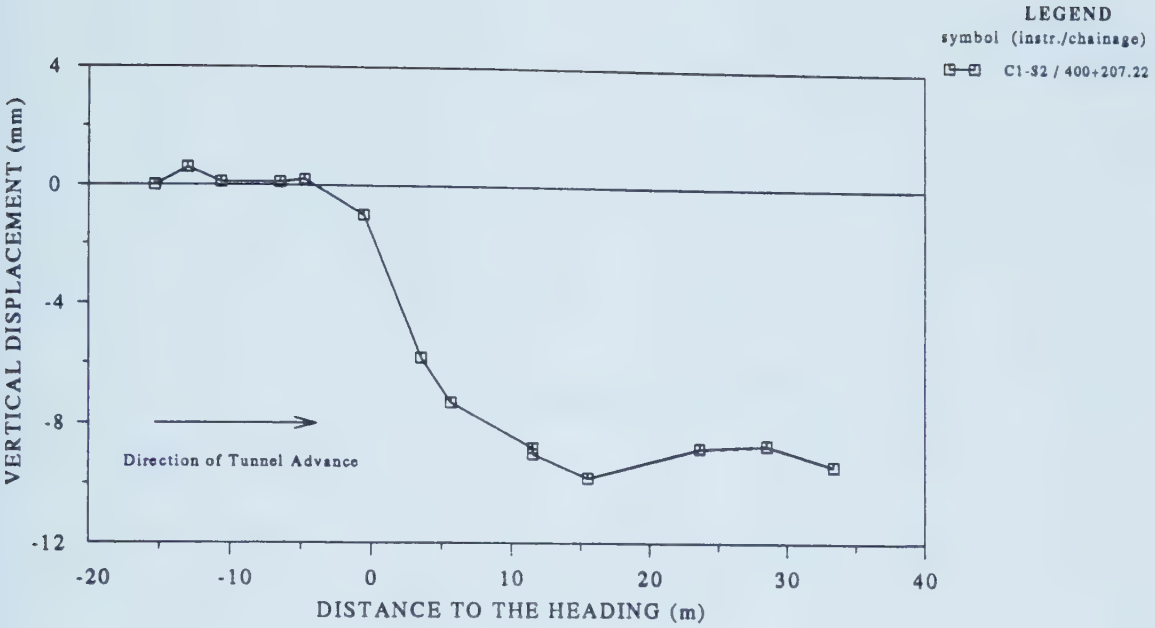


Figure A.10 Measured Vertical Displacements with Tunnel Heading Advancing, C1-S2

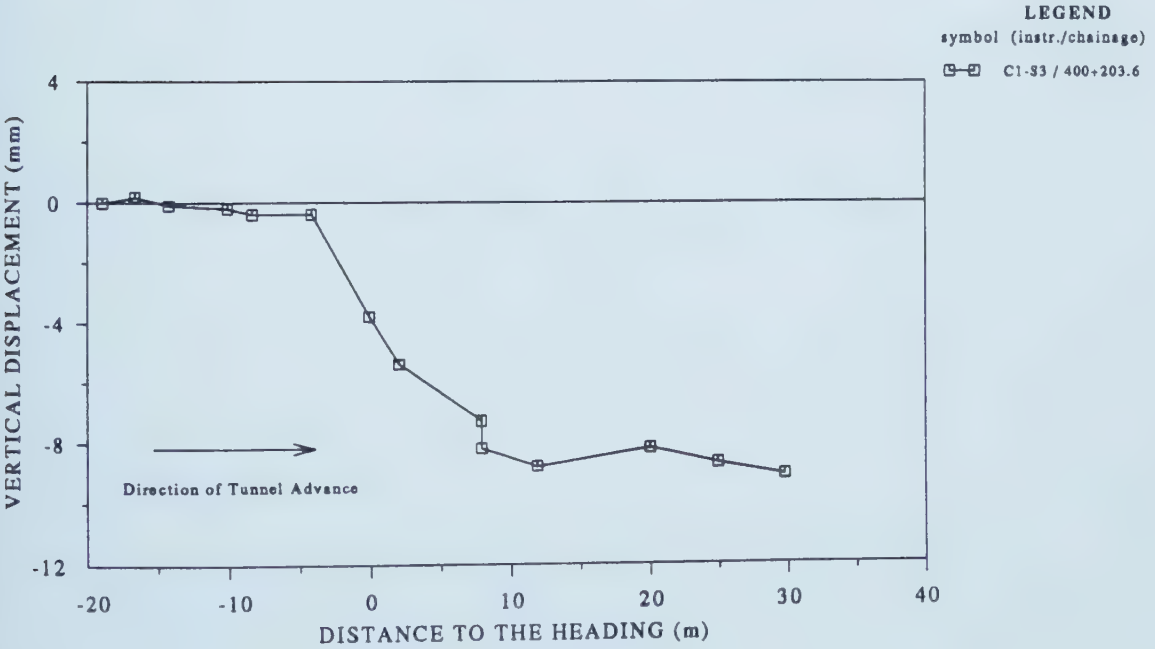


Figure A.11 Measured Vertical Displacements with Tunnel Heading Advancing, C1-S3

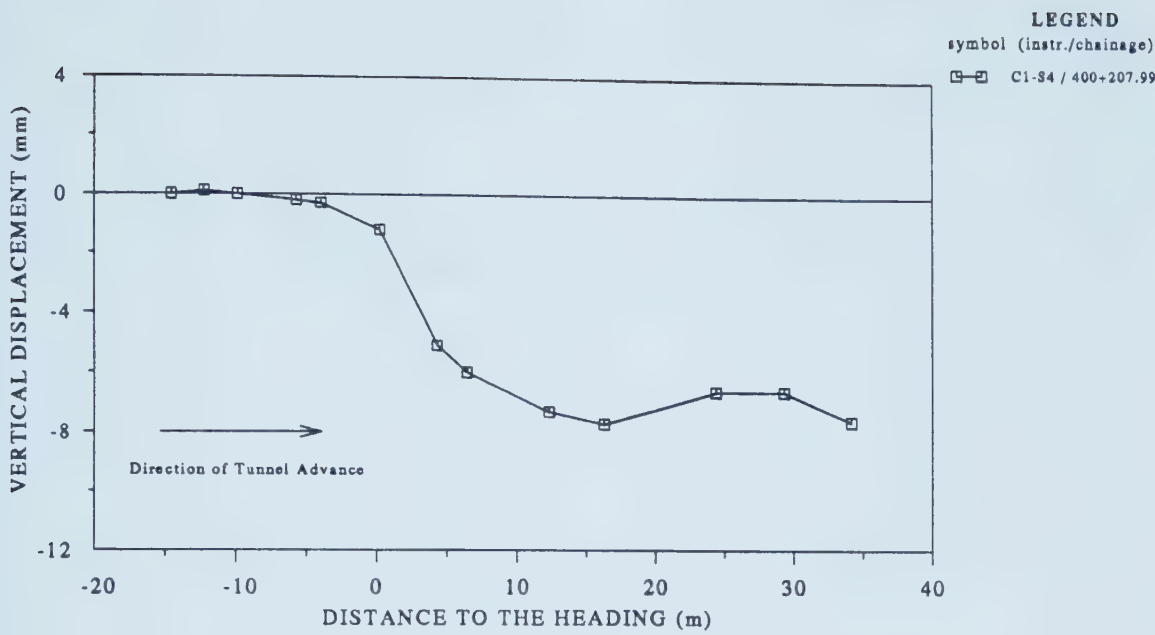


Figure A.12 Measured Vertical Displacements with Tunnel Heading Advancing, C1-S4

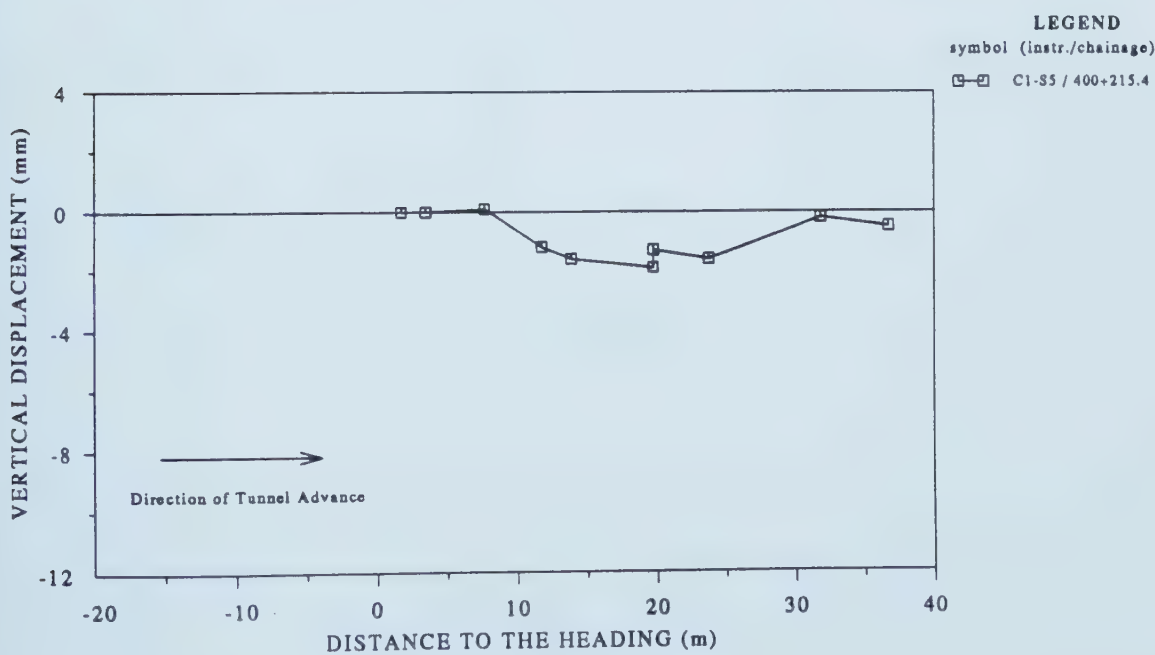


Figure A.13 Measured Vertical Displacements with Tunnel Heading Advancing, C1-S5

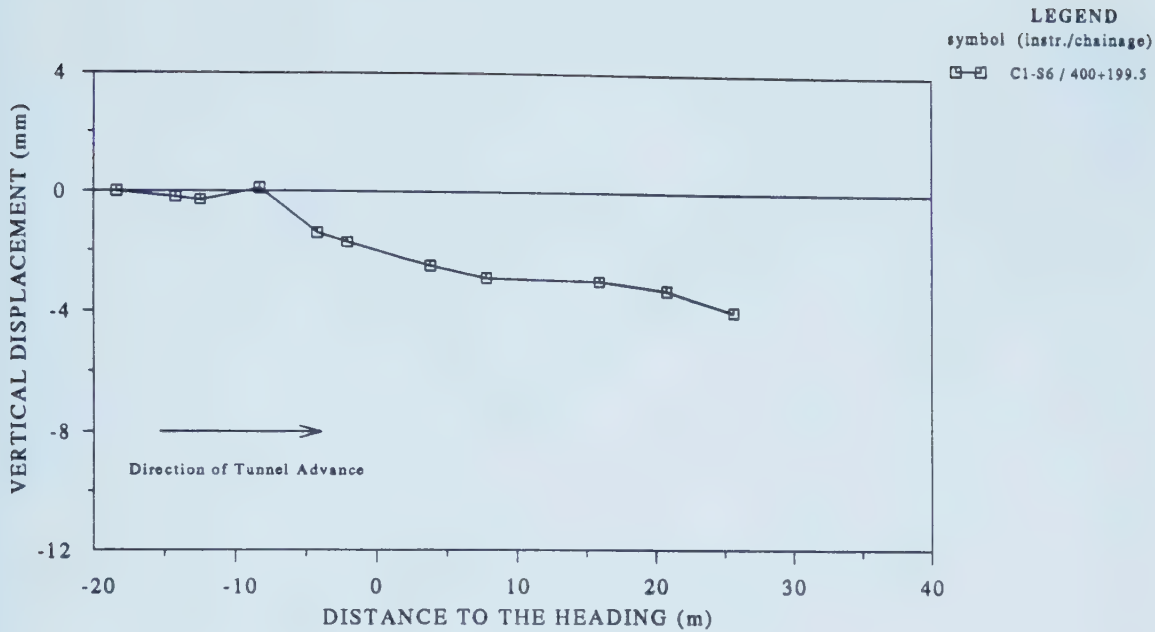


Figure A.14 Measured Vertical Displacements with Tunnel Heading Advancing, C1-S6

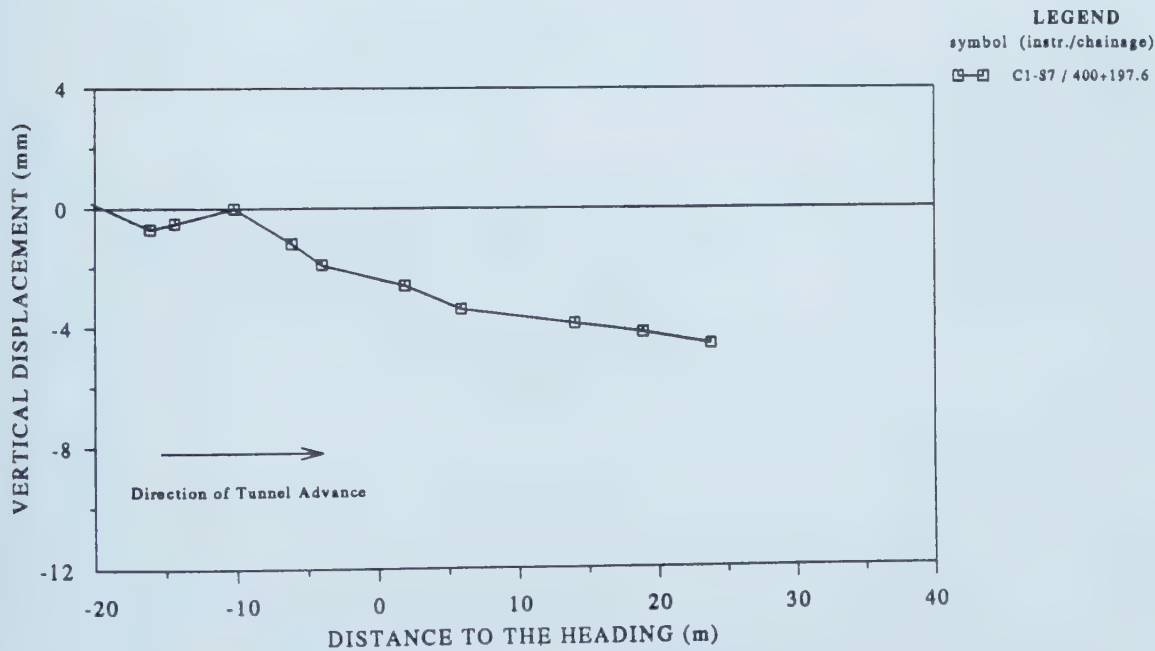


Figure A.15 Measured Vertical Displacements with Tunnel Heading Advancing, C1-S7

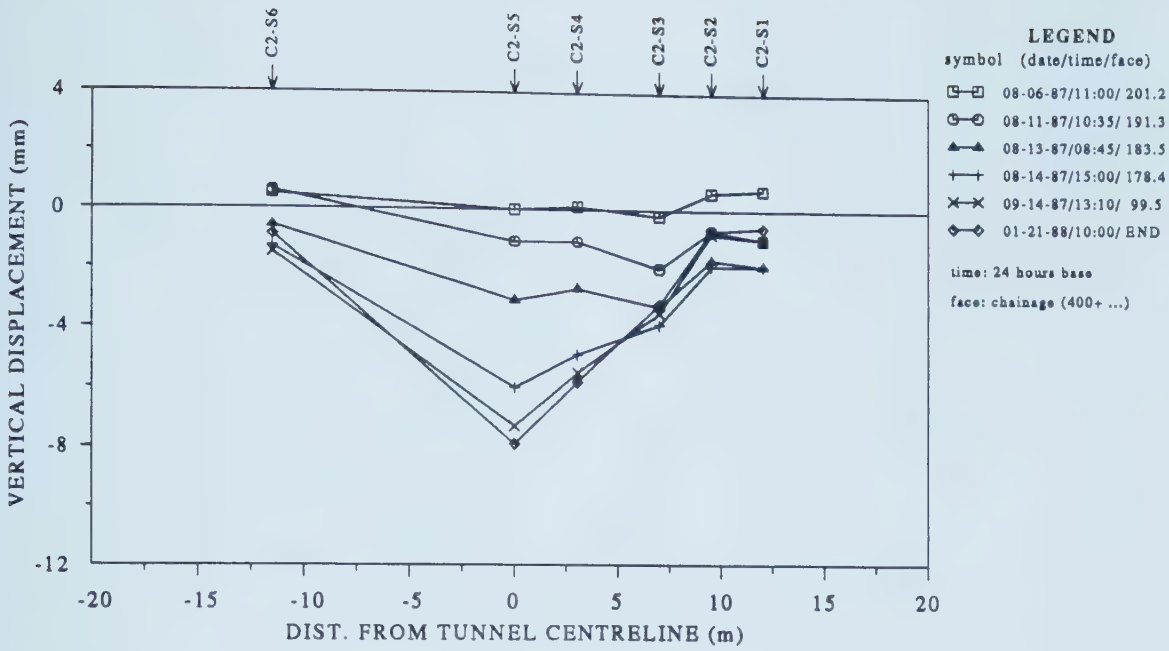


Figure A.16 Transverse Settlement Distribution, Main Section C2-1, Shallow Settlement Points

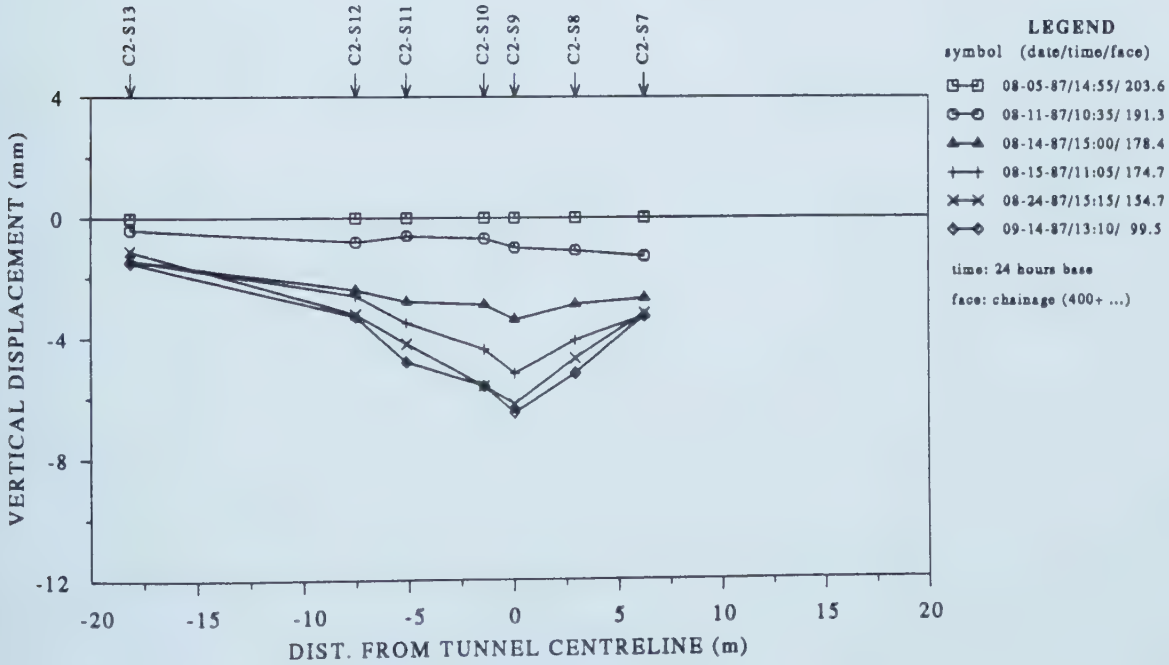


Figure A.17 Transverse Settlement Distribution, Main Section C2-2, Shallow Settlement Points

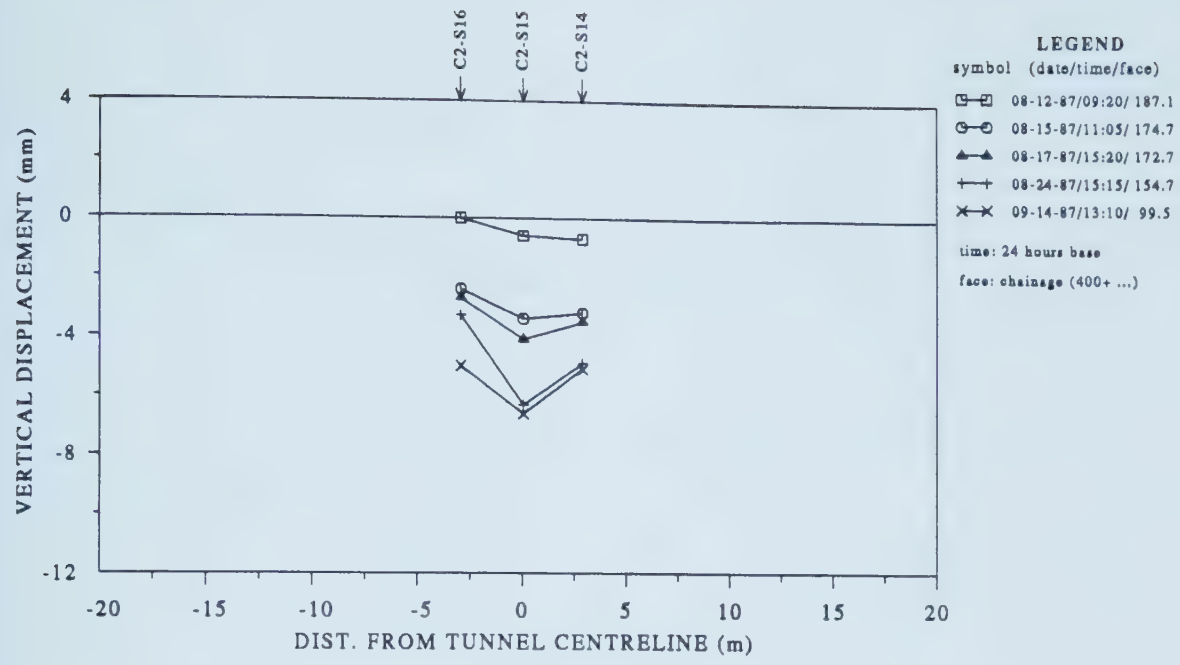


Figure A.18 Transverse Settlement Distribution, Main Section C2-3, Shallow Settlement Points

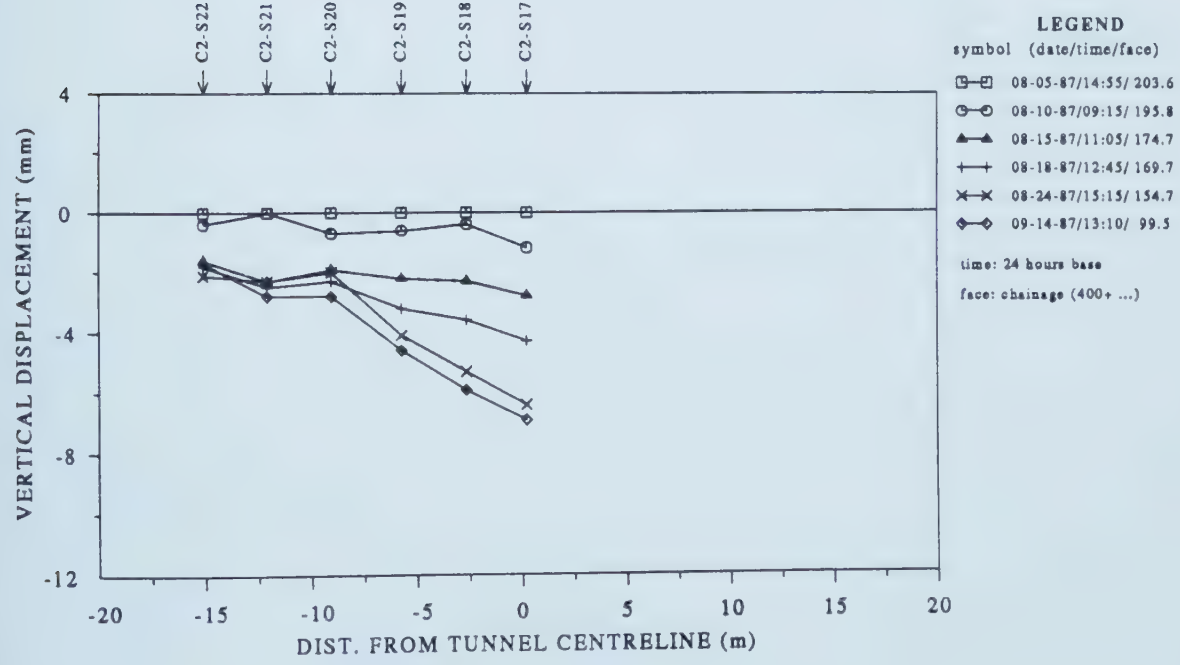


Figure A.19 Transverse Settlement Distribution, Main Section C2-4, Shallow Settlement Points

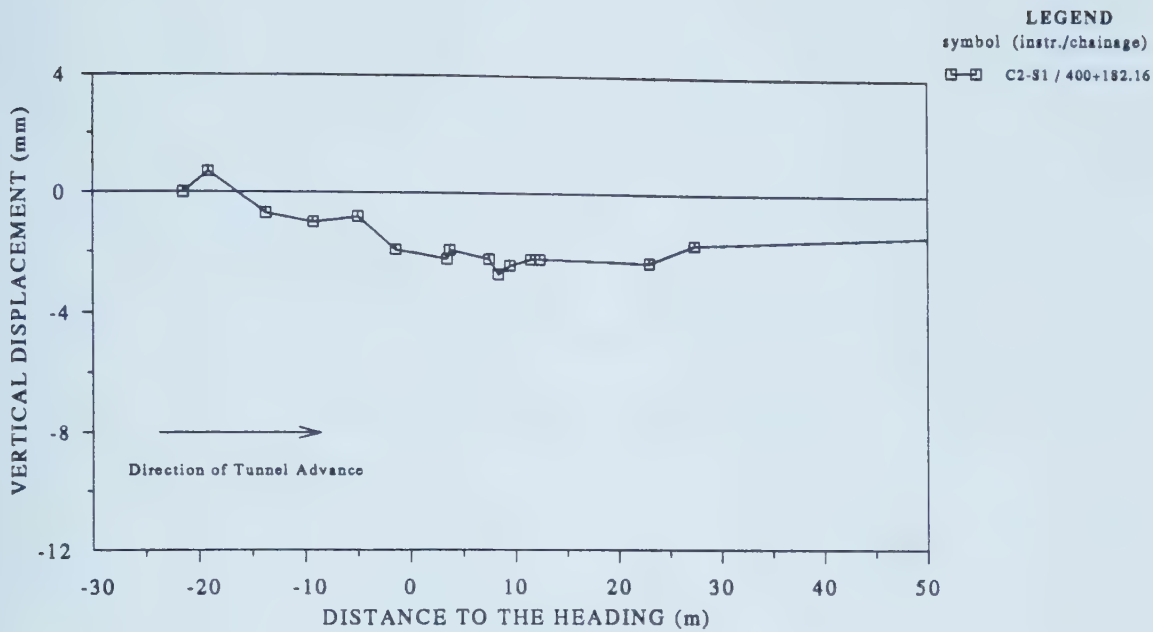


Figure A.20 Measured Vertical Displacements with Tunnel Heading Advancing, C2-S1

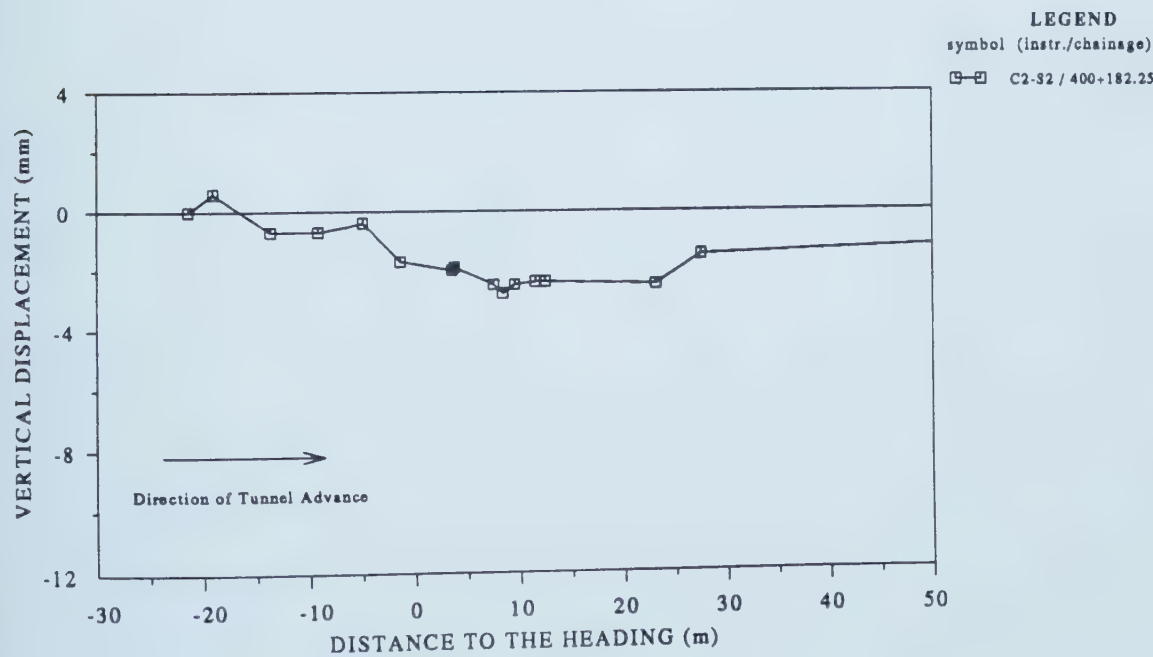


Figure A.21 Measured Vertical Displacements with Tunnel Heading Advancing, C2-S2

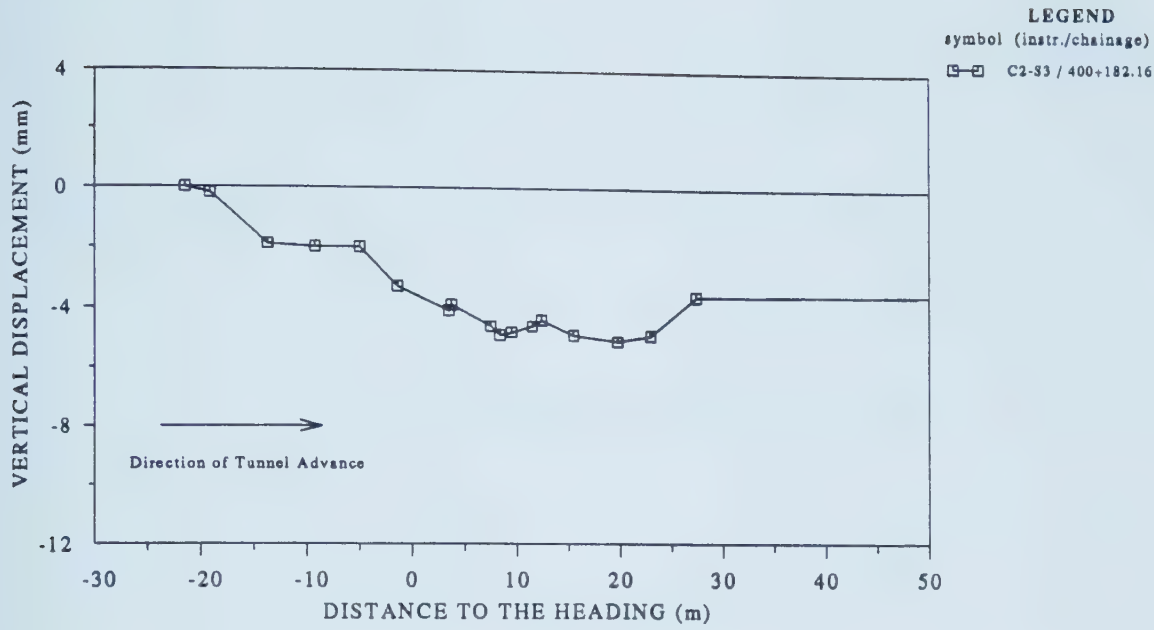


Figure A.22 Measured Vertical Displacements with Tunnel Heading Advancing, C2-S3

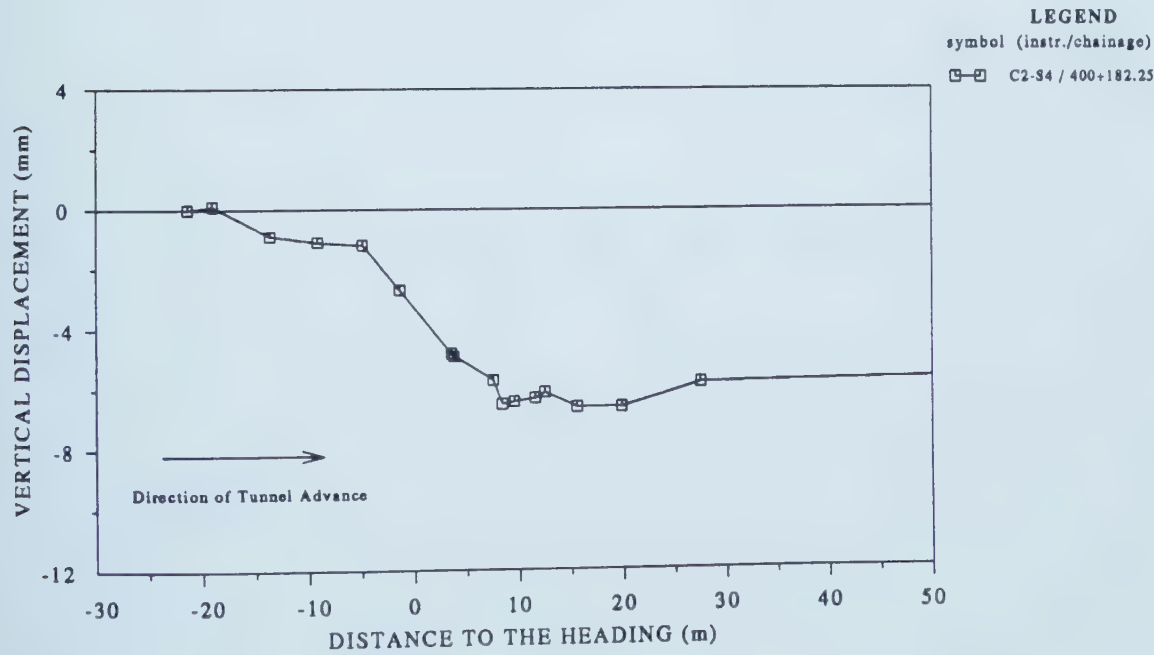


Figure A.23 Measured Vertical Displacements with Tunnel Heading Advancing, C2-S4

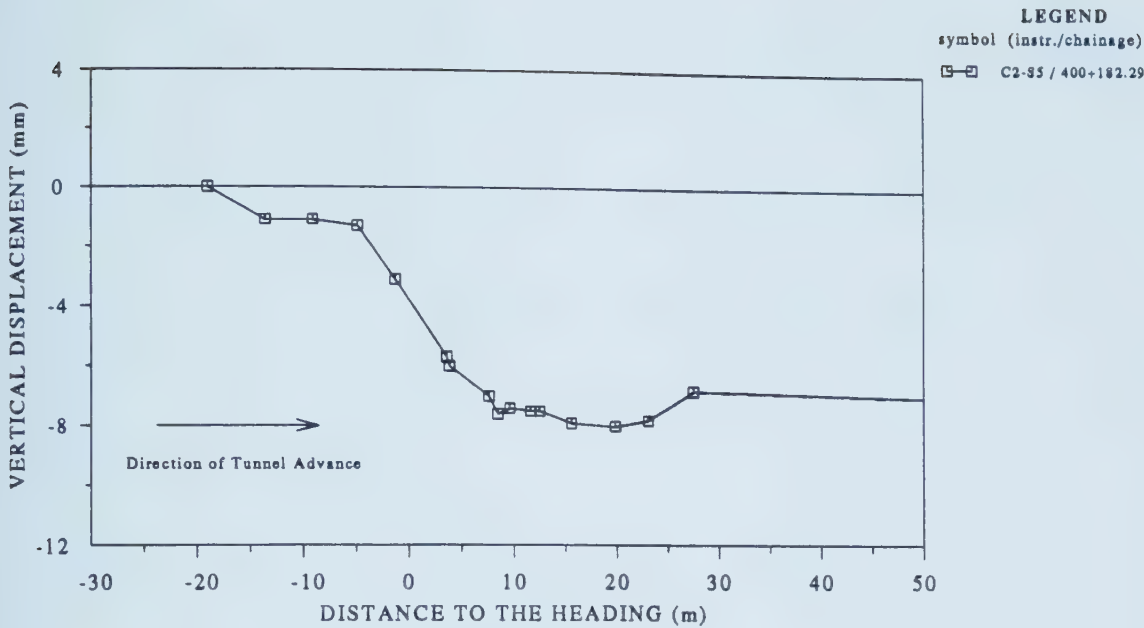


Figure A.24 Measured Vertical Displacements with Tunnel Heading Advancing, C2-S5

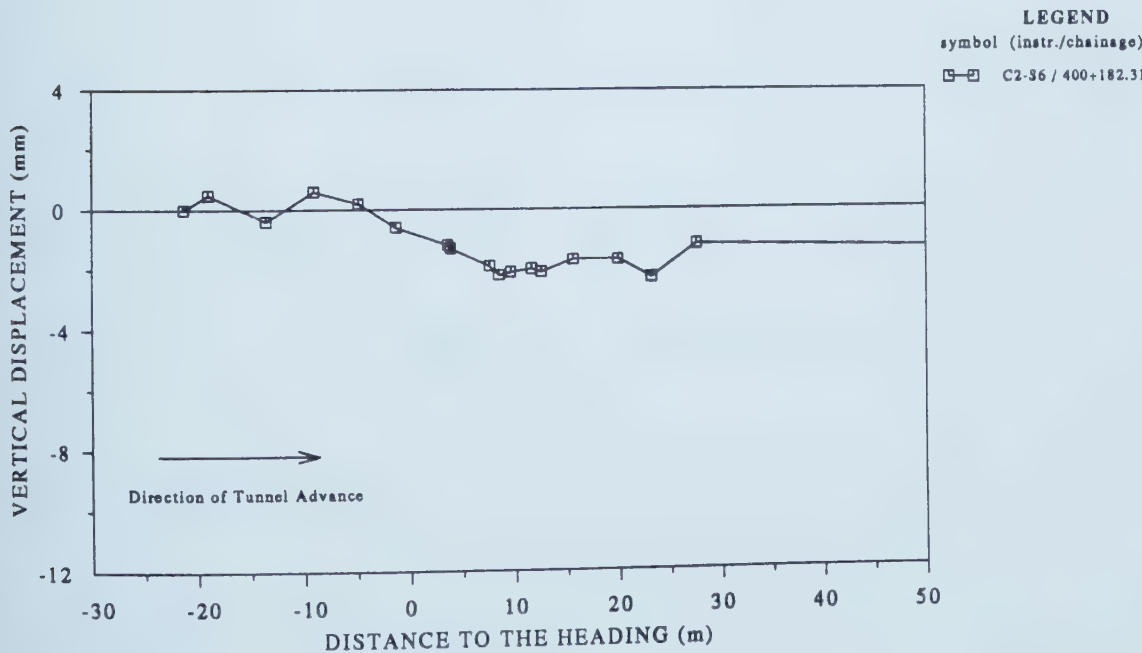


Figure A.25 Measured Vertical Displacements with Tunnel Heading Advancing, C2-S6

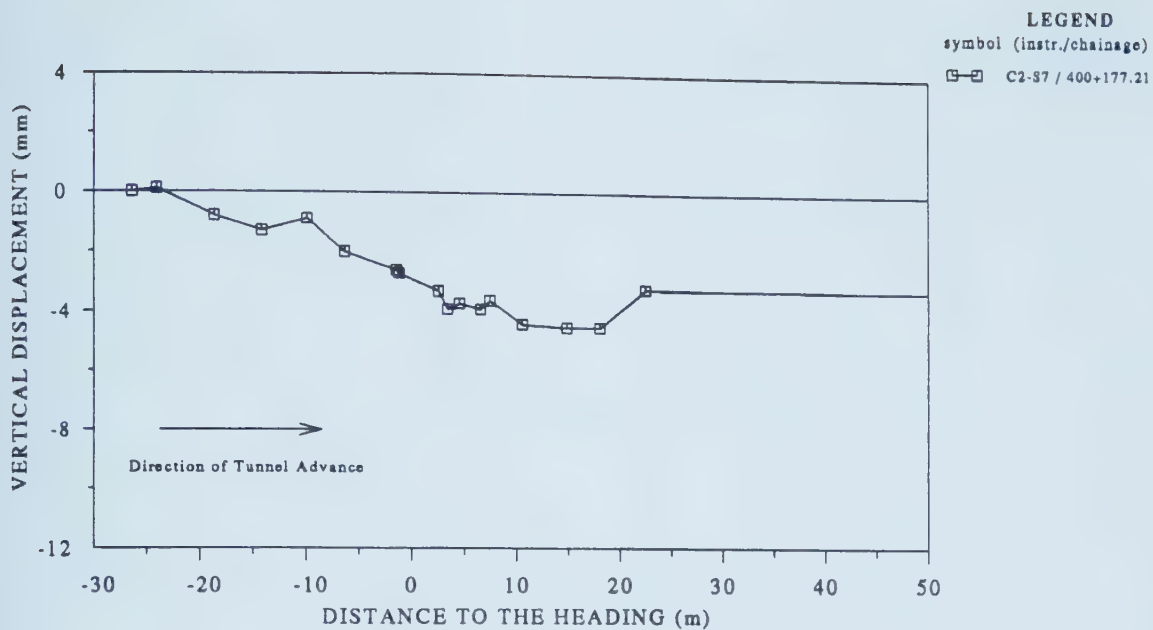


Figure A.26 Measured Vertical Displacements with Tunnel Heading Advancing, C2-S7

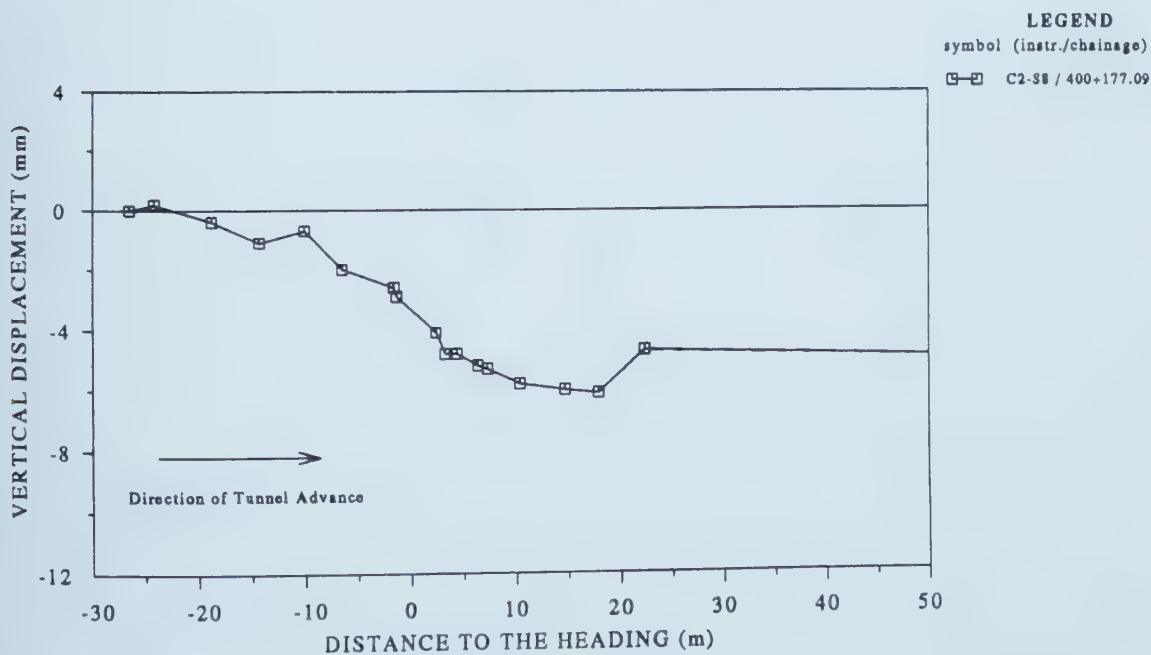


Figure A.27 Measured Vertical Displacements with Tunnel Heading Advancing, C2-S8

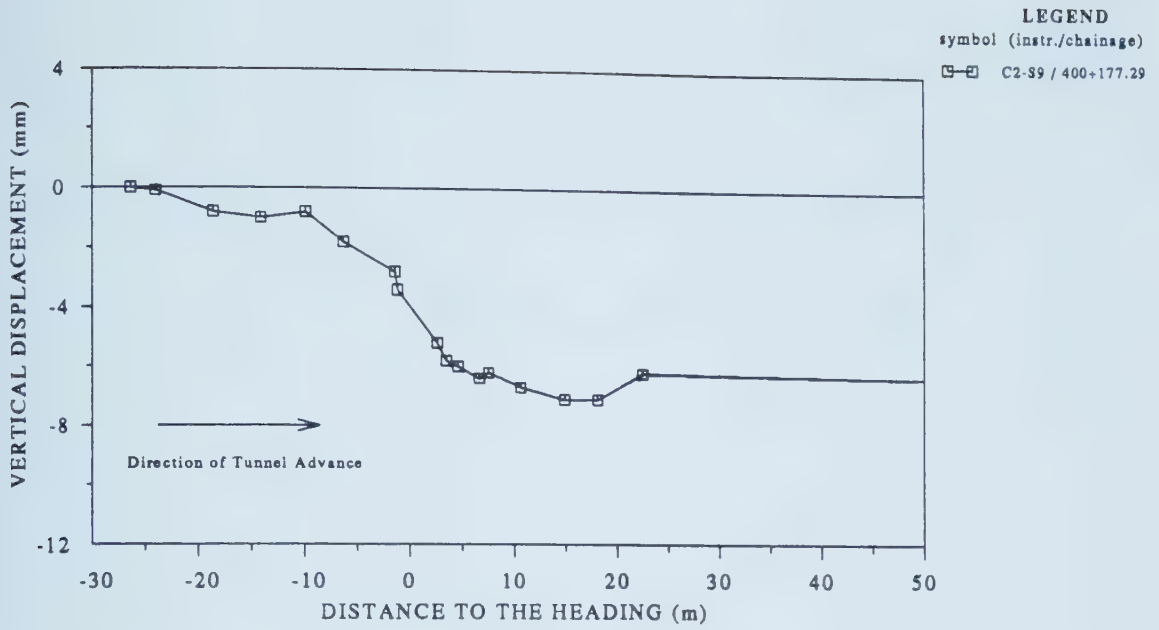


Figure A.28 Measured Vertical Displacements with Tunnel Heading Advancing, C2-S9

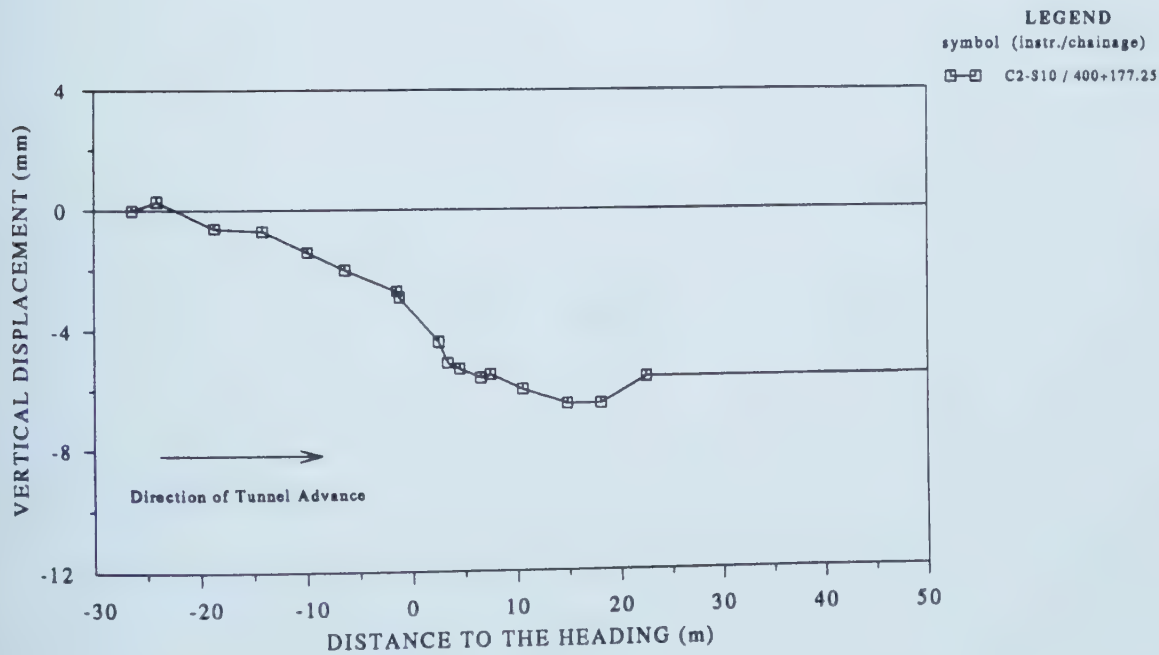


Figure A.29 Measured Vertical Displacements with Tunnel Heading Advancing, C2-S10

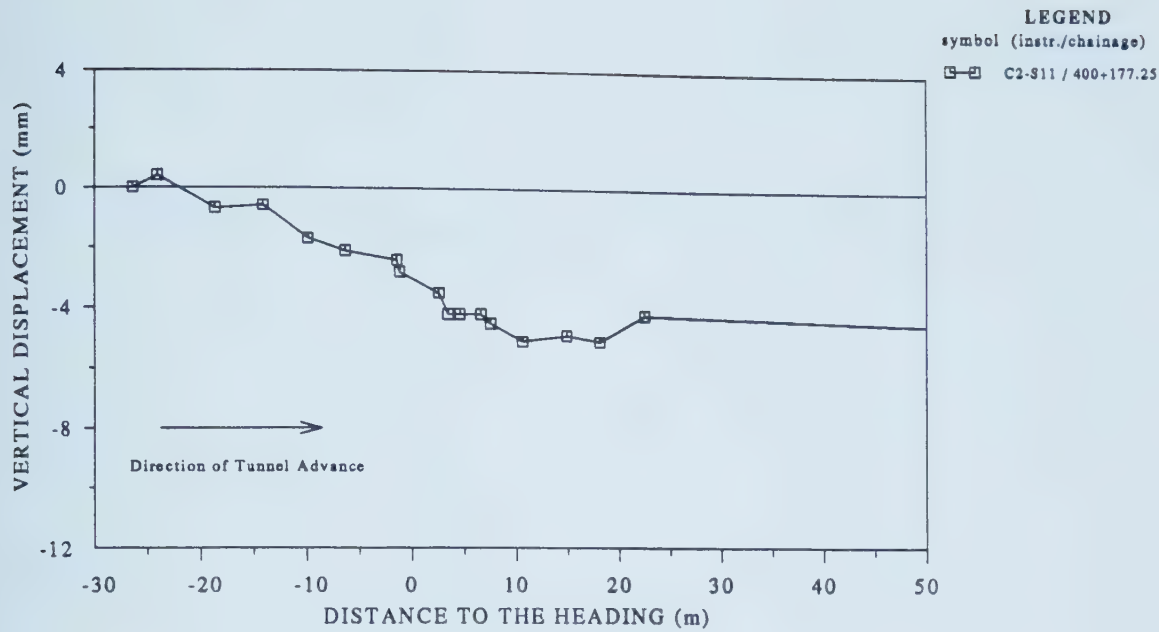


Figure A.30 Measured Vertical Displacements with Tunnel Heading Advancing, C2-S11

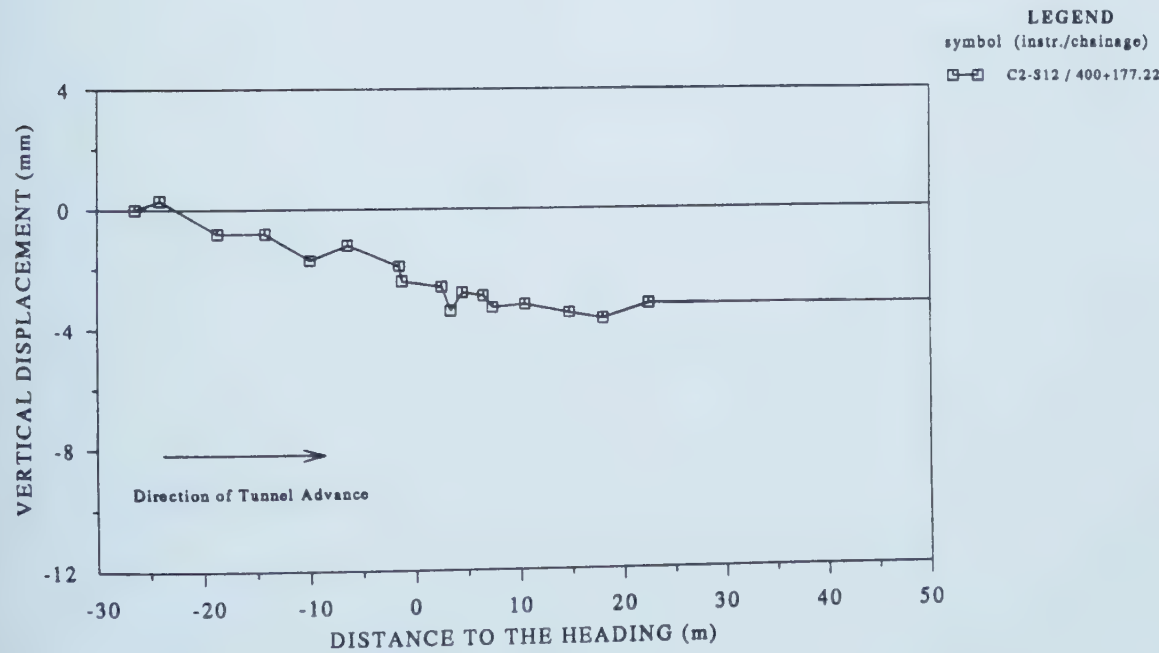


Figure A.31 Measured Vertical Displacements with Tunnel Heading Advancing, C2-S12

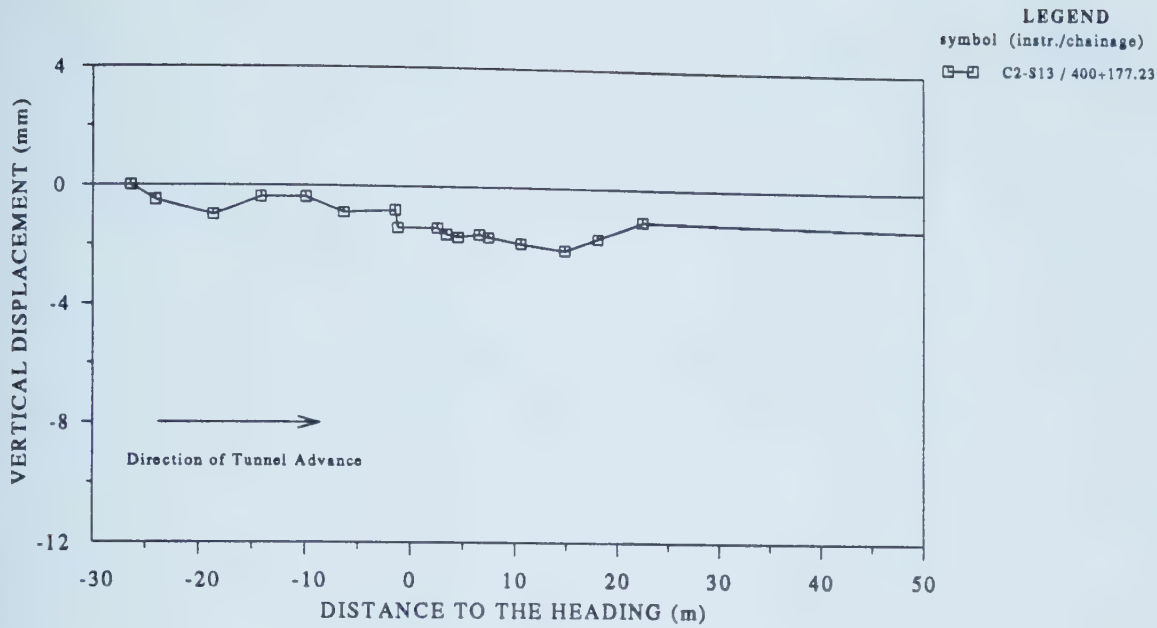


Figure A.32 Measured Vertical Displacements with Tunnel Heading Advancing, C2-S13

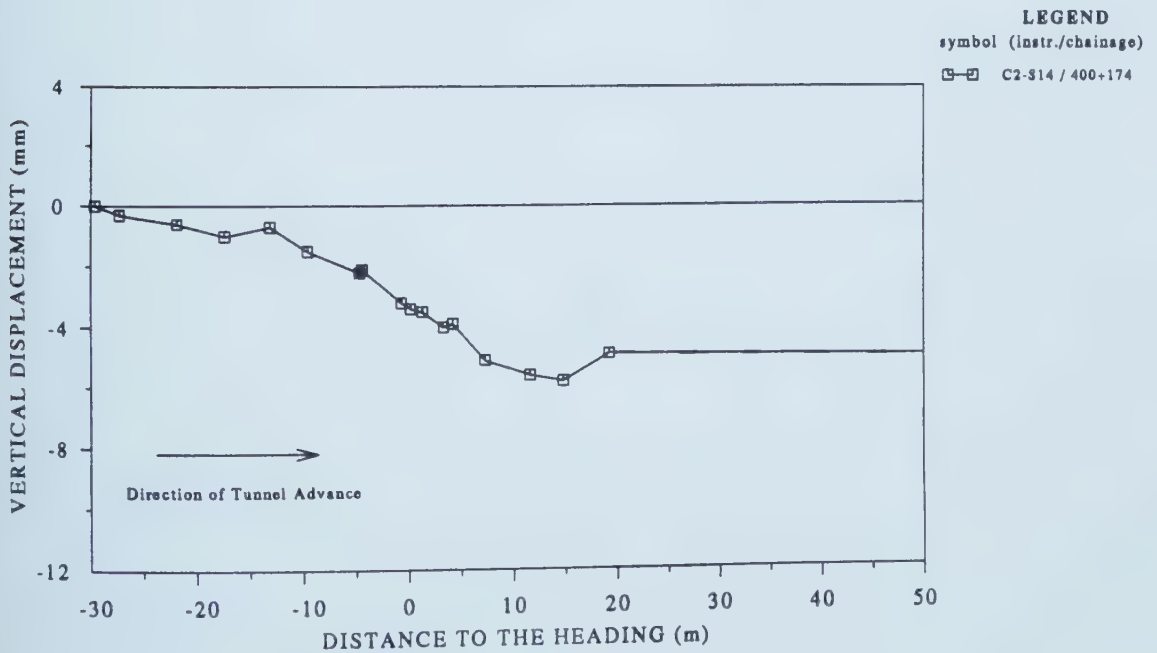


Figure A.33 Measured Vertical Displacements with Tunnel Heading Advancing, C2-S14

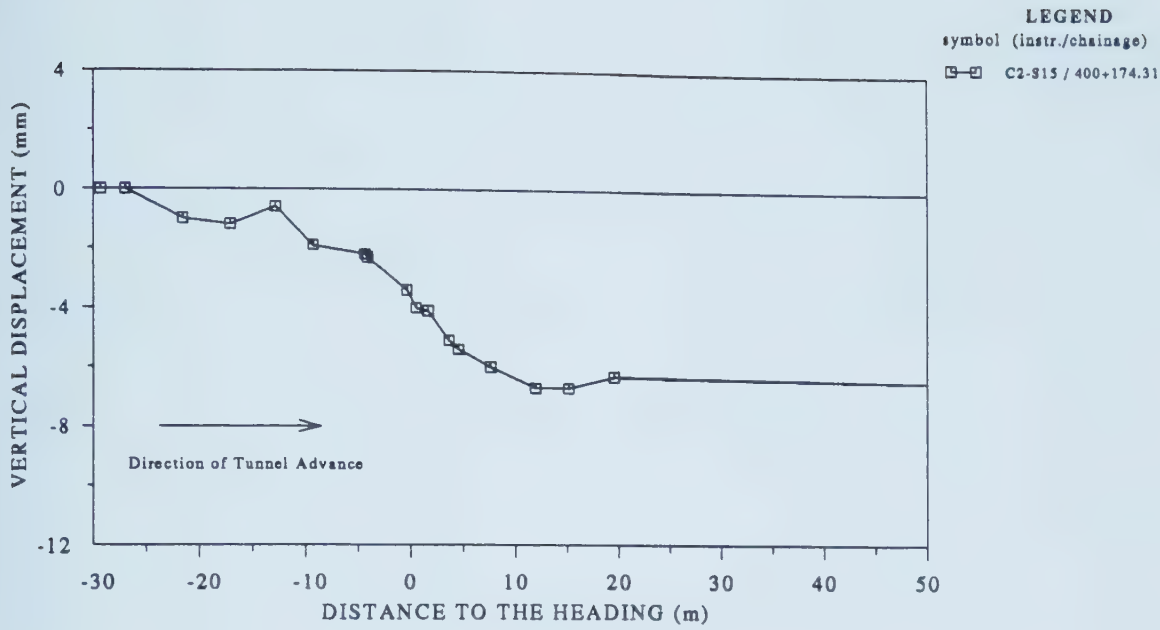


Figure A.34 Measured Vertical Displacements with Tunnel Heading Advancing, C2-S15

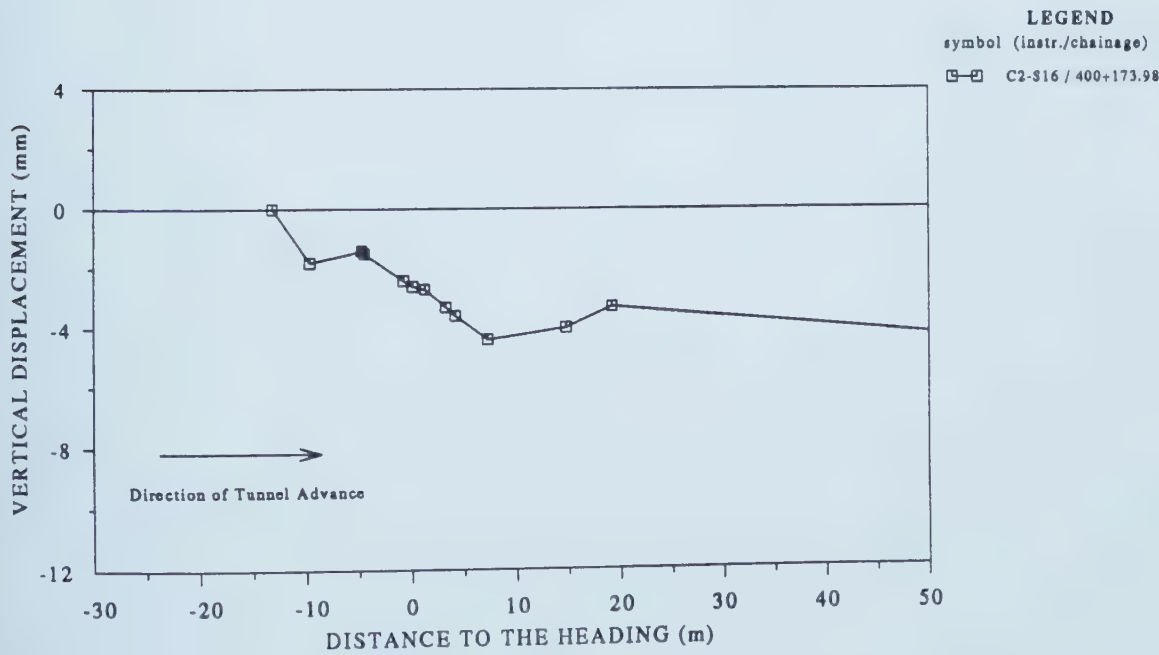


Figure A.35 Measured Vertical Displacements with Tunnel Heading Advancing, C2-S16

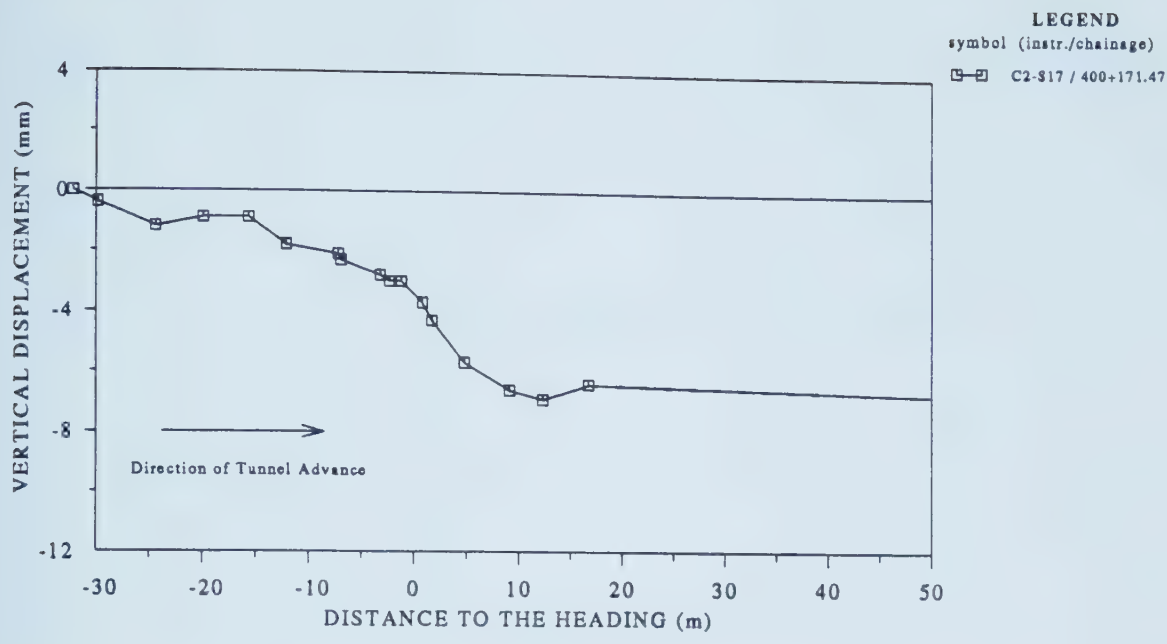


Figure A.36 Measured Vertical Displacements with Tunnel Heading Advancing, C2-S17

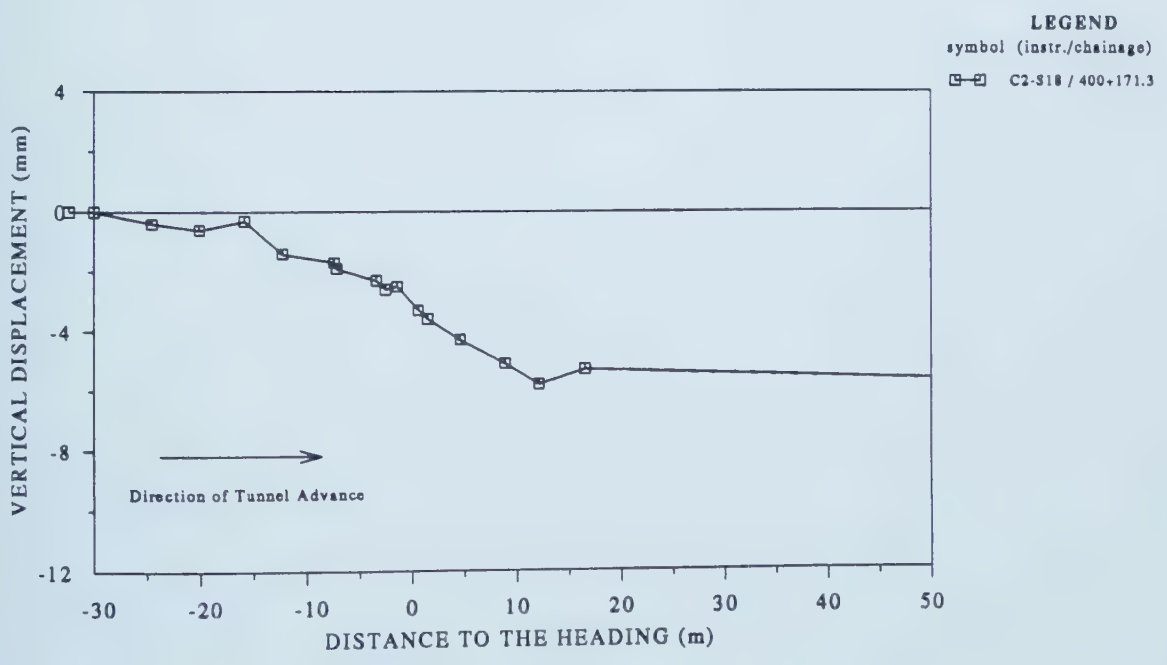


Figure A.37 Measured Vertical Displacements with Tunnel Heading Advancing, C2-S18

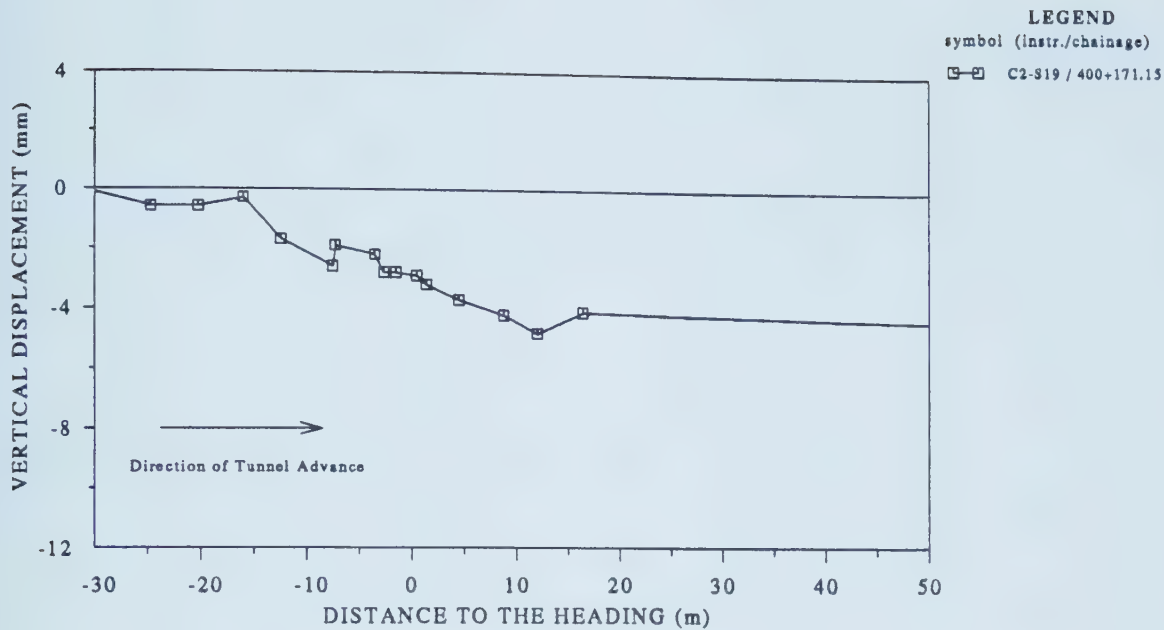


Figure A.38 Measured Vertical Displacements with Tunnel Heading Advancing, C2-S19

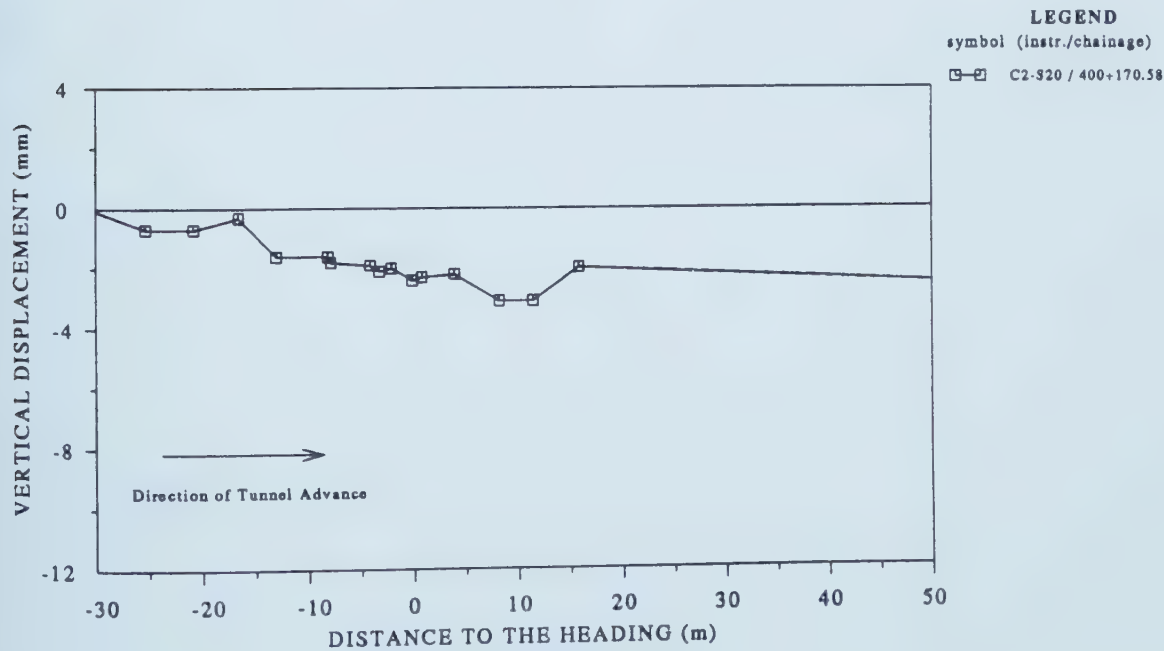


Figure A.39 Measured Vertical Displacements with Tunnel Heading Advancing, C2-S20

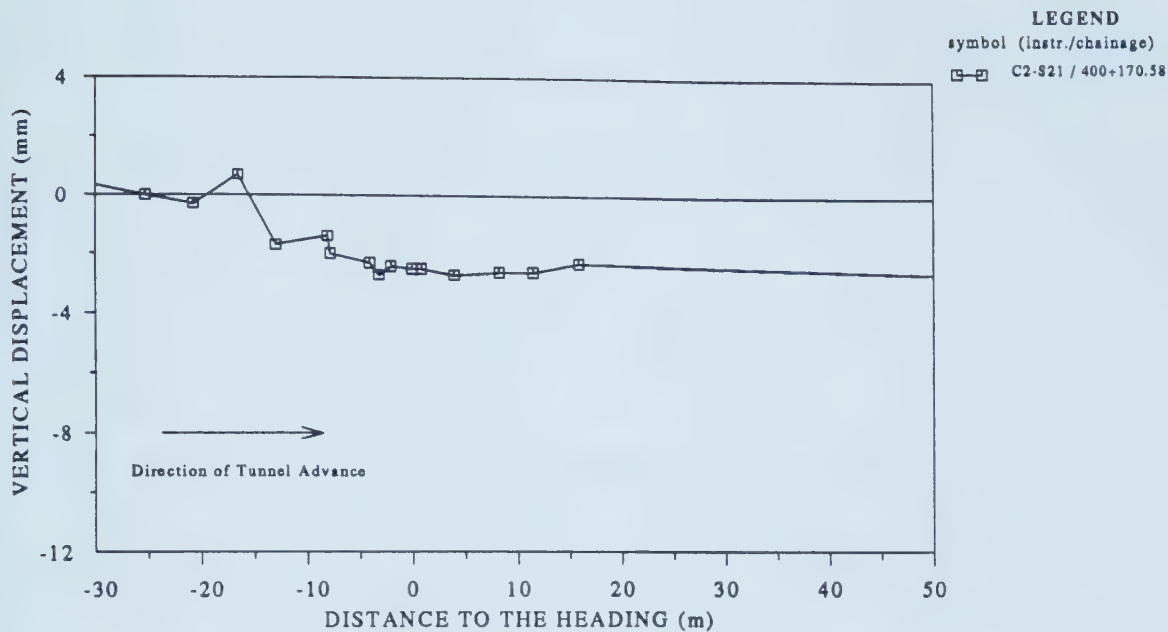


Figure A.40 Measured Vertical Displacements with Tunnel Heading Advancing, C2-S21

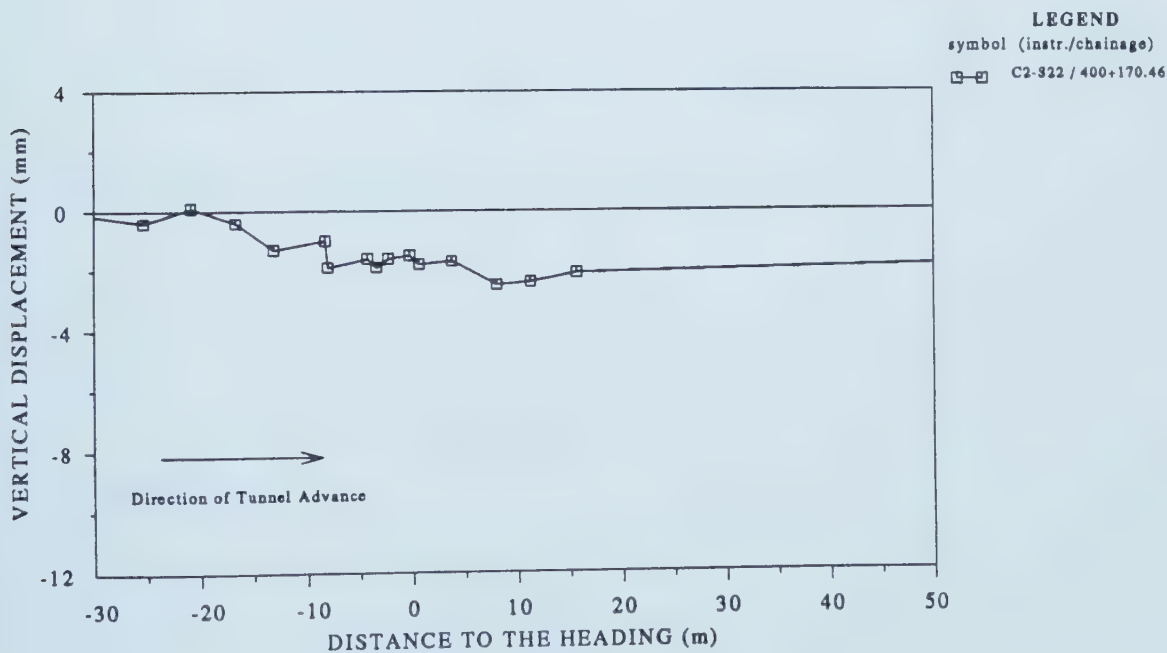


Figure A.41 Measured Vertical Displacements with Tunnel Heading Advancing, C2-S22

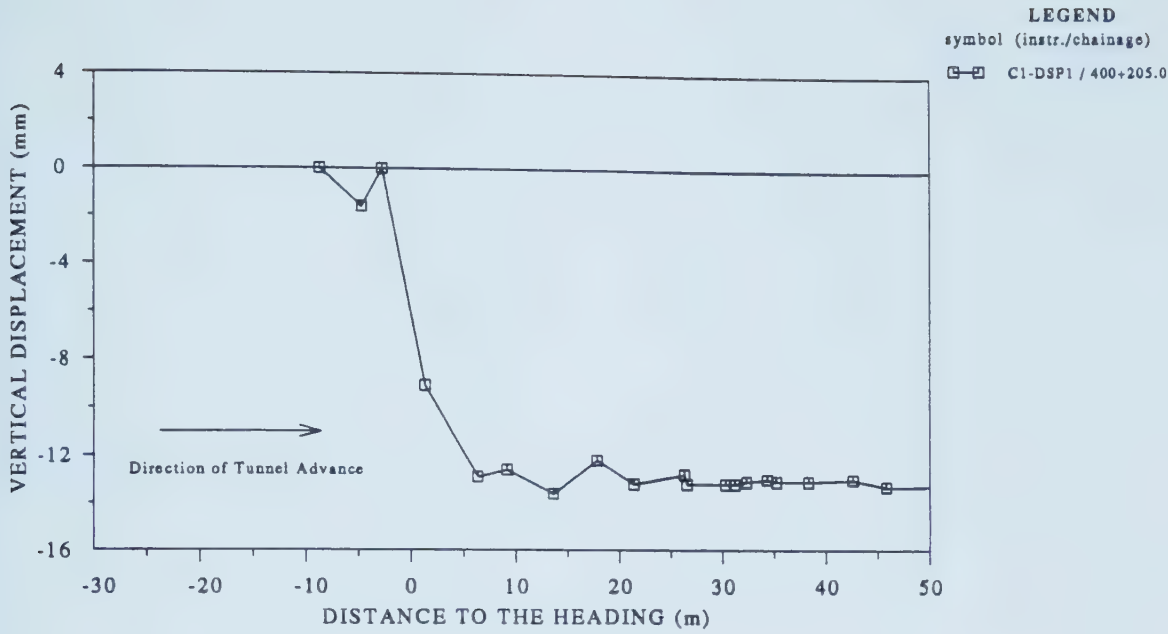


Figure A.42 Measured Vertical Displacements with Tunnel Heading Advancing, C1-DSP1 (Deep Settlement Point)

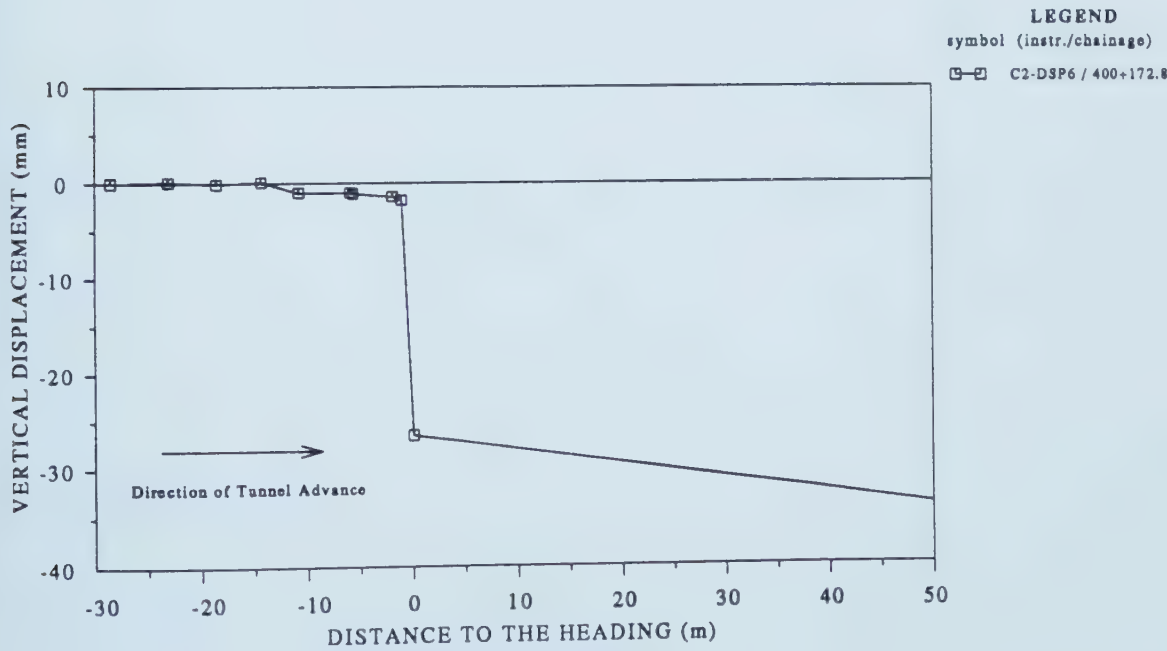


Figure A.43 Measured Vertical Displacements with Tunnel Heading Advancing, C2-DSP6 (Deep Settlement Point)

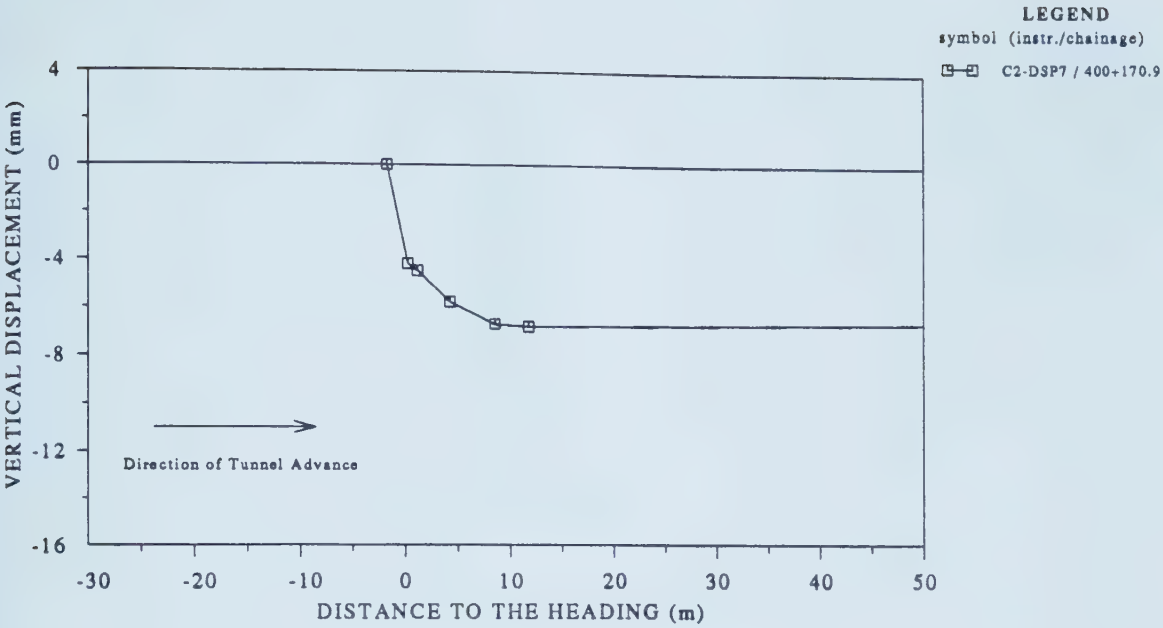


Figure A.44 Measured Vertical Displacements with Tunnel Heading Advancing, C2-DSP7 (Deep Settlement Point)

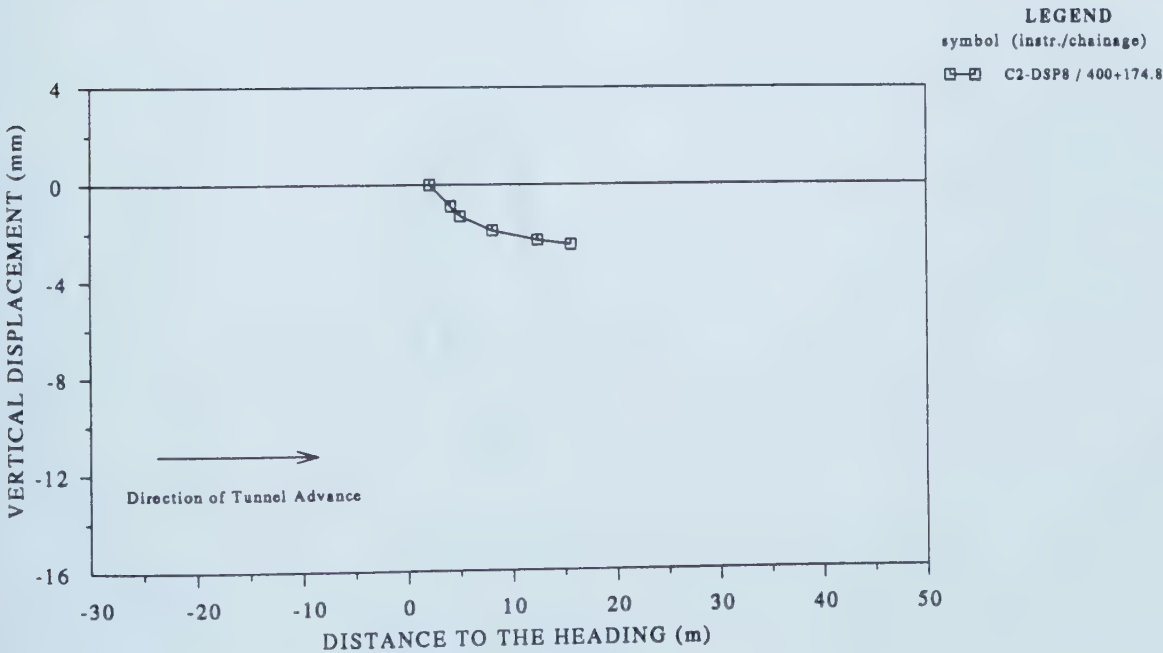


Figure A.45 Measured Vertical Displacements with Tunnel Heading Advancing, C2-DSP8 (Deep Settlement Point)

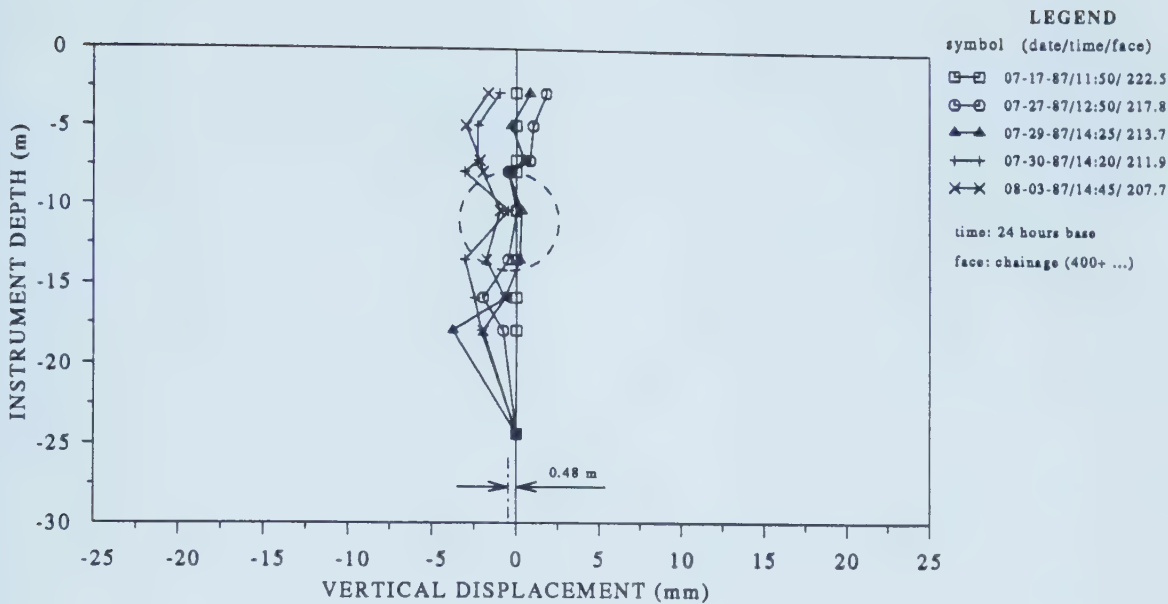


Figure A.46 Measured Vertical Displacement Profile, Multipoint Extensometer C1-M1

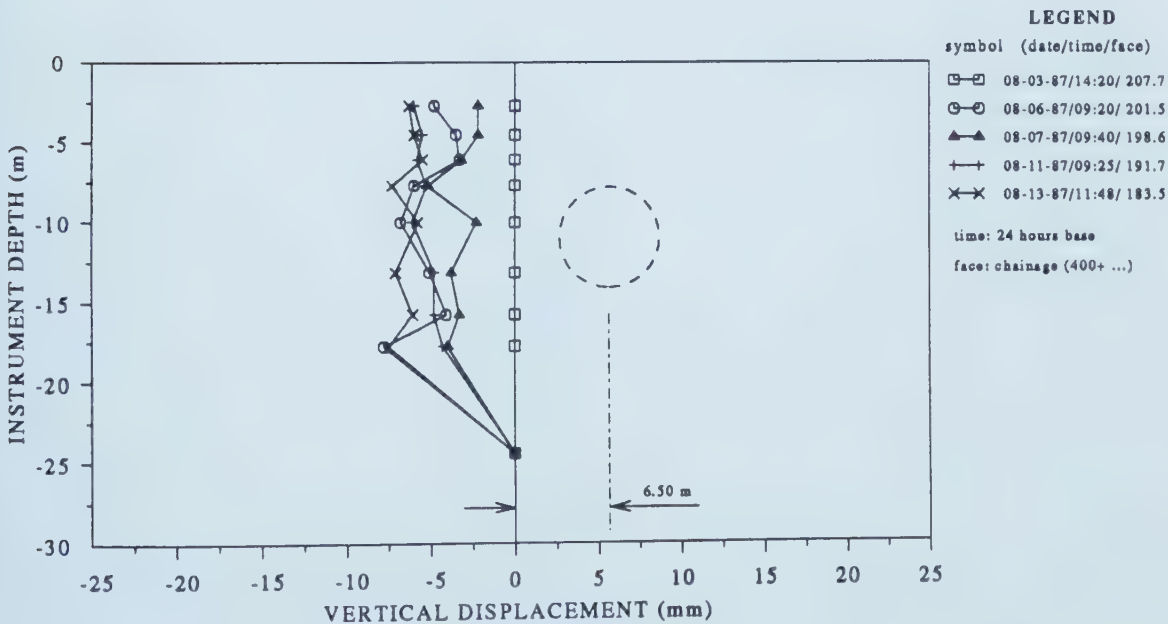


Figure A.47 Measured Vertical Displacement Profile, Multipoint Extensometer C1-M2

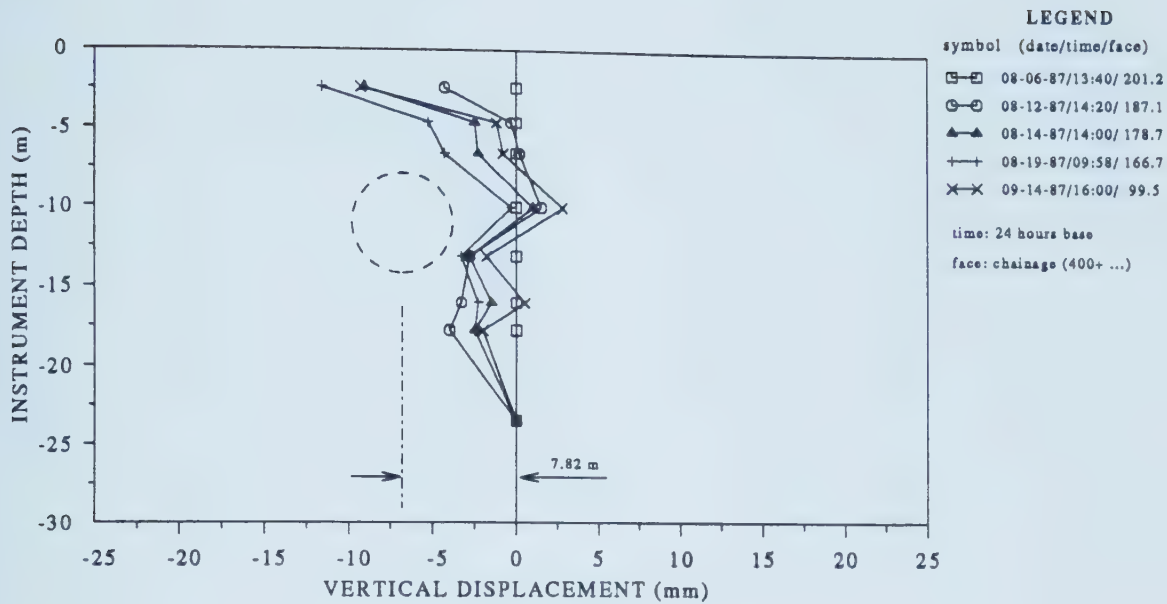


Figure A.48 Measured Vertical Displacement Profile, Multipoint Extensometer C2-M1

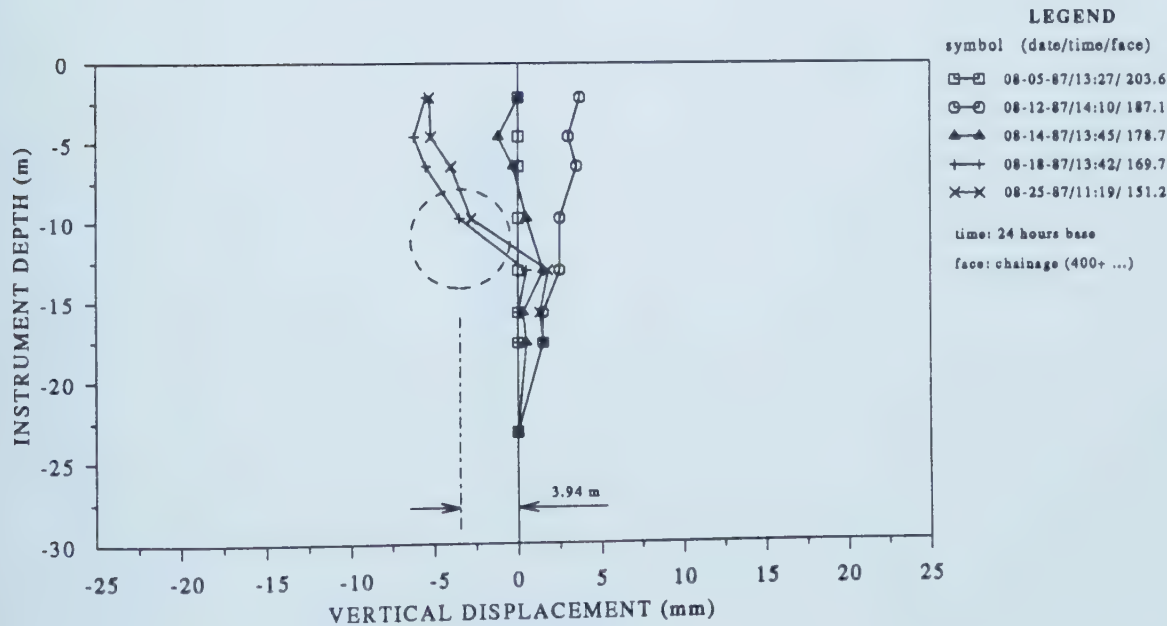


Figure A.49 Measured Vertical Displacement Profile, Multipoint Extensometer C2-M2

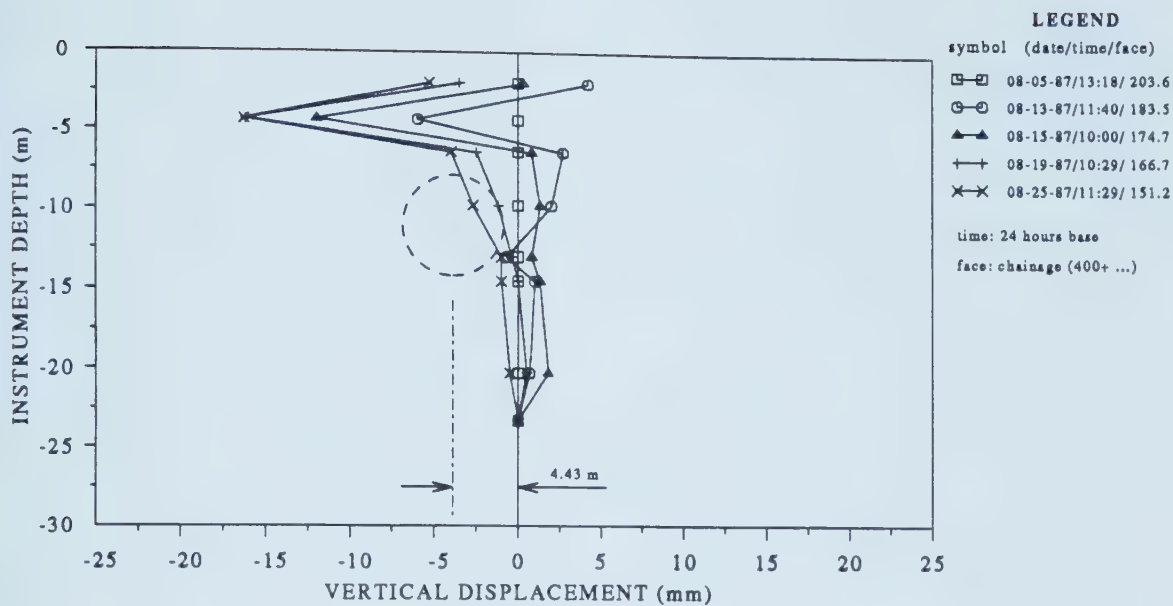


Figure A.50 Measured Vertical Displacement Profile, Multipoint Extensometer C2-M3

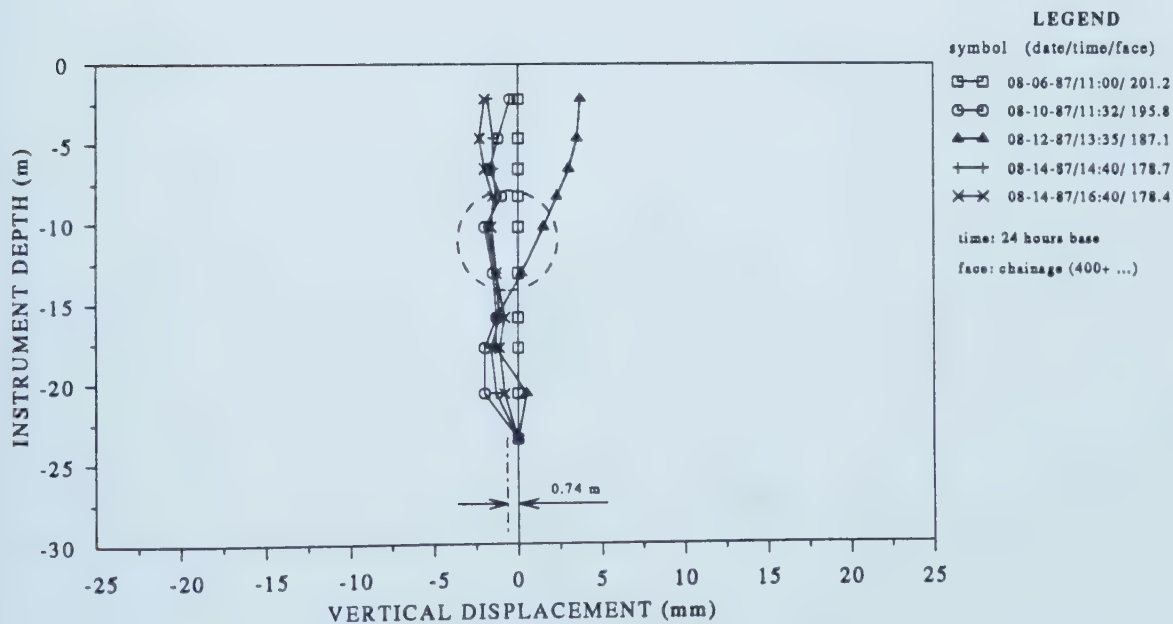


Figure A.51 Measured Vertical Displacement Profile, Multipoint Extensometer C2-M4

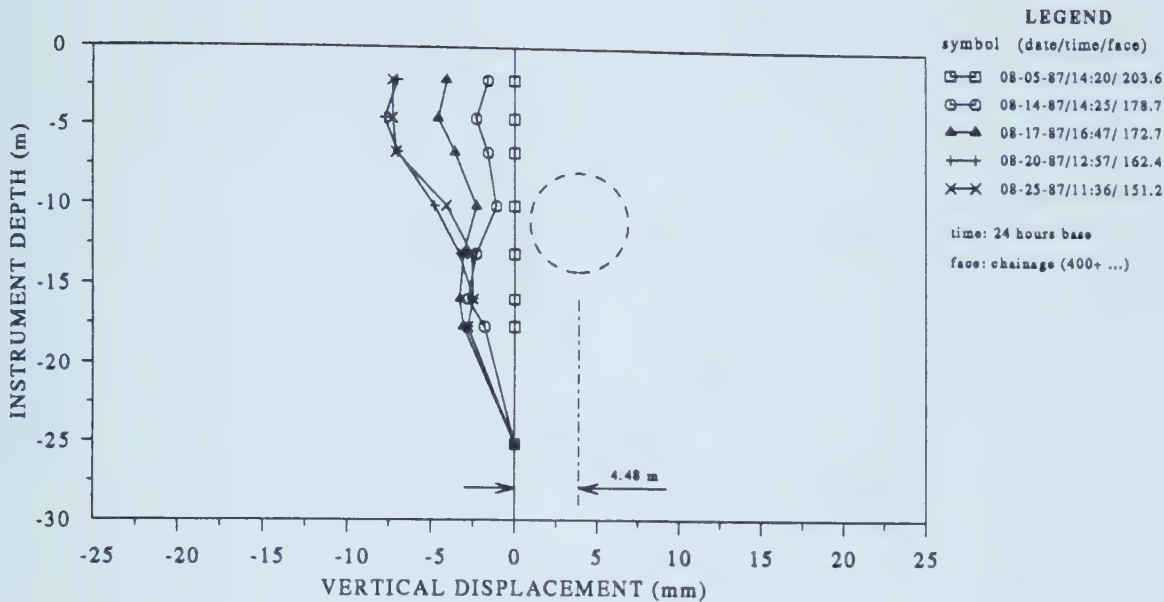


Figure A.52 Measured Vertical Displacement Profile, Multipoint Extensometer C2-M5

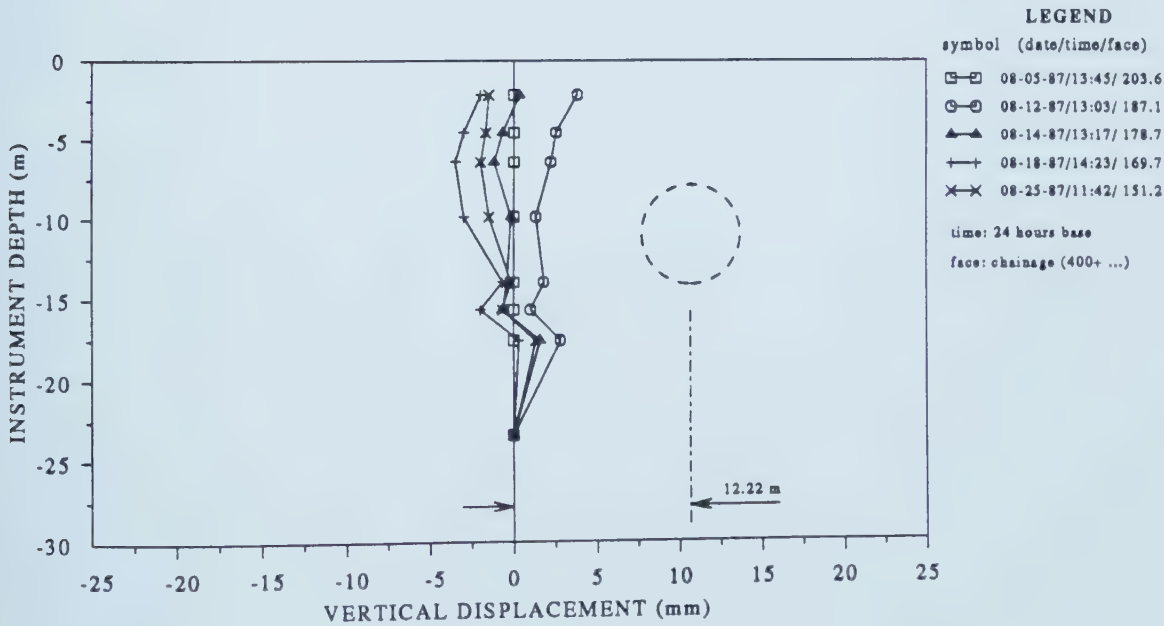


Figure A.53 Measured Vertical Displacement Profile, Multipoint Extensometer C2-M6

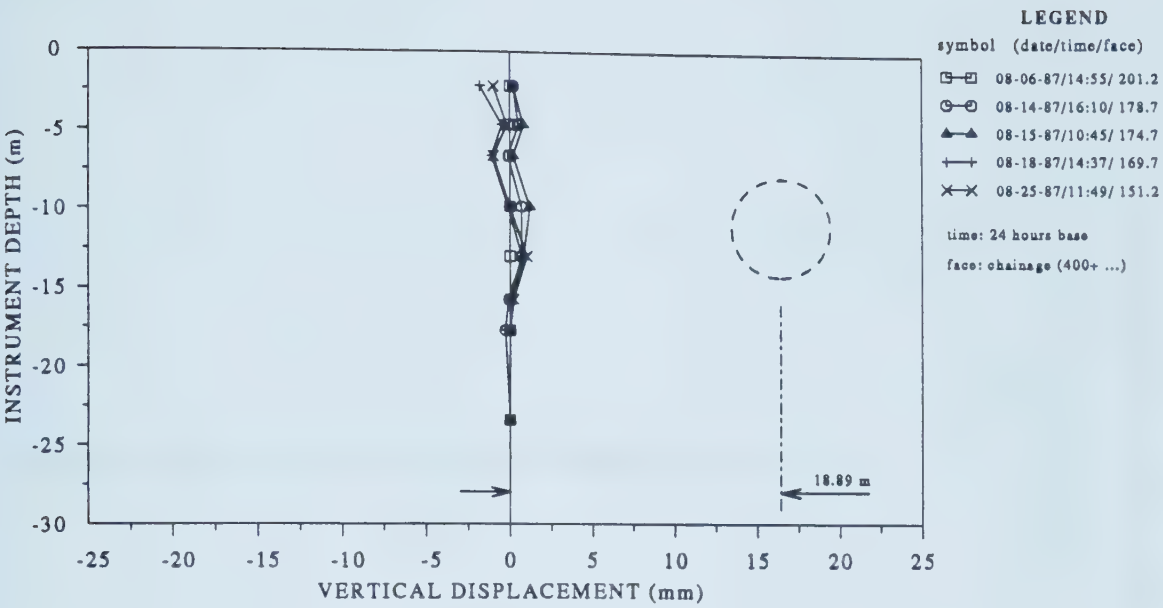


Figure A.54 Measured Vertical Displacement Profile, Multipoint Extensometer C2-M7

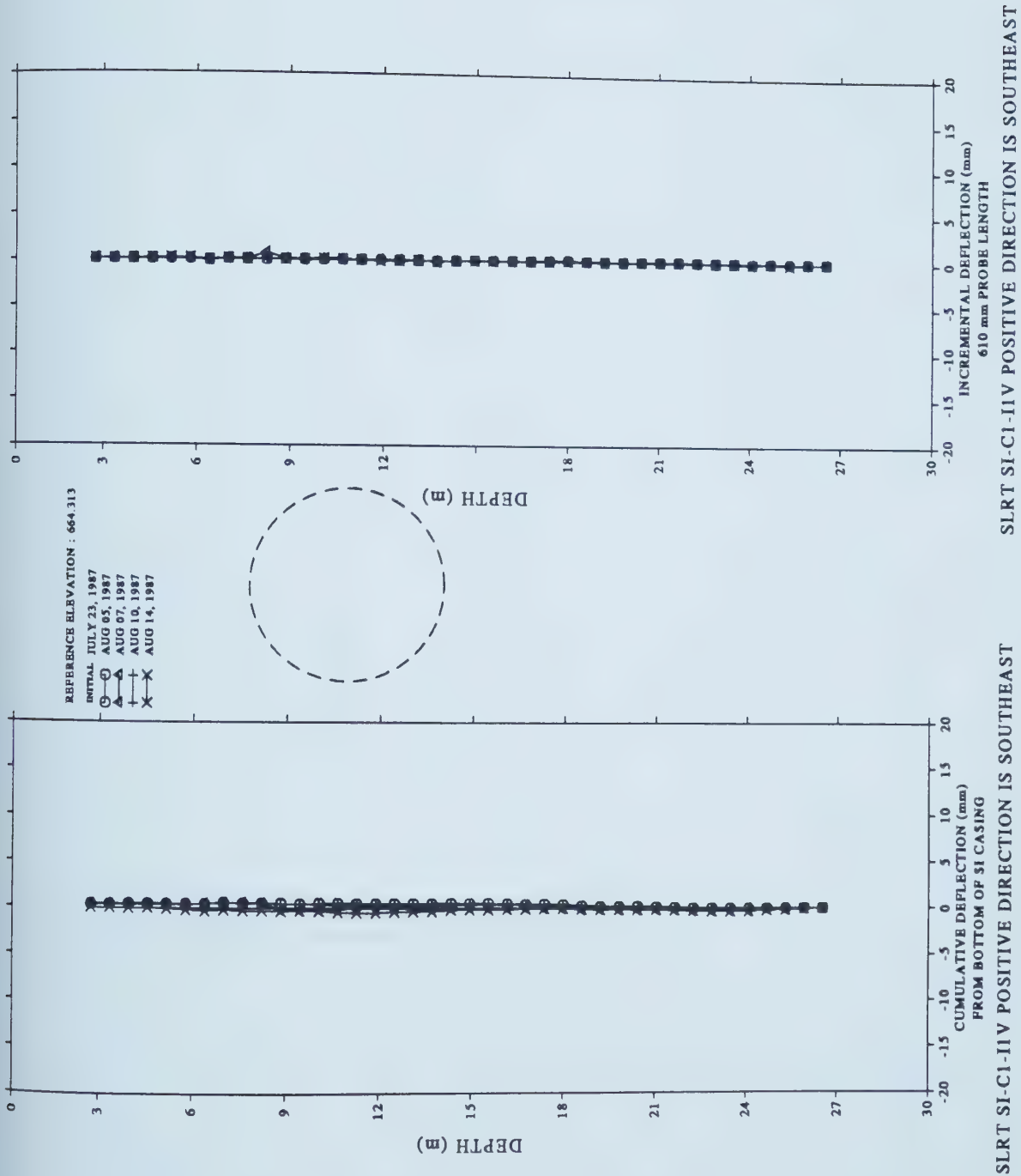


Figure A.55 Measured Horizontal Displacement Profile, Perpendicular to Tunnel Axis, Slope Indicator C1-II

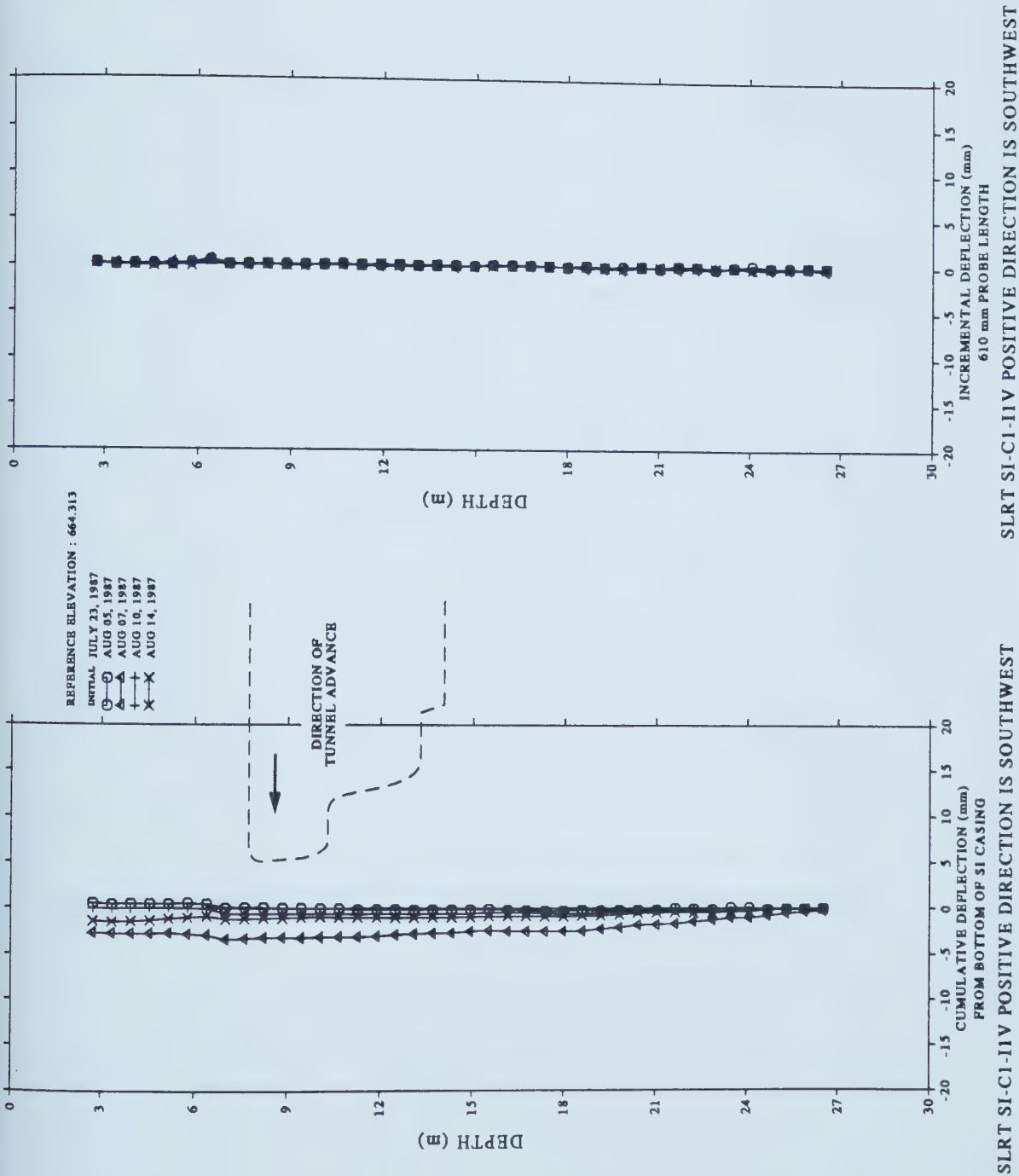


Figure A.56 Measured Horizontal Displacement Profile, Parallel to Tunnel Axis, Slope Indicator C1-I1

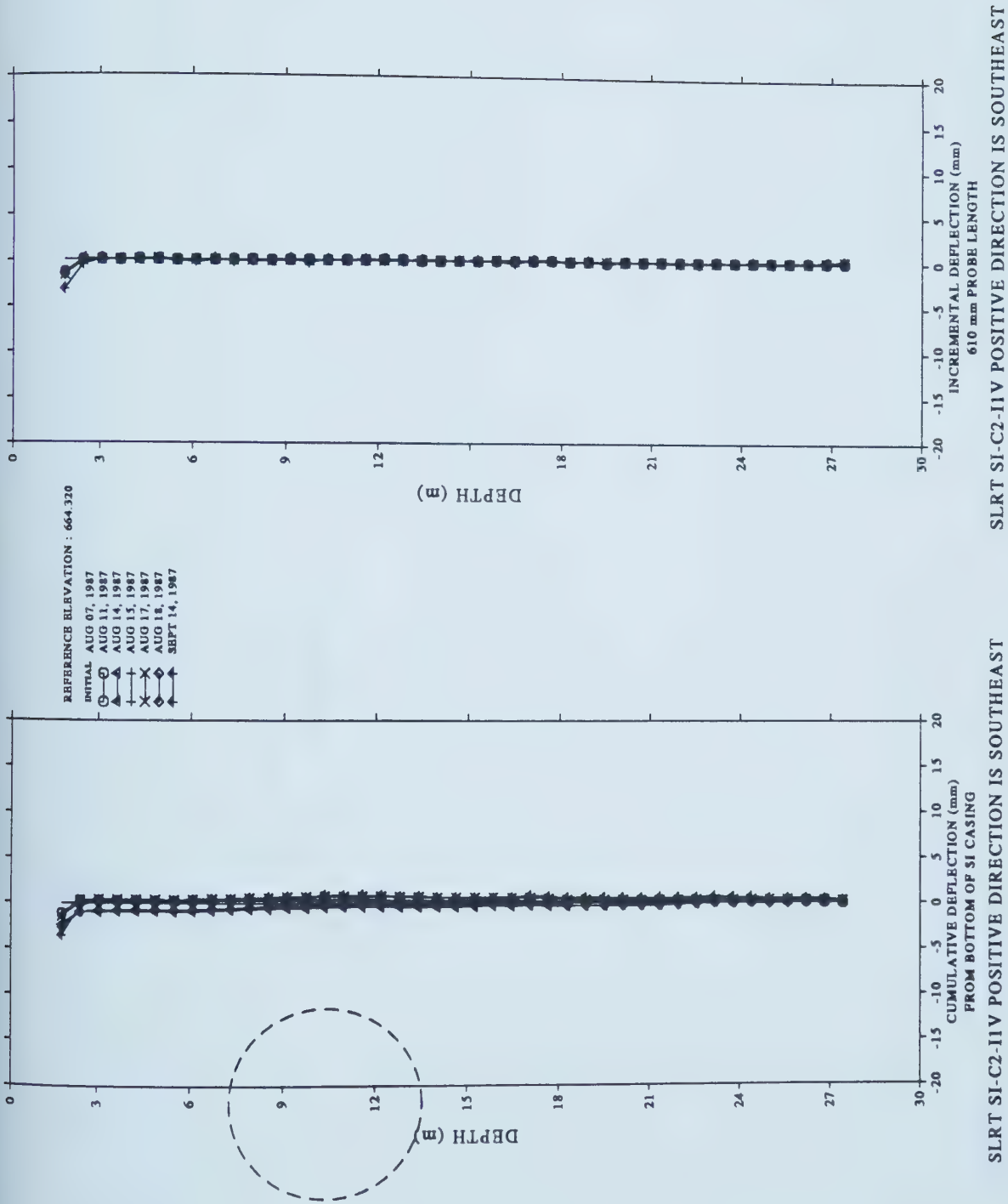


Figure A.57 Measured Horizontal Displacement Profile, Perpendicular to Tunnel Axis, Slope Indicator C2-I1

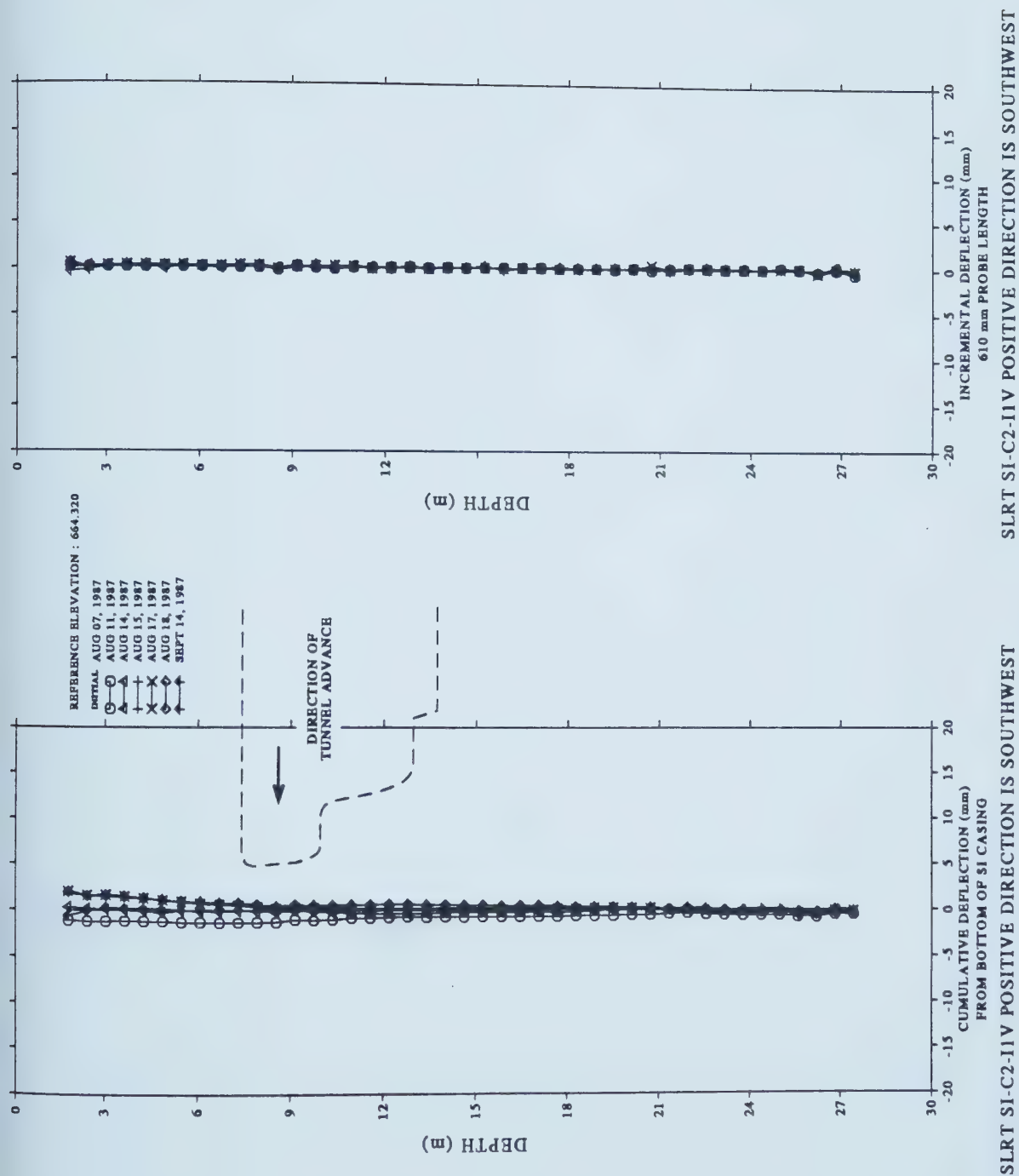


Figure A.58 Measured Horizontal Displacement Profile, Parallel to Tunnel Axis, Slope Indicator C2-I1

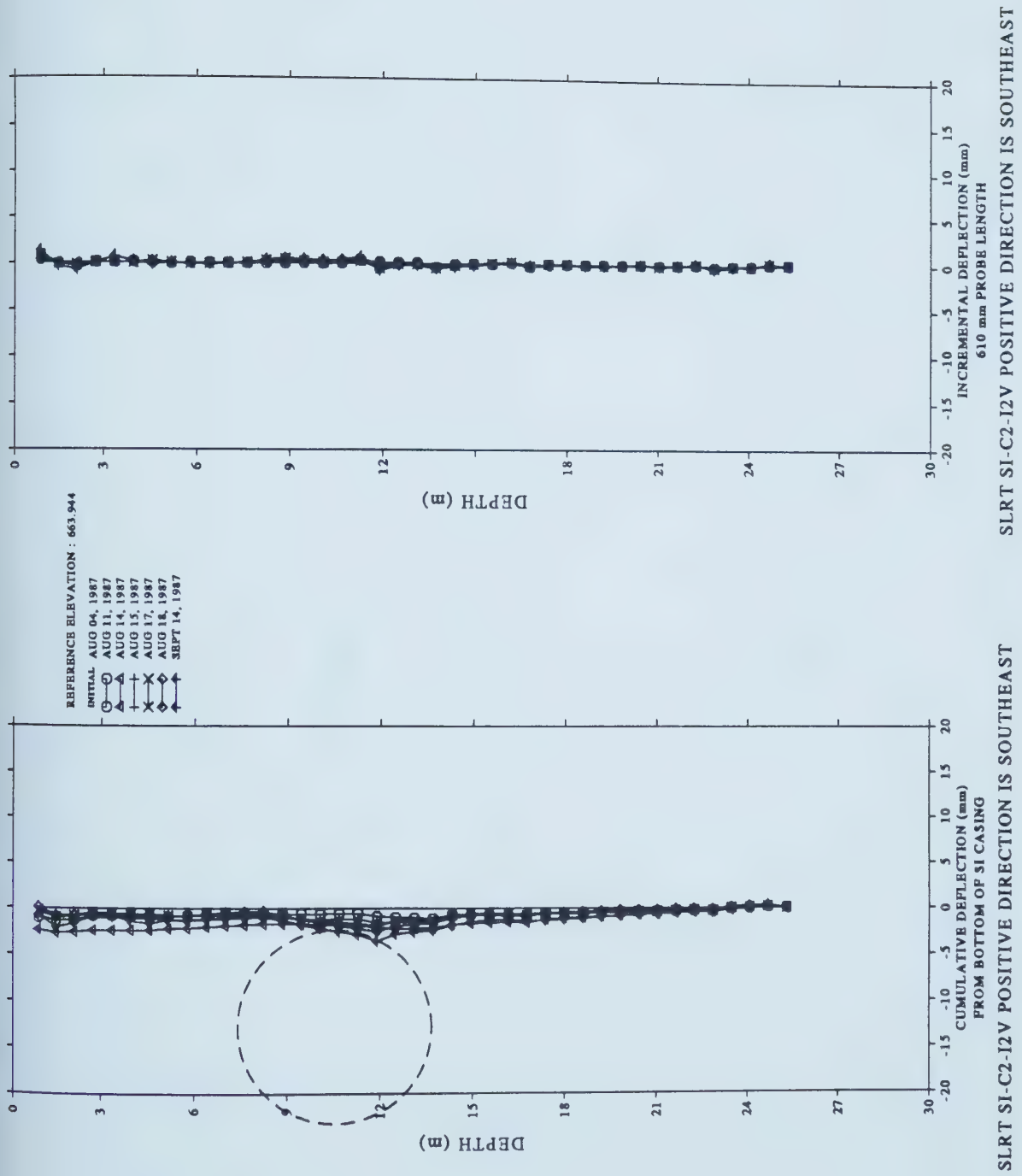


Figure A.59 Measured Horizontal Displacement Profile, Perpendicular to Tunnel Axis, Slope Indicator C2-I2

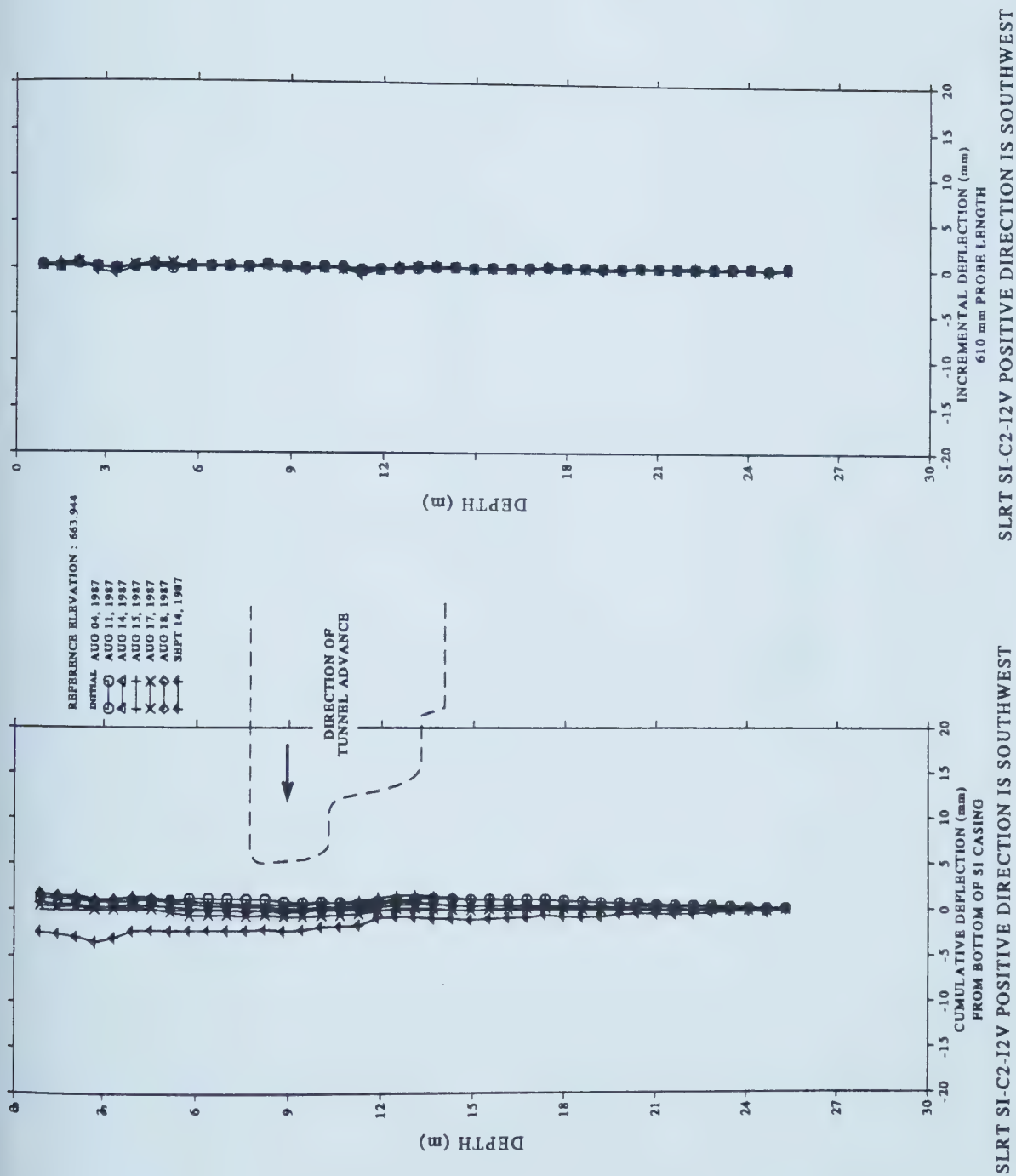


Figure A.60 Measured Horizontal Displacement Profile, Parallel to Tunnel Axis, Slope Indicator C2-12

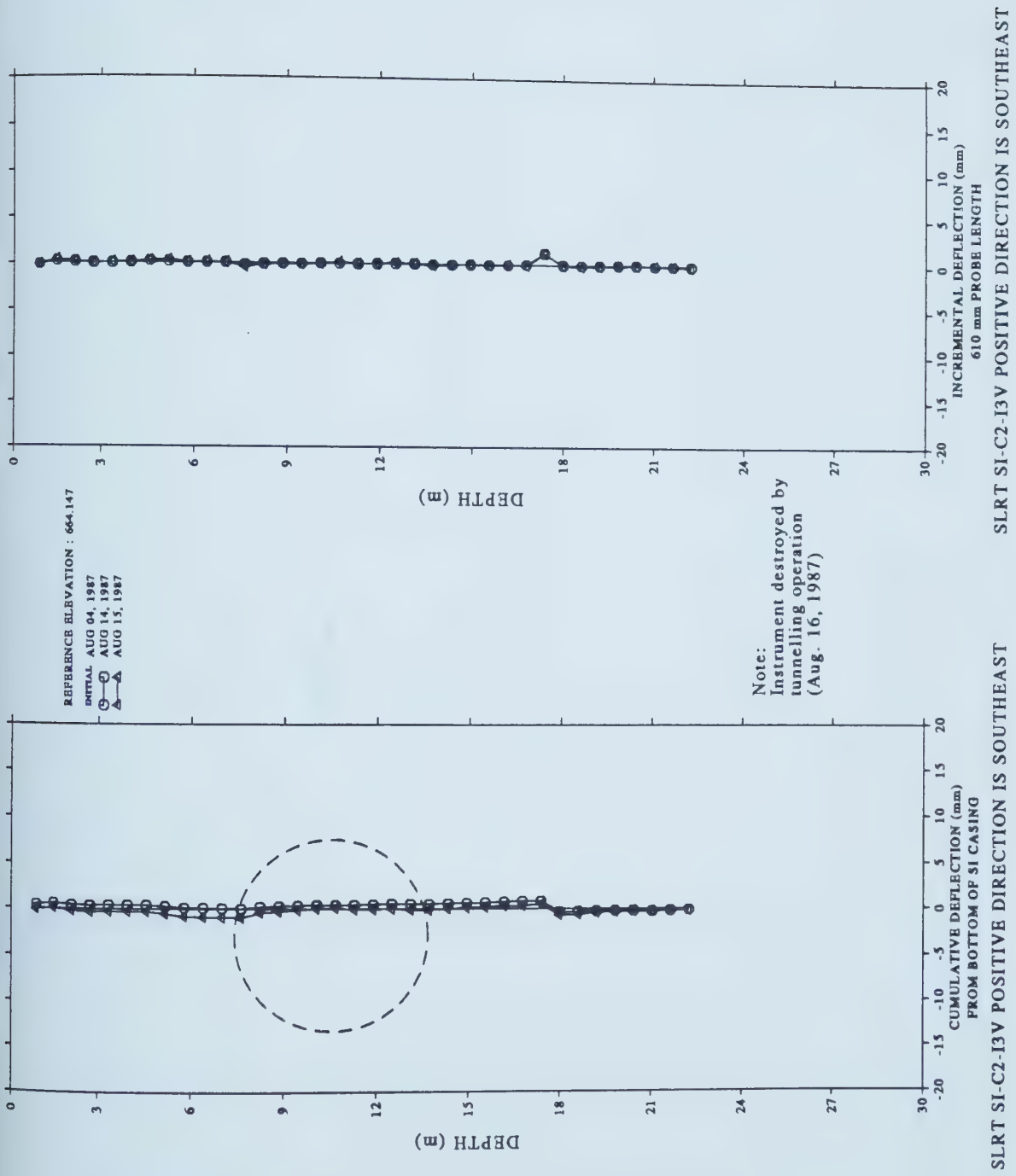


Figure A.61 Measured Horizontal Displacement Profile, Perpendicular to Tunnel Axis, Slope Indicator C2-I3

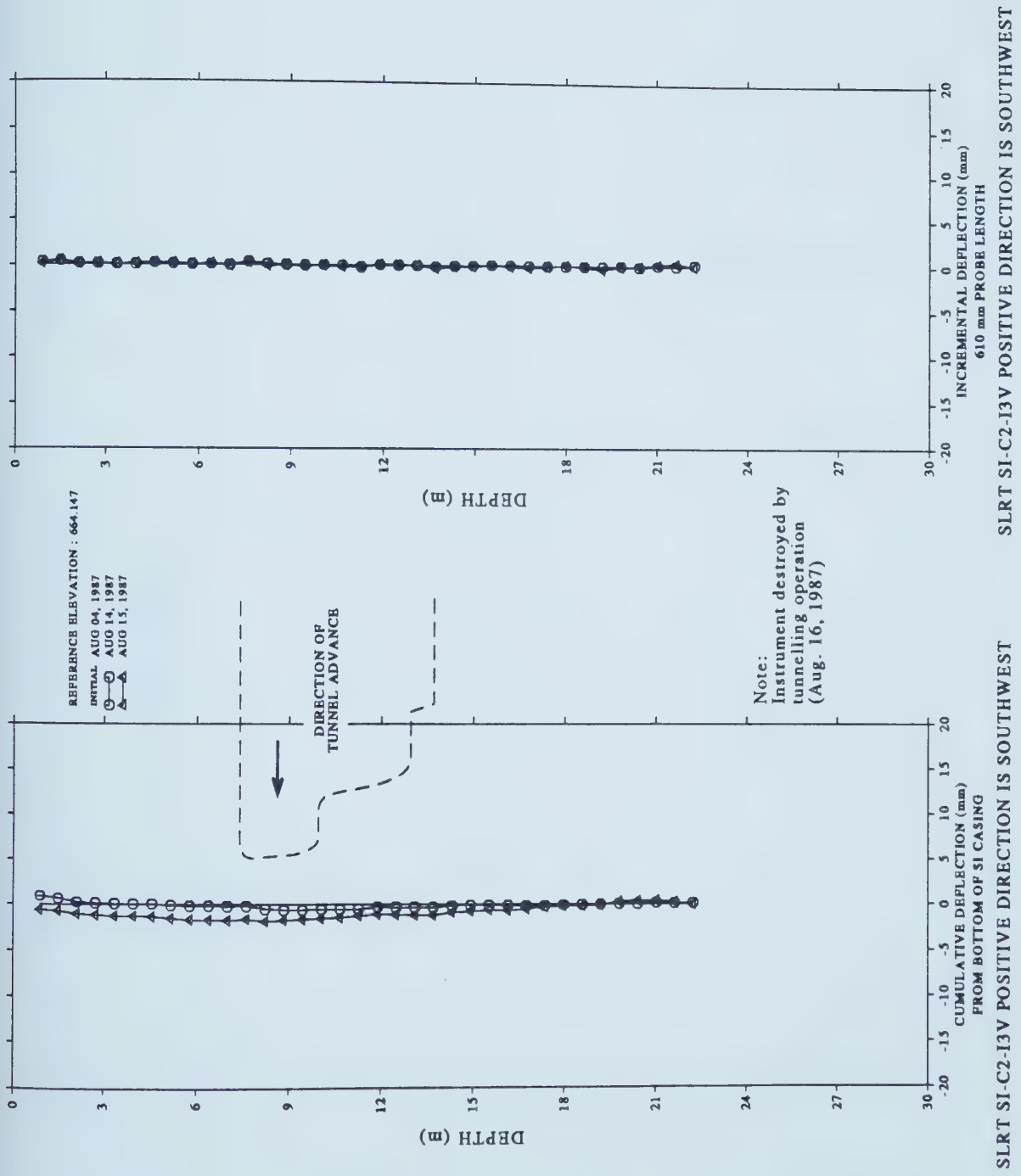


Figure A.62 Measured Horizontal Displacement Profile, Parallel to Tunnel Axis, Slope Indicator C2-13

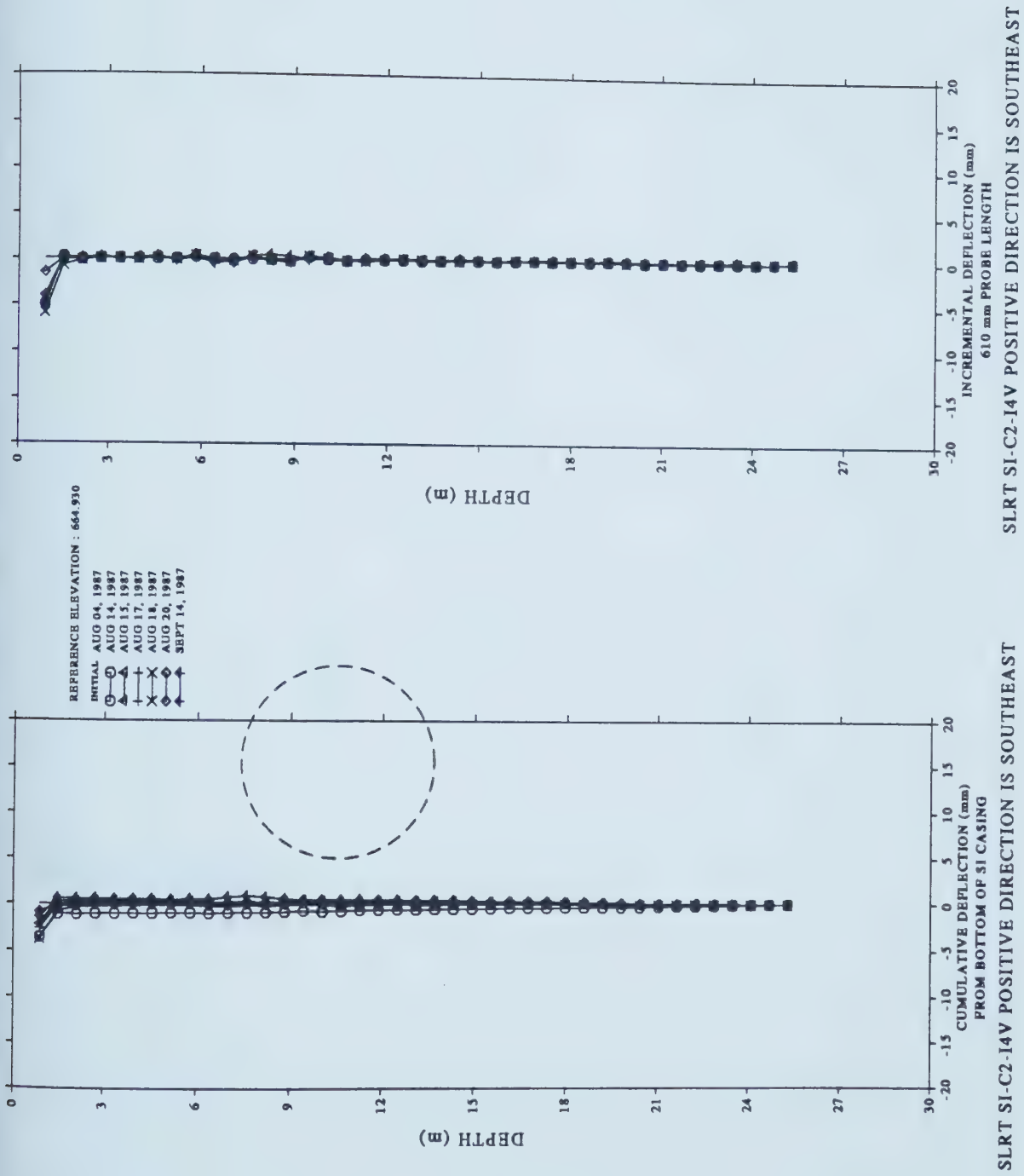


Figure A.63 Measured Horizontal Displacement Profile, Perpendicular to Tunnel Axis, Slope Indicator C2-14

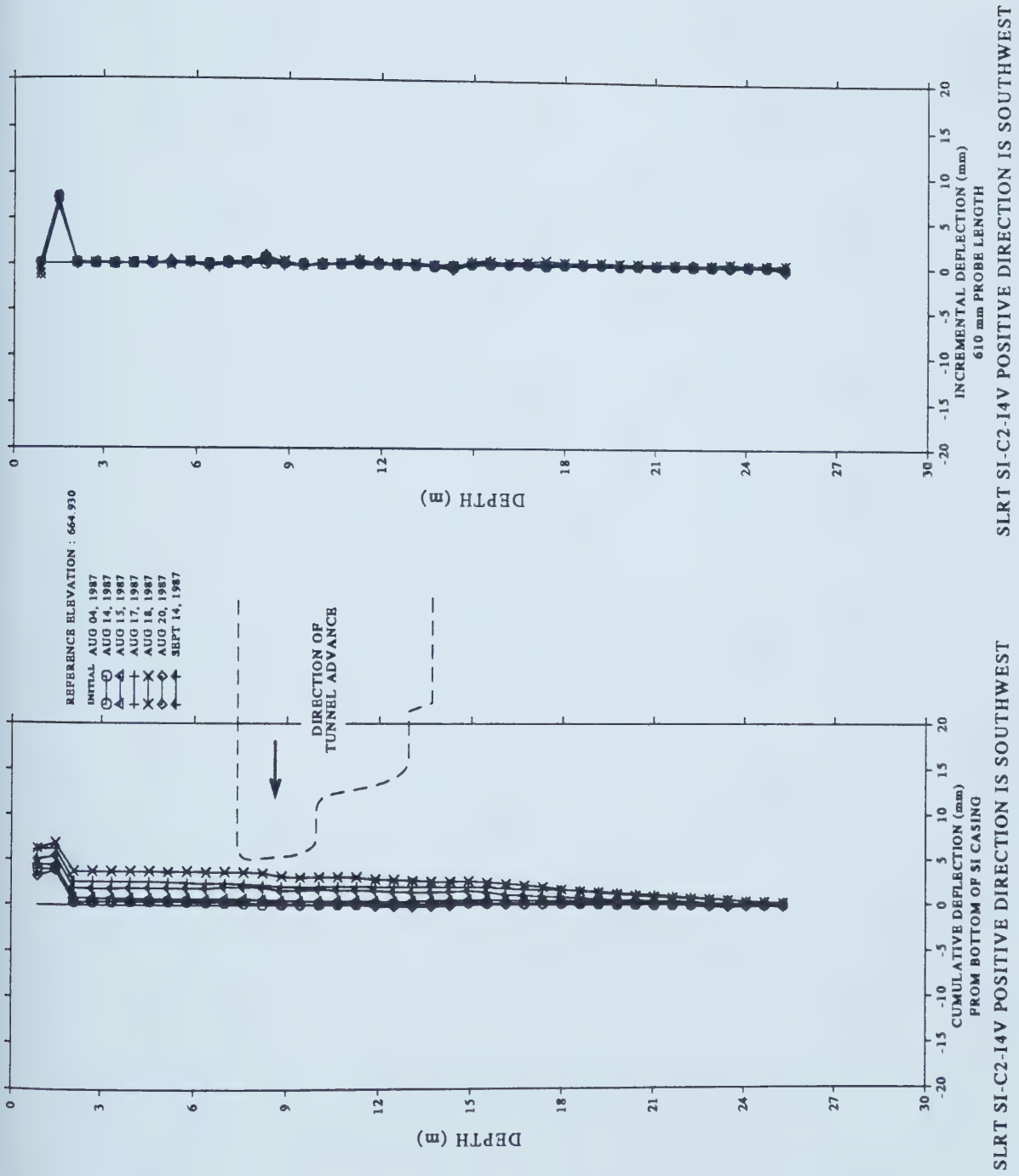


Figure A.64 Measured Horizontal Displacement Profile, Parallel to Tunnel Axis, Slope Indicator C2-14

APPENDIX B - Data from Lining Instrumentation of the SLRT Project

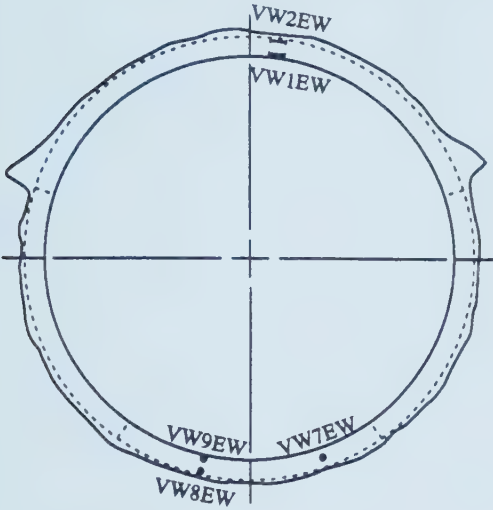
Table B.1 Timetable of Tunnel Lining Instrumentation

SECTION	REGION	END OF SHOTCRETE	INT. TYPE	LOCATION (STATION)	FIRST READING
C1	HEADING	07-Aug-87/02:50 PM	VW	400+201.2m	07-Aug-87/03:00 PM
	INVERT	11-Aug-87/12:30 AM	VW	400+201.2m	11-Aug-87/12:35 AM
C2I	HEADING	28-Aug-87/06:15 PM	VW	400+136.2 m	28-Aug-87/06:25 PM
			CG	400+136.2 m	28-Aug-87/06:20 PM
			RS	400+136.7 m	28-Aug-87/06:20 PM
	INVERT	31-Aug-87/07:55 PM	VW	400+136.2 m	31-Aug-87/08:05 PM
			TPC	400+136.2 m	31-Aug-87/07:55 PM
			CG	400+136.2 m	31-Aug-87/08:15 PM
			RS	400+136.7 m	31-Aug-87/08:00 PM
C2II	HEADING	31-Aug-87/02:30 PM	VW	400+132.2 m	31-Aug-87/02:35 PM
			TPC	400+132.2 m	31-Aug-87/03:00 PM
			CG	400+132.2 m	31-Aug-87/02:42 PM
	INVERT	01-Sep-87/11:40 PM	VW	400+132.2 m	01-Sep-87/11:45 PM
			TPC	400+132.3 m	01-Sep-87/11:55 PM
			RS	400+132.7 m	02-Sep-87/12:05 AM
C2III	HEADING	01-Sep-87/01:15 AM	VW	400+131.2 m	01-Sep-87/11:15 AM (*)
			TPC	400+131.2 m	01-Sep-87/11:22 AM (*)
			CG	400+131.2 m	01-Sep-87/08:00 AM (*)
			RS	400+131.7 m	01-Sep-87/08:00 AM (*)
	INVERT	01-Sep-87/11:40 PM	VW	400+131.2 m	01-Sep-87/11:45 PM
			CG	400+131.2 m	02-Sep-87/12:05 AM
			RS	400+131.7 m	02-Sep-87/12:05 AM

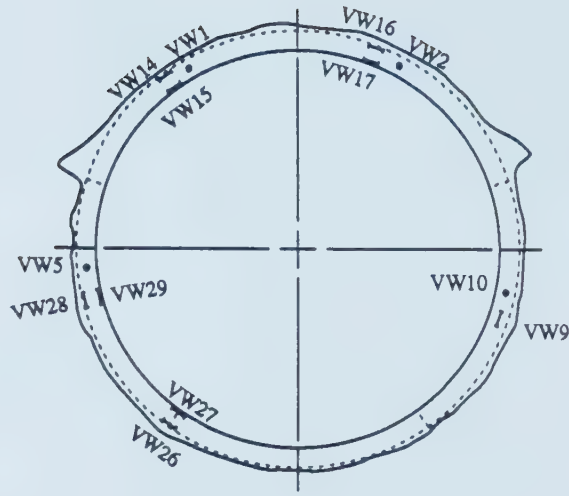
1. VW = Vibrating Wire strain gage embedded in shotcrete
2. TPC = Total Pressure Cell installed in the soil-lining interface
3. CG = Compression strain Gage embedded in shotcrete
4. RS = Resistance Strain gage bonded on steel rib
- 5 (*) = delayed first readings of the instruments

LEGEND:

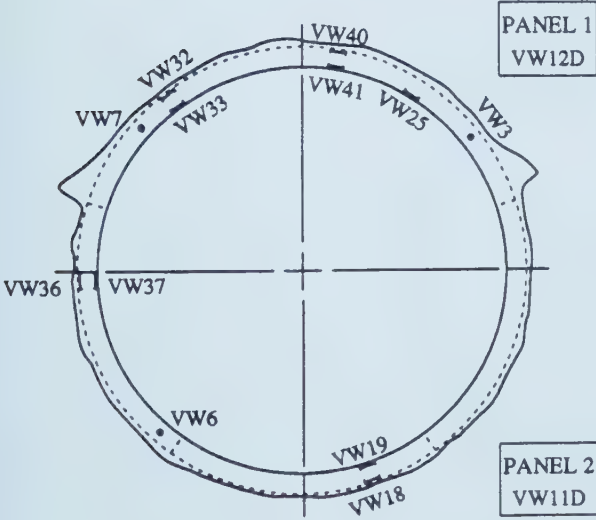
- parallel to tunnel axis
- perpendicular to tunnel axis



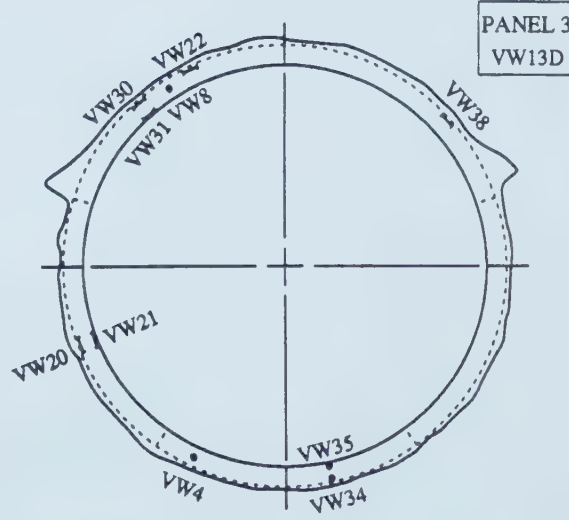
SECTION : C1I
 LOCATION : between ribs 26 and 27
 STATION : 400+201.7 m to 400+200.7 m



SECTION : C2I
 LOCATION : between ribs 87 and 88
 STATION : 400+136.7 m to 400+135.7 m



SECTION : C2II
 LOCATION : between ribs 91 and 92
 STATION : 400+132.7 m to 400+131.7 m

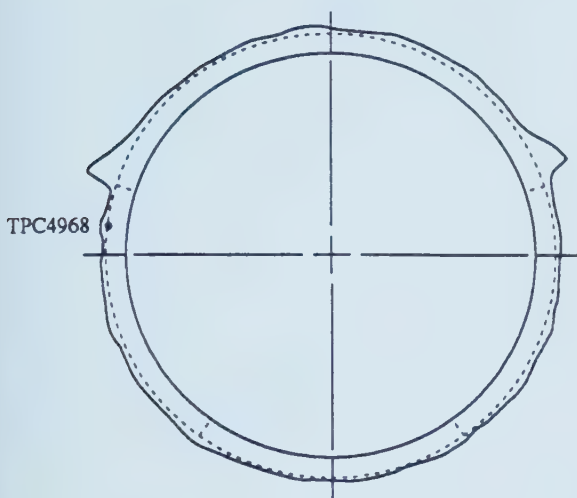


SECTION : C2III
 LOCATION : between ribs 92 and 93
 STATION : 400+131.7 m to 400+130.7 m

Figure B.1 Layout of Vibrating Wire Strain Gages (VW) Installed in Tunnel Lining

LEGEND:

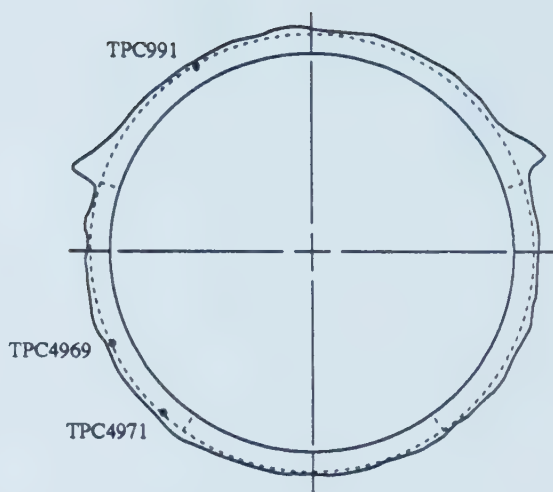
- parallel to tunnel axis
- perpendicular to tunnel axis



SECTION : C2I

LOCATION : between ribs 87 and 88

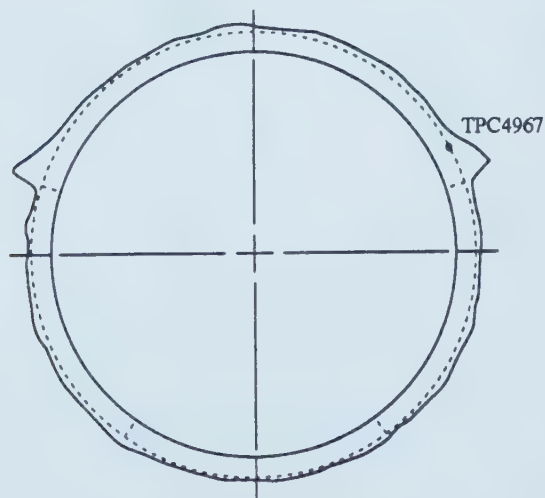
STATION : 400+136.7 m to 400+135.7 m



SECTION : C2II

LOCATION : between ribs 91 and 92

STATION : 400+132.7 m to 400+131.7 m



SECTION : C2III

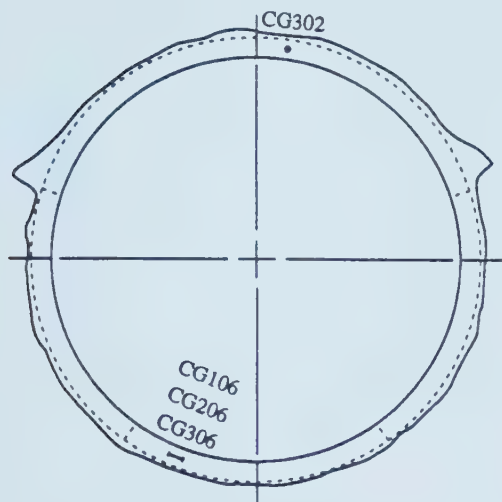
LOCATION : between ribs 92 and 93

STATION : 400+131.7 m to 400+130.7 m

Figure B.2 Layout of Total Pressure Cells (TPC) Installed in Tunnel Lining

LEGEND:

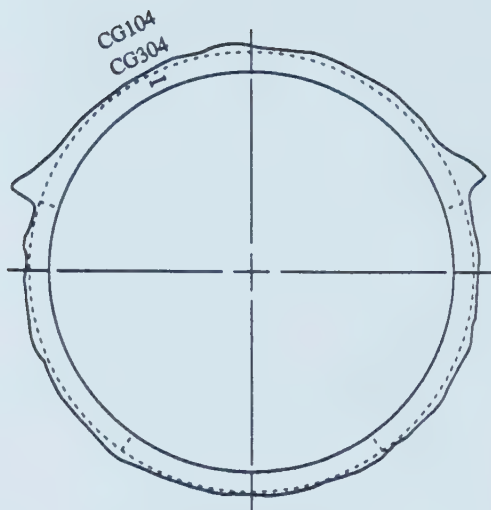
- parallel to tunnel axis
- perpendicular to tunnel axis



SECTION : C2I

LOCATION : between ribs 87 and 88

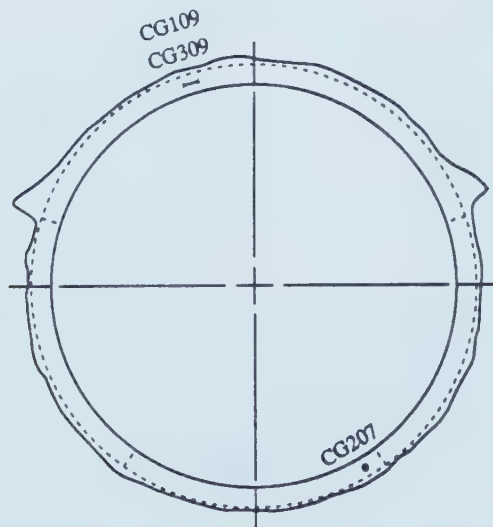
STATION : 400+136.7 m to 400+135.7 m



SECTION : C2II

LOCATION : between ribs 91 and 92

STATION : 400+132.7 m to 400+131.7 m

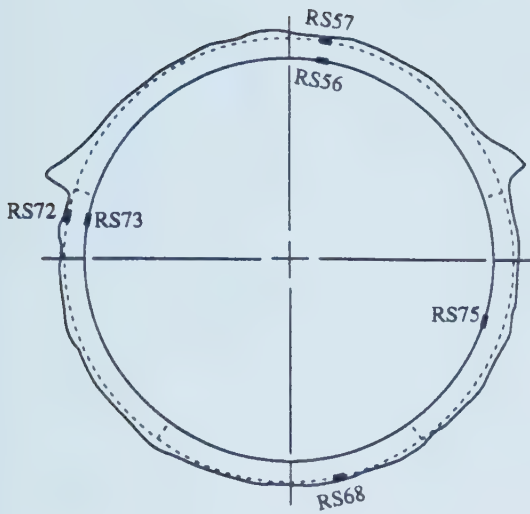


SECTION : C2III

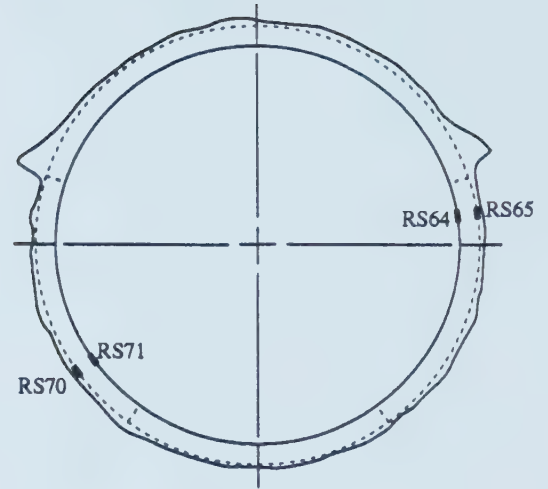
LOCATION : between ribs 92 and 93

STATION : 400+131.7 m to 400+130.7 m

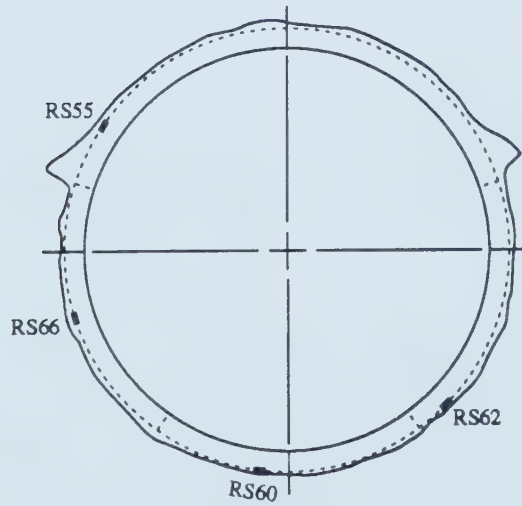
Figure B.3 Layout of Compression Gages (CG) Installed in Tunnel Lining



SECTION : C2I
 LOCATION : rib 87
 STATION : 400+136.7 m



SECTION : C2II
 LOCATION : rib 91
 STATION : 400+132.7 m



SECTION : C2III
 LOCATION : rib 92
 STATION : 400+131.7 m

Figure B.4 Layout of Resistance Strain Gages (RS) Bonded on Steel Ribs

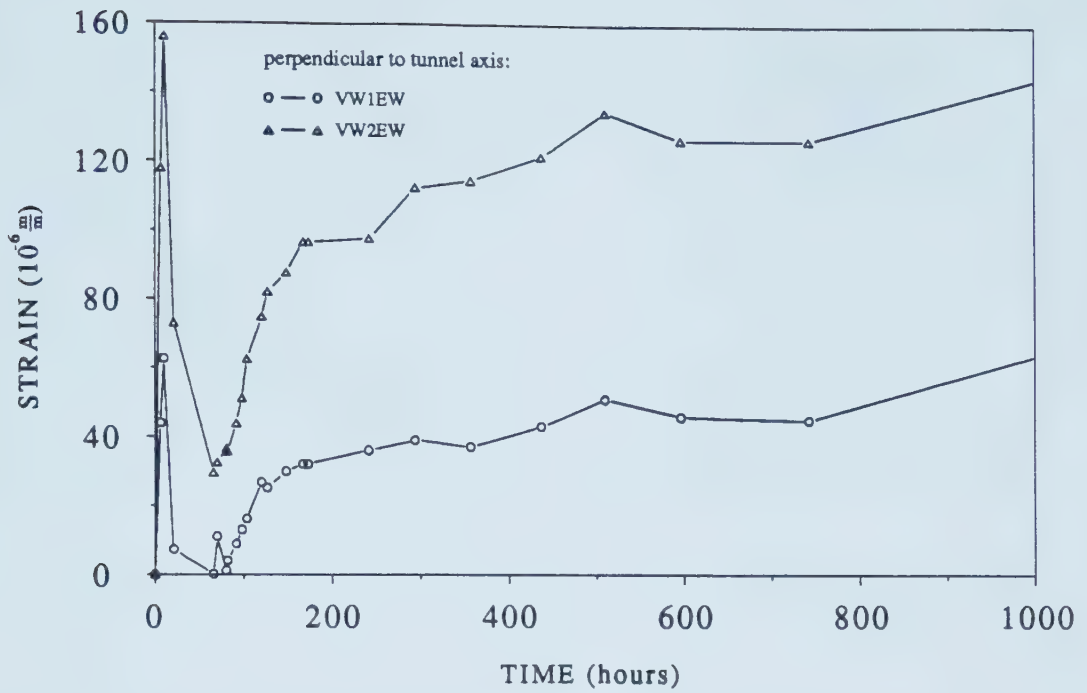


Figure B.5 Measured Strains from Gages Embedded in Shotcrete, Section C1I, Crown Region, Large Overcut

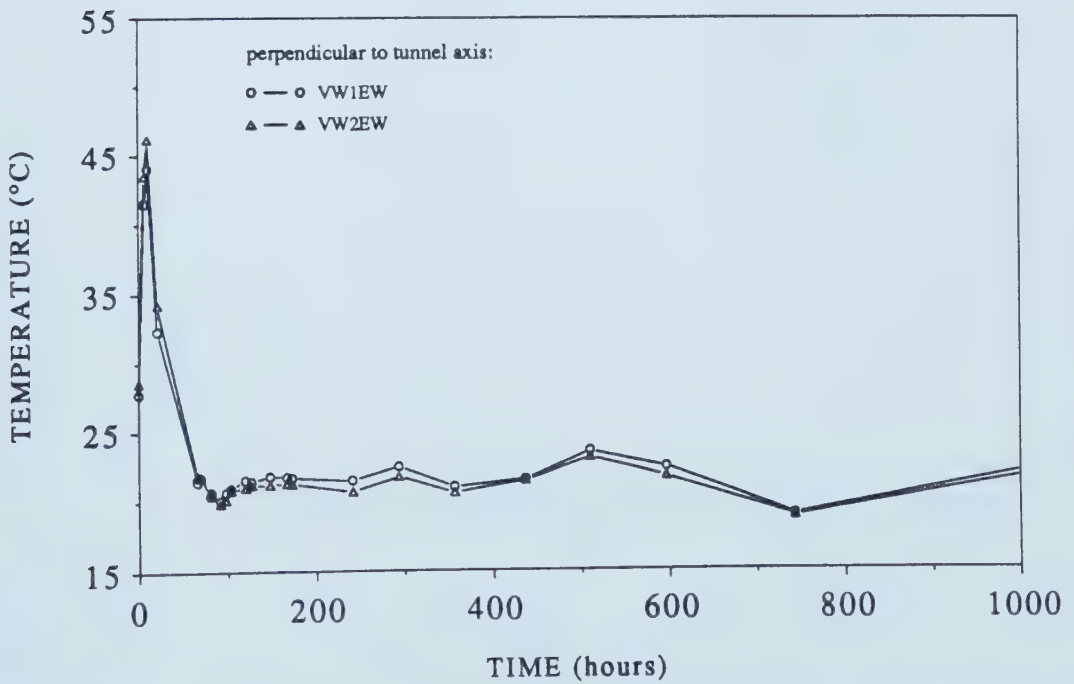


Figure B.6 Measured Temperatures from Gages Embedded in Shotcrete, Section C1I, Crown Region, Large Overcut

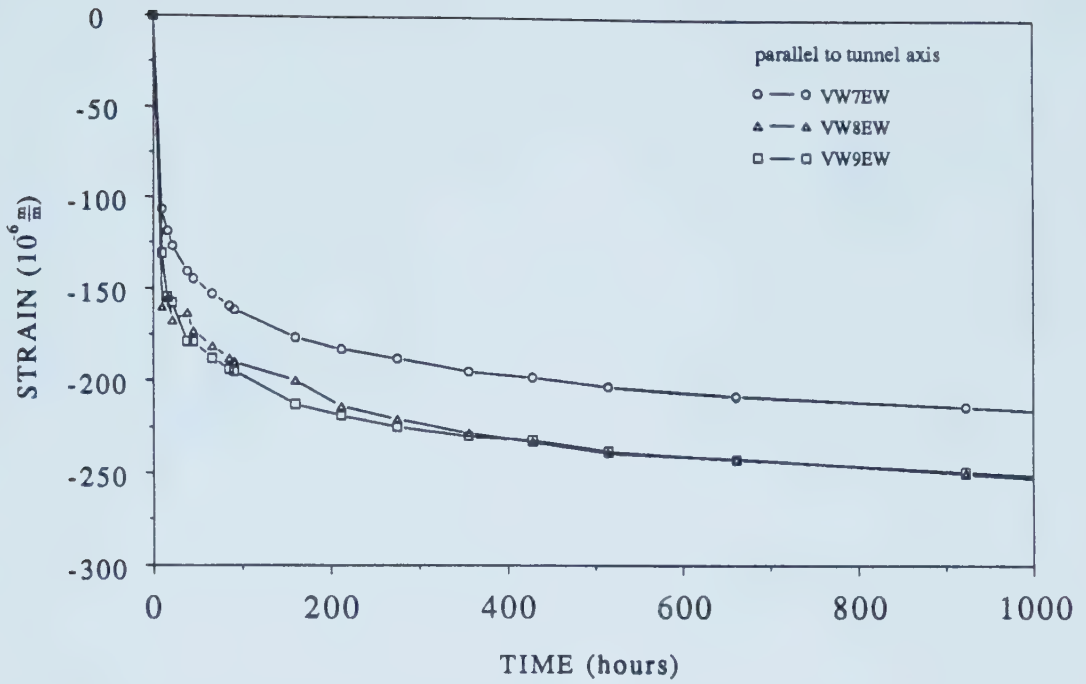


Figure B.7 Measured Strains from Gages Embedded in Shotcrete, Section C1I, Floor Region

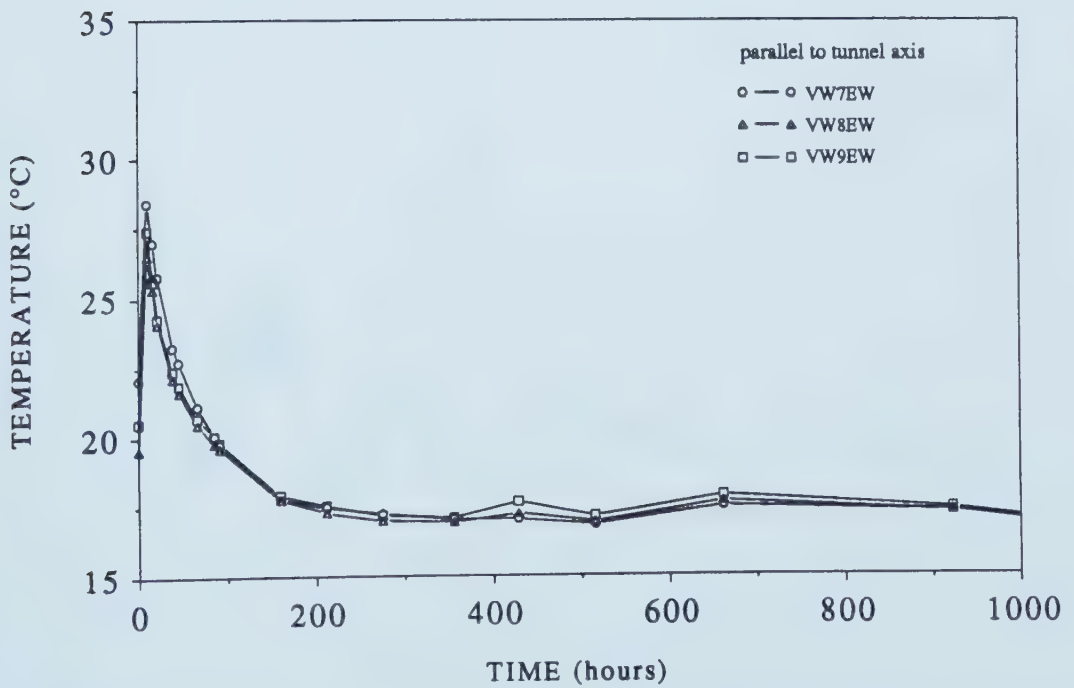


Figure B.8 Measured Temperatures from Gages Embedded in Shotcrete, Section C1I, Floor Region

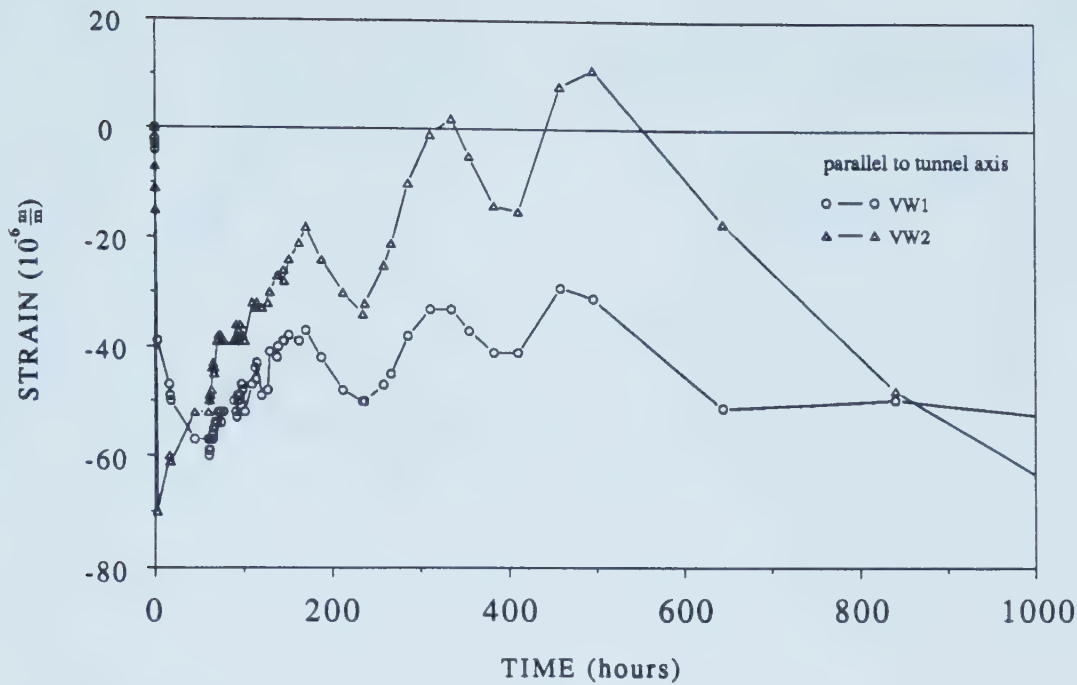


Figure B.9 Measured Strains from Gages Embedded in Shotcrete, Section C2I, Crown Region

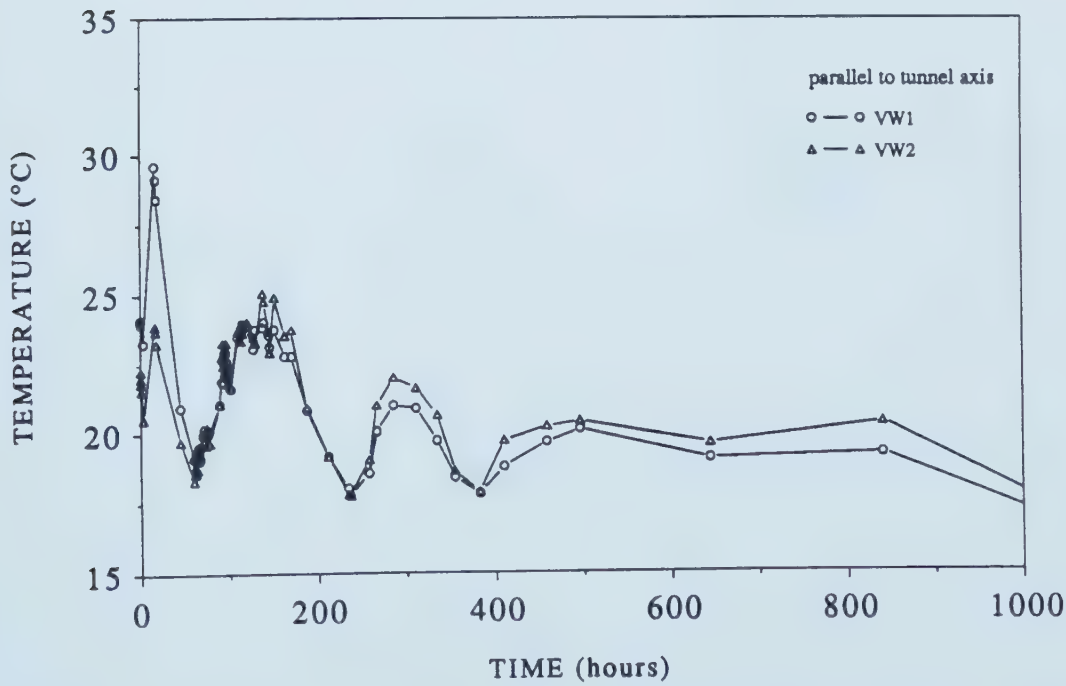


Figure B.10 Measured Temperatures from Gages Embedded in Shotcrete, Section C2I, Crown Region

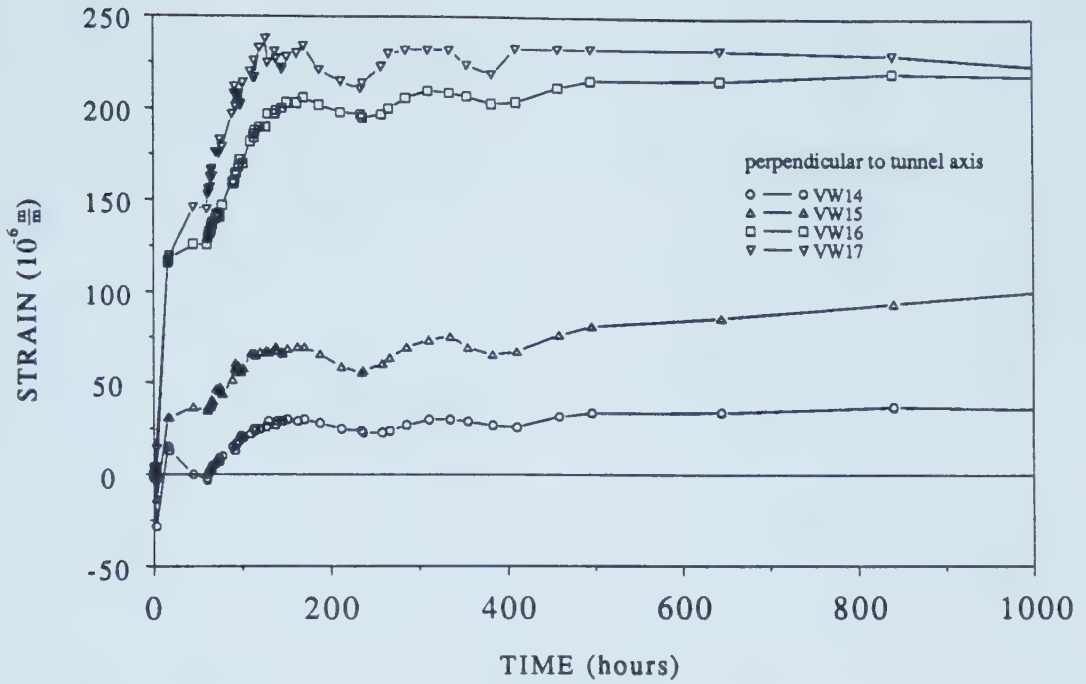


Figure B.11 Measured Strains from Gages Embedded in Shotcrete, Section C2I, Crown Region

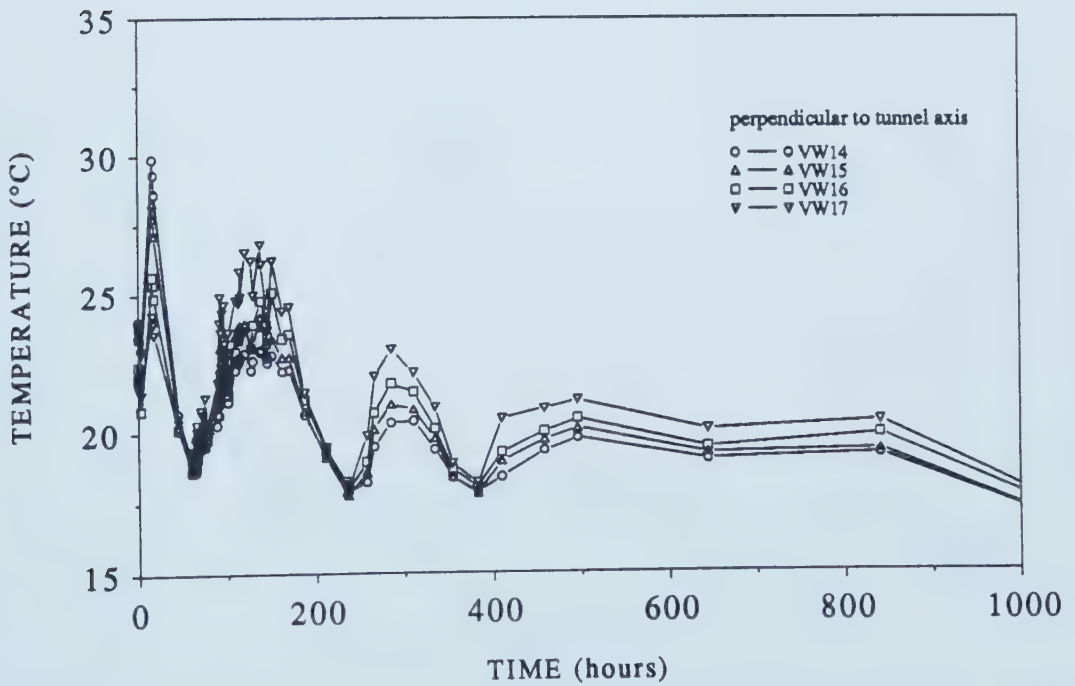


Figure B.12 Measured Temperatures from Gages Embedded in Shotcrete, Section C2I, Crown Region

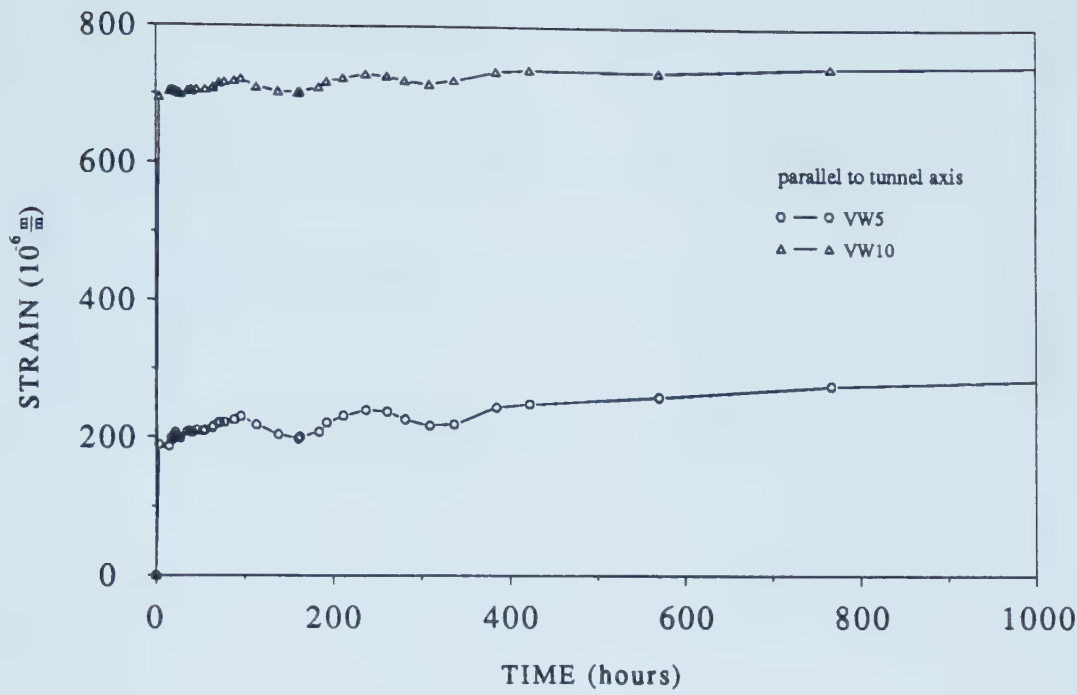


Figure B.13 Measured Strains from Gages Embedded in Shotcrete, Section C2I, Springline Region

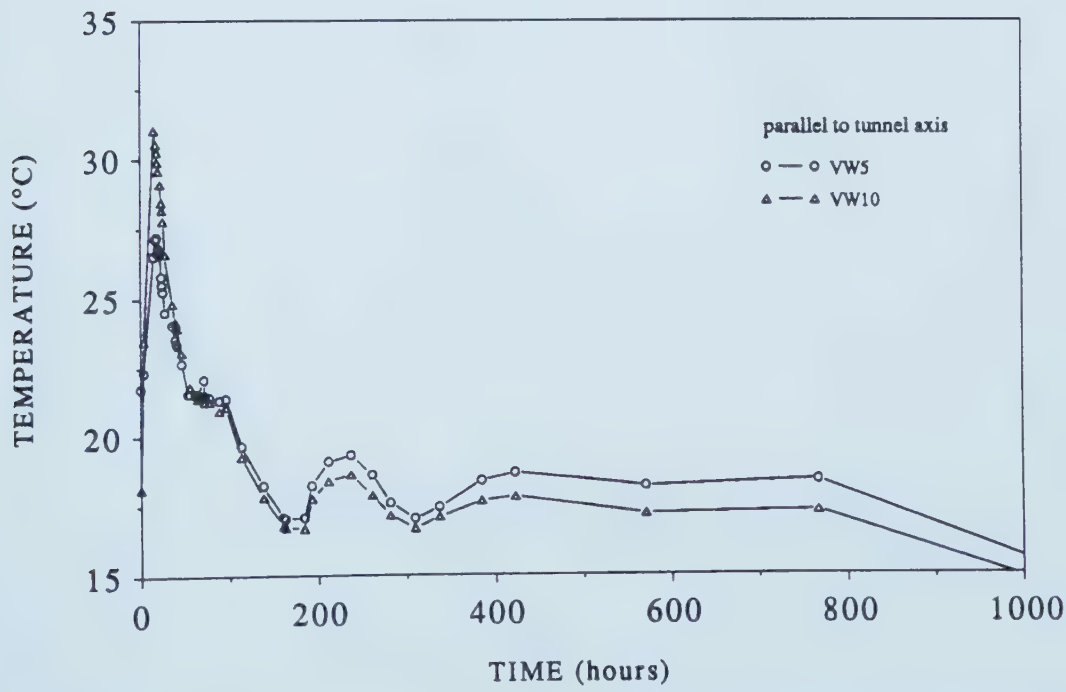


Figure B.14 Measured Temperatures from Gages Embedded in Shotcrete, Section C2I, Springline Region

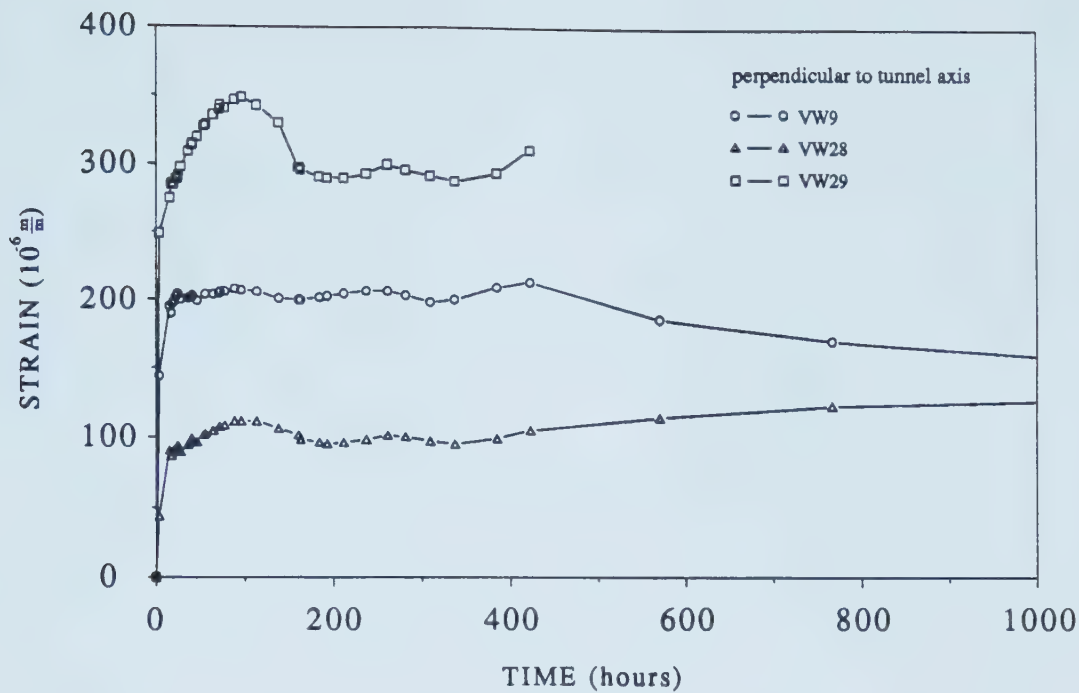


Figure B.15 Measured Strains from Gages Embedded in Shotcrete, Section C2I, Springline Region

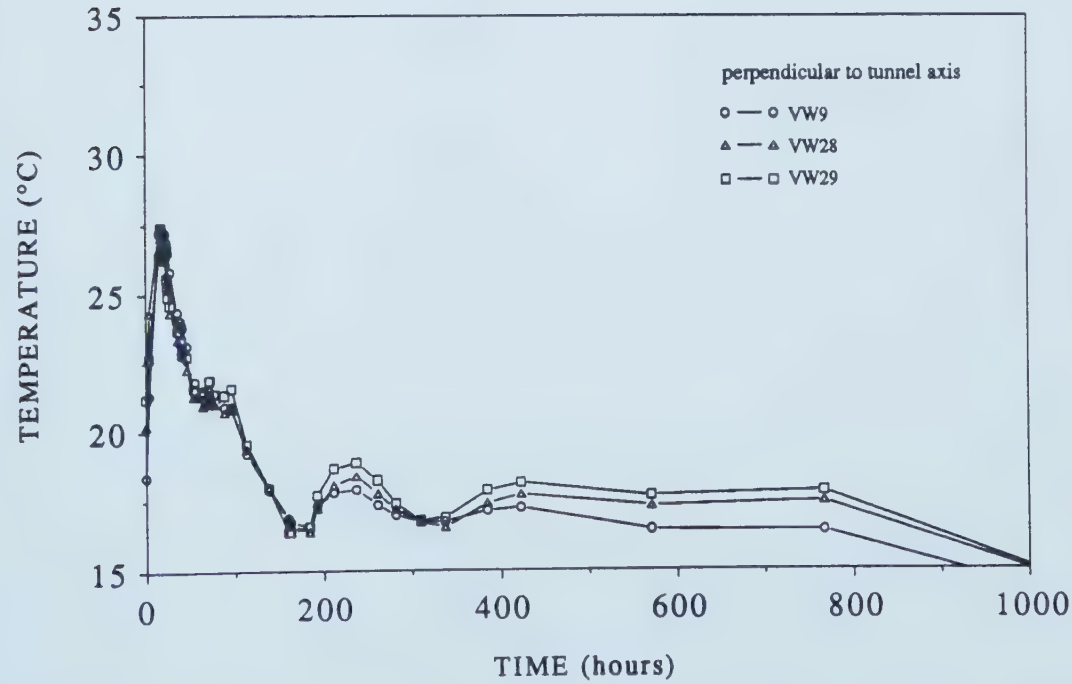


Figure B.16 Measured Temperatures from Gages Embedded in Shotcrete, Section C2I, Springline Region

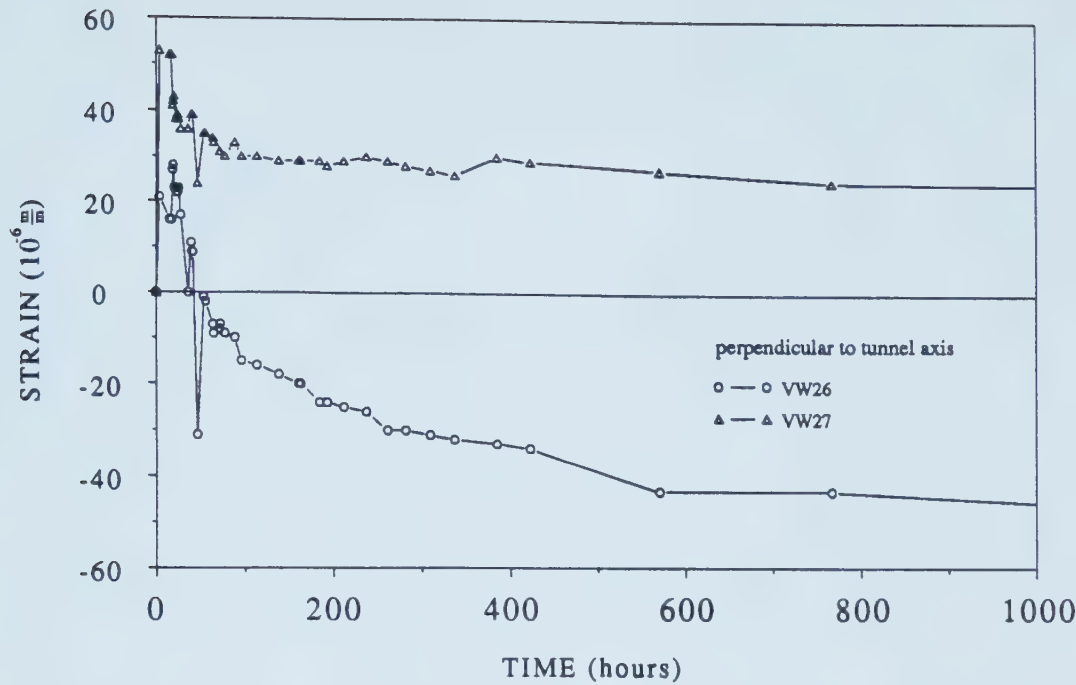


Figure B.17 Measured Strains from Gages Embedded in Shotcrete, Section C2I, Floor Region

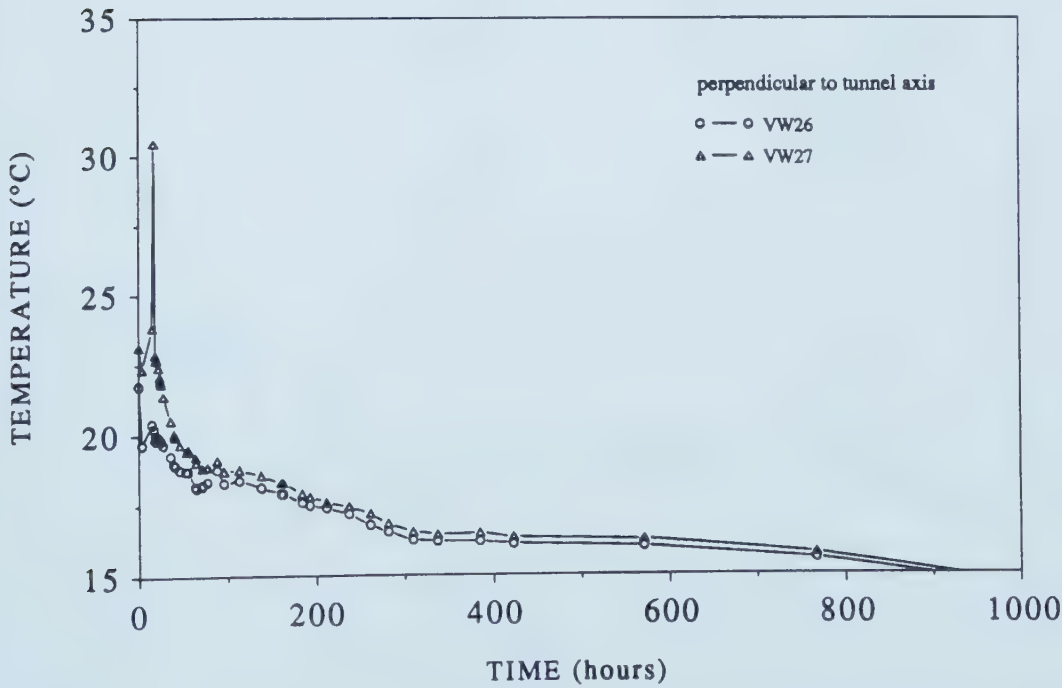


Figure B.18 Measured Temperatures from Gages Embedded in Shotcrete, Section C2I, Floor Region

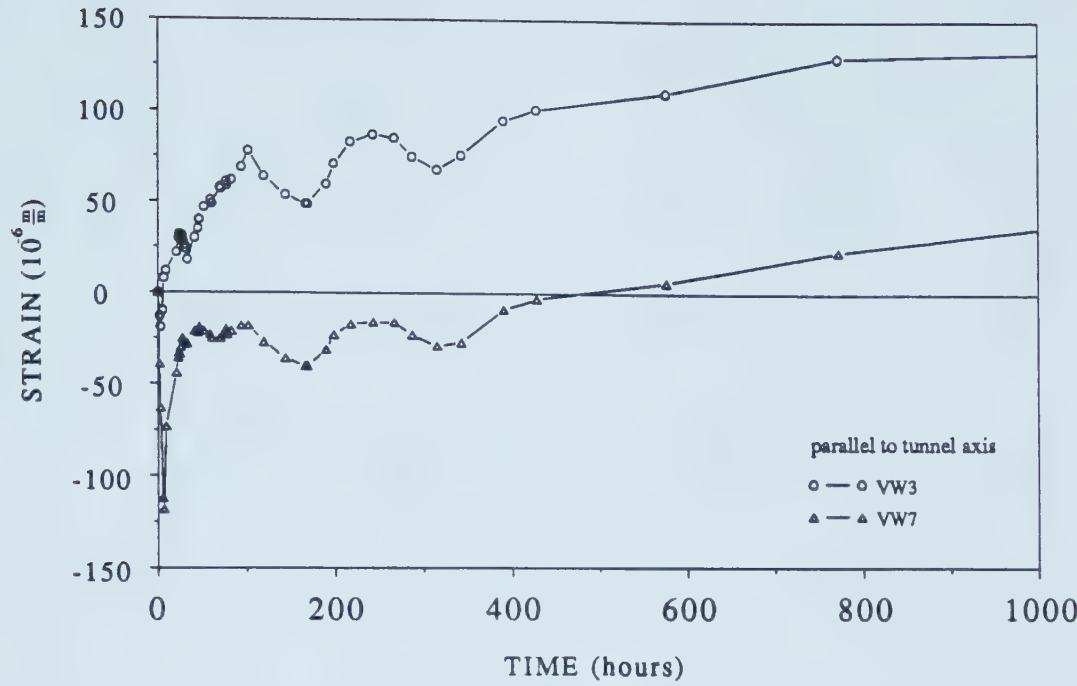


Figure B.19 Measured Strains from Gages Embedded in Shotcrete, Section C2II, Crown Region

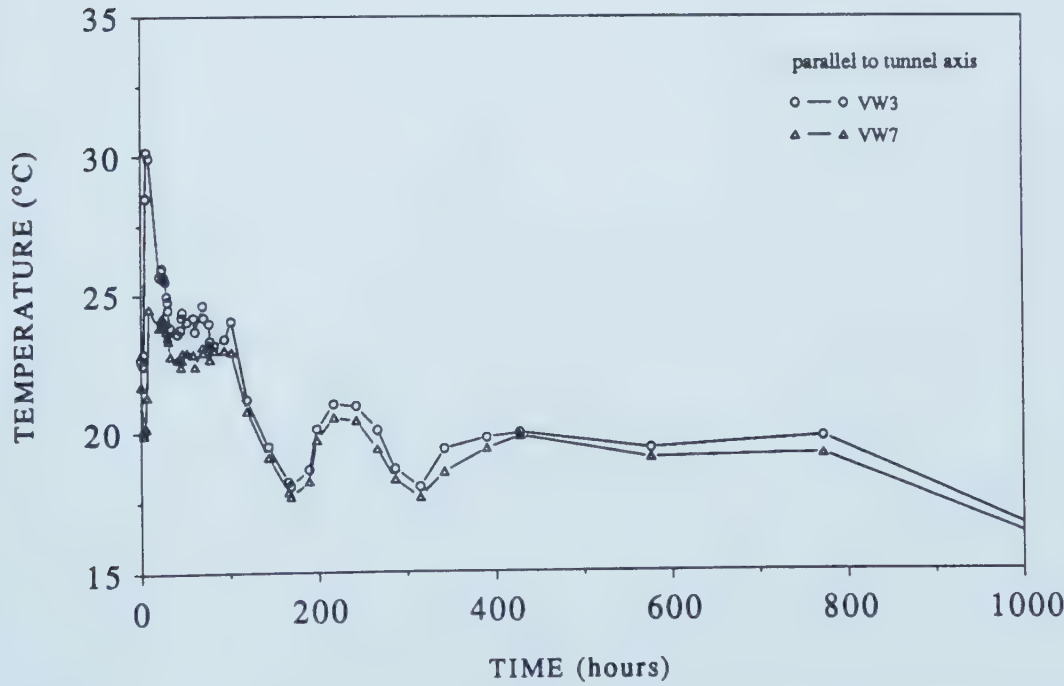


Figure B.20 Measured Temperatures from Gages Embedded in Shotcrete, Section C2II, Crown Region

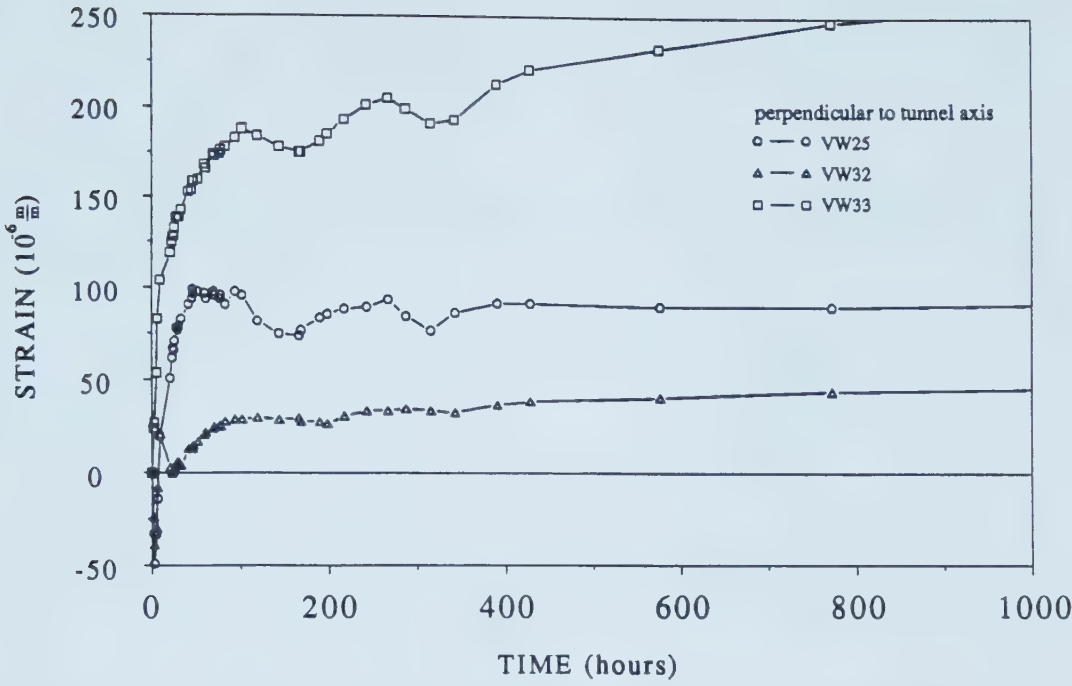


Figure B.21 Measured Strains from Gages Embedded in Shotcrete, Section C2II, Crown Region

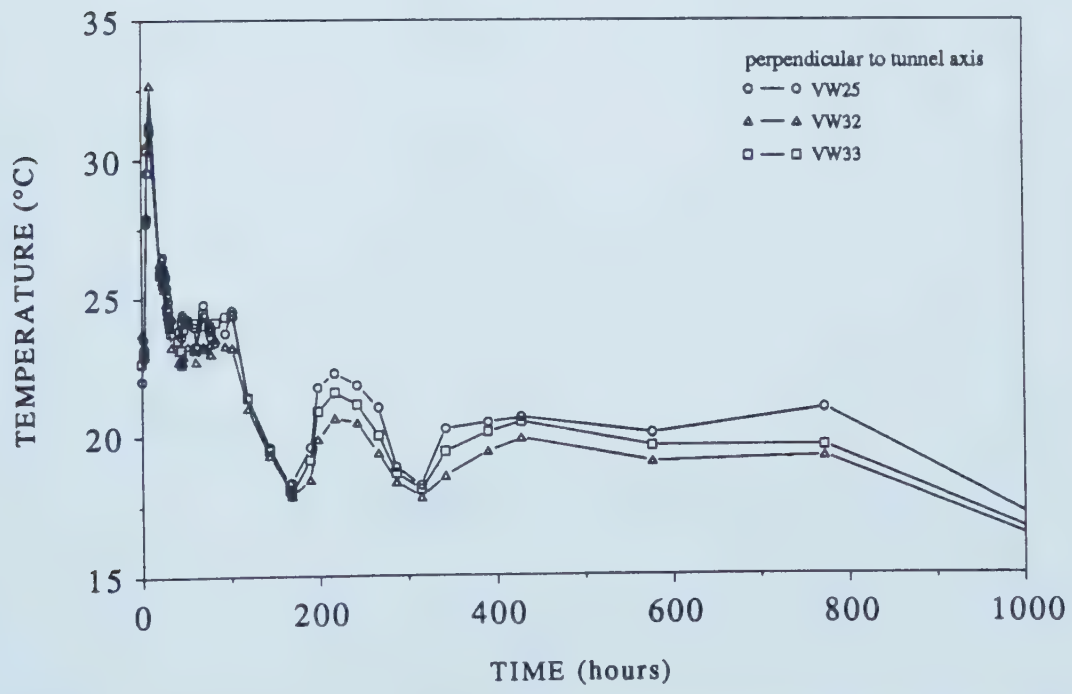


Figure B.22 Measured Temperatures from Gages Embedded in Shotcrete, Section C2II, Crown Region

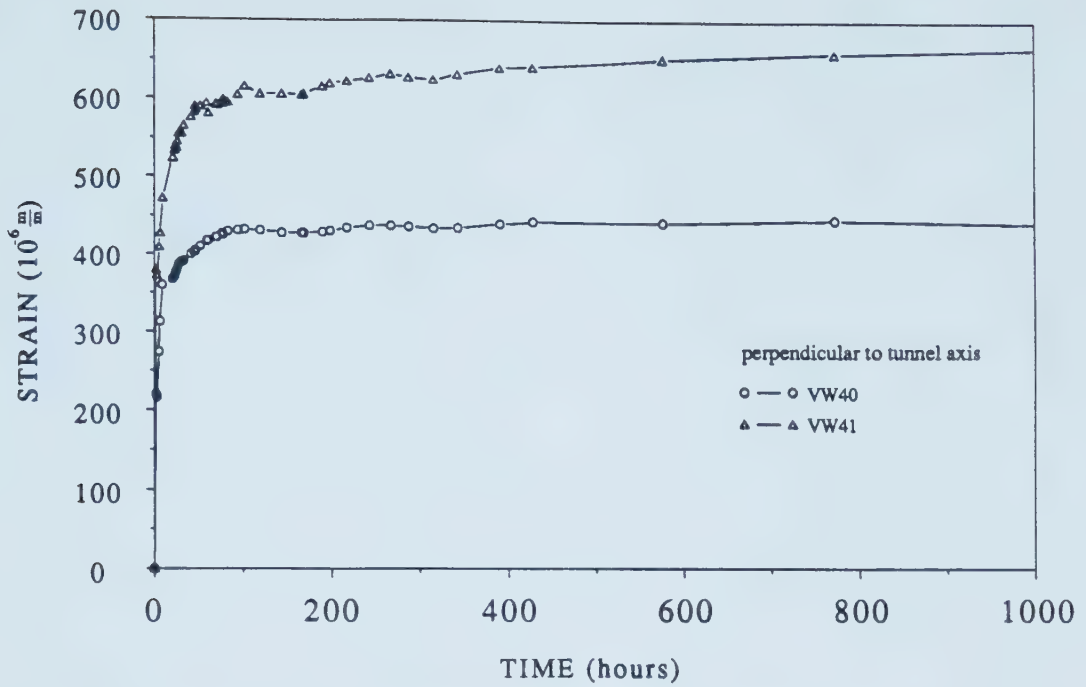


Figure B.23 Measured Strains from Gages Embedded in Shotcrete, Section C2II, Crown Region, Block Fall

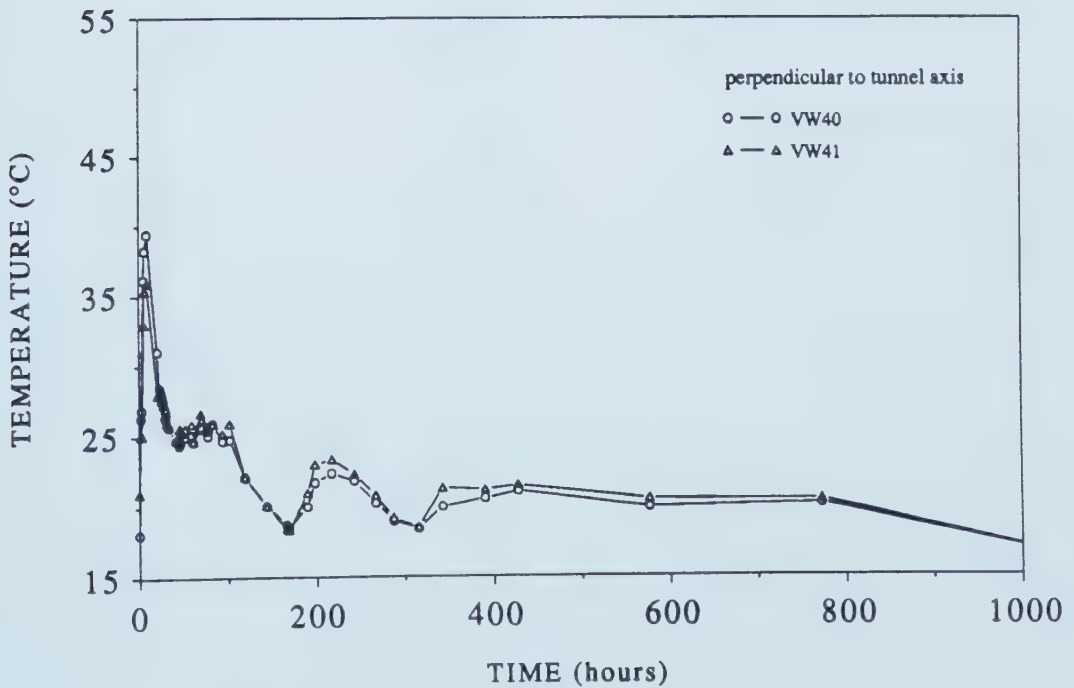


Figure B.24 Measured Temperatures from Gages Embedded in Shotcrete, Section C2II, Crown Region, Block Fall

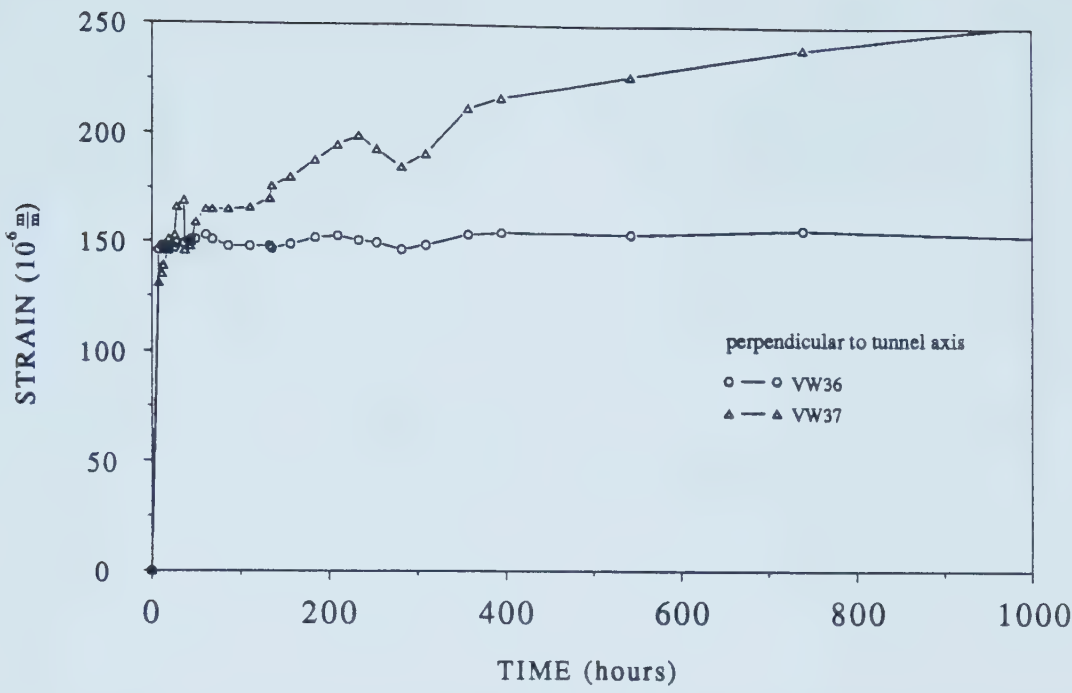


Figure B.25 Measured Strains from Gages Embedded in Shotcrete, Section C2II, Springline Region

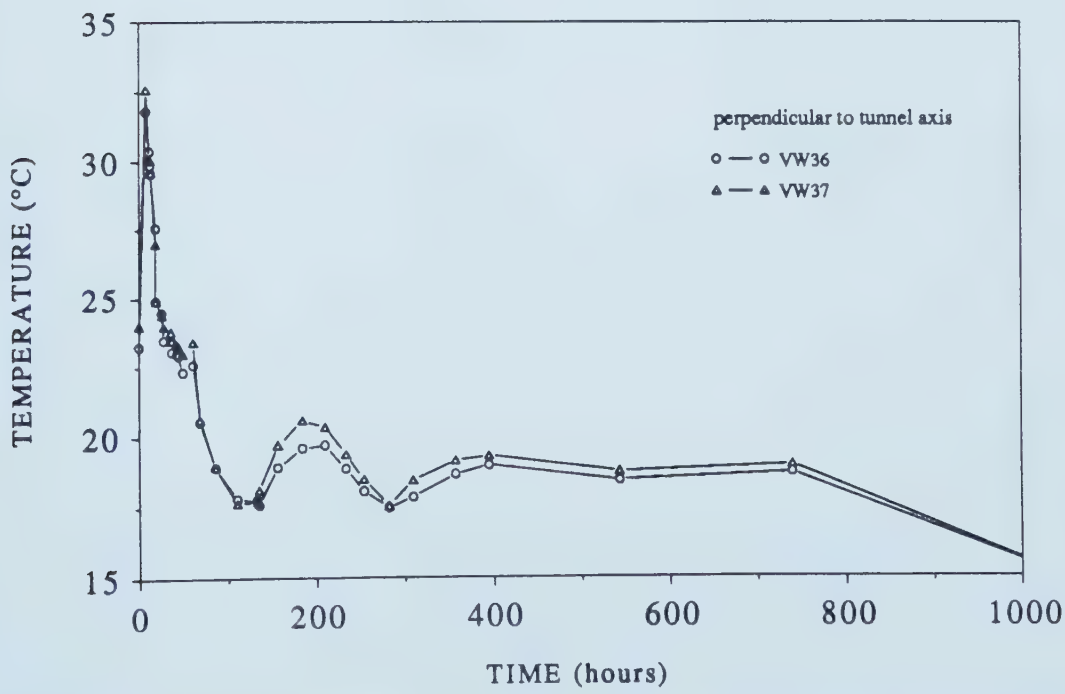


Figure B.26 Measured Temperatures from Gages Embedded in Shotcrete, Section C2II, Springline Region

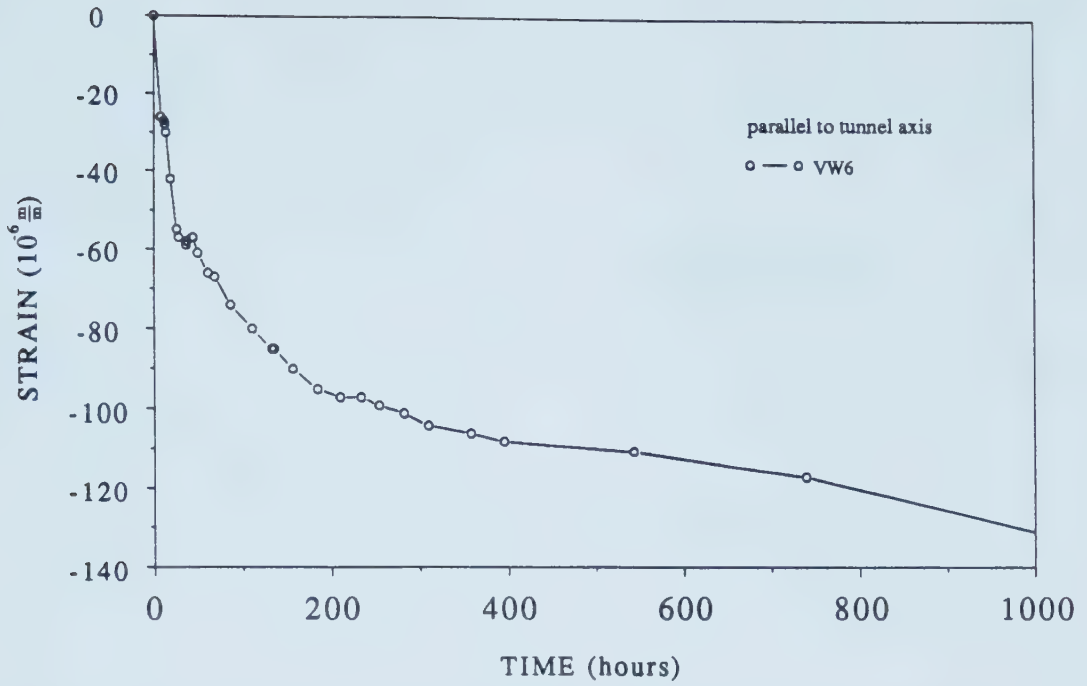


Figure B.27 Measured Strains from Gages Embedded in Shotcrete, Section C2II, Floor Region

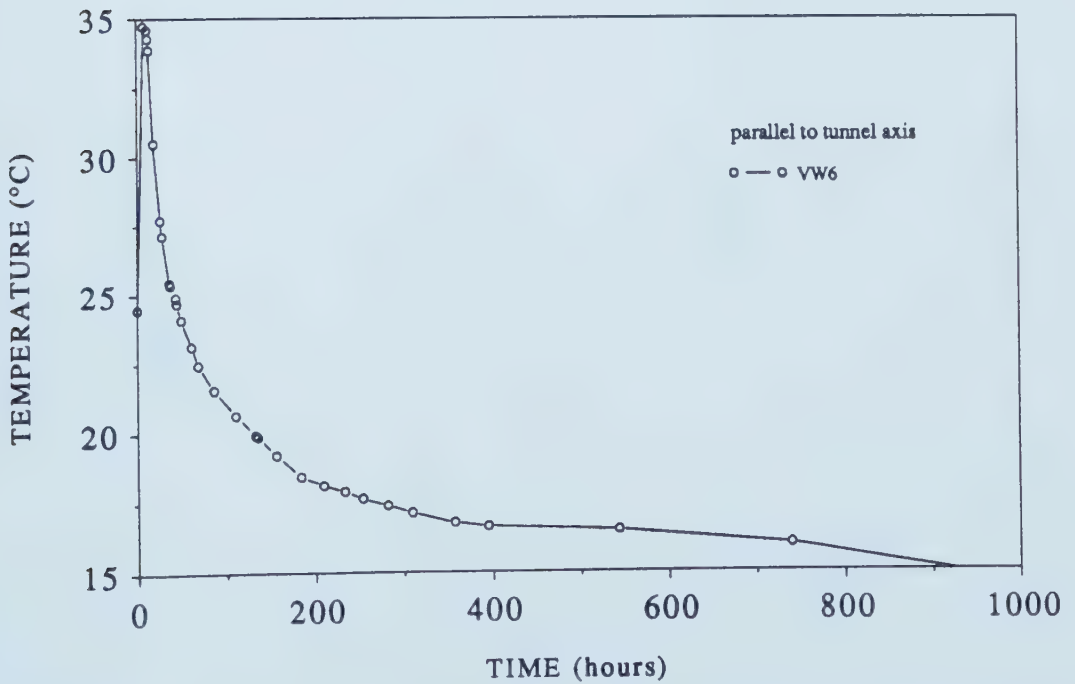


Figure B.28 Measured Temperatures from Gages Embedded in Shotcrete, Section C2II, Floor Region

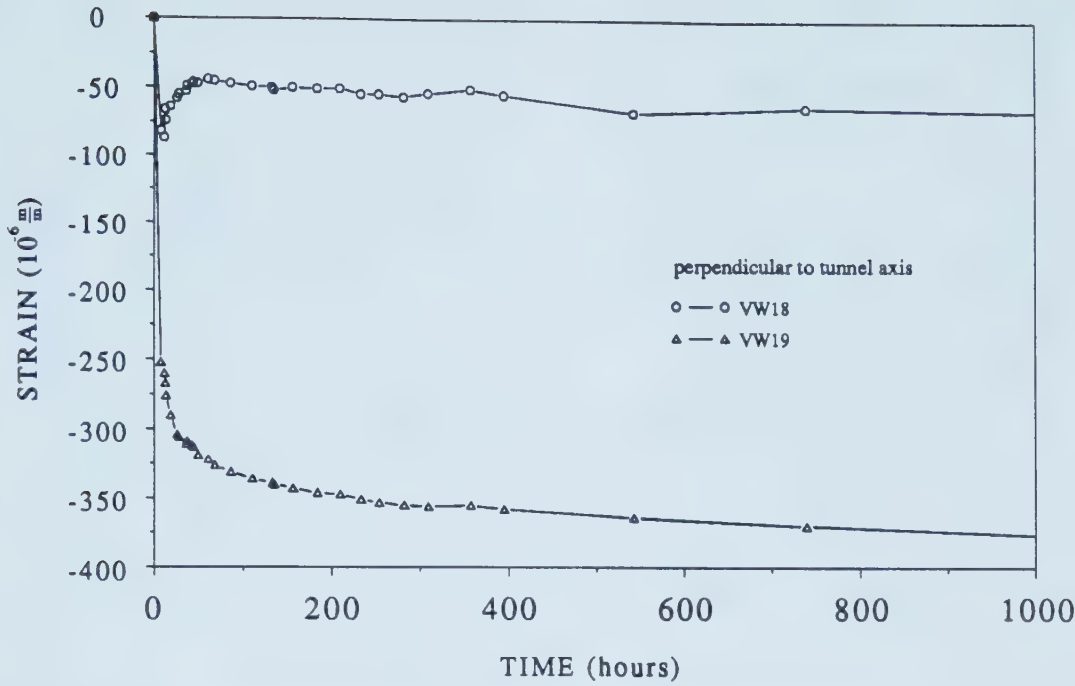


Figure B.29 Measured Strains from Gages Embedded in Shotcrete, Section C2II, Floor Region

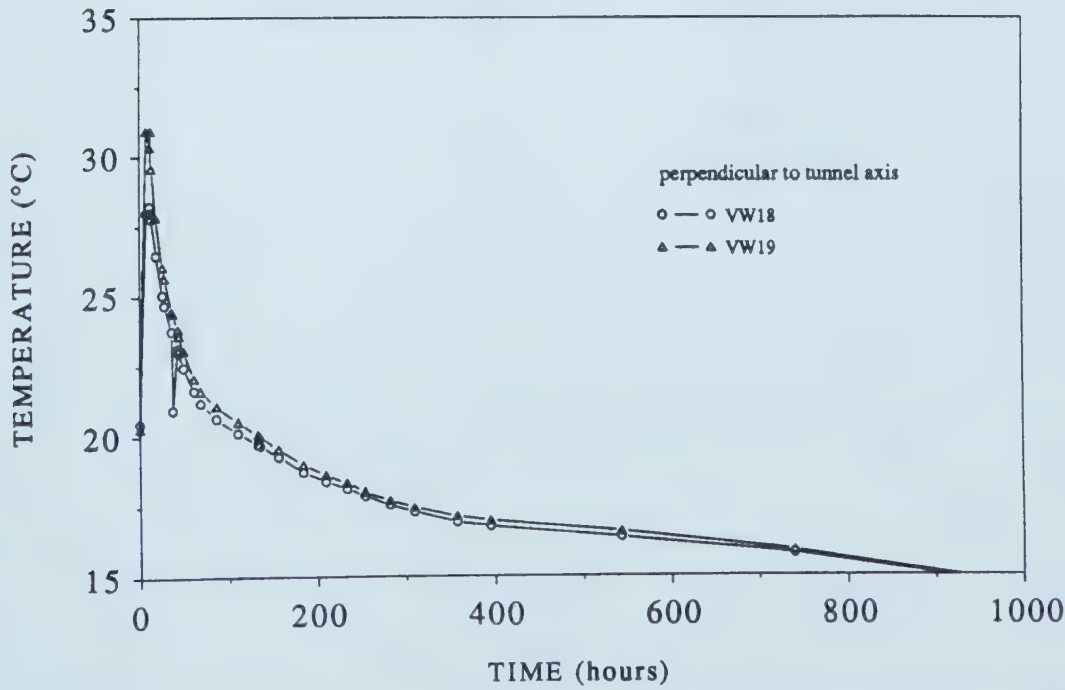


Figure B.30 Measured Temperatures from Gages Embedded in Shotcrete, Section C2II, Floor Region

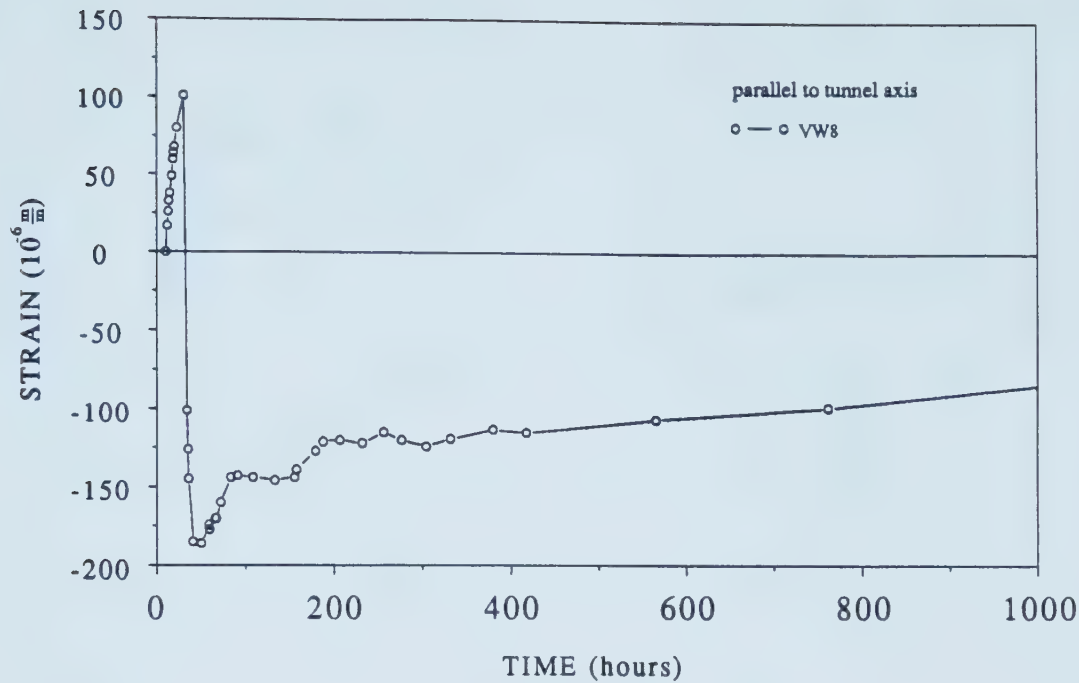


Figure B.31 Measured Strains from Gages Embedded in Shotcrete, Section C2III, Crown Region

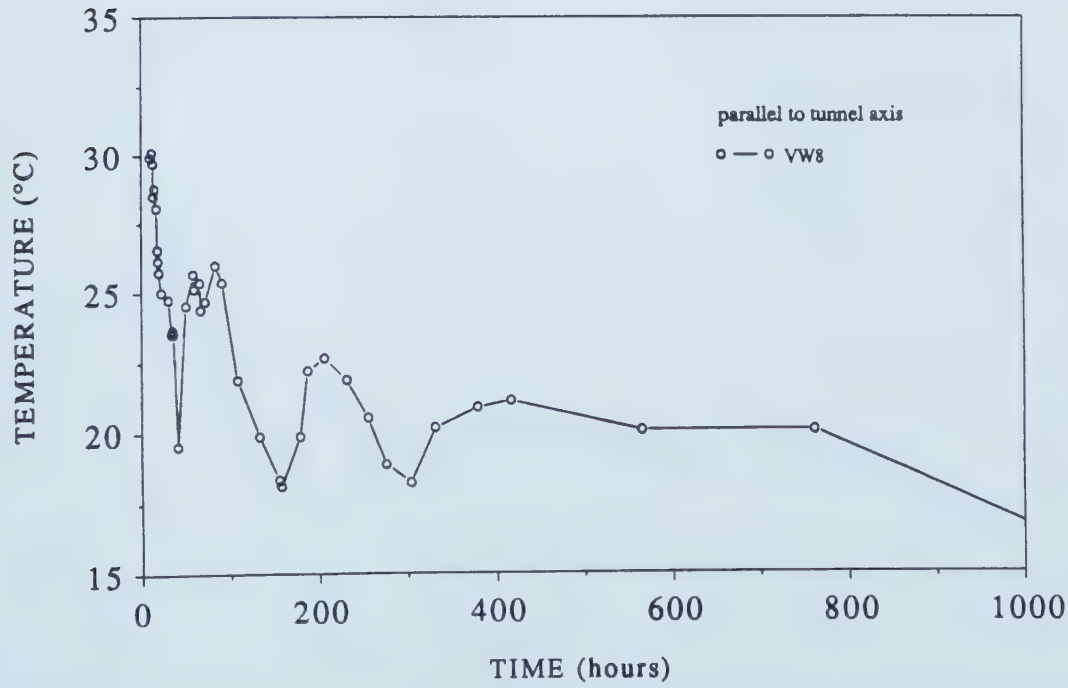


Figure B.32 Measured Temperatures from Gages Embedded in Shotcrete, Section C2III, Crown Region

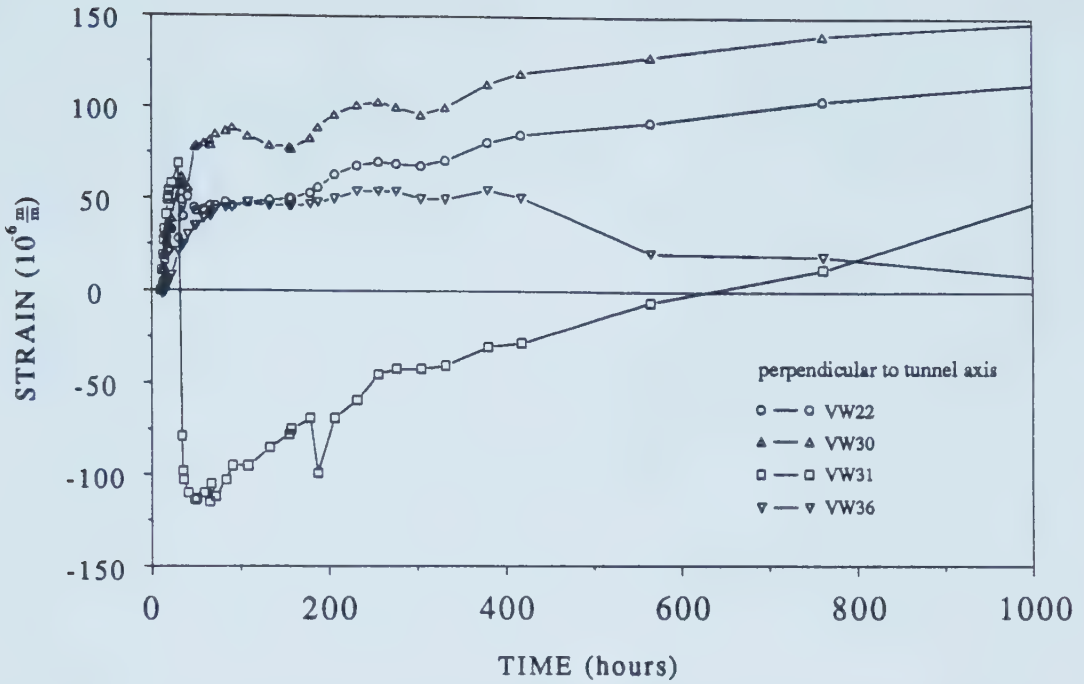


Figure B.33 Measured Strains from Gages Embedded in Shotcrete, Section C2III, Crown Region

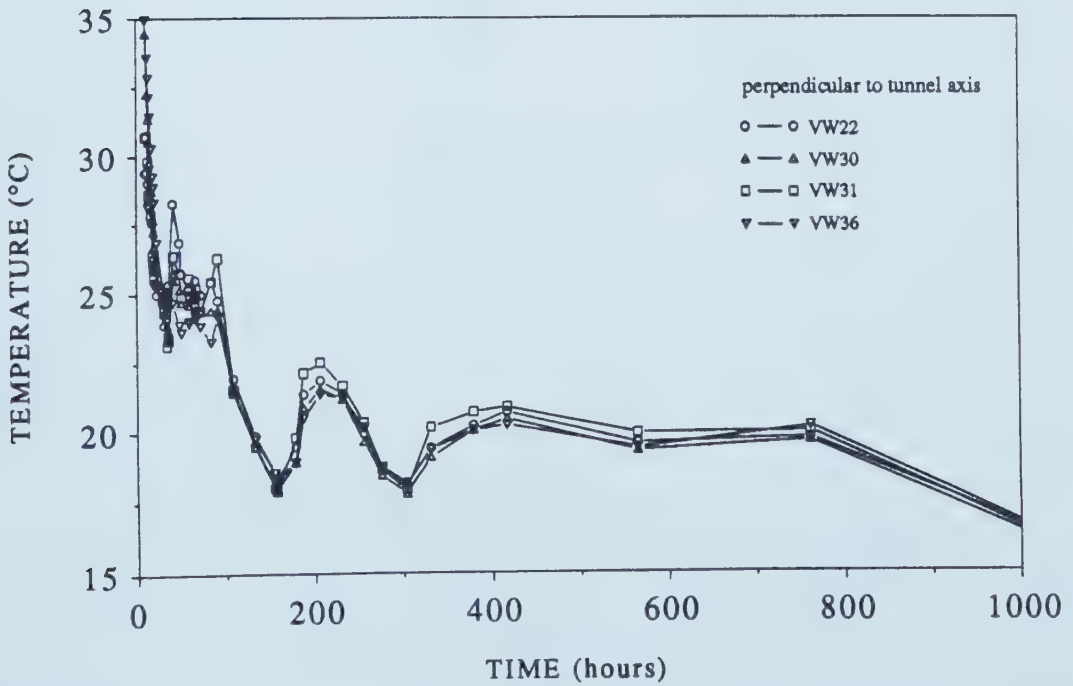


Figure B.34 Measured Temperatures from Gages Embedded in Shotcrete, Section C2III, Crown Region

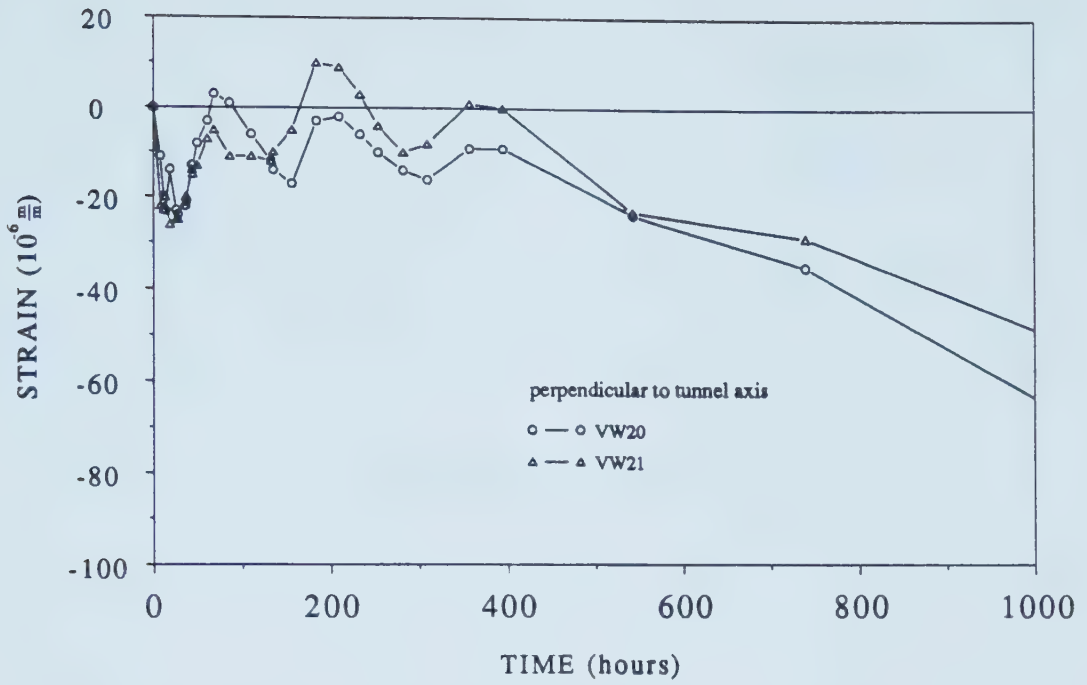


Figure B.35 Measured Strains from Gages Embedded in Shotcrete, Section C2III, Springline Region

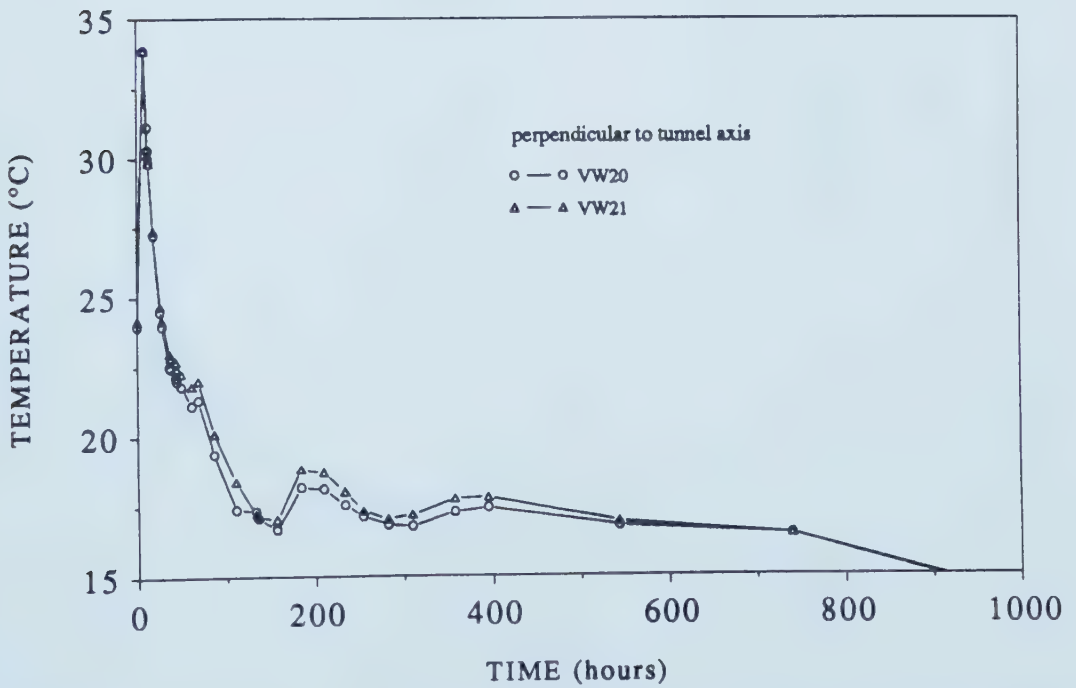


Figure B.36 Measured Temperatures from Gages Embedded in Shotcrete, Section C2III, Springline Region

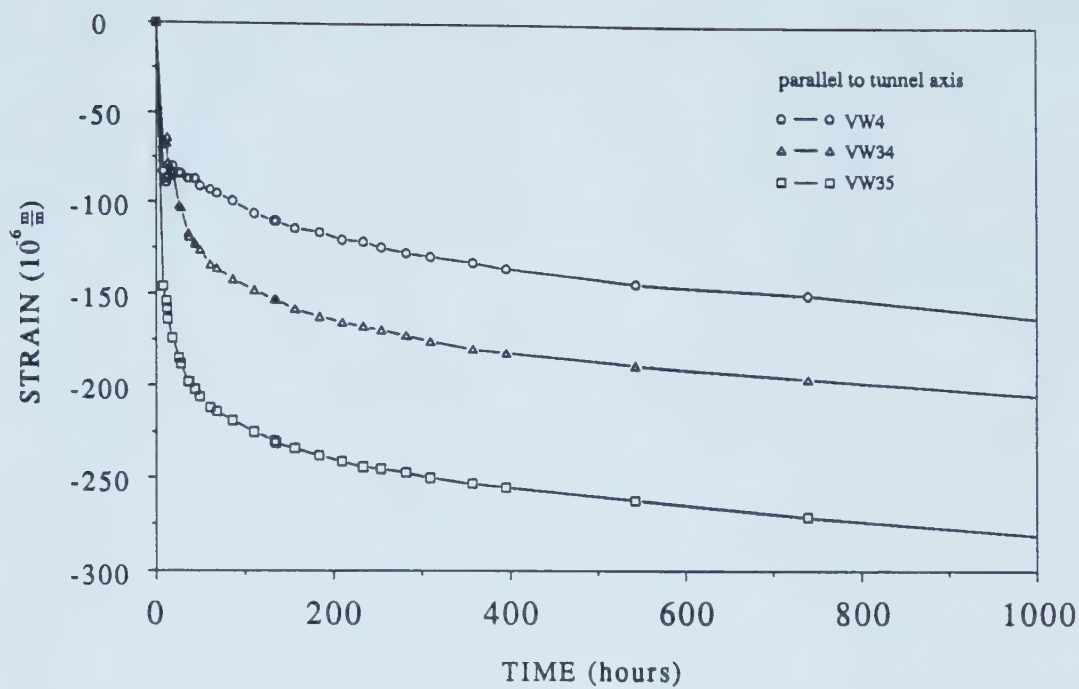


Figure B.37 Measured Strains from Gages Embedded in Shotcrete, Section C2III, Floor Region

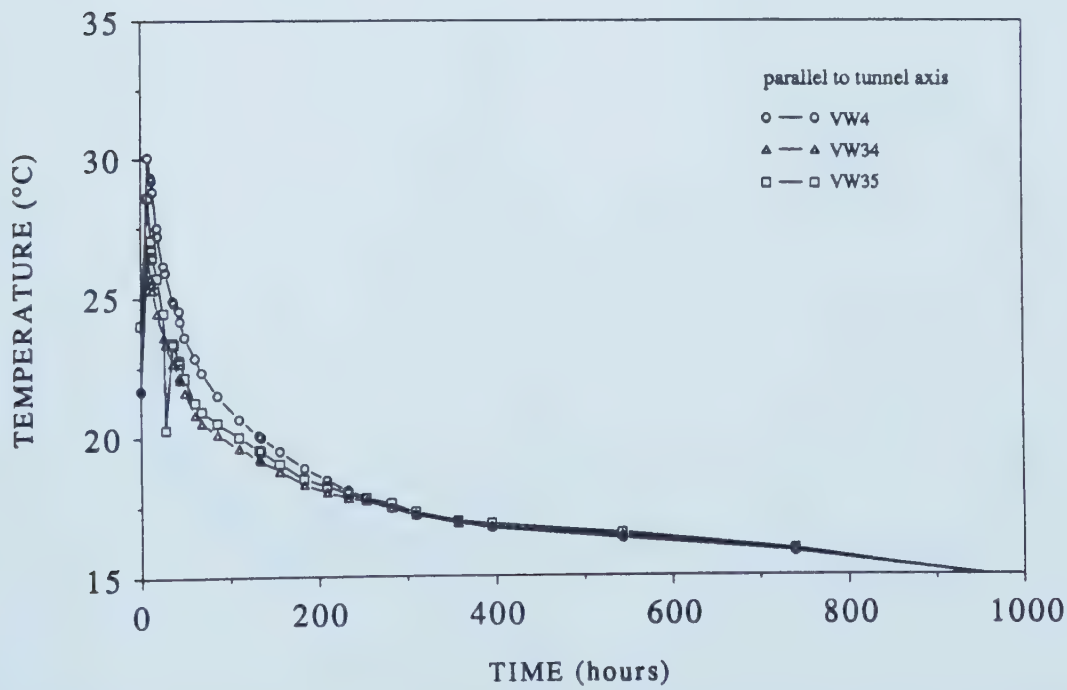


Figure B.38 Measured Temperatures from Gages Embedded in Shotcrete, Section C2III, Floor Region

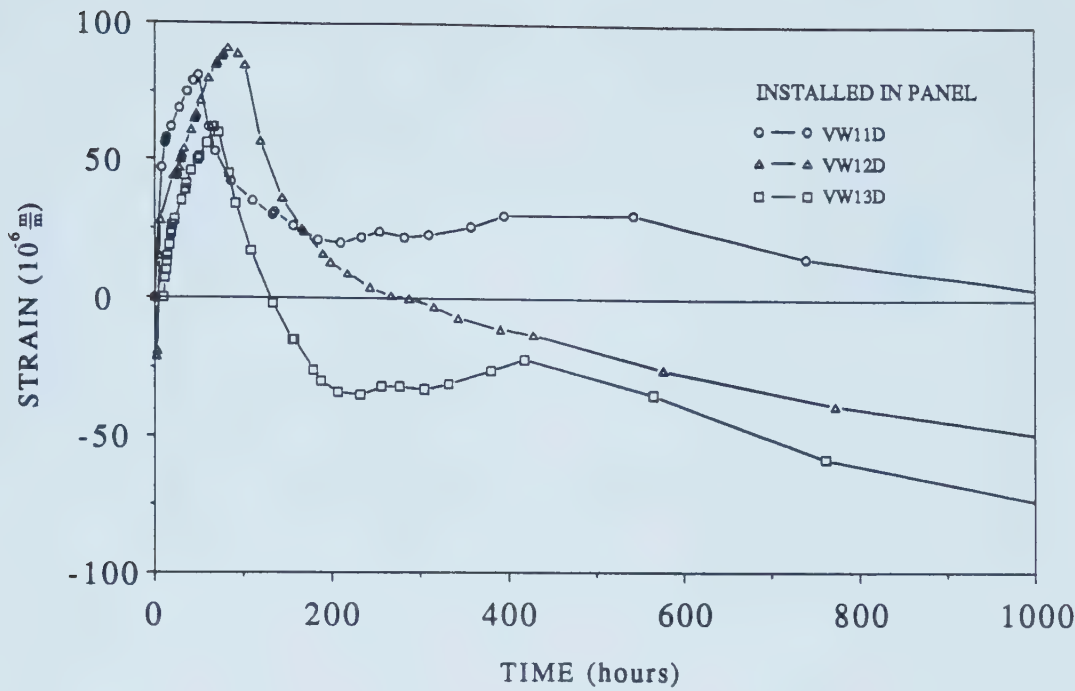


Figure B.39 Measured Strains from Dummy Gages Embedded in Shotcrete Panels and left inside the Tunnel

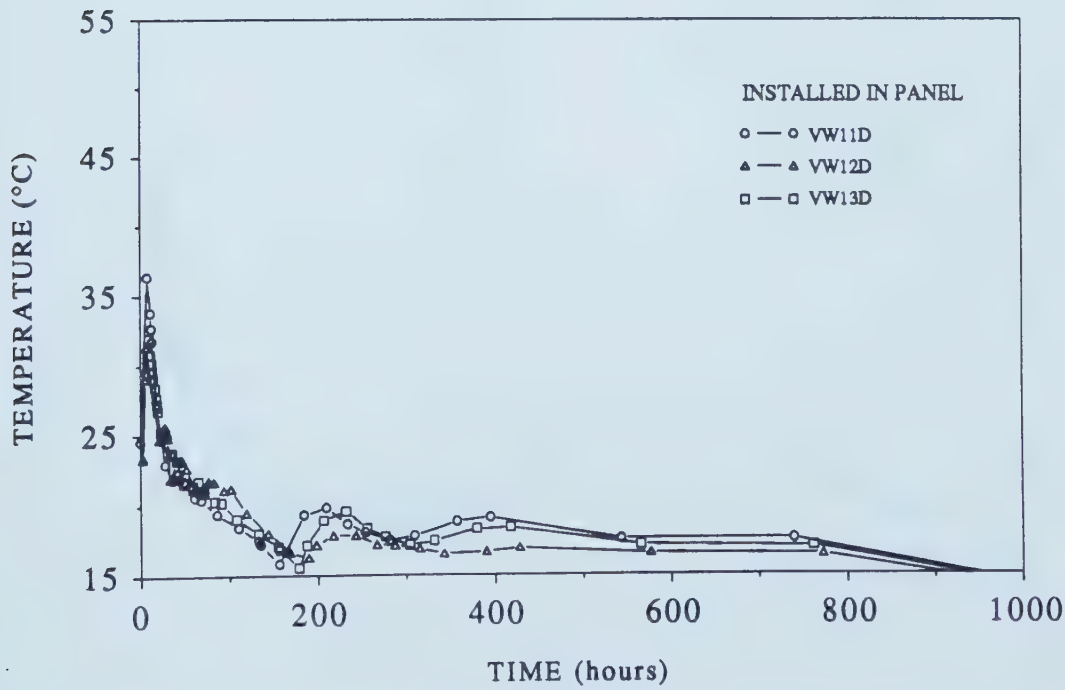


Figure B.40 Measured Temperatures from Dummy Gages Embedded in Shotcrete Panels and left inside the Tunnel

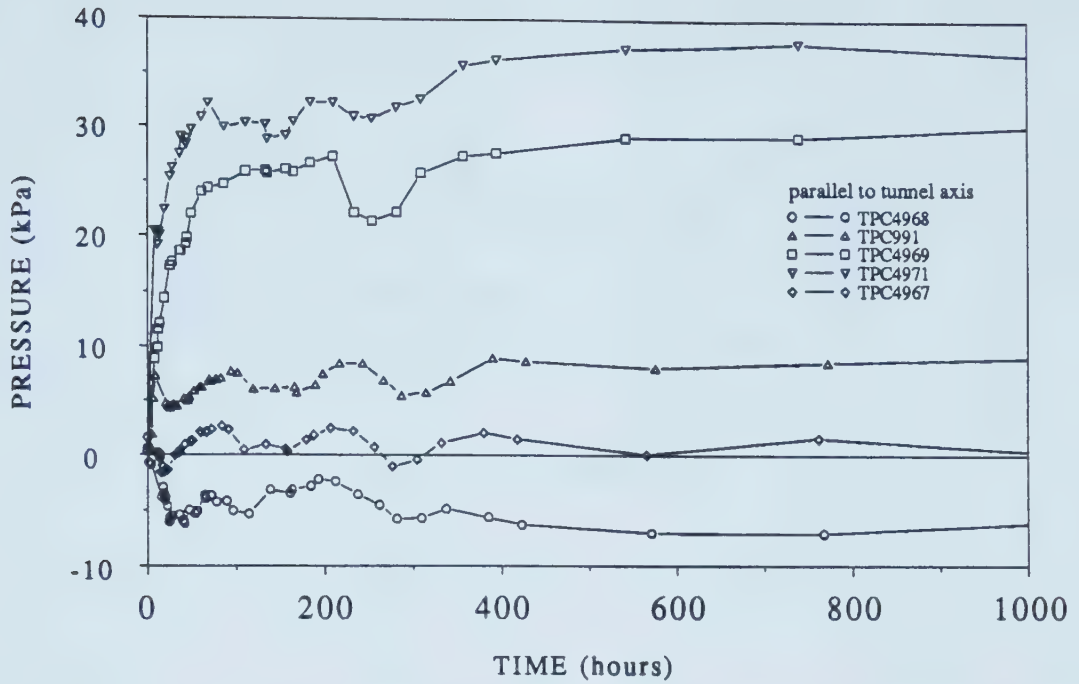


Figure B.41 Measured Pressures by Total Pressure Cells Installed at Interface Soil-Shotcrete, Temperature Compensated

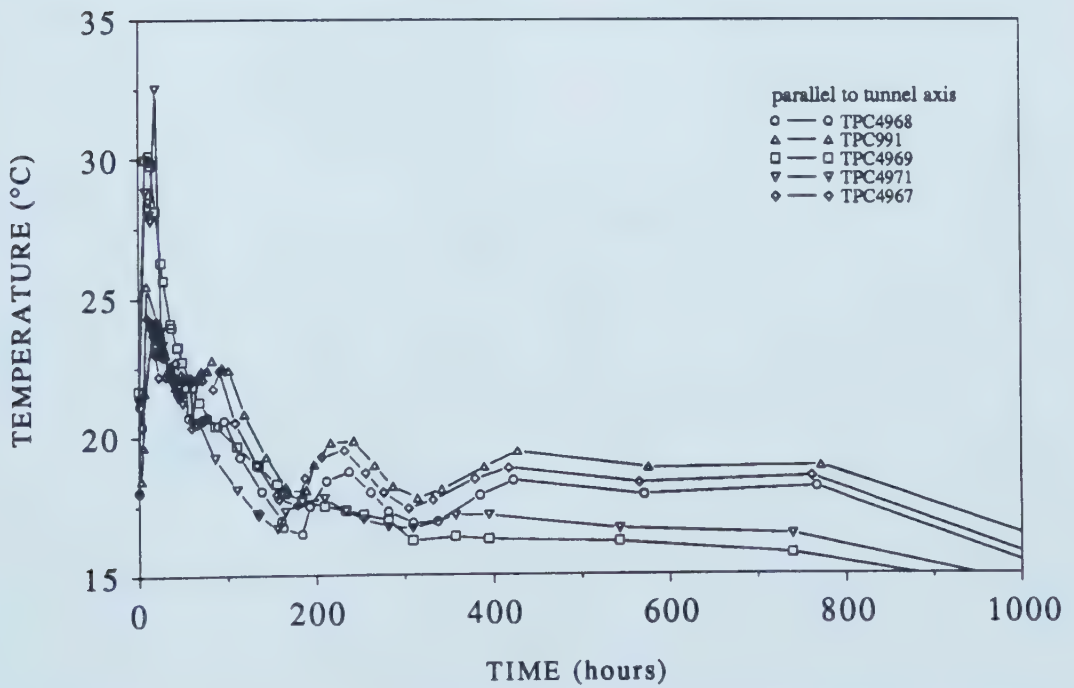


Figure B.42 Measured Temperatures in Total Pressure Cells Installed at Interface Soil-Shotcrete

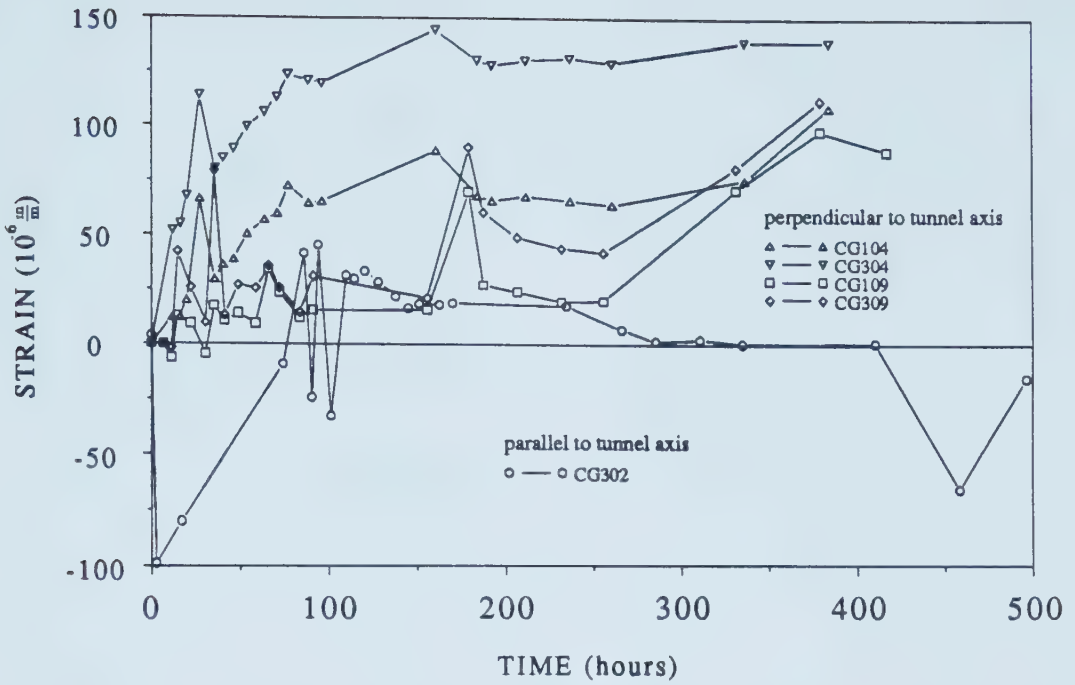


Figure B.43 Measured Strains from Compression Gages Embedded in Shotcrete, Crown Region, Temperature Compensated

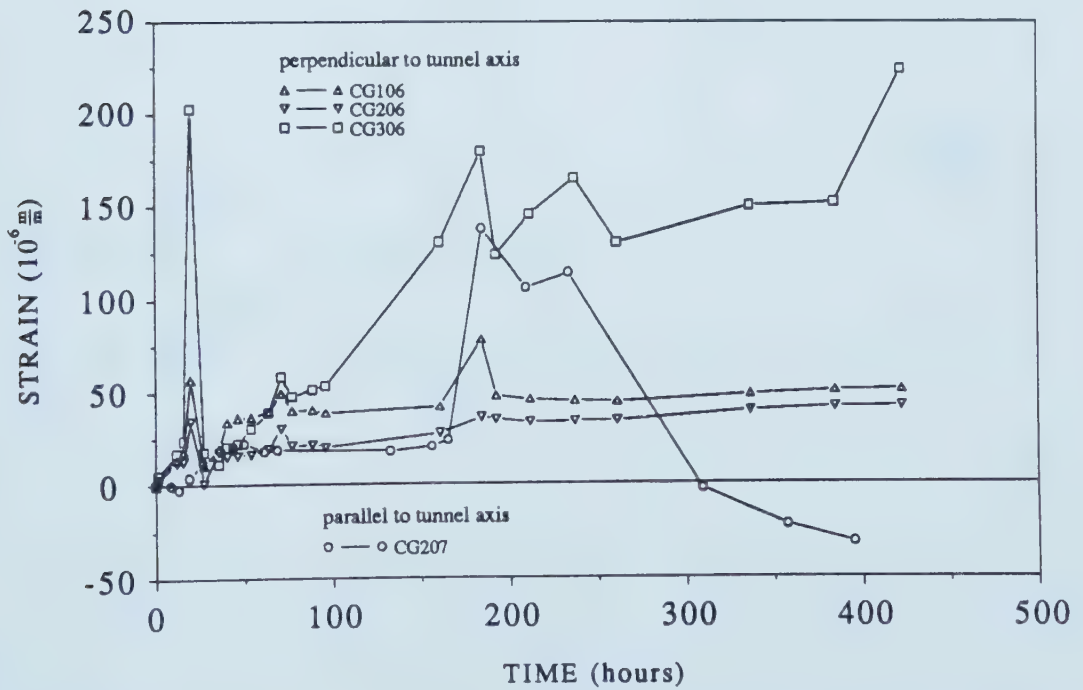


Figure B.44 Measured Strains from Compression Gages Embedded in Shotcrete, Floor Region, Temperature Compensated

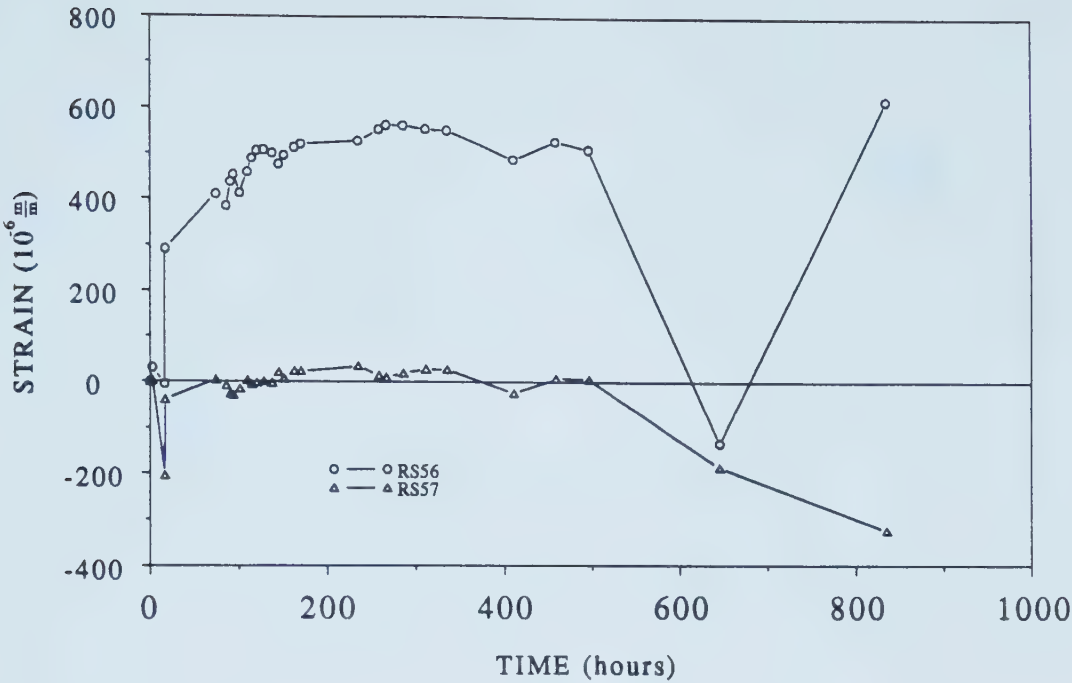


Figure B.45 Measured Strains from Resistance Gages Bonded in Steel Ribs, Section C2I, Heading, Temperature Compensated

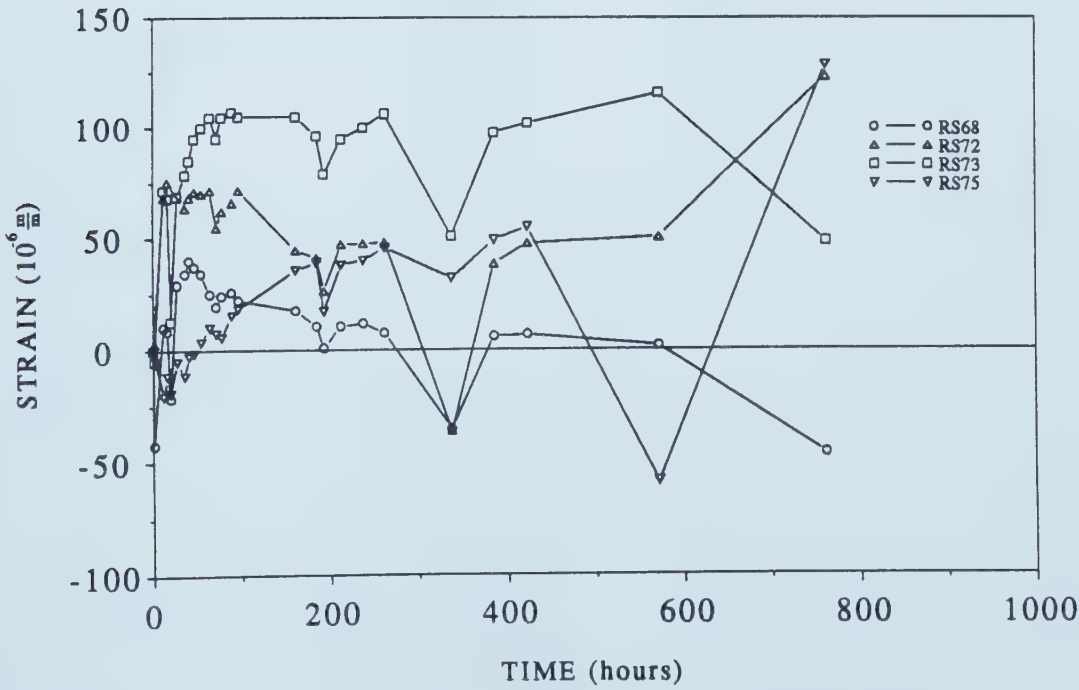


Figure B.46 Measured Strains from Resistance Gages Bonded in Steel Ribs, Section C2I, Invert, Temperature Compensated

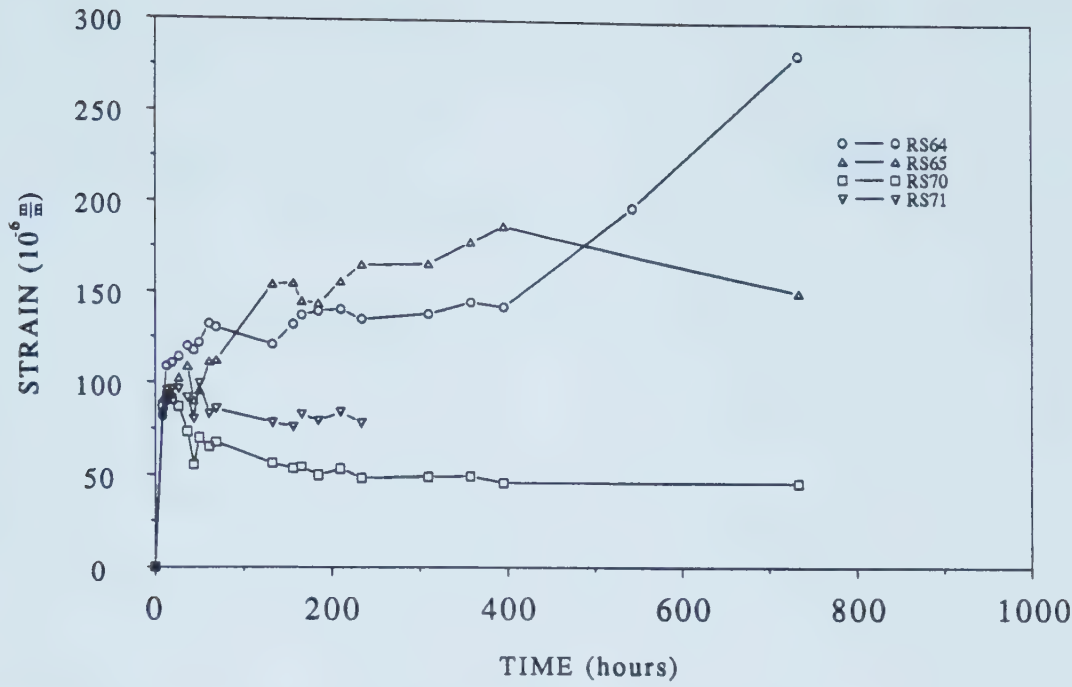


Figure B.47 Measured Strains from Resistance Gages Bonded in Steel Ribs, Section C2II, Invert, Temperature Compensated

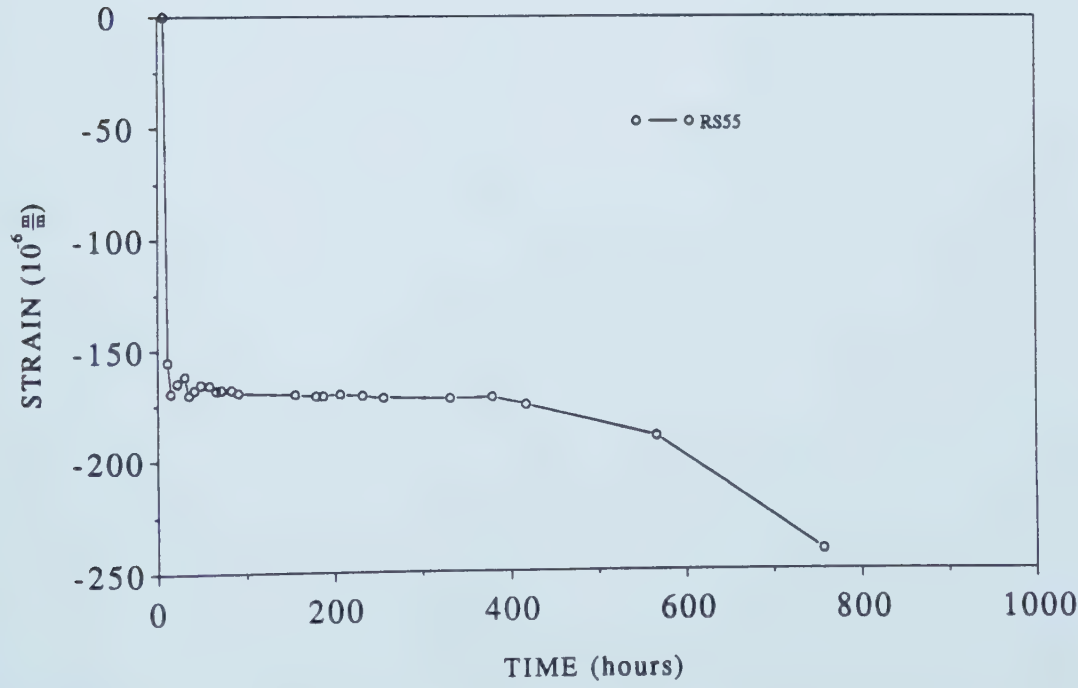


Figure B.48 Measured Strains from Resistance Gages Bonded in Steel Ribs, Section C2III, Heading, Temperature Compensated

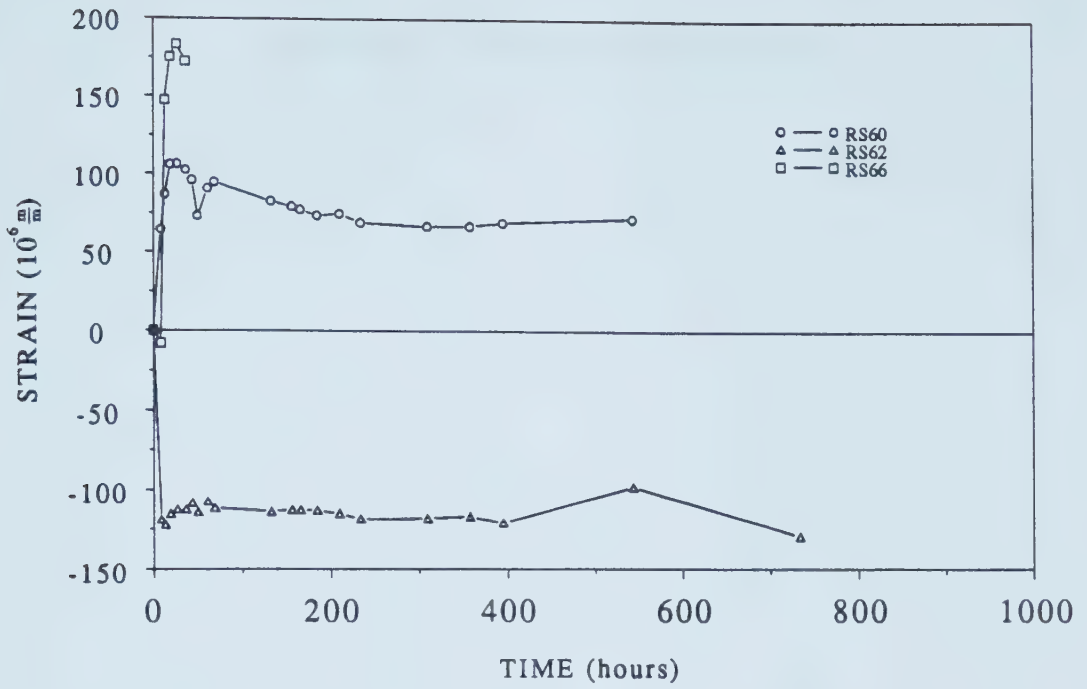


Figure B.49 Measured Strains from Resistance Gages Bonded in Steel Ribs, Section C2III, Invert, Temperature Compensated

APPENDIX C - Data from Flat Jack Tests

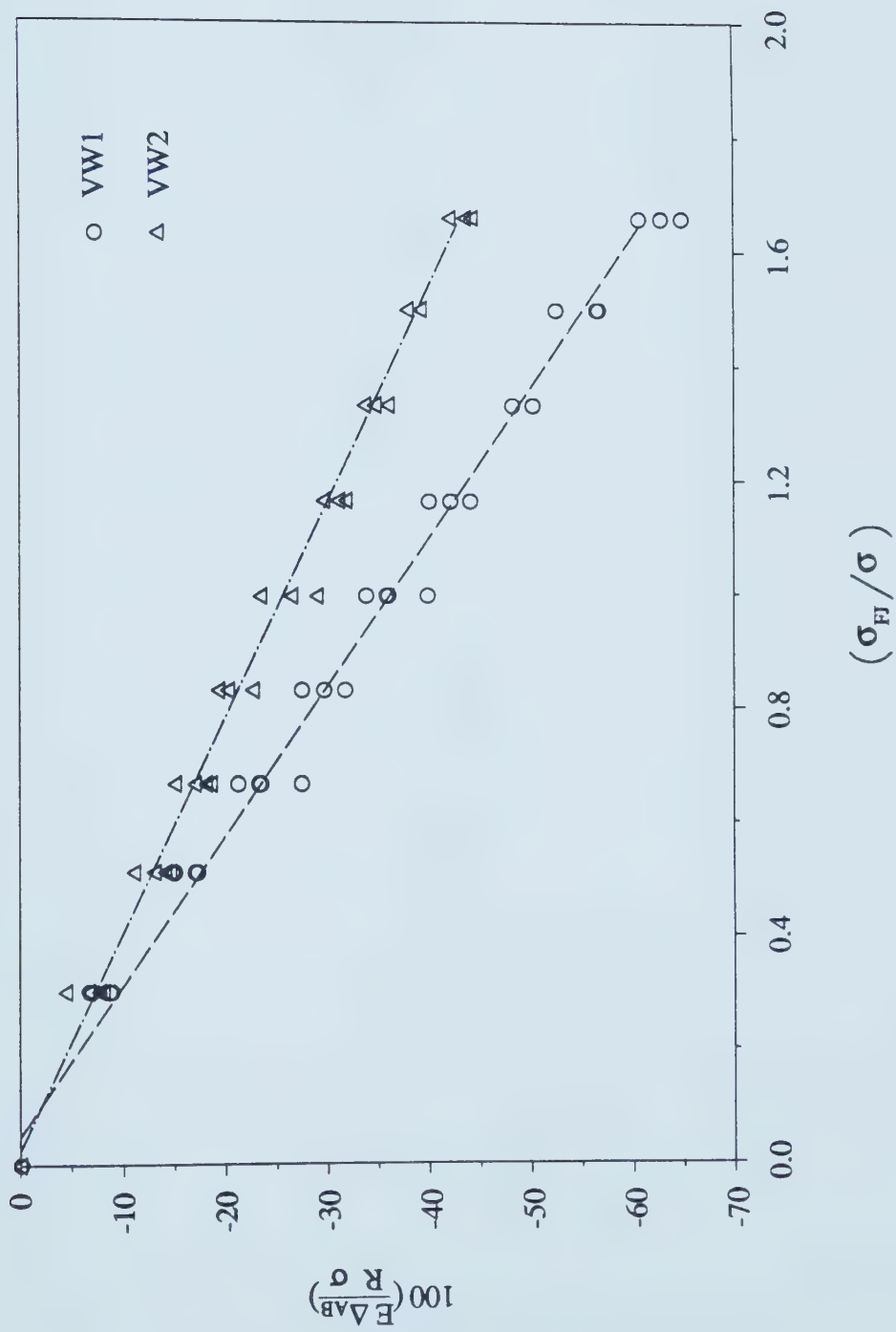


Figure C.1 Flat Jack Test CLMR1, Pressurization Stage

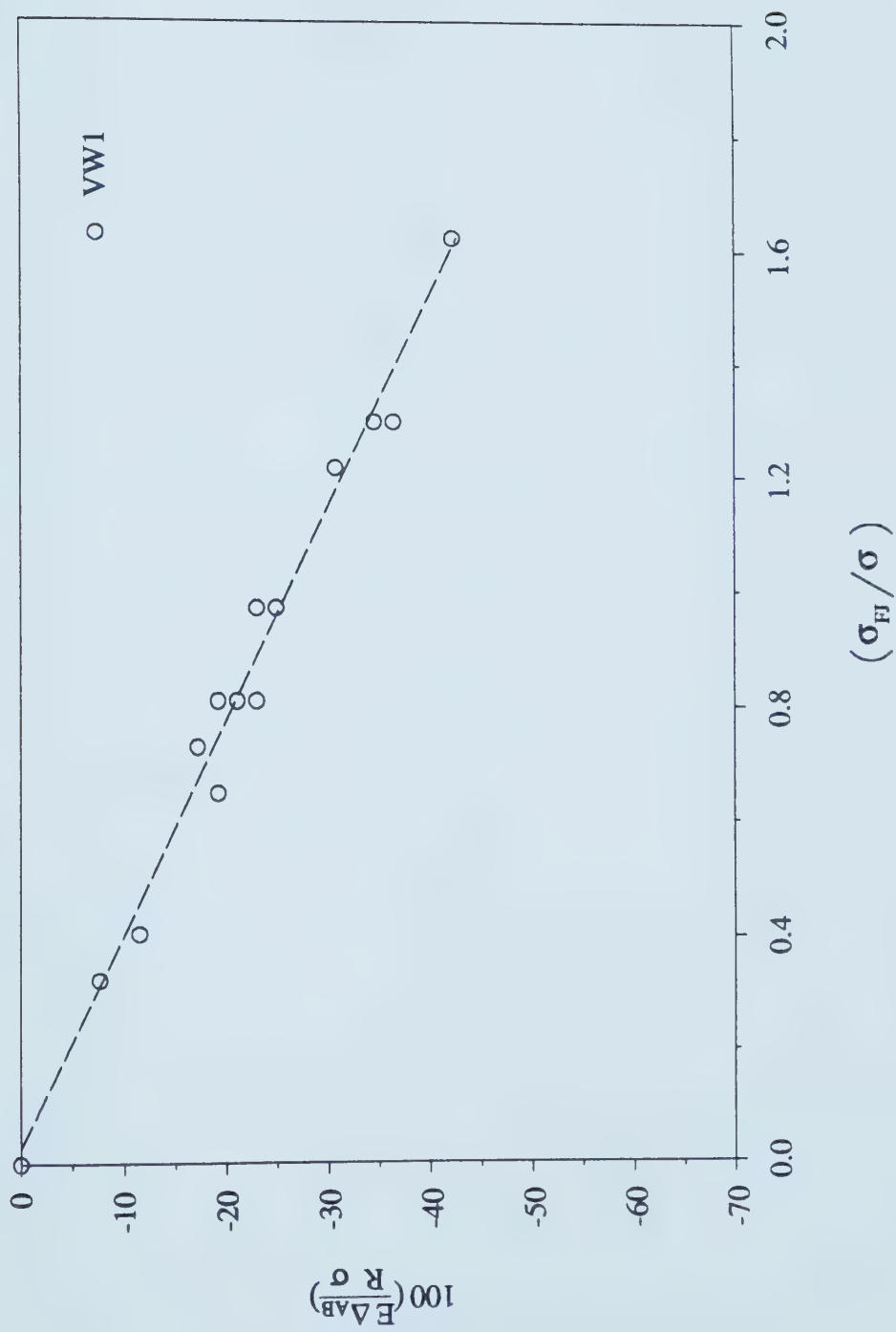


Figure C.2 Flat Jack Test CLMR2, Pressurization Stage

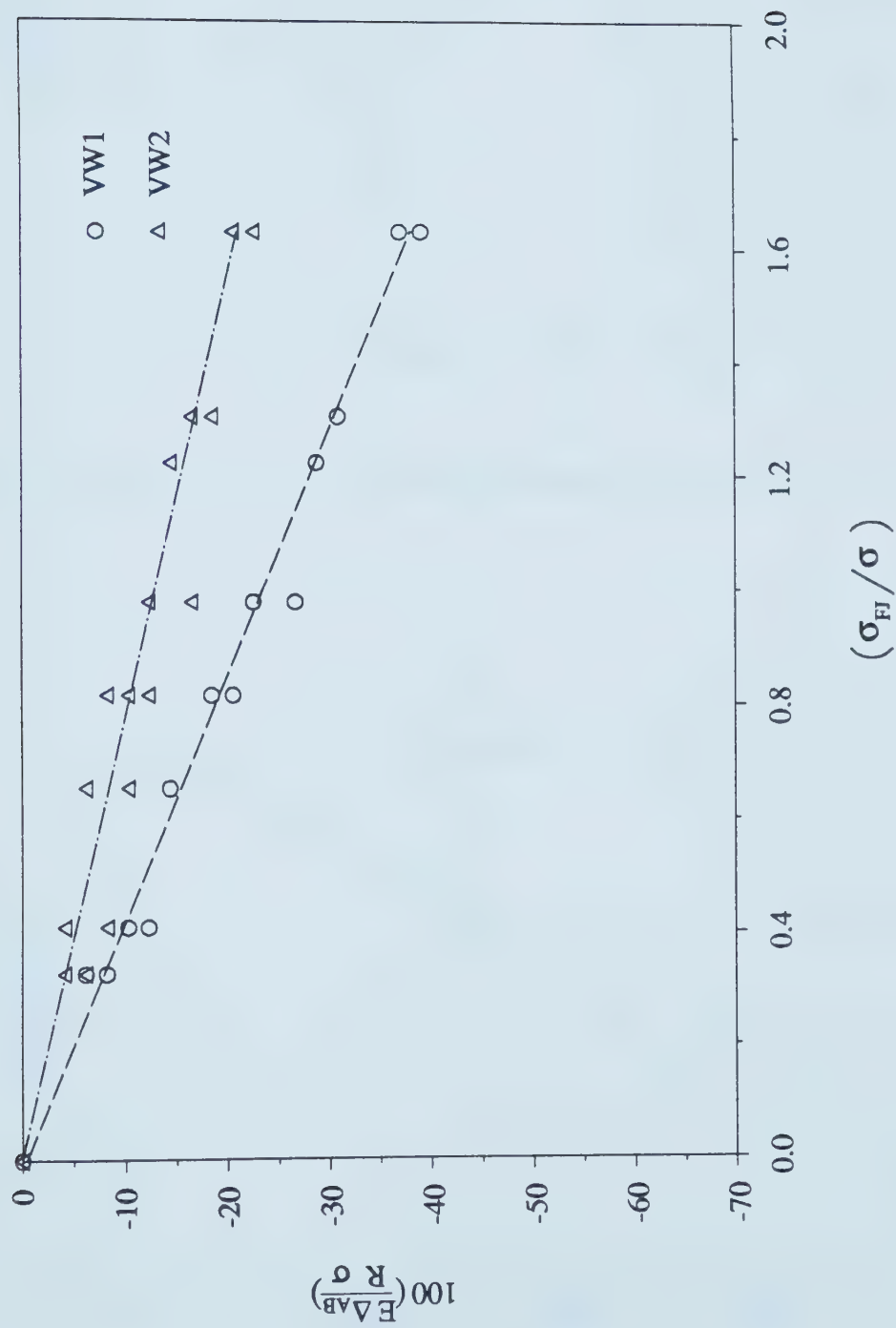


Figure C.3 Flat Jack Test CLNRH, Pressurization Stage

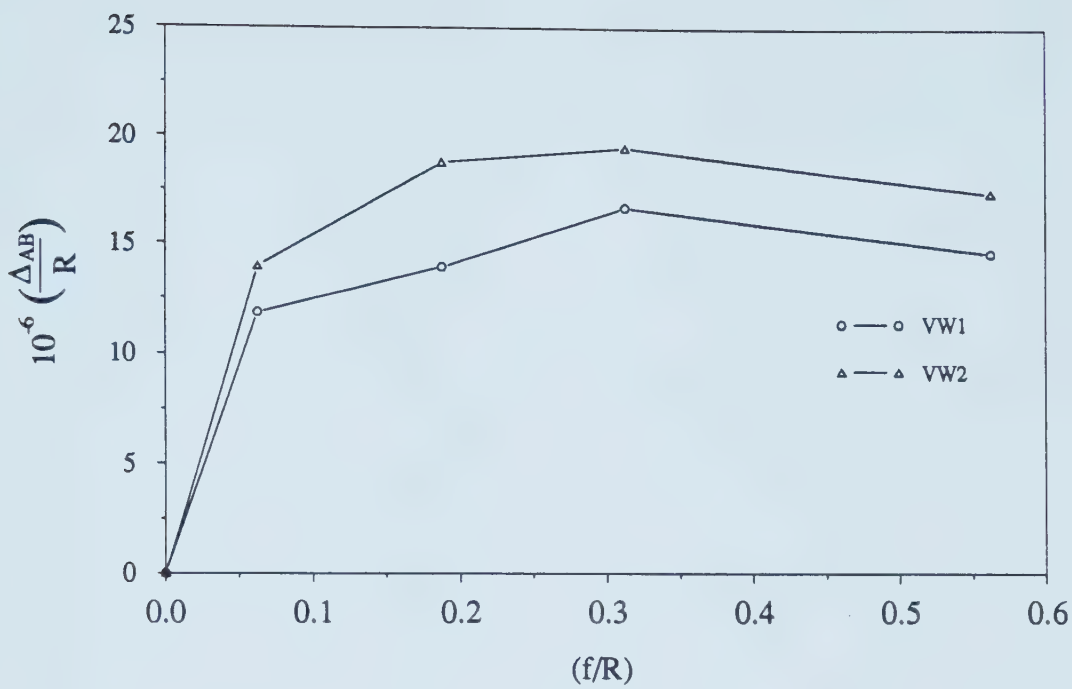


Figure C.4 Relative Displacements during the First Cutting, In Situ Test IST1/1

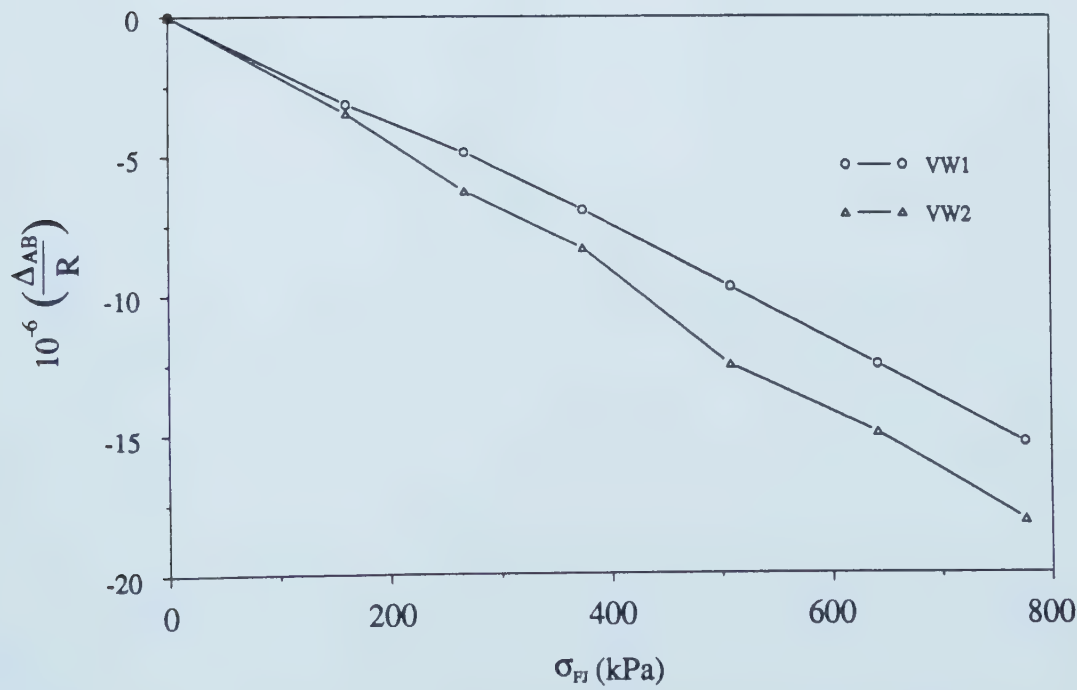


Figure C.5 Relative Displacements during Jack Pressurization Stage, In Situ Test IST1/1

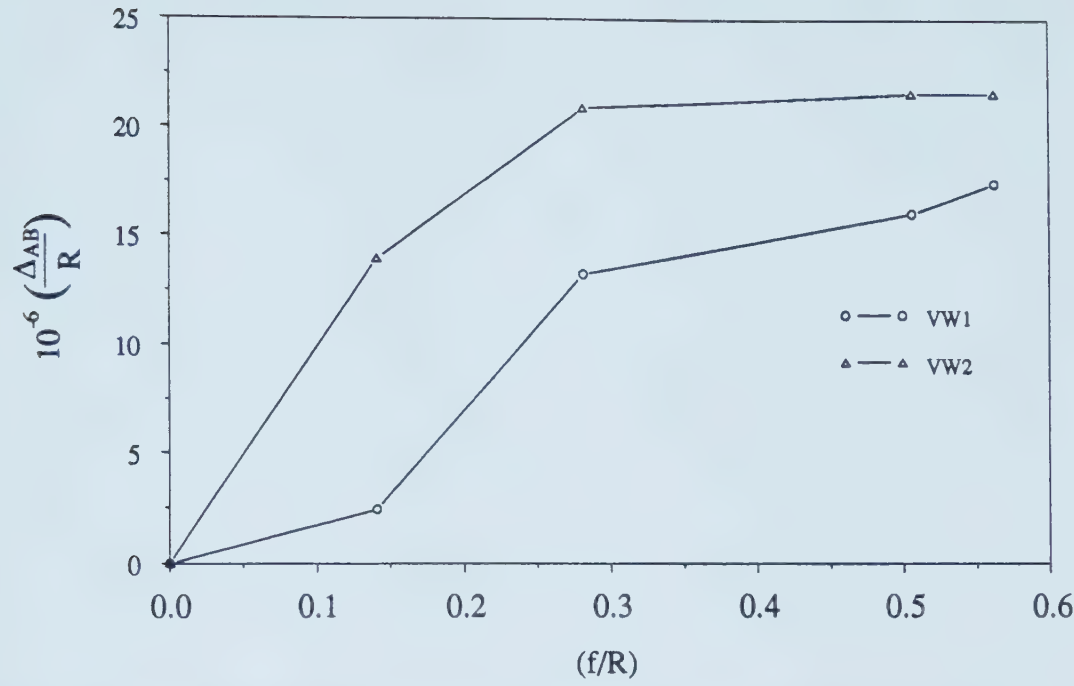


Figure C.6 Relative Displacements during the First Cutting, In Situ Test IST1/2

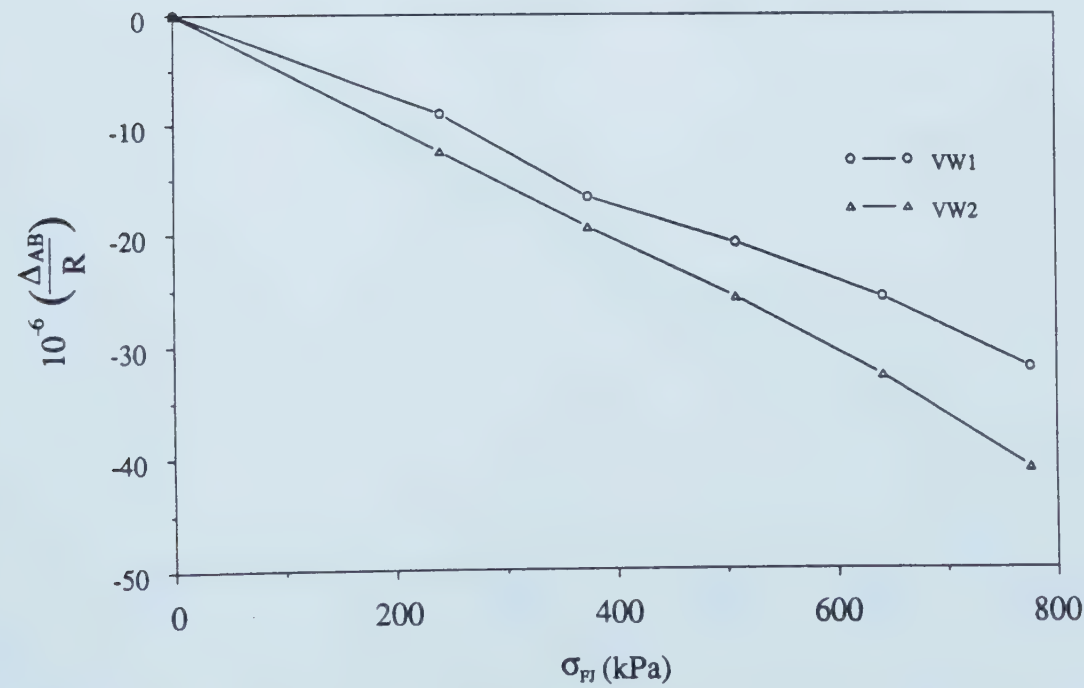


Figure C.7 Relative Displacements during Jack Pressurization Stage, In Situ Test IST1/2

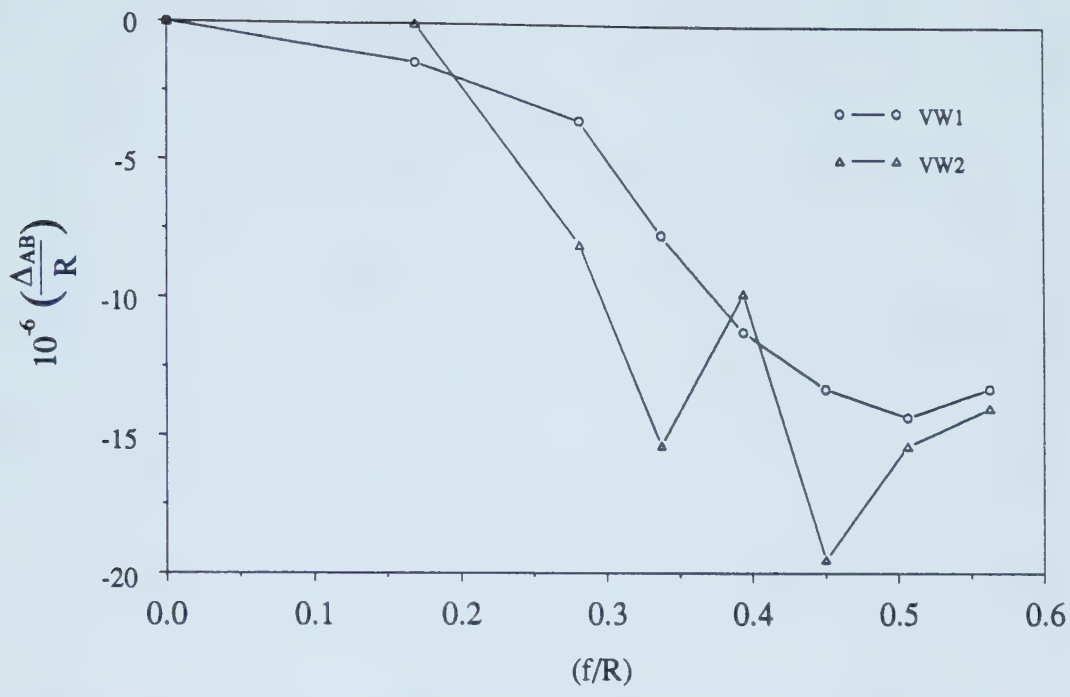


Figure C.8 Relative Displacements during the First Cutting, In Situ Test IST1/3

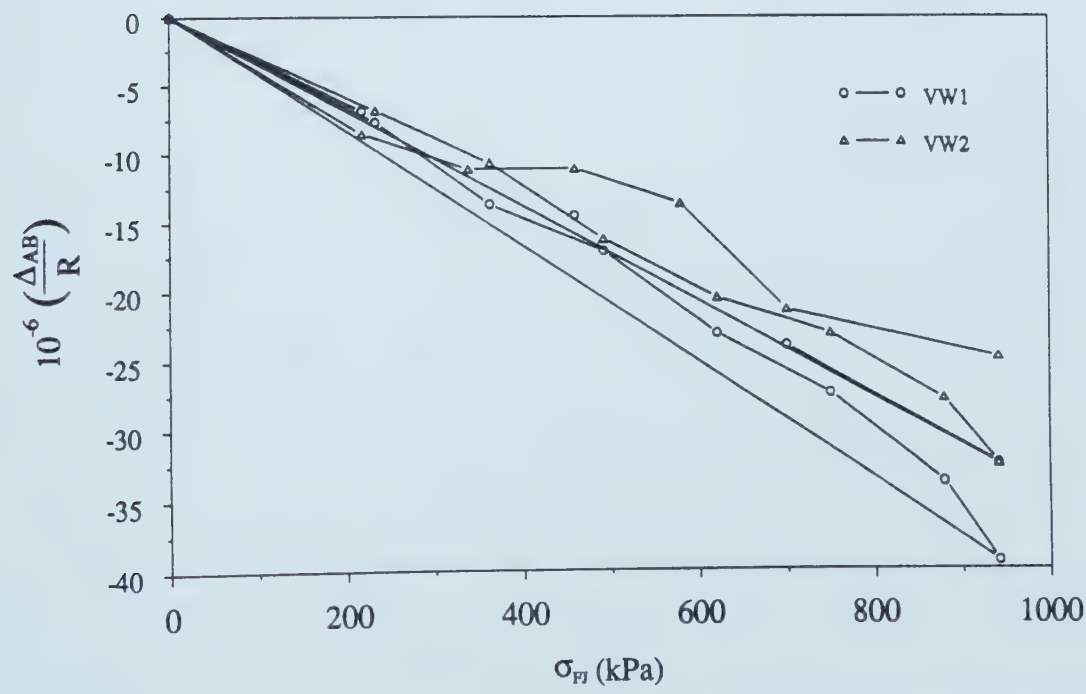


Figure C.9 Relative Displacements during Jack Pressurization Stage, In Situ Test IST1/3

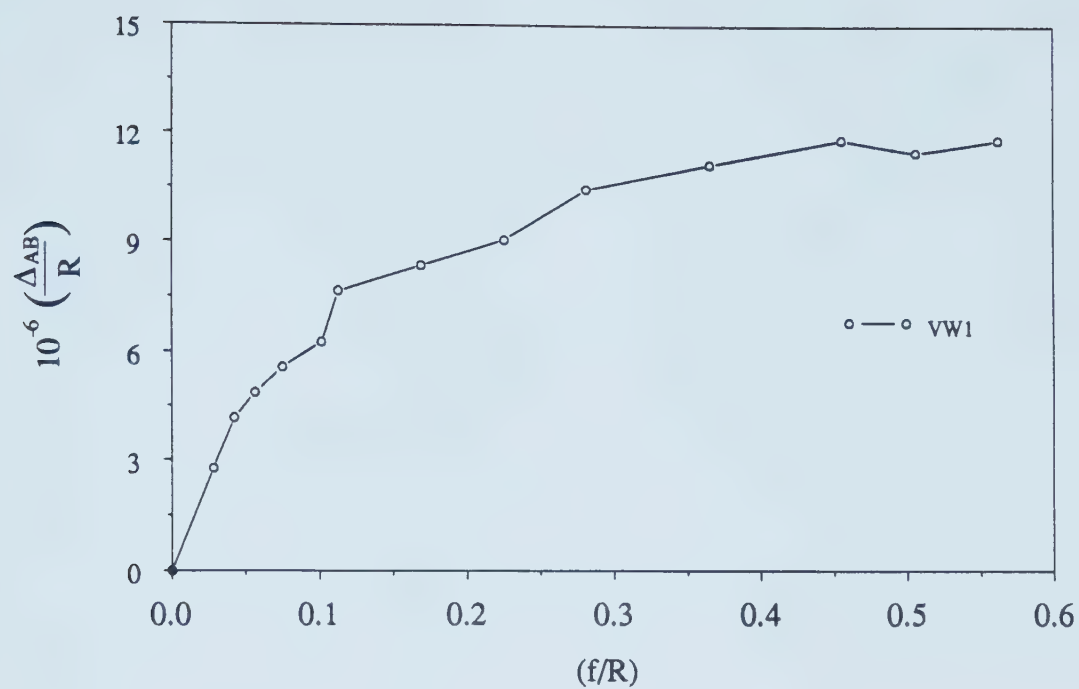


Figure C.10 Relative Displacements during the First Cutting, In Situ Test IST2/1

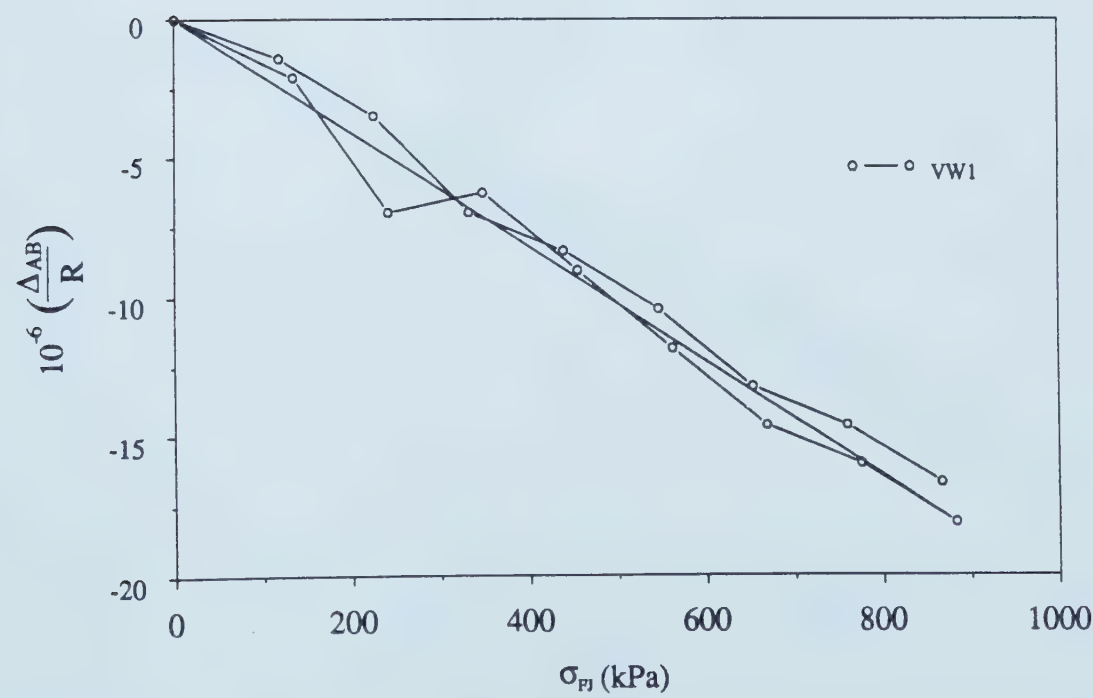


Figure C.11 Relative Displacements during Jack Pressurization Stage, In Situ Test IST2/1

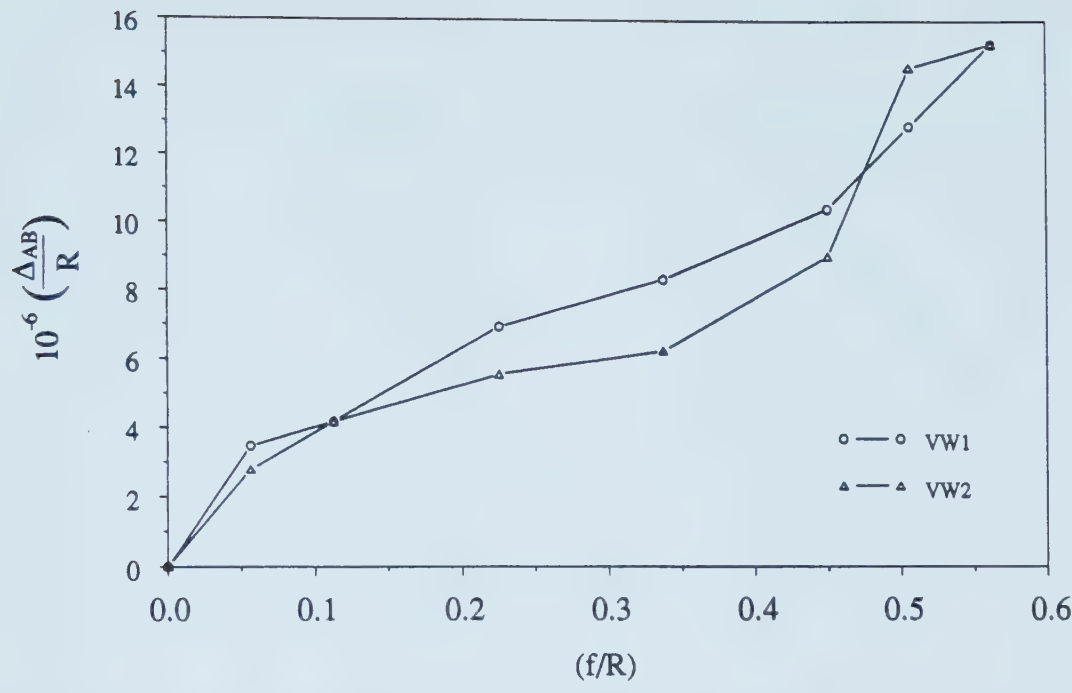


Figure C.12 Relative Displacements during the First Cutting, In Situ Test IST2/2

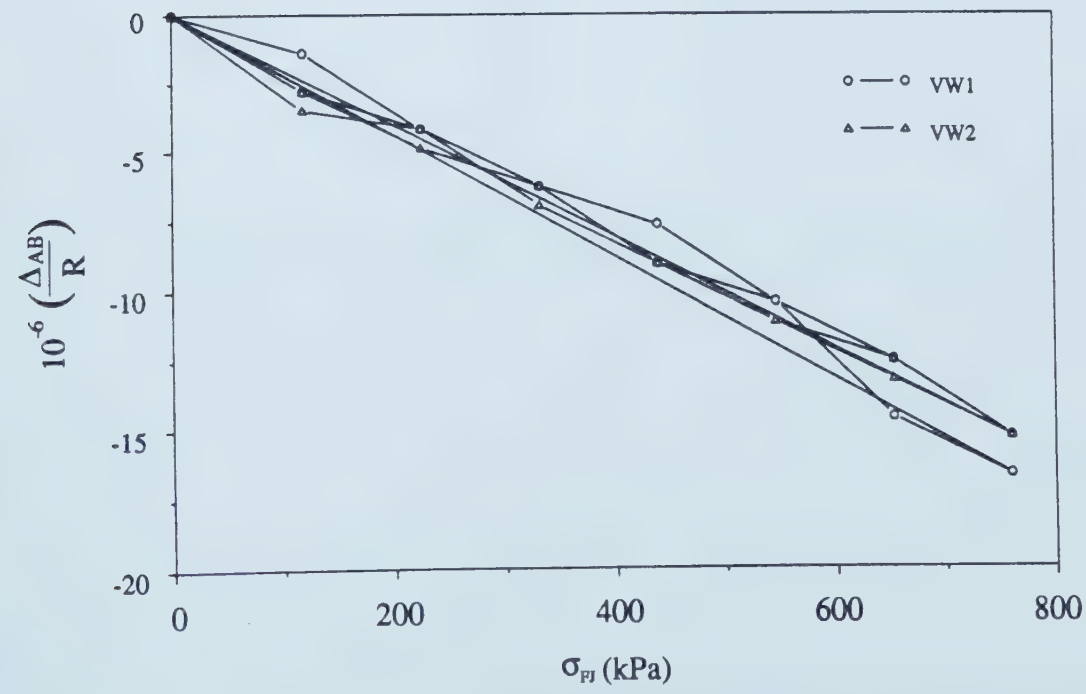


Figure C.13 Relative Displacements during Jack Pressurization Stage, In Situ Test IST2/2

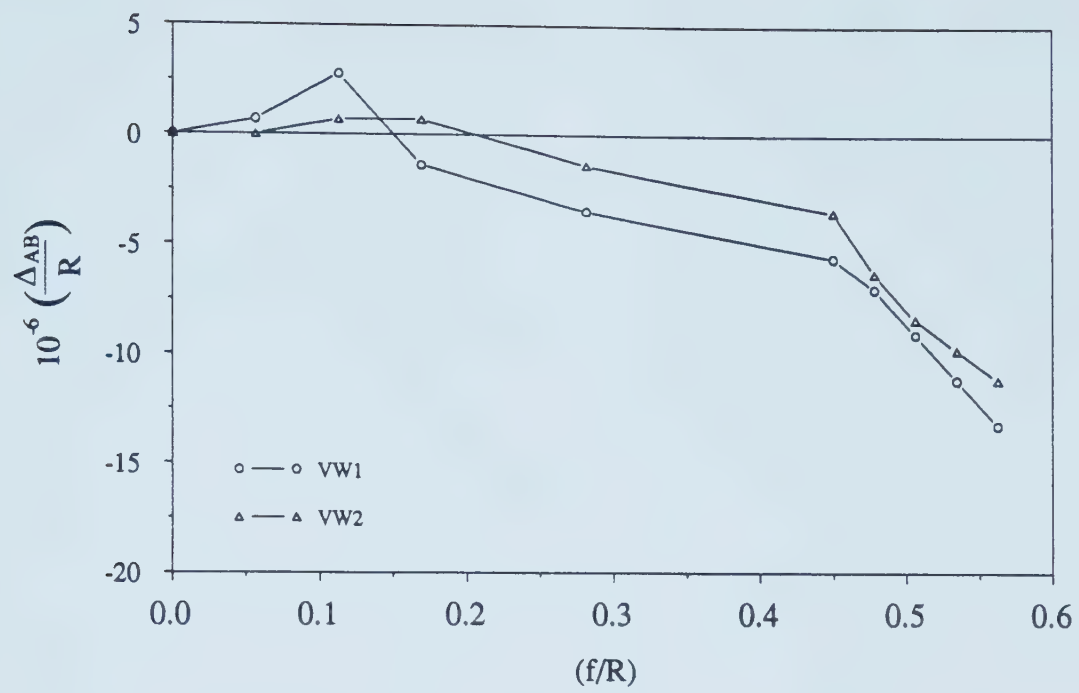


Figure C.14 Relative Displacements during the First Cutting, In Situ Test IST2/3

TEST IST2/3 WAS NOT SUBJECTED TO PRESSURIZATION

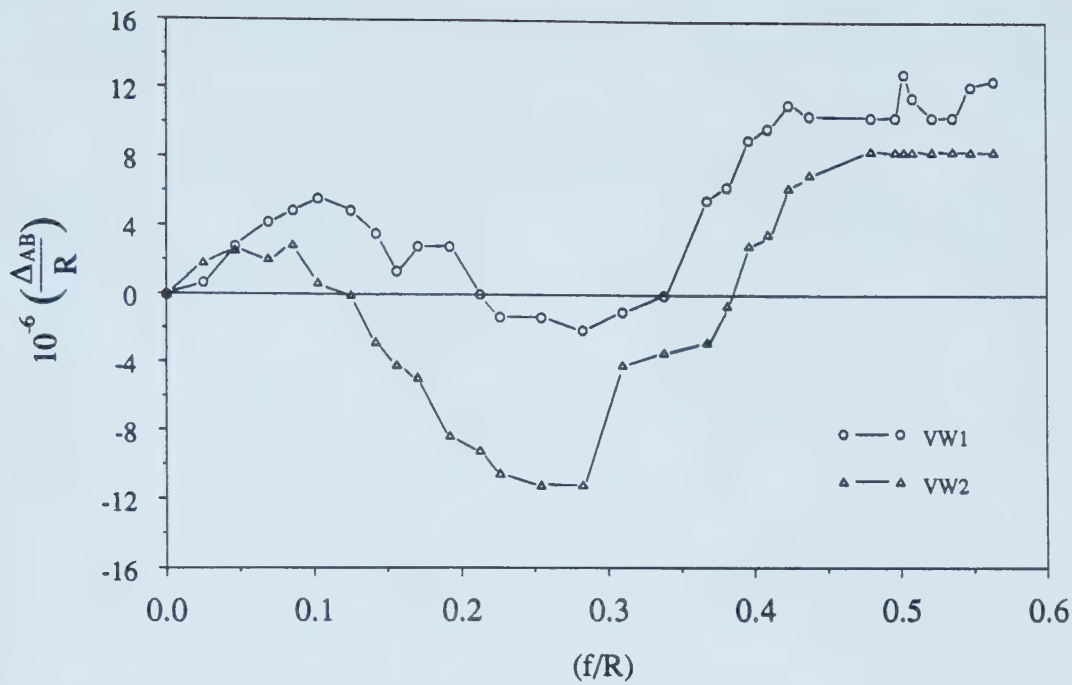


Figure C.15 Relative Displacements during the First Cutting, In Situ Test IST3/1

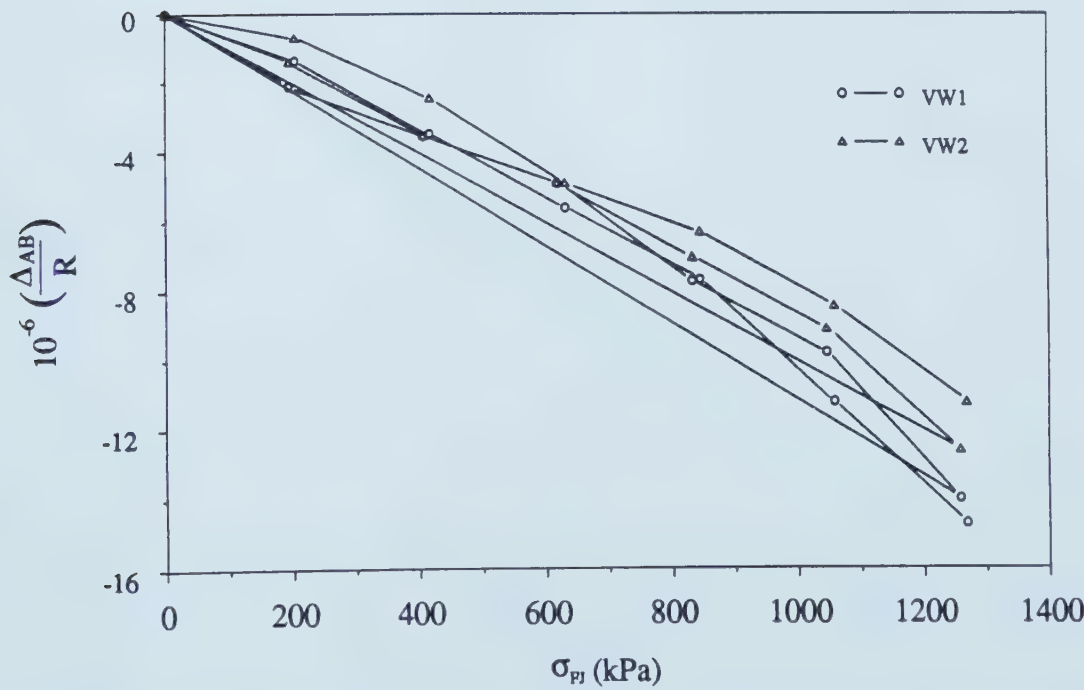


Figure C.16 Relative Displacements during Jack Pressurization Stage, In Situ Test IST3/1

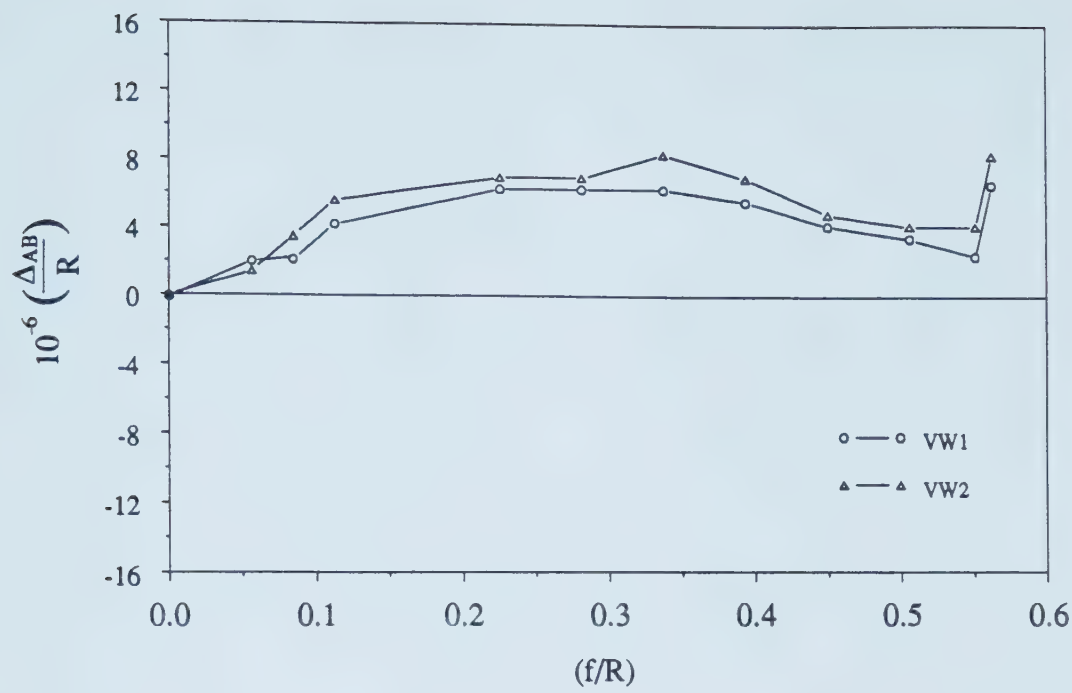


Figure C.17 Relative Displacements during the First Cutting, In Situ Test IST3/2

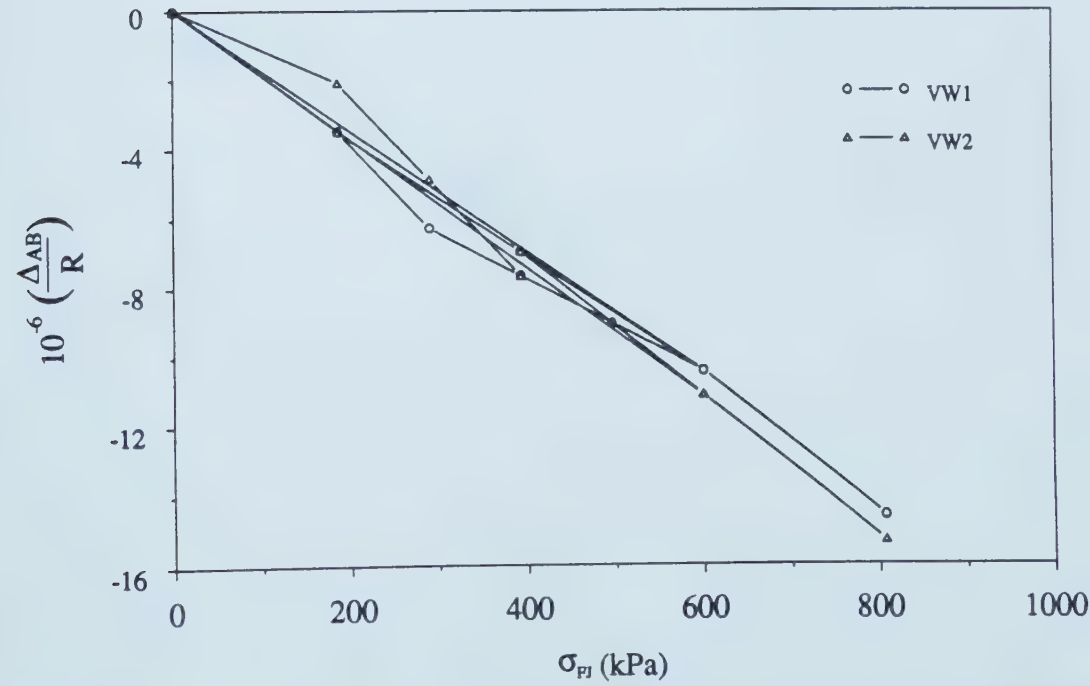


Figure C.18 Relative Displacements during Jack Pressurization Stage, In Situ Test IST3/2

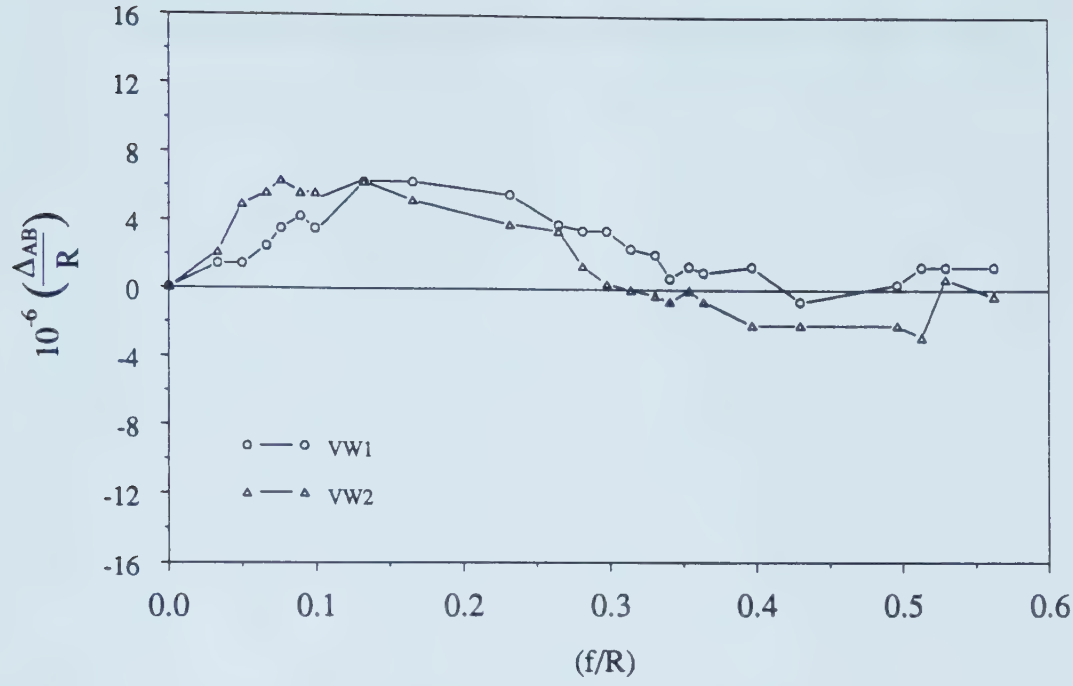


Figure C.19 Relative Displacements during the First Cutting, In Situ Test IST3/3

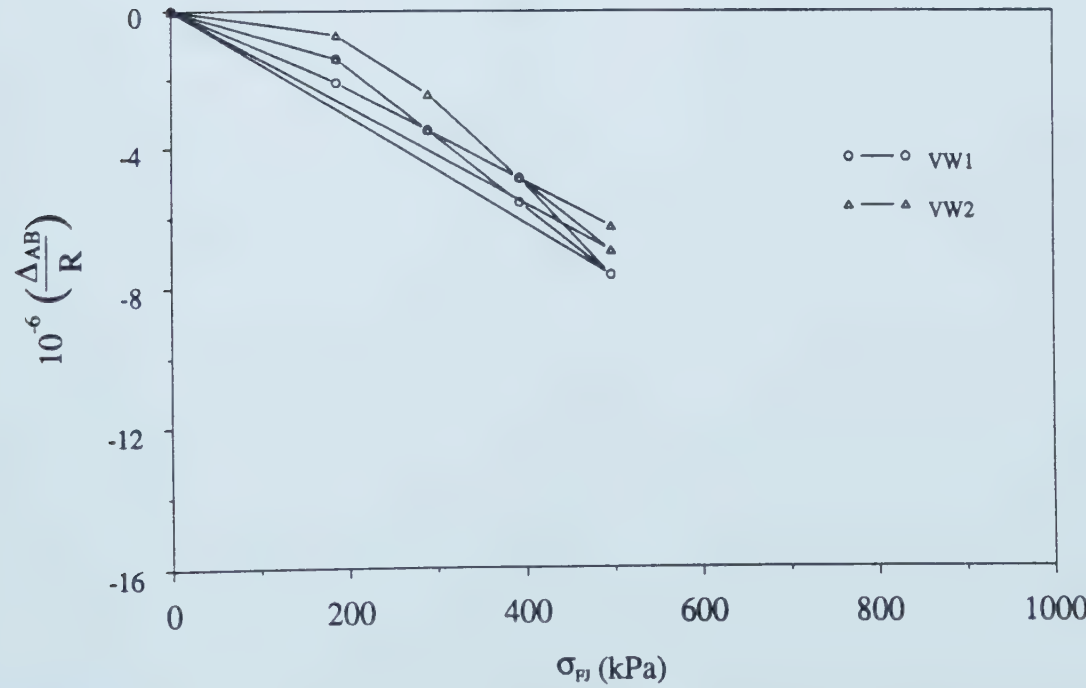


Figure C.20 Relative Displacements during Jack Pressurization Stage, In Situ Test IST3/3

APPENDIX D - Data from Creep Tests in Shotcrete at Early Age

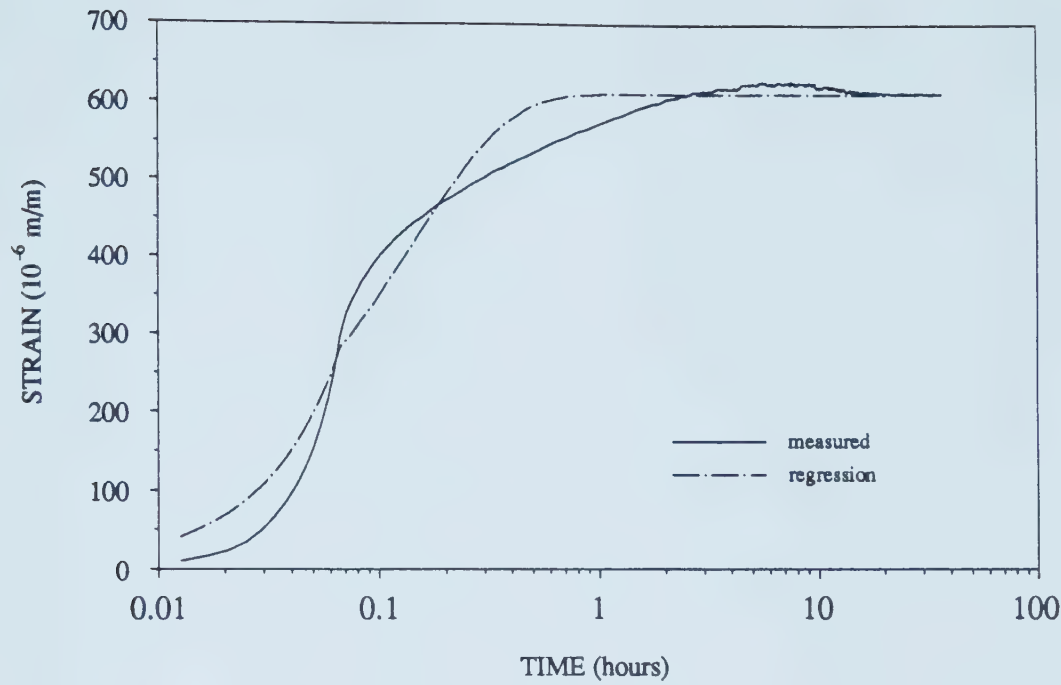


Figure D.1 Measured and Calculated Strains, Test CRSG4H

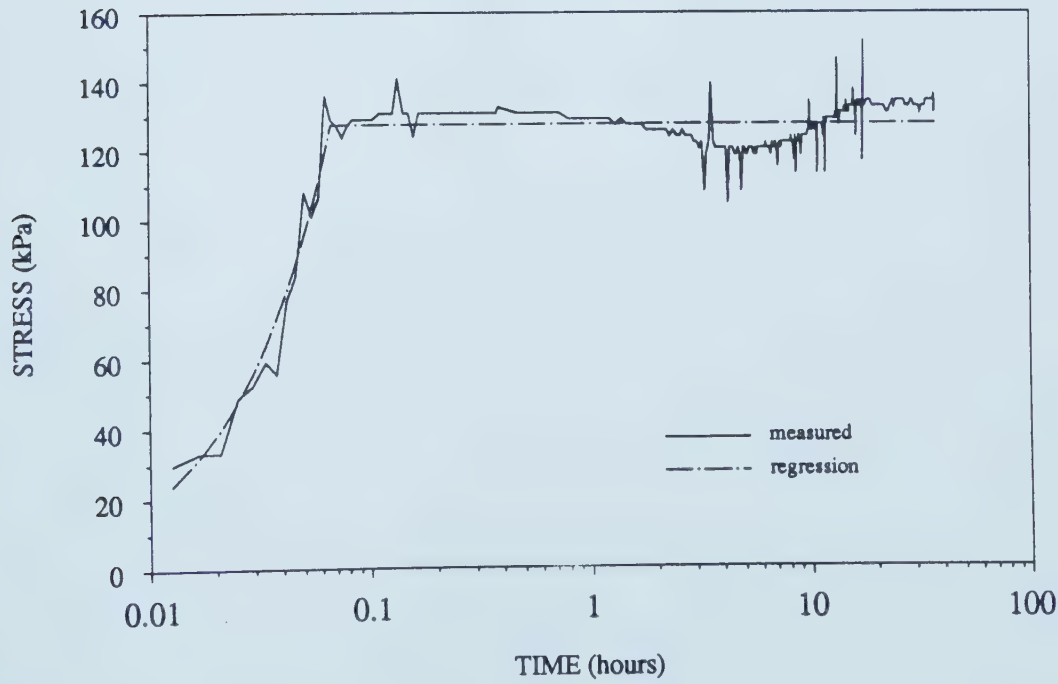


Figure D.2 Measured and Assumed Stresses, CRSG4H

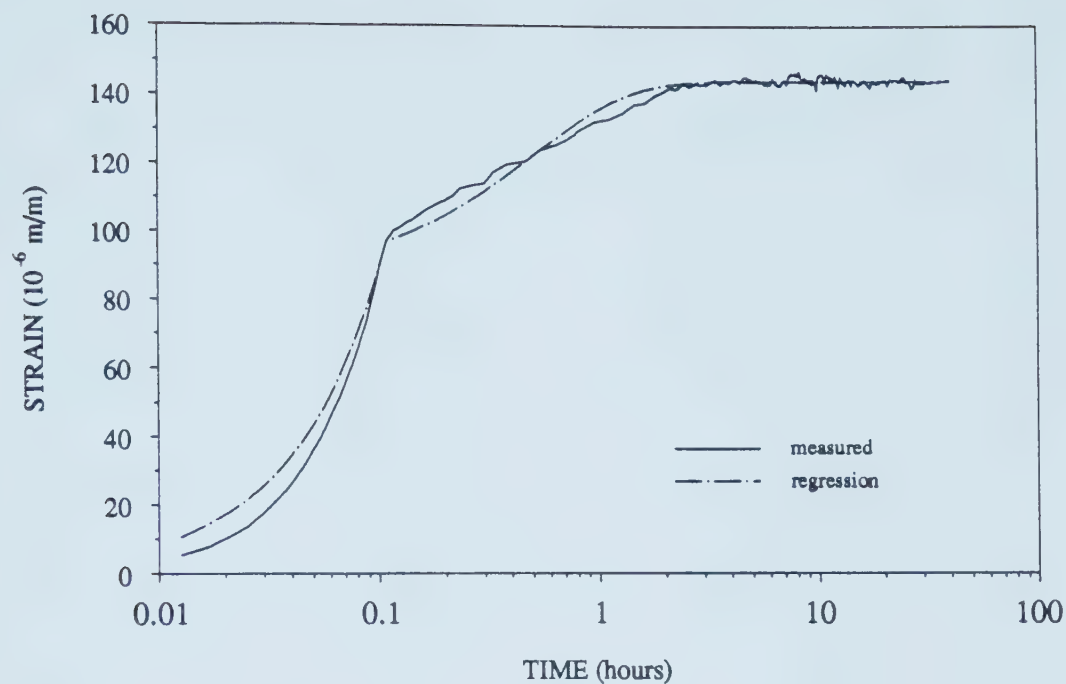


Figure D.3 Measured and Calculated Strains, Test CRSG8H

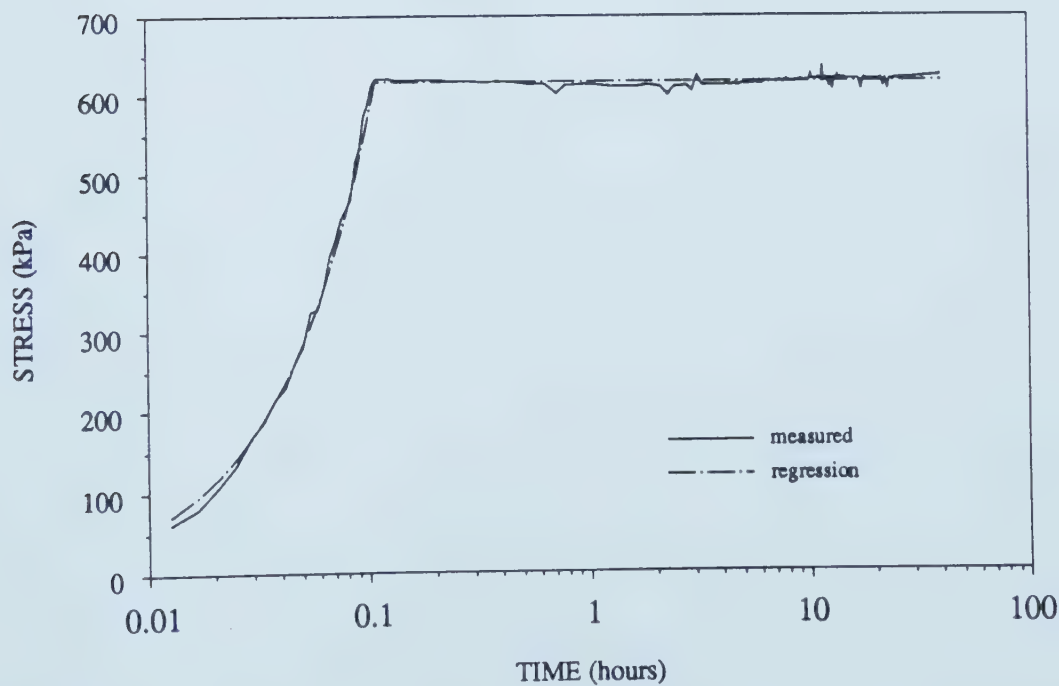


Figure D.4 Measured and Assumed Stresses, CRSG8H

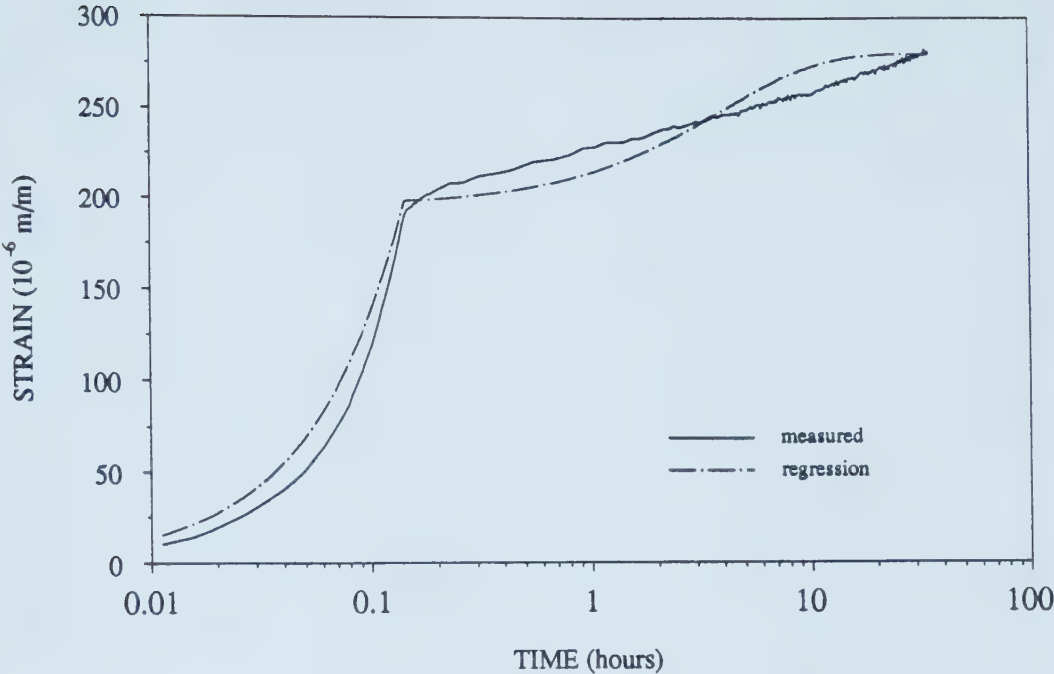


Figure D.5 Measured and Calculated Strains, Test CRSG12H

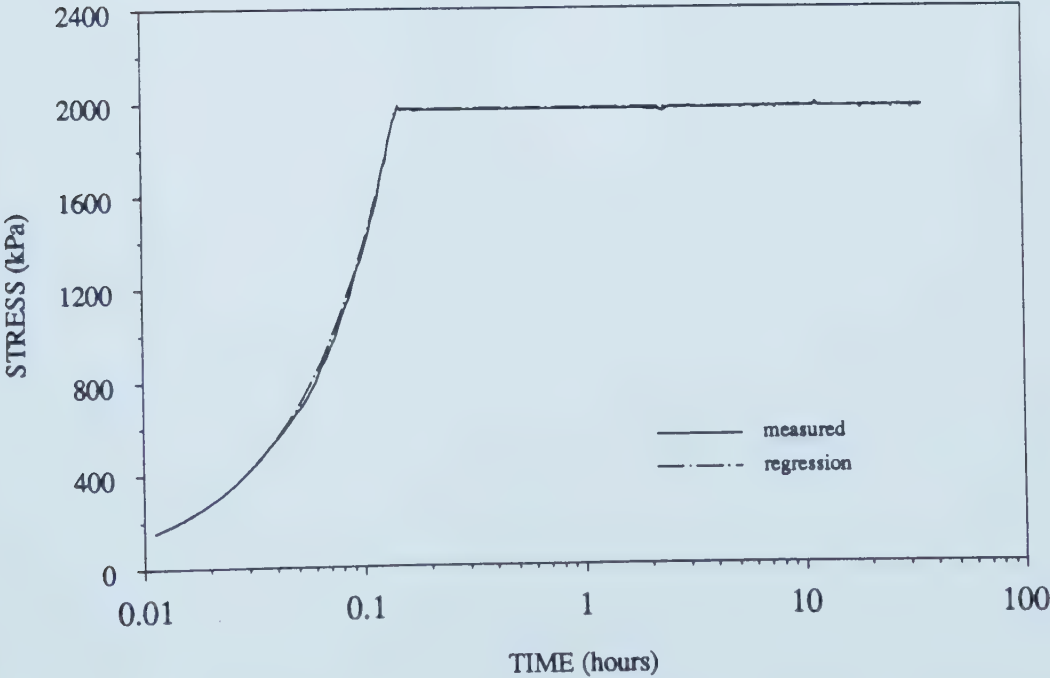


Figure D.6 Measured and Assumed Stresses, CRSG12H

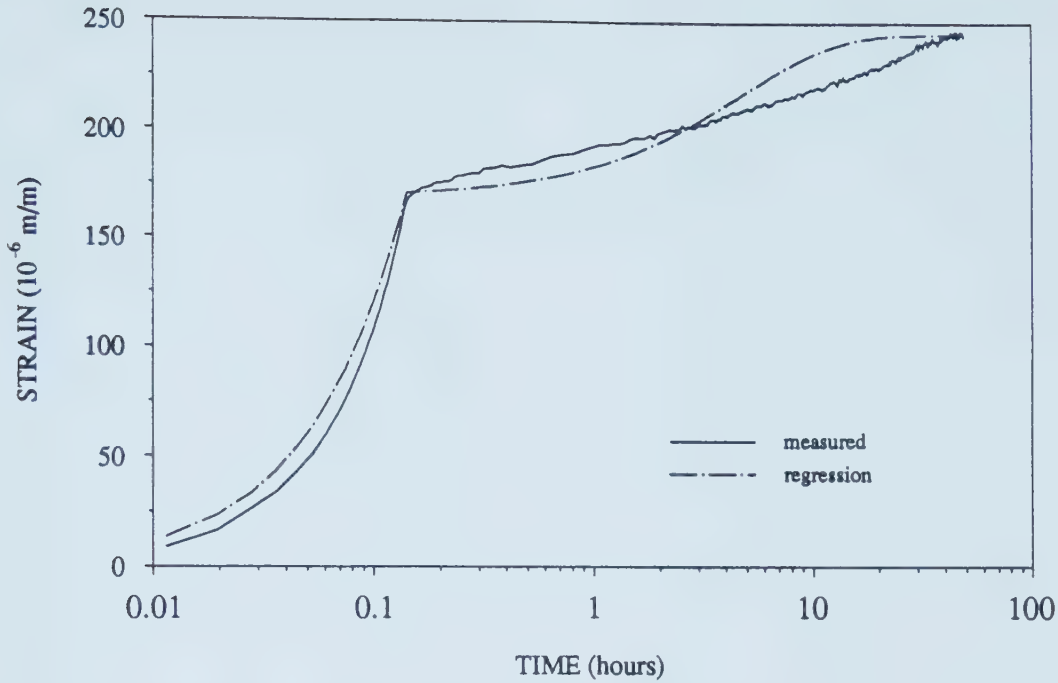


Figure D.7 Measured and Calculated Strains, Test CRSG16H

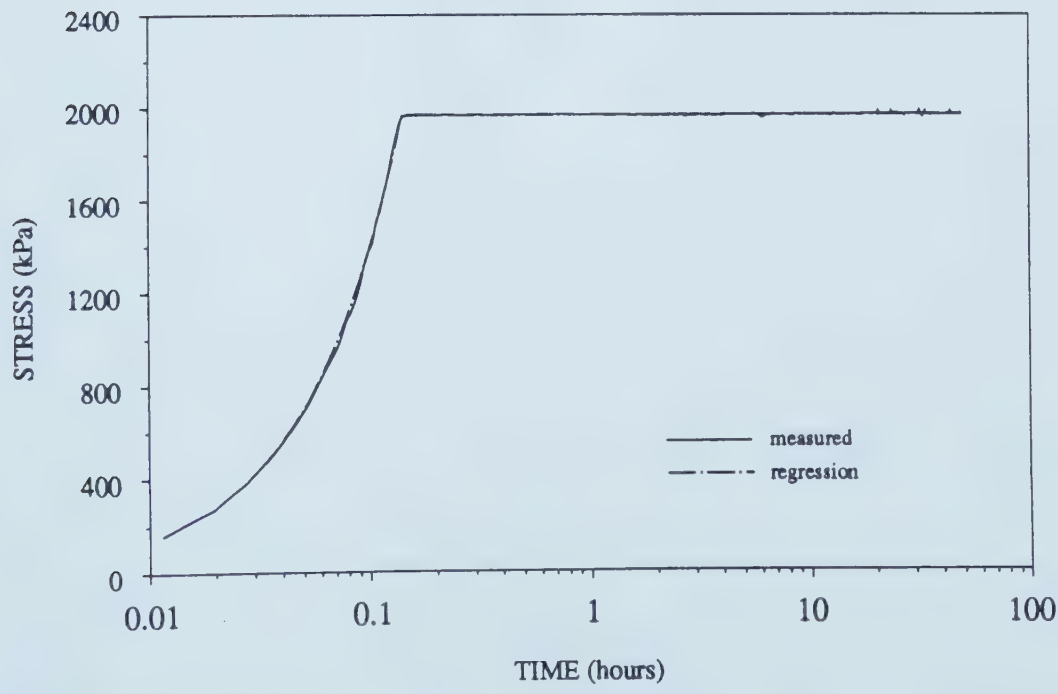


Figure D.8 Measured and Assumed Stresses, CRSG16H

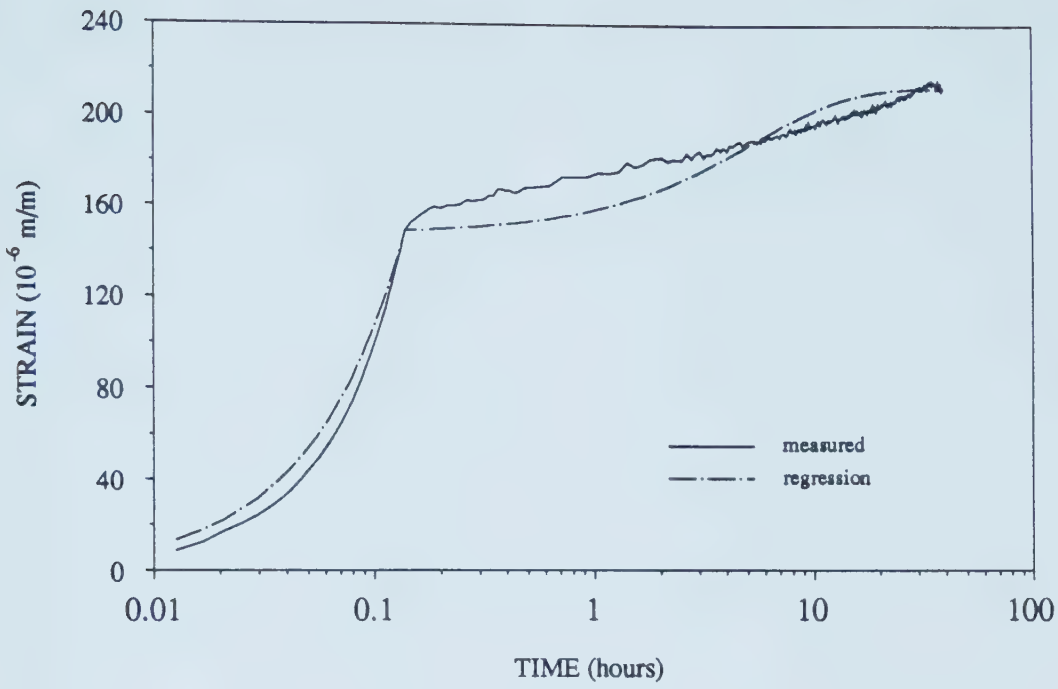


Figure D.9 Measured and Calculated Strains, Test CRSG24H

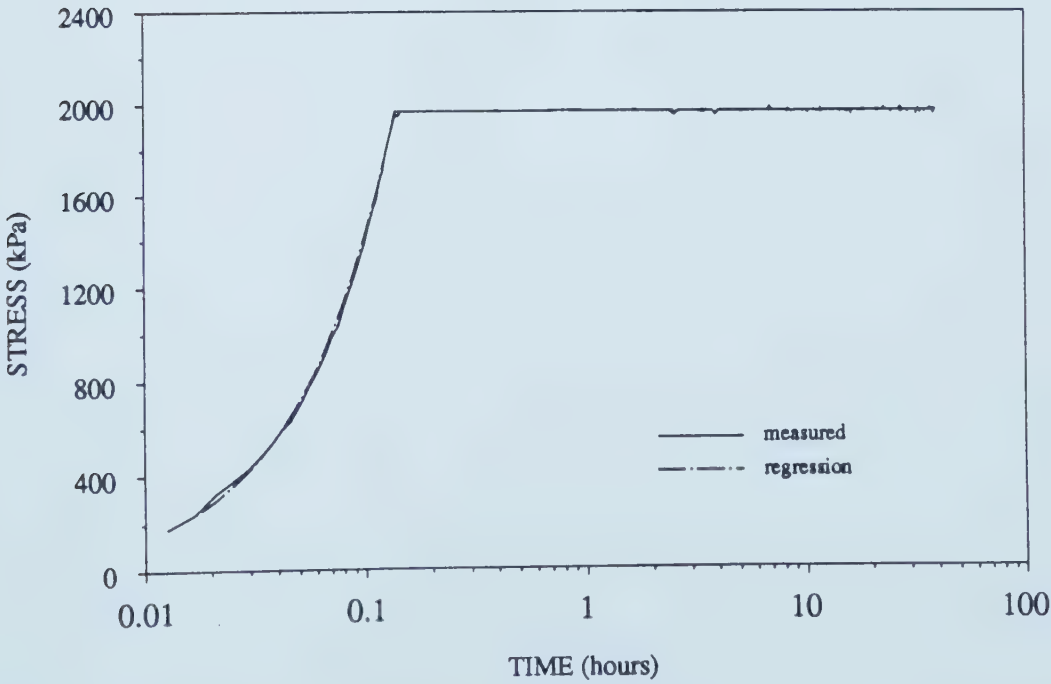


Figure D.10 Measured and Assumed Stresses, CRSG24H

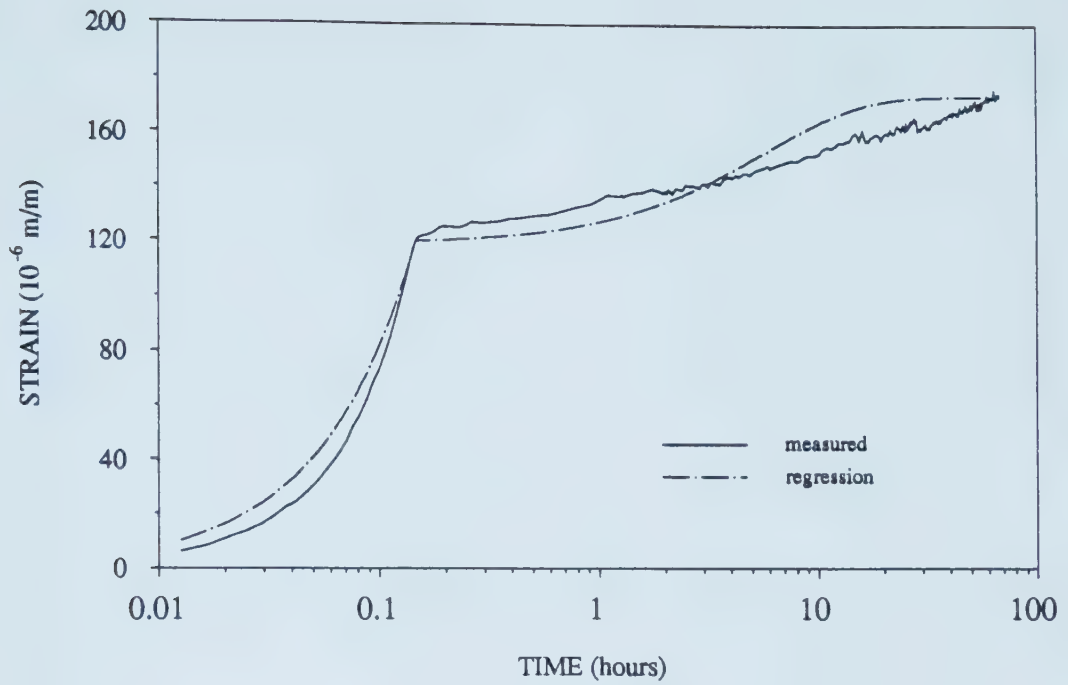


Figure D.11 Measured and Calculated Strains, Test CRSG36H

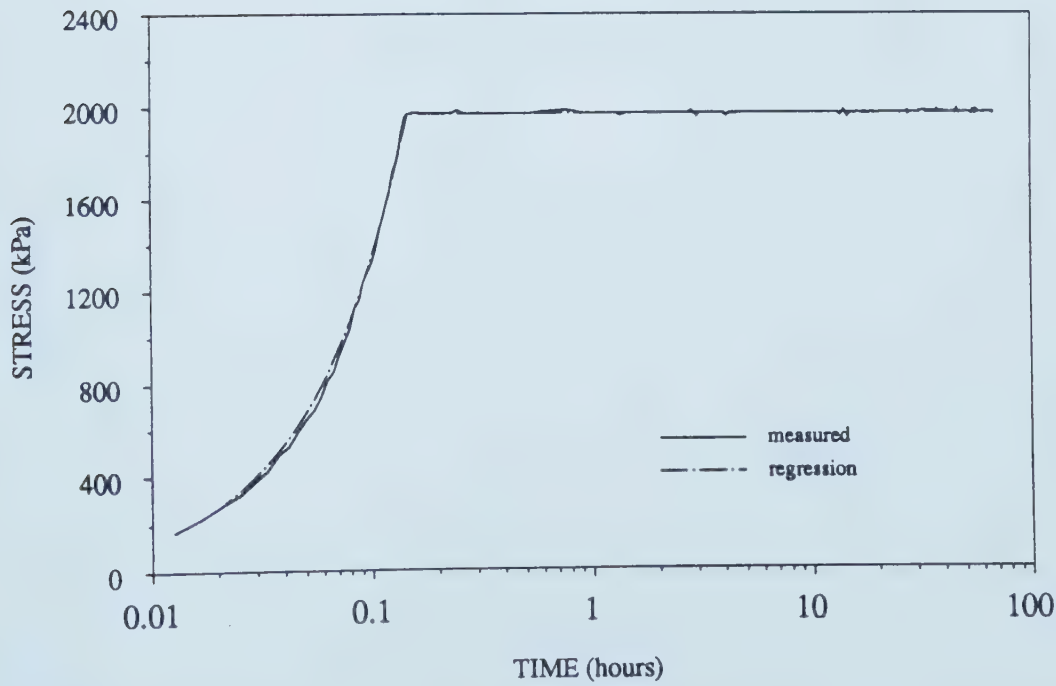


Figure D.12 Measured and Assumed Stresses, CRSG36H

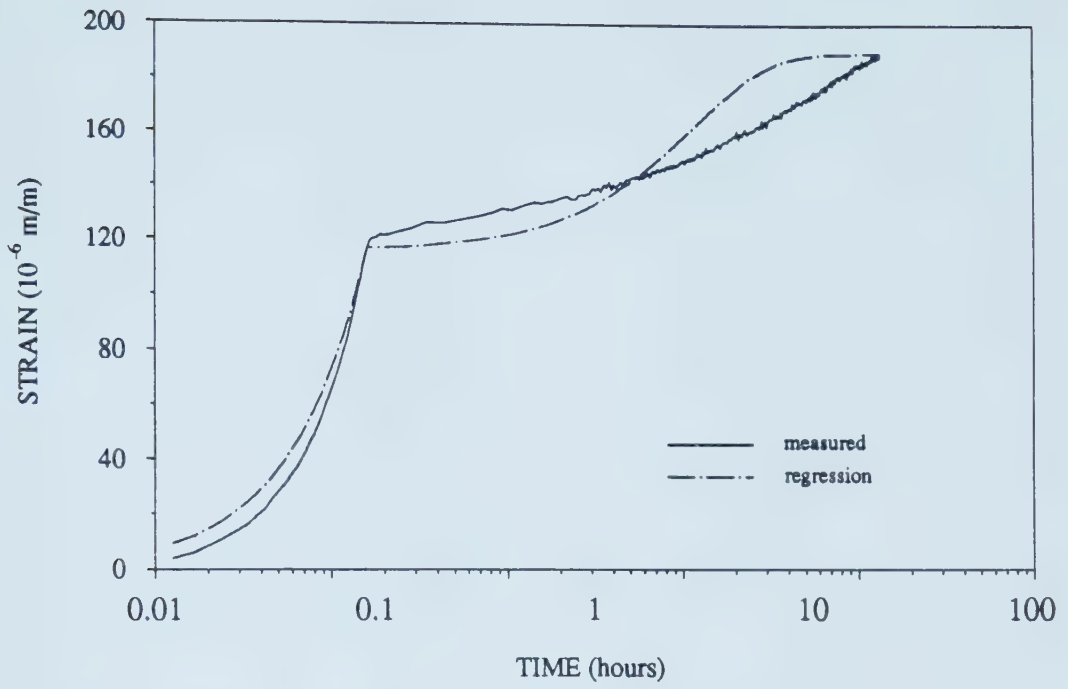


Figure D.13 Measured and Calculated Strains, Test CRS78H

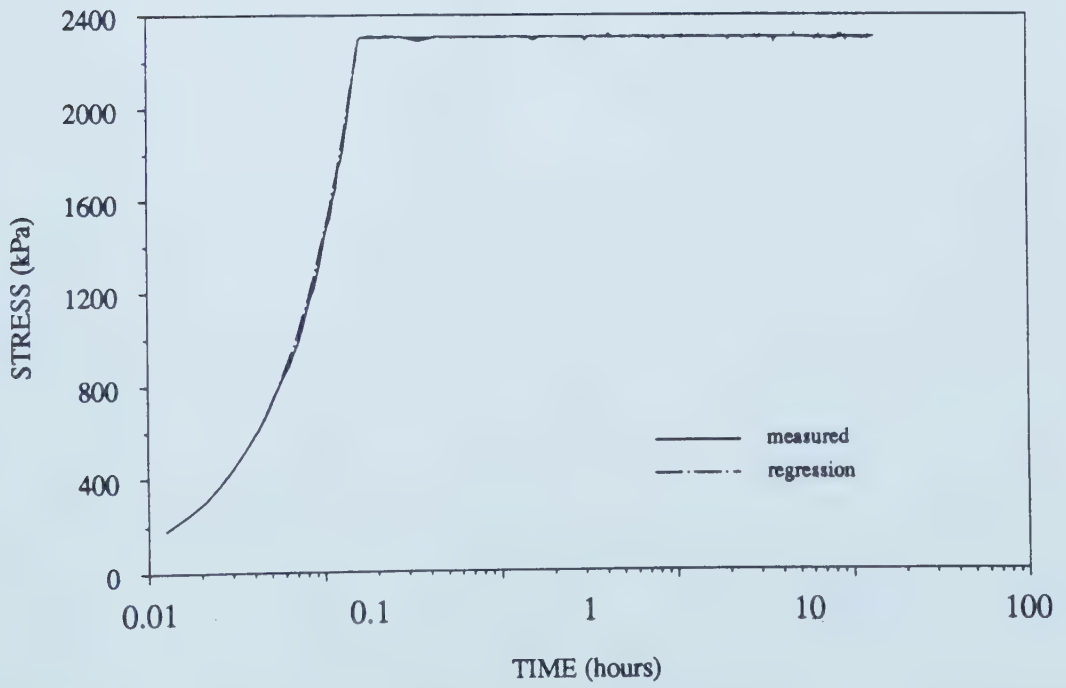


Figure D.14 Measured and Assumed Stresses, CRS78H

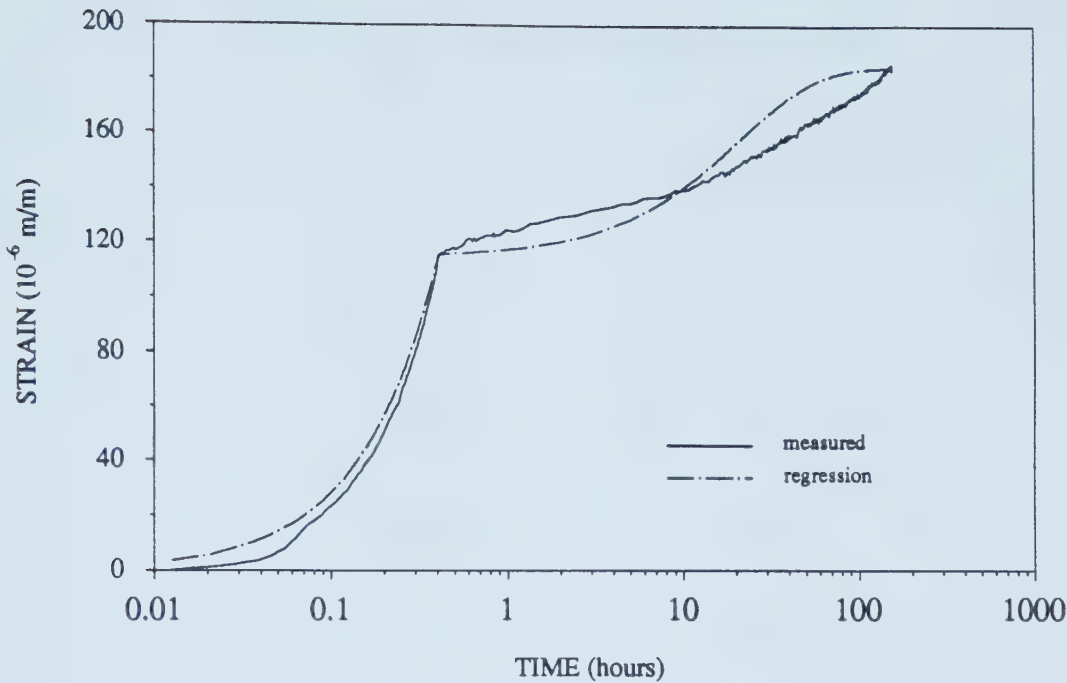


Figure D.15 Measured and Calculated Strains, Test CRSG168H

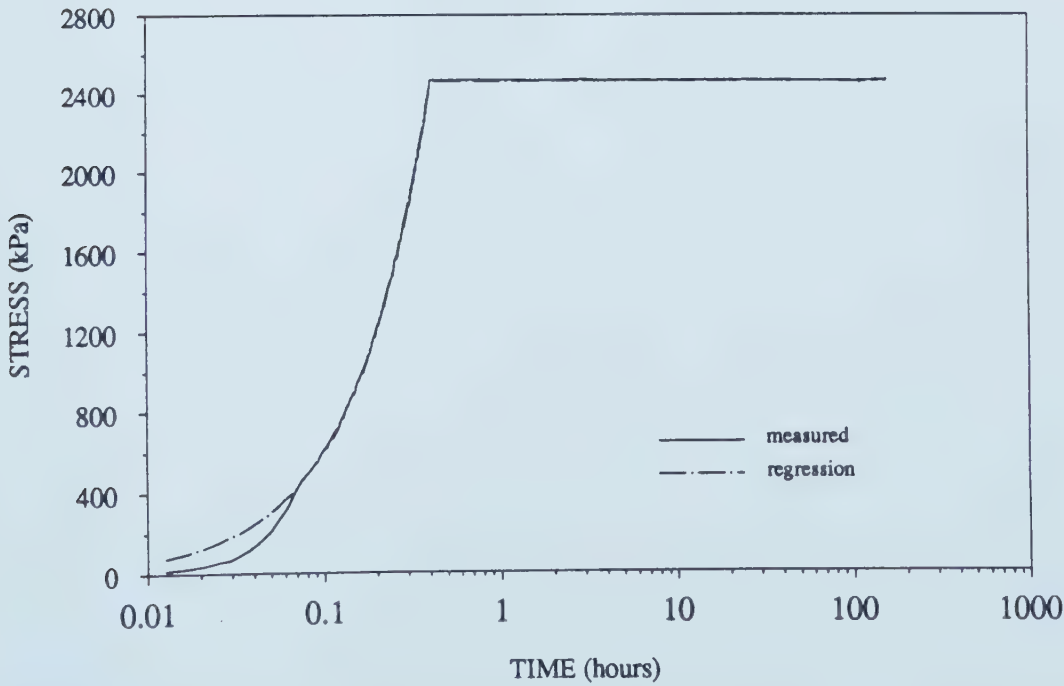


Figure D.16 Measured and Assumed Stresses, CRSG168H

APPENDIX E - Listing of Program ADVRATE


```

*****
PROGRAM ADVRATE
*****
MODIFICATION OF YUEN'S (1979) SOLUTION FOR ROCK LINER INTERACTION
*****
IN VISCOELASTIC MEDIUM
*****
APPLIED TO EMULATION OF
*****
TUNNEL ADVANCE RATE CONSTRUCTION IN LINEAR ELASTIC GROUND
*****
AND VISCOELASTIC LINER
*****
BY
*****
FLAVIO MASSAYUKI KUWAJIMA, 1990
*****
*****
*****
THIS BASIC PROGRAM WAS TRANSLATED FROM THE FORTRAN CODE BY
YUEN(1979) AND THEN MODIFIED AS INDICATED IN CHAPTER 4
*****
IN THIS CODE, ORDINARY COMMAND LINE TRANSFORMED INTO COMMENT
BY ', INDICATES LINES NOT NECESSARY TO THE PRESENT APPLICATION
*****
MODIFICATIONS FROM THE ORIGINAL PROGRAM IS INDICATED BY THE
COMMENT ':MODIFIED *****
*****
THIS PROGRAM FOLLOWS THE SAME STRUCTURE OF THE ORIGINAL PROGRAM
THE VARIABLES ALSO FOLLOW THE ORIGINAL DESIGNATION
*****
*****
DEFDBL A-Z
CLS
*****
*****
ROCK LINER INTERACTION IN VISCOELASTIC MEDIUM
*****
*****
DEFINITION OF INPUT PARAMETERS
PH=HORZ. INSITU STRESS
PV=VERT. INSITU STRESS
P0=(PV+PH)/2
Q0=(PH-PV)/2
R1=INNER RADIUS OF LINER
R2=OUTER RADIUS OF LINER

```


' R=RADIAL DISTANCE FROM CENTRE OF TUNNEL (m)
' EL=MODULUS OF LINER (kPa)
' VL=POISSON'S RATIO OF LINER
' ER=MODULUS OF ROCK (kPa)
' VR=POISSON'S RATIO OF ROCK
' ELT=CREEP/SWELL MODULUS OF LINER (kPa)
' ENL=VISCOSITY OF LINER (kPa*day)
' ERT=CREEP/SWELL MODULUS OF ROCK (kPa)
' ENR=VISCOSITY OF ROCK (kPa*day)
' T0=TIME OF INSTALLATION OF LINER (days)
' T1=TIME WHEN PRESSURES ARE EVALUATED (day)
' APHA1,APHA2=EXPONENTS IN STRESS REBUILD-UP FUNCTION (DISTORTIONAL)
' BETA1,BETA2=EXPONENTS IN STRESS REBUILD-UP FUNCTION (HYDROSTATIC)
' NO SLIP AT INTERFACE
' GAMA1,GAMA2=EXPONENTS IN STRESS REBUILD-UP FUNCTION (DISTORTIONAL)
' FULL SLIP AT INTERFACE
' N=0, WRITE OUTPUT FOR STRESS AND DISPL. IN ROCK
' N=1, WRITE OUTPUT FOR STRESS AND DISPL. IN LINER.
' NR=0, FLEXIBLE LINING.
' NR=1, RIGID LINING
' NCASE=1 NO SLIP AT ROCK-LINER INTERFACE.
' NCASE=2 FULL SLIP AT ROCK-LINER INTERFACE.
' NN=0, WRITE TITLE FOR SECOND SET OF RESULTS FOR LINER.
' PC=BENDING STRESS OF CONCRETE IN COMPRESSION (kPa)
'

' *****
' *
' * INPUT PARAMETERS *
' *
' *****

' *****
' *
' * CURVE FITTING USING 3D FEM SIMULATION (HANAFY & EMERY, 1980) *
' *
' * COEFICIENT k = 0.629399 *
' * COEFICIENT w = 1.098728 *
' *
' *****

coefk = .629399 ;'MODIFIED *****
coefw = 1.098728 ;'MODIFIED *****
' ;'MODIFIED *****
' ;'MODIFIED *****
KAKA = 0 ;'MODIFIED *****
' ;'MODIFIED *****
INPUT "ENTER INPUT FILENAME "; NOME1\$;'MODIFIED *****
OPEN "i", #1, NOME1\$;'MODIFIED *****
INPUT "ENTER OUTPUT FILENAME "; NOME\$;'MODIFIED *****
OPEN "o", #2, NOME\$;'MODIFIED *****

' *****
' * Note that the input data requirement was modified: *


```

' * PH,PV,R2,EL,VL,THIL,TLAML,PC,NCASE,NR have the same *
' * meaning as presented above. *
' * The others parameters: *
' * T - lining thickness (m) *
' * Eeq - equivalent Young's modulus of the ground (kPa) *
' * VR - Poisson's ratio of the ground *
' * ADVAN - rate of tunnel advancing (radius/day) *
' * T0 - delay of lining activation (days) *
' * (delay of lining installation + delay due to curing) *
' * (see Chapter 4) *
' *****

```

```

INPUT #1, PH, PV, R2, T :MODIFIED *****
INPUT #1, EL, VL, Eeq, VR :MODIFIED *****
INPUT #1, THIL, TLAML, ADVAN :MODIFIED *****
INPUT #1, T0, PC, NCASE, NR :MODIFIED *****

```

```

RX = (R2 - T) / R2 :MODIFIED *****
ER = Eeq / (1 - coefk) :MODIFIED *****
ERT = Eeq * ER / (ER - Eeq) :MODIFIED *****
THIR = ER / ERT :MODIFIED *****
SN = ER * (1 + VL) / (EL * (1 + VR)) :MODIFIED *****
TLAMR = coefw * ADVAN / 24 :MODIFIED *****

```

EVALUATION OF FUNDAMENTAL PARAMETERS

```

R1 = R2 * RX
TR = RX * RX
'ER = SN * EL * (1 + VR) / (1 + VL) :MODIFIED *****
'ERT = ER / THIR :MODIFIED *****
ELT = EL / THIL
GL = EL / (2 * (1 + VL))
GR = ER / (2 * (1 + VR))
GRT = ERT / (2 * (1 + VR))
GLT = ELT / (2 * (1 + VL))
ENR = 2 * GRT / TLAMR
ENL = 2 * GLT / TLAML
TLAMRD = TLAMR * (1 + THIR)
TLAMLD = TLAML * (1 + TLAML)
BMR = 1 + THIR
BML = 1 + THIL

```

```

P0 = (PV + PH) / 2
Q0 = (PH - PV) / 2
SK0 = PH / PV
SKK = (SK0 - 1) / (SK0 + 1)

```

```

DA = 5 - 6 * VR
DB = 4 - 6 * VR
DM = (1 + VR) / (3 * ER)
DN = (1 + VL) / (3 * EL * (1 - TR) ^ 3)
C1 = (ER * (1 + VL)) / (EL * (1 + VR))
C2 = ((1 - 2 * VL) * R2 * R2 + R1 * R1) / (R2 * R2 - R1 * R1)
C3 = DN / DM

```



```

'
' LAPLACE TRANSFORM PARAMETERS
'
GR = ER / (2 * (1 + VR))
GRT = ERT / (2 * (1 + VR))
GNR = ENR
GL = EL / (2 * (1 + VL))
GLT = ELT / (2 * (1 + VL))
GNL = ENL
'

PIRD = GNR / (2 * (GR + GRT))
QORD = 2 * GR * GRT / (GR + GRT)
Q1RD = GR * GNR / (GR + GRT)
'

PILD = GNL / (2 * (GL + GLT))
QOLD = 2 * GL * GLT / (GL + GLT)
Q1LD = GL * GNL / (GL + GLT)
'

' *****
' *
' *          PRINT OUT OF INPUT PARAMETERS          *
' *
' *****

CLS
PRINT : PRINT : PRINT : PRINT SPC(20); "INPUT PARAMETERS": PRINT : PRINT
PRINT "HORIZ. STRESS= "; PH: PRINT "VERT. STRESS= "; PV
PRINT "INNER RADIUS = "; R1: PRINT "OUTER RADIUS= "; R2
PRINT "MODULUS OF ROCK = "; ER: PRINT "MODULUS OF LINER= "; EL
PRINT "POISSON'S RATIO(ROCK) = "; VR: PRINT "POISSON'S RATIO(LINER)= "; VL
PRINT "CREEP MOD. OF ROCK = "; ERT: PRINT "CREEP MOD. OF LINER= "; ELT
PRINT "VISCOSITY OF ROCK = "; ENR: PRINT "VISCOSITY OF LINER= "; ENL
PRINT "TIME OF INSTALLATION(DAYS)= "; T0
PRINT "BENDING STRENGTH OF CONCRETE IN TENSION= "; PC
PRINT "RATIO OF TOTAL AND VISCOELASTIC DEFORMATION OF ROCK = "; BMR
PRINT "RATIO OF TOTAL AND VISCOELASTIC DEFORMATION OF LINER= "; BML
PRINT "MODULUS RATIO OF ROCK AND LINER = "; SN
PRINT "LAMBDA (ROCK) = "; TLAMR
PRINT "LAMBDA(LINER) = "; TLAML
PRINT "CASE No.= "; NCASE
PRINT "RIGIDITY = "; NR
PRINT "P0 = "; P0; " (kPa)"
PRINT "Q0 = "; Q0; " (kPa)"
PRINT "K0 = "; SK0
INPUT "PRESS ENTER TO CONTINUE ...", asdf$                                : 'MODIFIED *****
'
'
' PRINT TITLE LABELS
' INITIALIZE TIME
'
'
N = 0
T1 = 0

```



```

1380 PRINT : PRINT : PRINT T1; " DAYS AFTER EXCAVATION OF TUNNEL "; PRINT : PRINT
      PRINT #2, T1
      ;'MODIFIED *****
      ;
      ;
      ; TWO CASES OF INTERFACE CONDITIONS ARE CONSIDERED
      ;
      IF NCASE = 1 THEN PRINT " NO SLIP AT INTERFACE "; PRINT : PRINT
      IF NCASE = 2 THEN PRINT " FULL SLIP AT INTERFACE "; PRINT : PRINT
      IF (T1 - T0) <= 0 THEN GOTO 1460 ELSE GOTO 1490
1460 PRINT "STRESSES AND DISPLACEMENTS IN ROCK MASS BEFORE INSTALATION OF
LINING ": PRINT : PRINT
      PRINT " R2/R THETA RD.ST./P0 TG.ST./P0 SH.ST./P0 RD.DIS./R2 TG.DIS./R2"
      GOTO 1570
1490 IF N = 1 THEN GOTO 1500 ELSE GOTO 1540
1500 PRINT " STRESSES AND DISPLACEMENTS IN LINING "; PRINT : PRINT
      PRINT "THETA UR/R2 VR/R2 UR/R2 VR/R2 RD.PR. TG.PR./ M/P0* N/P0* TG.ST./ TG.ST./
FS"
      PRINT " (R2) (R2) (R1) (R1) /P0 P0 (R2-R1)^2 (R2-R1) P0(R1) P0(R2)CONC"
      GOTO 1570
1540 PRINT : PRINT : PRINT " STRESSES AND DISPLACEMENTS IN ROCK MASS ": PRINT :
PRINT
      PRINT " R2/R THETA RD.ST./P0 TG.ST./P0 SH.ST./P0 RD.DIS./R2 TG.DIS./R2"
      ;
1570 R = R2
1580 THETA = 0
      NN = 0
      RR = R / R2
      TD = T1 - T0
      FT2 = EXP(-TLAMR * T0) * THIR / (1 + THIR)
      FTR = 1 + THIR * (1 - EXP(-TLAMR * T1))
      FTR0 = 1 + THIR * (1 - EXP(-TLAMR * T0))
1650 IF T1 > T0 THEN GOTO 2130
      '*****
      '*
      '* DIMENSIONLESS STRESSES AND DISPLACEMENTS IN ROCK BEFORE
      '* INSTALLATION OF THE LINER
      '*
      '*****
      ;
      ; HYDROSTATIC STRESS COMPONENTS
      ;
      ; DIMENSIONLESS ELASTIC STRESSES AND DISPL. IN ROCK
      ;
      STRH = 1 - R2 * R2 / (R * R)
      STTH = 1 + R2 * R2 / (R * R)
      URH = P0 * (1 + VR) * R2 / (R * ER)
      ;
      ; DISTORTIONAL STRESS COMPONENT
      ;
      ; DIMENSIONLESS ELASTIC STRESSES AND DISPL. IN ROCK
      ;
      STRD = (1 + 3 * (R2 / R) ^ 4 - 4 * (R2 / R) ^ 2) * COS(2 * THETA)
      STTD = -(1 + 3 * (R2 / R) ^ 4) * COS(2 * THETA)
      SSD = -(1 - 3 * (R2 / R) ^ 4 + 2 * (R2 / R) ^ 2) * SIN(2 * THETA)

```



```

URD = ((1 + VR) / ER * (-Q0 * R2 ^ 3 / R ^ 3 + 4 * Q0 * R2 * (1 - VR) / R)) * COS(2 * THETA)
VRD = -((1 + VR) / ER * (Q0 * R2 ^ 3 / R ^ 3 + 2 * Q0 * R2 * (1 - 2 * VR) / R)) * SIN(2 * THETA)
*****
'
'*
'*      COMBINING STRESSES AND DISPLACEMENTS IN ROCK MASS          *
'*      UNDER HYDROSTATIC AND DISTORTIONAL STRESS COMP.           *
'*      (BEFORE LINER INSTALLATION)                                  *
'*                                                                    *
*****
'
IF T1 - T0 <= 0 THEN GOTO 2000 ELSE GOTO 2080
2000 SUME1 = STRH + STRD * SKK
    SUME2 = STTH + STTD * SKK
    SUME3 = SSD * SKK
    SUME4 = (URH + URD) * FTR
    SUME5 = VRD * FTR
    ANGLE = THETA * 180 / 3.141592654#
    PRINT USING " ###.#"; RR; ; PRINT USING " ###.#"; ANGLE; ; PRINT USING " ##.####^";
SUME1, SUME2, SUME3, SUME4, SUME5
'
                                                                MODIFIED *****
IF KAKA = 0 THEN
    IF ANGLE = 0 THEN PRINT #2, NOME$: PRINT #2, "   T       M(0)   T(0)   M(90)   T(90)"
ur(0) ur(90)"
        KAKA = 1
    END IF
    IF ANGLE = 0 THEN PRINT #2, USING "#####.###"                "#.#####"; T1,
SUME4;
    IF ANGLE = 90 THEN PRINT #2, USING "#####.###"; SUME4
'
                                                                MODIFIED *****
GOTO 5490
2080 *****
'
'*      EXTENSION TO VISCOELASTICITY -- HYDROSTATIC STRESS COMPONENT *
'*
'*
*****
2130 IF NR = 0 THEN GOTO 2200
'
'      RIGID LINING PRESSURE - HYDROSTATIC STRESS COMPONENT
'
PLHRT = (1 - EXP(-TLAMRD * TD)) * FT2
PLHT = PLHRT
GOTO 2530
2200 '
'      FLEXIBLE LINING PRESSURE
'
SA = Q0LD
SB = P1RD * Q0LD + Q1LD
SC = P1RD * Q1LD
SD = Q0LD + C2 * Q0RD
SE = P1RD * Q0LD + Q1LD + C2 * (Q1RD + P1LD * Q0RD)
SF = P1RD * Q1LD + C2 * Q1RD * P1LD
'
SDD = SD / SF

```


SED = SE / SF

BETA2 = (SED + SQR(SED * SED - 4 * SDD)) / 2

BETA1 = SDD / BETA2

A1 = SA / (BETA1 * BETA2)

A3 = (SB * BETA2 - SC * BETA2 * BETA2 - SA) / (BETA2 * (BETA1 - BETA2))

A2 = SC - A1 - A3

!*

!*

MAX PRESS. AND PRESS. AT TIME=T1 (DIMENSIONLESS)

!*

XBETA1 = BETA1: XTLAMR = TLAML: XTD = TD: XTHIR = THIL: 'PARAMETER TO FTIME

GOSUB 15000: TLNH = XTRNH: 'RETURN FROM FTIME

XBETA1 = BETA1: XTLAMR = TLAMR: XTD = TD: XTHIR = THIR: 'PARAMETER TO FTIME

GOSUB 15000: TRNH = XTRNH: 'RETURN FROM FTIME

POM = THIR * EXP(-TLAMR * T0) / (C1 * C2 * (1 + THIL) + 1 + THIR)

PLHT = POM * (1 - EXP(-BETA1 * TD))

!*

!*

NORMAL THRUST AND MOMENT IN LINER

!*

2530 '

SLHR1 = 2 * PLHT / (1 - TR)

SLHR2 = PLHT * (1 + TR) / (1 - TR)

SNHLT = PLHT * (3 + TR) / (2 * (1 - TR))

SMHLT = -PLHT / 12

!*

!*

STRESS DISTRIBUTION IN ROCK MASS AT TIME=T1

!*

STRHT = 1 - (1 - PLHT) * (R2 / R) ^ 2

STTHT = 1 + (1 - PLHT) * (R2 / R) ^ 2

!

!*

!*

DISPLACEMENT OF LINER AND ROCK

!*

IF NR = 0 THEN GOTO 2940

!

DISPL. IN ROCK AND LINER FOR RIGID LINER

!

ULHRT1 = 0

ULHRT2 = 0

VLHRT1 = 0

VLHRT2 = 0

!

URHRT = P0 * (1 + VR) / ER * R2 / R * FTR0

VRHRT = 0


```

ULHT1 = ULHRT1
ULHT2 = ULHRT2
VLHT1 = VLHRT1
VLHT2 = VLHRT2
URHT = URHRT
VRHT = VRHRT
GOTO 3110
'
'      DISPL. IN ROCK AND LINER FOR FLEXIBLE LINER
2940 '
  ULHFT2 = POM * C2 * (1 + VL) / EL * TLNH * P0
  ULHFT1 = POM * (1 + VL) / EL * 2 * (1 - VL) * R2 / (R2 * R2 - R1 * R1) * R1 * TLNH * P0
  ULHT1 = ULHFT1
  ULHT2 = ULHFT2
  VLHT1 = 0
  VLHT2 = 0
'
'      DISPLACEMENT IN ROCK
'
  URHFT = (1 + VR) * (R2 / R) / ER * (P0 * FTR - POM * TRNH * P0)
  URHT = URHFT
  VRHT = 0
  '*****
  '*
  '* EXTENTION TO VISCOELASTICITY --- DISTORTIONAL STRESS COMPONENT
  '*
3110 '*****
  C11 = TR ^ 3 * (5 - 6 * VL) + TR ^ 2 * (9 - 6 * VL) + TR * (15 - 18 * VL) + 3 - 2 * VL
  D = TR ^ 3 * (4 - 6 * VL) + TR ^ 2 * (12 - 6 * VL) - 6 * VL * TR + 2 * VL
  C12 = TR ^ 3 * (5 - 8 * VL) + TR ^ 2 * (9 - 6 * VL) - TR * (9 - 6 * VL) + 3 - 2 * VL
  C3 = C1 / ((1 - TR) ^ 3)
  IF NR = 0 THEN GOTO 3330
  IF NCASE = 2 THEN GOTO 3320
'
'      RIGID LINING - NO SLIP AT INTERFACE. DISTORTIONAL STRESS COMPONENT
'
'      LINER PRESSURE
'
3230 SNLR1 = (1 - EXP(-TLAMRD * TD)) * FT2
  STLR1 = SNLR1
  SNLT = SNLR1
  STLT = STLR1
  GOTO 4050
'
'      RIGID LINING - FULL SLIP AT INTERFACE. DISTORTIONAL STRESS COMPONENT
'
'      LINER PRESSURE
3320 GOTO 3230
3330 IF NCASE = 2 THEN GOTO 3760
'
'      FLEXIBLE LINING - NO SLIP AT INTERFACE - DISTORTIONAL
'      STRESS COMPONENT
'
'      LINER PRESSURE

```



```

DK = (1 - C3 * (D - C11)) / (1 + C3 * (C12 - D))
DJ1 = 3 * (3 - 4 * VR)
DJ2 = DA + DK * DB
DJ3 = (C11 + D * DK) / (1 - TR) ^ 3
DJ4 = DJ3 / DJ2
,
SG = Q0LD + DJ4 * Q0RD
SH = Q0LD * P1RD + Q1LD + DJ4 * (Q1RD + P1LD * Q0RD)
SM1 = P1RD * Q1LD + DJ4 * Q1RD * P1LD
,
SGD = SG / SM1
SHD = SH / SM1
APHA2 = (SHD + SQR(SHD * SHD - 4 * SGD)) / 2
APHA1 = SGD / APHA2
B1 = SA / (APHA1 * APHA2)
B3 = (SB * APHA2 - SC * APHA2 * APHA2 - SA) / ((APHA1 - APHA2) * APHA2)
B2 = SC - B1 - B3
*****
!*
!*          MAX PRESS. AND PRESS. AT TIME=T1 (DIMENSIONLESS)          *
!*
*****
,
                                                                MODIFIED *****
XBETA1 = APHA1: XTLAMR = TLAML: XTD = TD: XTHIR = THIL: 'PARAMETER TO FTIME
GOSUB 15000: TLND1 = XTRNH:          'RETURN FROM FTIME          '*
XBETA1 = APHA1: XTLAMR = TLAMR: XTD = TD: XTHIR = THIR: 'PARAMETER TO FTIME
GOSUB 15000: TRND1 = XTRNH:          'RETURN FROM FTIME          '*
,
                                                                MODIFIED *****
TK = (1 + THIR + C3 * (C11 - D) * (1 + THIL)) / (1 + THIR - C3 * (D - C12) * (1 + THIL))
Q0M = THIR * 3 * (3 - 4 * VR) * EXP(-TLAMR * T0) / (C3 * (C11 + D * TK) * (1 + THIL) + (DA
+ DB * TK) * (1 + THIR))
SNLF1 = Q0M * (1 - EXP(-APHA1 * TD))
SNLT = SNLF1
STLT = SNLF1 * TK
GOTO 4050
,
          FLEXIBLE LINING - FULL SLIP AT INTERFACE. DISTORTIONAL
          STRESS COMPONENT
,
3760 '
' LINER PRESSURE
,
DJ7 = C11 / (DA * (1 - TR) ^ 3)
,
SG1 = Q0LD + DJ7 * Q0RD
SH1 = Q0LD * P1RD + Q1LD + DJ7 * (Q1RD + Q0RD * P1LD)
SM2 = P1RD * Q1LD + DJ7 * Q1RD * P1LD
SG1D = SG1 / SM2
SH1D = SH1 / SM2
GAMA2 = (SH1D + SQR(SH1D * SH1D - 4 * SG1D)) / 2
GAMA1 = SG1D / GAMA2
,
D1 = SA / (GAMA1 * GAMA2)

```


$$D3 = (SB * GAMA2 - SC * GAMA2 * GAMA2 - SA) / ((GAMA1 - GAMA2) * GAMA2)$$

$$D2 = SC - D1 - D3$$

MODIFIED *****

```

XBETA1 = GAMA1: XTLAMR = TLAML: XTD = TD: XTHIR = THIL: 'PARAMETER TO FTIME
GOSUB 15000: TLND2 = XTRNH: 'RETURN FROM FTIME

```

```

XBETA1 = GAMA1: XTLAMR = TLAMR: XTD = TD: XTHIR = THIR: PARAMETER TO FTIME
GOSUB 15000: TRND2 = XTRNH: RETURN FROM FTIME

```

MODIFIED *****

```

Q0MS = THIR * (5 - 6 * VR) * EXP(-TLAMR * T0) / (C3 * C11 * (1 + THIL) + DA * (1 + THIR))
SNLF2 = Q0MS * (1 - EXP(-GAMA1 * TD))
SNLT = SNLF2
STLT = 0

```

—

! *

!

STRESS DISTRIBUTION IN ROCK MASS AT TIME=T1

✱

4050 #####

$$\text{STLR} = \text{STLT}$$
$$\text{SNLR} = \text{SNLT}$$
$$\text{STRDT} = (1 + (3 - \text{SNLR} - 2 * \text{STLR}) * (\text{R2} / \text{R})^4 - (4 - 2 * \text{STLR} - 2 * \text{SNLR}) * (\text{R2} / \text{R})^2) *$$

COS(2 * THETA)

$$STTDT = -(1 + (3 - 2 * STLR - SNLR) * (R2 / R)^4) * \cos(2 * THETA)$$
$$\text{SSDT} = -(1 - (3 - 2 * \text{STLR} - \text{SNLR}) * (\text{R2} / \text{R})^4 + (2 - \text{STLR} - \text{SNLR}) * (\text{R2} / \text{R})^2 * \sin(2 * \text{THETA}))$$

9

9

[illegible]

✱

✱

NORMAL STRESS AND MOMENT IN LINER

✱

一、

$$AA = (-SNLT * .5 * (2 * TR * TR + TR + 1) - STLT * TR * TR) / (1 - TR) ^ 3$$
$$BB = (SNLT * (3 * TR + 1) / (6 * R2 * R2) + STLT * (3 * TR - 1) / (6 * R2 * R2)) / (1 - TR) ^ 3$$
$$CC = (-SNLT * TR * TR * (TR + 3) * R2^4 / 6 - STLT * TR^3 * R2^4 / 3) / (1 - TR)^3$$
$$DD = (SNLT * TR * (TR * TR + TR + 2) * R2 * R2 / 2 + STLT * TR * TR * (TR + 1) * R2 * R2 / 2) / (1 - TR)^3$$
$$STLR1 = (2 * AA + 12 * BB * R1 * R1 + 6 * CC / R1 ^ 4) * COS(2 * THETA)$$
$$STLR2 = (2 * AA + 12 * BB * R2 * R2 + 6 * CC / R2 ^ 4) * \cos(2 * THETA)$$
$$SNDLT = (STLR1 + STLR2) / 2$$
$$SMDLT = (STLR2 - STLR1) / 12$$

```
IF NR = 0 THEN GOTO 4550
```

```
IF NCASE = 2 THEN GOTO 4540
```

[illegible]

✱

✱

DISPLACEMENT IN LINER AND ROCK

!

一

1

RIGID LINING - NO SLIP AT INTERFACE DISPL. IN ROCK AND LINER

1

DISPLACEMENT IN LINER

4370 ULDT1 = 0

ULDT2 = 0

VLDT = 0

DISPLACEMENT IN ROCK

URDRT = $Q0 / (2 * GR) * (-(R2 / R)^3 + 4 * (1 - VR) * R2 / R) * FTR0 * \cos(2 * THETA)$

VRDRT = $-Q0 / (2 * GR) * ((R2 / R)^3 + 2 * (1 - 2 * VR)) * FTR0 * \sin(2 * THETA)$

URDT = URDRT

VRDT = VRDRT

GOTO 5250

RIGID LINING - FULL SLIP AT INTERFACE. DISPLACEMENT IN ROCK
AND LINER

DISPLACEMENT IN LINER

4540 GOTO 4370

4550 BAD = $R1 * (2 * TR * TR + TR + 1) - TR * TR * (TR + 3) * R2^4 / (3 * R1^3) + 2 * TR * (TR * TR + TR + 2) * R2 * R2 / R1 * (1 - VL) - 2 * VL * R1^3 * (3 * TR + 1) / (3 * R2 * R2)$

BBD = $R1 * 2 * TR * TR - 2 * R2^4 * TR^3 / (3 * R1^3) + 2 * TR * TR * (TR + 1) * R2 * R2 / R1 * (1 - VL) - 2 * VL * R1^3 * (3 * TR - 1) / (3 * R2 * R2)$

BADD = $R1 * (2 * TR * TR + TR + 1) / 2 - (3 - 2 * VL) * (3 * TR + 1) * R1^3 / (6 * R2 * R2) + TR * TR * (TR + 3) * R2^4 / (6 * R1^3) + (1 - 2 * VL) * TR * (TR * TR + TR + 2) * R2 * R2 / (2 * R1)$

BBDD = $TR * TR * R1 - (3 - 2 * VL) * (3 * TR - 1) * R1^3 / (6 * R2 * R2) + TR^3 * R2^4 / (3 * R1^3) + (1 - 2 * VL) * TR * TR * (TR + 1) * R2 * R2 / (2 * R1)$

ED = $R2^4 / (3 * R^3) - 2 * (1 - VR) * R2 * R2 / R$

FD = $2 * R2^4 / (3 * R^3) - 2 * (1 - VR) * R2 * R2 / R$

EDD = $R2^4 / (3 * R^3) + (1 - 2 * VR) * R2 * R2 / R$

FDD = $2 * R2^4 / (3 * R^3) + (1 - 2 * VR) * R2 * R2 / R$

IF NCASE = 2 THEN GOTO 4880

FLEXIBLE LINING - NO SLIP AT INTERFACE. DISPLACEMENT IN ROCK AND
LINER

DISPLACEMENT IN LINER

ULDFT2 = $(1 + VL) / (EL * 3 * (1 - TR)^3) * (C11 + TK * D) * Q0M * TLND1 * \cos(2 * THETA) * Q0$

ULDFT1 = $(1 + VL) / (EL * (1 - TR)^3) * (BAD / R2 + TK * BBD / R2) * Q0M * TLND1 * \cos(2 * THETA) * Q0$

VLDFT2 = $-(1 + VL) / (EL * 3 * (1 - TR)^3) * (D + TK * C12) * Q0M * TLND1 * \sin(2 * THETA) * Q0$

VLDFT1 = $-2 * (1 + VL) / (EL * (1 - TR)^3) * (BADD / R2 + BBDD * TK / R2) * TLND1 * Q0M * Q0 * \sin(2 * THETA)$

ULDT1 = ULDFT1

ULDT2 = ULDFT2

VLDT1 = VLDFT1

VLDT2 = VLDFT2

DISPLACEMENT IN ROCK

URDFT = $Q0 * (1 + VR) / ER * (-(R2 / R)^3 + 4 * R2 / R * (1 - VR)) * FTR$

URLD = $Q0M * (1 + VR) / ER * (ED / R2 + FD * DK / R2) * TRND1 * Q0$

VRDFT = $-Q0 * (1 + VR) / ER * ((R2 / R)^3 + 2 * R2 / R * (1 - 2 * VR)) * FTR$

VRLD = $Q0M * (1 + VR) / ER * (EDD / R2 + FDD * DK / R2) * TRND1 * Q0$


```

URDT = (URDFT + URLD) * COS(2 * THETA)
VRDT = (VRDFT + VRLD) * SIN(2 * THETA)
GOTO 5250
4880 '
'
'   FLEXIBLE LINER - FULL SLIP AT INTERFACE. DISTORTIONAL STRESS
'   STRESS COMPONENT
'
'   DISPLACEMENT IN LINER
'
ULDFT2 = Q0MS * (1 + VL) / (3 * EL * (1 - TR) ^ 3) * C11 * TLND2 * COS(2 * THETA) * Q0
ULDFT1 = Q0MS * (1 + VL) / (EL * (1 - TR) ^ 3) * BAD / R2 * TLND2 * COS(2 * THETA) * Q0
VLDFT2 = -Q0MS * 2 * (1 + VL) / (EL * (1 - TR) ^ 3) * D * TLND2 * SIN(2 * THETA) * Q0
VLDFT1 = -Q0MS * 2 * (1 + VL) / (EL * (1 - TR) ^ 3) * BADD / R2 * TLND2 * SIN(2 * THETA) *
Q0
ULDT1 = ULDFT1
ULDT2 = ULDFT2
VLDT1 = VLDFT1
VLDT2 = VLDFT2
'
'   DISPLACEMENT IN ROCK
'
URDFT = (Q0 * (1 + VR) / ER * ((R2 / R) ^ 3 + 4 * R2 / R * (1 - VR)) * FTR + Q0MS * Q0 * (1 +
VR) / ER * ED / R2 * TRND2) * COS(2 * THETA)
VRDFT = (-Q0 * (1 + VR) / ER * ((R2 / R) ^ 3 + 2 * R2 / R * (1 - 2 * VR)) * FTR + Q0 * Q0MS * (1
+ VR) / ER * EDD / R2 * TRND2) * SIN(2 * THETA)
URDT = URDFT
VRDT = VRDFT
'*****
' *
' *   COMBINING STRESS SYSTEMS FROM HYDROSTATIC
' *   AND DISTORTIONAL STRESS COMPONENTS
' *   (AFTER INSTALLATION OF LINER)
' *
'*****
'   SUM1,SUM2   = SUM OF RAD. AND TANG. DISPL. OF LINER AT R2
'   SUM3,SUM4   = SUM OF RAD. AND TANG. DISPL. AT R1
'   SUM5,SUM6   = SUM OF RAD. AND TANG. PRESSURE OF LINER AT R2
'   SUM7,SUM8   = SUM OF MOMENT AND THRUST IN LINER
'   SUM9,SUM10  = SUM OF TANG. STRESSES AT R1 AND R2 RESPECTIVELY
'   FS          = FACTOR OF SAFETY OF CONC. AGAINST TENSILE FAILURE
'   SUM12,SUM13 = SUM OF RAD. AND TANG. STRESSES IN ROCK
'   SUM14       = SUM OF SHEAR STRESSES IN ROCK
5250 '   SUM15,SUM16 = SUM OF RAD. AND TANG. DISPL. IN ROCK
SUM1 = ULHT2 + ULDT2
SUM2 = VLHT2 + VLDT2
SUM3 = ULHT1 + ULDT1
SUM4 = VLHT1 + VLDT1
SUM5 = PLHT + SNLT * SKK * COS(2 * THETA)
SUM6 = STLT * SKK * SIN(2 * THETA)
SUM7 = SMHLT + SMDLT * SKK
SUM8 = SNHLT + SNDLT * SKK
SUM9 = SLHR1 + STLR1 * SKK
SUM10 = SLHR2 + STLR2 * SKK

```



```

FS = ABS(PC / (SUM9 * P0))
SUM12 = STRHT + STRDT * SKK
SUM13 = STTHT + STTDT * SKK
SUM14 = SSDT * SKK
SUM15 = URHT + URDT
SUM16 = VRHT + VRDT
SUM17 = URLD
SUM18 = VRLD
SUM19 = URDFT
SUM20 = VRDFT

```

```

ANGLE = THETA * 180 / 3.141592654#

```

MODIFIED *****

```

IF N <> 1 THEN

```

```

    PRINT USING " ###.#"; RR; : PRINT USING " ###.#"; ANGLE; : PRINT USING " ##.####^";
SUM12, SUM13, SUM14, SUM15, SUM16                                     '*
    IF ANGLE = 0 THEN PRINT #2, USING " #.#####"; SUM15;           '*
    IF ANGLE = 90 THEN PRINT #2, USING " #.#####"; SUM15           '*
    END IF                                                            '*

```

```

5490 IF N = 1 THEN

```

```

    PRINT USING " #.^"; ANGLE, SUM1, SUM2, SUM3, SUM4, SUM5, SUM6, SUM7, SUM8,
SUM9                                                                '*

```

```

    IF ANGLE = 0 THEN PRINT #2, USING "####.### ####.#### ####.####"; T1, SUM7, SUM8;
                                                                '*

```

```

    IF ANGLE = 90 THEN PRINT #2, USING " ####.#### ####.####"; SUM7, SUM8;
                                                                '*

```

```

    ELSE GOTO 5540

```

```

    END IF                                                            '*

```

```

IF THETA < 1.4 THEN THETA = THETA + 3.141592654# / 2: GOTO 1650

```

```

IF THETA < 1.4 THEN THETA = THETA + 3.141592654# / 2: GOTO 1650

```

MODIFIED *****

```

N = 0

```

```

GOTO 1490

```

```

5540 IF THETA < 1.4 THEN THETA = THETA + 3.141592654# / 2: GOTO 1650

```

MODIFIED *****

```

'R20=R2*20

```

MODIFIED *****

```

'R10=R2*10

```

MODIFIED *****

```

'R4=R2*4

```

MODIFIED *****

```

'R02=R2*2

```

MODIFIED *****

```

'IF R<R02 THEN R=R+R2*.25 : GOTO 1580

```

MODIFIED *****

```

'IF R<R4 THEN R=R+R2*1 : GOTO 1580

```

MODIFIED *****

```

'IF R<R10 THEN R=R+R2*2 : GOTO 1580

```

MODIFIED *****

```

'IF R<R20 THEN R=R+R2*5 : GOTO 1580

```

MODIFIED *****

```

'    INSERT CONTROL CARD FOR PRINTING OUT OF DATA IN CALCULATIO

```

```

'PRINT "THIR,THIL,TLAMR,TLAML,C1,C2,C3"

```

MODIFIED *****

```

'PRINT USING " #.####^";THIR,THIL,TLAMR,TLAML,C1,C2,C3

```

MODIFIED *****

```

'PRINT "P1RD,Q0RD,Q1RD,P1LD,Q0LD,Q1LD"

```

MODIFIED *****

```

'PRINT USING " #.####^";P1RD,Q0RD,Q1RD,P1LD,Q0LD,Q1LD

```

MODIFIED *****

```

'PRINT "SA,SB,SC,SD,SE,SF"

```

MODIFIED *****

```

'PRINT USING " #.####^";SA,SB,SC,SD,SE,SF

```

MODIFIED *****

```

'PRINT "SG,SH,SM1,SG1,SH1,SM2"

```

MODIFIED *****

```

'PRINT USING " #.####^";SG,SH,SM1,SG1,SH1,SM2

```

MODIFIED *****

```

'PRINT "BETA1,BETA2,APHA1.APHA2,GAMA1,GAMA2"

```

MODIFIED *****

```

'PRINT USING " #.####^";BETA1,BETA2,APHA1.APHA2,GAMA1,GAMA2MODIFIED *****

```

```

'PRINT "A1,A2,A3,B1,B2,B3,D1,D2,D3"

```

MODIFIED *****


```

'PRINT USING " #.###^";A1,A2,A3,B1,B2,B3,D1,D2,D3
'PRINT "DK,DJ1,DJ2,DJ3,DJ4,DJ7,TK"
'PRINT USING " #.###^";DK,DJ1,DJ2,DJ3,DJ4,DJ7,TK
'PRINT "TLNH,TLND1,TLND2,TRNH,TRND1,TRND2"
'PRINT USING " #.###^";TLNH,TLND1,TLND2,TRNH,TRND1,TRND2
'PRINT "AA,BB,CC,DD,C11,D,C12"
'PRINT USING " #.###^";AA,BB,CC,DD,C11,D,C12
'PRINT "BAD,BADD,BBD,BBDD,ED,FD,EDD,FDD"
'PRINT USING " #.###^";BAD,BADD,BBD,BBDD,ED,FD,EDD,FDD
'PRINT "POM,QOM,QOMS"
'PRINT USING " #.###^";POM,QOM,QOMS
'
      IF T1 >= T0 THEN N = 1
      IF T1 <= T0 THEN GOTO 5890 ELSE GOTO 5910
5890 T1 = T1 + T0 / 8
'
      IF T0 = 0 THEN T1 = (24 / ADVAN / 6)
      IF T1 > T0 THEN N = 1
      GOTO 1380
5910 IF T1 <= 720 THEN T1 = (T1 - T0) * 1.5 + T0: GOTO 1380
      END
'
15000 '*****
      '*
      '*          SUBROUTINE FTIME(BETA1,TLAMR,TD,THIR,TRNH)
      '*
      '*          MODIFIED TO FTIME(XBETA1,XTLAMR,XTD,XTHIR,XTRNH)
      '*
      '******
'
      IF XBETA1 * XTD > 20 THEN XA = 1 ELSE XA = 1 - EXP(-XBETA1 * XTD)
      IF XTLAMR * XTD > 20 THEN XB = 1 ELSE XB = 1 - EXP(-XTLAMR * XTD)
      IF XTLAMR > XBETA1 THEN GOTO 15130
      IF XTLAMR * XTD > 20 THEN XC = 0 ELSE XC = XTLAMR / (XBETA1 - XTLAMR) * EXP(-
XTLAMR * XTD) * (1 - EXP(-(XBETA1 - XTLAMR) * XTD))
      GOTO 15180
15130 IF XBETA1 * XTD > 20 THEN GOTO 15170
      IF XTLAMR * XTD > 20 THEN GOTO 15170
      XC = XTLAMR / (XTLAMR - XBETA1) * EXP(-XBETA1 * XTD) * (1 - EXP(-(XTLAMR -
XBETA1) * XTD))
      GOTO 15180
15170 XC = 0
15180 XTRNH = XA + XTHIR * (XB - XC)
      RETURN

```


B46177